

Separator Design and Thermal Study of Ionic Liquid Electrolyte Lithium-ion Cells

by

Candice Flora Jean Francis

*Thesis
Submitted to Flinders University
for the degree of*

Doctor of Philosophy
College of Science and Engineering
12th November 2018

Summary

Safety concerns surrounding the flammability of lithium-ion cells under abuse conditions inspired this thesis. It is widely accepted that the reactivity and volatility of conventional electrolytes are a significant contributing factor, hence the need for safer electrolyte alternatives. One such electrolyte is based on ionic liquids.

Ionic liquids are comprised entirely of ions and can be liquid at room temperature. Ionic liquids have negligible vapour pressure and therefore very low flammability, which is advantageous for lithium-ion batteries. However, compared to conventional electrolytes, ionic liquid electrolytes have poor wetting properties, due to their hydrophobic / hydrophilic characteristics, which can negatively affect the performance of a lithium-ion cell. This thesis aims to investigate the thermal characteristics of ionic liquid electrolytes and address the wetting issues through the development of a novel separator.

It was hypothesised that the surface of a separator could be modified to improve wettability with an ionic liquid electrolyte. The novel separator was developed using electrospinning to modify the surface of a support membrane. The physical and electrochemical properties of the separator were investigated. The support membrane provided mechanical integrity and thermal stability to the separator, and the electrospun layers successfully increased separator wetting and electrode-electrolyte interphase stability. However, cycling of lithium-ion cells containing the novel separator and ionic liquid electrolyte were still not comparable to conventional electrolyte cells.

It was further hypothesised that a lithium-ion cell containing ionic liquid electrolyte and the enhanced separator would display superior thermal stability. Using Differential Scanning Calorimetry and Thermalgravimetric Analysis, the exothermic decomposition characteristics of the ionic liquid electrolyte were evaluated with a number of commercial electrode materials. It was found that the total heat generation during decomposition of these electrodes was not necessarily lower with the ionic liquid electrolyte than with conventional electrolytes. However, with most electrodes, the ionic liquid electrolyte was found to delay the onset of exothermic decomposition, compared to conventional electrolytes.

Properties extracted from the thermal stability investigation were used to implement a thermal model for a lithium-ion cell with an ionic liquid electrolyte. A generic lumped thermal model was used, containing Arrhenius equations to describe internal heat sources. This model has been validated in the literature for conventional electrolyte lithium-ion batteries, however, to this author's knowledge, this is the first time the thermal decomposition of ionic liquid electrolyte in a lithium-ion cell has been modelled. Oven test simulation of the ionic liquid electrolyte lithium-ion cell revealed that the cell did not enter thermal runaway when exposed to 350 °C for 60 minutes. Whereas, simulation of an equivalent conventional electrolyte lithium-ion cell entered thermal runaway when exposed to 200 °C for approximately two minutes.

The investigations conducted in this thesis partially support the hypothesis that a lithium-ion cell containing ionic liquid electrolyte with the enhanced separator has greater thermal stability. In the event of thermal runaway, an ionic liquid electrolyte cell would release a larger amount of energy that could affect the safety of surrounding cells in a battery module. The delayed thermal runaway onset temperature provided by ionic liquid electrolytes, however, could give the battery management and cooling systems a greater opportunity to prevent a cell entering thermal runaway and resulting cell fires.

Declaration

I certify that this thesis does not incorporate without acknowledgment any material previously submitted for a degree or diploma in any university; and that to the best of my knowledge and belief it does not contain any material previously published or written by another person except where due reference is made in the text.

Signed.....

Date.....

Acknowledgements

I would like to thank my friends and family for their support during my candidature. This work would not have been possible without their encouragement and understanding.

I gratefully acknowledge the funding provided by PMB Defence Engineering and thank the engineering team for support throughout my candidature, specifically Rosalie Louey and Peter Chaplin.

I gratefully acknowledge funding provided by CSIRO Manufacturing High Performance Metal Industries Program and specifically thank Dr Adam S. Best for his support as my expert supervisor, who always went above and beyond. I am also thankful for the support provided by the staff of CSIRO Energy and Manufacturing groups for assistance with my testing.

I gratefully acknowledge the support of my supervisors Associate Professor Karl Sammut and Dr Andrew Lammas of Flinders University Centre for Maritime Engineering, Control and Imaging and their invaluable help throughout my candidature.

I gratefully acknowledge the support of the ARC Research Training Centre for Naval Design and Manufacturing (RTCNDM) in this investigation. The RTCNDM is a University-Industry partnership established under the Australian Research Council Industry Transformation grant scheme (ARC IC140100003).

I gratefully acknowledge Bryant Polzin at Argonne National Laboratory (USA) Cell Analysis, Modelling, and Prototyping (CAMP) Facility for kindly supplying high quality electrodes from their electrode library.

Acronyms

0D	Zero dimensional
1D	One dimensional
1G13TFSI	N-methyl-N-propyl-N,N,N,N-tetramethylguanidinium bis(trifluoromethanesulfonyl)imide
2D	Two dimensional
3D	Three dimensional
AC	Alternating Current
AgOTf	Silver triflate
Aramid	Poly(p-phenylene terephthamide)
ARC	Accelerating Rate Calorimetry
BF ₄ ⁻	Tetrafluoroborate
BMIBF ₄	N-butyl-N-methyl-imidazolium tetrafluoroborate
BMITFSI	N-butyl-N-methyl-imidazolium bis(trifluoromethanesulfonyl)imide
CPE	Constant Phase Element
CV	Cyclic Voltammetry
DEC	Diethyl carbonate
DMA	Dynamic Mechanical Analyser
DMAc	N,N-Dimethylacetamide
DMC	Dimethyl carbonate
DMF	Dimethylformamide
DSC	Differential Scanning Calorimetry
EC	Ethylene carbonate
EDX	Energy Dispersive X-Ray
EIS	Electrochemical Impedance Spectroscopy
EMC	Ethyl methyl carbonate
EMI ⁺	N-methyl-N-ethyl-imidazolium
EMIBF ₄	N-ethyl-N-methyl-imidazolium tetrafluoroborate
EMIFSI	N-ethyl-N-methyl-imidazolium bis(fluorosulfonyl)imide
EMINTf2	N-ethyl-N-methyl-imidazolium bis(trifluoromethylsulfonyl)imide
EMITFSI	N-ethyl-N-methyl-imidazolium bis(trifluoromethanesulfonyl)imide
EU	Electrolyte Uptake
FSI ⁻	Bis(fluorosulfonyl)imide
FTIR	Fourier-transform infrared spectroscopy
GF	Glass fibre
HDPE	High density PE
IL	Ionic liquid

IM ⁺	Imidazolium
LCO	LiCoO ₂
LFP	LiFePO ₄
Li	Lithium metal
LiBF ₄	Lithium tetrafluoroborate
LiBOB	Lithium bis(oxalato)borate
LiClO ₄	Lithium perchlorate
LiFSI	Lithium bis(fluorosulfonyl)imide
LiPF ₆	Lithium hexafluorophosphate
LiTf	Lithium trifluoromethanesulfonate
LiTFSI	Lithium bis(trifluoromethanesulfonyl)imide
LMNO	LiNi _{0.5} Mn _{1.5} O ₄
LMO	LiMn ₂ O ₄
LTO	Li ₄ Ti ₅ O ₁₂
MD	Machine direction
Melamine	Melamine formaldehyde
MP	Microporous membrane
MS	Mass Spectroscopy
Multi	Multi-layered membrane
NCA	LiNi _{0.8} Co _{0.15} Al _{0.05} O ₂
NCC	Non-crystalline cellulose
NMC	Li(Ni _{1/3} Co _{1/3} Mn _{1/3})O ₂
NW	Nonwoven membrane
ODE	Ordinary Differential Equations
P12O1FSI	N-methoxyethyl-N-methylpyrrolidinium bis(fluorosulfonyl)imide
P13FSI	N-methyl-N-propyl-pyrrolidinium bis(fluorosulfonyl)imide
P13TFSI	N-methyl-N-propyl-pyrrolidinium bis(trifluoromethanesulfonyl)imide
P14FSI	N-methyl-N-butyl-pyrrolidinium bis(fluorosulfonyl)imide
P14TFSI	N-methyl-N-butyl-pyrrolidinium bis(trifluoromethanesulfonyl)imide
P15TFSI	N-methyl-N-pentyl-pyrrolidinium bis(trifluoromethanesulfonyl)imide
P24FSI	N-ethyl-N-butyl-pyrrolidinium bis(fluorosulfonyl)imide
P24TFSI	N-ethyl-N-butyl-pyrrolidinium bis(trifluoromethanesulfonyl)imide
PAEK	Poly(aryl ether ketone)
PAN	Polyacrylonitrile
PC	Propylene carbonate
PDA	Polydopamine
PE	Polyethylene

PEEK	Poly(ether ether ketone)
PEG	Polyethylene glycol
PEI	Polyetherimide
PEO	Poly(phenylene oxide)
PES	Polyethersulfone
PET	Polyethylene terephthalate
PI	Polyimide
PMIA	Poly(m-phenylene isophthalamide)
PMIBF ₄	N-methyl-N-propyl-imidazolium tetrafluoroborate
PMITFSI	N-methyl-N-propyl-imidazolium bis(trifluoromethanesulfonyl)imide
PMMA	Poly(methylmethacrylate)
PMMA-AN-VAc	Poly(methyl methacrylate-acrylonitrile–vinyl acetate)
PP	Polypropylene
PSA	Polysulfonamide
PTFE	Polytetrafluoroethylene
PU	Polyurethane
PVC	Poly(vinyl chloride)
PVDF	Polyvinylidene fluoride
PVDF-HFP	Poly(vinylidene fluoride-hexafluoropropylene)
PVDF-TRFE	Poly(vinylidene fluoride-co-trifluoroethylene)
Pyr ⁺	Pyrrolidinium
SEI	Solid Electrolyte Interface
SEM	Scanning Electron Microscopy
SoC	State of Charge
STA	Simultaneous Thermal Analysis
TD	Transverse direction
TFSI ⁻	Bis(trifluoromethanesulfonyl)imide
TGA	Thermogravimetric Analysis
TIPS	Temperature Induced Phase Separation
TMA	Thermal Mechanical Analysis
TPGTA	Tripropylenglycol diacrylate
t.w.	Total wetting
UHMWPE	Ultra high molecular weight PE
UV	Ultra-violet
VC	Vinylene carbonate
v/v	Volume / volume ratio
w/w	Weight / weight ratio

Contents

Summary	i
Declaration	iii
Acknowledgements	iv
Acronyms	v
Contents	viii
Table of Figures	xii
Table of Tables	xxii
Chapter 1	1
1.1 Background information	2
1.1.1 Lithium-ion cell materials	3
1.1.2 Cell safety	6
1.1.3 IL electrolytes	8
1.1.4 Thermal modelling	10
1.2 Research motivation	11
1.3 Statement of contributions	11
1.3.1 Original contribution of thesis	11
1.3.2 Outline of thesis	12
1.3.3 Publications	13
Chapter 2	14
2.1 Introduction	15
2.2 Literature review	15
2.2.1 Separator properties	15
2.2.1.1 Chemical and electrochemical stability	16
2.2.1.2 Dimensional stability	16
2.2.1.3 Thickness	16
2.2.1.4 Porosity	16
2.2.1.5 Pore geometry	17
2.2.1.6 Tortuosity	18
2.2.1.7 Wettability	18
2.2.1.8 Ionic conductivity	19
2.2.1.9 Mechanical properties	19
2.2.1.10 Melt integrity	20
2.2.1.11 Shutdown temperature	20
2.2.1.12 Thermal dimensional stability	20
2.2.1.13 Thermal stability	20
2.2.2 Separator types	21
2.2.2.1 Microporous	21
2.2.2.2 Nonwoven	23
2.2.2.3 Composite	24
2.2.2.4 Surface treated	25
2.2.3 Novel separators	28
2.2.4 IL electrolytes and separators	36
2.2.4.1 Commercial separators	36

2.2.4.2	New separator materials.....	41
2.3	Conclusion.....	57
Chapter 3	60
3.1	Introduction.....	61
3.2	Experimental.....	63
3.2.1	Materials.....	63
3.2.2	Commercial separator wettability.....	64
3.2.3	Separator preparation.....	64
3.2.4	Separator characterisation.....	65
3.2.4.1	Separator morphology.....	65
3.2.4.2	Thickness measurement.....	66
3.2.4.3	Pore Size distribution.....	66
3.2.4.4	Porosity measurement.....	66
3.2.4.5	Tensile testing.....	67
3.2.4.6	Thermal testing.....	67
3.2.4.7	Thermal dimensional stability.....	67
3.2.4.8	Contact angle and electrolyte uptake measurement.....	68
3.2.4.9	Wicking rate testing.....	68
3.2.4.10	Ionic conductivity measurement.....	68
3.3	Results and discussion.....	69
3.3.1	Commercial separators.....	69
3.3.2	Novel separator characterisation.....	72
3.3.2.1	Separator morphology.....	72
3.3.2.2	Thickness and fibre diameters.....	79
3.3.2.3	Porosity and pore sizes.....	83
3.3.2.4	Mechanical properties.....	88
3.3.2.5	Thermal properties.....	91
3.3.2.6	Wetting properties.....	93
3.4	Conclusion.....	99
Chapter 4	101
4.1	Introduction.....	102
4.2	Literature review.....	103
4.2.1	Cyclic Voltammetry.....	103
4.2.2	Electrochemical Impedance Spectroscopy.....	103
4.2.3	Capacity testing.....	107
4.3	Experimental.....	108
4.3.1	Materials.....	109
4.3.2	Electrochemical characterisation.....	109
4.3.3	Cell preparation and cell testing.....	110
4.4	Results and discussion.....	111
4.4.1	FTIR polymer structure.....	112
4.4.2	Cyclic voltammetry.....	113
4.4.3	Open circuit voltage EIS.....	118
4.4.4	Lithium plating and stripping.....	125
4.4.5	Rate performance.....	132
4.4.6	Cycling performance.....	137
4.4.7	FTIR changes after cycling.....	147
4.5	Conclusion.....	152

Chapter 5	155
5.1 Introduction	156
5.2 Literature review	156
5.2.1 Thermal stability and IL electrolytes	158
5.3 Experimental	161
5.3.1 Materials	162
5.3.2 Sample preparation.....	162
5.3.3 Thermal characterisation	164
5.4 Results and discussion	165
5.4.1 P13FSI electrolyte thermal stability	167
5.4.1.1 LiFSI salt	168
5.4.1.2 LiFSI concentration in P13FSI electrolyte	170
5.4.1.3 P13FSI electrolyte and conventional electrolytes	172
5.4.2 Separators with P13FSI electrolyte	172
5.4.2.1 Celgard with P13FSI electrolyte	172
5.4.2.2 GF with P13FSI electrolyte	175
5.4.2.3 Electrospun PVDF-HFP with P13FSI electrolyte	177
5.4.3 Commercial electrodes with P13FSI electrolyte	179
5.4.3.1 NMC with P13FSI electrolyte.....	179
5.4.3.2 LCO with P13FSI electrolyte	183
5.4.3.3 LMNO with P13FSI electrolyte.....	186
5.4.3.4 LFP with P13FSI electrolyte	189
5.4.3.5 Graphite with P13FSI electrolyte	195
5.4.3.6 LTO with P13FSI electrolyte.....	199
5.4.4 Comparison of electrode thermal stability	204
5.5 Conclusion	206
Chapter 6	208
6.1 Introduction	209
6.2 Literature review	210
6.2.1 Thermal runaway	210
6.2.2 Thermal characterisation	212
6.2.3 Modelling	213
6.3 Physical and mathematical model.....	217
6.4 Thermal energy model	218
6.4.1 Reaction models for P13FSI electrolyte cell.....	219
6.4.1.1 Cathode reactions	220
6.4.1.2 Anode reactions	221
6.4.1.3 Electrolyte reactions	221
6.4.2 Estimation of kinetic parameters	222
6.4.3 Reaction models for conventional electrolyte cell.....	223
6.4.3.1 SEI reaction.....	224
6.4.3.2 Anode reactions	224
6.4.3.3 Cathode reactions	225
6.4.3.4 Electrolyte reactions	225
6.4.4 Modelling procedure	225
6.5 Experimental	228
6.5.1 Materials	228
6.5.2 Pouch cell preparation and formation.....	228

6.5.3	Thermal abuse testing	229
6.5.4	Pouch cell disassembly.....	230
6.6	Results and discussion	230
6.6.1	Thermal abuse tests	230
6.6.1.1	Formation.....	230
6.6.1.2	Oven tests.....	233
6.6.1.3	Cell disassembly	240
6.6.2	Thermal abuse model	245
6.6.2.1	Kinetic parameter estimation	245
6.6.2.2	Model validation	247
6.6.2.3	Heat transfer coefficient.....	250
6.6.2.4	Oven test temperature simulations	253
6.6.2.5	Ohmic heating from internal short circuit	263
6.7	Conclusion	266
Chapter 7	268
7.1	Summary	269
7.2	Implications for IL electrolyte lithium-ion batteries	272
7.3	Conclusions	272
7.4	Limitations of work	273
7.5	Directions for future work	274
References	276
Appendices	289
Appendix A	Ideal separator properties	289
Appendix B	Commercial separator data sheets	290
Appendix C	Commercial separator wetting	296
Appendix D	Energy Dispersive X-Ray of glass fibre membrane	297
Appendix E	Energy Dispersive X-Ray of separators containing LiFSI	298
Appendix F	Scanning Electron Microscopy images.....	299
Appendix G	Thermal dimensional stability.....	303
Appendix H	Wicking rate images.....	304
Appendix I	Cycling voltage-capacity.....	305
Appendix J	Disassembly images.....	306
Appendix K	DSC at different heating rates.....	307
Appendix L	DSC graphite and LFP overlay	308
Appendix M	Biot number and V_{cell} calculations	309
Appendix N	Additional oven tests.....	311
Appendix O	Kinetic parameter estimation.....	313
Appendix P	Different h values for oven test simulations.....	315

Table of Figures

Figure 1.1 schematic diagram of the lithium intercalation–de-intercalation reaction mechanism in a rechargeable lithium-ion battery containing graphite LiCoO ₂ (LCO) electrodes and a liquid electrolyte. Taken from Roy and Srivastava [7].	2
Figure 2.2 SEM images of six different separators (a) Polypropylene (PP) / polyethylene (PE) / PP trilayer microporous; (b) PP dry-stretch microporous; (c) PP nonwoven; (d) Polyamide microporous; (e) Cellulose nonwoven; (f) Polyethylene terephthalate (PET) / ceramic. Taken from Kirchhöfer, et al. [96].	18
Figure 2.3 Typical presentation of contact angle results: optical images of IL contact angle on different separator types; captured with a Kyowa DropMaster DM501. Taken from Huie, et al. [18]. 1M3PIm-TFSI = N-methyl-N-propyl-imidazolium bis(trifluoromethanesulfonyl)imide (PMITFSI). 1M3PIm-BF ₄ = N-methyl-N-propyl-imidazolium tetrafluoroborate (PMIBF ₄).	19
Figure 2.4 Wetting behaviour with time: optical images of membrane wetting with IL electrolyte recorded as a function of wetting time. 5 μL of electrolyte was dropped onto each membrane. PVDF = polyvinylidene fluoride. LiTFSI = lithium bis(trifluoromethanesulfonyl)imide. Taken from Truong, et al. [95].	19
Figure 2.5 Photographs of separators, pristine PE (a) before treating and (b) after treating under 140 °C for 0.5 h, (c) P(MMA–AN–VAc), (d) Al ₂ O ₃ /P(MMA–AN–VAc), (e) Al ₂ O ₃ /P(MMA–AN–VAc)/2.5% H ₂ O, (f) Al ₂ O ₃ /P(MMA–AN–VAc)/5% H ₂ O, (g) Al ₂ O ₃ /P(MMA–AN–VAc)/7.5% H ₂ O, and (h) SiO ₂ /P(MMA–AN–VAc)/2.5% H ₂ O. Taken from Liao, et al. [99].	20
Figure 2.6 Schematic representation of the experimental procedure for the preparation of the PVDF-TRFE composite membranes. Taken from Nunes-Pereira, et al. [104].	23
Figure 2.7 Schematic of single nozzle electrospinning device. Taken from Alcoutlabi, et al. [107].	24
Figure 2.8 (a) Discharge capacities of the 1st, 5th, and 10th cycles for LFP Li cells with IL hybrid electrolytes with 0.5 M lithium salt. (b) Contact angles for electrolytes consisting of 50:50 volume/volume (v/v) (1M3PIm-BF ₄ (N-methyl-N-propyl-imidazolium tetrafluoroborate, PMIBF ₄), 1E3MIm-BF ₄ (EMIBF ₄), or 1M3PIm-TFSI (N-methyl-N-propyl-imidazolium bis(trifluoromethanesulfonyl)imide, PMITFSI)) and (EC or PC), and 0.5 M lithium salt (LiBF ₄ or LiTFSI). Neat IL with no carbonate and no lithium salt is also plotted for reference. Error bars represent one standard deviation of ten measurements for each IL and separator combination. Taken from Huie, et al. [18].	41
Figure 2.9 Left: Porosity and IL uptake of the microporous membranes composed of various amounts of PMMA. Right: Temperature dependence of ionic conductivity of all synthesized polymer electrolytes. Taken from Zhai, et al. [274].	46
Figure 2.10 Impedance spectra of cell Li gel polymer electrolyte Li at open circuit potential with electrospun PAN / PMMA, PAN and Celgard PE; Inset: the variation of interfacial resistance of cell Li gel polymer electrolyte Li with storage time. Taken from Rao, et al. [278].	49

Figure 2.11 Rate study of NMC half-cells containing N-methyl-N-propyl-pyrrolidinium bis(fluorosulfonyl)imide (P13FSI) (1.2 M LiFSI) comparing performance of a GF separator and the electrospun PAN microfibre separator. Electrochemical cycling was performed at room temperature between 3 and 4.2 V vs. Li | Li. Taken from Evans, et al. [105]. 51

Figure 2.12 Variation of storage modulus with temperature of PVDF-HFP and PVDF-HFP + 2 wt% NCC (non-crystalline cellulose) electrospun mats activated with 1 M LiTFSI in BMPyrTFSI (P14TFSI) electrolyte. Taken from Lalia, et al. [283]. 54

Figure 2.13 Thermogravimetric analysis (left) and DSC (right) of the separators. Taken from Truong, et al. [95]. 56

Figure 3.14 Schematic of novel separator with multi-layer design. PAN = polyacrylonitrile, PVDF-HFP = poly(vinylidene fluoride-hexafluoropropylene), and LiFSI = lithium bis(fluorosulfonyl)imide. 62

Figure 3.15 Dynamic contact angle measurements for commercial separators with P13FSI electrolyte. 71

Figure 3.16 SEM images of (a) GF (magnification 8000x), (b) PAN support (magnification 8000x) (c) FSI-0 (magnification 15000x), (d) FSI-A (magnification 12000x), (e) FSI-B (magnification 12000x) and (f) FSI-C (magnification 8000x). Red arrow indicates an area containing *beading*. Red circle indicates a region of melted polymer. 73

Figure 3.17 EDX spectrum of (a) FSI-A, (b) FSI-B and (c) FSI-C. Inserts: (i) SEM image for EDX, (ii) fluorine distribution map, (iii) elemental percentage on surface. 75

Figure 3.18 SEM images of separators (a) Tfd (magnification 30000x), (b) FSId (magnification 30000x) (c) TFSId (magnification 16000x), (d) FSI-B (magnification 30000x) and (e) TFSI-B (magnification 24000x). 78

Figure 3.19 Fibre diameter distributions for separators (a) GF, (b) PAN support, (c) FSI-0, (d) FSI-A, (e) FSI-B and (f) FSI-C. 81

Figure 3.20 Fibre diameter distributions for separators (a) Tfd, (b) FSId, (c) TFSId, (d) FSI1 and (e) TFSI1. 83

Figure 3.21 Pore size distribution for separators (a) GF (one measurement), (b) FSI-0 (average of two measurements), (c) FSI-A (average of two measurements), (d) FSI-B (average of three measurements) and (e) FSI-C (average of three measurements). 84

Figure 3.22 Pore size distribution for separators (a) FSI-B (average of three measurements) and (b) TFSI-B (average of three measurements). 87

Figure 3.23 Stress-strain plots for (a) Celgard 3501 (four samples); (b) GF (four samples); and (c) FSI-C (eight samples). FSI-C shows variation in tensile strength, yield strength and yield profile for different samples - samples that showed a two-part yield profile are shown in dashed lines. 89

Figure 3.24 Simultaneous thermal analysis: (a) DSC and (b) TGA of dry separators: PAN, FSI-0, FSI-A, FSI-B and FSI-C, at a heating rate of 10 °C min⁻¹. 92

Figure 3.25 Contact angle measurements of P13FSI electrolyte on (a) Celgard 3501, (b) FSI-0 and

(c) FSI-C separators at time = 0.....	94
Figure 3.26 Wicking rate and electrolyte uptake for the separators containing LiFSI salt with P13FSI electrolyte.....	96
Figure 4.27 (a) Randle's circuit diagram (from Z Fit EC-Lab® software) and (b) Typical Nyquist plot of Randle's circuit numerical fitting. Taken from Fernández-Sánchez, et al. [330]. R_e is electrolyte resistance; C_{dl} is the electrode surface double layer capacity; R_{ct} and C are the electrode reaction resistance and capacity, respectively. Ω is the frequency.	105
Figure 4.28 Electrode-electrolyte interphase formed on lithium metal in the presence of electrolyte.	106
Figure 4.29 Fitted impedance spectrum obtained from a cycled symmetrical lithium cell containing 0.5 mol kg^{-1} LiTFSI-P13TFSI electrolyte. The spectrum is fitted to a four-element layer model equivalent circuit; the error of the fit is shown. Taken from Howlett, et al. [336].....	107
Figure 4.30 FTIR of dry separators containing LiFSI salt and PAN support. Characteristic PAN peaks circled in red. Characteristic PVDF-HFP peaks indicated with red dashed line. LiFSI peak indicated by red dotted line and red label.....	112
Figure 4.31 CV at a glassy carbon electrode in P13FSI electrolyte with (a) no separator, (b) GF, (c) FIS-B and (d) FSI-C.....	114
Figure 4.32 (a) 1 st and(b) 5 th scan of CV at a glassy carbon electrode in P13FSI electrolyte.....	115
Figure 4.33 (a) Typical Nyquist plot obtained for novel separators in Li P13FSI electrolyte Li cell. (b) Equivalent electrical circuit for fitting impedance data. (c) Numerical fitting for equivalent circuit. R_{ele} is the resistance associated with the electrolyte + separator phase. R_{SEI} is the resistance associated with the SEI. R_{cell} is the total resistance.....	119
Figure 4.34 Nyquist plots of Li P13FSI electrolyte Li cells with (a) GF, (b) FSI-0, (c) FSI-A, (d) FSI-B and (e) FSI-C separators at different times during storage at open circuit voltage.....	120
Figure 4.35 Nyquist plots for EIS of Li separator + P13FSI electrolyte Li cell (a) at time of cell assembly and (b) after 15 hours at open circuit voltage at room temperature.	122
Figure 4.36 Nyquist plots of Li P13FSI electrolyte Li cells with (a) Tfd, (b) FSId, (c) TFSId, (d) FSI-B and (e) TFSI-B separators at different times during storage at open circuit voltage.....	123
Figure 4.37 Nyquist plots for EIS of Li separator + P13FSI electrolyte Li cell (a) at time of cell assembly and (b) after 15 hours at open circuit voltage at room temperature.	124
Figure 4.38 Galvanic cycling of Li Li cells with P13FSI electrolyte and (a) GF, (b) Celgard 3501, (c) FSI-0, (d) FSI-A, (e) FSI-B and (f) FSI-C separator.....	126
Figure 4.39 Galvanic cycling of Li Li cells with P13FSI electrolyte and (a) Tfd, (b) FSId, (c) TFSId, (d) FSI-B and (e) TFSI-B separator.....	130
Figure 4.40 Rate study of LFP P13FSI electrolyte Li cells with GF, FSI-A, FSI-B and FSI-C separators cycling at C/10, C/5 and C/2 rates between 1.0 and 2.5 V. Red arrow indicates reduced capacity in first cycle at C/10 rate following C/2 charge.....	133

Figure 4.41 Rate study of LFP | P13FSI electrolyte | Li cells with Tfd, FSI_d, TFSI_d, FSI-B and TFSI-B separators cycling at C/10, C/5 and C/2 rates between 1.0 and 2.5 V. Red arrow indicates reduced capacity in first cycle at C/10 rate following C/2 charge. 135

Figure 4.42 Capacity plot of C/10 cycling of LFP | P13FSI electrolyte | LTO cells with GF, FSI-0, FSI-A, FSI-B and FSI-C separators. Average and standard deviation (error bars) presented for three replicate cells for each separator. 138

Figure 4.43 Voltage curves for 1st, 10th, 25th and 50th cycles of representative LFP | P13FSI electrolyte | LTO cell with (a) GF and (b) FSI-B separators, cycling at current density 0.126 mA cm⁻². Theoretical capacity 170 mAh (g LFP)⁻¹. 140

Figure 4.44 Resistances during C/10 cycling of LFP | P13FSI electrolyte | LTO cells with GF, FSI-0, FSI-A, FSI-B, FSI-C and TFSI-B separators. Calculated from difference between voltage plateau median of charge and discharge curves. 141

Figure 4.45 Capacity plot of C/10 cycling of LFP | P13FSI electrolyte | LTO cells with FSI_d, TFSI_d, FSI1, and TFSI1 separators. 143

Figure 4.46 Capacity plot of C/10 cycling of LFP | FSI-B | LTO cells with ILE (P13FSI electrolyte), ILE with PC (P13FSI / PC electrolyte) and conventional electrolyte at 30 °C as well as ILE at 50 °C. 145

Figure 4.47 Capacity plot of C/10 cycling of LFP | conventional electrolyte | LTO cells with GF, FSI-B and FSI_d separators. 146

Figure 4.48 Capacity plot of C/10 cycling of LFP | P13FSI / PC electrolyte | LTO cells with FSI-0, FSI-A, FSI-B, FSI-C and TFSI_d separators. 147

Figure 4.49 (a) FTIR spectra of P13FSI electrolyte alone and each separator with P13FSI electrolyte before (—) and after (.....) cycling in an LFP | LTO coin cell. (b) In range 2500 to 3200 cm⁻¹. (c) In range 500 to 1600 cm⁻¹, characteristic P13FSI electrolyte peaks indicated with red dashed lines. Grey arrows indicate peaks altered after cycling in separator containing LiFSI. 149

Figure 4.50 FTIR of cycled LFP harvested from P13FSI electrolyte LFP | LTO cells with different separators (GF, FSI-0, FSI-A, FSI-B and FSI-C), alongside dry LFP for comparison. In range 500 to 1800 cm⁻¹. Black dashed lines indicate dry LFP peaks. Red dashed lines indicate peaks that appear on cycling. 151

Figure 4.51 FTIR of cycled LTO harvested from P13FSI electrolyte LFP | LTO cells with different separators (GF, FSI-0, FSI-A, FSI-B and FSI-C). 152

Figure 5.52 DSC thermogram for dry LTO electrode material in different DSC crucibles, hermetically sealed high pressure stainless steel crucible (—) and standard aluminium DSC crucible (.....). 166

Figure 5.53 DSC thermogram (—) and TGA trace (.....) for (a) LiFSI powder, (b) P13FSI IL and (c) P13FSI electrolyte (1.17 mol kg⁻¹ LiFSI). 167

Figure 5.54 TGA trace of LiFSI powder, P13FSI IL, P13FSI electrolyte (1.57 M LiFSI) and P13FSI

electrolyte with different salt concentrations: 0.67, 1.34, 1.61 and 2.01 M LiFSI in P13FSI. Inset of 200 to 300 °C temperature range..... 171

Figure 5.55 DSC thermogram (—) for (a) Celgard 3501, (b) Celgard 3501 (uncycled) with P13FSI electrolyte (including P13FSI electrolyte (.....)), and (c) Celgard 3501 (cycled) in P13FSI electrolyte LFP | Li cell. 173

Figure 5.56 DSC thermogram (—) for (a) GF, (b) GF (uncycled) with P13FSI electrolyte (including P13FSI electrolyte (.....)) and (c) GF (cycled) in P13FSI electrolyte LTO | Li cell. 176

Figure 5.57 DSC thermogram (—) for (a) Electrospun PVDF-HFP, (b) Electrospun PVDF-HFP (uncycled) with P13FSI electrolyte (including P13FSI electrolyte (.....)) and (c) Electrospun PVDF-HFP (uncycled) with conventional electrolyte. 178

Figure 5.58 Discharge and recharge curve of NMC vs lithium metal with P13FSI electrolyte. Reversible capacity 210 mAh (g NMC)⁻¹. Current density 0.242 mA cm⁻². 179

Figure 5.59 DSC thermograms (—) and TGA trace (.....) for (a) uncycled NMC with 1.2 M LiPF₆ EC / EMC (2:1 v/v) electrolyte, (b) uncycled NMC with P13FSI electrolyte, (c) delithiated NMC from half-cell with P13FSI electrolyte and (d) lithiated NMC from half-cell with P13FSI electrolyte. 181

Figure 5.60 Discharge and recharge curve of LCO vs lithium metal with P13FSI electrolyte. Reversible capacity 105 mAh (g LCO)⁻¹. Current density 0.316 mA cm⁻². 184

Figure 5.61 DSC thermogram for (a) uncycled LCO with P13FSI electrolyte and (b) delithiated LCO from half-cell with P13FSI electrolyte. 184

Figure 5.62 Discharge and recharge curve of LMNO vs lithium metal with P13FSI electrolyte. Reversible capacity 125 mAh (g LMNO)⁻¹. Current density 0.100 mA cm⁻². 187

Figure 5.63 DSC thermogram for (a) uncycled LMNO with P13FSI electrolyte, (b) delithiated LMNO from half-cell with P13FSI electrolyte and (c) lithiated LMNO from half-cell with P13FSI electrolyte. 187

Figure 5.64 Discharge and recharge curve of LFP vs lithium metal with P13FSI electrolyte. Theoretical capacity 170 mAh (g LFP)⁻¹ [6, 352]. Current density 0.063 mA cm⁻². 189

Figure 5.65 DSC thermogram (—) and TGA trace (.....) for (a) uncycled LFP with P13FSI electrolyte, LFP from half-cell with P13FSI electrolyte charged to (b) 100% SoC (c) 75% SoC, (d) 50% SoC, (e) 25% SoC and (f) 0% SoC. 191

Figure 5.66 Discharge and recharge curve of LiC₆ vs lithium metal with P13FSI electrolyte. Reversible capacity 330 mAh (g Graphite)⁻¹. Current density 0.400 mA cm⁻². 195

Figure 5.67 DSC thermogram (—) and TGA trace (.....) for (a) uncycled graphite with P13FSI electrolyte, (b) lithiated graphite from half-cell with P13FSI electrolyte and (c) delithiated graphite from half-cell with P13FSI electrolyte. 196

Figure 5.68 Discharge and recharge curve of LTO vs lithium metal with P13FSI electrolyte. Theoretical capacity 175 mAh (g LTO)⁻¹ [6, 389]. Current density 0.071 mA cm⁻². 200

Figure 5.69 DSC thermogram (—) and TGA trace (.....) for (a) uncycled LTO with P13FSI

electrolyte, LTO from half-cell with P13FSI electrolyte charged to (b) 100% SoC (c) 75% SoC, (d) 50% SoC, (e) 25% SoC and (f) 0% SoC and P13FSI electrolyte (---)..... 201

Figure 5.70 Total heat and exothermic onset temperature for cycled electrodes from P13FSI electrolyte cells. The instrument measurement error for temperature and heat values displayed is 0.2 K and 0.04 μ W, respectively..... 204

Figure 6.71 Temperature ranges for different stages of thermal runaway in a NMC | graphite lithium-ion cell with conventional electrolyte from Accelerating Rate Calorimetry (ARC) testing. Taken from Feng, et al. [365]. 211

Figure 6.72 Thermocouple placement for oven test. 230

Figure 6.73 Voltage plots of formation cycles at current density 0.0315 mA cm⁻² with different separators and P13FSI electrolyte or conventional electrolyte (1.2 M LiPF₆ EC / EMC (2:1 v/v)). Cycle number indicated in grey. Plateau voltage difference (for 3rd cycle) indicated by red arrows. 232

Figure 6.74 Temperature vs time plot for oven test of LFP | P13FSI electrolyte-Celgard 3501 | LTO pouch cell. Oven temperature at 150 °C for approximately 60 minutes, then raised to 180 °C for approximately 45 minutes. Including ambient thermocouple, five thermocouples recorded temperature over the surface of the pouch and provided average dT/dt from cell thermocouples. 234

Figure 6.75 Oven test (a) before and (b) after photos of LFP | P13FSI electrolyte-Celgard 3501 | LTO pouch cell. Discolouration on pouch surface before and after oven testing circled in red..... 235

Figure 6.76 Temperature vs time plot for oven test of LFP | conventional electrolyte-Celgard 3501 | LTO pouch cell. Oven temperature at 150 °C for approximately 60 minutes, then raised to 180 °C for approximately 45 minutes. Including ambient thermocouple, five thermocouples over surface of the pouch and average dT/dt from cell thermocouples. 236

Figure 6.77 Oven test (a) before and (b) after photos of LFP | conventional electrolyte-Celgard 3501 | LTO pouch cell. 236

Figure 6.78 Temperature vs time plot for LFP | Celgard 3501 | LTO pouch cells during the temperature increased region of the oven tests. Overlay of the average cell temperature of pouch cells with P13FSI electrolyte (dashed blue line) and conventional electrolyte (solid black line). Standard deviation for five thermocouple measurements over the surface of the cell is shown every minute during the test. 237

Figure 6.79 Temperature vs time plot for oven test of LFP | conventional electrolyte-GF | LTO pouch cell. Oven temperature at 150 °C for approximately 60 minutes, then raised to 180 °C for approximately 45 minutes. Including ambient thermocouple, five thermocouples over surface of the pouch and average dT/dt from cell thermocouples. 238

Figure 6.80 Oven test after photos of LFP | conventional electrolyte-GF | LTO pouch cell, showing severe swelling (a) pouch surface and (b) pouch side..... 239

Figure 6.81 Disassembly photos of a LFP | P13FSI electrolyte-Celgard 3501 | LTO pouch cell following oven testing..... 240

Figure 6.82 Disassembly photos of a LFP | conventional electrolyte-Celgard 3501 | LTO pouch cell following oven testing..... 241

Figure 6.83 Disassembly photos of a LFP | P13FSI electrolyte-FSI-C | LTO pouch cell following oven testing. 242

Figure 6.84 Disassembly photos of a LFP | conventional electrolyte-FSI-C | LTO pouch cell following oven testing..... 243

Figure 6.85 Disassembly photos of a LFP | conventional electrolyte-GF | LTO pouch cell following oven testing. 244

Figure 6.86 Temperature range and heat release for sequence of reactions selected to simulate thermal abuse of LFP | P13FSI electrolyte | LTO cell: (i) electrode-electrolyte interphase decomposition on cathode, (e1) first reaction of P13FSI electrolyte, (a) anode-electrolyte reaction, (c) cathode-electrolyte reaction and (e2) decomposition of P13FSI electrolyte. Cathode reactions shown in red. Anode reaction shown in blue. Electrolyte reactions shown in yellow..... 245

Figure 6.87 $\ln(k)$ vs $1/T$ plot for e2, the 355 °C peak in P13FSI electrolyte thermogram, used to calculate E and A reaction parameters for $n = 1$. Markers are data points and the dotted line is the linear fit. Fit equation and R^2 value shown in plot. 246

Figure 6.88 Simulation and experimental temperature evolution of LFP | P13FSI electrolyte | LTO pouch cell oven test, oven temperature of 150 °C for 70 minutes and 180 °C for 50 minutes. $h = 4.5 \text{ W m}^{-2} \text{ K}^{-1}$ 248

Figure 6.89 Simulation and experimental temperature evolution of LFP | conventional electrolyte | LTO pouch cell oven test, oven temperature of 150 °C for 70 minutes and 180 °C for 50 minutes. $h = 4.5 \text{ W m}^{-2} \text{ K}^{-1}$ 250

Figure 6.90 Temperature profile of LFP | P13FSI electrolyte | LTO pouch cell during 250 °C oven test simulations, $h = 0.1, 1.5, 4.5, 7.17, 20$ and $45 \text{ W m}^{-2} \text{ K}^{-1}$ 251

Figure 6.91 Heat generation contributions of different reactions for LFP | P13FSI electrolyte | LTO pouch cell during 250 °C oven test simulation (a) $h = 4.5 \text{ W m}^{-2} \text{ K}^{-1}$ and (b) $h = 20 \text{ W m}^{-2} \text{ K}^{-1}$; electrode-electrolyte interphase heat generation Q_i , cathode heat generation Q_c , anode heat generation Q_a , and electrolyte heat generation Q_{e1} and Q_{e2} 252

Figure 6.92 Heat generation profile of LFP | P13FSI electrolyte | LTO pouch cell during 250 °C oven test simulations, total heat generation (Q_{gen}). $h = 0.1, 1.5, 4.5, 7.17, 20$ and $45 \text{ W m}^{-2} \text{ K}^{-1}$.. 253

Figure 6.93 Equivalent heat transfer coefficient (h) vs total heat release for LFP | P13FSI electrolyte | LTO pouch cell during 250 °C oven test simulations. 253

Figure 6.94 LFP | P13FSI electrolyte | LTO pouch cell temperature evolution during 150, 200, 300, 350 and 370 °C oven test simulations. $h = 4.5 \text{ W m}^{-2} \text{ K}^{-1}$ 254

Figure 6.95 LFP | P13FSI electrolyte | LTO pouch cell 200, 300 and 370 °C oven test simulations

conversion degree in for (a) electrode-electrolyte interphase decomposition x_i , (b) anode electrolyte reactions x_a , (c) cathode electrolyte reactions x_c , (d) first electrolyte decomposition x_{e1} and (e) second electrolyte decomposition x_{e2} . $h = 4.5 \text{ W m}^{-2} \text{ K}^{-1}$ 255

Figure 6.96 Heat generation profile during LFP | P13FSI electrolyte | LTO pouch cell 300 °C oven test simulation, (a) total heat generation Q_{gen} , (b) exothermic heat generation for different reactions, (c) cathode heat generation $Q_i + Q_c$, (d) anode heat generation Q_a , and (e) electrolyte heat generation $Q_{e1}+Q_{e2}$. $h = 4.5 \text{ W m}^{-2} \text{ K}^{-1}$ 257

Figure 6.97 Heat generation profile during LFP | P13FSI electrolyte | LTO pouch cell 350 °C oven test simulation, (a) total heat generation Q_{gen} , (b) exothermic heat generation for different reactions, (c) cathode heat generation $Q_i + Q_c$, (d) anode heat generation Q_a , and (e) electrolyte heat generation $Q_{e1}+Q_{e2}$. $h = 4.5 \text{ W m}^{-2} \text{ K}^{-1}$ 258

Figure 6.98 LFP | conventional electrolyte | LTO pouch cell temperature evolution during 150 and 200 °C oven test simulations. $h = 4.5 \text{ W m}^{-2} \text{ K}^{-1}$ 259

Figure 6.99 LFP | conventional electrolyte | LTO pouch cell 150 and 200 °C oven test simulations conversion degree in for (a) electrode-electrolyte interphase decomposition x_i , (b) anode electrolyte reactions x_a , (c) cathode electrolyte reactions x_c and (d) electrolyte decomposition x_e . $h = 4.5 \text{ W m}^{-2} \text{ K}^{-1}$. 260

Figure 6.100 Heat generation contribution of different reactions for LFP | conventional electrolyte | LTO pouch cell during 150 °C oven test simulation; electrode-electrolyte interphase heat generation Q_i , cathode heat generation Q_c , anode heat generation Q_a , and electrolyte heat generation Q_e . Inset shows Q_i , Q_c and Q_e . $h = 4.5 \text{ W m}^{-2} \text{ K}^{-1}$ 261

Figure 6.101 Heat generation contribution of different reactions for LFP | conventional electrolyte | LTO pouch cell during 200 °C oven test simulation; electrode-electrolyte interphase heat generation Q_i , cathode heat generation Q_c , anode heat generation Q_a , and electrolyte heat generation Q_e . Inset shows Q_i , Q_c and Q_e . $h = 4.5 \text{ W m}^{-2} \text{ K}^{-1}$ 262

Figure 6.102 Temperature profile of LFP | P13FSI electrolyte | LTO pouch cells of varying capacity, during 200 °C oven test simulations including internal short circuit ohmic heating, $h = 4.5 \text{ W m}^{-2} \text{ K}^{-1}$ 265

Figure 6.103 Temperature profile of LFP | P13FSI electrolyte | LTO pouch cells of varying capacity, during 350 °C oven test simulations including internal short circuit ohmic heating, $h = 4.5 \text{ W m}^{-2} \text{ K}^{-1}$ 266

Figure A.104 EDX spectrum of GF: (a) elemental count with SEM image (insert); (b) distribution mapping (i) silicon, (ii) oxygen and (iii) sodium; and (c) atomic percentage on surface. 297

Figure A.105 EDX spectrum of (a) FSI-A, (b) FSI-B and (c) FSI-C. Left: SEM image of EDX region. Right: sulphur distribution map..... 298

Figure A.106 SEM image of FSI-0, magnification 30000x and 1000x..... 299

Figure A.107 SEM image of FSI-A, magnification 25000x and 1500x. 299

Figure A.108 SEM image of FSI-B, magnification 30000x and 2000x.	300
Figure A.109 SEM image of FSI-C, magnification 50000x and 2000x.	300
Figure A.110 SEM image of TFSI-B, magnification 120000x and 1500x.	301
Figure A.111 SEM image of Tfd, magnification 8000x and 1000x.	301
Figure A.112 SEM image of FSId, magnification 4000x and 1000x.	302
Figure A.113 SEM image of TFSId, magnification 4000x and 1000x.	302
Figure A.114 Voltage curves for 1 st , 10 th , 25 th and 50 th cycles of representative LFP P13FSI electrolyte LTO cell with FSI-0 separator, cycling at current density 0.126 mA cm ⁻² . Theoretical capacity 127 mAh (g LFP) ⁻¹	305
Figure A.115 DSC thermogram of LiFSI powder at 5 °C min ⁻¹ (—) and 10 °C min ⁻¹ (.....) heating rates.	307
Figure A.116 DSC thermogram of uncycled LFP with P13FSI electrolyte at 5 °C min ⁻¹ (—) and 10 °C min ⁻¹ (.....) heating rates.	307
Figure A.117 DSC thermogram of uncycled LTO with P13FSI electrolyte at 5 °C min ⁻¹ (—) and 10 °C min ⁻¹ (.....) heating rates.	307
Figure A.118 DSC thermogram overlay of discharged (delithiated) graphite (—) and discharged (0% SoC) LFP (.....) from half-cells with P13FSI electrolyte.	308
Figure A.119 Temperature vs time plot for oven test of LFP P13FSI electrolyte-FSI-C LTO pouch cell. Oven temperature at 150 °C for approximately 60 minutes, then raised to 200 °C for approximately 60 minutes. Including ambient thermocouple and five thermocouples over surface of the pouch.	311
Figure A.120 Oven test (a) before and (b) after photos of LFP P13FSI electrolyte-FSI-C LTO pouch cell. Discolouration from electrolyte leakage from pouch cell prior to oven test.	311
Figure A.121 Temperature vs time plot for oven test of LFP conventional electrolyte-FSI-C LTO pouch cell. Oven temperature at 150 °C for approximately 60 minutes, then raised to 200 °C for approximately 60 minutes. Including ambient thermocouple and five thermocouples over surface of the pouch.	312
Figure A.122 Oven test (a) before and (b) after photos of LFP conventional electrolyte-FSI-C LTO pouch cell. Swelling obvious after oven test.	312
Figure A.123 log(k) vs 1/T plot for i, the 204 °C peak in charged LFP P13FSI electrolyte thermogram, used to calculate E and A reaction parameters for n=1. Markers are data points and the dotted line is the linear fit. Fit equation and R ² value shown in plot.	313
Figure A.124 log(k) vs 1/T plot for e1, the 269 °C peak in P13FSI electrolyte thermogram, used to calculate E and A reaction parameters for n=1. Markers are data points and the dotted line is the linear fit. Fit equation and R ² value shown in plot.	313
Figure A.125 log(k) vs 1/T plot for a, the 294 °C peak in charged LTO P13FSI electrolyte thermogram, used to calculate E and A reaction parameters for n=1. Markers are data points and	

the dotted line is the linear fit. Fit equation and R^2 value shown in plot. 313

Figure A.126 $\log(k)$ vs $1/T$ plot for c, the 352 °C peak in charged LFP P13FSI electrolyte thermogram, used to calculate E and A reaction parameters for $n=1$. Markers are data points and the dotted line is the linear fit. Fit equation and R^2 value shown in plot. 314

Figure A.127 Temperature profile of LFP | P13FSI electrolyte | LTO pouch cell during oven profile experimental temperature and simulated temperature with $h = 1.5, 3, 4.5$ and $7.17 \text{ W m}^{-2} \text{ K}^{-1}$ 315

Table of Tables

Table 1.1 Anode materials for lithium-ion cells.....	4
Table 1.2 Cathode materials for lithium-ion cells.....	5
Table 1.3 Structures for Pyr ⁺ and IM ⁺ cations and FIS ⁻ and TFSI ⁻ anions. Taken from Wang and Zhong [75].....	10
Table 1.4 Publications included in this thesis.....	13
Table 2.5 Properties of three commercial separator materials along with ideal specifications from literature.....	17
Table 2.6 Separator modification techniques.....	26
Table 2.7 Polymers being investigated for novel separators; including membrane type; separator material and manufacturing; tensile strength; and thermal dimensional stability. MP = microporous membrane. NW = nonwoven membrane. Multi = multi-layered membrane.....	32
Table 2.8 Commercial separators contact angle measurement summary.....	40
Table 2.9 Summary of new separator materials for IL electrolytes from literature survey. MP = microporous membrane. NW = nonwoven membrane.....	43
Table 3.10 Electrospinning process variables.....	65
Table 3.11 Properties of six commercial separators including material, thickness, porosity and contact angle (time = 0.2, 2 and 10 seconds) with P13FSI electrolyte.....	70
Table 3.12 Material, thickness and fibre diameters for two commercial separators as well as the separators containing LiFSI salt prepared in this work.....	80
Table 3.13 Material, thickness and fibre diameters for different salt-type separators prepared in this work.....	82
Table 3.14 Porosity and pore size distribution for GF, Celgard 3501, PAN and the separators containing LiFSI salt.....	86
Table 3.15 Pore size distribution for the DMAc separators, FSI-B and TFSI-B.....	87
Table 3.16 Mechanical properties: tensile strength, yield strength, modulus and elongation at break.....	88
Table 3.17 Peak temperature and decomposition temperature (by 5% weight loss) and shrinkage of Celgard 3501, PAN support and the four separators containing LiFSI salt.....	91
Table 3.18 Wicking rate, electrolyte uptake, ionic conductivity and MacMullin number for the separators containing LiFSI salt with P13FSI electrolyte.....	95
Table 3.19 Ionic conductivity and MacMullin number for FSI-B, TFSI-B and the DMAc separators with P13FSI electrolyte.....	99
Table 4.20 Coulombic efficiency and oxidation voltage and current peak of GF, FSI-B and FSI-C from Cyclic Voltammetry (CV) at a glassy carbon electrode in P13FSI electrolyte.....	116
Table 4.21 Equivalent circuit fitted parameters.....	121
Table 4.22 Average cell resistance in P13FSI electrolyte symmetrical lithium cells with different	

separators, 1 st and 100 th cycle at 0.1 mA cm ⁻²	127
Table 4.23 Discharge capacity for LFP P13FSI electrolyte Li cells with GF, FSI-A, FSI-B and FSI-C separators cycling at C/10, C/5 and C/2. Capacity shown for last cycle performed at each rate.	134
Table 4.24 Discharge capacity of LFP P13FSI electrolyte LTO cells at current density 0.126 mA cm ⁻² with different separators. Average values and standard deviation are taken from three replicate cells with a specific separator.	139
Table 5.25 Summary of thermal stability of carbonate solvent, conventional electrolyte, ILs and IL electrolytes.....	159
Table 5.26 Commercial electrodes supplied by Argonne National Laboratory (USA) Cell Analysis, Modelling, and Prototyping (CAMP) Facility Electrode Library.....	162
Table 5.27 TGA test methods for different samples	165
Table 5.28 Comparison of DSC thermograms for P13FSI electrolyte components and conventional electrolyte components: LiFSI, LiPF ₆ , P13FSI IL, EC / EMC (1:1) solvent, P13FSI electrolyte, 1 M LiPF ₆ EC / EMC (1:1) electrolyte and 1 M LiPF ₆ EC / DMC (1:1 w/w) electrolyte.....	168
Table 5.29 Comparison of DSC results for Celgard 3501, GF and electrospun PVDF-HFP: alone, with P13FSI electrolyte (uncycled) and harvested from a P13FSI electrolyte cell.....	174
Table 5.30 Comparison of DSC results for uncycled NMC with 1.2 M LiPF ₆ EC / EMC (2:1 v/v) electrolyte, uncycled NMC with P13FSI electrolyte, delithiated NMC from half-cell with P13FSI electrolyte, lithiated NMC from half-cell with P13FSI electrolyte and Li _x NMC cycled with 1 M LiPF ₆ EC / DMC (1:1 w/w) electrolyte.	182
Table 5.31 Comparison of DSC results for uncycled LCO with P13FSI electrolyte, delithiated LCO from half-cell with P13FSI electrolyte and Li _x CoO ₂ cycled with 1 M LiPF ₆ EC / DMC (1:1 w/w) electrolyte.	185
Table 5.32 Details of DSC results for uncycled LMNO with P13FSI electrolyte, delithiated LMNO from half-cell with P13FSI electrolyte, lithiated LMNO from half-cell with P13FSI electrolyte and Li _x Mn _{1.5} Ni _{0.5} O ₄ cycled with 1 M LiPF ₆ EC / DMC (1:1 w/w) electrolyte.	188
Table 5.33 Details of DSC results for uncycled LFP with P13FSI electrolyte, LFP from half-cell with P13FSI electrolyte charged to 100% SoC, 75% SoC, 50% SoC, 25% SoC and 0% SoC, and Li _x FePO ₄ cycles with 1 M LiPF ₆ EC / DMC (1:1 w/w) electrolyte.....	192
Table 5.34 Comparison of DSC results for uncycled LiC ₆ with P13FSI electrolyte, lithiated graphite from half-cell with P13FSI electrolyte, delithiated graphite from half-cell with P13FSI electrolyte, lithiated graphite with 1 M LiPF ₆ EC / DEC (1:1) and charged graphite with 1 M LiPF ₆ EC / DMC (1:1 w/w) electrolyte.	197
Table 5.35 Comparison of DSC results for uncycled LTO with P13FSI electrolyte, LTO from half-cell with P13FSI electrolyte charged to 100% SoC, 75% SoC, 50% SoC, 25% SoC, 0% SoC and Li _x Ti ₅ O ₁₂ with 1 M LiPF ₆ EC / DMC (1:1 w/w) electrolyte.	202

Table 6.36 Symbols used in thermal model, including units and description.	218
Table 6.37 IL electrolyte model parameters	226
Table 6.38 Conventional electrolyte model parameters.....	227
Table 6.39 Formation cycling capacities of LFP LTO cells at current density $0.0315 \text{ mA cm}^{-2}$ with different separators and P13FSI electrolyte or conventional electrolyte (1.2 M LiPF_6 EC / EMC (2:1 v/v)). Values shown with standard deviation are average capacity calculated from replicate cells with a specific separator.....	231
Table 6.40 $\ln(k)$ vs $1/T$ linear fit equations for P13FSI electrolyte cell reactions: i, c, a, e1 and e2. Resulting kinetic parameters are shown in Table 6.37.	247
Table 6.41 Theoretical heat values for the LFP LTO pouch cells with P13FSI electrolyte or conventional electrolyte.....	263
Table 6.42 Internal short circuit reaction parameters.....	264
Table A.43 Ideal separator properties including typical measurement standards and methods. ...	289
Table A.44 Representative contact angle image for eight commercial separators with P13FSI electrolyte at time = 0.2 seconds.....	296
Table A.45 Images of shrinkage of Celgard, PAN and the four separators manufactured in this work after exposure to $150 \text{ }^\circ\text{C}$ for 60 minutes.	303
Table A.46 Images of wicking rate of separators containing LiFSI salt with P13FSI.	304
Table A.47 Images of LFP P13FSI electrolyte LTO cells with GF, FSI-0, FSI-A, FSI-B and FSI-C separators, following 50 cycles at C/10 discharge rate.....	306

CHAPTER 1

Introduction

1.1 Background information

A battery stores electrical energy as chemical energy. In recent years, larger battery packs have been applied to electric vehicles and large-scale energy storage [1-6]. Batteries are integral in our society. Increasing energy and power demands have stimulated research into “greener” energy production and storage solutions. Therefore, continuous battery improvement is required to keep up with the developing technologies.

This thesis focusses on application of a safer electrolyte alternative in lithium-ion batteries. The original contribution to knowledge is the development of a novel separator for ionic liquid (IL) electrolyte and the analysis of a lithium-ion cell containing an IL electrolyte under thermal abuse conditions.

There are a range of rechargeable battery chemistries available each with different voltage and capacity characteristics. Common chemistries include lithium-ion, nickel-metal hydride, lead acid, redox flow and sodium-sulphur [2]. A battery can be designed for either high-power or high-energy, depending on the intended application. A high-power battery can deliver a large amount of capacity in a short amount of time, whereas a high energy battery delivers a lower capacity over a longer period. Different chemistries and cell designs have advantages for each application [2]. However, the amount of energy able to be stored and delivered is still limited by the theoretical energy density of the material. A large amount of research has been done to engineer new materials for improved batteries.

A battery is made up of one or more cells connected in parallel or series. A typical cell contains electrodes, a separator and an electrolyte, as shown in Figure 1.1. In lithium-ion cells the electrodes are metallic current collectors coated with an active material that participates in the electrochemical reactions [2]. Positive and negative electrodes are known as the cathode and anode, respectively. The electrodes are responsible for storage and release of charged ions during cell operation. Reversibility of ion storage and release in a secondary cell is important for life expectancy of the cell.

Figure has been removed due to Copyright restrictions.

Figure 1.1 schematic diagram of the lithium intercalation–de-intercalation reaction mechanism in a rechargeable lithium-ion battery containing graphite | LiCoO₂ (LCO) electrodes and a liquid electrolyte. Taken from Roy and Srivastava [7].

1.1.1 Lithium-ion cell materials

Lithium-ion is a popular battery chemistry for a variety of consumer products, such as mobile phones, laptops, hybrid and electric vehicles as well as large format energy storage [1, 3, 5, 6]. Lithium-ion cells contain active material in the form of positive and negative electrodes, separated by an electrically insulative polymer membrane called the separator. The electrodes and separator are porous materials that are layered together and wet with a liquid electrolyte to enable ionic transport between the electrodes (Figure 1.1).

Lithium-ion cells were commercialised in 1991 by Sony [8]. The battery chemistry has since developed into a varied and widely used product. The electrodes are usually a lithium-containing material mixed with conductive carbon(s) to facilitate electron transfer, and a binder for adherence to the current collector. There are several different active materials used in electrodes for lithium-ion cells. The active materials can be selected to provide different performance, i.e. capacity, rate capability and / or safety characteristics to the cell. To achieve a good cell efficiency, the active materials undergo reversible lithium intercalation by either insertion or displacement reactions [9].

The most common lithium-ion anode is graphite. Its layered structure facilitates reversible intercalation of lithium ions. Graphite reacts with lithium at a low potential [10] which provides a wide voltage window for the device when this material is used as an anode. Although graphite has been widely commercialised, there are a few disadvantages. Firstly, the lithiation potential of graphite is close to the lithium plating voltage which is dangerous for cell safety [7]; and secondly the graphite structure swells when lithium is intercalated causing mechanical stress and ageing of the cell with continued cycling. Alternative anode materials have been developed that do not induce mechanical stress within the cell, the most successful of which is lithium titanate ($\text{Li}_4\text{Ti}_5\text{O}_{12}$, LTO) [10]. Although LTO intercalates lithium at a higher potential, 1.5 V vs. lithium metal ($\text{Li} \mid \text{Li}^+$) [7], reducing the cell voltage window, it has enhanced stability and safety characteristics. Hayner, et al. [11] discusses the major challenges facing anode material development: volumetric stability, cycling stability and active material reaction with electrolyte. Advantages and disadvantages for anode materials have been summarised in Table 1.1.

Table 1.1 Anode materials for lithium-ion cells.

Material	Compound	Advantages	Disadvantages	Ref.
Lithium metal	Li	High theoretical capacity, low density, low negative electrochemical potential	Dendritic growth, poor cycle life	[6, 12]
Graphite	LiC ₆ (and carbon allotropes)	Inexpensive, easy to handle, abundant material, cycling stability	SEI* formation, volumetric changes	[11]
LTO	Li ₄ Ti ₅ O ₁₂ (transition metal oxide)	Minimal SEI* formation, calendar life, volumetric stability, safety	Reduced electrochemical operating window	[9, 11]
Lithium-metal alloys	Li _x Si and Li _x Sn, including carbon-based nanocomposites	High theoretical capacity, abundant materials, low cost, high electrical conductivity	Decreased reversible capacity, volumetric changes	[6, 7, 13]

* Solid Electrolyte Interphase (SEI)

The cathode material can be a range of different chemistries. Zhao, et al. [14], Hayner, et al. [11] and Goodenough and Park [9] discuss common cathode materials and advancements. Several cathode materials are in use commercially including lithium cobalt oxide (LiCoO₂, LCO), lithium nickel cobalt aluminium oxide (LiNi_{0.8}Co_{0.15}Al_{0.05}O₂, NCA), lithium iron phosphate (LiFePO₄, LFP), lithium manganese oxide (LiMn₂O₄, LMO), lithium nickel manganese cobalt oxide (Li(Ni_{1/3}Co_{1/3}Mn_{1/3})O₂, NMC). The chemistries and properties of these cathodes are summarised in Table 1.2. New cathode materials are continually being developed to bridge the gap that exists between performance and safety with the current materials. Lithium manganese nickel oxide (LMNO) (LiNi_{0.5}Mn_{1.5}O₄) and lithium manganese iron phosphate (LiMn_yFe_{1-y}PO₄) are potential new cathodes being investigated for high voltage capabilities [10].

Table 1.2 Cathode materials for lithium-ion cells.

Material	Compound	Advantages	Disadvantages	Ref.
LCO	LiCoO ₂	Energy density, conductivity, diffusivity, theoretical capacity, cycle life, operating voltage, specific energy	Thermally unstable (safety), high cost	[11, 14, 15]
LMO	LiMn ₂ O ₄	Low cost, operating voltage, specific energy	Conductivity, theoretical capacity	[14]
LFP	LiFePO ₄	Safety, environmental compatibility, low cost	Conductivity, diffusivity, theoretical capacity, high cost, operating voltage	[14]
NCA	LiNi _{0.8} Co _{0.15} Al _{0.05} O ₂	Energy density, diffusivity, theoretical capacity, cycle life, specific energy	High cost, cycle life	[14]
NMC	LiNi _x Co _y Mn _z O ₂ (x+y+z = 1)	Low cost, operating voltage, theoretical capacity	Cycle life	[9, 14]

The recommended voltage range is different for each electrode combination based on their electrochemical stabilities. However, the electrochemical stability of conventional electrolytes is currently hindering the use of high voltage materials [10].

The liquid electrolyte used in lithium-ion cells contains dissolved lithium salts in a solvent to facilitate lithium ion transport. The electrolyte is absorbed into the pores of the electrodes and separator, enabling ions to flow between the anode and cathode. Electrolyte properties such as salt solubility, ionic conductivity, lithium reactivity and electrochemical stability are very important properties for an effective electrolyte [16]. Electrolyte wetting of the electrode and separator can directly impact cell performance [17, 18]. The electrolyte is also integral to cell safety [14, 19], and this is discussed further in Section 1.1.2.

The electrolyte is a critical material for cell performance. The transport properties of an electrolyte can limit the charge and discharge rates possible in a cell. Conventional lithium-ion cell electrolytes (conventional electrolyte) consist of: an organic solvent blend, a lithium salt and occasionally additives to increase electrolyte stability. Solvents are usually a mixture of ethylene carbonate (EC), diethyl carbonate (DEC), dimethyl carbonate (DMC), ethyl methyl carbonate (EMC) and / or propylene carbonate (PC) [11, 13, 20]. The organic solvents need to possess excellent transport properties and be electrochemically and thermally stable under the operating conditions of the cell. The most common lithium salt is lithium hexafluorophosphate (LiPF₆); other salts, such as lithium tetrafluoroborate (LiBF₄), lithium bis(oxalato)borate (LiBOB) and lithium perchlorate (LiClO₄), have also been used [11]. The lithium salt in the electrolyte must be stable in the cell while being able to dissociate in the solvent and effectively diffuse through the electrolyte. Conventional electrolytes have been used for decades in lithium-ion cells, however, the use of organic solvents presents

safety issue relating to their volatility and flammability. This thesis investigates a safer electrolyte alternative with negligible volatility and flammability, introduced in Section 1.1.3.

Electrolyte solvents react with the electrode active materials and the resultant reaction products form a protective film on the electrode surface [21], known as the electrode-electrolyte interphase. The electrode-electrolyte interphase is commonly called the Solid Electrolyte Interphase (SEI) when formed on the negative electrode [11]. This protective film is necessary to prevent further reaction between the electrolyte and electrode active materials. Some lithium ions are used up in these reactions, depleting the amount of lithium available in the cell for cycling. Therefore, stability of the SEI strongly influences cell efficiency throughout life. A stable SEI provides a protective electrode film that does not need replenishing throughout the life of the cell. When the SEI is damaged or becomes unstable, further electrolyte reaction will occur at the electrode to replenish the SEI, leading to further electrolyte depletion and subsequent capacity loss. Electrolyte additives have been introduced to improve the SEI stability on some electrode materials [22]. These materials typically react “sacrificially” with the electrode to form a stable SEI film instead of reacting with the electrolyte.

A porous separator membrane is placed between the electrodes to provide electrical insulation [23], while allowing ion transport between the electrodes. The separator is required to meet a range of material requirements: mechanical, thermal and electrochemical stability as well as having appropriate transport properties when wet with electrolyte. Since the commercialisation of lithium-ion cells, the separator material has commonly been a polyolefin membrane such as polypropylene (PP) or polyethylene (PE) based [24]. Designing a separator with sufficient thermal and mechanical stability whilst also trying to minimise the thickness of the separator is a significant challenge. Since the separator is an inert material in the cell, any volume and weight added to the cell by the separator decreases the energy density of the final device. The energy density of a cell depends on the volume and weight of the cell compared to the theoretical capacity being delivered. Therefore, the deliverable capacity is directly related to the amount of active material in the electrodes. A separator with minimal thickness, while meeting the insulation requirements for cell safety, is ideal [24]. This thesis includes the design of a novel separator material for use with the alternative electrolyte.

1.1.2 Cell safety

Commercial lithium-ion cells have one major safety issue: the occurrence of fires generating intense heat. Catastrophic failure of lithium-ion cells in recent years has led to public safety concerns [19, 25-29]. Such failures can occur from manufacturing defects or cell operation under

abuse conditions, such as high temperature, mechanical crush, short circuit, over charge or over discharge, to name a few.

When lithium-ion cells are subjected to abuse conditions, they can enter a state known as thermal runaway. Thermal runaway occurs when heat accumulates in the cell causing temperatures to increase and reach the onset temperature for decomposition reactions, known as the thermal runaway onset temperature. Heat accumulation can be a result of electrical and / or chemical heat being generated by the cell, coupled with insufficient cooling. Material decomposition reactions are exothermic, which compounds the heating effects within the cell. In conventional electrolyte lithium-ion cells the sequence of reactions is generally [30]:

1. SEI decomposition
2. Separator melting and decomposition
3. Negative active material reaction with electrolyte
4. Electrolyte decomposition
5. Positive active material reaction with electrolyte

When a cell experiences a high temperature, the electrolyte and SEI thermal stability can have a major impact on cell decomposition [31-34]. The organic solvents in conventional electrolytes begin decomposing into volatile compounds at temperatures not much higher than the operating range for conventional lithium-ion cells [34-37]. Consequently, separator and electrolyte materials with increased thermal stability and heat capacity may decrease the occurrence or delay the onset of thermal runaway events [28, 38, 39]. During thermal runaway, conventional lithium-ion cells typically exhibit what is commonly described as catastrophic failure which results in fire, explosion and release of toxic fumes. An electrolyte with improved thermal stability, including formation of an SEI with increased thermal stability, may increase the safety of lithium-ion cells under abuse conditions. In this thesis, increased safety is determined as a lower likelihood of a thermal runaway event.

When the cell experiences increased temperatures, some cell cooling can be done via the tabs and packaging. Therefore, getting heat from a local hot spot within the cell to the cell edge and packaging can help to prevent thermal runaway from occurring. The electrodes and electrolyte have relatively good thermal conduction, however, the separator is the most thermally insulating material within the cell [40], with the highest thermal resistance at the interphase between the separator and the electrodes [41]. Increasing the thermal conductivity of the separator may therefore increase cell safety by allowing the cell to dissipate more effectively. The difficulty is that materials with good thermal conductivity are often electrically conductive as well. Since the separator must first provide electrical insulation, it is challenging to increase the thermal conduction while maintaining no increase in electrical conductivity.

The separator has a critical impact on cell safety, despite being the least reactive material in the cell. Delaying the occurrence of an internal short circuit from separator melting may prevent the cell from heating further, therefore allowing existing heat to be effectively dissipated within the cell to reduce the formation of hot spots. Thus, the ability of a separator to prevent contact between the electrodes at elevated temperatures may deter the cell from entering thermal runaway.

Investigations into the flammability and explosion of lithium-ion cells under abuse conditions revealed the reactivity and volatility of solvents in conventional electrolytes are major contributors [13, 42, 43]. This inspired investigations into alternative electrolyte materials with improved safety characteristics, i.e. low volatility and flammability, while providing equivalent performance in a complex electrochemical system. The safety advantages of incorporating a safer alternative electrolyte material will be investigated along with the effects on cell performance.

Considering the safety issues surrounding conventional electrolytes, there is a requirement for new electrolytes, and as a result, new separator materials are also required. Conventional electrolytes use volatile, toxic and flammable materials and the separator is designed specifically for these materials to support their performance. The use of a novel liquid electrolyte can introduce complexities related to viscosity, reduced ionic conductivity and reduced wetting of commercial separator materials, all of which have the potential to strongly influence the electrochemical performance of the device. To address these issues, there is a need to design new separator materials that can not only act as a robust separator between the electrodes, but also facilitate ion transfer and, potentially, stabilise the electrode-electrolyte interphase at both the cathode and anode.

Alternative electrolyte materials have been explored in the literature, but have not yet been implemented in commercial cells, due to compatibility issues with other cell materials. In cells using a liquid electrolyte, the separator is a critical component that needs to be compatible with the electrolyte in order to produce a cell with acceptable performance [16, 24]. While separator advancements have been investigated for use with conventional electrolyte cells, the safety issues surrounding these electrolytes still dominate the thermal runaway behaviour of a conventional electrolyte lithium-ion cell. Therefore, to create a safer lithium-ion cell, both the electrolyte and separator safety characteristics must be improved, while maintaining compatibility with current electrode materials.

1.1.3 IL electrolytes

IL based electrolytes have been widely investigated in the literature as an alternative electrolyte for lithium-ion cells. ILs are liquids comprised entirely on ions and are desirable due to typically low

melting points and flame retardant properties [44]. Many different anion and cation combinations exist, each with unique material properties. ILs with the following properties suitable for lithium-ion cells have been suggested as alternative electrolytes [44-56]:

- ionic conductivity
- viscosity
- lithium ion transport number
- wide electrochemical stability
- reversible lithium plating and stripping
- low flammability
- improved thermal stability
- low volatility
- low melting temperature

ILs are typically liquid at room temperatures and can therefore eliminate the need for volatile organic solvents used in conventional electrolytes. However, there are some issues limiting the use of ILs as an alternative to conventional electrolytes, such as high viscosity, compatibility with selected electrodes, poor separator and electrode wettability, and high cost of production [48, 57-59].

For cell applications, dissolving a sufficient concentration of lithium salt into an IL forms an electrolyte that can be used in lithium-ion cells. ILs with imidazolium (IM^+) or pyrrolidinium (Pyr^+) cations and bis(trifluoromethanesulfonyl)imide ($TFSI^-$) or bis(fluorosulfonyl)imide (FSI^-) anions have been widely investigated as IL electrolytes [60-65], structures are shown in Table 1.3. Specifically, Pyr^+ and FSI^- IL electrolytes have been investigated for their suitability in lithium-ion cells [45, 66-69]. Although the charge / discharge rate of this IL is limited to low rate applications due to the low ionic conductivity, the safety characteristics and electrochemical and thermal stability advantages make it a suitable IL choice to investigate safer electrolyte substitution.

Researchers [70-74] have investigated the use of IL and organic solvent blends to increase electrolyte ionic conductivity while retaining the flame-retardant properties of ILs. Blend compositions are determined by the safety and performance requirements of the cell [70]. Electrochemical and thermal stability studies of lithium-ion cells containing IL electrolytes have been widely published, as reviewed by Lewandowski and Świdarska-Mocek [44].

Table 1.3 Structures for Pyr⁺ and IM⁺ cations and FIS⁻ and TFSI⁻ anions. Taken from Wang and Zhong [75].

Table has been removed due to Copyright restrictions.

Along with IL electrolytes, improving the separator material may also help with controlling thermal runaway. Common commercial separators are made from PE or PP, and these materials have melting temperatures of approximately 135 to 160 °C, respectively [76, 77]. The proposed benefit of IL electrolytes is that the decomposition reactions would occur at higher temperatures. Therefore, coupled with a more thermally stable separator, this could potentially create a larger window for cell cooling to prevent the cell from entering thermal runaway. Although, the thermal stability of the IL electrode-electrolyte interphase film is unknown and this will be an important factor to investigate in this thesis.

The formation of a stable SEI film is still necessary with ILs to prevent uncontrolled and continuous reaction with the electrode active materials. Lewandowski and Świdarska-Mocek [44] summarise SEI film formation in various IL electrolyte systems and discuss the use of SEI forming additives to improve electrochemical stability of the cells. Although ILs have been widely reported as a potential lithium-ion electrolyte, they have not yet been proven as a competitive replacement for conventional electrolytes in the commercial industry due to high cost, high viscosity and SEI challenges [50, 75].

1.1.4 Thermal modelling

There are many variables relating to thermal stability of lithium-ion cells when substituting new materials and modelling is a tool that can be used to help predict behaviours of a cell under normal and abuse conditions. There are three main physical phenomena occurring inside the cell; electrical, chemical and thermal processes and these are used to model lithium-ion cells [78]. Creating a model to simulate an electrochemical cell with thermal effects can be complex, due to internal interactions and the model complexity is directly dependent on desired accuracy and intended application of the model. Models have been developed in zero dimension (0D), one dimension (1D), two dimension (2D) and three dimension (3D) and dimensionality is determined by the resolution required inside the cell.

Thermal models for lithium-ion cells have been developed to simulate cell decomposition under abuse conditions. Since most abuse conditions result in material decomposition and thermal runaway, abuse models should incorporate decomposition reactions in high temperature simulations. Decomposition reactions are added to thermal models to simulate loss of active materials and heat released during decomposition. Decomposition reactions are typically in the

form of Arrhenius equations to account for temperature dependence [79] and the heat of reaction during decomposition is found experimentally. These equations can be coupled to the thermal model to simulate the influence of cell temperature and subsequent decomposition rates.

Thermal abuse modelling of lithium-ion cells with conventional electrolyte has been extensively reported in the literature [1, 30, 78, 80-86], however, no literature could be found applying thermal abuse models to IL electrolyte cells. In models used to simulate conventional electrolyte lithium-ion cell behaviour under standard operating and abuse conditions, averaged material properties, such as density, thermal conductivity and heat capacity, have often been used to decrease computational time. Further, a limited number of models have included separator properties as a function of cell conditions. Thermal abuse models available in literature for lithium-ion cells are further reviewed in Chapter 6.

1.2 Research motivation

This study is focussed on improving lithium-ion cell safety by increasing thermal stability of the cell with an alternative electrolyte and a novel separator. A more thermally stable cell will mean an increased thermal runaway onset temperature and therefore a larger operation window for cell cooling to avoid a thermal runaway event. A key to successfully exploiting an electrolyte with increased thermal stability is coupling it with a safer separator material.

An IL electrolyte with improved chemical and thermal stability as well as flame-retardant properties will be investigated. An unknown for this electrolyte substitution is the thermal stability of the IL electrode-electrolyte interphase on both the cathode and anode. Designing a safer separator means materials with improved wetting, increased melting temperatures and dimensional stability at high temperatures to provide enhanced safety characteristics under abuse conditions. Coupling a more thermally stable electrolyte with a novel separator of enhanced safety characteristics is hypothesised to decrease the likelihood of a thermal runaway event.

1.3 Statement of contributions

1.3.1 Original contribution of thesis

The novel contribution is the evaluation of safer separator and electrolyte materials with respect to overall safety in a lithium-ion cell. A separator with favourable wetting characteristics with the IL electrolyte will be developed. The IL electrolyte and safer separator will be assembled into a lithium-ion cell for performance and safety analysis testing. The impact of safer materials on the

cell safety under abuse conditions will be investigated experimentally and theoretically. This thesis aims to show that the use of IL electrolyte along with modified separator materials can reduce the likelihood of a thermal runaway event in lithium-ion cells.

1.3.2 Outline of thesis

Chapter 2 contains a comprehensive literature review of lithium-ion battery separators, including relevant material properties for separator membranes, enhanced separator materials for conventional electrolytes and novel separator materials in literature for IL electrolytes. The discussion focusses on correlating separator properties and performance with IL electrolytes, leading into the IL electrolyte and separators developed in Chapter 3.

Chapter 3 presents the development and physical characterisation of a novel electrospun separator designed for IL electrolyte. The effects of solvent type, salt type and salt concentration in the electrospinning solution are investigated and discussed. The following physical characteristics are reported: separator morphology (thickness, fibre diameter, pore size, porosity), tensile strength, thermal stability, and wetting and ionic conductivity of the separator with IL electrolyte. The discussion compares the physical characteristic and wetting properties of the electrospun separators and point to the expected electrochemical performance to be investigated in Chapter 4.

Chapter 4 contains a summary of pertinent literature for electrochemical performance of IL electrolytes in lithium metal and lithium-ion cells. Electrochemical characterisation and cell testing of the novel separators with IL electrolyte are presented and discussed. The following electrochemical characterisations are reported: Cyclic Voltammetry (CV), Electrochemical Impedance Spectroscopy (EIS) and lithium stripping / plating behaviour. Cell testing was also reported: rate performance in LFP | Li cells and cycling performance in LFP | LTO cells. The discussion compares the electrochemical performance of the electrospun separators and recommends the best separator to be used with the IL electrolyte and thermally stable electrodes investigated in Chapter 5.

Chapter 5 begins with an overview of literature surrounding thermal stability of lithium-ion cells, specifically including IL electrolytes. A Differential Scanning Calorimetry (DSC) thermal investigation, is conducted and discussed. The thermal investigation includes the IL electrolyte with different separators and a range of commercially available electrode materials at different states of charge from cells cycled with the IL electrolyte. The discussion compares the thermal stability of electrode materials with the IL electrolyte and determines the electrodes to be used in the cell abuse investigations in Chapter 6.

Chapter 6 gives a literature summary of thermal abuse testing and modelling of lithium-ion cells.

The implementation of a thermal abuse model for a lithium-ion cell containing IL electrolyte is presented and discussed. Kinetic analysis of the thermal data from Chapter 5 is undertaken to extract decomposition reaction parameters. Simulations of the IL cell under thermal abuse conditions are presented using the extracted reaction parameters. Single-plate pair pouch cells containing LFP | LTO and the IL electrolyte are prepared and tested under thermal abuse conditions for comparison to the model. The discussion compares the IL electrolyte and conventional electrolyte thermal runaway reaction predictions of the model and discusses the implications for cell safety.

Chapter 7 presents a brief summary and conclusion of the overall thesis findings, along with recommendations for future work.

1.3.3 Publications

Table 1.4 Publications included in this thesis.

	Publication title	Authors / Journal	Status	Inclusion in thesis
# 1	Thermal stability of Pyrrolidinium-FSI IL electrolyte and lithium-ion electrodes at elevated temperatures	C. Francis, R. Louey, K. Sammut, A.S. Best, Journal of The Electrochemical Society, 165 (2018) A1204-A1221.	Published April 25, 2018	Chapter 5 (majority of 5.3 Experimental and 5.4 Results and Discussion)
# 2	Lithium-ion battery separators for IL electrolytes: a review	Candice Francis, Ilias Louis Kyratzis, Adam S. Best, Journal of Membrane Science	Manuscript finalisation	Chapter 2 (2.2.4 IL electrolytes and separators)

CHAPTER 2

Literature Review of Lithium-ion Battery Separators

2.1 Introduction

Ionic liquids (ILs) have been widely studied as a safer alternative electrolyte for lithium-ion batteries. The desirable properties of ILs, which were discussed in Chapter 1, make ILs a more thermally stable option compared with conventional electrolytes but ILs have inferior wetting characteristics with commercial separator materials. In a lithium-ion cell, the electrolyte should completely wet out the separator and electrode materials to reduce internal resistances in a cell. Investigations of cell materials with IL electrolytes have shown the wetting issues in IL electrolyte cells are most likely due to poor separator compatibility, not electrode compatibility [17, 18].

Commercial separators have been designed for compatibility with organic solvent based conventional electrolytes and are therefore not compatible with IL based electrolytes. The surface properties of separators must be modified for use with IL electrolytes. This modification must take place without sacrificing any of the performance or safety characteristics of the separator. New polymers, material combinations and improved manufacturing processes have been highly researched in the past decade [87]. Research has been done in parallel to modify surface properties and improve electrolyte separator wettability.

This chapter reviews separator developments and investigations, specifically focussing on separators for IL electrolytes, including commercial and novel separator materials. Firstly, the ideal properties for a separator are summarised. Secondly, different types of membranes used as separators are introduced. Thirdly, separators with different processing methods, polymers and additive materials for use with conventional electrolyte are discussed. Lastly, separators developed for use with IL electrolytes are reviewed. Section 2.2.4 below is part of a review paper manuscript in preparation, see Table 1.4 publication #2 for authorship details.

2.2 Literature review

2.2.1 Separator properties

Separators are thin porous membranes. New polymers, material combinations and improved manufacturing processes have been highly researched in the past decade to develop more effective separators [87]. Development research includes modifying surface properties of current materials, as well as investigating new materials and additives, to improve wettability with liquid electrolytes. There are ideal property requirements that determine if a membrane is suitable as a separator. Although a separator should not contribute to electrochemical reactions, its design is important for functionality of the cell [88, 89]. Separator properties can be related to interfacial characteristics, internal resistance, capacity, cycling and safety of the cell [90-92]. Ideal separator properties have

been summarised in Table 2.5, alongside the properties of three commercial separators: Celgard 3501, Solupor 7P03A and Separion S240P30, for comparison. A table of properties and measurement methods that are industry standard for separator characterisation can be found in Appendix A. Each separator property is discussed below with respect to impact on cell performance and safety.

2.2.1.1 *Chemical and electrochemical stability*

A separator should have no or very low chemical reactivity with other cell materials [89]. It should be electrochemically stable under the reductive and oxidative conditions encountered during charge and discharge [91].

2.2.1.2 *Dimensional stability*

Separators should lay flat and not bow or skew [87]. The dimensional stability of a separator should be maintained when the separator is wet with liquid electrolyte [89]. One measure of this is shrinkage; shrinkage of the separator in either direction once the cell is assembled may allow the electrodes to contact at the edges, causing a short circuit. Typically, shrinkage should be <5% in all directions when the separator is wet with electrolyte [87]. Instability of the separator dimensions could also cause misalignment during cell assembly [91].

2.2.1.3 *Thickness*

Ideally, a separator should be less than 25 μm in thickness [87]. Moreover, the separator should have uniform thickness to promote even current distribution during cell operation. Minimising the separator thickness reduces the volume taken up by the separator, together with less electrolyte required, leading to an increase in overall energy density of the cell [91]. However, the minimum membrane thickness is limited by the mechanical requirements to prevent separator rupture during cell assembly and through life [89].

2.2.1.4 *Porosity*

The porosity of separators should be greater than 40% with pore dimensions typically less than 1 μm [87]. The porosity must allow sufficient electrolyte retention to minimise cell internal resistance [89], however, the separator should not be too porous as this will decrease the membrane mechanical integrity [91].

Table 2.5 Properties of three commercial separator materials along with ideal specifications from literature.

Property	Celgard 3501*	Solupor 7P03A*	Separion S240P30*	Ideal Specification	Ref.
	Polypropylene (PP) monolayer, surfactant coated	Ultra-high molecular weight polyethylene (UHMWPE) fibrils	Polyethylene terephthalate (PET), Al ₂ O ₃ and SiO ₂ coated		
Chemical stability			Superior chemical resistance	Stable in battery for ten years	[93]
Thickness	25 µm	50 µm	30 µm	≤ 25 µm	[91, 93]
Porosity	55%	85%	> 40%	40 to 60%	[91]
Pore size	64 nm	300 nm	240 nm	< 1 µm	[91, 93]
Permeability (Gurley number)	200 seconds	10 seconds	15 to 30 seconds	< 35 seconds, per 10 cm ⁻³	[93]
Wettability	Surfactant-coated for rapid wetting		Excellent for dimethyl carbonate (DMC), ethylene carbonate (EC) and propylene carbonate (PC)	Quick and complete wetting	[91, 93]
Dimensional stability				No curl when wet, < 2 mm m ⁻¹ skew	[91, 93]
MacMullin number				< 11	[93]
Tensile strength	13.24 MPa in transverse direction (TD) 103.46 MPa in machine direction (MD)	15 MPa (MD)	> 3 N, per cm sample width (MD)	≥ 98.06 MPa	[91]
Puncture strength	335 g	300 g		≥ 300g for 25.4 µm thickness	[93]
Melt integrity			> 210 °C	≥ 200 °C	[93]
Thermal dimensional stability	5% after one hour at 90 °C (MD)	< 2% at 80 °C (MD and TD)	< 1% after 24 hours at 200 °C (MD and TD)	< 5% after 60 minutes at 90 °C <5% shrinkage at 200 °C	[91, 93]

* from manufacturer data sheet / information sheet, shown in Appendix B

2.2.1.5 Pore geometry

The separator should have a uniform morphology and tight pore size distribution, this can affect the current distribution within a cell [91]. The pore size should be small enough to prevent internal short circuits [91] but large enough to allow transport of lithium ions through the liquid electrolyte phase.

Scanning Electron Microscopy (SEM) images of separators from various manufacturers with different pore structures and dimensions are shown in Figure 2.2.

2.2.1.6 Tortuosity

Tortuosity relates the actual mean path of lithium ions through a porous structure as compared to the direct distance travelled [93]. Increasing the tortuosity of a separator can impede dendritic growth [89] but may also increase ionic resistance [93]. When separator thickness and porosity are constant, tortuosity is reflected in the Gurley number, which quantifies permeability [87, 89]. The typical Gurley number for a separator is < 0.025 seconds μm^{-1} [91]. Permeability is directly proportional to lithium ion transport through the electrolyte-filled separator pore structure.

2.2.1.7 Wettability

An electrolyte should completely wet out the separator pores to reduce internal resistance in the cell [93]. The speed of wetting is associated with the materials, porosity and pore size; faster wetting is favourable for cell manufacturing processes [91]. Incomplete wetting of the separator can produce uneven current distribution [94]. Retention of electrolyte in the separator is also important for the cycle life of the cell [89]. If the electrolyte is not held within the separator, a dry spot will emerge that leads to the adjacent electrode active material not being fully utilised. Contact angle and electrolyte uptake are widely used as an indicator, however, there is no standard method for assessing wettability which can make comparisons very difficult.

Common tests used to indicate the electrolyte affinity for the separator are as follows:

- 1 Place a drop of electrolyte on the separator surface and record the contact angle [89] (e.g. Figure 2.3).
- 2 Place a constant volume of electrolyte on the separator surface and observe the wetting behaviour over time [95] (e.g. Figure 2.4).
- 3 Place the separator vertically in liquid electrolyte and measure the absorption rate (capillary rise) or wicking height [93].

Figure has been removed due to Copyright restrictions.

Figure 2.2 SEM images of six different separators (a) Polypropylene (PP) / polyethylene (PE) / PP trilayer microporous; (b) PP dry-stretch microporous; (c) PP nonwoven; (d) Polyamide microporous; (e) Cellulose nonwoven; (f) Polyethylene terephthalate (PET) / ceramic. Taken from Kirchhöfer, et al. [96].

Contact angle is obtained by placing an electrolyte drop on a dry separator and measuring the drop shape with time [96]. A contact angle greater than 90° indicates poor wetting. The lower the contact

angle, the greater the affinity. Example of contact angle measurements are shown in Figure 2.3, the left images show good wetting and the right images show poor wetting. In the case of fast drop absorption, it is often difficult to get a precise measurement since the angle changes rapidly as the electrolyte is absorbed by the separator.

Figure has been removed due to Copyright restrictions.

Figure 2.3 Typical presentation of contact angle results: optical images of IL contact angle on different separator types; captured with a Kyowa DropMaster DM501. Taken from Huie, et al. [18]. 1M3PIIm-TFSI = N-methyl-N-propyl-imidazolium bis(trifluoromethanesulfonyl)imide (PMITFSI). 1M3PIIm-BF₄ = N-methyl-N-propyl-imidazolium tetrafluoroborate (PMIBF₄).

2.2.1.8 Ionic conductivity

The conductivity of lithium ions between the electrodes relates to transport properties of the electrolyte absorbed in the separator. The ionic conductivity of a separator containing electrolyte is typically in the range 10^{-3} to 10^{-1} S cm⁻¹ [91]. In an investigation correlating separator properties to cell performance, Lee, et al. [92] observed that Gurley number and ionic conductivity have a stronger relationship to rate capability than the commonly discussed properties of thickness and porosity.

The MacMullin number is commonly used to predict the ionic conductivity expected in an assembled cell [91]. The MacMullin number is defined as the ratio of ionic conductivity of a wet separator compared to that of the electrolyte alone. A lower MacMullin number is preferable for good performance and safety of the cell [89], ideally the MacMullin number would be close to one [93]. However, in reality less than eight is accepted for a separator [87] when taking into account the structural and mechanical limitations of other design requirements on the separator.

Figure has been removed due to Copyright restrictions.

Figure 2.4 Wetting behaviour with time: optical images of membrane wetting with IL electrolyte recorded as a function of wetting time. 5 μ L of electrolyte was dropped onto each membrane. PVDF = polyvinylidene fluoride. LiTFSI = lithium bis(trifluoromethanesulfonyl)imide. Taken from Truong, et al. [95].

2.2.1.9 Mechanical properties

Sufficient mechanical properties are important to withstand physical stress during cell assembly, cell operation and under abuse conditions [93]. A high tensile strength increases separator robustness during handling [89]. During standard operating conditions the separator is subjected to mechanical

deformation due to external compression and electrode expansion. A high puncture strength increases separator resistance to dendrite penetration during operation and under abuse conditions [91]. The mechanical properties of a separator can change substantially once the separator has been wet with electrolyte [97].

2.2.1.10 Melt integrity

The mechanical integrity of a separator at elevated temperatures can be analysed to assess the expected thermal stability of a separator [87]. Melt integrity temperature is the temperature at which a separator can no longer maintain its mechanical properties. Ideally separators would have a melt integrity temperature of ≥ 200 °C [93].

2.2.1.11 Shutdown temperature

The 'shutdown' functionality of a separator is the ability to limit or stop the current flow at an elevated temperature [89]. Upon reaching shutdown temperature the separator polymer begins to melt and flow closing the pores [93]. However, the separator must maintain mechanical integrity after undergoing shutdown to prevent contact between the electrodes which could cause an internal short circuit [98]. Impedance measurement with increasing temperature of a cell containing the separator of interest can be used to quantify the temperature at which shutdown occurs and the degree of shutdown experienced [98]. Venugopal, et al. [98] observed an impedance increase of at least three orders of magnitude following separator shutdown was required for successful prevention of a thermal runaway event. To act as a safety mechanism the shutdown temperature is required to be below the thermal runaway onset temperature of the cell [89].

2.2.1.12 Thermal dimensional stability

Thermal dimensional stability of a separator is important for cell safety. Membranes used as separators should maintain dimensional stability, even at high temperatures, to increase cell safety [93]. Separator shrinkage under high temperature conditions may allow the electrodes to come into contact, causing an internal short circuit. The thermal shrinkage for a separator is required to be < 5% after 60 minutes at 90 °C [89]. An example of the change in dimension of a separator following heat treatment is shown in Figure 2.5.

Figure has been removed due to Copyright restrictions.

Figure 2.5 Photographs of separators, pristine PE (a) before treating and (b) after treating under 140 °C for 0.5 h, (c) P(MMA-AN-VAc), (d) Al₂O₃/P(MMA-AN-VAc), (e) Al₂O₃P(MMA-AN-VAc)/2.5% H₂O, (f) Al₂O₃/P(MMA-AN-VAc)/5% H₂O, (g) Al₂O₃/P(MMA-AN-VAc)/7.5% H₂O, and (h) SiO₂/P(MMA-AN-VAc)/2.5% H₂O. Taken from Liao, et al. [99].

2.2.1.13 Thermal stability

The entire battery thermal stability, including the separator, can be tested according to IEEE standards 1725 5.6.5 [100], and 1625 5.6.6 and 5.6.7.2 [101]. The test procedure involves heating the cell at $5\text{ }^{\circ}\text{C min}^{-1}$ to $130\text{ }^{\circ}\text{C}$ then holding at $130\text{ }^{\circ}\text{C}$ for one hour [100, 101].

2.2.2 Separator types

There are two main membrane structures used as lithium-ion cell separator materials; microporous and nonwoven membranes.

2.2.2.1 Microporous

Microporous membranes typically show good mechanical strength and chemical stability [91]. However, there are issues associated with their use in lithium-ion cells, such as, low thermal stability, low interconnection of pores and poor electrolyte retention [91]. Low interconnection of pores is an issue as it results in low separator wettability with electrolyte. Common commercial separators are microporous polypropylene (PP) and polyethylene (PE) based membranes [88, 102], other polymers materials that have been researched are discussed below. Microporous membranes with co-polymers, polymer blends and / or additives have also been investigated to obtain separators with the advantageous properties of each material.

Microporous separators are generally made from polyolefins. A micrograph of a tri-layer microporous PP / PE / PP separator made by Celgard is shown in Figure 2.2a, showing typical pore structures of microporous separators. Material selection is limited by the required polymer properties in the manufacturing process. Dry processing is only applicable to crystalline polymers while wet processing is applicable to both crystalline and amorphous structures [89].

Dry processing involves three stages; extruding, annealing and stretching [89]. The polymer resin is heated above its melting temperature and extruded into a precursor film. This film is annealed just below the melting temperature to improve the crystal structure and then stretched to form pores. Pore structure can be tailored by stretching process variables such as temperature, strain rate and stretch direction; stretching can be done in the machine direction (MD), transverse direction (TD) or both [89]. Secondly, wet processing involves mixing a polymer and solvent solution, extruding a film and then extracting the solvent [89]. A stretching step may also be applied depending on the polymer material and desired pore structure. In both cases, the thickness of the separator can be minimised to reduce internal resistance in a cell, but the separator must be thick enough to provide mechanical integrity, as discussed in Section 2.2.1.

Chen, et al. [103] compared the tensile strength and fracture behaviour of microporous separators made by wet and dry processing using a micro-stage tensile tester. The properties were tested in the machine direction and transverse direction. Wet processed separators had higher overall

strength due to isotropic pore structure, however, the dry processed separators had a higher strength in the machine direction [103]. Chen, et al. [103] tested dry separators which provides useful information regarding separator handling during cell assembly.

Lee, et al. [91] discussed phase inversion processing as an alternative manufacturing method, however, the resulting separators typically exhibit an asymmetrical pore structure that can lead to uneven current distribution in a lithium-ion cell. The casting and drying process of a poly(vinylidene fluoride-co-trifluoroethylene (PVDF-TRFE) polymer solution containing ceramic fillers to create a microporous separator is shown in Figure 2.6.

Figure has been removed due to Copyright restrictions.

Figure 2.6 Schematic representation of the experimental procedure for the preparation of the PVDF-TRFE composite membranes. Taken from Nunes-Pereira, et al. [104].

2.2.2.2 Nonwoven

Nonwoven membranes have been investigated as an alternative separator material due to their highly interconnected pore structure, which is advantageous for a separator [91]. Nonwoven separators have shown excellent ionic transport properties due to their higher porosity and open pore structures compared to microporous membranes [105]. Nonwoven membranes are manufactured from fibres being randomly laid or directionally oriented into a sheet format [102]. Nonwoven membranes are made up of individual fibres that have been bonded together chemically, physically or mechanically [89], manufacturing methods include wet- or dry- laid process, melt blowing and electrospinning [93]. The manufacturing methods used to make nonwovens allow a wide range of compositions and designs to be considered [106]. This means different materials with enhanced thermal properties and electrolyte affinity can be investigated to improve cell safety and performance, such as polyesters, polyamides, polyimides [93]. However, nonwoven membranes have a large pore size and lower mechanical integrity compared to microporous membranes, which may limit their suitability for lithium-ion separators [91], but these properties may be controlled through manufacturing processes to produce nonwoven membranes that are suitable as lithium-ion separators.

Electrospinning is a popular method for fabricating nanofibre-based nonwovens as it is an easy fabrication method that allows for good control and optimisation of physical properties in the nonwoven separator [105]; porosity, pore size, fibre diameter and membrane thickness [91, 95]. Electrospinning parameters that can be varied include solution concentration, collector distance, voltage and solution flow rate [89]. Electrospun membranes are formed by applying a voltage between a needle containing polymer solution and a collector plate to induce fibre formation and collection into a randomly oriented sheet mat. The electrospinning setup for preparation of an electrospun nonwoven separator is shown in Figure 2.7.

Figure has been removed due to Copyright restrictions.

Figure 2.7 Schematic of single nozzle electrospinning device. Taken from Alcoutlabi, et al. [107].

2.2.2.3 Composite

Composite membranes are separators that contain ceramic particles [108]. Ceramics are non-metallic inorganic materials that have high thermal, chemical and dimensional stability [109]. Therefore, composite separators generally have good wettability, thermal stability and thermal conductivity compared to non-composite polymer-based separators [109]. Composite membranes have increased wettability due to hydrophilic surface properties enhancing the electrolyte affinity [109]. Higher thermal stability and thermal conductivity of the separator, provided by the ceramic particles, can improve cell safety by decreasing the possibility of internal short circuits and hot-spot formation, as well as improving heat dissipation in the cell [93].

Halalay, et al. [110] tested the elastic modulus and hardness of various separator materials through nanoindentation to assess puncture resistance. It was found that generally composite separators had enhanced mechanical properties however the inclusion of ceramic particles does not necessarily lead to improved properties [110]. The authors [110] found that the ceramic material choice and manufacturing conditions had a large influence on mechanical properties. Composite separators, however, do introduce disadvantages, such as an increase in membrane weight, a decrease in tensile strength and the possibility of particulate shedding during the life of the cell [93].

Ceramic particles can be added to the separator either as a coating or as a membrane filler. Polymer separators can be coated with ceramic particles to enhance their safety properties. Coating methods include spraying, casting, dip-coating or roll coating of the polymer separator in a ceramic suspension solution [109]. Often a binder material is required in the solution to ensure the particles bind to the polymer surface [91]. Membranes that contain a ceramic filler have been manufactured with the ceramic particles dispersed in the polymer solution [91]. This technique can be applied to microporous and nonwoven membrane manufacturing techniques [91]. Separators with ceramic fillers, compared to ceramic coatings, have a reduced risk of particulate shedding while retaining the improved thermal properties of ceramics.

Composite membranes can be manufactured with a variety of ceramic materials. The development of composite separators has been previously reviewed by Nunes-Pereira, et al. [108]. The most common ceramic particles are aluminium oxide (Al_2O_3), silica (SiO_2) and titania (TiO_2), although other ceramic materials have been investigated [108]. Development of composite separator materials in the literature have been discussed inside the relevant membrane type section below:

surface treated, microporous and nonwoven separators.

2.2.2.4 *Surface treated*

Common manufacturing and modification methods for separators have been previously reviewed [24, 88, 89]. Membrane surface treatments have been investigated to improve separator performance and safety. Contact between the electrodes and separator, along with electrolyte wettability, are important characteristics for the safety and performance of a lithium-ion cell [89]. These characteristics are dependent on the separator morphology and surface properties. Surface treatments have been investigated to improve interphase interactions by modifying the surface properties of a separator.

Polyolefin separators have been modified to produce a more hydrophilic separator by treatment with wetting agents, grafting functional groups onto the surface, i.e. plasma, ultra-violet (UV), electron beam or chemical treatment; or application of a thin coating to the separator surface [24, 88, 89]. These modification methods have been similarly applied to other microporous and nonwoven separators to produce membranes with enhanced surface properties. A summary of common surface treatments is shown in Table 2.6.

Table 2.6 Separator modification techniques.

Treatment	Materials	Ref.
Plasma treatment	Argon plasma	[111]
	Ethane / nitrogen plasma	[112]
	Argon / oxygen plasma	[113]
Polymer coating	Polydopamine (PDA) coating + UV irradiation	[114-117]
	Ethylene-vinyl acetate copolymer microspheres	[118]
	Poly(phenylene oxide) (PEO) coating + hydrogen induced cross-linking	[119]
	Poly(methylmethacrylate) (PMMA) coating	[120]
	PMMA via atom transfer radical polymerisation	[121]
Ceramic coating	Pulse microwave surface deposition of ceramic (TiO ₂)	[122]
	Radio-frequency magnetron sputtering of ceramic (Al ₂ O ₃)	[123]
	UV grafting of ceramic	[124]
	Molecular self-assembly of ceramic layer (SiO ₂)	[125]
	Ceramic deposition by electron beam evaporation (SiO ₂)	[126]
	Surface coating (ZrO ₂ , SiO ₂ , NiO, Li _{1.5} Al _{0.5} Ge _{1.5} (PO ₄) ₃)	[127-132]

Plasma treatment of commercial separators prior to cell assembly has been investigated to enhance electrolyte wetting and interphase properties in the assembled cell. The plasma type determines the type of change seen in the surface properties. Argon, ethane / nitrogen and argon / oxygen plasma treatments have been used to modify the surface of PP monolayer and PP / PE / PP separators [111-113], all investigations found that the electrolyte affinity increased following plasma treatment. To enhance adherence Li, et al. [133] investigated plasma treatment and grafting functional groups onto the separator surface before dip coating to increase adherence between cell layers.

Adherence to commercial polyolefin separators can be difficult due to their hydrophobic surface properties. Fang, et al. [134] and Kim and Park [135] used an oxygen plasma to alter the surface properties of a PE separator prior to dip coating in an SiO₂ solution. A SiO₂ and cellulose diacetate coating was investigated by Chen, et al. [136] following air plasma treatment of a PE commercial separator. The plasma treatment enhanced the coating layer adherence and morphology while the cellulose acetate and SiO₂ particles provided enhanced thermal properties.

Irradiation can cause a change in surface properties and has been studied to enhance the adherence of coating material on commercial polyolefin separators. Ko, et al. [137] used electron beam irradiation to graft hydrophilic glycidyl methacrylate on the hydrophobic surface of a PE separator. The electron beam irradiation showed good crosslinking and successful grafting of the coating solution to create a modified separator with good adherence. The modified hydrophilic surface improved the electrolyte affinity and subsequent cell performance. Electron beam irradiation was also used by Zhu, et al. [138] to achieve grafting of TiO₂ nanoparticles onto a PE separator. The modified separator had enhanced electrochemical performance and thermal dimensional stability.

Kim, et al. [139] used gamma ray irradiation to alter the surface properties of a PE separator prior to cell assembly. The treatment caused crosslinking in the polymer that enhanced the separator thermal properties, without negatively effecting the electrochemical performance. Kim, et al. [140] modified a PE separator by using gamma ray irradiation to change the surface properties prior to dip coating in poly(vinylidene fluoride-hexafluoropropylene) (PVDF-HFP). The modified separator showed enhanced electrolyte affinity due to the presence of PVDF-HFP and increased thermal stability which the authors [140] attributed to some crosslinking of the PE during irradiation.

Radiation induced grafting of poly(methylmethacrylate) (PMMA) onto a PE separator was investigated by Gwon, et al. [141] to enhance the interfacial properties and electrochemical performance of the separator. Grafting of methyl acrylate and SiO₂ nanoparticles onto PE surface was achieved by ultraviolet irradiation prior to dip coating [124]. The modified separator had a good microporous structure, improved wetting and enhanced thermal stability, due to the presence of the ceramic particles. Gao, et al. [117] modified the surface of a PE separator by applying ultraviolet irradiation to alter the polymer chain structure. The irradiated separator shows good electrolyte affinity and increased thermal stability due to the modified chains and crosslinking.

Tamaño-Machiavello, et al. [142] studied the properties of a hybrid hydrophilic / hydrophobic separator. A PVDF-TRFE hydrophobic microporous support was formed then poly(hydroxyethyl acrylate) was polymerised onto pore surfaces with dip coating and in situ polymerisation. The authors [142] stated many uses for a membrane with tuneable surface properties, including application to a lithium-ion separator due to the possibility of tuning surface characteristics for optimal wetting with the desired electrolyte.

Dip coating of a polymer solution onto a commercial PE separator was studied to obtain the advantageous properties the second material. Kim, et al. [143] used a poly(phenylene oxide) (PEO) dip coating solution to improve separator conductivity. Jeong and Kim [144] and Chen, et al. [145] used co-polymers of polyacrylonitrile (PAN) and PMMA to enhance the wetting and thermal characteristics of the separator. A microporous polyvinylidene fluoride (PVDF) coating was investigated to enhance separator wettability. Fang, et al. [146] expected the polar PVDF surface to have a better affinity with the polar conventional electrolytes, however, the microporous structure of the coating layer needed to be optimised for application to a separator. A microporous PP separator was dipped in a suspension of PVDF particles by Xu, et al. [147] to apply an even coating and improve the wetting and electrochemical properties of the separator. Coating of PE separators with more thermally resistance polymer was expected to improve overall cell safety.

The other modification technique involves ceramic particle coating of PE separators to improve wetting and thermal dimensional stability. A polymer binder was used in the solution containing ceramic particles to ensure good adherence. PVDF and its co-polymers were a common choice of

binding polymer due to good affinity with electrolytes and SiO_2 or Al_2O_3 particles [76, 148-154]. Although the ceramic particles provided good electrolyte affinity and enhanced thermal stability to the separator, the pore structure and adherence of the ceramic layer was not optimal for separator requirements. Choi, et al. [155], Ko, et al. [156] and Shi, et al. [157] investigated poly(lithium 4-styrenesulfonate), polyethylene terephthalate (PET) and styrene-butadiene rubber, respectively, as alternative binders to improve the wetting and thermal properties of ceramic layers.

Kang, et al. [158] and Kim, et al. [159] investigated ceramic particle deposition directly onto the PE microporous structure by surface functionalisation and plasma modification. Lee, et al. [123] introduced Al_2O_3 particles onto the surface of a PE separator via radio frequency magnetron sputtering. The ceramic particles improved the wetting and thermal characteristics without sacrificing the electrochemical properties or the morphology. Yeon, et al. [160] investigated the effects of coating metal hydroxides with PVDF-HFP binder on to an existing PE separator. The metal hydroxides had fire-retardant properties and were found to improve the thermal dimensional stability of the separator.

Another approach investigated to improve the wettability of a separator is to apply an electrospun layer on the sides of a polyolefin microporous separator. This approach has been pursued to combine the high chemical stability and tensile strength of a polyolefin separator with the high porosity and surface area of an electrospun layer [107], to produce a superior separator. Liu, et al. [161] added an electrospun polyether sulfone (PES) layer onto both sides of a microporous PE separator to improve the meltdown properties. Specifically, PVDF co-polymers have been used to coat commercial polyolefin separators due to their high affinity with electrolytes [162, 163].

PP commercial separators were used as supports and modified to enhance their properties for use as a separator. Wang and Gao [164] used a PP melt-blown support sandwiched between two PVDF-HFP microporous membranes coated with SiO_2 . Ceramic particles in polymer suspensions were dip coated [165-167] or electrospun [107, 163, 168] onto PP separators to increase the thermal stability and electrochemical performance of the separator. Modification of polyolefin separators by adding layers can prove difficult to gain sufficient adherence between the layers. The modified separators also remain limited by the low thermal properties of the polyolefin therefore alternate separator materials have been investigated.

2.2.3 Novel separators

The wetting and thermal properties of microporous PP or PE based separators can be improved using polymer blends or ceramic additives, however, overall separator thermal stability is still limited by the melting point of the PP or PE. Alternative polymer materials have been investigated in place

of PP or PE to produce microporous membranes with suitable properties for use as a lithium-ion cell separator. New polymers, material combinations and improved manufacturing processes have been highly researched in the past decade [87] to develop enhanced separators to address these problems.

Dry stretched high density PE (HDPE) and ultra-high molecular weight PE (UHMWPE) have been investigated as enhanced separators [169]. Shi, et al. [170] investigated blending HDPE with PE-co-polyethylene glycol (PEG) polymer to manufacture a hydrophilic microporous separator with improved wetting properties. The authors [170] found that the separator with hydrophilic properties had a lower interfacial resistance which led to improved electrochemical performance.

PVDF and its co-polymers have been highly reported for application to lithium-ion cell separators. PVDF has been investigated as separator material due to its high affinity with electrolyte materials [171, 172]. Although a pure PVDF based polymer membrane does not have the mechanical integrity required to survive the cell assembly process, the excellent wetting and electrochemical properties of PVDF based polymers makes them ideal for polymer blends or multi-layer separator designs.

Ceramic particles [173, 174] and nanocrystalline cellulose [175] have both been investigated as additives to PVDF membranes to enhance wetting and thermal stability of the separator. Zhu, et al. [176] studied the use of a glass fibre (GF) mat to provide dimensional thermal stability while dip coating in PVDF to produce suitable separator pore structure and increase the mechanical properties of the separator.

Electrospun PVDF has been widely studied for lithium-ion cell separators, Costa, et al. [87] has summarised investigations into PVDF, co- and blended polymers for separator materials. Liang, et al. [177] manufactured a pure PVDF nonwoven separator by electrospinning followed by heat treatment to increase the mechanical properties. Since pure polymer PVDF membranes do not have sufficient thermal or mechanical properties to be applicable to separators. Kim, et al. [178] manufactured a PMMA microporous separator dipped in a PVDF and ceramic solution to provide thermal and mechanical stability to the PMMA core.

PVDF-HFP has also been investigated for separators due to a high affinity for electrolytes as well as having excellent electrochemical stability for use in lithium-ion cells [179, 180]. Pure PVDF-HFP microporous separators have been investigated [181-184], as well as composite PVDF-HFP separators containing ceramic fillers [185-188].

Numerous different PVDF-HFP polymer blends have been investigated to enhance the mechanical and thermal properties of the separator. PMMA has been blended with PVDF-HFP to enhance the physical and wetting properties of an electrospun separator [189]. Huang, et al. [190] combined

cellulose acetate with PVDF-HFP by coaxial electrospinning to increase the thermal, mechanical and wetting properties of the separator. A polysulfonamide (PSA) separator electrospun in a core-shell structure with PVDF-HFP showed thermal stability while maintaining the advantageous wetting characteristics of PVDF-HFP [180]. Expanded polytetrafluoroethylene (PTFE) [191] and poly(vinyl chloride) (PVC) [192] membranes have both been used as mechanical supports and coated with electrospun PVDF-HFP to form membranes suitable for use as lithium-ion cell separators.

PVDF-HFP composite separators have also been manufactured via electrospinning [193, 194]. Incorporating ceramic fillers has been successful at enhancing the thermal and mechanical properties of a separator as well as resulting in an increased ionic conductivity [193]. Song, et al. [188] manufactured a PVDF-HFP and PMMA separator containing titania (TiO_2) via solution casting. The addition of TiO_2 improved the pore morphology and increased interfacial stability between the electrolyte and the electrode.

The co-polymer PVDF-TRFE was investigated due to superior thermal and mechanical properties as well as good electrolyte affinity. Temperature Induced Phase Separation (TIPS) and solvent extraction methods were studied by Costa et al. [195, 196] to produce a suitable PVDF-TRFE microporous separator. Nunes-Pereira, et al. [104] investigated PVDF-TRFE microporous membranes with different additives (montmorillonite, NaY zeolite, BaTiO_3 and multiwalled-carbon nanotubes) for separators with enhanced safety and performance. The authors [104] found that improvement in membrane morphology and electrochemical performance were highly dependent on the filler type but montmorillonite was concluded to make the best composite separators for lithium-ion cell applications.

Cellulose can also provide enhanced mechanical support to a separator and increase the thermal stability. Zhang, et al. [197] electrospun a cellulose separator from a cellulose acetate solution followed by hydrolysis and then used PVDF-HFP dip-coating to provide the separator good wetting and electrochemical properties. Cellulose fibres have also been investigated for use in separators by the papermaking method with various polymer binders and additives [89, 198-203].

The papermaking process has been used to manufacture separators from other fibre materials selected for advantageous mechanical or thermal properties: PET, para-phenylene terephthalamide and GFs [106, 204-206]. A microfiber glass support was made by Zhang, et al. [207] via the paper making process then dip coated in polyimide (PI) to increase the mechanical properties of the separator. The high thermal stability of both materials was expected to produce a separator with very high thermal dimensional stability.

The wide range of physical, chemical, thermal and mechanical requirements summarised in Table 2.5 is difficult to find in a single material. Despite the disadvantages of commercial separator

materials, no alternatives have been developed with simple low-cost manufacturing that can compete with polyolefin microporous separators. A summary of some novel polymers investigated for enhanced mechanical and thermal properties in a separator is shown in Table 2.7; including membrane type, separator material/s and manufacturing method, as well as tensile strength and thermal dimensional stability of the membrane. Polymers summarised in Table 2.7 include poly(aryl ether ketone) (PAEK), PAN, poly(ether ether ketone) (PEEK), polyetherimide (PEI), PET, PI, poly(m-phenylene isophthalamide) (PMIA), PMMA, PSA, PTFE, polyurethane (PU), PVC, melamine formaldehyde (Melamine), and poly(p-phenylene terephthamide) (Aramid).

PAN has been investigated as a separator material with enhanced thermal stability [208-212]. Seven separators that contain PAN are summarised in Table 2.7, including the tensile strength and thermal dimensional stability of the membranes. PAN is specifically suitable for nonwoven membranes due to the formation of thin fibres during electrospinning, which results in an improved morphology [208] and a high thermal stability, which leads to improved thermal stability in a cell [211]. Electrospinning the polymer blend PAN and PU was investigated to improve the separator wettability and thermal properties by Zainab, et al. [213]. Gopalan, et al. [214] studied an electrospun PVDF and PAN polymer blend to obtain a separator with the positive characteristics of both; PVDF has high affinity for electrolyte and a wide electrochemical stability while PAN has high thermal stability and good morphology for a separator. PAN nonwoven separators with ceramic SiO₂ additives were studied to improve the separator dimensional stability [215-218].

Table 2.7 Polymers being investigated for novel separators; including membrane type; separator material and manufacturing; tensile strength; and thermal dimensional stability. MP = microporous membrane. NW = nonwoven membrane. Multi = multi-layered membrane.

Polymer	Type	Separator materials and manufacturing method	Tensile strength, MPa	Temperature, °C	Time, hours	Thermal dimensional stability Shrinkage, %	Ref.
PVC	NW	PVC, electrospun, coated with PVDF-HFP, electrospun	1 to 2	150		0.2	[192]
PU	NW	Electrospun PU with 12 wt% PAN	10	170	0.5	None	[213]
PEEK	MP	PEEK, phase inversion	12	150	1	37	[219]
	MP	PEEK hydroxymethyl functionalized, phase inversion		240	12	18	[220]
PTFE	MP	PTFE (porous) commercial, impregnated with PVDF-HFP, phase inversion	20	5% length reduction at 160 °C Thermal Mechanical Analysis (TMA)			[191]
Melamine	NW	Melamine formaldehyde resin, electrospun	12	120	4	None	[221]
	NW	Glass fibres (GFs), paper making, immersed in melamine formaldehyde resin, thermally cured	21	150	1	None	[222]
PSA	NW	PSA electrospun onto PET support	17	170	0.5	None	[223]
PMIA	MP	PMIA, phase inversion	10	160	1	None	[224]
	NW	PMIA electrospun	36	180	1	None	[225]
	NW	PMIA fluoro-doped, electrospun		260	1.5	None	[226]
	NW	PMIA, electrospun, coated with PVDF, electrospun	14	180	1	None	[225]
PAN	MP	PAN / PVDF 4:6 w/w*, TIPS	1	160	1	12	[227]
	NW	PAN, electrospun	4 to 12	200	1	None	[209, 215, 218, 228]
	NW	PAN, electrospun, thermal calendared / heat treated	22 to 49	180 180	1 12	None 4	[211, 229]
	NW	PAN, centrifugal spun	14	180	0.5	None	[230]
	NW	PAN containing SiO ₂ nanoparticles, electrospun	4	150	0.5	None	[218]
	NW	PAN, electrospun, immersed in SiO ₂ with	7	200	0.5	None	[228]

Polymer	Type	Separator materials and manufacturing method	Tensile strength, MPa	Thermal stability, °C	dimensional stability, Time, hours	Shrinkage, %	Ref.
	NW	TEGDA, thermally crosslinked PAN / PVDF 1:1 w/w, centrifugal spun	18	180	0.5	None	[230]
PEI	MP	PEI, phase inversion	12 to 16	200	1	None	[231]
	MP	PEI containing nano SiO ₂ surface treated with octylsilane, phase inversion	Up to 16	No deformation up to 220 °C (Dynamic Mechanical Analyser (DMA))			[232]
	NW	PEI, electrospun, thermal crosslinking	Up to 38	150	1	None	[233]
	Multi	PEI / PU 1:1 w/w, electrospun, immersed in SiO ₂ with PVDF-HFP	15	180	0.5	5	[234]
PI	MP	PI, phase inversion	12 to 33	180	1	None	[235,
	NW	PI, electrospun	4 to 39	200	0.5	1	236]
	NW	PI, electrospun, mechanical pressing	31	500	2	None	[237-240]
	NW	PI, electrospun, thermal crosslinking	37	150	1	None	[241]
	NW	PI containing Al ₂ O ₃ or SiO ₂ nanoparticles, electrospun	5 to 38	300	2	None	[242]
	NW	PI containing TiO ₂ , co-electrospun with PVDF-HFP, thermal calendaring	11	250	1	None	[243, 244]
	NW	PI containing glass microfibre, paper-making	24	200	0.5	None	[245]
	NW	PVDF, electrospun, coated with PI, electrospun	8	180	2	3	[246]
	NW	PI co-electrospun with PVDF-HFP, thermal calendaring	7.5	180	0.5	None	[247]
	NW	PI / PVDF-HFP, core / shell electrospun, mechanical pressing	53	150	1	None	[179]
	Multi	PI, electrospun, immersed in nano Al ₂ O ₃ with PVDF-HFP		200	0.5	None	[248]
PET	NW	PET, electrospun	12				[249]
	NW	PET fibres, paper making, thermal calendaring,	57	180	1	None	[204]

Polymer	Type	Separator materials and manufacturing method	Tensile strength, MPa	Thermal dimensional stability			Ref.
				Temperature, °C	Time, hours	Shrinkage, %	
	Multi	impregnated with cellulose nanofibres Wet-laid PET, immersed in PAN and Poly(ethylene glycol)dimethacrylate solution, thermally crosslinked	32	130	5	< 5	[250]
	Multi	PET nonwoven, immersed in SiO ₂ with ethoxylated trimethylolpropane triacrylate, UV-cured and etched	50	150	0.5	None	[251]
	Multi	PET nonwoven, immersed in NaA microparticles with PVDF-HFP		170	1	2	[252]
PAEK	MP	PAEK / PVDF / PEG 1:1:1 w/w/w, phase inversion	59	160	2	8	[253]
PMMA	Multi	PMMA, phase inversion, coated with PVDF, electrospun	7				[254]
	MP	PMMA, phase inversion, immersed in Al ₂ O ₃ with PVDF-HFP	35	150	0.3	Some	[178]
	MP	HDPE, TIPS, PDA and PMMA grafted on surface	54 to 77	170	1	10	[121]
	NW	PSA / PVDF-HFP, core / shell electrospun, mechanically pressed	24	200	0.5	None	[180]
	NW	Cellulose / PSA 3:1 w/w, paper-making, thermal calendaring	17	200	0.5	None	[200]
Aramid	NW	Aramid fibres / pulp, paper making, thermal calendaring	31	250	0.5	None	[255]
	NW	Aramid nanofibres and PEG, vacuum filtration	50	200	0.5	None	[256]
	NW	Para-phenylene terephthalamide and PET microfibres, paper making, thermal calendaring	13 to 23	After ten minutes at 180 °C, 45% of strength remains			[205]
	NW	PEO and aramid nanofibres, layer-by-layer deposition	170	200	0.16	None	[257]

* w/w = weight/weight

PAN-co-PMMA has been studied to develop a suitable microporous separator. Different polymer blends and additives were investigated to improve the pore morphology of a PAN-co-PMMA based microporous separator [258-260]. Zhang, et al. [261] considered a PAN-co-PMMA separator with incorporated SnO₂ nanoparticles to further improve the pore structure and poly(ethylene glycol diacrylate) crosslinking to improve the mechanical properties.

PEI has been investigated as a separator material because it has a higher thermal stability than typical polyolefins [232, 262], which would be advantageous for safer separator materials. Four separators that contain PEI are summarised in Table 2.7, including the tensile strength and thermal dimensional stability of the membranes.

PET nonwoven membrane has been investigated as a mechanical support due to its interconnected pore structure and thermal dimensional stability. Five separators that contain PET are summarised in Table 2.7, including the tensile strength and thermal dimensional stability of the membranes. PET was studied as a pure polymer electrospun separator by Hao, et al. [249] with high porosity and good thermal properties. Ding, et al. [263] added an electrospun PI layer to improve the ionic conductivity while maintaining good support provided by the PET nonwoven membrane.

Electrospinning of poly(vinyl alcohol)-co-PE onto both sides of a PET support was investigated by Xia, et al. [264] to provide a hierarchical pore structure through the separator with good wetting and thermal stability. PSA was also electrospun onto both sides of a PET support to provide a separator with high thermal, mechanical and electrolyte affinity properties [223]. Ding, et al. [265] attempted to cast a PI and PEG polymer blend onto a PET nonwoven support. The PI and PEG blend was thought to improve the pore structure and ionic conductivity as well as have high thermal stability itself. To further improve the pore structure and electrolyte affinity, solutions containing ceramic particles were also investigated on PET nonwoven supports. SiO₂ particles were widely studied with a PVDF-HFP polymer binder [266-268].

PI shows excellent thermal and mechanical properties. A summary of 11 separators that contain PI is shown in Table 2.7, including the tensile strength and thermal dimensional stability of the membranes. Pure PI electrospun membranes [239, 241, 269, 270] as well as different polymer blends and additives [179, 245, 247] have been studied for use as separators with enhanced safety. Shi, et al. [271] used a PI nonwoven membrane for high temperature mechanical support and coated PEG on either side to decrease the pore size for applicability to lithium-ion separators.

Aramid fibres have been specifically investigated as a separator material due to high thermal stability and flame retardant properties which could improve the safety of lithium-ion cells [255, 256]. Four separators that contain aramid fibres are summarised in Table 2.7, including the tensile strength and thermal dimensional stability of the membranes. As can be seen in Table 2.7, aramid based separators have very high mechanical and thermal properties, compared to the other

polymers presented. A nonwoven separator containing nano-sized aramid fibres and a PEO binder was made by Tung, et al. [257] using the layer-by-layer deposition method. Unfortunately, the processing of this polymer is not simple, which would complicate large scale manufacturing techniques [272].

2.2.4 IL electrolytes and separators¹

IL electrolytes have different wetting characteristics and reactivity, as compared to conventional electrolytes which affect the electrolytes interaction with the other cell components, specifically wetting of the separator [17, 18, 96] and reactions with the electrode active material at the electrode-electrolyte interphase [48, 273]. Conventional electrolytes show good wetting properties with commercially available hydrophobic polyolefin based separators, while IL electrolytes show poor wetting with these commercially available separators [17, 96]. Similarly, reactivity of the electrolyte with electrode active materials is an essential and crucial aspect of a lithium-ion cell. Initial reactions between the electrolyte and the electrode active materials is essential to form a passivating film on the electrode surface that inhibits further reactions [11, 273]. The separator can affect the stability of the passivation film during cycling [96].

The separator material appears to be the limiting material when it comes to cell wetting with IL electrolyte [17, 18]. The hydrophobicity of ILs is very different from those of commonly used organic solvents, meaning separator materials must be modified to have different surface properties to enable wetting with IL electrolytes.

New separator materials are needed to fully realise the safety benefits of IL electrolyte lithium-ion batteries. Microporous and nonwoven separators have been investigated with new polymers, copolymers, polymer blends and additives to increase the affinity of separators with IL electrolytes, while maintaining the necessary characteristics of a separator (Table 2.5).

2.2.4.1 Commercial separators

Alternative electrolyte materials would be most effectively taken up by commercial cell manufacturers if they could be simply exchanged with existing organic electrolytes. This would require good compatibility with currently available electrode and separator materials. IL electrolytes possess very different properties to organic solvent electrolytes. These properties make them attractive as safer electrolytes but also mean they interact differently with other cell components.

¹ Section 2.2.4 is from a review paper manuscript in preparation, see Table 1.4 publication #2 for authorship details.

Stefan, et al. [17] conducted a study on the compatibility of pyrrolidinium (Pyr^+) and bis(trifluoromethanesulfonyl)imide (TFSI^-) based ILs with common separator and electrode materials. Compatibility was quantified with calculated interfacial free energy and contact angle measurements. The authors [17] tested four ILs of varying side chain lengths (N-methyl-N-propyl-pyrrolidinium bis(trifluoromethanesulfonyl)imide (P13TFSI), N-methyl-N-butyl-pyrrolidinium bis(trifluoromethanesulfonyl)imide (P14TFSI), N-methyl-N-pentyl-pyrrolidinium bis(trifluoromethanesulfonyl)imide (P15TFSI), N-ethyl-N-butyl-pyrrolidinium bis(trifluoromethanesulfonyl)imide (P24TFSI)) with commercially available separators by Celgard (2730, 2500, 2400 and 2320) and Separion. All IL and separator combinations had a contact angle below 90° indicating the ILs investigated could 'wet' the separators.

Separion showed far better compatibility in terms of wetting than any of the Celgard separators due to the Al_2O_3 and SiO_2 coating. Stefan, et al. [17] pointed out that Al_2O_3 and SiO_2 oxides have high surface free energies which means they have better wetting properties than polymeric materials. Of the Celgard materials, Celgard 2730 showed the lowest contact angle and interfacial free energy with all ILs measured, indicating the best compatibility. However, wetting characteristics were measured with pure ILs, and would most likely change when lithium salt was added to form an electrolyte [18].

From the Stefan, et al. [17] investigation it was concluded that wetting issues in cells containing IL electrolyte were most likely due to poor separator compatibility, not electrode compatibility. This supports the notion of the separator being extremely important for improved lithium-ion cell development.

A similar investigation was done by Kirchhöfer, et al. [96] on a range of commercially available separator materials using IL electrolytes with the Pyr^+ cation and either TFSI^- or bis(fluorosulfonyl)imide (FSI^-) anion. In addition to contact angle measurements, the authors [96] also determined the Gurley number, the MacMullin number, Solid Electrolyte Interphase (SEI) resistance and lithium plating / stripping characteristics of a separator with IL electrolyte in a symmetrical lithium metal (Li) | Li cell. Celgard, Separion and Freudenberg commercial separators were investigated as well as other membranes made from polyamide, cellulose and GFs.

Kirchhöfer, et al. [96] related contact angle to porosity, surface roughness, separator-electrolyte affinity and electrolyte viscosity. GF/C showed the fastest wetting and had a MacMullin number of 1, which was attributed to the high porosity and low Gurley number. The Freudenberg commercial separator, FS2190 PP nonwoven membrane, had the lowest Gurley number but did not show fast wetting due to low affinity of the IL electrolyte with polyolefin. This was supported by the two Celgard separators that had the highest contact angles due to a combination of the low porosity and poor electrolyte affinity. Celgard 2500, however, had a low MacMullin number of five with P14TFSI, which

Kirchhöfer, et al. [96] said could make it a good alternative to GF separators for IL electrolytes.

The Separion and Polyamide separators showed good wetting with IL electrolytes that the authors [96] attribute to their hydrophilic surface. Kirchhöfer, et al. [96] concluded that IL electrolytes with FSI⁻ anode had a poor affinity for polyolefin separators but suggested these separators could be wet by TFSI⁻ IL electrolyte.

During the SEI resistance and lithium stripping / plating investigations, the Celgard separators with P14TFSI had the lowest resistance which Kirchhöfer, et al. [96] suggested was due to low surface roughness and low chemical reactivity. Separion was found to be not suitable when combined with TFSI⁻ electrolytes. The ceramic particles were suggested to induce cracks in the SEI during cycling leading to increased resistance. However, when combined with FSI⁻ based electrolytes, Separion had one of the lowest resistances. Overall, the separator morphology was found to have a greater influence on the SEI resistance during cycling than the separator reactivity. FS2190, which is chemically stable with cell materials, was found to have the highest SEI resistance due to its rough surface causing SEI damage requiring continual repair during cycling.

Kirchhöfer, et al. [96] found that IL electrolytes based on FSI⁻ had lower resistances compared to those based on TFSI⁻. Specifically, the combination of Separion and N-methoxyethyl-N-methylpyrrolidinium bis(fluorosulfonyl)imide (P12O1FSI) showed excellent cycling behaviour. The authors [96] attributed this to the synergistic high electrolyte conductivity, good SEI formation, good wettability and low separator thickness. Similar to Stefan, et al. [17], Kirchhöfer, et al. [96] concluded that Separion is the best commercial separator option for IL based electrolytes.

Huie, et al. [18] also investigated the compatibility of commercial polyolefin separators with ILs and IL electrolytes. The effects of IL properties on separator compatibility were investigated; including cation type, cation chain length, anion type, IL viscosity, lithium salt concentration and the presence of carbonate solvent additives. Commercial polyolefin separators were used in the investigation; Celgard 2325, Celgard 2500 and Tonen E25.

Huie, et al. [18] tested saturated and unsaturated cations of different sizes to determine the effects on wettability. They used contact angle to quantify wetting. The larger pyridinium cation had a lower contact angle with unsaturated side chains. Whereas the smaller Pyr⁺ cation had a lower contact angle with saturated side chains. The authors [18] suggested that the size and chain saturation level of the cation can have a conflicting influence on separator wettability. Unfortunately Stefan, et al. [17] and Kirchhöfer, et al. [96] did not vary the IL cation so no other comparison of this kind could be made from the reviewed literature.

Huie, et al. [18] also varied cation chain length in an imidazolium (IM⁺) IL and found that, generally,

the contact angle decreased with increasing chain length. This result was also observed by Stefan, et al. [17] with Pyr⁺ and TFSI⁻ ILs on Celgard separators, for which the contact angles all followed the same trend: N-methyl-N-pentyl- < N-ethyl-N-butyl < N-methyl-N-butyl- < N-methyl-N-propyl. Huie, et al. [18] suggested longer chains increase the IL hydrophobicity which increases compatibility with hydrophobic separators.

Similarly, they also observed that the size of the anion influences the wetting, with larger anions increasing the hydrophobicity of the IL. The contact angle of IM⁺ ILs on Celgard 2500 and Tonen separators are shown in Figure 2.3. The authors [18] observed Pyr⁺ based IL electrolyte with TFSI⁻ anions were better able to wet the hydrophobic polyolefin separators than those with the tetrafluoroborate (BF₄⁻) anion.

In general, the hydrophilic separators showed consistently superior wetting with ILs and IL electrolytes [17, 96]. The superior wetting of hydrophilic commercial separator Separion was observed by Kirchhöfer, et al. [96] and Stefan, et al. [17] with the IL electrolytes tested. Kirchhöfer, et al. [96] saw superior wetting of hydrophilic separators (polyamide, cellulose and GFs) over the hydrophobic separators investigated (Celgard 2325 and Celgard 2500 and FS2190).

Huie, et al. [18] investigated the effect on contact angle of adding lithium salt to the IL. An overall trend of increasing contact angle with increasing salt concentration was observed for all ILs. A similar trend can be observed in the contact angle measurements with pure P14TFSI IL by Stefan, et al. [17] and 10 mol% lithium bis(trifluoromethanesulfonyl)imide (LiTFSI) electrolyte by Kirchhöfer, et al. [96] on Celgard 2500 and Separion, see Table 2.8 for values. Huie, et al. [18] further investigated the effect on contact angle of a carbonate solvent additive in IL electrolytes. Carbonate solvents have been added to IL electrolytes to reduce electrolyte viscosity, increase ionic conductivity and improve device performance. Contrary to expectation, TFSI⁻ ILs were observed to have the same or higher contact angle with the addition of ethylene carbonate (EC) or propylene carbonate (PC).

Huie, et al. [18] looked at the performance of cells containing electrolytes with IL, carbonate solvents and lithium salts. Evidence of gradual separator wetting was seen during cycling with 0.5 M LiTFSI in N-methyl-N-propyl-imidazolium bis(trifluoromethanesulfonyl)imide (PMITFSI): PC. The performance results from Huie, et al. [18] suggest a strong interaction between separator and anion type. Cell performance results agreed with contact angle measurements; electrolytes with lowest contact angle showed highest cell performance (Figure 2.8). This is expected as incomplete wetting can lead to increased internal resistance in a cell [93]. Also, one function of the separator is to absorb and distribute electrolyte within the cell, if separator wetting is poor this may lead to poor utilisation of the electrode active material and a resulting lower capacity of the cell. Huie, et al. [18] conclude that separator wetting is more critical than electrolyte ionic conductivity for electrochemical

performance of a cell.

Table 2.8 Commercial separators contact angle measurement summary.

Separator		IL	[§] Contact angle, °	Ref.
Celgard 2320 and Celgard 2325	Tri-layer membrane with one PE layer between two PP layers (Polypore).	P13TFSI	60.9	[17]
		P14TFSI	60.5	[17]
		P15TFSI	49	[17]
		P24TFSI	52.3	[17]
		P13TFSI	56	[18]
		P14FSI + 10 mol% LiTFSI	83	[96]
		P14TFSI + 10 mol% LiTFSI	66	[96]
Celgard 2500	Monolayer PP membrane (Polypore).	P13TFSI	67.3, 52*	[17, 18]
		P14FSI + 10 mol% LiTFSI	83	[96]
		P14TFSI	58.5	[17]
		P14TFSI + 10 mol% LiTFSI	65	[96]
		P15TFSI	52.6	[17]
		P24TFSI	53.9	[17]
Celgard 2730	Monolayer PE membrane (Polypore).	P13TFSI	53.1	[17]
		P14TFSI	46.9	[17]
		P15TFSI	38.4	[17]
		P24TFSI	46.4	[17]
Copa Spacer	Cellulose (Spez. Papierfabrik Oberschmitt GmbH)	P14FSI + 10 mol% LiTFSI	35	[96]
		P14TFSI + 10 mol% LiTFSI	34	[96]
FS2190	Monolayer PP membrane, nonwoven (Freudenberg and Co. KG).	P14FSI + 10 mol% LiTFSI	74	[96]
		P14TFSI + 10 mol% LiTFSI	46	[96]
GF/C	Glass fibre (Whatman)	P14FSI + 10 mol% LiTFSI	19	[96]
		P14TFSI + 10 mol% LiTFSI	33.5	[96]
Polyamide	Polyamide, 0.2um (Sartotius Stedium Biotech GmbH)	P14FSI + 10 mol% LiTFSI	25.5	[96]
		P14TFSI + 10 mol% LiTFSI	35	[96]
Separion	Ceramic (Al ₂ O ₃ , SiO ₂) impregnated and coated PET polymer nonwoven film (Evonik).	P14FSI + 10 mol% LiTFSI	30	[96]
		P14TFSI	15.8	[17]
		P14TFSI + 10 mol% LiTFSI	44	[96]
		P15TFSI	t.w.	[17]
		P24TFSI	t.w.	[17]
Tonen E25	PE (Toray Battery Separator Co, Ltd.)	P13TFSI	21.6	[17]
			46	[18]

[§] [17] and [18] measured contact angle with the sessile drop method. [96] measured contact angle with the drop shape analysis method.

t.w. = total wetting

Huie, et al. [18] and Stefan, et al. [17] investigated the compatibility of IL electrolytes with commercially available lithium-ion cell components. Both studies concluded that separator materials are more likely to have wetting issues with IL electrolytes than current electrode materials, electrodes investigated: LiFePO_4 (LFP), LiCoO_2 (LCO), $\text{Li}_4\text{Ti}_5\text{O}_{12}$ (LTO) and graphite. Kirchhöfer, et al. [96] investigated a variety of commercial separators with IL electrolytes. Separator compatibility was evaluated using wetting measurements as well as effect on internal resistances and SEI stability in a cell. Most studies with IL electrolytes use a GF mat as the separator that shows excellent wetting characteristics but is not used as a commercial separator due to its undesirable thickness [96]. These investigations of commercial separators with IL electrolytes suggests that no existing separator products are suitable for use with IL electrolytes. Therefore, a compatible separator material must be developed before IL electrolytes can be used in commercial lithium-ion batteries.

Figure has been removed due to Copyright restrictions.

Figure 2.8 (a) Discharge capacities of the 1st, 5th, and 10th cycles for LFP | Li cells with IL hybrid electrolytes with 0.5 M lithium salt. (b) Contact angles for electrolytes consisting of 50:50 volume/volume (v/v) (1M3PIm-BF₄ (N-methyl-N-propyl-imidazolium tetrafluoroborate, PMIBF₄), 1E3MIm-BF₄ (EMIBF₄), or 1M3PIm-TFSI (N-methyl-N-propyl-imidazolium bis(trifluoromethanesulfonyl)imide, PMITFSI)) and (EC or PC), and 0.5 M lithium salt (LiBF₄ or LiTFSI). Neat IL with no carbonate and no lithium salt is also plotted for reference. Error bars represent one standard deviation of ten measurements for each IL and separator combination. Taken from Huie, et al. [18].

2.2.4.2 New separator materials

New separator materials, the electrolyte, and electrodes that they were tested with are summarised in Table 2.9, as well as some key separator properties.

Microporous separators

Commercial microporous separators for conventional electrolytes are generally PP or PE. These polyolefin membranes are typically hydrophobic and do not have good compatibility with IL electrolytes, resulting in poor wetting. Less hydrophobic polymers are expected to have better compatibility with IL electrolytes. New materials have been investigated for microporous separators in IL electrolyte based lithium-ion batteries.

Liao, et al. [99] investigated dip coating a commercial PE microporous separator with poly(methyl methacrylate-acrylonitrile–vinyl acetate) (PMMA-AN-VAc) containing SiO_2 and Al_2O_3 to improve wetting characteristics with IL electrolyte. Low interconnection between pores is a common issue in

microporous separators causing decreased transport pathways available to lithium ions. SEM images showed that PMMA-AN-VAc only coating resulted in good interconnected pores. However, when Al_2O_3 was included in the coating solution, a water additive was required to achieve uniform particle dispersion within the coating layer. Only a small increase in Gurley number was observed for the Al_2O_3 / PMMA-AN-VAc / PE separator, suggesting the ceramic containing layer had an interconnected pore structure.

The inclusion of SiO_2 and Al_2O_3 nanoparticles was expected to increase the thermal stability of the separator [99]. Thermal shrinkage was calculated following exposure to 140 °C for 0.5 hours. Separator shrinkage after heating is shown in Figure 2.5, the blue background is the original area of the untreated separator. As expected, the authors [99] observed less shrinkage in the separators coated with polymer layers containing nanoparticles. Similarly, thermal gravimetric analysis showed a slower decomposition rate for the separators containing ceramic particles. In a study of SiO_2 coatings applied to a PE separator [76], decreased thermal shrinkage of the ceramic coated separator was attributed to the heat-resistant SiO_2 particles preventing shrinkage in the separator structure.

The separators were investigated with 0.7 M LiTFSI in P14TFSI IL electrolyte. Liao, et al. [99] observed an increase in lithium with ceramic coated separators, indicated by a low SEI resistance compared to the PMMA-AN-VAc coated separator. The authors [99] attribute this increased compatibility to the ceramic coated separator's ability to trap more electrolyte, due to the high surface area of nanoparticles, and therefore limit electrolyte reaction with lithium metal. Electrochemical stability indicated the presence of PMMA-AN-VAc and ceramic particles increased the decomposition potential above 5.25 V. Liao, et al. [99] suggested this was due to the polymer and ceramic particles reducing the IL activity.

Table 2.9 Summary of new separator materials for IL electrolytes from literature survey. MP = microporous membrane. NW = nonwoven membrane.

Type	Materials	Processing	Electrolyte	Thickness, μm	Porosity, %	Electrolyte Uptake, %	Ionic conductivity, mS cm^{-1}	Tensile strength, MPa	Electrode (vs. Li)	Ref.
MP	PE PMMA-AN- VAc Al_2O_3 or SiO_2	Dip coating commercial separator	0.7 M LiTFSI in P14TFSI / VC	22	-	-	1.1-1.2	-	LFP	[99]
MP	PVDF-HFP PMMA	Casting and phase inversion	LiClO in BMIBF ₄		56.8	234	1.4	-	LFP	[274]
MP	PVDF-TRFE PVDF-HFP PEO	Casting	0.37 M LiTFSI in P14TFSI		60-72	245 300	0.4 0.4	-	LFP	[275]
MP	PVDF-HFP	Casting and solvent extraction	1.1 M LiTFSI in 1G13TFSI	200	-	670	0.316	-	LFP	[276]
MP	PVDF	Casting	EMINTf2	45 \pm 5	20	-	0.23	-	C-LFP	[277]
NW	PAN	Electrospinning	1.2 M LiFSI in P13FSI 0.6 M LiTFSI in P13TFSI	200	83	-	-	16.4	NMC	[105]
NW	PAN PMMA	Electrospinning	1 M LiTFSI in P14TFSI / Poly(ethylene glycol) dimethylether		78-86	420 480	2.3 3.63	-	LFP	[278]
NW	PVDF-HFP	Electrospinning	0.5 M LiTFSI in BMITFSI 0.5 M LiBF ₄ in BMIBF ₄	80	-	750 600	2.3 2.3	-	LFP	[279]

Separator Design and Thermal Study of Ionic Liquid Electrolyte Lithium-ion Cells, C. Francis, 2018

NW	PVDF-HFP Al ₂ O ₃ or SiO ₂ or BaTiO ₃	Electrospinning	0.5 M LiTFSI in BMITFSI	150	84-87	650 725 740 750	2.3 3.6 4.4 5.2	-	LFP	[280]
NW	PVDF-HFP SiO ₂	Electrospinning	0.5 M LiTFSI in BMITFSI	100-120	87-88	400	2.3-4.3	-	LFP	[281]
NW	PVDF-HFP SiO ₂	Electrospinning	1 M LiBF ₄ in EMIBF ₄ / DEC	98	86	469	3.48	-	LFP	[282]
NW	PVDF-HFP Cellulose	Electrospinning	1 M LiTFSI in P14TFSI	60-70	>80	438 712	0.18 0.35	-	LFP	[283]
NW	PVDF LiTFSI TPGTA Poly(ethylene glycol)dimetha crylate	Electrospinning with thermal or ultraviolet crosslinking	0.7 M LiTFSI in P14TFSI		91-95	-	-	1.54 6.33 8.45 8.50	Li	[95]

The ceramic coated separators showed good capacity in LFP | Li cells tested at C/10. Liao, et al. [99] concluded the SiO₂ / PMMA-AN-VAc / PE separator is suitable for P14TFSI IL electrolyte lithium-ion batteries. Despite modifying the PE separator for the express purpose of improving wetting with IL electrolyte this study did not report the porosity or wetting behaviour of the modified separator. Unfortunately, the mechanical properties were not reported by Liao, et al. [99] either, but investigations into mechanical properties would be useful to assess the robustness of coatings applied by the dip method to survive handling and cell assembly.

PVDF-HFP is a popular material investigated for separators, all novel PVDF-HFP separators reviewed use the material *Kynar 2801* which has a molecular weight of 477000 g mol⁻¹ and a VDF:HFP ratio of 88:12 [274, 276, 279-283], except for Costa, et al. [275] who uses a PVDF-HFP with the same VDF / HFP ratio but a molecular weight of 600000 g mol⁻¹.

A microporous PVDF-HFP and PMMA separator was investigated by Zhai, et al. [274]. The separator was produced by solution casting and phase inversion. The polymer ratio of 40 wt% PVDF-HFP to 60 wt% PMMA was found to produce the best separator for application to lithium-ion batteries. The separator was tested with lithium perchlorate (LiClO₄) in N-butyl-N-methyl-imidazolium tetrafluoroborate (BMIBF₄) IL electrolyte. Unfortunately, no commercial or control separators were tested so a direct comparison could not be made regarding the benefits of this separator directly. The PVDF-HFP and PMMA separator has some of the lowest electrolyte uptake (234%) and ionic conductivity (1.4 mS cm⁻¹) values among those reported in Table 2.9. Zhai, et al. [274] suggest ionic conductivity is strongly related to the electrolyte uptake of the separator, since the fastest lithium ion transport occurs in the liquid electrolyte. This is evidenced by correlation between electrolyte uptake (left) and ionic conductivity (right) shown in Figure 2.9, the separator with the highest electrolyte uptake and porosity (PVDF-HFP / PMMA 40:60 weight/weight (w/w)) also has the highest ionic conductivity.

Figure has been removed due to Copyright restrictions.

Figure 2.9 Left: Porosity and IL uptake of the microporous membranes composed of various amounts of PMMA. Right: Temperature dependence of ionic conductivity of all synthesized polymer electrolytes. Taken from Zhai, et al. [274].

Zhai, et al. [274] performed Differential Scanning Calorimetry (DSC) on separator samples wet with IL electrolyte. The authors [274] saw a decrease in the glass transition temperature with increasing PMMA content and proposed this was due to the IL electrolyte interacting with the PVDF-HFP and the lowering membrane crystallinity. Thermal gravimetric analysis showed that decomposition temperatures for the components in the electrolyte-wet separator were higher than for the individual components alone.

Transport properties of the PMMA and PVDF-HFP separator in a cell assembly were investigated by measuring bulk electrolyte resistance during storage. A Li | Li cell with the separator and IL electrolyte showed fluctuations in resistance for eight days before stabilizing. Zhai, et al. [274] suggested this was due to elastic deformation changes in the separator thickness combined with SEI formation. The stabilisation was attributed to a stable ion-conducting film, the SEI, forming between the PMMA and lithium, indicating good compatibility of the separator with other cell components. The PMMA and PVDF-HFP separator showed good performance in a LFP | Li cell [274]. The capacity decrease observed with increasing discharge rate is typical for high viscosity electrolytes and is not a reflection on the separator. The capacity was seen to increase over the first five cycles which could indicate poor initial wetting of the LFP electrode. The mechanical properties of the separator were not investigated by the authors [274] so comments could not be made regarding mechanically robustness to survive cell assembly and handling. The results from Liao, et al. [99] and Zhai, et al. [274] indicate PMMA is a compatible polymer material for IL electrolytes.

PVDF-HFP, PVDF-TRFE and PEO separators were investigated by Costa, et al. [275] with carbonate-based electrolytes and 0.37 M LiTFSI in P14TFSI IL electrolyte. The separators were produced by solution casting with solvent evaporation and the separator thickness was not reported. SEM images showed different microstructures for each polymer separator. The PVDF-TRFE and PVDF-HFP separators appeared to have open interconnected pore structures while the PVDF-TRFE / PEO blend separator had highly dispersed smaller pores. An interconnected pore structure within the separator is desirable to allow the electrolyte to fill every pore and for lithium ion transport.

The PVDF-TRFE / PEO separator had a noticeably lower porosity. The low porosity and low interconnected pore structure is strongly reflected in a lower electrolyte uptake (only 31.6%) with

regards to IL electrolytes. Interestingly, while the PVDF-TRFE separator had the highest porosity, the PVDF-HFP separator had a higher electrolyte uptake. This may suggest a better affinity between PVDF-HFP and the IL electrolyte. The same ionic conductivity was reported for the PVDF-TRFE and PVDF-HFP separators [275]. The PVDF-TRFE / PEO separator had a much lower ionic conductivity, as expected based on the low porosity and electrolyte uptake. This correlation between separator porosity and ionic conductivity is observed in a number of these studies [105, 274, 278, 282].

The melting temperature of PEO in the PVDF-TRFE / PEO separator is below 100 °C [275]. The PVDF-TRFE has a melting temperature of approximately 140 °C which is lower than the specification for an ideal separator (see Table 2.5). A separator with higher thermal stability is desirable for IL electrolytes in order to exploit their characteristic safety advantages. The electrochemical performance of the separators with IL electrolyte was not tested in this study. The electrochemical and mechanical properties of these separators need to be investigated further to determine their suitability for lithium-ion cell applications.

Li, et al. [276] manufactured a microporous PVDF-HFP separator with a plasticiser to assist pore formation. The separator was produced with a doctor blade process at a thickness of 200 µm followed by immersion in water bath to remove the plasticiser. SEM images showed large uniform pores in the PVDF-HFP separator after wetting with 1.1 M LiTFSI in N-methyl-N-propyl-N,N,N,N-tetramethylguanidinium bis(trifluoromethanesulfonyl)imide (1G13TFSI) IL electrolyte. Unfortunately, porosity was not reported so comparison to other separators is not possible. The PVDF-HFP separator showed a high electrolyte uptake (670%) which the authors [276] attributed to the large pores and high poor interconnectivity of the separator. An ionic conductivity of 0.316 mS cm⁻¹ was measured for the separator with the IL electrolyte. Unfortunately no comparison could be made since Li, et al. [276] did not include a control separator in the investigation. The IL 1G13TFSI is not widely published, so literature values could not be found for comparison.

The PVDF-HFP separator was electrochemically stable up to 5.3 V with the IL electrolyte, suggesting it may be compatible with high voltage cathode materials [276], however this has not been investigated to date. The PVDF-HFP separator interfacial resistance with lithium metal was measured over seven days in a Li | Li cell, the resistance stabilised after five days suggesting an effective SEI film had been established. Cyclic Voltammetry (CV) was performed and after ten cycles the current peaks were constant, indicating a stable SEI had formed, and a reversible process was observed. In a LFP | Li cell, stable cycling behaviour was reported but evidence of gradual separator and / or electrode wetting was seen during the first few cycles [276]. This study shows further evidence that PVDF-HFP has good compatibility with IL electrolytes and should be

considered for further materials development. However, the thermal and mechanical properties of this specific separator design have not yet been investigated.

Costa, et al. [277] manufactured a PVDF microporous separator via solution casting with a 'green' solvent N,N'-dimethylpropyleneurea. The polymer solution was spread with a doctor blade and oven air dried at 50 °C for one month to produce a separator with uniform pore distribution. The separator had a thickness of $45 \pm 5 \mu\text{m}$ and a porosity of approximately 20% with pores less than 1 μm diameter. The slow drying and low porosity could be attributed to the low volatility of the solvent N,N'-dimethylpropyleneurea. Although the separator has a low porosity compared to commercial separators (approximately 40%), the low porosity increases the mechanical properties of the separator. DSC confirms the separator is stable up to 100 °C and Thermogravimetric Analysis (TGA) shows the thermal stability is similar to a PP separator [277]. The authors [277] report thermal and mechanical properties that are suitable for separators.

Electrochemical properties and cell performance of the microporous PVDF separator were tested with electrolytes 1 M lithium hexafluorophosphate (LiPF_6) EC / diethyl carbonate (DEC) as well as the IL 1-ethyl-3-methylimidazolium bis(trifluoromethylsulfonyl)imide (EMINTf2) [277]. The IL electrolyte was tested as an environmentally friendly option. The IL EMINTf2 was chosen for its high conductivity, improved thermal properties and immiscibility with water. The ionic conductivity for the IL alone is 11 mS cm^{-1} , this decreases to 0.23 mS cm^{-1} for the separator wet with IL, which correlates to a MacMullin number of 48. The separator and IL show a stable voltage window between 1.0 to 5.0 V. The interfacial resistance is seen to increase with cycling in a LFP | Li cell indicating SEI resistance increasing and consequential reduced lithium ion diffusion. This is confirmed by the cycling in a LFP | Li cell at C/5 rate where the capacity retention is 60% after ten only cycles, which the authors [277] attribute to SEI thickening and a low compatibility with the lithium anode.

Nonwoven separators

Rao, et al. [278] investigated the suitability of PAN / PMMA blended electrospun separator. With SEM imaging the authors [278] observed a small fibre diameter (approximately 450 nm) and high porosity (86%) in the separator. The electrolyte uptake and ionic conductivity of the separator was tested with 1 M LiTFSI in P14TFSI and poly(ethylene glycol)dimethylether IL electrolyte. The PAN / PMMA separator had a faster electrolyte uptake and higher ionic conductivity than a Celgard PE separator wet with the same IL electrolyte. The authors [278] attribute the higher ionic conductivity to high porosity and interconnected pores in the electrospun membrane which allows faster transport of ions.

The PAN / PMMA separator showed electrochemical stability up to 5.2 V, while the PAN separator

began to decompose approximately 5 V, which indicates that electrochemical stability in the blend separator was provided by the PMMA. Rao, et al. [278] suggested this was due to a high affinity between PMMA polar functional groups and the electrolyte. The PAN / PMMA separator showed a more stable interfacial resistance in a symmetrical Li | Li cell, compared to the PAN and Celgard separators. The change in resistance with storage time can be seen in Figure 2.10 (insert). The lower interfacial resistance of the PAN / PMMA separator suggests these materials are more compatible with a lithium electrode than the PAN or Celgard separators. This was reflected in the good rate and cycling performance observed in a LFP | Li cell. These results suggest that both PAN and PMMA are compatible, individually or in a blend material, for an IL electrolyte lithium-ion cell.

Figure has been removed due to Copyright restrictions.

Figure 2.10 Impedance spectra of cell Li | gel polymer electrolyte | Li at open circuit potential with electrospun PAN / PMMA, PAN and Celgard PE; Inset: the variation of interfacial resistance of cell Li | gel polymer electrolyte | Li with storage time. Taken from Rao, et al. [278].

Evans, et al. [105] investigated an electrospun PAN separator with 1.2 M lithium bis(fluorosulfonyl)imide (LiFSI) in N-methyl-N-butyl-pyrrolidinium bis(fluorosulfonyl)imide (P14FSI) and 0.6 M LiTFSI in P14TFSI IL electrolytes. The PAN separator was manufactured with a large fibre diameter (1 μm) which the authors [105] proposed would increase the wettability with high viscosity IL electrolytes. The PAN separator had a similar high porosity (83%) to that of the PAN / PMMA separator (86%) [278], despite having a fibre diameter twice the size (approximately 1 μm for PAN and 450 nm for PAN / PMMA). Wetting behaviour of the PAN separator was similar to a Whatman GF membrane, which is widely published as having good wettability with IL electrolytes [105]. Evans, et al. [105] suggest the low contact angle and fast wetting rate of the PAN separator with both electrolytes (contact angle approximately 70° at time = 0 seconds decreases to approximately 30° after 0.3 seconds) proves the separator can readily absorb and distribute IL electrolyte in a cell.

The tensile strength of the PAN separator was found to be 16.4MPa [105], which is lower than the specification in Table 2.5. The PAN separator had better mechanical properties than the GF (GF/F, Whatman) membrane (1.13 MPa), but was not as strong as the Celgard PP separator (114.03 MPa). Poor mechanical properties are a significant downfall of Whatman membranes making them not suitable for commercial cells.

The PAN separator had a low MacMullin number (<5), which Evans, et al. [105] attribute to high porosity and wettability, facilitating good lithium ion transport. The PAN separator showed good

rate and cycling capacity with 1.2 M LiFSI P14FSI electrolyte in a $\text{Li}(\text{Ni}_{1/3}\text{Co}_{1/3}\text{Mn}_{1/3})\text{O}_2$ (NMC) | Li cell. The PAN separator performance is superior to the Whatman GF control cell, as shown in Figure 2.11. The authors [105] attribute this performance to the open pore structure, low MacMullin number and high electrochemical stability of the separator.

Morphological changes were observed in the PAN separator after 100 cycles, SEM images revealed physical evidence of fibre swelling from electrolyte absorption and fibre compaction from cell assembly. The authors [105] claim the observed changes did not have negative effects on the separator performance. Evans, et al. [105] conclude that the PAN separator shows good compatibility in their study but suggest further safety and thermal analysis should be performed before application to a lithium-ion cell.

Figure has been removed due to Copyright restrictions.

Figure 2.11 Rate study of NMC half-cells containing N-methyl-N-propyl-pyrrolidinium bis(fluorosulfonyl)imide (P13FSI) (1.2 M LiFSI) comparing performance of a GF separator and the electrospun PAN microfibre separator. Electrochemical cycling was performed at room temperature between 3 and 4.2 V vs. Li | Li. Taken from Evans, et al. [105].

Cheruvally, et al. [279] investigated an electrospun PVDF-HFP separator. The PVDF-HFP had the same fibre diameter (1 μm) as Evans PAN separator [105] resulting in similar separator morphology with an interconnected pore structure and high surface area [279]. Separator porosity was not reported so comparison was not possible. The PVDF-HFP separator was investigated with two IL electrolytes, 0.5 M LiTFSI in N-butyl-N-methyl-imidazolium bis(trifluoromethanesulfonyl)imide (BMITFSI) and 0.5 M lithium tetrafluoroborate (LiBF_4) in BMIBF₄.

The highest electrolyte uptake was seen with 0.5 M LiTFSI in BMITFSI, which was related to the lower viscosity of BMITFSI [279]. Concerns regarding limited electrolyte retention in nonwoven separators with high electrolyte uptake were raised but the authors [279] did not investigate further. The ionic conductivity of the PVDF-HFP separator was the same for both IL electrolytes tested (2.3 mS cm^{-1}) [279]. The authors [279] expected a decrease in separator ionic conductivity compared to the pure IL ($\geq 3.5 \text{ mS cm}^{-1}$) from the combined effects of lithium salt addition and transport limitations in the separator pore structure. In other studies of microporous PVDF separators (approximately 70% porosity) with conventional electrolytes [284], a greater drop in ionic conductivity was observed from the pure electrolyte (9 mS cm^{-1} for 1 M LiPF₆ in EC / dimethyl carbonate (DMC) at 30 °C) to the wet separator (0.015 mS cm^{-1} at 30 °C). Cheruvally, et al. [279] noted that the drop in ionic conductivity from the pure IL electrolyte to the wet PVDF-HFP nonwoven separator was lower than expected, compared to previous studies, specifically microporous PVDF separators with conventional electrolytes.

Cell performance was investigated in an LFP | Li cell. The BMITFSI electrolyte showed a higher capacity than the BMIBF₄ which the authors [279] suggested may be due to the presence of a thicker SEI film with the BMIBF₄ electrolyte. Compared to a commercial Celgard separator, performance of the PVDF-HFP separator was superior. The PVDF-HFP separator showed good reversibility during cycling, however, capacity reduction was seen at high discharge rates, as is typical in high viscosity electrolytes. Cheruvally, et al. [279] propose their PVDF-HFP separator is suitable for low current density applications at room temperature.

Continuing on from the PVDF-HFP electrospun separator investigated by Cheruvally, et al. [279], Raghavan, et al. [280] studied the effect of dispersing nano-sized ceramic fillers within this

separator. The ceramic fillers investigated were SiO_2 , Al_2O_3 and BaTiO_3 . Incorporating ceramic fillers can enhance the mechanical, thermal and flame retardant properties of a separator [280]. A slight increase in porosity was seen with the addition of the ceramic fillers. The fibre diameter of the PVDF-HFP separator was increased by the presence of the fillers, while the polymer crystallinity decreased. The authors [280] proposed the polar C-F bonds in the PVDF-HFP formed a weak Acid-base complex with the -OH groups on the surface of the nano-sized fillers, resulting in reduced ordering in the crystalline regions. The separators were investigated with 0.5 M LiTFSI in BMITFSI IL electrolyte and an increased electrolyte uptake was observed in the presence of fillers [280]. The BaTiO_3 / PVDF-HFP separator had the lowest bulk electrolyte resistance and highest ionic conductivity. The authors [280] attributed the increase in ionic conductivity to interactions between the ceramic particles and the electrolyte polar groups.

In a symmetrical Li | Li cell a stable SEI film was formed in the first five days for separators incorporating fillers [280]. The separator without fillers formed a SEI much more slowly without stabilising during the experiment. Raghavan, et al. [280] proposed ceramic filled separators had increased interfacial stability because the high surface area of the fillers resulted in more electrolyte being held in the wet separator, which limited the reaction between the electrolyte and lithium metal. Since cyclable lithium is consumed in these reactions, minimising the reactions has a positive effect on the cell performance through life. The PVDF-HFP separator was electrochemically stable up to 5.5 V and the authors [280] suggested application of separators with ceramic fillers for high voltage cathodes. CV studies confirmed reversible plating / stripping of lithium in the PVDF-HFP separator regardless of the presence of a ceramic filler(s). The capacity retention after 20 cycles at C/10 in a LFP | Li cell was highest for the BaTiO_3 filled separator and lowest for the non-filled separator. Raghavan, et al. [280] concluded the ceramic filled PVDF-HFP electrospun separators were suitable for IL lithium-ion cells as they allow for good ion transport as well as having a good compatibility with the electrolytes and electrodes.

Kim, et al. [281] investigated a SiO_2 filled PVDF-HFP electrospun nonwoven separator with 0.5 M LiTFSI in BMITFSI IL electrolyte. The pure PVDF-HFP electrospun separator in this work had a much larger fibre diameter (2 μm) than the PVDF-HFP separator produced in Cheruvally, et al. [279] and Raghavan, et al. [280] (1 μm and 630 nm, respectively), despite reporting using the same solution and applied voltage for electrospinning. This highlights the influence that the unreported electrospinning conditions, such as humidity, temperature, solution flow rate and collector distance, can have on the resulting separator. The addition of SiO_2 resulted in an increase in the average fibre diameter and a lack of uniform fibre diameter distribution as well as a branched morphology [281]. The separator porosity was not significantly affected by SiO_2 which the authors [281] attributed to packing of larger less uniform diameter fibres, causing many smaller pores with a similar overall porosity. The authors [281] reported an electrolyte uptake of approximately 400%

when the separator was immersed in IL electrolyte.

In a symmetrical Li | Li cell, Kim, et al. [281] observed the electrolyte resistance was relatively constant with storage time however the interfacial resistance continued to increase over the seven day storage period. This indicated the separators with ceramic fillers were more compatible with lithium electrodes than those without, as was reported by Raghavan, et al. [280]. CV showed good electrochemical stability and reversible plating and stripping which the authors [281] attributed to a stabilising effect of lithium salt in the IL electrolyte. The separator and electrolyte were tested in an LFP | Li cell to investigate the performance and cycling characteristics. A higher discharge capacity was seen with the 6% SiO₂ / PVDF-HFP separator. Kim, et al. [281] concluded the SiO₂ filled PVDF-HFP separator and 0.5 M LiTFSI in BMITFSI IL electrolyte investigated were compatible with LFP cells.

Yang, et al. [282] investigated SiO₂ content in PVDF-HFP electrospun separators, similar to Kim, et al. [281], but with 1 M LiBF₄ in EMIBF₄ IL electrolyte. The authors [282] observed fibre diameters between one and 3 µm with homogeneously dispersed SiO₂ nanoparticles. The highest porosity and electrolyte uptake were directly related to the highest ionic conductivity as seen with the 5% SiO₂ / PVDF-HFP separator. The electrolyte uptake of the SiO₂ / PVDF-HFP separators (460 to 470%) was noticeably higher than for the pristine PVDF-HFP separator (approximately 405%). Yang, et al. [282] found the crystallinity of the separator was lowered by the addition of SiO₂, which was also previously observed by Raghavan, et al. [280].

The 5% SiO₂ / PVDF-HFP separator was investigated with a 1 M LiBF₄ in EMIBF₄ IL electrolyte containing different amounts of DEC [282]. As expected, based on viscosities, the ionic conductivity increased in proportion with the amount of DEC additive in the electrolyte. During TGA studies the authors [282] observed that the separator wet with pure IL electrolyte was stable up to 318 °C (5% weight loss), while the separators wet with the IL and DEC electrolytes were only stable up to 94 °C, depending on the amount of DEC present in the electrolyte. However, this increase in thermal stability observed for pure IL electrolyte was at the expense of cell performance, which is lower in the absence of DEC additive.

Electrochemical studies were performed with the 5% SiO₂ / PVDF-HFP separator only so no comparison was made between the ceramic filled and the non-filled separator. Yang, et al. [282] showed that DEC additive increased the electrochemical stability of the system. Further, they suggested that the improved electrochemical properties were due to formation of a thin, stable SEI in the presence of the DEC additive that prevented further reaction between EMIBF₄ and the lithium electrode. In an LFP | Li cell the 5% SiO₂ / PVDF-HFP separator with pure IL electrolyte, Yang, et al. [282] saw serious capacity fade, however, the cell with DEC additive showed stable cycling performance.

Cell testing was also performed at elevated temperatures to determine the temperature effects on cell performance, with and without DEC additive in the electrolyte [282]. In a similar test, Cheruvally, et al. [279] saw enhanced performance with the 0.5 M LiTFSI in BMITFSI IL electrolyte by increasing the operating temperature from 25 °C to 40 °C, which resulted in lower viscosity and higher ionic conductivity of the IL electrolyte at the elevated temperature. For pure IL electrolyte at 55 °C with the SiO₂/ PVDF-HFP separator, increased operating temperature did not increase the performance, in fact a higher capacity fade was observed at higher operating temperatures [282]. Yang, et al. [282] suggested that EMIBF₄ was reacting with the lithium electrode and could not form a stable SEI film, consistent with their other findings regarding this electrolyte, and at higher temperatures the reaction rates were accelerated. In contrast, at 55 °C only a small amount of capacity loss was seen in the cell with the IL and DEC electrolyte. The authors [282] concluded that the electrospun 5% SiO₂/ PVDF-HFP separator is suitable for use with EMIBF₄ IL electrolyte with an organic solvent additive to stabilise the SEI film.

Lalia, et al. [283] investigated a PVDF-HFP electrospun separator containing a cellulose additive for mechanical reinforcement. Nanocrystalline cellulose was dispersed in the PVDF-HFP solution prior to electrospinning. The separators were tested with 1 M LiTFSI in P14TFSI IL electrolyte. The authors [283] observed a higher electrolyte uptake and correspondingly higher ionic conductivity in the cellulose PVDF-HFP separator. The contact angle was also measured, and although the PVDF-HFP separator already had a low contact angle with the IL electrolyte, the addition of cellulose resulted in an even lower contact angle. Lalia, et al. [283] hypothesised that the low contact angle combined with the high porosity would lead to an increased electrolyte retention in the cellulose PVDF-HFP separator, compared to the pure PVDF-HFP separator.

The storage modulus of the separator wet with electrolyte was determined with dynamic mechanical analysis, the storage modulus relates to the amount of elastic energy stored in a material [285]. The mechanical properties of a separator can change once it has been saturated with electrolyte [97, 286], therefore the mechanical properties of an electrolyte wet separator are likely to give a more realistic estimate of the mechanical properties of the separator in an assembled cell. Lalia, et al. [283] found that the cellulose additive increased the separator storage modulus by approximately 15% up to 90 °C. Above 90 °C, they found that the cellulose additive was no longer an advantage due to softening of the polymer. The change in storage modulus of the separators is shown in Figure 2.12 over a temperature range of 30 °C to 150 °C.

Figure has been removed due to Copyright restrictions.

Figure 2.12 Variation of storage modulus with temperature of PVDF-HFP and PVDF-HFP + 2 wt% NCC (non-crystalline cellulose) electrospun mats activated with 1 M LiTFSI in BMPyrTFSI (P14TFSI) electrolyte. Taken from Lalia, et al. [283].

CV showed reversible lithium plating and stripping and electrochemical stability up to 5 V in the cellulose PVDF-HFP separator. The cellulose PVDF-HFP separator was tested in an LFP | Li cell with IL electrolyte. Lalia, et al. [283] observed the discharge capacity increasing gradually during the first ten cycles at C/10. This behaviour is commonly seen in cells that are initially not sufficiently wet with electrolyte and gradually wet out during cycling as the electrodes and separator absorb the electrolyte. A reduced discharge capacity was observed at higher discharge rates, as is characteristic of higher viscosity electrolytes. No decrease in capacity was observed during extended cycling which suggests suitability of the separator and IL electrolyte for use in a lithium-ion cell.

Evidence of this stability was also seen by the capacity being fully recovered when the cell was discharged at C/10 following higher rate discharge [283]. This recovered capacity means that if a cell not designed for high rate discharge encounters a high rate discharge, the cell will not be irreversibly affected. The performance and mechanical properties of this separator are promising for application to lithium-ion batteries. Mechanical results, however, indicate that polymer softening occurs from 90 °C which is not ideal for applications with high thermal stability electrolytes. The thermal stability of these materials needs to be further investigated especially regarding lithium-ion cell safety.

In an attempt to increase separator wettability with ILs, Truong, et al. [95] investigated electrospinning of PVDF separators containing lithium salt additive. Manufacturing a separator containing the same salt as the IL electrolyte was hypothesised to increase the separator-electrolyte affinity. The authors [95] also investigated separator post treatments to increase mechanical stability through fibre cross-linking. Pure PVDF had the largest fibre diameter (600 nm) and the addition of LiTFSI to the electrospinning solution halved the fibre diameter (300 nm). Post-treated separators showed smaller fibre diameters again, 200 nm and 100 nm for ultraviolet- and thermally-crosslinked membranes, respectively. The commercial separator, Solupor was used for comparison.

Wetting was investigated with 0.7 M LiTFSI in P14TFSI IL electrolyte. The Solupor and pure PVDF separators showed similar wetting; after 30 minutes Truong, et al. [95] observed electrolyte still present on the separator surface. The LiTFSI / PVDF separator showed complete wetting within four minutes, supporting the authors' [95] hypothesis of enhanced wetting with a lithium salt additive. Complete wetting was observed for the post-treated separators in equivalent or less time which indicated the post-treatments were not detrimental to separator wetting. The electrospun separators had a higher porosity (approximately 90%), larger mean pore size and more uniform pore distribution than Solupor. Truong, et al. [95] suggested the larger pore size could account for

the increased wetting, however, they noted that surface interactions may also have contributed. The physical and wetting properties of these membranes are promising for lithium-ion cell separators however the ionic transport properties of the wet separator were not reported so comparison to other separators was not possible.

Truong, et al. [95] found the pure PVDF separator and LiTFSI / PVDF separators were not mechanically suitable for application as a separator. However, the post-treated separators had increased tensile strength, within the acceptable range for lithium-ion batteries mechanically superior to the commercial Solupor separator. Thermal analysis showed an increased thermal stability compared to Solupor for all electrospun separators excluding the ultraviolet crosslinked separator. The TGA and DSC curves for each separator are shown in Figure 2.13. This lower thermal stability in the UV cross-linked separator was attributed to incomplete cross linking of the tripropylenglycol diacrylate (TPGTA) [95].

The separators were assembled into Li | Li cells for electrochemical testing and the surface morphology of the fibre and membrane surfaces observed via SEM before and after cycling [95]. Both Solupor and pure PVDF had altered morphologies after cycling, suggesting they had interacted with the electrolyte. Fibre swelling observed in the PVDF separator could be evidence of the electrolyte acting as a slight solvent to the polymer, which suggests poor life for this separator in a cell. The LiTFSI / PVDF separator and both post-treated separators showed no indication of changed morphology after cycling. The cross-linking in the post-treated separators appears to have maintained the membrane morphology during cycling, which is highly desirable for long-life in a lithium-ion cell.

Figure has been removed due to Copyright restrictions.

Figure 2.13 Thermogravimetric analysis (left) and DSC (right) of the separators. Taken from Truong, et al. [95].

The cell resistance with cycling was used to indicate performance [95]. The LiTFSI / PVDF separator performed better than the pure PVDF which the authors [95] suggested was due to favourable interactions allowing more electrolyte to be contained within the pores. The ultraviolet crosslinked separator showed an extremely high resistance indicating the post-treatment has a negative effect on electrochemical performance. The thermally crosslinked separator showed stable cycling and the lowest resistance. Truong, et al. [95] suggested the thermally crosslinked PVDF separator containing LiTFSI may be applicable to IL batteries. Cell tests were conducted in symmetrical Li | Li cells to reduce the effects of complex cell reactions for comparison of the separators. It is suggested that investigations with composite electrode materials would help to

determine the suitability of the thermally crosslinked separator for lithium-ion batteries.

Mechanical properties of the novel separators were consistently lower than microporous commercial separators. Lower mechanical properties may become an issue during manufacture of the cells, any damage or rupture that occurs to the separator during cell assembly will likely result in a short circuit in the cell. Therefore, an appropriate mechanical strength is necessary for a separator to become a competitive alternative to existing commercial separators. The tensile strength at 30 °C of the materials for which mechanical properties were reported can be ranked as follows: Celgard PP (114.03 MPa) [105] > electrospun PAN (16.39 MPa) [105] > electrospun PVDF-HFP and cellulose (8 MPa) [283] > microporous PVDF (6.4 MPa) [277] > electrospun PVDF and LiTFSI (6.33 MPa) [95] > electrospun PVDF (1.54 MPa) [95]. It is postulated that the mechanical properties of novel separator may be improved through the use of post-treatments, as shown by Truong, et al. [95], and this would be a necessary development step for any novel separator being considered for commercial applications.

2.3 Conclusion

Published studies of separator materials for use in conventional electrolyte and IL electrolyte lithium-ion batteries have been discussed in this review. Among the IL electrolyte papers reviewed, microporous separators consistently demonstrated a lower porosity than nonwoven separators, which is expected given the open pore structure in nonwoven membranes. IL electrolyte uptake increased with porosity in the separators without additives, however, in separators with additives the electrolyte uptake appeared to more strongly relate to the additive-electrolyte affinity. The IL electrolyte separators were tested mainly with IM^+ (TFSI⁻ or BF₄⁻ anion) or Pyr⁺ (TFSI⁻ anion) ILs and electrolytes thereof. Separators using hydrophilic materials were studied due to their favourable wetting characteristics with IL electrolytes. All the studies found that porosity, pore structure and surface properties have a strong influence on separator wetting.

For the reviewed separators, the nonwoven separators containing electrolyte had consistently higher ionic conductivities compared to microporous separators tested with the same electrolyte. The high porosity and open pore structure of nonwoven separators appear to maximise transport properties of the IL electrolytes. Separators containing ceramic additives showed consistently higher ionic conductivities than those without for IM^+ based electrolytes [280, 281]. Whereas, with Pyr⁺ based electrolytes, PAN based separators appeared to facilitate the highest conductivities, this did not necessarily correlate with highest electrolyte uptake values.

Separators using LiTFSI P14TFSI showed ionic conductivities ranging from 0.006 mS cm⁻¹ (0.37 M

LiTFSI) for a microporous separator with 30% porosity up to 3.6 mS cm^{-1} (1 M LiTFSI) for a nonwoven separator with 86% porosity. Of note, the PAN separators with Pyr⁺ based electrolytes had conductivities an order of magnitude greater than PVDF or co-polymer based separators with the same electrolyte. This could suggest a better affinity of IL electrolyte with PAN over PVDF and co-polymers, but could also be indicative of more favourable membrane morphologies obtained with one material over another. However, as the lithium salt concentration in the electrolyte were not constant across all papers, the conductivities are not directly comparable between studies.

Overall, there is a stronger correlation between ionic conductivity and membrane porosity than any other property, including electrolyte type. This highlights the impact separator porosity can have on cell performance even though the separator is not an active material in electrochemical reactions. The electrochemical stability of the separators appears to be related to electrolyte type. Additionally, within each electrolyte type, separators incorporating ceramic additives showed higher electrochemical stabilities due to the activity of the IL being reduced by the presence of the ceramic nanoparticles [99, 280]. This suggests that a ceramic separator may be a part of the separator answer for IL electrolytes.

Since IL electrolytes offer a wider operating temperature range it is important for the separators being developed to have a high thermal stability to take advantage of the enhanced thermal properties. Thermal stability of the materials reviewed can be ranked based on the melting temperatures reported: PMMA-AN-VAc > PVDF-HFP and PMMA blend > PVDF electrospun pristine and with lithium salt additive > PVDF-HFP pristine and with ceramic additive > PE commercial separator > PVDF-TRFE > PVDF microporous. The thermal properties of a PAN based separator were unfortunately not reported in the reviewed studies.

The mechanical properties of the developed separators were lower than commercial separator products. The tensile strength at 30 °C of the materials for which mechanical properties were reported can be ranked: Celgard PP (114.03 MPa) [105] > electrospun PAN (16.39 MPa) [105] > electrospun PVDF-HFP and cellulose (8 MPa) [283] > microporous PVDF (6.4 MPa) [277] > electrospun PVDF and LiTFSI (6.33 MPa) [95] > electrospun PVDF (1.54 MPa) [95]. Appropriate mechanical strength is necessary for a separator product to become a competitive alternative.

Among the studies reviewed mechanical properties are the least reported. This could be due to the design priorities for separators; i.e. the morphological, transport and electrochemical properties that effect cell performance are determined first to decide if the material is suitable for further development. Many studies have not presented the secondary - mechanical and thermal - properties that effect cell safety. For a separator material to be recommended for use in a lithium-ion cell, all properties need to be investigated.

The challenge of a suitable separator material for IL electrolytes has not been solved yet. Based on the reported studies the solution will most likely require a combination of a high thermally / mechanically stable polymer, ceramic additives and an optimised manufacturing process to produce a suitable separator. A novel separator for an IL electrolyte will be presented in Chapter 3 and Chapter 4. The separator morphology, porosity, wettability and ionic conductivity will be investigated in Chapter 3, along with thermal and mechanical stability. The electrochemical and cycling performance of the separator with an IL electrolyte cell will be investigated in Chapter 4.

The use of IL electrolytes in the cell is expected to increase the decomposition temperature of other cell materials [287]. This hypothesis will be investigated in Chapter 5 with different separator and electrode materials. Materials with increased thermal stability may delay self-heating reactions and therefore suppress thermal runaway from occurring in a cell [288, 289]. For these properties to improve the safety of a cell it must be coupled with a separator that also has an increased thermal stability to allow the cell cooling to take effect and decrease heat accumulation within the cell. The novel separator should have a thermal dimensional stability above the decomposition temperatures of individual components to ensure it can maintain electrical isolation between the electrodes under abuse conditions, therefore delaying an internal short circuit that may lead into thermal runaway. The thermal runaway process in an IL electrolyte lithium-ion cell will be investigated in Chapter 6.

CHAPTER 3

Properties of the Novel Separator

3.1 Introduction

Ionic liquid (IL) electrolytes are suggested as safer electrolyte alternatives due to their low volatility and flame retardant properties, as discussed in Chapter 1. A separator with increased thermal stability would allow separation of the electrodes to be maintained at higher temperatures, compared to commercial polyolefin based separators, which the cell may experience under abuse conditions. A higher melting temperature for the separator provides a larger time frame for engineering and software controls to take effect before the cell reaches a critical temperature and enters thermal runaway. Combining IL electrolyte with an enhanced separator material is hypothesised to increase cell safety by delaying the temperature of an internal short circuit occurring from separator melting.

Despite the benefits of increased electrochemical and thermal stability, IL electrolyte compatibility with commercial separator products is generally poor [17, 18, 96], leading to a decrease in electrochemical performance with current separator materials. To avoid this, new separator materials must be developed to achieve good separator wetting for IL electrolytes in lithium-ion batteries. In this chapter, the compatibility of an IL electrolyte with a range of commercial separators will be characterised to compare wettability of different materials and membrane types. A commercial IL electrolyte product will be investigated in this thesis, based on the pyrrolidinium (Pyr^+) cation and the bis(fluorosulfonyl)imide (FSI^-) anion with dissolved lithium bis(fluorosulfonyl)imide (LiFSI), otherwise known as N-methyl-N-propyl-pyrrolidinium bis(fluorosulfonyl)imide (P13FSI) electrolyte, ILs of which are known to have a wide electrochemical window and relatively high conductivity [290, 291].

The wetting of a selection of commercial separators with P13FSI electrolyte will be investigated through contact angle measurements. Then a new polymer membrane for use as a separator in lithium-ion cells with the same electrolyte will be suggested based on the lithium-ion separator materials and manufacturing processes, reviewed in Chapter 2. Considering the high thermal stability and IL electrolyte compatibility of the separator discussed above, a novel separator was developed (Figure 3.14): polyacrylonitrile (PAN) coated with electrospun poly(vinylidene fluoride-hexafluoropropylene) (PVDF-HFP) containing different concentrations of lithium salt. The commercial PAN electrospun membrane was selected from the polymers in Table 2.7 due to good mechanical and thermal properties as well as high affinity with IL electrolytes, shown in Section 2.2.4.

On either side of the PAN support, a layer of electrospun PVDF-HFP containing a lithium salt was applied. PVDF-HFP was selected for electrospinning due to a good affinity with IL electrolytes and flexibility of processing, discussed in Sections 2.2.3 and 2.2.4. The lithium salt additive in the

electrospinning solution was hypothesised to further improve IL electrolyte affinity and retention as well as providing increased electrode-electrolyte interphase stability in an IL electrolyte cell, discussed in Section 2.2.4.2. Electrospinning was selected to produce a multi-layer membrane with suitable thickness and morphology for use as a separator. Electrospinning was used due to the range of possible material combinations and the ability to control the fibre and membrane morphology, discussed in Section 2.2.2.2.

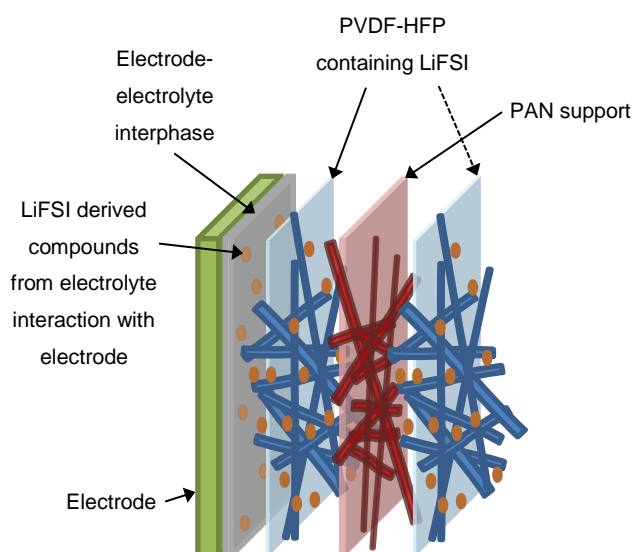


Figure 3.14 Schematic of novel separator with multi-layer design. PAN = polyacrylonitrile, PVDF-HFP = poly(vinylidene fluoride-hexafluoropropylene), and LiFSI = lithium bis(fluorosulfonyl)imide.

In Chapter 2 the ideal properties for a lithium-ion cell separator were discussed (Section 2.2.1). Therefore, the novel separator properties will be characterised against these properties to assess the suitability of the final structure as a separator material. The aim of this chapter was to develop a novel separator and evaluate the physical, thermal, mechanical and wetting properties. In this chapter the following physical properties of the novel separator will be evaluated to determine suitability of the separator to a P13FSI electrolyte lithium-ion cell: thickness, pore size and structure, porosity, fibre diameter distribution, tensile strength, thermal stability and wetting characteristics with IL electrolyte. Wetting characteristics were determined by examining contact angle, electrolyte wicking rate, electrolyte uptake and ionic conductivity results. The electrochemical properties and cycling performance of the novel separator with P13FSI electrolyte assembled into a cell will be evaluated in Chapter 4.

3.2 Experimental

PVDF-HFP containing different concentrations of lithium salt was electrospun onto a PAN support membrane and evaluated for use as a separator in an IL electrolyte lithium-ion cell. The materials, preparation method and characterisation techniques employed are outlined below.

3.2.1 Materials

PVDF-HFP (average Mw ~455,000) pellets were purchased from Sigma-Aldrich (USA). LiFSI (>99.5% purity) was purchased from CoorsTek Fluorochemicals (USA). Lithium bis(trifluoromethanesulfonyl)imide (LiTFSI) was purchased from 3M (USA). Lithium trifluoromethanesulfonate (LiTf, 99.995% purity) was purchased from Sigma-Aldrich (USA). Dimethylformamide (DMF, 100 ppm, 99.9% purity) was purchased from RCI Labscan Limited (Thailand). Acetone (analytical reagent grade, 99.8% purity) was purchased from Chem-Supply Pty Ltd (Australia). N,N-Dimethylacetamide (DMAc, ReagentPlus, 99%) was purchased from Sigma-Aldrich (USA). These materials were used as received to produce the electrospinning solutions, since electrospinning was undertaken in a lab environment, material drying before mixing the solution was not necessary.

The IL electrolyte was a commercial product containing 1-methyl-3-propylpyrrolidinium bis(fluorosulfonyl)imide (P13FSI) with 1.17 mol kg^{-1} LiFSI in P13FSI (P13FSI electrolyte, >99.5% purity) also purchased from CoorsTek Fluorochemicals (USA). P13FSI electrolyte was used as received from the manufacturer, the electrolyte was transferred into the glovebox in the sealed condition from the manufacturer therefore material drying was not necessary.

Nanofibrous PAN support membrane (NnF MBRANE - PAN, typical fibre diameter 200-600 nm, grammage $0.5\text{-}15 \text{ g m}^{-2}$) was purchased from Pardam, s.r.o (Ltd.) (Czech Republic). Glass fibre (GF) membrane (GA558X10IN, Advantech) was purchased from Sterlitech Limited (USA). Commercial polypropylene separators Celgard 3501 and Celgard 2400 were purchased from Celgard, LLC (USA). Commercial ultra-high molecular weight polyethylene (UHMWPE) separator (Solupor 7P03A) was purchased from Lydall Inc. (The Netherlands). Commercial ceramic coated polyethylene terephthalate (PET) nonwoven separator (SEPARION S240 P30) was purchased from LITARION GMBH (Germany). Commercial nonwoven separators Dreamweaver Gold and Silver were purchased from Dreamweaver International (USA). Separator materials were dried overnight in a vacuum oven at $50 \text{ }^\circ\text{C}$ before use.

3.2.2 Commercial separator wettability

To confirm the requirement of alternate separator materials for use with IL electrolytes, the wettability of P13FSI electrolyte on six commercial separators was measured with the contact angle method [17, 18]. Contact angle was measured with a Pocket Goniometer (PG-3, FIBRO System AB, Sweden) at CSIRO (Clayton, VIC) using a manual drop applicator. Material samples were cut into strips approximately one by 12 cm and taped onto stiff plastic to aid sample loading on the goniometer stage. The prepared material strips along with the goniometer were transferred inside an argon atmosphere glovebox ($H_2O < 100$ ppm, $O_2 < 50$ ppm) at CSIRO (Clayton, VIC) and P13FSI electrolyte was loaded into the manual drop applicator. The Pocket Goniometer was operated in static and dynamic modes with image capture automatically triggered when the drop touched the separator surface. The images shown are the first image captured for each sample. Three measurements were performed for each separator type. The dynamic contact angle of P13FSI electrolyte on each commercial separator will be used to assess their compatibility.

3.2.3 Separator preparation

The separators were prepared via electrospinning method [210, 221, 241, 249, 292], introduced in Section 2.2.2.2. To make up the electrospinning solutions, PVDF-HFP and the lithium salt additive were dissolved in the solvents DMF / acetone (7:3 weight/weight (w/w)) or DMAc (100%). The solution was 10 wt% PVDF-HFP and 90 wt% solvent, plus lithium salt additive of 0 wt%, 0.5 wt%, 1 wt% or 2 wt% of PVDF-HFP weight. The solution ingredients were weighed into a schott bottle and after adding a Polytetrafluoroethylene (PTFE) magnetic stirring bar the bottle was sealed with paraffin. The sealed solution bottle was placed on a hot plate at 75 °C with a magnetic stirrer for four days to ensure the polymer and salts were dissolved before electrospinning.

Electrospinning was conducted with a Nanofiber Electrospinning Unit using a rotating collector drum (NEU-01, NaBond Technologies Co., Limited, China) at Flinders (Tonsley, SA). A 20 by 20 cm piece of PAN support was cut and taped to aluminium foil. The foil was then wrapped around the collector drum with the PAN support facing out. The polymer solution was loaded into the syringe and connected to the syringe pump. The syringe needle was connected to an arm with 19 cm axial slide along the length of the drum. The needle arm was aligned at a 90° angle to the collector drum and with a distance of 12 cm from the needle tip to the drum surface. The flow rate and applied voltage were set to the values outlined in Table 3.10.

Table 3.10 Electrospinning process variables

	Separator	Salt	Salt, wt% of polymer	Solvent	Flow rate, mL hour ⁻¹	Applied voltage, kV	Spinning time per side, hours
FSI separators	FSI-0	LiFSI	0	DMF/acetone	1.6	15	2.0
	FSI-A	LiFSI	0.5	DMF/acetone	0.7	18	2.0
	FSI-B	LiFSI	1.0	DMF/acetone	0.6	18	2.0
	FSI-C	LiFSI	2.0	DMF/acetone	0.5	18	2.0
	TFSI-B	LiTFSI	1.0	DMF/acetone	0.6	18	2.0
DMAc separators	TFSId	LiTFSI	1.0	DMAc	0.8	15	1.5
	FSId	LiFSI	1.0	DMAc	0.9	15	1.5
	Tfd	LiTf	1.0	DMAc	0.8	15	1.5

Electrospinning was performed for the spinning time indicated in Table 3.10. Then aluminium foil containing the polymer coated PAN was removed from the drum. The polymer coated PAN was transferred onto a new piece of aluminium foil with the uncoated PAN facing out. The electrospinning process was repeated to obtain an equal layer on both sides of the PAN support.

3.2.4 Separator characterisation

Characterisation of properties is critical to determining the suitability of the novel separator for use in a lithium-ion cell. The morphology, mechanical properties, thermal stability and wetting characteristics of the novel separator were investigated using the methods outlined below.

3.2.4.1 Separator morphology

Separator morphology was imaged using a Scanning Electron Microscopy (SEM) with an Energy Dispersive X-Ray (EDX) Analyser (MX2500, CAMScan, USA) at Flinders (Tonsley, SA) with an accelerating voltage of 2 kV and a spot size of 3. Prior to SEM the separator samples were sputter coated with platinum (K757X Sputter coater, Emitech, UK) at Flinders (Tonsley, SA). The DMAc, GF and PAN separators were coated with 5 nm platinum (coarser features) while the separators containing LiFSI salt were coated with 2 nm platinum (finer features). The separators prepared in this work were imaged on the aluminium collection foil from electrospinning to decrease disruption of the fibre morphology before SEM imaging and mounted on the SEM stump with double-sided carbon tape. EDX was performed during SEM on FSI-A, FSI-B, FSI-C and GF with an accelerating voltage of 10 kV and a spot size of 5.5, with distribution mapping of elements: carbon, oxygen, fluorine, aluminium, silicon and sulphur. From the SEM images, fibre diameters were measured with ImageJ software line segment and measurement tools. The diameter of every fibre appearing at the surface in the image was measured to gain a representative distribution of fibre diameter over the separator surface, typically more than 50 fibre diameter measurements per SEM image

capture.

3.2.4.2 Thickness measurement

Separator thickness was measured with a Digital Indicator, 0-25 mm, 0.001 mm (S229, Sylvac, Switzerland) at CSIRO (Clayton, VIC). Two electrospun sheets were produced for the separators containing LiFSI salt prepared in this work. The thickness of each electrospun separator sheet was measured at four points distributed over the sheet. The total sheet thickness was measured with the separator was still on the aluminium collection foil to reduce disruption of the separator layers before measurement. The bare aluminium foil thickness was measured. Separator thicknesses were calculated from the difference in thickness between the sheet and the bare foil. The thickness was determined from the average of all measurements for each separator type.

3.2.4.3 Pore Size distribution

The pore size distribution was measured with a Capillary Flow Porometer (CFP-1500AEXIH, Porous Materials, Inc., USA) at CSIRO (Clayton, VIC). Material samples were stamped into 12.7 mm diameter discs and loaded into the porometer. The sample was saturated with Galwick (approximately seven drops, surface tension 15.9 dynes cm⁻¹, Porous Materials, Inc., USA). The pressure limits were set as 1.0 to 35.0 PSI for the measurement. At least three repetitions were tested for each separator type using a fresh material sample for each test, except GF for which only one repetition was obtained due to the brittleness of the membrane under high pressures. The pore size distribution of PAN was not able to be measured with the porometer due to the thinness of the membrane. Pore size estimates for the PAN support and DMAc separators were obtained by measuring pore diameters in the SEM images with ImageJ software line segment and measurement tools. The diameter of each pore appearing at the surface in the image was measured to gain a representative distribution of pore diameter over the separator surface. There were at least 30 pore diameter measurements in one SEM image capture.

3.2.4.4 Porosity measurement

Porosity of the separators was determined using the known material densities along with the mass and volume of separator samples [105]. Separator porosity was calculated with **Eq. (1)**:

$$\varepsilon = 1 - \frac{V_{polymer}}{V_{membrane}} \quad \text{Eq. (1)}$$

where ε is porosity, $V_{polymer}$ is the volume occupied by polymer and $V_{membrane}$ is the total volume of the membrane. The calculations were obtained from two by two cm square of separator with two repetitions for each separator type. $V_{membrane}$ was calculated from the area and thickness of the sample. $V_{polymer}$ was calculated by determining the volume occupied by the polymer from material densities and the sample weight. To account for the layered structure in the electrospun

separators, the known weight of the PAN layer was subtracted to determine the weight of the PVDF-HFP and LiFSI electrospun layers on each separator. Material densities for calculations were: PAN (1.184 g cm⁻³), PVDF-HFP (1.78 g cm⁻³), LiFSI (2.32 g cm⁻³) and SiO₂ (2.65 g cm⁻³). GFs were assumed to have a density equal to SiO₂ for these calculations.

3.2.4.5 Tensile testing

Tensile properties were determined from a stress-strain test performed on an Instron 5500R Frame (Instron, Illinois Tool Works, USA) at CSIRO (Clayton, VIC), controlled by Instron Bluehills 3 software (version 3.3), with a 10 N load cell at a strain rate of 10 mm min⁻¹. Testing was performed at 23 °C and 50% relative humidity. The samples were conditioned for at least 48 hours prior to testing. Air clamps were used to grip the samples during testing. The materials were cut into dog bone samples with 4.3 mm width and 12 mm length (gauge length). A minimum of five samples were tested for each material.

3.2.4.6 Thermal testing

Thermal analysis was performed using Simultaneous Thermal Analysis (STA) with a PerkinElmer STA8000 at Flinders (Bedford Park, SA). The samples were tested from 40 to 700 °C at a heating rate of 10 °C min⁻¹ with a nitrogen purge gas. Sample weight was between 7 and 8 mg. The samples were not dried prior to STA analysis, therefore evaporation of absorbed moisture from the polymer matrix was expected towards the beginning of the heating stage. The PerkinElmer Pyris software was used to calculate mass loss and heat release for each thermal event.

3.2.4.7 Thermal dimensional stability

For thermal dimensional stability testing, separator samples were cut into five by five cm squares and placed on aluminium foil with 25 cm² area marked for each sample. Each sample was photographed alongside a ruler to obtain sample measurements. The aluminium foil was placed inside an oven heated to 150 °C. When the oven stabilised at 150 °C again after sample insertion, a timer was set for 60 minutes. After 60 minutes the samples were removed and photographed again alongside a ruler. ImageJ was used to measure the sample dimensions. The same ruler was used in each photo to set the scale. The length of each edge of the square was measured to obtain the sample dimensions before entering the oven. The measurements were repeated after oven exposure, the length of each edge was measured by point-to-point measurement assuming a straight line in between (curved edges not accounted for in length measurements). The thermal shrinkage was calculated with **Eq. (2)**:

$$S = \frac{A_b - A_a}{A_b} \times 100 \quad \text{Eq. (2)}$$

where S is shrinkage (%), A_b and A_a are the sample areas (cm²) before and after oven exposure,

respectively.

3.2.4.8 Contact angle and electrolyte uptake measurement

Contact angle was measured as described previously in Section 2.2.1 *Wettability*.

For electrolyte uptake tests, two by two cm squares of separator sample were cut and placed in a vacuum oven at 50 °C overnight to dry before being transferred into an argon atmosphere glovebox (H₂O <100 ppm, O₂ <50 ppm) at CSIRO (Clayton, VIC). The dried samples were weighed in individual weighing pans. 1 mL of P13FSI electrolyte was added to the centre of each sample and the samples were left to soak for 12 hours. After 12 hours, the samples were taken out and excess electrolyte was removed by dabbing both sides with KimWipes. The wet samples were weighed. The electrolyte uptake % was calculated with **Eq. (3)** [293]:

$$EU = \frac{M_{wet} - M_{dry}}{M_{dry}} \times 100\% \quad \text{Eq. (3)}$$

where EU is the electrolyte uptake %, and M_{dry} and M_{wet} are the sample weight before and after wetting, respectively. Five replicates were performed per separator sample. Due to the gel-like behaviour of the PVDF-HFP electrospun layer, separator integrity was not well maintained after wetting with P13FSI electrolyte, therefore electrolyte retention experiments could not be performed.

3.2.4.9 Wicking rate testing

For electrolyte wicking rate tests a one by five cm strip of separator material was cut. The strips were placed upright in glass vials and secured at the top edge with a paper clip to ensure the end of the strip was flush with the bottom of the glass vial. A mark was placed on the side of the vial at a vertical height of 4 cm. The glass vials with mounted separator samples were dried in a vacuum oven overnight before taking them into an argon atmosphere glovebox (H₂O <100 ppm, O₂ <50 ppm) at CSIRO (Clayton, VIC) for testing with the P13FSI electrolyte. 1 mL of electrolyte was added to the vial and the time was recorded. The electrolyte volume ensured 1 to 2 mm of the strip was submerged for the wicking process. The samples were observed until the wicking height reached the 4 cm indicator on the vial and the time was recorded. The wicking rate was calculated with **Eq. (4)**:

$$W_{rate} = \frac{h}{t} \quad \text{Eq. (4)}$$

where W_{rate} is the wicking rate in cm h⁻¹, h is the height in cm and t is the time in hours. Two replicates were performed per separator type.

3.2.4.10 Ionic conductivity measurement

The separators were cut into 15.9 mm diameter disks and dried overnight in a vacuum oven at

50 °C before transferring into an argon atmosphere glovebox (H₂O <100 ppm, O₂ <50 ppm) at CSIRO (Clayton, VIC). Once inside the glovebox, the separators were assembled into symmetrical coin cells (CR2032 coin cells) with stainless steel (coin cell spacer, 16 mm diameter) electrodes. 150 µL of P13FSI electrolyte was added directly onto the separator surface during coin cell assembly. Within one hour of assembly, the coin cells were removed from the glovebox and tested at room temperature on a potentiostat (VMP3, BioLogic Science Instruments, France) at CSIRO (Clayton, VIC). The potentiostat was configured for a two-electrode cell with the reference electrode lead piggybacked onto the counter electrode lead. The cells underwent Electrochemical Impedance Spectroscopy (EIS) with an amplitude of 10 mV from 0.1 MHz to 0.1 Hz. The cells were scanned at least three times each to obtain multiple measurements per sample. Equivalent circuit fitting, using Randles circuit, was performed with Z Fit (EC-Lab V11.16, BioLogic Science Instruments, France) to determine the bulk (electrolyte and separator) resistance. The conductivity was calculated with **Eq. (5)** [293]:

$$\sigma = \frac{d}{R_{bulk}A} \quad \text{Eq. (5)}$$

where σ is the conductivity, d is the separator thickness, R_{bulk} is the bulk resistance and A is the sample area. The MacMullin Number (N_M) was calculated with **Eq. (6)** [105]:

$$N_M = \frac{\sigma_{ele}}{\sigma} \quad \text{Eq. (6)}$$

where σ is the conductivity of the separator and P13FSI electrolyte (calculated in **Eq. (5)**), σ_{ele} is the conductivity of P13FSI electrolyte (6.6 mS cm⁻¹ at 25 °C, from manufacturers datasheet). The tortuosity was calculated with **Eq. (7)** [293]:

$$\sigma = \sigma_{ele} \frac{\varepsilon}{\tau^2} \quad \text{Eq. (7)}$$

where, ε is the porosity (calculated in **Eq. (1)**) of the separator and τ is the tortuosity.

3.3 Results and discussion

3.3.1 Commercial separators

The wetting properties of a separator with electrolyte can have a strong influence on the cell performance, particularly when incomplete wetting occurs. The contact angle of an electrolyte drop on the surface of a separator can be representative of the electrolyte-separator affinity [17, 18], the lower the contact angle the greater the affinity. Six commercial separators were investigated for

wettability with P13FSI electrolyte. Two Celgard separators were selected: Celgard 2400, which has been widely evaluated in literature [172, 175, 195, 220, 232, 235, 253, 294-298], and Celgard 3501, which is a surfactant-coated material for rapid wetting. Solupor [95, 199, 299-301], Separion [17, 89, 96, 102, 106, 302-304] and Dreamweaver Gold and Silver [305-307] were also selected to compare different materials and membrane types. Manufacturer data sheets for commercial separators can be found in Appendix B. The material, thickness, porosity and contact angle is shown in Table 3.11 for six commercial separators and Figure 3.15 shows the dynamic contact angle results with P13FSI electrolyte (images in Appendix C).

Table 3.11 Properties of six commercial separators including material, thickness, porosity and contact angle (time = 0.2, 2 and 10 seconds) with P13FSI electrolyte.

Separator	Membrane type	Materials	Thickness*, µm	Porosity*, %	Contact Angle, °		
					0.2 seconds	2 seconds	10 seconds
Dreamweaver Silver40 (DW Silver)	Nonwoven	Micro- and nanofibres blend, including PAN nanofibres	29	53	50 ±1	28 ±4	19 ±4
Dreamweaver Gold40 (DW Gold)	Nonwoven	Micro- and nanofibres blend, including para-aramid fibres	40	68	54 ±2	29 ±2	22 ±3
Separion S240P30	Nonwoven, ceramic coated	Polyethylene terephthalate (PET) / Al ₂ O ₃ +SiO ₂	30	> 40	74 ±1	46 ±1	33 ±6
Solupor 7P03A	Microporous	UHMWPE fibrils	50	85	91 [§]	73 ±3	70 ±5
Celgard 3501	Microporous	Polypropylene (PP) monolayer + surfactant coated	25	55	79 ±3	74 ±3	73 ±3
Celgard 2400	Microporous	PP monolayer	25	~ 40	79 ±9	80 ±2	78 ±2

* from manufacturer data sheets, shown in Appendix B

§ only one measurement captured at 0.2 seconds

The contact angles of Celgard 2400 and Solupor with conventional electrolytes have been reported in the literature. Martinez-Cisneros, et al. [301] found contact angles of 70° and 68° for Celgard 2400 and Solupor 10P05A, respectively, with 1 M lithium hexafluorophosphate (LiPF₆) ethylene

carbonate (EC) / dimethyl carbonate (DMC) (1:1 w/w) electrolyte. The contact angle of water on these two separators was also reported, 111° and 124° for Celgard 2400 and Solupor 10P05A, respectively [301]. From these results the authors [301] concluded that the polyethylene (PE) separator (Solupor) was more hydrophobic than the polypropylene (PP) separator (Celgard). As only a single contact angle value was reported and static or dynamic method was not stated, it is assumed that the contact angles reported by Martinez-Cisneros, et al. [301] were from the first captured image after the drop made contact with the separator. Interestingly, the contact angle for Celgard 2400 with same electrolyte was reported to be approximately 20° by Xie, et al. [253], this elucidates the variability in contact angle depending on the measurement method. Dynamic contact angle measurements are useful for substrates in which liquid absorption is expected; static contact angle measurements if that case could vary greatly depending on the time between liquid contact and the angle measurement. Therefore, comparison to contact angles reported in literature should not be done without noting the method and time frame of angle measurement. Contact angles for Celgard 3501, Separion and Dreamweaver separators with conventional electrolytes could not be located in the literature.

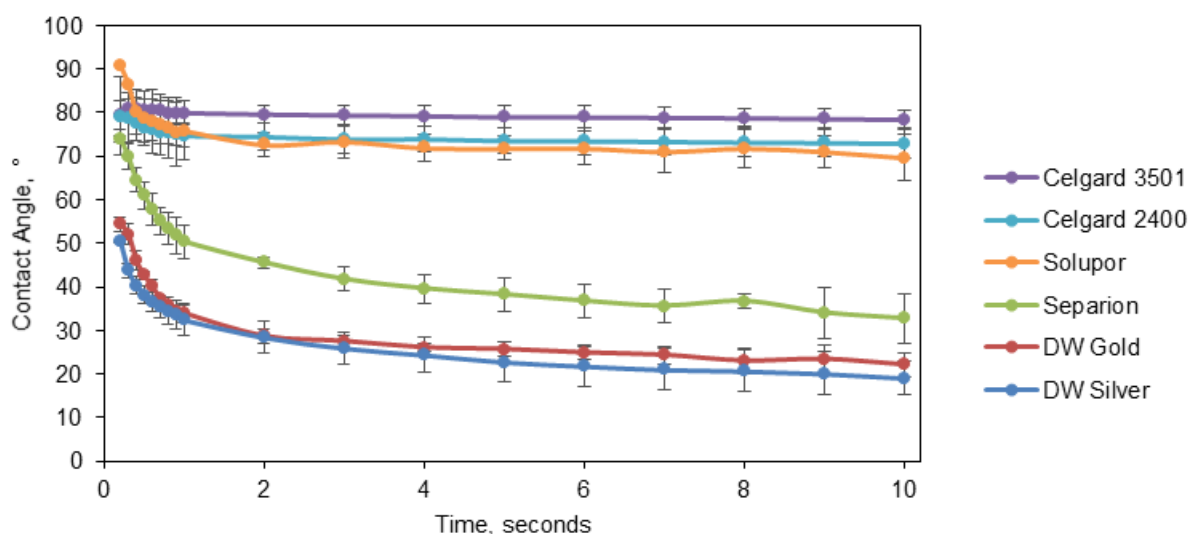


Figure 3.15 Dynamic contact angle measurements for commercial separators with P13FSI electrolyte.

In this work the highest contact angles were on Celgard 3501, Celgard 2400 and Solupor separators, which all had contact angles greater than 70°, measured two seconds after the drop was placed on the surface. The contact angles of Celgard 3501, Celgard 2400 and Solupor, shown in Figure 3.15, remain constant from approximately two seconds with very little gradual wetting observed, suggesting poor wetting with P13FSI electrolyte.

The third best wetting separator was Separion which had a contact angle of 46° at time = 2 seconds. Initially, there is a rapid decrease of the contact angle on Separion in the first second to approximately 50° , after this the contact angle continues to decrease slowly to approximately 33° at ten seconds (Figure 3.15); this indicates gradual wetting of the separator with P13FSI electrolyte. The improved wetting of Separion with P13FSI electrolyte, compared to the polyolefin separators (Celgard 3501, Celgard 2400 and Solupor), is not surprising considering the hydrophilic and hydrophobic surface properties, respectively, of these separators [96]. The contact angles of different separators with pyrrolidinium (Pyr^+) and bis(trifluoromethanesulfonyl)imide (TFSI $^-$) based ILs and IL electrolytes have been reported by Stefan, et al. [17] and Kirchhöfer, et al. [96], in both cases the authors report better wetting of Separion, over the polyolefin separators with Pyr^+ based ILs and electrolytes. Kirchhöfer, et al. [96] attributed this to the hydrophilic SiO_2 surface of Separion.

The best wetting was seen on the Dreamweaver separators with contact angles of 28° and 29° for Silver and Gold, respectively, at time = 2 seconds. The higher wetting of the Dreamweaver separators is likely due to a combination of the open porosity facilitating fast wetting [96] and the hydrophilicity of aramids [256, 272] giving the separators a higher affinity for IL electrolytes. Similar to Separion, the Dreamweaver separators also show gradual wetting with P13FSI electrolyte, with the contact angles approximately 34° after one second and decreasing to 19° and 20° after ten seconds, for Silver and Gold, respectively.

Although the Dreamweaver separators showed the best wetting, there was still electrolyte left on the separator surface after ten seconds, which indicates that a separator with better wetting and wicking properties could be developed for use with P13FSI electrolyte.

3.3.2 Novel separator characterisation

3.3.2.1 Separator morphology

The morphology of GF, PAN support and the electrospun separators FSI-0, FSI-A, FSI-B and FSI-C is shown in Figure 3.16. The GF membrane (Figure 3.16a) shows a much larger fibre size and corresponding pore size compared to the electrospun separators. The variation in fibre and pore sizes visible in Figure 3.16a suggests high non-uniformity across the GF membrane surface. There are also fractured fibres visible indicating a brittle membrane, which is to be expected of GFs. EDX was performed on GF during SEM imaging to confirm the composition of GFs (results in Appendix D). The majority of fibres appear to be composed of SiO_2 , with silicon and oxygen accounting for approximately 44 and 40 atomic% of the surface, respectively.

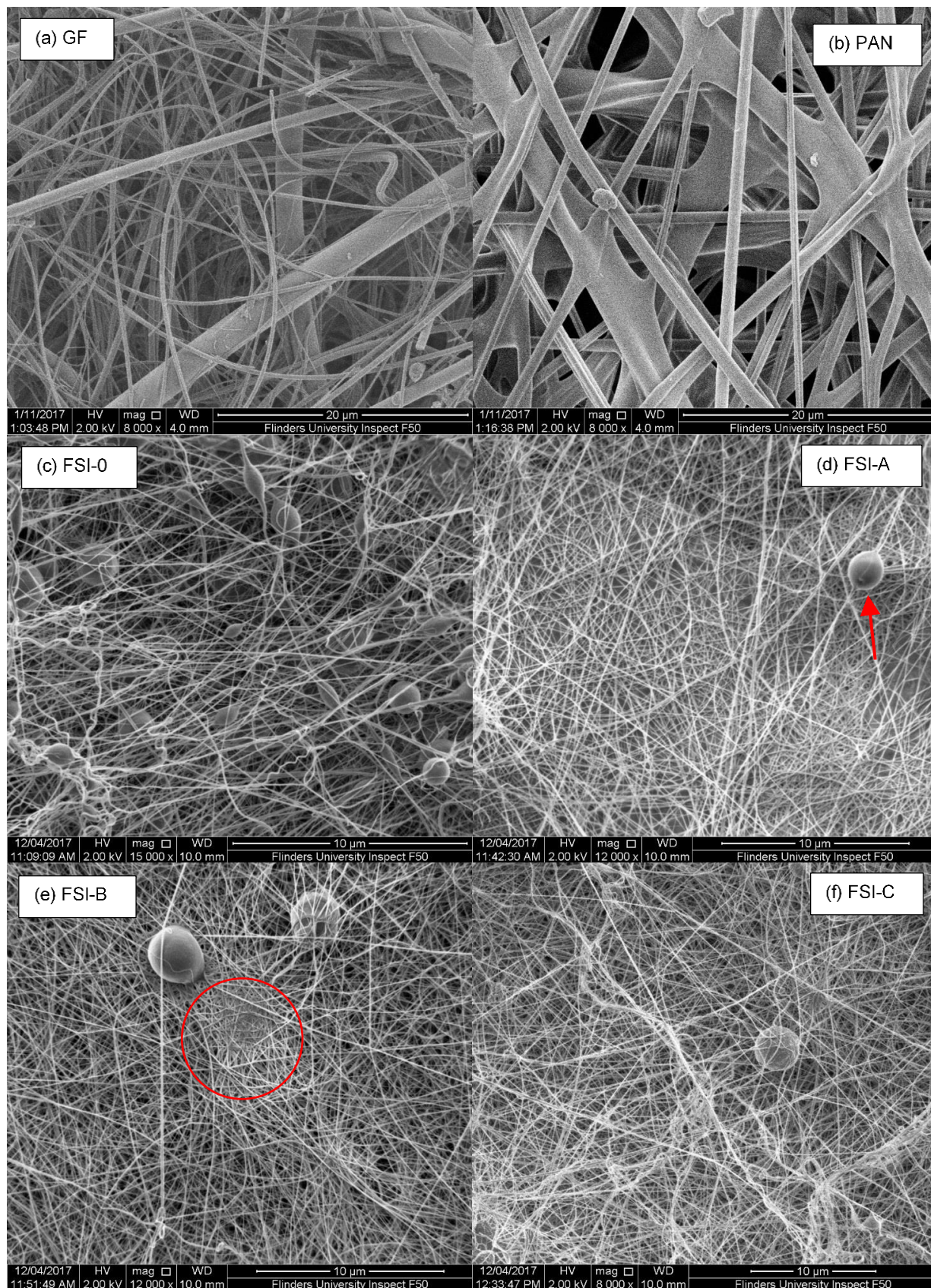


Figure 3.16 SEM images of (a) GF (magnification 8000x), (b) PAN support (magnification 8000x) (c) FSI-0 (magnification 15000x), (d) FSI-A (magnification 12000x), (e) FSI-B (magnification 12000x) and (f) FSI-C (magnification 8000x). Red arrow indicates an area containing *beading*. Red circle indicates a region of melted polymer.

The PAN support (Figure 3.16b) has an even larger fibre diameter than the GF membrane and shows a highly branched morphology, which is not typical of an electrospun membrane. The branched morphology and flattened appearance suggests the membrane has undergone some post-processing treatment, such as hot pressing [212], which would account for the fibre fusion observed with SEM. Although hot pressing generally compresses the pores structure in an electrospun membrane, it can also increase the mechanical integrity of the membrane by creating anchor points for crosslinking of the fibres. The large fibre and pore size of the PAN support membrane means it is not directly suitable for use as a separator as the large pores increase the possibility for electrode contact or active material migration during cell operation.

The morphology of fibres and nonwoven membranes produced via electrospinning is dependent on the solution properties, such as solvent type, polymer concentration, viscosity and electrical conductivity; electrospinning parameters, such as applied voltage, solution flow rate, collection distance, collector plate / rotating drum; and environmental conditions, such as temperature and humidity [308]. The processing conditions used in this thesis are shown in Table 3.10. The solution flow rate and applied voltage were altered for each solution to obtain consistent fibre formation at the needle tip, while the needle aperture, collection distance, drum rotation speed and ambient conditions were kept constant. Although solution viscosities were not measured, the electrospinning solutions had noticeably higher viscosities with increasing salt concentration. An increase in salt concentration in the polymer solution is expected to result in a higher solution viscosity and is also expected to increase the electrical conductivity [309]. Changes in the viscosity and electrical conductivity of the polymer solution impact the flow rate and applied voltage necessary for ideal fibre formation. The aim during electrospinning is to form of a continuous defect-free fibre with a consistent diameter [310]. It was found that slower flow rates and a higher applied voltage resulted in a more consistent fibre formation as the LiFSI salt concentration increased in the polymer solution.

The solvents DMF and acetone were used to dissolve the PVDF-HFP for electrospinning [247], the polymer solution was mechanically stirred on a hot plate at 75 °C for four days to facilitate LiFSI dissolving and to obtain a homogenous solution. The electrospinning variables were tuned to reduce beading at the end of the electrospinning needle, with the aim of continuous fibre formation from. As seen in the SEM images (Figure 3.16c-f) the electrospun fibres overlay with random orientation to form the nonwoven separator.

EDX spectra collected during SEM imaging of FSI-A, FSI-B and FSI-C are shown in Figure 3.17. Images containing beads and / or melted regions were chosen for EDX to help determine their composition. For SEM, the separators were left on the aluminium collection foil used during electrospinning to decrease separator disruption prior to imaging. This accounts for the aluminium

detected in EDX elemental spectra.

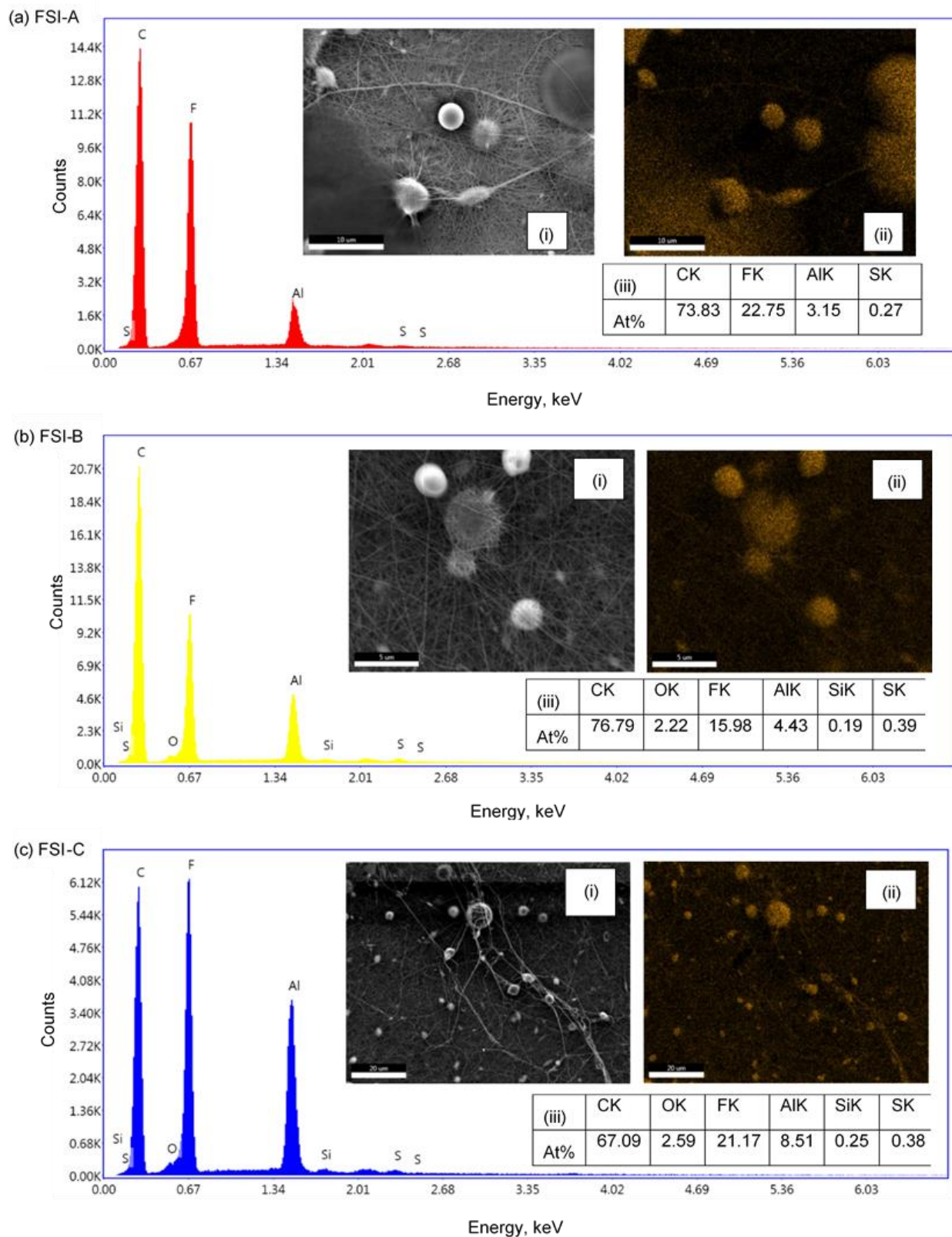


Figure 3.17 EDX spectrum of (a) FSI-A, (b) FSI-B and (c) FSI-C. Inserts: (i) SEM image for EDX, (ii) fluorine distribution map, (iii) elemental percentage on surface.

The carbon and fluorine detected in the spectra confirm the presence of PVDF-HFP polymer. In all the EDX images, with and without LiFSI in the PVDF-HFP polymer, the beads and melts contain dense areas of fluorine, see fluorine distribution map Figure 3.17 inset (ii), indicating areas of solid polymer, irrespective of LiFSI concentration in the electrospinning solution. This suggests the irregularities seen on the separator are polymer from the electrospinning, not contaminants on the separator surface. Sulphur was included in the elemental mapping to identify any dense regions of LiFSI in the separators. Very little (<1 At%) sulphur was detected in the separator samples, which indicates that LiFSI has been dissolved homogeneously in the polymer solution, so no sulphur rich regions could be identified (see Appendix E).

Carbon accounts for approximately 70 At% and fluorine is 15 – 22 At% of the separator samples, as expected from the PVDF-HFP polymer. Some fibre definition is seen in the fluorine distribution maps for the larger surface fibres. The non-uniform presence of fluorine over the separator, i.e. beading in Figure 3.17, suggests that the LiFSI may not have been effectively dissolved in the solvent. However, EDX sulphur mapping (Appendix E) shows a uniform distribution of sulphur from the LiFSI, leading to the conclusion that they are beads of polymer.

The presence of beading and regions of melted polymer in the electrospun separators (Figure 3.16 and Figure 3.17) indicate that further optimisation of the electrospinning conditions is required to form a single continuous fibre using the polymer solutions in this work. The extent of non-uniformities across the surface of the electrospun separators can be further seen in SEM images at lower magnifications in Appendix F. The implication of a non-uniform separator morphology was discussed in Section 2.2.1 *Pore geometry*. Regions of melted polymer indicate incomplete evaporation of the solvent prior to fibre collection on the drum, this could be addressed with alternative solvents. Beading occurred frequently in the FSI-0 separator (Figure 3.16c), fewer beads were formed with the addition of LiFSI salt to the electrospinning solution (Figure 3.16d-f). This is likely due to an increase in the electrospinning solution electrical conductivity with increasing LiFSI salt concentration [309]. Beading may be address through changes to the solvents, polymer concentration, applied voltage, distance to the collector, or a combination of these [309-311].

It is possible that other solvents, i.e. DMAc [95], could produce a PVDF-HFP and LiFSI solution that is better suited to electrospinning. An electrospun PVDF separator was produced by Truong, et al. [95] containing LiTFSI salt using DMAc solvent. The authors [95] obtained fibres with diameters approximately 300 nm without any evidence of beading. DMAc may be an improved solvent for the PVDF-HFP and LiFSI electrospinning solution in this work to produce more uniform separators without beading.

SEM images of electrospun separators with different lithium salts at a concentration of 1 wt% are

shown in Figure 3.18, including a comparison between separators produced with different electrospinning solutions, DMF / acetone solvent mixture versus DMAc solvent. The separators produced with DMF / acetone (Figure 3.18d,e) have highly branched fibre morphology. TFSI-B (Figure 3.18e) appears to be more uniform than FSI-B (Figure 3.18d), suggesting that the electrospinning solution containing 1 wt% LiTFSI likely has a viscosity and an electrical conductivity more suited to the electrospinning conditions used than the solution containing 1 wt% LiFSI. As discussed above, the electrical conductivity of a solution changes when a salt is added [309], in addition, the electrical conductivity would also change depending on the type of salt. SEM images at lower magnifications (Appendix F) confirm substantial inhomogeneity in LiFSI and LiTFSI DMF / acetone electrospun separators, which led to the investigation with an alternate solvent.

Electrospun PVDF-HFP fibres containing 1 wt% LiTf, LiFSI and LiTFSI were produced using DMAc as the solvent (Figure 3.18a-c). The fibres have a less branched morphology compared to the DMF / acetone based fibres, suggesting the use of DMAc produces a solution with properties more suited to single fibre formation with the electrospinning conditions used. The salt type (LiTf, LiFSI or LiTFSI) does not appear to have a substantial effect on the separator morphology with DMAc. Compared to the DMF / acetone separators, it appears that the electrospinning solution salt concentration and solvent type have a larger impact on the resulting separator than the salt type. The lower magnification SEM images (Appendix F) show that overall, solutions with DMAc produce separators with improved uniformity. However, further optimisation is required to eliminate beading and melted regions still present in the separators, as discussed above.

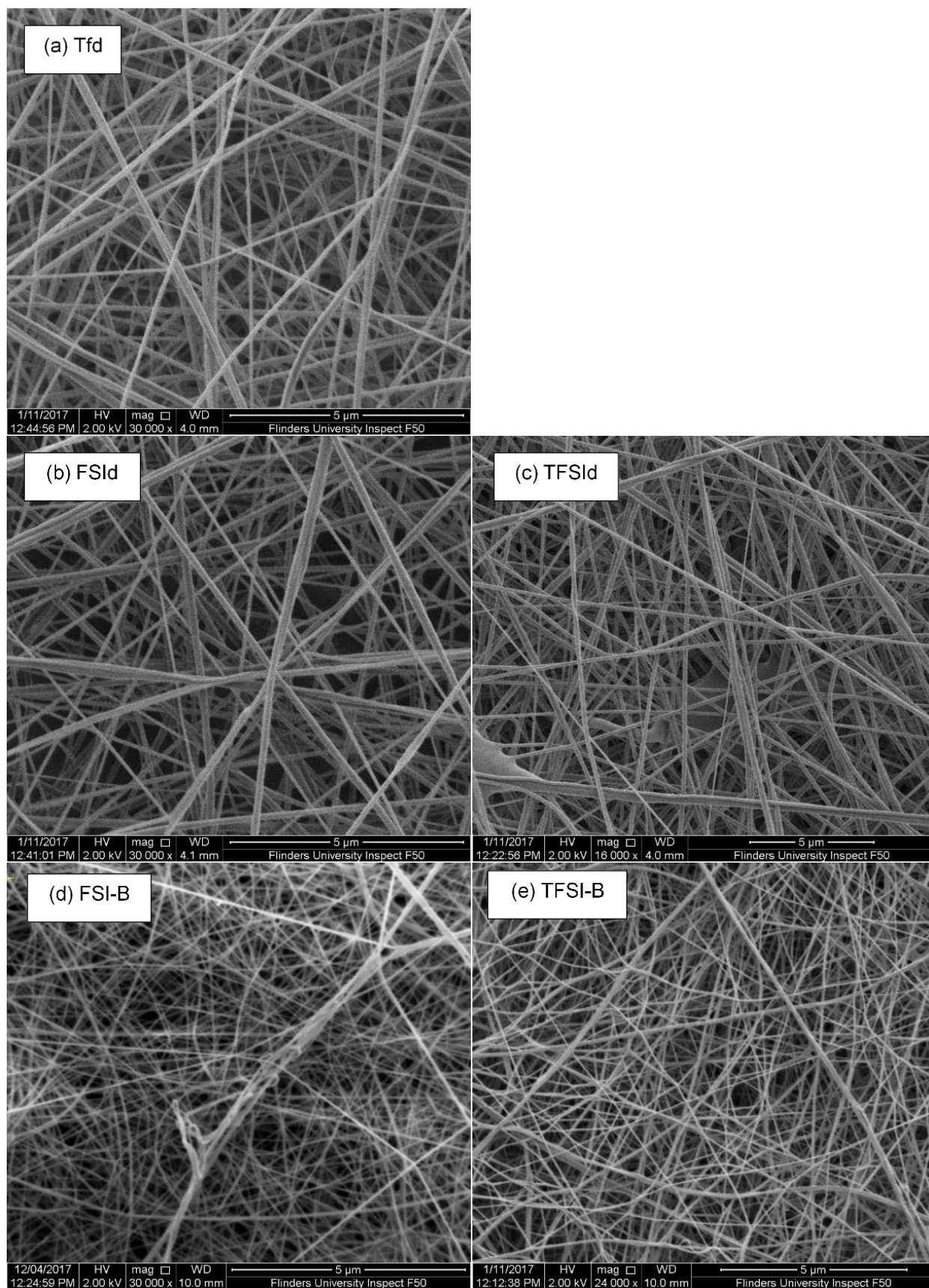


Figure 3.18 SEM images of separators (a) Tfd (magnification 30000x), (b) FSI-d (magnification 30000x) (c) TFSI-d (magnification 16000x), (d) FSI-B (magnification 30000x) and (e) TFSI-B (magnification 24000x).

3.3.2.2 Thickness and fibre diameters

The materials, thickness and fibre diameters of Celgard 3501, the GF and the separators containing LiFSI salt prepared in this work are shown in Table 3.12. The spinning time was kept constant for each sample to obtain a similar thickness for each separator. The separators were electrospun onto a collector drum with a collection area of approximately 18 by 20 cm. The thickness measurement and corresponding error shown in Table 3.12 were averaged from ten measurements taken across the surface of each separator. The separators prepared with DMF / acetone solvents have a thickness between 20 and 38 μm , which is comparable to the commercial separators shown in Table 3.11. The variation of $\pm 25\%$ in separator thickness indicates variation in fibre collection over the surface of the collector drum. This could be related to the axial sliding of the needle along the drum during electrospinning, although the axial slide speed was kept constant for each membrane the thickness of collected fibres was expected to be lower at each end of the drum at the edges of the axial sliding track of the needle. The GF membrane is a commercial product, not specifically designed for lithium-ion cell applications, with a thickness of 210 μm . It should be noted that researchers using IL electrolytes typically use GF membranes as separator materials [62, 63, 67, 96, 287, 312]. The GF is approximately seven times as thick as the separators prepared in this work.

The fibre diameter distribution for the separators containing LiFSI salt prepared in this work are shown in Figure 3.19, the PAN support material and the commercial GF for comparison. The GF membrane has much larger fibres with a large variation in fibre diameter. The average fibre diameter was 479 nm and the largest fibre observed had a diameter of 1.9 μm . This would likely result in a high surface roughness for the membrane, and once assembled into a cell, it could affect the electrode-electrolyte interphase stability [96]. The PAN support showed an even larger fibre diameter distribution, with fibres observed in the range 500 nm up to 4.0 μm , which could be a result of the branched morphology (Figure 3.16). The larger fibre diameter likely resulted in a high surface roughness of the PAN support.

Table 3.12 Material, thickness and fibre diameters for two commercial separators as well as the separators containing LiFSI salt prepared in this work.

Separator	Material	LiFSI, wt%	Thickness, μm	Fibre diameter, nm		
				Smallest	Average	Largest
Celgard 3501	PP, surfactant coated	-	25*	N/A		
GF	Glass fibre mat	-	210*	115	479 \pm 301	1873
PAN	PAN	-	15 \pm 2	522	1440 \pm 724	4034
FSI-0	PAN/PVDF-HFP	0	30 \pm 7	35	70 \pm 20	143
FSI-A	PAN/PVDF-HFP	0.5	32 \pm 6	43	70 \pm 23	192
FSI-B	PAN/PVDF-HFP	1	28 \pm 8	26	53 \pm 13	89
FSI-C	PAN/PVDF-HFP	2	30 \pm 6	40	85 \pm 40	275

* from manufacturer data sheet, shown in Appendix B

The fibre diameters of FSI-0 (Figure 3.19c) and FSI-A (Figure 3.19d) show a tight distribution with average fibre diameters of 70 nm for both separators (see Table 3.12). The fibre distribution for FSI-B (Figure 3.19e) is not ideally distributed but the difference between smallest and largest fibre diameter for this separator is narrow which indicates a more uniform fibre formation compared to the other separators. The fibre distribution for FSI-C (Figure 3.19f) is discontinuous with an average fibre diameter of 85 nm, the largest fibre observed was 275 nm. This indicates variability in fibre formation during electrospinning, potentially due to the higher salt concentration in the polymer solution affecting the homogeneity.

The material, thickness and fibre diameters for electrospun separators with different salt and solvent types are shown in Table 3.13. TFSI-B has a thickness of approximately 29 μm , within the range of thicknesses obtained for separators containing LiFSI salt above. The separators electrospun with DMAc were thicker than those using DMF / acetone solvents. The flow rates and applied voltages were changed for each solution to reduce beading effects at the tip of the needle. Since higher flow rates were used with the DMAc solutions, the spinning time was decreased (see Table 3.10) in an attempt to obtain separators of similar thickness.

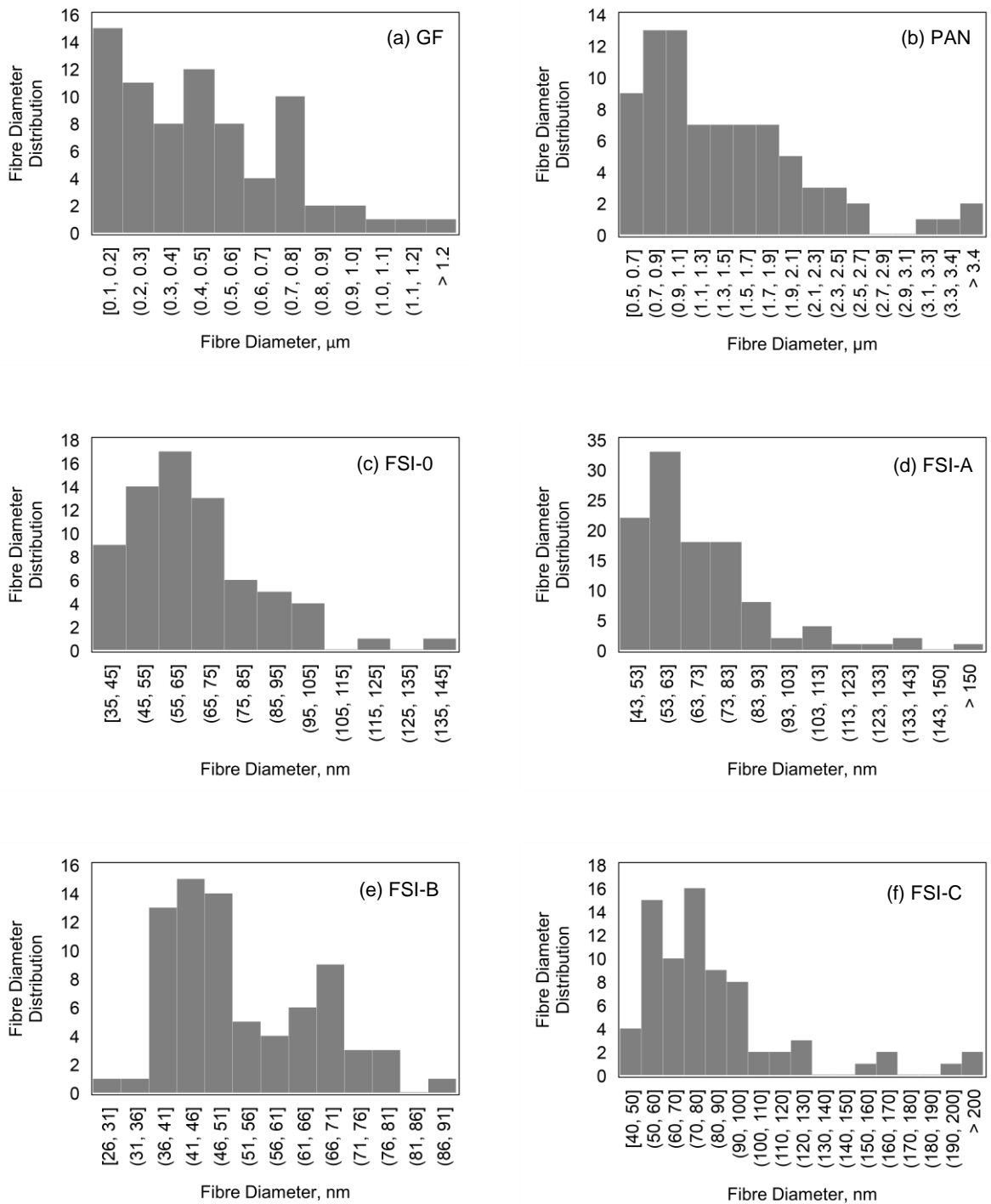


Figure 3.19 Fibre diameter distributions for separators (a) GF, (b) PAN support, (c) FSI-0, (d) FSI-A, (e) FSI-B and (f) FSI-C.

Table 3.13 Material, thickness and fibre diameters for different salt-type separators prepared in this work.

Separator	Solvent	Salt, 1 wt%	Thickness, μm	Fibre diameter, nm		
				Smallest	Average	Largest
Tfd	DMAc	LiTf	43 \pm 5	35	102 \pm 33	220
FSId	DMAc	LiFSI	76 \pm 21	37	107 \pm 50	331
TFSId	DMAc	LiTFSI	59 \pm 4	82	185 \pm 57	338
FSI-B	DMF/acetone	LiFSI	28 \pm 8	26	53 \pm 13	89
TFSI-B	DMF/acetone	LiTFSI	29 \pm 3	38	67 \pm 25	207

The Tfd separator has a thickness of 43 μm , only 5 μm thicker than the thickest DMF / acetone separator. The TFSId and FSId separators, however, are substantially thicker. TFSId is approximately 59 μm and FSId is approximately 76 μm , more than double the thickness of the DMF / acetone separators, it should be noted that the variation in thickness across the FSId separator is \pm 21 μm . The high amount of variation in FSId thickness supports the previous suggestion that further optimisation of the electrospinning variables is required.

The fibre diameters and corresponding distributions for different salt-type separators are shown in Table 3.13 and Figure 3.20, respectively. TFSI-B has similar fibre diameters to those of the other DMF / acetone separators (Table 3.12 and Table 3.13), the average fibre diameter of TFSI-B is 67 nm. This suggests that changing the salt from LiFSI to LiTFSI does not substantially change the resulting fibre diameters. There is, however, a noticeable change in the fibre diameter when a different solvent is used, the separators that had DMAc solvent for electrospinning have higher average fibre diameters. Tfd and FSId have a similar average fibre diameter of approximately 100 nm, but Tfd has a lower standard deviation (\pm 33 nm) than FSId (\pm 50 nm) which suggests a more uniform fibre diameter was achieved with the polymer solution containing LiTf. This is supported by the tighter grouping of fibre diameters in the Tfd distribution shown in Figure 3.20a. TFSId has a much larger average fibre diameter (approximately 185 nm) than the other DMAc separators. Since the only difference during electrospinning was the salt type in the polymer solution, it is possible that LiTFSI affected the solution viscosity and / or conductivity [309], resulting in the larger fibre diameter.

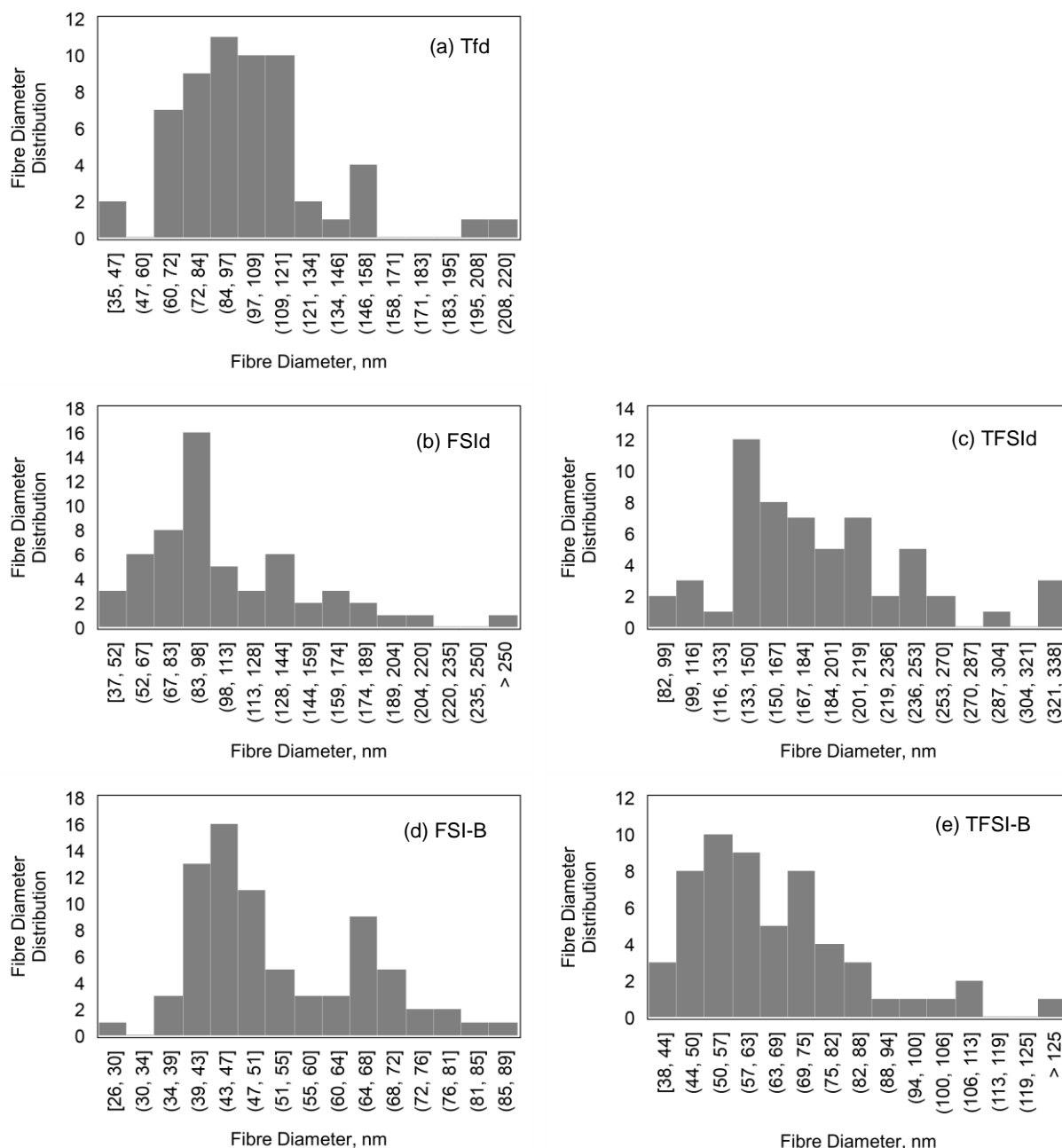


Figure 3.20 Fibre diameter distributions for separators (a) Tfd, (b) FSId, (c) TFSId, (d) FSI1 and (e) TFSI1.

3.3.2.3 Porosity and pore sizes

Pore size distributions of the separators containing LiFSI salt and GF are shown in Figure 3.21. The GF pore size distribution (Figure 3.21a) is from a single measurement and shows a wide distribution with pores between 0.9 and 4.8 μm diameter. The pore size estimates for PAN, shown in Table 3.14, have been taken from an SEM image as described in Section 3.2.4.3. The average pore size of the PAN support is approximately 7.2 μm , which is much larger than the maximum 1 μm pore size ideal for separators [91, 93].

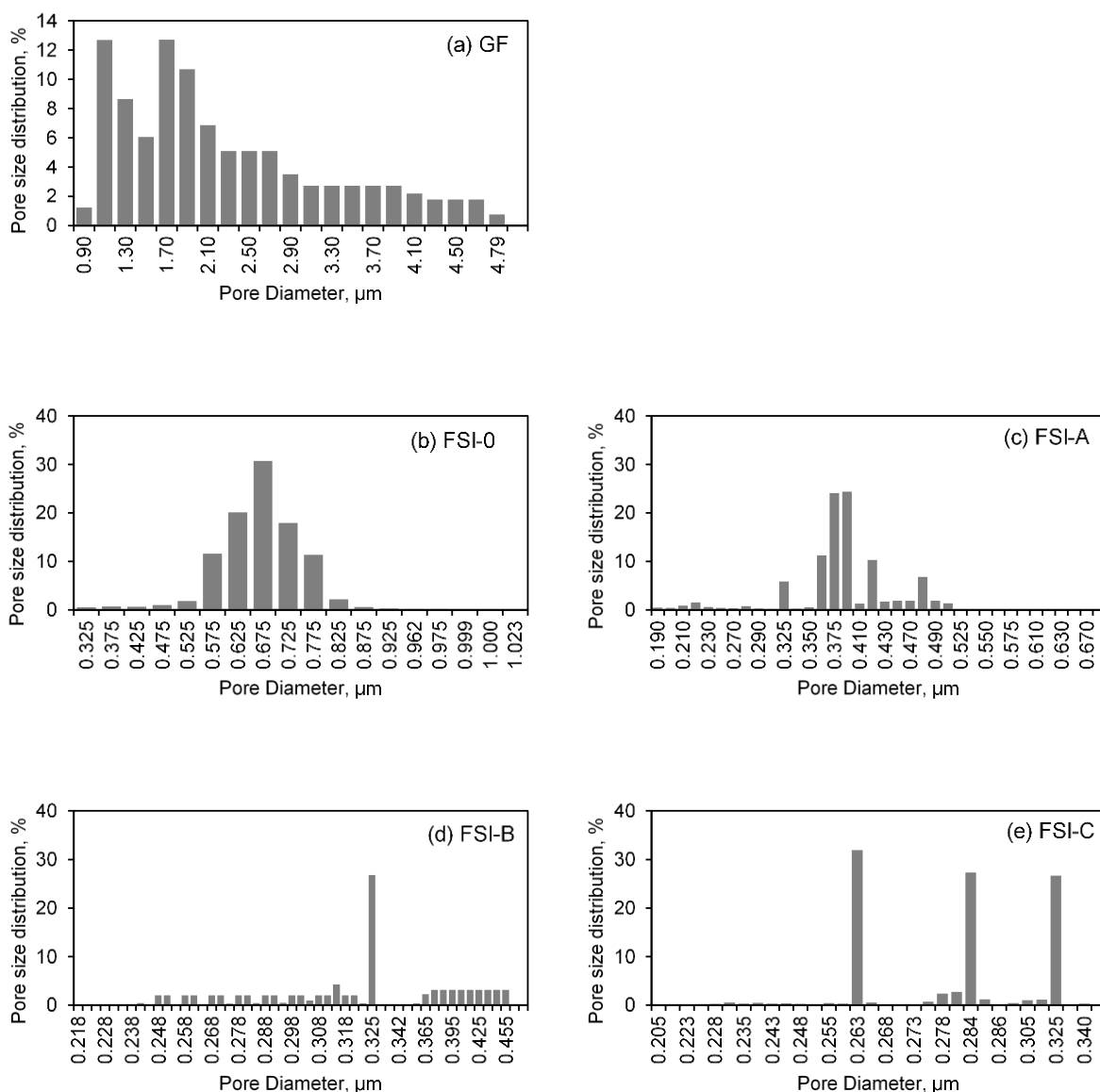


Figure 3.21 Pore size distribution for separators (a) GF (one measurement), (b) FSI-0 (average of two measurements), (c) FSI-A (average of two measurements), (d) FSI-B (average of three measurements) and (e) FSI-C (average of three measurements).

The FSI-0 separator pore distribution (Figure 3.21b) is the average of two measurements with most pores between 500 and 800 nm diameter. The effects of separator pore-size distribution were discussed in Section 2.2.1 *Pore geometry*, the pore-size distribution can be indicative of the membrane uniformity with a smaller distribution pointing to a more uniform morphology. The FSI-A separator pore distribution (Figure 3.21c) is an average of two measurements and shows a discontinuous pore distribution. Most pores in FSI-A are between 300 and 500 nm but approximately 2% are in the range 200 to 230 nm diameter, indicating some non-uniformity in the separator morphology, as observed with SEM. It should be noted that the porometry process includes pressurisation of the membrane, which can cause compression of pores in a nonwoven

membrane. Although comparison between the samples in this work is valid, comparison to other literature sources is not directly possible unless the porosity was measured using the same experimental technique. It is expected that the separator pores are larger than the values shown in Table 3.14 for the electrospun separators before they experienced the compressive forces.

The FSI-B separator pore distribution (Figure 3.21d) is an average of three measurements showing a wide distribution: 30% of the pores are between 250 and 320 nm diameter, 30% of the pores are 325 nm diameter and 30% are between 360 and 460 nm diameter. This distribution shape comes from averaging three measurements with widely varying results, the average was used to gain a characteristic pore distribution for the separator. The different measurements could indicate a non-uniform separator morphology for FSI-B, which could be due to the effects of beading and melted regions, described earlier. The FSI-C separator pore size distribution (Figure 3.21e) is an average of three measurements and shows a discontinuous pore distribution, similar to FSI-B but more segmented. Pore diameters of 263 nm, 284 nm and 325 nm make up 32%, 27% and 27% of pore diameters in the FSI-C separator, respectively. Again, the difference in pore size distributions for three measurements of the same material indicates a non-uniform separator morphology, as observed with SEM.

The smallest, largest and mean pore diameter for each separator is shown in Table 3.14. The pore diameter decreases as salt concentration increases in the polymer. This is reflected in both the largest detected pore diameter in each separator as well as the mean pore diameter for each separator. The smallest detected pore diameter is a little different with FSI-B showing the smallest pore, however the smallest pore size in a separator is not significant unless it begins to restrict ion flow or effect electrolyte wetting, which has not been observed for the separators prepared in this work. The largest detected pore diameter is important since this relates to the ability of a separator to prevent contact between the electrodes, as well as discourage lithium metal dendrite growth during cell operation or abuse conditions.

The porosity of the separators was calculated using **Eq. (1)**. The GF separator was found to have the highest porosity, which is not surprising based on the large fibre diameter and pore size of the membrane. Although a high porosity is not directly detrimental to a membrane's suitability as a separator, the larger pore sizes that often accompany high porosity membranes may allow dendrite growth or particle migration from the electrodes within the cell, both of which are detrimental to the performance of a cell [88].

Table 3.14 Porosity and pore size distribution for GF, Celgard 3501, PAN and the separators containing LiFSI salt.

Separator	Porosity, %	Pore diameter, μm		
		Smallest	Mean	Largest
Celgard 3501*	55.00		0.064	
GF	89.7	0.941	1.958	4.885
PAN	76.6	$\text{\$}2.5$	$\text{\$}7.2 \pm 3.5$	$\text{\$}17.6$
FSI-0	60.8	0.339 ± 0.057	0.661 ± 0.025	1.012 ± 0.016
FSI-A	69.2	0.229 ± 0.044	0.444 ± 0.083	0.772 ± 0.028
FSI-B	70.1	0.194 ± 0.048	0.337 ± 0.062	0.378 ± 0.072
FSI-C	67.9	0.223 ± 0.010	0.290 ± 0.029	0.302 ± 0.039

$\text{\$}$ repeatable porometer results not obtained, SEM image pore sizes measured with ImageJ, mean and error reported for 31 measurements

* from manufacturer data sheet, shown in Appendix B

The electrospun separators all have higher porosities than the commercial Celgard 3501 microporous separator (55%). This was expected due to the open, well-interconnected pore structure typical of nonwoven membranes [91, 105]. The suitable porosity for a separator is between 40 and 60%, a low porosity can influence electrolyte uptake and ionic transport in the separator, while a high porosity can decrease the separators mechanical properties [91]. The electrospun separators in this work have porosities of approximately 60 to 70%, which should provide good electrolyte uptake. Of the electrospun separators, FSI-0 (60.8%) and FSI-B (70.1%) have the lowest and highest porosities, respectively. The other two separators, FSI-A and FSI-C, have similar porosities of 69.2% and 68.0%, respectively. The porosities do not appear to correlate to either fibre diameter or pore dimension of the separators, which indicates another influence on the porosity of an electrospun membrane, possibly the fibre placement and packing during electrospinning.

The pore size distribution of FSI-B and TFSI-B are shown in Figure 3.22. Porometry of the DMAc separators was not performed; however, pore size estimates were obtained from pore diameter measurements on SEM images. The pore sizes of FSI-B, TFSI-B and the DMAc separators are shown in Table 3.15. Comparing the DMF / acetone separator with 1 wt% salt, TFSI-B has larger pore diameters by approximately 100 μm , average pore size is 0.337 and 0.428 μm for FSI-B and TFSI-B, respectively. In both cases the pores are less than 1 μm , the ideal pore size requirement for lithium-ion cell separators [91, 93]. The larger pore size of TFSI-B may result in enhanced conductivity in the separator from a decrease in resistance to lithium ion transport due to the larger pores.

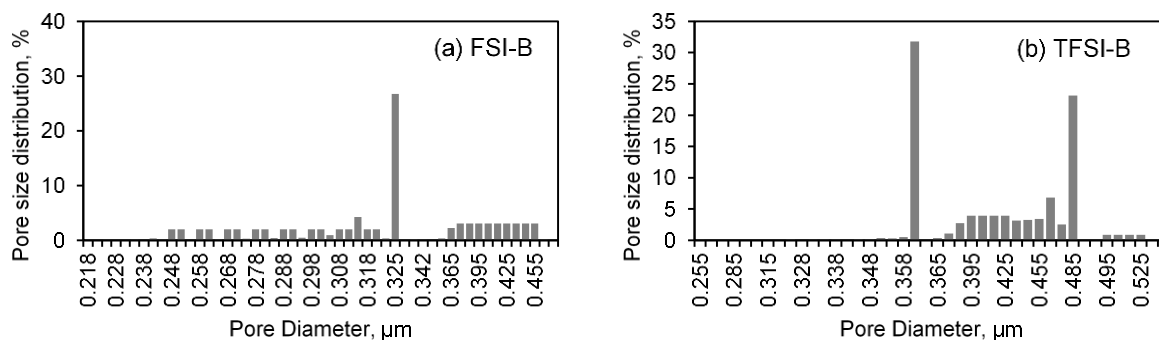


Figure 3.22 Pore size distribution for separators (a) FSI-B (average of three measurements) and (b) TFSI-B (average of three measurements).

The pore size of the DMAc separators was found to be larger than the DMF / acetone separators, which is not surprising considering the larger fibre diameters observed above. Although, the different measurement methods should be noted when comparing the results, i.e. pore diameter measurement from SEM image for DMAc separators and porometry measurements for DMF / acetone separators. Within the DMAc separators, the average pore size is smallest for Tfd (0.643 μm), and largest for TFSId (1.140 μm), this corresponds to the fibre diameters which were also smallest in Tfd and largest in TFSId. The membrane pore size is related to the fibre orientation, and the fibre orientation is depends on electrospinning parameters, particularly the rotating drum speed [310].

Table 3.15 Pore size distribution for the DMAc separators, FSI-B and TFSI-B.

Separator	Pore diameter, μm		
	Smallest	Mean	Largest
Tfd [§]	0.176	0.643 ±0.258	1.103
FSId [§]	0.442	0.906 ±0.280	1.645
TFSId [§]	0.497	1.140 ±0.411	2.263
FSI-B	0.194 ±0.048	0.337 ±0.062	0.378 ±0.072
TFSI-B	0.303 ±0.038	0.428 ±0.063	0.462 ±0.087

[§] SEM image pore sizes measured with ImageJ, mean and error reported for a minimum of 30 measurements

For the DMAc separators, the electrospinning parameters, including the drum rotation speed, were kept constant. Therefore, the variation seen is most likely due to different lithium salts changing the solution viscosity and conductivity, resulting in different behaviours of the fibres in the applied electric field between the needle and collector drum. The largest measured pore size for the three DMAc separators is greater than 1 μm, which falls outside of the pore size requirements for a

separator [91, 93], however the separators are not necessarily eliminated as the membrane thickness and tortuosity may be such that the possibility for short circuits are decreased, despite the larger pore size. This is demonstrated with the GF separator that has a much larger pore size, average of approximately 2 μm (Table 3.14), but also a higher membrane thickness.

3.3.2.4 Mechanical properties

The mechanical properties of a separator are important to determine the ability of the membrane to withstand cell assembly [105]. The mechanical requirements previously set for a lithium-ion cell separator are a tensile strength of at least 98.06 MPa [91] and less than 2% strain elongation at 6.89 MPa [93]. The tensile strength, yield strength, modulus and elongation at break are shown in Table 3.16 for Celgard 3501, GF and FSI-C. The stress-strain plots for Celgard 3501, GF and FSI-C are shown in Figure 3.23.

Table 3.16 Mechanical properties: tensile strength, yield strength, modulus and elongation at break.

Separator	^a Tensile strength, MPa	^b Yield strength, MPa	Modulus, MPa	Elongation at break, %
Celgard 3501	11.2 \pm 0.9	11.2 \pm 0.9	380.8 \pm 36.2	481 \pm 150
GF	0.3 \pm 0.1	-	36.9 \pm 12.6	-
FSI-C	6.6 \pm 1.4	5.8 \pm 1.6	159.2 \pm 45.0	25 \pm 5

^a maximum stress during test

^b stress at yield

Celgard 3501 (Figure 3.23a) was found to have a tensile strength approximately 11 MPa, which corresponds to the tensile strength in the transverse direction (13 MPa) provided by the manufacturer (from product information sheet). The tensile strength of Celgard 3501 in the machine direction is substantially higher, approximately 103 MPa (from product information sheet). The average elongation at break is approximately 480% for Celgard 3501. The GF (Figure 3.23b) was found to have a tensile strength of only 0.35 MPa, which was expected due to the brittle nature of GFs. The FSI-C (Figure 3.23c) showed an average tensile strength of 6.6 MPa at the maximum stress and an elongation of approximately 25% at point of rupture. Although FSI-C has a lower tensile strength than Celgard 3501, it has substantially improved mechanical properties over the GF. Unfortunately, the mechanical properties of FSI-C do not meet the ideal requirements for a separator, however, with continued development, the mechanical properties of layered electrospun separators could be improved.

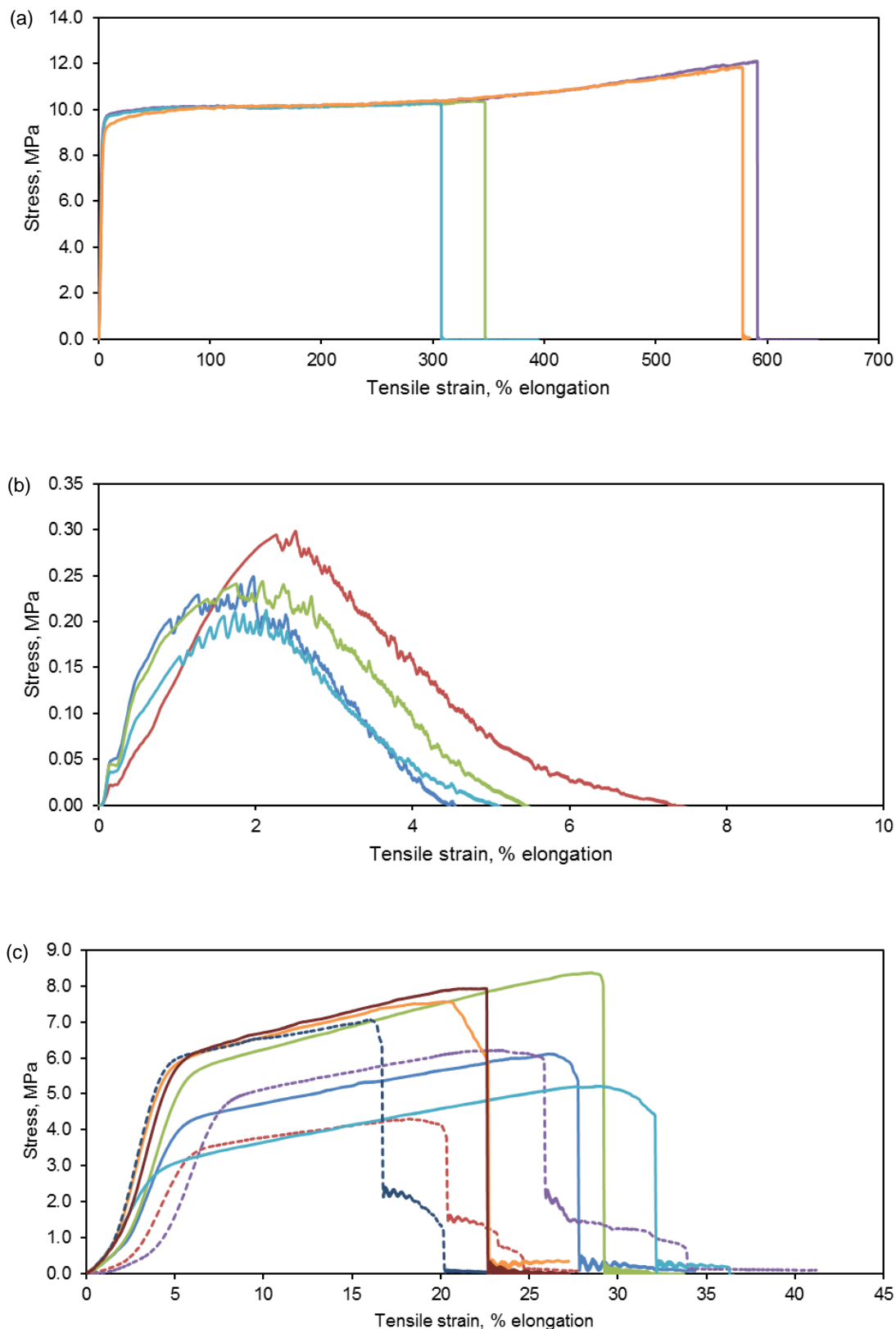


Figure 3.23 Stress-strain plots for (a) Celgard 3501 (four samples); (b) GF (four samples); and (c) FSI-C (eight samples). FSI-C shows variation in tensile strength, yield strength and yield profile for different samples - samples that showed a two-part yield profile are shown in dashed lines.

There was a large variance in the stress-strain plots obtained for eight samples of the FSI-C separator (Figure 3.23c). This could be from either a variation in thickness of the layers over the electrospun separator or variation in adhesion properties between the layers, or a combination of both. In three samples, a two-part yield profile was observed (dashed plots in Figure 3.23c). In these samples, the yield strengths for the first and second yields were 5.3 ± 1.4 MPa and 1.1 ± 0.4 MPa, respectively. This behaviour could be explained by delamination resulting in the PAN and PVDF-HFP layers rupturing separately during the test. This may indicate the layers are not well matched in tensile strength and / or elasticity properties; therefore, delamination occurred according to the properties of each individual layer. In the other five samples, the yield profile was a single step (yield strength 6 ± 1.75 MPa), suggesting during these tests the three layers behaved as one membrane.

The tensile strength of other electrospun PAN separators have been reported in the literature, however the tensile strength varies greatly. Evans, et al. [105] reported an ultimate tensile strength of 16.39 MPa for a 200 μm electrospun separator. Other electrospun PAN separators were reported to have tensile strengths from 3.7 to 13.5 MPa for separators between 26 and 250 μm thick, respectively [210, 215, 218, 228, 230]. The variability in these tensile strengths may be related to the separator thickness, but a correlation is not immediately obvious, suggesting that other properties also affect the tensile strength of an electrospun membrane. Carol, et al. [210] suggests that during electrospinning, the molecular chains in PAN are aligned by the electric field, causing the PAN to be more flexible compared to other PAN membranes, such as microporous membranes. It is possible that different electrospinning parameters used in the above studies resulted in different levels of polymer chain alignment, affecting the mechanical properties of each electrospun separator.

Similarly, the mechanical properties of PVDF-HFP electrospun separators also vary, with tensile strengths from 0.95 up to 8 MPa reported for separators with varying thickness (35 to 250 μm) [189, 192, 202, 313]. The tensile strength obtained for FSI-C was approximately 6.6 MPa, which falls within the expected range of tensile strength based on the reports for other PAN and PVDF-HFP separators. It should be noted that FSI-C consists of one 15 μm PAN layer with PVDF-HFP layers approximately 8 μm thick on each side. Considering the expected tensile strengths from other literature, the inclusion of LiFSI salt in the PVDF-HFP layers does not appear to impact the overall tensile strength of the separators. Layering of different materials did not appear to increase the tensile strength of the separator, but it also did not negatively affect the mechanical properties either.

3.3.2.5 Thermal properties

The Differential Scanning Calorimetry (DSC) and Thermogravimetric Analysis (TGA) results from STA of separators in the temperature range 100 °C to 600 °C are shown in Figure 3.24, at a heating rate of 10 °C min⁻¹. The peak temperature and decomposition temperature (by 5% weight loss) is shown in Table 3.17. The DSC thermogram (Figure 3.24a) for PAN shows an exothermic peak between 240 °C and 330 °C with a maximum at 301 °C, this agrees with other DSC results for electrospun PAN [212, 314]. The polymer PAN does not melt endothermically with heating like other polymers, but instead undergoes backbone crystallization followed by exothermic decomposition [314]. The TGA trace for PAN (Figure 3.24b) also indicates decomposition by the major mass loss between 272 °C and 347 °C. There is also a smaller mass loss at approximately 160 °C which could be attributed to residual solvent from the original preparation process. This is observed in all separators containing LiFSI salt with weight % loss corresponding to the weight portion of PAN present in the separator.

When an electrospun layer of PVDF-HFP is added (Figure 3.24a FSI-0) an endothermic event is seen between 136 °C and 165 °C, with a peak of 153 °C, and an exothermic peak is seen between 447 °C and 483 °C with a peak of 468 °C. The endothermic peak at 153 °C is most likely due to melting of PVDF-HFP, this is similar to other DSC results showing a melting point of 159 °C for PVDF-HFP [280]. The TGA trace (Figure 3.24b) shows a substantial mass loss between 367 °C and 515 °C which confirms the exothermic event at 468 °C is due to PVDF-HFP decomposition. The PVDF-HFP melting endotherm and exotherms from PAN and PVDF-HFP decompositions are observed in all four separators containing LiFSI salt in Figure 3.24a with average peak temperatures of 160 ±6 °C, 302 ±7 °C and 469 ±2 °C, respectively.

Table 3.17 Peak temperature and decomposition temperature (by 5% weight loss) and shrinkage of Celgard 3501, PAN support and the four separators containing LiFSI salt.

Separator	T _{peak} ^a , °C	T _{decomp} ^b , °C	Shrinkage ^c , %
Celgard 3501	-	-	78.0
PAN	301	296	8.0
FSI-0	303	305	16.0
FSI-A	320	323	6.0
FSI-B	312	312	20.0
FSI-C	308	304	6.0

^a peak temperature of decomposition event during DSC

^b decomposition temperature determined by 5% weight loss during TGA

^c shrinkage after 60 minutes at 150°C

The additional LiFSI salt to the PVDF-HFP electrospun layer (Figure 3.24a FSI-A, FSI-B and FSI-C) does not appear to affect the decomposition profile of the separator as no additional peaks were

observed in the thermogram of FSI-A, FSI-B and FSI-C, compared to FSI-0 (no salt). Since the lithium salt makes up less than 2% (by weight) of the electrospun layer, any LiFSI melting or decomposition reactions may not have been detected during STA. The decomposition of LiFSI has been previously reported to occur between 300 and 350 °C [31] so any exothermic event from LiFSI decomposition would likely have been engulfed by the PAN decomposition peak.

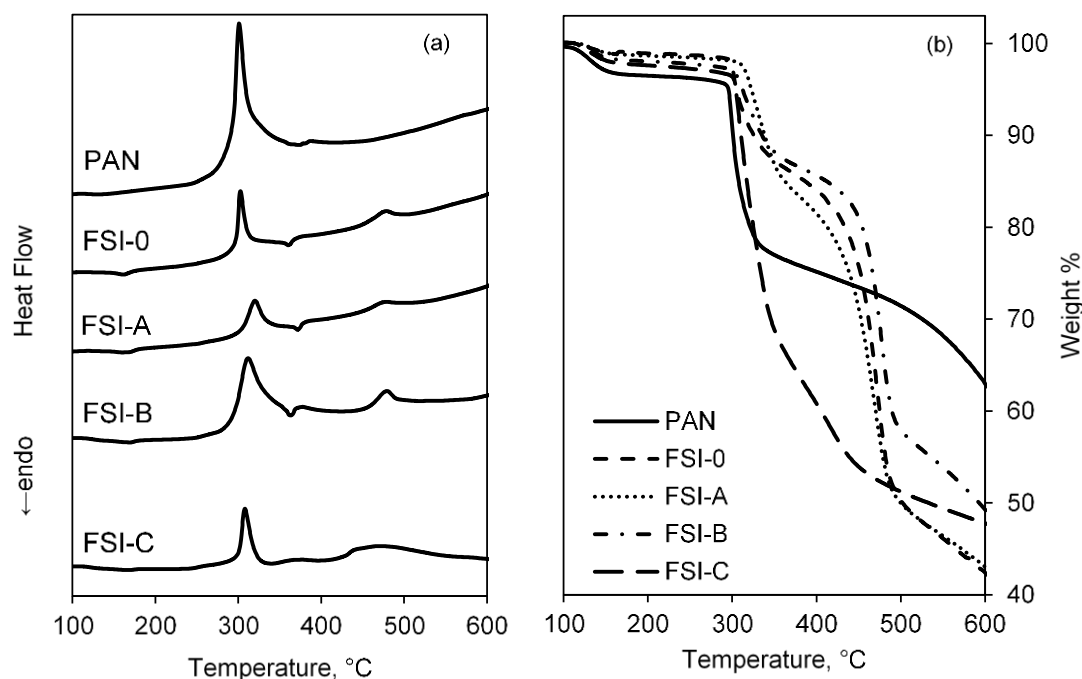


Figure 3.24 Simultaneous thermal analysis: (a) DSC and (b) TGA of dry separators: PAN, FSI-0, FSI-A, FSI-B and FSI-C, at a heating rate of 10 °C min⁻¹.

The DSC and TGA of FSI-C show a different profile to the other separators containing LiFSI salt. In the DSC thermogram the PVDF-HFP melting and decomposition peaks are less well defined. Also, in TGA the main mass loss occurs at PAN decomposition and no mass loss is observed at PVDF-HFP decomposition seen in the other separators containing LiFSI salt. Since presence of the electrospun layer was confirmed previously on the FSI-C sample, one possible explanation for the different thermal properties could be the higher lithium salt concentration in the polymer solution resulted in a non-continuous polymer matrix with decreased thermal stability.

The thermal dimensional stability of a separator can be related to the safety of a cell at high temperatures. The amount of dimensional change (shrinkage) experienced by a separator has been determined through hot oven tests where the separator is exposed to an elevated temperature for a set amount of time [190, 209, 211, 215, 218, 228], although the specific temperature and time of the oven test is not consistently described in the literature. The shrinkage

of Celgard 3501, the PAN support and the four separators containing LiFSI salt was determined after 60 minutes exposure to 150 °C. The values are shown in Table 3.17, and the before and after images can be seen in Appendix G. Celgard 3501 shows a shrinkage of approximately 78%, including obvious effects of warping and curl, as seen in the images. FSI-A and FSI-C had the least shrinkage with dimensional changes of only 6% based on area. FSI-0 and FSI-B showed the most shrinkage at 16 and 20%, respectively. There does not appear to be any correlation between the concentration of LiFSI in the PVDF-HFP layer and the thermal shrinkage. The low shrinkage of FSI-A and FSI-C suggest that the presence of LiFSI does not decrease the thermal stability of PVDF-HFP. However, this is not supported by FSI-B which has the highest shrinkage (excluding Celgard 3501), indicating a lower thermal dimensional stability than the other separators containing LiFSI salt. Some delamination between the layers is evident at the edges of the oven temperature samples and this could have affected the measured shrinkage. Huang, et al. [190] investigated the thermal shrinkage of an electrospun PVDF-HFP separator after 60 minutes at 200 °C. Based on the images published by Huang, et al. [190] (which included a scale), the shrinkage can be estimated approximately 85% (based on area, calculated from the images). Compared to this estimation, the 16% shrinkage observed for FSI-0 separator at 150 °C in this work is not surprising, especially considering the melting temperature of PVDF-HFP is approximately 160 °C [280].

The PAN support had a shrinkage of 8%. Electrospun PAN separators have been reported to have negligible thermal shrinkage at 150 to 200 °C for 30 or 60 minutes; in all instances this has been attributed to the high thermal stability of PAN [209, 215, 218, 228]. Huang, et al. [215] suggested that alignment of the PAN chains during electrospinning allow interactions between adjacent nitrile groups, therefore increasing the separators' resistance to dimensional changes at elevated temperatures. In the same study, an electrospun PAN separator wet with 1 M LiPF₆ EC / diethyl carbonate (DEC) 1:2 volume/volume (v/v) electrolyte and was found to experience 16% shrinkage and obvious warping after 60 minutes at 140 °C. The authors [215] attribute this to the plasticising effect of carbonate solvents in the electrolyte that disturb the nitrile group interactions. A similar investigation by Cho, et al. [209] showed that negligible shrinkage was seen for a dry electrospun PAN separator after 60 minutes at 200 °C, however once the separator had been harvested from a cell containing 1 M LiPF₆ EC / DEC 1:1 v/v electrolyte, an oven test at 150 °C for 60 minutes showed a thermal dimensional shrinkage of approximately 26%. This highlights the need for whole cell testing to determine the high temperature response of a separator in the cell environment.

3.3.2.6 *Wetting properties*

The wetting properties of a separator with electrolyte can have a strong impact on the cell performance, specifically ionic transport, particularly when incomplete wetting occurs. The contact angle of an electrolyte drop on the surface of a separator can be representative of the electrolyte-separator affinity, the lower the contact angle the greater the affinity. Evans, et al. [105] previously

compared the wetting properties of an electrospun PAN separator to a commercial PP separator and a GF separator (GF/F Whatman), with an IL electrolyte (1.2 M LiFSI P13FSI) and a conventional electrolyte (1 M LiPF₆ EC / DEC 1:1). With both electrolytes, the PAN separator showed superior wetting over the other membranes [105]. Similarly, PVDF-HFP has also been shown to have superior wetting with conventional electrolytes, compared to commercial PP and PE separators [120, 179, 180, 190]. Based on these results, the wetting of the PVDF-HFP / PAN separators prepared in this work are hypothesised to also have superior wetting with conventional electrolytes, compared to commercial PP and PE separators.

As discussed in Section 2.2.4.1, a contact angle investigation of various pure ILs and IL electrolytes on electrode and separator materials was undertaken by Huie, et al. [18]. For all ILs a trend of increasing contact angle was observed on commercial separators when salt was added to the IL to form an IL electrolyte. To determine wetting properties of the separators prepared in this work the wetting of separators containing LiFSI salt with P13FSI electrolyte was investigated via contact angle and compared to Celgard 3501. Contact angles of 86.9°, 54.8° and 37.9° are shown in Figure 3.25 for a drop of P13FSI electrolyte on Celgard 3501, FSI-0 and FSI-C separators, respectively (at time = 0 seconds).

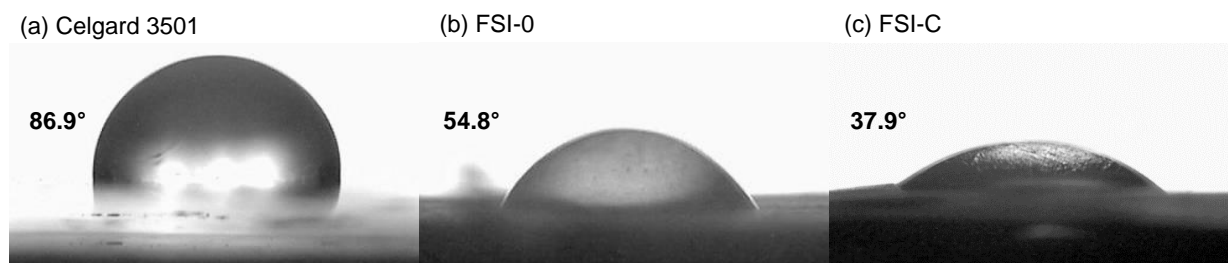


Figure 3.25 Contact angle measurements of P13FSI electrolyte on (a) Celgard 3501, (b) FSI-0 and (c) FSI-C separators at time = 0.

On FSI-0 and FSI-C the electrolyte drop was observed to be absorbed within a few seconds whereas on Celgard 3501 the drop of electrolyte remained on the surface for one minute, at which time the test was terminated. The contact angle of P13FSI electrolyte on Celgard 3501 (Figure 3.25a) is close to 90° which suggests poor wetting characteristics. The contact angle is smaller for P13FSI electrolyte on FSI-0 (Figure 3.25b), suggesting better wetting, which could be attributed to PVDF-HFP having a higher affinity for the IL electrolyte. The contact angle is even smaller for FSI-C (Figure 3.25c), suggesting better wetting than the Celgard 3501 and the FSI-0 separators. This is likely from the presence of LiFSI in the PVDF-HFP matrix increasing the separator affinity with

P13FSI electrolyte due to the common anion.

To overcome the challenges of fast absorption of IL electrolyte during the contact angle measurements, the wicking rate of P13FSI electrolyte with each separator was measured over several hours. The superior wetting of the separators prepared in this work with P13FSI electrolyte, compared to Celgard 3501, was shown with contact angle measurements. Therefore, wicking rate tests were used to further differentiate the effect of LiFSI concentration in the electrospun layer on wetting behaviour of the separators containing LiFSI salt (images in Appendix H). The values for wicking rate, electrolyte uptake, ionic conductivity, MacMullin number and tortuosity of the separators containing LiFSI salt with P13FSI electrolyte are shown in Table 3.18. The wicking rate and electrolyte uptake for the separators containing LiFSI salt with P13FSI electrolyte are shown in Figure 3.26.

Table 3.18 Wicking rate, electrolyte uptake, ionic conductivity and MacMullin number for the separators containing LiFSI salt with P13FSI electrolyte.

Separator	Wicking rate, cm hour ⁻¹	Electrolyte uptake, %	Ionic conductivity, mS cm ⁻¹	MacMullin number	Tortuosity
P13FSI electrolyte	-	-	6.6 ^a	-	-
GF	-	-	1.4 ±0.3	5 ±4	21
Celgard 3501	-	-	0.003 ±0.001	2300 ±1100	-
PAN	-	4200 ±800	-	-	-
FSI-0	2.1 ±0.7	5000 ±900	0.2 ±0.2	29 ±6	45
FSI-A	4.8 ±0.1	2900 ±800	0.2 ±0.2	32 ±6	44
FSI-B	4.7 ±0.3	8000 ±400	0.4 ±0.1	17 ±7	33
FSI-C	5.2 ±0.5	6100 ±1500	0.3 ±0.3	25 ±3	40

^a from manufacturers datasheet, error associated with P13FSI electrolyte ionic conductivity estimated to be ±1 mS cm⁻¹ for calculation of MacMullin number error.

The wicking rate can be seen to increase with the presence of LiFSI in the polymer matrix (Figure 3.26). The wicking rate more than doubles when 0.5 wt% LiFSI is added to the PVDF-HFP matrix, the wicking rate of 2.1 cm hour⁻¹ for the base polymer increases to 4.8 cm hour⁻¹ for FSI-A. FSI-B has a similar wicking rate to FSI-A suggesting there is no obvious wetting advantage obtained by increasing the salt concentration from 0.5 to 1 wt% LiFSI. The FSI-C separator has the highest wicking rate with a small increase seen from 4.7 cm hour⁻¹ for FSI-A and FSI-B up to 5.2 cm hour⁻¹ for FSI-C. This agrees with the contact angle measurements, that incorporating LiFSI into the polymer matrix does improve the separator wetting with P13FSI electrolyte. However, whilst the

presence of LiFSI in the polymer matrix favourably influences electrolyte wetting, the wetting does not necessarily increase in proportion to the LiFSI concentration in the polymer.

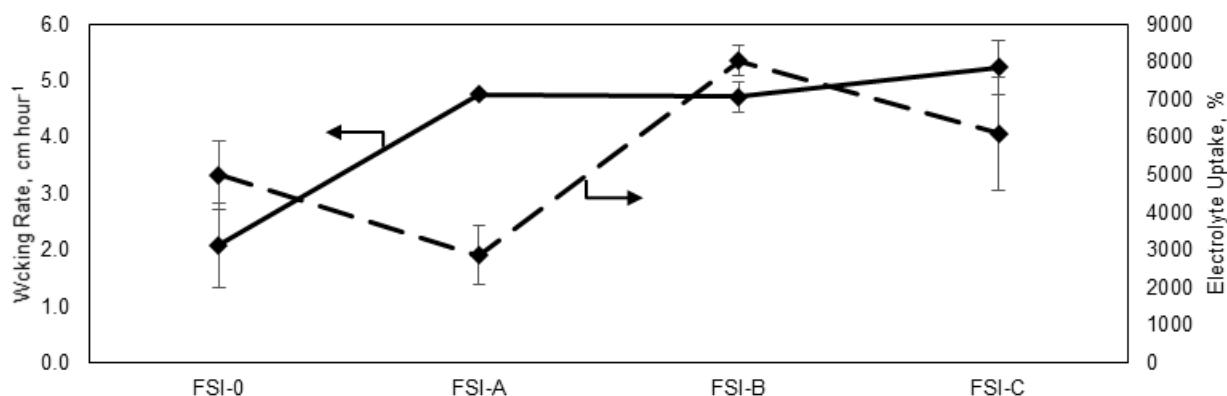


Figure 3.26 Wicking rate and electrolyte uptake for the separators containing LiFSI salt with P13FSI electrolyte.

The electrolyte uptake is another way of assessing separator wetting characteristics. Swelling of the separator when wet with electrolyte is common due to interactions between the electrolyte and polymer material [277]. The high affinity between PAN and P13FSI electrolyte has been previously demonstrated by Evans, et al. [105]. The PAN support membrane used in this work was found to have electrolyte uptake of 4200% ($\pm 800\%$) with P13FSI electrolyte. This confirms the favourable affinity of PAN with the electrolyte, and suggests that the presence of PAN in the separators prepared in this work will not negatively impact separator wetting with P13FSI electrolyte. However, ionic conductivity, McMullin number and tortuosity measurements for the PAN support material was not possible in this work due to the material being too thin and having large diameter pores ($\sim 10 \mu\text{m}$ as estimated from SEM), compared to the materials used by Evans, et al. [105].

Due to the open pore structure and high electrolyte affinity with the electrospun separators, the P13FSI electrolyte uptake values are very high for the separators containing LiFSI salt. Additionally, the process of removing excess electrolyte by dabbing the separator surface before measuring the wet weight can be imprecise due to polymer swelling, so a larger variation was seen in the electrolyte uptake values. The electrolyte uptake for the separators containing LiFSI salt can be seen in Figure 3.26 and the values can be found in Table 3.18. FSI-A has the lowest electrolyte uptake (approximately 2900%) and the largest electrolyte uptake was FSI-B with approximately 8000%, almost three times larger than that of FSI-A. FSI-0 and FSI-C have intermediate electrolyte uptake values of approximately 5000% and 6100%, respectively. There is no clear relationship between the electrolyte uptake and the concentration of LiFSI in the separator, which could be

ascribed to the challenges of preparing uniform electrospun materials. More specifically, there is no discernible advantage gained for electrolyte uptake by including LiFSI in the polymer matrix. It is likely that the PVDF-HFP fibres swell when activated with P13FSI electrolyte to form a gelatinous layer, as observed by Raghavan, et al. [315] with electrospun PVDF-HFP and IM-TFSI based IL electrolyte. This may help explain the high and varied electrolyte uptake values obtained for the four separators.

The ionic conductivity and corresponding MacMullin numbers for each separator can be found in Table 3.18. The ionic conductivity values for each separator were evaluated from the average of two samples, each scanned at least three times. There was a high variation observed in the measured resistance during EIS scanning between the two samples, which is reflected in the relatively large error values for ionic conductivity shown in Table 3.18. This variation could be due to polymer swelling, forming a gel-like layer, when the separator is wet with electrolyte. This results in a separator with a compressible thickness when assembled into a coin cell. It should be noted that within error there is no difference in the ionic conductivities measured for all electrospun separators, regardless of the salt or solvent used in the electrospinning solution. However, the ionic conductivity of the separators containing LiFSI salt can be correlated with the electrolyte uptake values, FSI-B and FSI-A have the highest (0.4 mS cm^{-1}) and lowest (0.2 mS cm^{-1}) ionic conductivities, respectively. As observed with electrolyte uptake values FSI-C has an intermediate ionic conductivity. The calculated MacMullin numbers for FSI-A, FSI-B and FSI-C also inversely correlate to the electrolyte uptake and ionic conductivities measured, with FSI-B and FSI-A having the lowest and highest MacMullin numbers, respectively. This indicates the ionic conductivity measurements suitably reflect the effects of separator tortuosity. It should be noted that the ionic conductivity of FSI-0 does not correlate to the electrolyte uptake and MacMullin number, which may suggest exterior influences, such as reduced electrolyte availability, effected the FSI-0 ionic conductivity measurement. The MacMullin number for FSI-B is 17, which is higher than the typical MacMullin numbers (10 to 12) for commercial separators [102]. This suggests the morphology - thickness, pore size, porosity and tortuosity - of the separators containing LiFSI salt could be further optimised to decrease the MacMullin number below 12, for use in a lithium-ion cell with P13FSI electrolyte.

Ionic conductivity of GF and Celgard 3501 with P13FSI electrolyte was also measured. The GF had an ionic conductivity over three times higher (1.4 mS cm^{-1}) than the best separators containing LiFSI salt, corresponding to a low MacMullin number of 5. This was expected due to the high pore size in the GF membrane which provides a lower impediment to transport, when wet with P13FSI electrolyte, compared to the electrospun separators with pores less than one-third the size. Despite providing good transport properties, the large pore size of GF is also a reason this membrane has not been used in commercial lithium-ion batteries. The separator pores must be small enough

(typically less than 1 μm) to prevent contact between the electrodes and stop migration of electrode particles during cell operation [91]. The commercial Celgard 3501 separator has the lowest ionic conductivity (0.003 mS cm^{-1}) with P13FSI electrolyte, approximately two orders of magnitude lower than the separators containing LiFSI salt. This is not surprising when considering the small pore size of 64 nm (from product information sheet) in this separator and the poor wetting with P13FSI electrolyte indicated by a high contact angle (86.9° (Figure 3.25)).

The tortuosity of each separator was calculated using **Eq. (7)**, which relates the measured ionic conductivity and porosity values for the separator to the tortuosity. FSI-0 has the highest tortuosity ($\tau = 45$) which results from having the highest porosity of the electrospun separators but the second lowest ionic conductivity. This means that although there is a high amount of pore volume for the ions to travel through, the pathway is tortuous, which leads to a reduced ionic conductivity through the thickness of the separator. FSI-A has the second highest tortuosity ($\tau = 44$) which is a result of the lowest porosity as well as the lowest ionic conductivity. FSI-C has an intermediate tortuosity ($\tau = 40$) which aligns with an intermediate porosity and ionic conductivity. The lowest tortuosity belongs to FSI-B which has the corresponding highest ionic conductivity along with the second highest porosity. A higher ionic conductivity in a separator with high porosity indicates the pathway for ionic transport is less tortuous than the other electrospun separators, as introduced in Section 2.2.1. The ideal tortuosity value in terms of transport properties would be equal to 1, a decrease in tortuosity correlates to an increase in ionic transport [316]. A higher tortuosity decreases the tendency of dendritic growth through the separator but can also increase the ionic resistance in the cell [93]. Since the tortuosities of the electrospun separators are all much greater than one it can be assumed that the separators are all tortuous enough to impede dendritic growth. Therefore, the separator with the lowest tortuosity can be described as having the best separator morphology for enabling ionic transport as determined with P13FSI electrolyte.

The ionic conductivity and MacMullin numbers for FSI-B, TFSI-B and the DMAc separator are shown in Table 3.19. FSI-B had the highest ionic conductivity (0.4 mS cm^{-1}) out of the separators containing LiFSI salt above. TFSI-B has a higher ionic conductivity (0.5 mS cm^{-1}) and corresponding lower MacMullin number of approximately 13. This suggests that, at the same salt concentration, incorporation of TFSI-B may increase the ionic conductivity of the separator. However, the thickness and pore structure of the separators can substantially influence the ionic conductivity. Since FSI-B and TFSI-B have similar thicknesses (approximately $28 \mu\text{m}$), the higher average pore size in TFSI-B compared to FSI-B is likely influencing the separator's ionic conductivity with P13FSI electrolyte, along with porosity and tortuosity properties of the separator.

Table 3.19 Ionic conductivity and MacMullin number for FSI-B, TFSI-B and the DMAc separators with P13FSI electrolyte.

Separator	Ionic conductivity, mS cm ⁻¹	MacMullin number
Tfd	0.4 ±0.1	18 ±10
FSId	0.5 ±0.3	12 ±3
TFSId	0.4 ±0.3	17 ±3
FSI-B	0.4 ±0.1	17 ±7
TFSI-B	0.5 ±0.3	13 ±3

^a from manufacturers datasheet, error associated with P13FSI electrolyte ionic conductivity estimated to be ±1 mS cm⁻¹ for calculation of MacMullin number error

Tfd and TFSId have the same ionic conductivity, 0.4 mS cm⁻¹, which is comparable to that of FSI-B. The larger thickness and larger pore size of these separators appear to have opposing effects, which result in similar ionic conductivities. The ionic conductivity of FSId is the highest (0.5 mS cm⁻¹), despite having the largest thickness. This is likely due to a favourable pore structure, in combination with the same anion FSI⁻ being present in the separator and electrolyte providing good affinity between the materials.

3.4 Conclusion

A novel separator with a multi-layer structure was prepared via electrospinning of PVDF-HFP, containing a lithium salt, onto both sides of an electrospun PAN support. The solvent type, salt type and concentration thereof in the PVDF-HFP solution were varied to investigate the effects on the resulting fibres and separator. Electrospinning PVDF-HFP solutions, with and without lithium salts, presented issues around continuous fibre formation and the final membrane morphology uniformity. Of the separators with the LiFSI salt, electrospun PVDF-HFP containing 0.5 wt% LiFSI showed the best morphology, fibre diameter distribution and pore size distribution. Although, overall, the separators electrospun with DMAc solvent showed improved fibre formation and membrane uniformity, with less beading visible from electrospinning.

The mechanical properties of the separator coated with PVDF-HFP containing 2.0 wt% LiFSI were higher than the GF membrane but not as high as the commercial Celgard 3501 separator. The separator coated with PVDF-HFP containing 0.5 wt% LiFSI showed the best thermal stability with the major mass loss delayed to a higher temperature during TGA. At higher salt concentrations it is likely the presence of lithium salt caused a discontinuous polymer matrix which resulted in a lower thermal stability in the electrospun layer.

The wetting characteristics of PVDF-HFP with P13FSI electrolyte were shown to increase with the

concentration of LiFSI in the polymer matrix. Separators containing 1 wt% LiFSI in the PVDF-HFP matrix showed the best electrolyte uptake and ionic conductivity in the presence of the P13FSI electrolyte, with the DMAc LiFSI separator having the highest overall ionic conductivity. This indicates that incorporation of a small amount of lithium salt with the same anion as the IL into the polymer matrix may increase separator wetting with IL electrolytes. The membrane morphology, thermal characteristics and favourable wetting with P13FSI electrolyte indicate the novel separators may be suitable for use in lithium-ion batteries with IL electrolyte.

In the next chapter, the electrochemical properties and cycling performance of the novel separator with P13FSI electrolyte will be evaluated. After determining the properties and performance of the novel separator, the thermal stability of P13FSI electrolyte in combination with a range of separators and electrodes will be evaluated in Chapter 5, then the thermal runaway process of a cell containing the novel separator and P13FSI electrolyte will be assessed in Chapter 6.

CHAPTER 4

Electrochemical Performance of the Novel Separator

4.1 Introduction

While enhancing cell safety is the primary concern in this thesis, the ability of the novel separator and 1.17 mol kg⁻¹ lithium bis(fluorosulfonyl)imide (LiFSI) in 1-methyl-3-propylpyrrolidinium bis(fluorosulfonyl)imide electrolyte (P13FSI electrolyte) to function in a cell is very important. Predicting the compatibility of a material in an assembled cell is not always straightforward. The novel separator characterised in Chapter 3 was found to have suitable separator morphology and good wetting with P13FSI electrolyte, which suggests good performance in a cell. Next, the separator compatibility needs to be determined against lithium metal and lithium-ion electrodes with P13FSI electrolyte to assess the separator's suitability for ionic liquid (IL) lithium-ion batteries.

Substituting a new material into a cell can introduce a number of unexpected reactions. Cells must be performance tested as close as possible to operational conditions in order to accurately design the cell for the intended application. This will help to determine potential parasitic reactions that could decrease cell performance and the conditions at which they occur. The use of an IL electrolyte, introduced in Chapter 1, removes the potentially hazardous reactions of organic solvents, but also introduces another set of reactions. Those reactions must be assessed and controlled in order for the cell to function as intended. The separator material must be tested to ensure it is inert in the cell and to determine any changes in pore structure and general integrity over the life of the cell that could impact the overall performance.

In this chapter, the novel separators manufactured and characterised in Chapter 3 were tested in lithium metal and lithium-ion cells. The methods of Electrochemical Impedance Spectroscopy (EIS), Cyclic Voltammetry (CV) and cell cycling performance was used to evaluate the cells. The techniques are introduced briefly in Section 4.2. The interphase stability of the separator and electrolyte on a lithium metal electrode were investigated with EIS. This allowed for investigation into effects of the electrolyte and / or separator, while minimising electrode material effects, however, due to complex interactions during operation, the only way to actually determine performance was to assemble a cell with all the intended components. The separators were assembled into half-cells, with an LiFePO₄ (LFP) electrode, for performance investigation at different current densities. Then full cells with an LFP cathode and an Li₄Ti₅O₁₂ (LTO) anode electrodes were assembled and subjected to cycling at a C/10 rate with different cycling temperatures and different electrolytes for assessment of the separator. Cycling efficiency of the novel separator and P13FSI electrolyte cell is an important factor to investigate for through life performance considerations. The impact of different salts (lithium trifluoromethanesulfonate (LiTf), lithium bis(fluorosulfonyl)imide (LiFSI) and lithium bis(trifluoromethanesulfonyl)imide (LiTFSI)) and concentrations (0, 0.5, 1 and 2 wt%) incorporated into the electrospun layer on separator performance was investigated.

4.2 Literature review

The physical properties of a separator are important, as discussed in Chapter 3, however the suitability of a separator for lithium-ion cells needs to be determined by cell testing. CV can provide information on the lithium transport properties of the separator wet with electrolyte. EIS can provide information on the resistance provided by electrode-electrolyte interphase films present in the cell. Cell cycling can provide information on the chemical stability and integrity of the separator wet with electrolyte in contact with the electrodes. All of these properties affect the performance of a separator when assembled into a cell.

4.2.1 Cyclic Voltammetry

The electrochemical stability of each material in a cell is crucial to functionality of the cell and is used to determine operational limits thereof. In an electrochemical cell, the materials experience voltage polarisation during cycling that can result in material decomposition [317]. Therefore the cell voltage must be limited to potentials at which the cell materials, including the separator and electrolyte, are chemically stable and do not undergo oxidation or reduction reactions [317]. The voltage range at which a material is stable is known as the electrochemical stability window [317]. Linear Sweep Voltammetry [62, 72, 318-322] and CV [67, 69, 323-327] methods have both been commonly used to determine the electrochemical stability of cell components. CV can also be used to investigate the electrochemical and transport properties of an electrolyte and / or separator [325], including the plating and stripping characteristics of lithium [69]. The plating and stripping characteristics can be obtained by cycling the potential below and above the plating and stripping potentials, respectively, ensuring not to operate outside the electrochemical stability window to avoid the effects of oxidative or reductive decomposition. Pyrrolidinium (Pyr⁺) based IL electrolytes are known to be stable with lithium metal and the presence of FSI has been shown to provide cathodic stability [326]. The ability of the electrolyte to form an Solid Electrolyte Interphase (SEI) on the plated lithium during the first cycle is important as it protects the electrode in subsequent plating-stripping cycles [65].

4.2.2 Electrochemical Impedance Spectroscopy

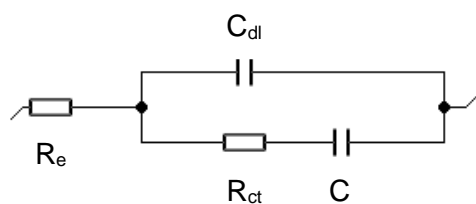
EIS is a characterisation method that allows analysis of dynamic elemental processes inside a cell; including electron migration, charger-transfer at the electrodes, lithium ion migration in the electrolyte and lithium ion diffusion in electrode active materials particles [328]. EIS can be carried out on a cell in an equilibrium state by imposing an Alternating Current (AC) and measuring the response, which is made up of alternating anodic and cathodic components [329]. EIS has been

used to investigate the charge-transfer resistance, film resistance and electric double layer capacitance of electrodes [329]. In a lithium metal or lithium-ion cell the film resistance refers to the electrode-electrolyte interphase formed on the electrode surface/s, introduced in Chapter 1.

Impedance can be physically described as the complex resistance response to an AC flowing in a circuit with real resistive components and imaginary capacitive components [330]. Therefore, the impedance of an electrochemical cell can be fitted to the impedance output of an equivalent electrical circuit of resistors and capacitors [330]. The design of a physically meaningful equivalent circuit requires an understanding of the reactions, interphase films and layers present in a cell [328, 331]. The general impedance of a cell can be fitted to simple equivalent circuits, however, it should be noted that analysis of complex electrochemical processes is limited by the accuracy of the equivalent circuit design [332].

Randles [333] introduced an equivalent electrical circuit to represent an electrode system, commonly known as Randle's circuit (Figure 4.27a). When exposed to an AC, the electrode reaction was found to be electrically equivalent to a resistor and capacitor in series [333]. The equivalent circuit includes the electrolyte resistance (R_e), the electrode surface double layer capacity (C_{dl}) and the electrode reaction resistance and capacity (R_{ct} and C , respectively) [333]. Randle's circuit is a simple equivalent circuit used to describe a single Faradaic process [330], generally a Nyquist plot with one semicircle (Figure 4.27b). Electrochemical systems with multiple phases present or complicated Faradaic processes will typically display more than one semicircle in a Nyquist plot [330], and requires additional equivalent circuit components to model the impedance.

(a) Randle's circuit



(b) Nyquist plot of Randle's circuit numerical fitting

Figure has been removed due to Copyright restrictions.

Figure 4.27 (a) Randle's circuit diagram (from Z Fit EC-Lab® software) and (b) Typical Nyquist plot of Randle's circuit numerical fitting. Taken from Fernández-Sánchez, et al. [330]. R_e is electrolyte resistance; C_{dl} is the electrode surface double layer capacity; R_{ct} and C are the electrode reaction resistance and capacity, respectively. Ω is the frequency.

Within a lithium metal or lithium-ion cell, the lithium electrolyte interphase has been suggested to consist of multiple layers, parallel to the electrode surface, with different characteristics i.e. porosity, resistance and capacitance, depending on the distance from the electrode surface (Figure 4.28) [65, 331, 334-336]. The layer adjacent to the lithium electrode is more compact because amount of reduction is higher and the electronic conductivity is also high, allowing more electrolyte of the species to be reduced [331]. Aurbach, et al. [334] suggested that the lithium electrolyte interphase forms within a few seconds of contact between electrolyte and the lithium metal, therefore the changes observed with impedance, at intervals of hours or days, is the interphase ageing process. The impedance spectrum represents time constants for the following complex processes: diffusion of lithium ions in the electrolyte; migration of lithium ions in the SEI; charge transfer between the lithium electrode and the SEI; charging of the SEI; solid-state diffusion of lithium; and lithium accumulation in the active material [21, 334].

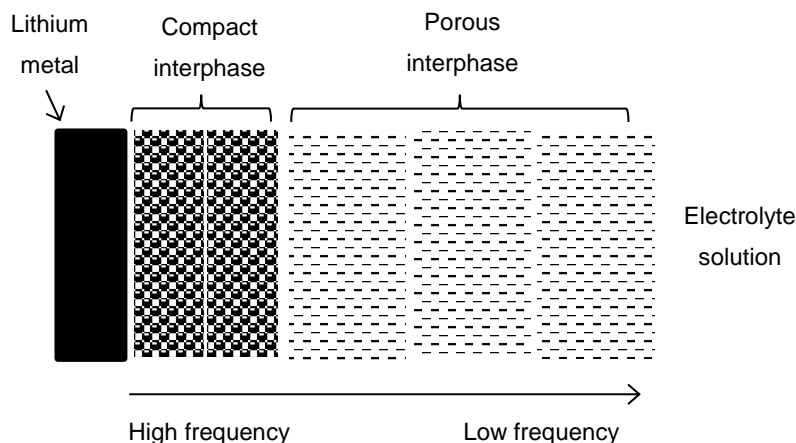


Figure 4.28 Electrode-electrolyte interphase formed on lithium metal in the presence of electrolyte.

Typically, EIS of lithium metal in contact with an electrolyte has one or more depressed semicircles in the high to mid frequency range, and been has been fitted to a multilayer model with at least four parallel resistor / capacitors in series with one resistor (e.g. Figure 4.29) [331, 334-337]. The high-frequency intercept with the real axis indicates the bulk resistance of the electrolyte [65, 326, 331, 338]. The depressed semicircle/s in the high to mid-frequency range represent the resistance and capacitance of the lithium electrolyte interphase [65, 326, 331, 334-336, 338]. The SEI formed on a lithium metal electrode with IL electrolytes has been investigated with AC impedance and equivalent circuit modelling [65, 336, 339]. Constant Phase Elements (CPEs) have been introduced into the multilayer equivalent circuit to better fit the complex SEI (with non-ideal capacitance(s)) formed on lithium with IL electrolytes [65, 336]. Each resistor / capacitor in the multilayer model represents a layer of the lithium electrolyte interphase with differing thickness, porosity, uniformity, resistivity and capacitance [331, 334].

Figure has been removed due to Copyright restrictions.

Figure 4.29 Fitted impedance spectrum obtained from a cycled symmetrical lithium cell containing 0.5 mol kg^{-1} LiTFSI-P13TFSI electrolyte. The spectrum is fitted to a four-element layer model equivalent circuit; the error of the fit is shown. Taken from Howlett, et al. [336].

EIS of porous electrodes was fitted to an equivalent circuit model of a pore by de Levie [337], who discussed the following system assumptions: uniformity of pore size distribution, electrolyte homogeneously filling pores and amount of electrolyte present, interconnectivity of pores, resistivity of electrode material and roughness of electrode surface. Although, de Levie [337] was referring to the pores in a porous electrode, these assumptions should be considered when analysing the impedance of a lithium metal electrode in the presence of electrolyte, a separator and the porous lithium electrolyte interphase formed on the electrode surface.

Electrode-electrolyte interphase stability is an important factor determining the through life performance of a cell and the separator can influence this stability. Kirchhöfer, et al. [96] found that both the morphology and chemical composition of the separator influence the SEI formed on lithium metal electrode with Pyr⁺ based ILs. Any structural changes in the separator may cause decreased lithium ion transport in the electrolyte which would increase cell resistance. Additionally, any chemical reaction that may occur with the separator and other cell components will cause reaction product to build up on the separator and reduce mass transport.

During cell operation the SEI may be disturbed, causing the electrode to become exposed and further reaction to occur with the electrolyte [340]. This can be caused by a rough electrode or separator surface causing exfoliation of the SEI at the interphase. The stability of the SEI compounds is also important [340]. If the compounds are stable against the electrolyte and active materials then they will remain in the SEI. However, if the SEI compounds are not stable in the cell environment then they may react further during cell operation causing further loss of electrolyte and accumulation of SEI. The electrode-electrolyte interphase film is expected to stabilise within the first few cycles in a cell with compatible materials. Once the cell resistance stabilises it is assumed that a sufficient electrode-electrolyte interphase has formed to prevent further reaction at the interphase. This indicates that components are no longer reacting and a stable passivating electrode-electrolyte interphase film has formed [21].

4.2.3 Capacity testing

Electrochemical testing at different rates is also an evaluation of performance. Each individual cell component has transport limitations that, together, determine the maximum transport rates

possible in an assembled cell. The separator does not actively participate in lithium ion transport however the transport of lithium ions in the electrolyte is influenced by the electrolyte-filled pore structure of the separator, i.e. porosity, tortuosity and electrolyte wettability [18]. Transport behaviour of the electrode is dictated by electrode properties, such as diffusion of lithium ions and conductivity of electrons [2, 6], as well electrode wettability with the electrolyte [17]. Transport in the electrolyte is affected by ionic conductivity as well as wettability of the electrolyte on the electrodes and separator [18].

Cycling efficiency of a cell is a good indication of life expectancy. The temperature is important as it influences transport mechanisms in the cell as well as the rate of parasitic side reactions [341]. The cell performance can be stated by two metrics; the discharge capacity at a specified rate and the coulombic efficiency. Coulombic efficiency of the cell is the amount of capacity delivered by the cell during discharge, compared to the capacity accepted by the cell in the charge immediately previous. The cycling efficiency of a cell is the amount of capacity delivered during a discharge compared to the amount of capacity delivered in the first discharge after formation. A cell intended for an extended cycling application would ideally have a cycling efficiency very close to 100% over extended cycling.

4.3 Experimental

The novel separators manufactured and characterised in Chapter 3 will be tested with P13FSI electrolyte in cells containing lithium metal and lithium-ion electrodes to compare performance of the separators assembled in a cell.

4.3.1 Materials

Novel separators: FSI-0, FSI-A, FSI-B, FSI-C, TFSI-B, Tfd, FSI_d and TFSI_d, were manufactured as described in Section 3.2 Experimental. Glass fibre (GF) membrane (GA558X10IN, Advantech), 210 µm thickness and 0.6 µm nominal pore size, was purchased from Sterlitech Limited (USA). Commercial microporous polypropylene separator (Celgard 3501), 25 µm thickness and 0.064 µm average pore size, was purchased from Celgard, LLC (USA).

The IL electrolyte was a commercial product containing 1-methyl-3-propylpyrrolidinium bis(fluorosulfonyl)imide (P13FSI) with 1.17 mol kg⁻¹ LiFSI (P13FSI electrolyte, >99.5%) purchased from CoorsTek Fluorochemicals (USA). LiFePO₄ (LFP, 10.0 mg cm⁻² coating loading, approximately 48% porosity) was purchased from MTI Corporation (USA). Li₄Ti₅O₁₂ (LTO, 13.59 mg cm⁻² coating loading, 31.7% porosity) was supplied through Argonne National Laboratory (USA) Cell Analysis, Modelling, and Prototyping (CAMP) Facility Electrode Library. The conventional electrolyte was 1.2 M lithium hexafluorophosphate (LiPF₆) in ethylene carbonate (EC): ethyl methyl carbonate (EMC) 2:1 volume/volume (v/v), purchased from *soulbrain* MI (USA). Propylene carbonate (PC, anhydrous, 99.7%) was purchased from Sigma-Aldrich (USA).

4.3.2 Electrochemical characterisation

The P13FSI electrolyte, dry and wet separators, dry electrodes and cycled cell materials were characterised with Fourier-transform infrared spectroscopy (FTIR). The materials were then tested in cells and evaluated using CV, EIS, lithium plating and stripping, capacity performance, and cycling performance.

FTIR was performed with a Spectrum 400 (PerkinElmer, USA) at CSIRO (Clayton, VIC) from 4000 cm⁻¹ to 570 cm⁻¹ (machine range), 16 scans were collected per sample. Before beginning measurements, a background scan was performed to correct for the relevant atmosphere to be used for the samples. The dry separators and electrodes were measured in an air atmosphere. The P13FSI electrolyte, wet separators and cycled separators and electrodes were measured in an argon atmosphere. The FTIR stage was transferred into an argon atmosphere glovebox (H₂O < 100 ppm, O₂ < 50 ppm) at CSIRO (Clayton, VIC) and the samples were mounted and sealed with an O-ring fitting prior to leaving the glovebox atmosphere to minimise the sample absorbing moisture during scanning.

CV was performed with a µ-Autolab III PGSTAT 302N potentiostat (Metrohm Eco Chemie, Netherlands) at CSIRO (Clayton, VIC) and using GPES software version 4.9.007, inside an argon atmosphere glovebox (H₂O <100 ppm, O₂ <50 ppm) at CSIRO (Clayton, VIC), between 0 and -4.5 V at a scan rate of 20 mV s⁻¹. CV was completed using a three-electrode cell: glassy carbon

working electrode, platinum wire counter electrode and a silver reference electrode (Ag | Ag⁺ (0.01 M silver triflate (AgOTf) in P13FSI)). The working electrode had an area of 0.0707 cm² and the counter electrode had a large surface area. The glassy carbon electrode was washed, polished and dried before each use. Before immersing in the electrolyte, the separator was wrapped tightly around the glassy carbon electrode, secured with Teflon tape and fastened with an O-ring to ensure good contact between the separator and electrode while immersed in P13FSI electrolyte.

The separators were cut into 15.9 mm diameter disks and dried overnight in a vacuum oven at 50 °C before transferring into an argon atmosphere glovebox through a vacuum antechamber. Once inside the glovebox, the separators were assembled into coin cells (CR2032 cells). For open circuit EIS and lithium plating / stripping tests, the separators were assembled into symmetrical lithium metal coin cells (lithium chips: 12 mm diameter, 0.4 mm thick). 150 µL of P13FSI electrolyte was added directly onto the separator surface during coin cell assembly.

EIS coin cells were removed from the glovebox and tested at room temperature on a potentiostat (VMP3, BioLogic Science Instruments, France) at CSIRO (Clayton, VIC). The cells were tested within one hour of assembly to reduce variation in the cell resistance from extended standing time. The potentiostat was configured for a two-electrode cell with the reference electrode lead piggybacked onto the counter electrode lead. EIS cells were scanned with an amplitude of 10 mV from 0.1 MHz to 0.1 Hz (within standard range [282]). An EIS scan was performed within one hour of cell assembly (as soon as practicable) and each consecutive hour for at least 15 hours with the cell at open circuit and room temperature in between scans. Equivalent electrical circuit fitting was performed using Z Fit (EC-Lab® V11.16, BioLogic Science Instruments, France).

Lithium plating / stripping cells were removed from the glovebox and tested on a MACCOR unit (Series 4000, MACCOR, Inc., USA) at CSIRO (Clayton, VIC). A cycle consisted of 0.1 mA cm⁻² current applied for 16 minutes then the current was reversed for 16 minutes [95, 342], with a one minute rest at open circuit in between each current reversal. This cycle was completed 100 times.

4.3.3 Cell preparation and cell testing

LFP and LTO electrodes were cut into 11 mm diameter disks and dried overnight in a vacuum oven at 50 °C before transferring into an argon atmosphere glovebox (H₂O <100 ppm, O₂ <50 ppm) at CSIRO (Clayton, VIC). For coin cell testing at different discharge rates, the separators were assembled into LFP half-cells with lithium metal as the counter electrode and P13FSI electrolyte. For cell cycle testing the separators were assembled into LFP | LTO coin cells. Three different electrolytes were used for comparison. P13FSI electrolyte cells used 150 µL of P13FSI electrolyte. P13FSI / PC electrolyte cells used 120 µL of P13FSI electrolyte containing 6.3 wt% PC

additive. Conventional cells used 100 μL of 1.2 M LiPF_6 EC / EMC (2:1 v/v).

The coin cells were removed from the glovebox and tested on a MACCOR unit. Cells for rate performance testing were cycled at room temperature in the voltage range 3.0 to 3.8 V. The typical LFP | lithium metal (Li) voltage range in literature is 2.5 to 4.2 V [199, 218], however, a narrower voltage range was selected to reduce the effects of electrode ageing during cycling in an attempt to focus on separator effects. Some variation in the room temperature during testing was expected so cells were contained in a thermally insulated container at room temperature to minimise the effect of temperature variation during the test, approximately 12 days duration. Additionally, all cells were tested at the same time therefore direct comparison between cell can be made. Prior to testing at different rates, the cells underwent three formation cycles at C/20. One cycle is defined as a discharge followed by a recharge at the same rate with three minutes rest at the end of each discharge and charge. The cells were then cycled five times at C/10, five times at C/5, five times at C/2 and five times at C/10 again, for comparison. The cells were cycled at a C/10 rate following the higher rate tests to determine the degree of reversibility for lower capacities observed at higher rates.

Cells for cycle testing were cycled at 30 $^{\circ}\text{C}$ in the voltage range 1.0 to 2.5 V. The cells were tested in a temperature-controlled environment to minimise the effect of temperature variation during the test, approximately six weeks duration. Before cycle testing the cells underwent three formation cycles at C/20. The cells were then cycled at C/10 rate for 50 cycles. Cycling was also performed on some cells at 50 $^{\circ}\text{C}$ in a temperature-controlled environment.

The cycle tested coin cells were transferred back into the glovebox for disassembly. Separators and electrodes were harvested from the coin cells by using a coin cell uncrimping device (MTI Corporation (USA), MSK-110) at CSIRO (Clayton, VIC) to ensure that the cells were not short circuited. The electrodes and separators were harvested without washing with solvent to avoid disturbing any electrode-electrolyte interphase that may have been present on the sample surface. FTIR was performed on the harvested samples. The FTIR obtained for cycled electrodes was compared to the FTIR of P13FSI electrolyte to identify peaks that may originate from the excess electrolyte present on the harvested electrodes.

4.4 Results and discussion

FTIR was performed on the novel separators manufactured in Chapter 3 dry and with P13FSI electrolyte to determine interactions between the separator and electrolyte materials. CV, EIS and cell testing of the novel separators with P13FSI electrolyte was performed to assess the performance of the separators when assembled into a lithium-ion cell.

4.4.1 FTIR polymer structure

The FTIR spectra for dry separators containing LiFSI salt, including the polyacrylonitrile (PAN) support membrane, are shown in Figure 4.30. FTIR was used to determine the effects of LiFSI addition on the poly(vinylidene fluoride-hexafluoropropylene) (PVDF-HFP) polymer structure in the electrospun separators and confirm the structure of the PAN support membrane. The PAN support shows peaks at 2243 and 1454 cm^{-1} from -CN stretching vibration and C-H bending vibration, respectively, which are characteristic of PAN [210, 228] (indicated by red circles in Figure 4.30). An additional peak can also be seen at approximately 1667 cm^{-1} of unknown origin but is consistent with FTIR spectrum of electrospun PAN reported previously by Yanilmaz, et al. [218].

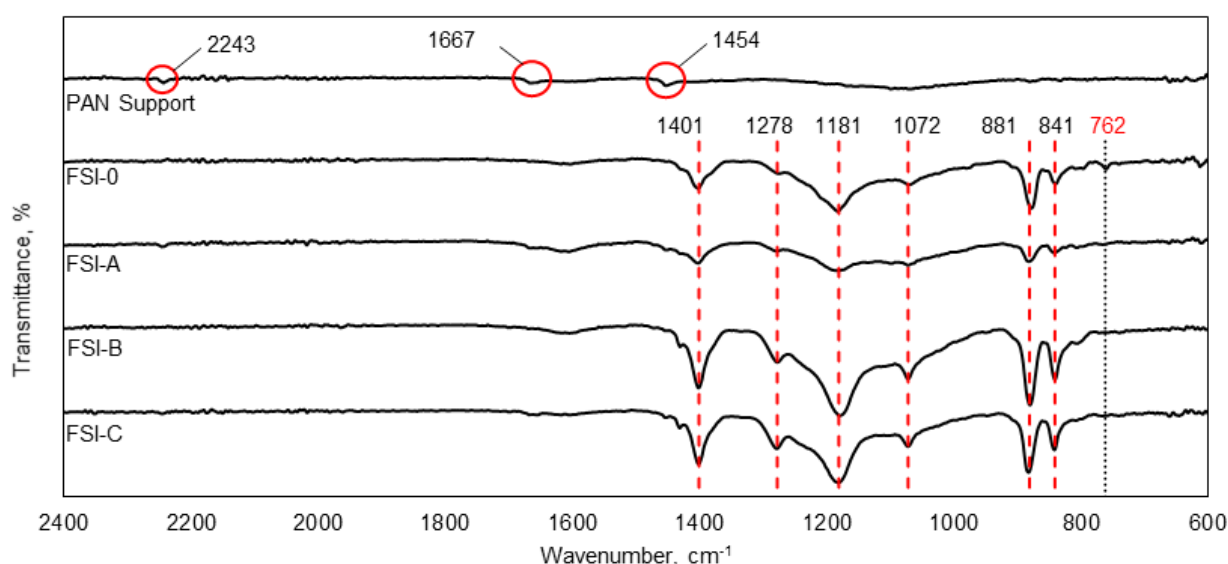


Figure 4.30 FTIR of dry separators containing LiFSI salt and PAN support. Characteristic PAN peaks circled in red. Characteristic PVDF-HFP peaks indicated with red dashed line. LiFSI peak indicated by red dotted line and red label.

The separators containing LiFSI salt with different salt concentrations all show peaks characteristic of PVDF-HFP that align well with previously reported FTIR spectrum of PVDF-HFP [182, 189]. The six peaks identified in Figure 4.30 (indicated by red dashed lines with black labels) can be assigned to the following vibrations: 1401 cm^{-1} - CH_2 wagging vibration; 1278 cm^{-1} - CF_2 asymmetrical stretching vibration; 1181 cm^{-1} - CF_2 symmetrical stretching vibration; 881 cm^{-1} - CF_2 rocking vibration; and, 1072 and 841 cm^{-1} - CF_3 rocking vibration [189]. Sousa, et al. [182] identify the 881 cm^{-1} peak from the amorphous phase of PVDF-HFP and the 1401 and 841 cm^{-1} peaks from the crystalline phase of the copolymer. FSI-B and FSI-C show the strongest peaks which suggests the addition of 1 or 2 wt% LiFSI salt to PVDF-HFP does not noticeably alter the

amorphous or crystalline phases of the copolymer. FSI-A has weaker characteristic PVDF-HFP peaks than the other electrospun separators but does show the characteristic -CN stretching vibration peak at 2243 cm^{-1} from the PAN support. This could be due to the electrospun coating being thinner on this part of the sample or from disturbance of the electrospun fibres, both which would allow the PAN spectrum to be detected during FTIR.

The FTIR spectra of the PVDF-HFP fibres containing LiFSI salt (FSI-A, FSI-B and FSI-C) are not very different from that of the pure PVDF-HFP fibres (FSI-0). The only visible difference is one small peak at 762 cm^{-1} that occurs in the FSI-0 spectrum and is noticeably absent from the FSI-A, FSI-B and FSI-C spectra (Figure 4.30 indicated by grey dotted line with red label). Detailed FTIR of LiFSI, previously reported by Huang and Hollenkamp [64], identifies a peak at 759 cm^{-1} as being from -SNS symmetrical stretching vibration. The exact cause of peak reduction at 762 cm^{-1} in PVDF-HFP containing LiFSI salt is not known but could be due to interaction between the salt and PVDF-HFP.

4.4.2 Cyclic voltammetry

Cells containing the GF, FSI-B and FSI-C separators with P13FSI electrolyte underwent CV. Five CV scans are shown in Figure 4.31 for GF, FSI-B and FSI-C in P13FSI electrolyte and one scan of P13FSI electrolyte with no separator. The current density has been normalised based on the glassy carbon electrode surface area (0.0707 cm^2). CV was performed at a glassy carbon working electrode with a $\text{Ag} | \text{Ag}^+$ reference electrode [343] and platinum counter electrode, in the voltage range 0 V to -4.5 V and a scan rate of 20 mV s^{-1} . Non-porous electrodes, such as glassy carbon or platinum, typically have small capacitive currents and therefore the effects of capacitive current during electrochemical stability testing can be assumed negligible with these electrodes [317]. An overlay of the first and fifth CV scans are shown in Figure 4.32 for comparison between the separators. The coulombic efficiencies, lithium plating and stripping peak potentials and magnitudes for each scan of GF, FSI-B and FSI-C shown Figure 4.31 can be found in Table 4.20.

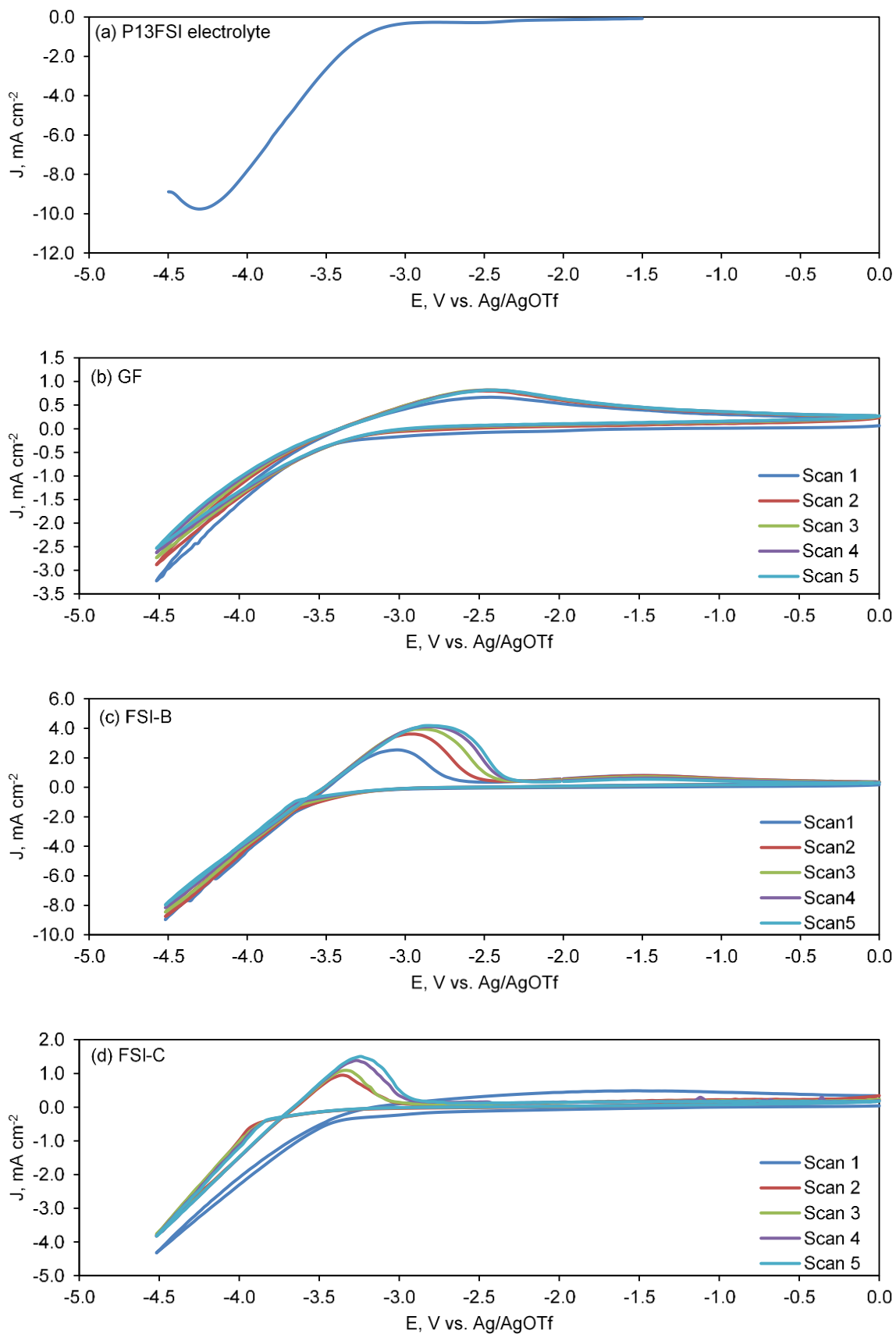


Figure 4.31 CV at a glassy carbon electrode in P13FSI electrolyte with (a) no separator, (b) GF, (c) FIS-B and (d) FIS-C.

The P13FSI electrolyte, without a separator, was scanned one from -1.5 V down to -4.5 V (Figure 4.31a). The lithium plating peak begins at approximately -3 V and continues until -4.5 V. The plating peak has a maximum current density of approximately -9.8 mA cm^{-2} at approximately -4.3 V. The P13FSI electrolyte plating peak can be compared to the lithium plating with the separators to investigate the effect of the separator on lithium plating behaviour.

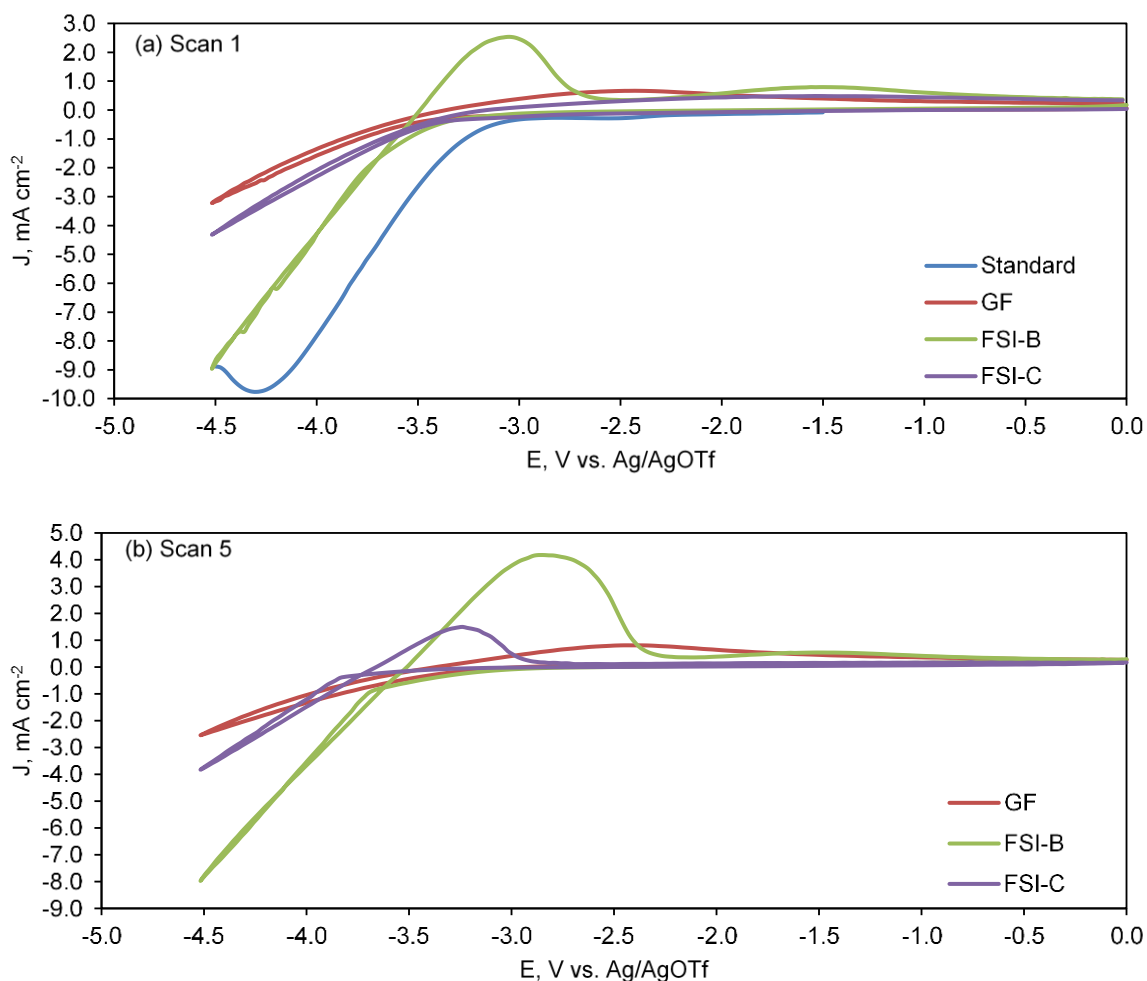


Figure 4.32 (a) 1st and (b) 5th scan of CV at a glassy carbon electrode in P13FSI electrolyte.

With GF (Figure 4.31b) lithium plating peak begins at approximately -3.3 V and reaches a maximum at -4.5 V, when the specified voltage limit was reached and the reverse scan commenced, as in all the samples. During the reverse scans the lithium stripping begins at approximately -3.3 V and continues in a broad peak until just before 0 V. The maximum plating current density decreases with each scan, in the first scan the plating current density reached approximately -3.2 mA cm^{-2} and by the fifth scan the maximum current density had reduced to

approximately -2.5 mA cm^{-2} . The stripping peak current density increases slightly after the first scan then remains relatively constant at approximately 0.8 mA cm^{-2} . The initial coulombic efficiency is approximately 60% and increases each scan to approximately 93% in the fifth scan, this indicates that irreversible reactions occur during the first scan, after which the reversibility increases successively in further scans. The increasing coulombic efficiency could be due to formation of SEI on the electrode surface [344].

Table 4.20 Coulombic efficiency and oxidation voltage and current peak of GF, FSI-B and FSI-C from Cyclic Voltammetry (CV) at a glassy carbon electrode in P13FSI electrolyte.

		Scan 1	Scan 2	Scan 3	Scan 4	Scan 5
GF	Coulombic efficiency, %	59.5	80.0	86.5	90.0	92.5
	E^{red} , V	$-4.52 \pm 0.2^{\S}$	-4.52 ± 0.2	-4.52 ± 0.2	-4.52 ± 0.2	-4.52 ± 0.2
	I^{red} , mA cm^{-2}	$-3.23 \pm 0.16^{\S}$	-2.88 ± 0.16	-2.73 ± 0.16	-2.63 ± 0.16	-2.54 ± 0.16
	E^{ox} , V	-2.42 ± 0.2	-2.48 ± 0.2	-2.44 ± 0.2	-2.46 ± 0.2	-2.44 ± 0.2
	I^{ox} , mA cm^{-2}	0.67 ± 0.16	0.80 ± 0.16	0.82 ± 0.16	0.82 ± 0.16	0.81 ± 0.16
FSI-B	Coulombic efficiency, %	26.6	45.4	58.4	64.9	71.0
	E^{red} , V	-4.52 ± 0.2	-4.52 ± 0.2	-4.52 ± 0.2	-4.52 ± 0.2	-4.52 ± 0.2
	I^{red} , mA cm^{-2}	-8.97 ± 0.16	-8.74 ± 0.16	-8.46 ± 0.16	-8.17 ± 0.16	-7.97 ± 0.16
	E^{ox} , V	-3.04 ± 0.2	-2.96 ± 0.2	-2.88 ± 0.2	-2.84 ± 0.2	-2.86 ± 0.2
	I^{ox} , mA cm^{-2}	2.54 ± 0.16	3.62 ± 0.16	3.94 ± 0.16	4.10 ± 0.16	4.19 ± 0.16
FSI-C	Coulombic efficiency, %	26.1	18.7	21.1	31.8	37.4
	E^{red} , V	-4.52 ± 0.2	-4.52 ± 0.2	-4.52 ± 0.2	-4.52 ± 0.2	-4.52 ± 0.2
	I^{red} , mA cm^{-2}	-4.32 ± 0.16	-3.81 ± 0.16	-3.77 ± 0.16	-3.82 ± 0.16	-3.83 ± 0.16
	E^{ox} , V	-1.54 ± 0.2	-3.36 ± 0.2	-3.34 ± 0.2	-3.26 ± 0.2	-3.24 ± 0.2
	I^{ox} , mA cm^{-2}	0.49 ± 0.16	0.95 ± 0.16	1.09 ± 0.16	1.38 ± 0.16	1.50 ± 0.16

* E^{red} = plating peak potential, E^{ox} = stripping peak potential, I^{red} = plating peak magnitude, I^{ox} = stripping peak magnitude.

\S Since replicates not performed, all errors were calculated from voltage and capacity accuracy of AUTOLAB potentiostat.

With FSI-B (Figure 4.31c) lithium plating peak begins at approximately -3.6 V . Similar to GF, the maximum plating current density decreases with each scan, in the first scan the plating peak maximum current density was approximately -9 mA cm^{-2} and by the fifth scan the current density had reduced to approximately -8 mA cm^{-2} . During the reverse scans the lithium stripping begins at approximately -3.5 V and ends at approximately -2.6 V in the first scan. In successive scans the stripping peak becomes broader and the peak magnitude increases. The stripping current density peaks at approximately 2.5 mA cm^{-2} in the first scan and increases to at approximately 4.2 mA cm^{-2} in the fifth scan. The initial coulombic efficiency is approximately 27% and increases each scan to approximately 71% in the fifth scan, indicating a low reversibility in the first scan with some

improvement in consecutive scans, which could be due to SEI formation on the electrode surface [344]. The coulombic efficiency of FSI-B is substantially lower than GF, however, the current densities achieved with FSI-B are higher. Despite GF having a substantially higher ionic conductivity in Chapter 3 compared to the prepared electrospun separators, the lithium stripping and plating performance of GF was not correspondingly superior. This suggests factors other than lithium ion transport in the electrolyte wetted separator can also impact the lithium stripping and plating behaviour, such as the uneven surface of GF likely resulting in poor SEI formation on the plated lithium, as introduced in section 4.2.1.

With FSI-C (Figure 4.31c) first scan is substantially different from the shape of consecutive scans, the first scan is similar in shape to that obtained with GF (Figure 4.32a), while the following scans are more similar to the shape obtained with FSI-B (Figure 4.32b). In the first scan the lithium plating peak begins at approximately -3.3 V and reaches a maximum current density of -4.3 mA cm^{-2} at -4.5 V. However, in the second scan the plating peak begins at approximately -0.5 V lower and has a smaller peak current density of approximately -3.8 mA cm^{-2} , this remains relatively constant for the remaining scans. During the first reverse scans the lithium stripping peak is a broad peak beginning at approximately -3.3 V and continuing until almost 0 V, as in GF. In the second scan the stripping peak begins at approximately -3.7 V and ends at approximately -3 V. In successive scans the stripping peak becomes broader and the peak magnitude increases. The stripping current density peaks of approximately 0.95 mA cm^{-2} in the second scan and increases to approximately 1.5 mA cm^{-2} in the fifth scan. The initial coulombic efficiency is approximately 27%, this decreases to approximately 19% in the second scan then and increases each scan to approximately 37% in the fifth scan, this indicates that irreversible reactions occur during the first and second scans, after which the reversibility increases however still remains below 40% coulombic efficiency in the fifth scan. The low coulombic efficiency could suggest that a stable SEI has not formed on the plated lithium with FSI-C and P13FSI electrolyte [344].

The lithium plating current density for P13FSI electrolyte without a separator reached a maximum of approximately -9.8 mA cm^{-2} . This is similar to the current densities of approximately -8 and -9 mA cm^{-2} observed by Bhatt, et al. [326] for 0.45 mol kg^{-1} LiFSI in P13FSI at platinum and nickel working electrodes, respectively. Although it should be noted that the lithium salt concentration was lower in the study performed by [326] than for the P13FSI electrolyte used in this thesis. The plating current density for P13FSI electrolyte without a separator is similar to the plating current density obtained during the first scan of FSI-B (approximately -8 mA cm^{-2}), however the current density decreases in subsequent scans with FSI-B. The next largest plating current density is FSI-C with approximately -4.3 mA cm^{-2} in the first scan, approximately half that of P13FSI electrolyte without a separator, and decreased current density in subsequent scans. GF has the lowest plating current density, approximately -3.2 mA cm^{-2} in the first scan. This suggests that FSI-C and GF do

impede the lithium plating of P13FSI electrolyte which will affect the performance of these separators in a P13FSI electrolyte lithium-ion cell.

4.4.3 Open circuit voltage EIS

EIS was performed on lithium symmetrical cells with P13FSI electrolyte, using the GF and novel separators manufactured in this work (Section 3.2.3), at open circuit voltage. The EIS data is plotted as Nyquist plots in Figure 4.34 and Figure 4.36. The equivalent circuit and numerical representation used to fit the impedance data is shown in Figure 4.33 and the fitted parameters are shown in Table 4.21. All the separators produce a Nyquist plot with two semicircles. The Warburg contribution is not observed in this work due to 0.1 Hz set as the lower frequency limit in the test specification. The impedance spectra of the separators at 0 and 15 hours are compared in Figure 4.35 and Figure 4.37, experimental results shown by markers and fitted results shown by solid lines.

Along with the complex multilayer SEI (discussed in Section 4.2.2) [65, 331, 334-336], the impedance spectrum is also likely influenced by the separator structure. The separator consists of three layers, each with different thickness, porosity and tortuosity. Additionally, the outer PVDF-HFP layers become gelatinous when activated with the IL electrolyte and the gel electrolyte likely interacts with the electrode, especially the separators containing LiFSI in the polymer matrix, which could undergo reduction at the lithium electrode and form part of the SEI.

The SEI formed on the lithium electrode with P13FSI electrolyte is shown as two semicircles in the Nyquist plot (Figure 4.33a), which has also previously been observed by Liu, et al. [324] for piperidinium-FSI IL electrolyte in a Li | GF | Li cell. The use of CPEs help fit the complex SEI formed on lithium metal with P13FSI electrolyte [65, 336]. Together the two semicircles in the Nyquist plot represent the SEI [65, 326, 331, 334-336, 338]. The two semicircles are depressed, suggesting multiple overlapping semicircles in the same frequency ranges. Semicircle depression could indicate the complex nature of the SEI, i.e. multilayer with varying porosity, lithium ion resistance, charge-transfer resistance and electrical capacitance in each layer [65, 326, 331, 334-336, 338].

The impedance data was fitted with the equivalent circuit shows in Figure 4.33b. R_1 (R_{ele} in Table 4.21) represents the resistance of the bulk electrolyte [65, 326, 331, 338]. This resistance is associated with the transport limitations of lithium ions through the electrolyte-separator matrix. The parallel blocks, Q_2/R_2 and Q_3/R_3 , together represent the total resistance and capacitance of the SEI and the lithium electrode. The resistance and capacitance of the SEI are shown as R_{SEI} and Q_{SEI} , respectively, in Table 4.21.

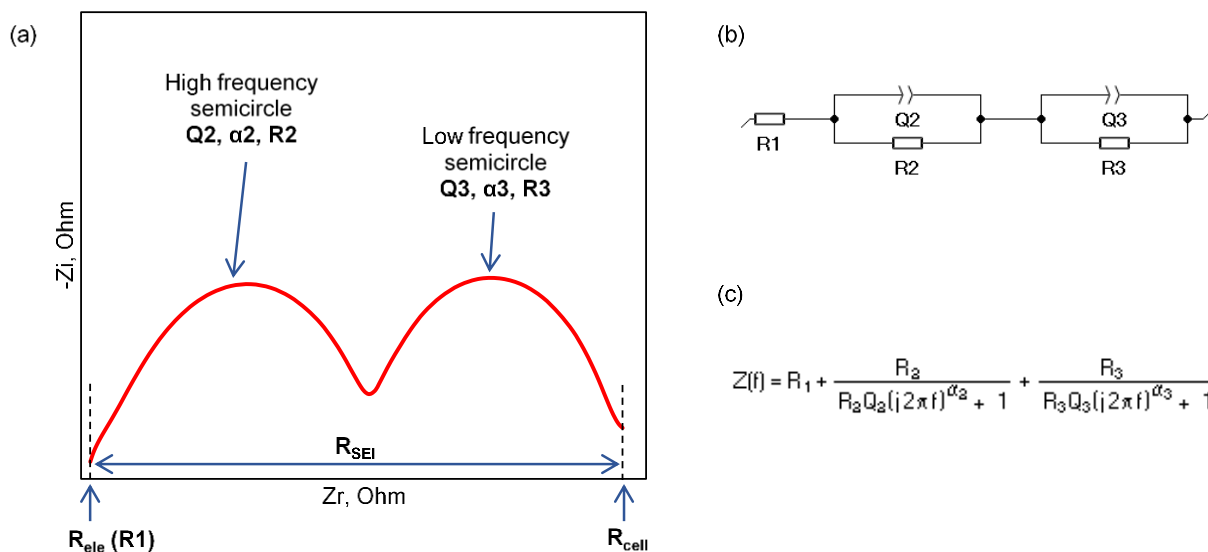


Figure 4.33 (a) Typical Nyquist plot obtained for novel separators in Li | P13FSI electrolyte | Li cell. (b) Equivalent electrical circuit for fitting impedance data. (c) Numerical fitting for equivalent circuit. R_{ele} is the resistance associated with the electrolyte + separator phase. R_{SEI} is the resistance associated with the SEI. R_{cell} is the total resistance.

The SEI is a porous film of electrolyte reduction products with electrolyte filled pores. Two parallel Q/R blocks were used to model the resistance and capacitance of the SEI [342]. In literature, the higher frequency semicircle has been associated with lithium ion diffusion through the SEI and the lower frequency semicircle with lithium transport at the SEI / active material interphase [21]. Specifically, R_2 and Q_2 are the impedance and capacitance of the SEI, respectively; and R_3 and Q_3 are the charge transfer resistance and double layer capacitance at the interphase, respectively [74].

In both instances the capacitance was modelled with a CPE, Q in Figure 4.33, to account for the complex structure of the SEI, as indicated by depressed semicircles [342]. The SEI is made up of various reduction products, each with different conducting properties. Additionally, the porosity and tortuosity of the SEI changes through the depth of the interphase with the least porous region existing immediately adjacent to the lithium electrode where the electrical conductivity is highest, and the most porous region is at the electrolyte edge where electrolyte is readily available for reduction but the electrical conductivity is much lower.

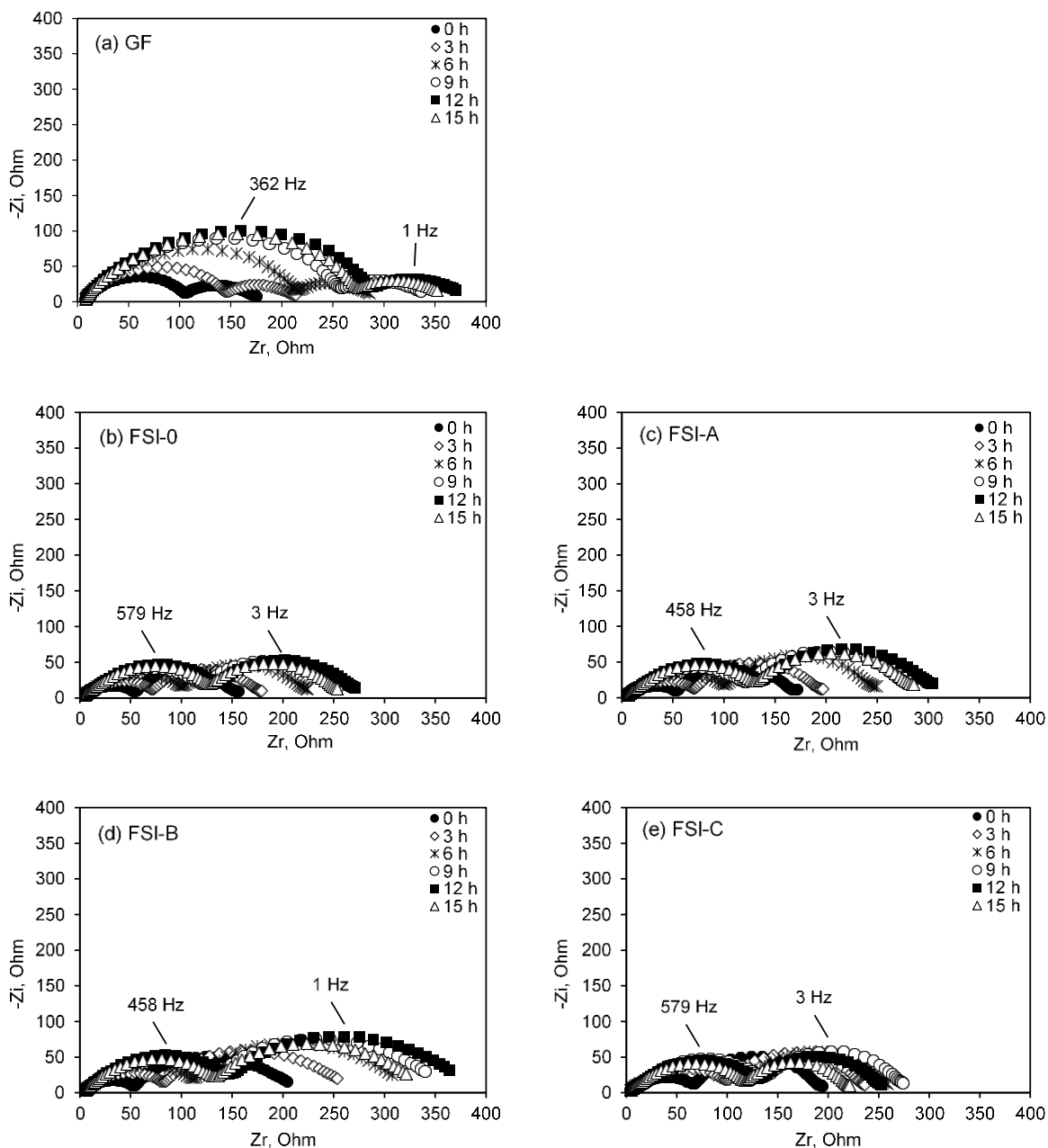


Figure 4.34 Nyquist plots of Li | P13FSI electrolyte | Li cells with (a) GF, (b) FSI-0, (c) FSI-A, (d) FSI-B and (e) FSI-C separators at different times during storage at open circuit voltage.

In all separators, including GF, the overall resistance can be observed to increase with storage time (Figure 4.34), reaching a maximum at 12 hours (9 hours for FSI-C), then decreasing in the 15 and 18 hour impedance spectra. This has similarly been observed for a N-ethyl-N-butylpyrrolidinium bis(fluorosulfonyl)imide (P24FSI) IL electrolyte (P24FSI:LiFSI 9:1 mole ratio) on lithium metal electrode [63]. Moreno, et al. [63] observed an increase in interfacial resistance over approximately the first ten hours, followed by a gradual decrease over the next 50 hours and a subsequent stable interfacial resistance over 200 hours storage. The authors [63] attribute the

enhanced interfacial stability, compared to an equivalent bis(trifluoromethanesulfonyl)imide (TFSI⁻) IL electrolyte, to the reduction products of FSI⁻ being able to form an effective passivation film on the lithium electrode. The results observed by Moreno, et al. [63] suggest that following the maximum resistance at approximately 12 hours and subsequent decrease observed in this work, the resistance could be expected to continue decreasing before stabilising at approximately the same resistance as time 0 hour.

Table 4.21 Equivalent circuit fitted parameters

		^a R _{cell} , Ohms cm ⁻²	^b R _{ele} , Ohms cm ⁻²	^c R _{SEI} , Ohms cm ⁻²	^d Q _{SEI} , μF s ^(a-1) cm ⁻²
GF	0	156 ±4	4.9 ±0.2	151 ±4	1240 ±38
	15	313 ±3	5.2 ±0.3	308 ±2	3083 ±164
FSI-0	0	136 ±4	2.2 ±0.3	133 ±4	491 ±24
	15	221 ±7	2.3 ±0.4	219 ±6	730 ±24
FSI-A	0	149 ±4	2.6 ±0.3	146 ±4	400 ±22
	15	250 ±7	3.0 ±0.4	247 ±7	580 ±18
FSI-B	0	181 ±4	2.7 ±0.1	179 ±3	646 ±16
	15	298 ±6	3.0 ±0.4	295 ±5	820 ±12
FSI-C	0	169 ±4	1.5 ±0.1	168 ±4	385 ±18
	15	193 ±6	1.4 ±0.4	191 ±6	744 ±36
TFSI-B	0	152 ±4	1.8 ±0.1	150 ±4	446 ±24
	15	183 ±6	2.0 ±0.4	181 ±6	767 ±37
Tfd	0	83 ±6	3.5 ±0.2	80 ±6	1466 ±100
	15	197 ±5	3.8 ±0.3	193 ±5	1887 ±54
FSId	0	92 ±5	6.9 ±0.3	85 ±5	910 ±77
	15	202 ±6	5.8 ±0.3	196 ±5	1205 ±30

^a R_{cell} = R_{ele} + R_{SEI}

^b R_{ele} is equal to R1 in Figure 4.33

^c R_{SEI} = R2 + R3

^d Q_{SEI} = Q2 + Q3

The electrolyte resistance, R_{ele} (R1), makes up only 1 to 2% of the total cell resistance, R_{cell} (R_{ele} + R_{SEI}) (see Table 4.21), therefore small changes observed are considered to have a negligible impact on the overall resistance. Since R_{ele} is associated with the transport limitations of lithium ions through the electrolyte-separator matrix, the variation seen in R_{ele} for different separators wet with the same electrolyte (i.e. P13FSI) is most likely due to separator properties, such as thickness, porosity and tortuosity, as well as separator wettability. FSI-C has the lowest R_{ele} value (Figure 4.34e), 1.5 and 1.4 ohms cm⁻² at 0 and 15 hours, respectively. FSI-C and FSId (Figure 4.34b), are the only separators in which the R_{ele} value at 15 hours is lower than the initial R_{ele} value. FSId has the largest R_{ele} (5.8 ohms cm⁻² at 15 hours) of all the separators and the thickness of FSId (75 ±20 μm) could have contributed to the high R_{ele}. TFSI-B has an R_{ele} below 2 ohms cm⁻²,

FSI-0, FSI-A and FSI-B have R_{ele} values between 2 and 3 ohms cm^{-2} , T_{fd} is approximately 4 ohms cm^{-2} , GF is approximately 5 ohms cm^{-2} , and FSI-d is approximately 6 ohms cm^{-2} .

For GF (Figure 4.34a), R_{SEI} doubles from 151 ohms cm^{-2} at 0 h, to 308 ohms cm^{-2} at 12 hours. R_{SEI} then decreases in the 15 and 18 hour scans, which suggests stabilisation of the SEI. In the GF impedance spectrum, the lower frequency semicircle remains relatively constant, while the higher frequency semicircle is responsible for the increase observed in R_{SEI} from 0 to 15 hours storage time.

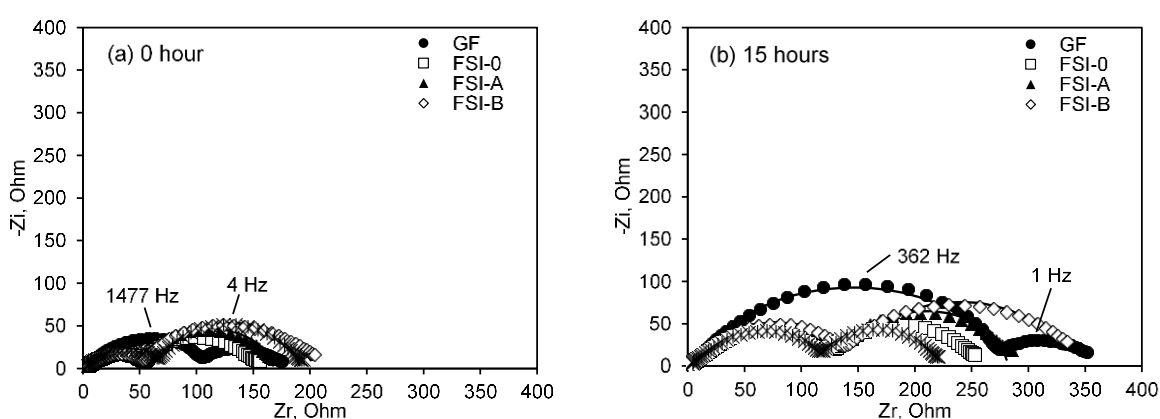


Figure 4.35 Nyquist plots for EIS of Li | separator + P13FSI electrolyte | Li cell (a) at time of cell assembly and (b) after 15 hours at open circuit voltage at room temperature.

R_{SEI} for FSI-0, FSI-A and FSI-B increases with LiFSI concentration in the polymer matrix (Figure 4.34b-d). At 0 hours R_{SEI} is 133, 146 and 179 ohms cm^{-2} and a 15 hours R_{SEI} is 219, 247 and 295 ohms cm^{-2} , for FSI-0, FSI-A and FSI-B, respectively. Although the higher frequency semicircle is smaller than the lower frequency semicircle in the FSI-0, FSI-A and FSI-B impedance spectra, from 0 hours to 15 hours the lower frequency semicircle only increases by a small amount while the higher frequency semicircle contributes most of the increase observed in R_{SEI} . At 15 hours FSI-B has the highest R_{SEI} of all the separators, except for GF.

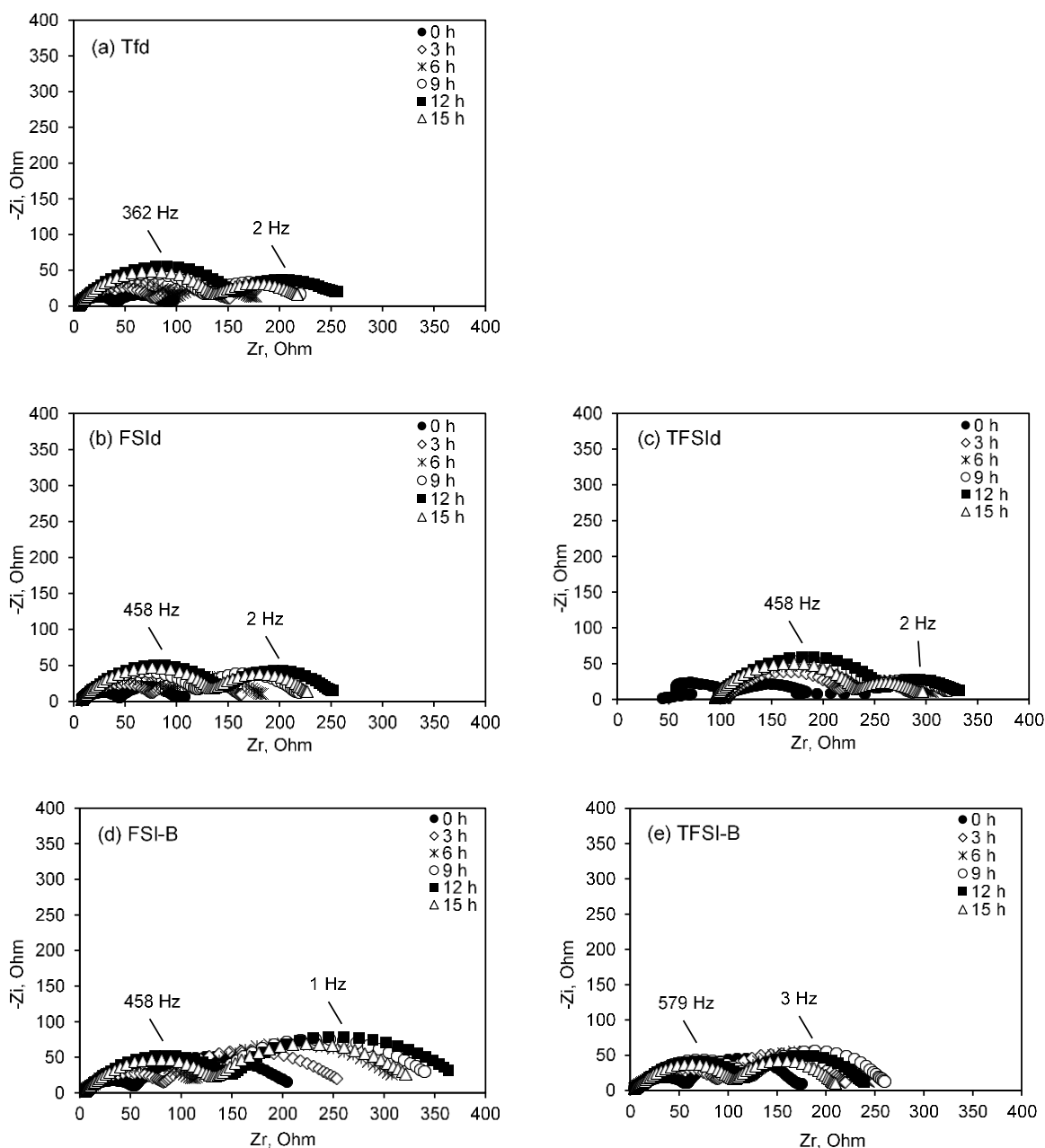


Figure 4.36 Nyquist plots of Li | P13FSI electrolyte | Li cells with (a) Tfd, (b) FSI-d, (c) TFSI-d, (d) FSI-B and (e) TFSI-B separators at different times during storage at open circuit voltage.

The resistance increases from FSI-0 to FSI-A to FSI-B with 0, 0.5 and 1 wt% LiFSI, respectively, suggesting that incorporation of LiFSI does not reduce the resistance of the SEI. However, the FSI-C separator does not match this trend and at 15 hours FSI-C (Figure 4.34e) has a lower R_{SEI} (191 ohms cm^{-2}) than GF, FSI-0, FSI-A and FSI-B. Unlike the other separators, the FSI-C R_{SEI} reaches a maximum at nine hours and shows decreasing resistances at 12 and 15 hours. Although FIS-C has a high initial R_{SEI} (Figure 4.35a), the resistance increase from 0 to 15 hours is much lower than the other separators containing LiFSI salt (Figure 4.35a). The lower resistance indicates

a more stable SEI is able to form with this separator, this could be due to the 2 wt% LiFSI in the polymer interacting with the lithium metal surface, which would reduce the amount of interaction between the lithium metal and P13FSI electrolyte and the subsequent SEI formation.

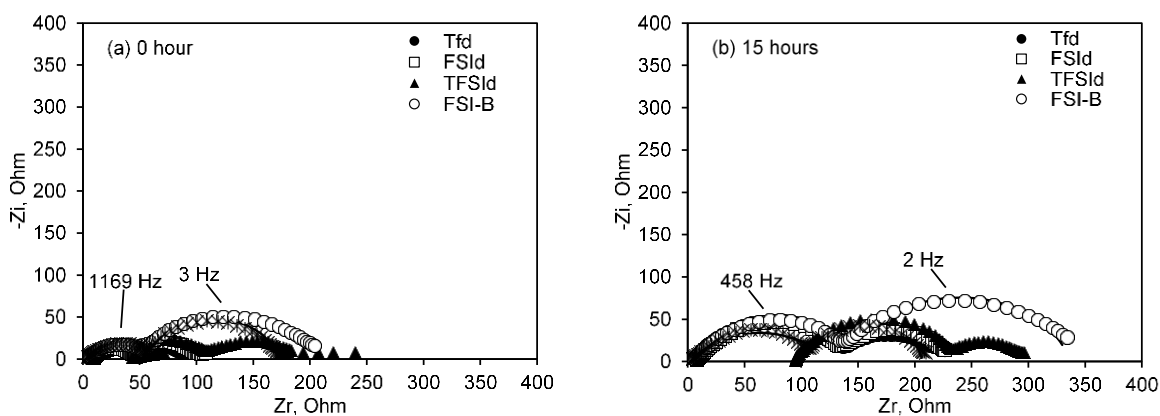


Figure 4.37 Nyquist plots for EIS of Li | separator + P13FSI electrolyte | Li cell (a) at time of cell assembly and (b) after 15 hours at open circuit voltage at room temperature.

The most obvious difference between the GF and the electrospun separators impedance spectrum in Figure 4.35 is that GF is the only one in which the higher frequency semicircle is larger than the lower frequency semicircle. This suggests the resistance of lithium migration through the surface interphase is larger than the charge transfer resistance between the electrode and electrolyte. It should be noted that the GF is approximately five times thicker than the electrospun separators, which could account for the difference in resistances.

In order to further investigate the impact of an incorporated lithium salt in the separator on electrode-electrolyte interphase stability with lithium metal, 1 wt% LiTFSI was incorporated. Similar to FSI-C, R_{SEI} for TFSI-B reached a maximum at nine hours and shows decreasing values at 12 and 15 hours (Figure 4.36e). R_{SEI} for TFSI-B is similar to FSI-A initially (approximately 150 ohms cm^{-2}), but by 15 hours the resistance has increased very little and R_{SEI} is the lowest of all the separators, including all the separators containing LiFSI salt and the N,N-Dimethylacetamide (DMAc) separators. This could be due to early stabilisation of the SEI, a maximum was reached after nine hours instead of 12 hours seen in other separators.

Due to the non-uniform morphologies obtained by electrospinning with dimethylformamide (DMF) / acetone solutions, an alternative solvent, DMAc, was investigated to produce uniform electrospun PVDF-HFP separators incorporating lithium salts. The salt concentration was kept constant at 1 wt% of the polymer but three different lithium salts were investigated: LiTf, LiFSI and LiTFSI

(Figure 4.36a-c). These separators can be compared to FSI-B and TFSI-B, which contain the same salt content. Electrospinning with the different solvents and salts resulted in solutions with varying properties. The electrospinning conditions were altered to optimise fibre formation for each solution, the electrospinning time, however, was not changed, this resulted in separators of varying thickness produced with DMAc solvent.

Tfd and FSId (Figure 4.36a-b) are thicker than the other separators (excluding GF). This could have contributed to the slightly larger R_{ele} values observed, 3.5 and 6.9 ohms cm^{-2} at 0 hours for Tfd and FSId, respectively. Tfd and FSId had the lowest initial R_{SEI} values of all the separators (approximately 80 ohms cm^{-2} at 0 h), however after 15 hours R_{SEI} was no longer the lowest. R_{SEI} more than doubled in both Tfd and FSId from 0 to 15 hours. For Tfd and FSId, the higher frequency semicircle is consistently larger than the lower frequency semicircle, this is similar to GF, but opposite to all the other electrospun separator where the lower frequency semicircle is larger.

4.4.4 Lithium plating and stripping

To investigate the lithium plating / stripping process and effects of cycling on the SEI, the separators were assembled into symmetrical lithium cells with P13FSI electrolyte. The cells were polarised at 0.1 mA cm^{-2} for 16 minutes, moving one coulomb of lithium, then the current was reversed for 16 minutes [95, 342, 345], with a one minute rest at open circuit in between each reversal. This cycle was repeated 100 times. Voltage-time plots of cycling are shown in Figure 4.38 and Figure 4.39. The average cell resistance in cycle one and cycle 100 is shown in Table 4.22, estimated from P13FSI electrolyte lithium symmetrical cells with different separators.

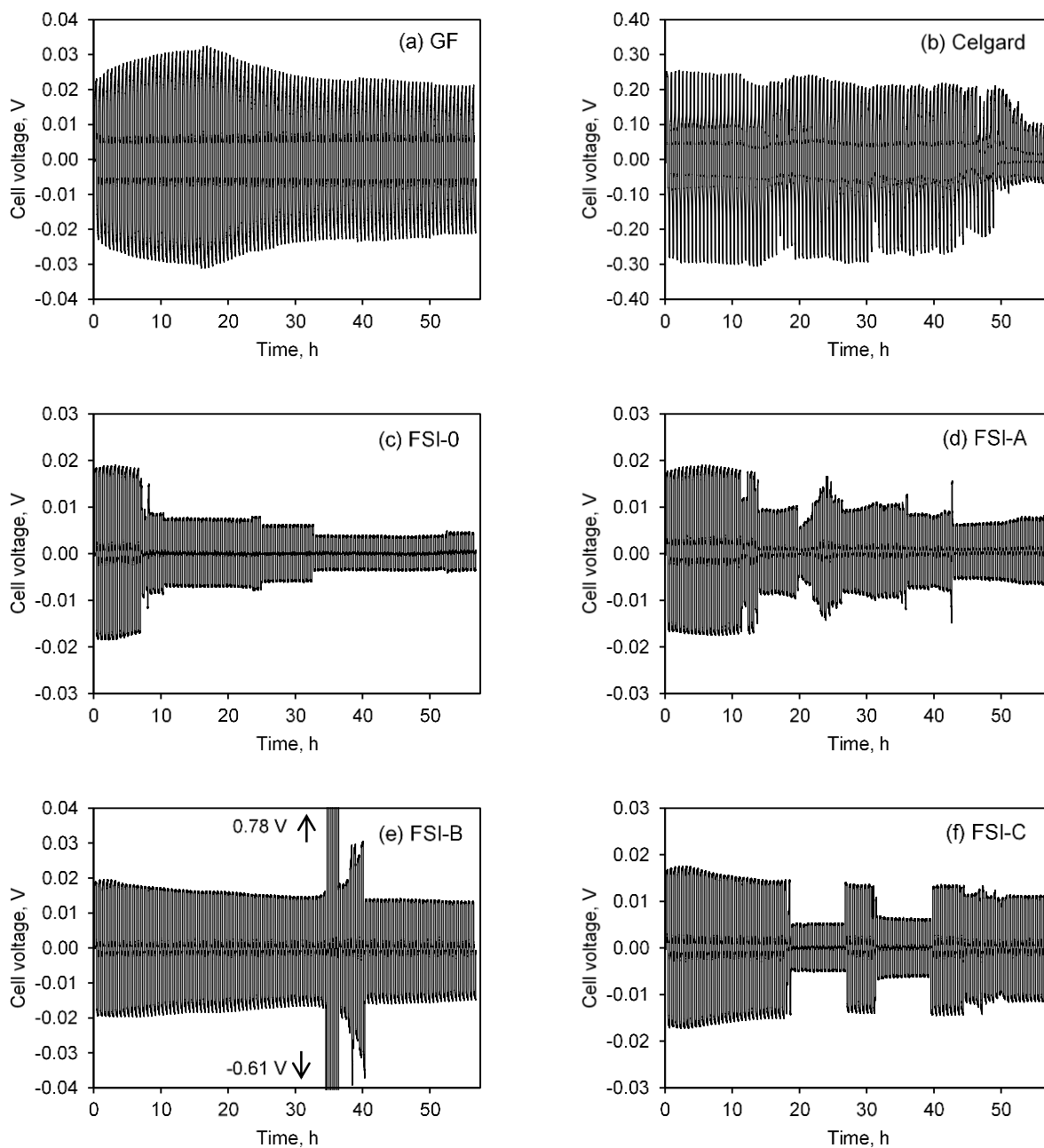


Figure 4.38 Galvanic cycling of Li | Li cells with P13FSI electrolyte and (a) GF, (b) Celgard 3501, (c) FSI-0, (d) FSI-A, (e) FSI-B and (f) FSI-C separator.

For the cell containing GF (Figure 4.38a) the maximum voltage during each cycle increases steadily in the first 30 cycles then decreases in the remaining cycles to a value lower than at the start, initially 23.1 mV and down to 21.3 mV after 100 cycles. The cell internal resistance can be estimated from the overvoltage and current density [65, 318, 326]. The overvoltage has been taken as the average overvoltage during each charge reversal, rather than the maximum voltage reached [326]. GF shows an average overvoltage of 20.1 mV in the first cycle, corresponding to a cell resistance of approximately 200 ohms cm² and an approximate resistance of 100 ohms cm² on

one electrode. The cell resistance calculated from the overpotential is an apparent cell resistance calculated based on the initial lithium electrode surface area. The cell resistance, directly proportional to overvoltage due to constant current density, increases during the first 30 cycles, to a maximum of 270 ohms cm⁻² in the 31st cycle. The overpotential then decreases slowly in the remaining cycles and reaches a minimum value of 15.8 mV in the 100th cycle. The decrease in overpotential could be accounted for by an increase in the surface area of the lithium, i.e. mossy morphology of plated lithium [65].

Basile, et al. [68] suggests that changes in the cell resistance could be due to the electrical conductivity of SEI products (LiF, Li₂O, LiOH and decomposition products of FSI⁻) forming on the lithium metal surface affecting the cell resistance. The increase in cell resistance over the first 17 hours could be due to reorganisation of the SEI and subsequent decrease could be due to reorganisation of the SEI during cycling [318]. The voltage does not spike or collapse during cycling which suggests that lithium did not form dendritic morphology or otherwise increase substantially in surface area during cycling [65, 326].

Table 4.22 Average cell resistance in P13FSI electrolyte symmetrical lithium cells with different separators, 1st and 100th cycle at 0.1 mA cm⁻².

	Cell resistance* (apparent), ohms cm ⁻² , error [§] ±20 ohms cm ⁻²	
	1 st cycle	100 th cycle
GF	200	160
Celgard 3501	2440	900
FSI-0	180	40
FSI-A	170	80
FSI-B	190	130
FSI-C	160	110
TFSI-B	180	150
Tfd	190	190
FSId	210	170
TFSId	170	150

* Cell resistance calculated based on initial electrode surface area (1.13 cm²).

§ Since replicates not performed, the error for cell resistance was calculated using voltage accuracy of MACCOR unit to be approximately ±20 ohms cm⁻².

The maximum overpotential during the cycling of the cell containing Celgard 3501 (Figure 4.38b) remains relatively constant during the first 20 cycles, with a small decrease from approximately 250 mV initially, to approximately 224 mV in the 22nd cycle. The overpotentials for Celgard 3501 are approximately one order of magnitude larger than those observed for GF. The maximum voltage then fluctuates by approximately ±20 mV over the next 65 cycles. The internal cell resistance is initially 2440 ohms cm⁻² (from average overvoltage during first cycle) and is unstable

during cycling with a decrease seen in the last 20 cycles to 900 ohms cm^{-2} in the last cycle, an approximate resistance of 450 ohms cm^{-2} on one electrode. The fluctuations observed in the voltage could indicate non-uniform lithium deposition or instability of the SEI [346]. Both phenomena could be a result of poor wetting of Celgard 3501 with P13FSI electrolyte. This could cause an uneven distribution of electrolyte, and therefore current flow, within the cell. Poor wetting with P13FSI electrolyte could also account for the high cell resistances observed, compared to GF. It should be noted that the Celgard 3501 cell voltage profile is not centred over 0 V. For example, cycle one has a positive maximum voltage of 250.6 mV and a negative maximum voltage of -280.8 mV. This continues during all 100 cycles and the imbalance becomes more pronounced after the 88th cycle. This irreversibility of the peak voltages could also be associated with the uneven electrolyte distribution from poor wetting of Celgard 3501 with P13FSI electrolyte.

The overvoltage of FSI-0 (Figure 4.38c) remains relatively constant at approximately 18 mV for the first 12 cycles (cell resistance of approximately 170 ohms cm^{-2}). During the cycling, the maximum voltage appears to step down at random intervals, as would be expected with a change in current density, except the applied current was kept constant at 0.1 mA cm^{-2} throughout cycling. After this, the overvoltage reduces to approximately 8 mV for seven cycles, except for one maximum voltage spike to approximately 15 mV in the 15th cycle. Voltage spikes during initial cycling could be from rearrangement of the lithium surface [68] or detachment of a dendrite causing a sudden change in surface area of the lithium electrode. The overvoltage remains constant again at approximately 7.5 mV for approximately 20 cycles, then increases to 8 mV for three cycles, then decreases to 5.5 mV for 14 cycles, then decreases to approximately 3.5 mV for 36 cycles before increasing to approximately 4 mV for the last seven cycles. As there are no voltage spikes followed by a collapse in the voltage, it is unlikely that a short circuit has occurred [68]. The decreasing cell resistance, proportional to overvoltage, indicates that either the electrode surface area or the cell resistance is changing with ongoing cycling. The decrease in overpotential could be accounted for by an increase in the surface area of the lithium, i.e. mossy morphology of plated lithium, however, this is unlikely due to the definite steps seen in the overvoltage. A decrease in the overpotential could also occur if the SEI was reorganising and becoming more conductive, which would reduce the cell resistance. A reduction in cell resistance may also be from changes to the bulk electrolyte resistance, which may include changes in the gel polymer (separator)-electrolyte morphology with cycling.

The maximum voltage in FSI-A (Figure 4.38d) remains relatively constant for approximately 20 cycles with an overvoltage (average) of 17.6 mV, approximately 180 ohms cm^{-2} cell resistance. Following this, the overvoltage fluctuates substantially. There are a few blocks of similar consecutive cell resistance, between 100 and 90 ohms cm^{-2} , but they are broken up by intermittent voltage spikes. The unstable voltage likely indicates dendritic lithium morphology [65, 326], but the

absence of voltage collapse suggests that a short circuit did not occur [68]. After the 80th cycle, the maximum voltage is stable, with a slight increase observed to the 100th cycle which has a maximum voltage of 8.2 mV, a cell resistance of approximately 80 ohms cm⁻² and an approximate resistance of 40 ohms cm⁻² on one electrode.

The maximum voltage has an overall decreasing trend for FSI-B (Figure 4.38e), excluding the presence of voltage spikes at approximately the 60th cycle. The initial overvoltage is approximately 18.5 mV. A steady decrease is observed to approximately 14.6 mV overvoltage in the 60th cycle. The stable decrease in over potential, and therefore cell resistance, suggests uniform lithium deposition and formation of a stable SEI [346]. After the 60th cycle the voltage fluctuates for approximately 12 cycles and spikes to a maximum of 780 mV, internal cell resistance of 7800 ohms cm⁻², an approximate resistance of 3900 ohms cm⁻² on one electrode. The sudden appearance of a voltage spike suggests formation of a lithium dendrite and the following fluctuations in maximum voltage could be due to subsequent rearranging of the surface morphology [68]. Following the voltage spikes, the overvoltage continues to decrease with the same trend as before the voltage spikes. By the 100th cycle the overvoltage has decreased to approximately 13 mV, a cell resistance of 130 ohms cm⁻² and an approximate resistance of 65 ohms cm⁻² on one electrode.

The cell containing FSI-C (Figure 4.38f) has a stable maximum voltage with a steady decrease over the first 33 cycles. Initially the overvoltage is approximately 16 mV (160 ohms cm⁻²), and after 33 cycles this has decreased to approximately 14.5 mV (150 ohms cm⁻², an approximate resistance of 75 ohms cm⁻² on one electrode). This suggests the formation of a stable SEI on the lithium electrode [346]. Following this, there are two blocks of reduced cell resistance over the next 40 cycles. 12 cycles with a cell resistance of approximately 50 ohms cm⁻², then eight cycles back at approximately 140 ohms cm⁻², followed by another 12 cycles with a cell resistance of approximately 70 ohms cm⁻² which ends at approximately the 70th cycle. Since the cell voltage does not go to zero during these decreased overvoltage blocks it is unlikely that a short circuit occurred. Additionally, as there are no fluctuations observed, only defined steps in the overvoltage, it is also unlikely that dendritic growths or changes in surface area are responsible for the decreased overvoltage [68]. The definite change in overvoltage during these blocks suggests an external influence on the cell, i.e. temperature change causing change in cell resistance or a change in current. However, as the cells all underwent cycling at the same time and no corresponding trends are observed in the other cells, it is unlikely that temperature or current changes are responsible. This suggests that internal cell properties, such as SEI or bulk separator-electrolyte resistances may be responsible for these blocks of reduced cell voltage. In the last 30 cycles the overvoltage returns to the trend seen in the first 33 cycles with fluctuations and an overall decreasing trend from approximately 13 mV (130 ohms cm⁻²) in the 71st cycle to 11 mV

(110 ohms cm⁻²) in the last cycle.

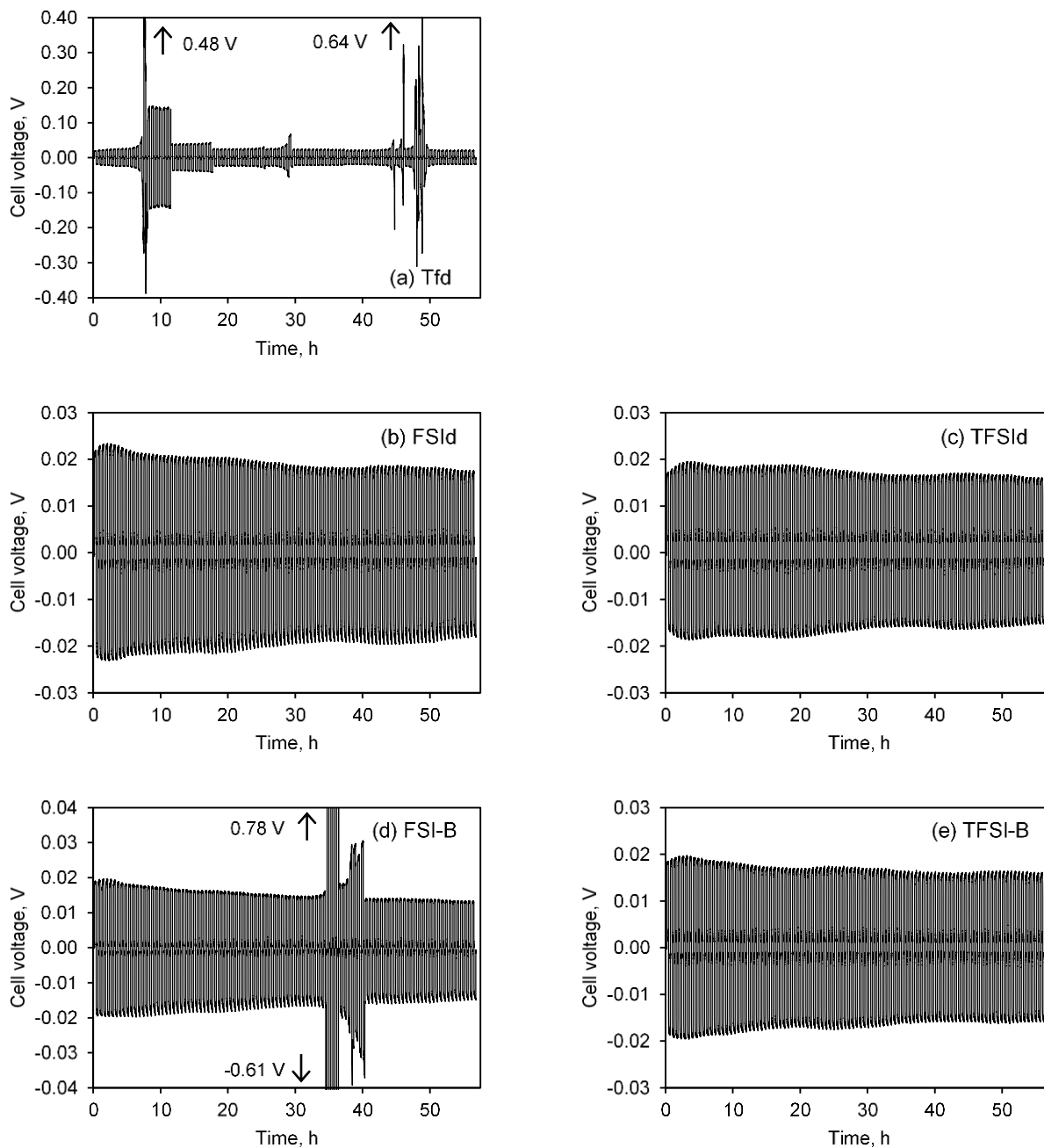


Figure 4.39 Galvanic cycling of Li | Li cells with P13FSI electrolyte and (a) Tfd, (b) FSId, (c) TFSId, (d) FSI-B and (e) TFSI-B separator.

The cycling of the cell containing the Tfd separator (Figure 4.39a) shows an initial over voltage similar to previous separators, approximately 19 mV (or 190 ohms cm⁻²) in the first cycle. During the first 12 cycles there is a steady increase in the cell resistance, to approximately 340 ohms cm⁻², immediately before a voltage spike to 480 mV (cell resistance of 4800 ohms cm⁻²). The sudden appearance of this voltage spike suggests the formation and subsequent detachment of a dendrite

on the electrode surface [65], which cannot be confirmed since the cells were not disassembled for inspection following cycling, however, the absence of a voltage collapse indicates that a short circuit did not occur [68]. The cell resistance then decreases over the next 65 cycles with a cell resistance of approximately 1440 ohms cm^{-2} for five cycles, 360 ohms cm^{-2} for eight cycles, then between 220 and 240 ohms cm^{-2} for the next 40 cycles. The stepped profile of overvoltage could indicate rearranging of the SEI, resulting in lower cell resistances with ongoing cycling, excluding the voltage spike seen at approximately the 52nd cycle with a maximum voltage of approximately 62 mV (approximately 60 ohms cm^{-2}), which could be due to formation and detachment of a lithium dendrite [65]. In the last 20 cycles there are multiple voltage spikes, with a maximum voltage of 640 mV. The overvoltage then appears to stabilise in the last ten cycles and the cell resistance in the final cycle is approximately 190 ohms cm^{-2} (an approximate resistance of 95 ohms cm^{-2} on one electrode), the same as in the first cycle.

The FSI_d, TFSI_d and TFSI-B cells (Figure 4.39b,c,f) all show stable overvoltage and cell resistance values throughout the 100 cycles, with no spike or collapse of voltage observed. The initial cell resistances are approximately 210, 160 and 180 ohms cm^{-2} for FSI_d, TFSI_d and TFSI-B, respectively. There is an increase in the cell resistance during the first few cycles (maximum reached in the 6th cycle for FSI_d and TFSI-B and the 9th cycle for TFSI_d), probably due to SEI formation and reorganisation on the lithium electrode [318]. However, this is followed by a gradual decrease in the cell resistance over approximately the next 90 cycles, suggesting a stable SEI was formed [346] and that dendritic morphology is not favoured in these systems [186]. The cell resistances in the final cycle are lower than in the first cycle (approximately 165, 150 and 150 ohms cm^{-2} for FSI_d, TFSI_d and TFSI-B, respectively). A lower cell resistance in the final cycle, along with the absence of voltage fluctuations, suggests that P13FSI electrolyte, along with these separators, are able to form stable SEIs on the lithium metal electrode and that reorganisation of the interphase during cycling results in an SEI structure with increased ionic conductivity, compared to the interphase initially formed.

The initial cell resistance of each separator can be compared: FSI-C (160 ohms cm^{-2}) had the lowest resistance; then TFSI_d (170 ohms cm^{-2}) and FSI-A (170 ohms cm^{-2}) were similar; then FSI-0 (180 ohms cm^{-2}) and TFSI-B (180 ohms cm^{-2}) were similar; then Tfd (190 ohms cm^{-2}); GF (200 ohms cm^{-2}); FSI_d (210 ohms cm^{-2}); and Celgard 3501 (2440 ohms cm^{-2}). The initial cell resistance is likely to relate to the conductivity of the first SEI formed, along with the thickness of the separator. The variation in the initial cell resistances, excluding Celgard 3501, is only 50 ohms cm^{-2} . There is no clear pattern relating initial cell resistance to the salt type or salt concentration in the separator electrospun layer. The cell resistance after 100 cycles could also be used to compare the separators, however, the fluctuating voltage profiles in six of the separators (FSI-0, FSI-A, FSI-B, FSI-C, Tfd and Celgard 3501) indicates that those separators may not be

suitable for cycling, and therefore the resistances at the end of their cycling may not be comparable. The four separators that maintained a stable overvoltage profile during the 100 cycles have variable thickness that may affect the cell resistance values. Of these four cells, the lowest cell resistance after 100 cycles was 150 ohms cm^{-2} for TFSI-B (29 μm thick) and 150 ohms cm^{-2} for TFSId (59 μm thick); then 160 ohms cm^{-2} for GF (210 μm thick) and finally 210 ohms cm^{-2} for FSI (80 μm thick). TFSI-B and TFSId both maintained stable overvoltage during 100 cycles and ended up with very similar cell resistances (lowest of the successfully cycled separator), despite the disparity in separator thickness. This suggests that the SEI formed by P13FSI electrolyte with the separators containing LiTFSI in the electrospun layers has higher stability than the other separators. Although FSI was able to complete 100 cycles, the cell resistance was higher than either of the LiTFSI separators.

4.4.5 Rate performance

The performance of GF and the FSI (-A, -B and -C) separators in LFP | P13FSI electrolyte | Li cells cycled at different current densities is shown in Figure 4.40. After assembly, the cells underwent formation (three C/20 charge / discharge cycles, 0.063 mA cm^{-2}). The cells then performed five consecutive cycles at each C/10, C/5, C/2 and C/10 discharge rates; current densities of 0.126, 0.253 and 0.633 mA cm^{-2} for C/10, C/5 and C/2, respectively. The discharge capacity for LFP | Li cells with P13FSI electrolyte and different separators at discharge rates of C/20, C/10, C/5 and C/2 are shown in Table 4.23. The discharge capacities shown in Table 4.23 are for the last cycle performed at each rate, to eliminate the effects of charge and / or discharge performance at previous current densities.

In Figure 4.40, FSI-C consistently has the highest discharge capacity at all current densities. At C/10, the FSI-C cell delivered an average of 121 mAh (g LFP)^{-1} , which is 71% of the theoretical capacity (170 mAh (g LFP)^{-1}). At C/5 and C/2, the average delivered capacity decreases to approximately 115 and 103 mAh (g LFP)^{-1} (68 and 60% of the theoretical capacity), respectively. The decrease in discharge capacity with increasing current density has also been reported with other IL electrolytes in LFP | Li half-cells [347-350], which Kim, et al. [347] attribute to high electrolyte viscosities. After cycling at C/2, the cell was cycled again at C/10 to determine if any irreversible capacity loss occurred during cycling at higher discharge rates. The final C/10 cycles had an average discharge capacity of 121 mAh (g LFP)^{-1} , a slight decrease from the initial C/10 discharge capacity. It should be noted that the first final C/10 cycle (indicated by red arrows) is characteristically lower in all cells (Figure 4.40 and Figure 4.41), due to the charge immediately previous being at the C/2 rate, and the average discharge capacity for the final C/10 cycles have been calculated from the last four C/10 cycles.

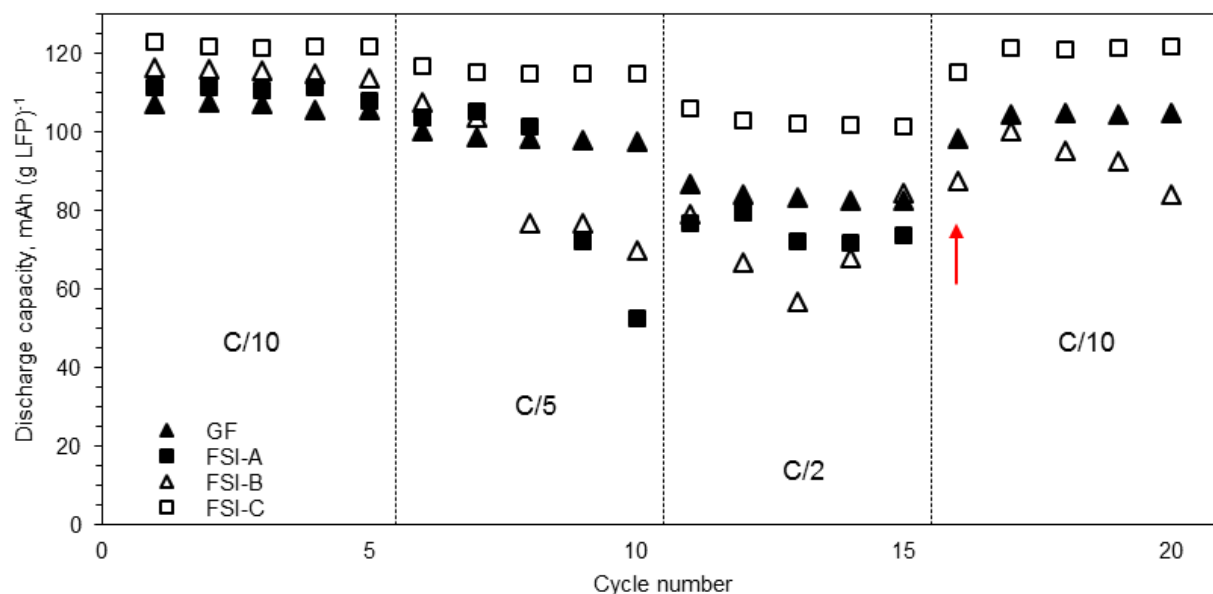


Figure 4.40 Rate study of LFP | P13FSI electrolyte | Li cells with GF, FSI-A, FSI-B and FSI-C separators cycling at C/10, C/5 and C/2 rates between 1.0 and 2.5 V. Red arrow indicates reduced capacity in first cycle at C/10 rate following C/2 charge.

During the first C/10 cycles, FSI-B has the second highest capacity (average $115 \text{ mAh (g LFP)}^{-1}$, 91% theoretical capacity). Although the FSI-B cell appeared to have stable cycling performance during the C/10 cycles, unfortunately the cell has an erratic discharge capacity at C/5, C/2 and during the final C/10 cycles (Figure 4.40), making comparison of average capacities impossible. A similar behaviour was observed for the FSI-A cell. FSI-A had an average discharge capacity of $111 \text{ mAh (g LFP)}^{-1}$, 65% theoretical capacity, at the C/10 rate. The first three cycles at C/5 appeared to be stable, with an average discharge capacity of $103 \text{ mAh (g LFP)}^{-1}$, 61% theoretical capacity, however in the following C/5 cycles the capacity dropped considerably (72 and $52 \text{ mAh (g LFP)}^{-1}$), suggesting a fault in the cell. At the C/2 discharge rate the FSI-A cell appeared to have recovered delivering an average discharge capacity of approximately $75 \text{ mAh (g LFP)}^{-1}$, 44% theoretical capacity, however the cell failed after this and the final C/10 cycles were not able to be performed.

Table 4.23 Discharge capacity for LFP | P13FSI electrolyte | Li cells with GF, FSI-A, FSI-B and FSI-C separators cycling at C/10, C/5 and C/2. Capacity shown for last cycle performed at each rate.

Rate (Current density)	Discharge capacity, mAh (g LFP) ⁻¹				
	C/20 (0.063 mA cm ⁻²)	C/10 (0.126 mA cm ⁻²)	C/5 (0.253 mA cm ⁻²)	C/2 (0.633 mA cm ⁻²)	C/10 (0.126 mA cm ⁻²)
GF	110.1	106.5	98.5	83.7	104.6
FSI-A	113.7	110.5	103.4	74.7	-
FSI-B	119.1	115.3	86.8	71.0	92.9
FSI-C	126.6	121.8	115.3	102.7	121.4
TFSI-B	132.7	128.1	121.5	104.0	118.8
Tfd	122.3 ±10.8	118.1 ±10.0	110.8 ±10.6	95.4 ±11.4	117.5 ±11.6
FSId	123.4	118.9	110.9	99.00	117.7
TFSId	106.5	103.7	96.6	84.7	102.2

The GF cell, although showing the lowest discharge capacity at C/10, showed a stable cycling profile. The GF cell had an average discharge capacity of 106, 98 and 84 mAh (g LFP)⁻¹ (63, 58 and 49% of the theoretical capacity) at C/10, C/5 and C/2, respectively. The GF cell did not recover all the initial discharge capacity during the final C/10 cycling (average 104 mAh (g LFP)⁻¹, 82% of the theoretical capacity), suggesting some irreversible loss of capacity. This could be from side reactions or increased cell polarisation that may have occurred at the higher discharge rates, due to the low ionic conductivity of P13FSI electrolyte, which would result in less active material being available [74].

Throughout rate testing, the GF cell capacities are noticeably lower than the FSI-C cell. This was not expected as the separator ionic conductivities, 1.41 mS cm⁻¹ for GF and 0.26 mS cm⁻¹ for FSI-C, suggested that the transport properties of the GF separator were superior to those of the FSI-C separator, when wet with P13FSI electrolyte. This, however, was not reflected in the performance of the separators in LFP half-cells with P13FSI electrolyte, which indicates that, along with electrolyte transport properties, the electrode-electrolyte interphase in a cell can also have an impact on the cycling performance. The rate performance results suggest that the FSI-C separator may have an enhanced electrode-electrolyte interphase compatibility with other materials when assembled in a cell.

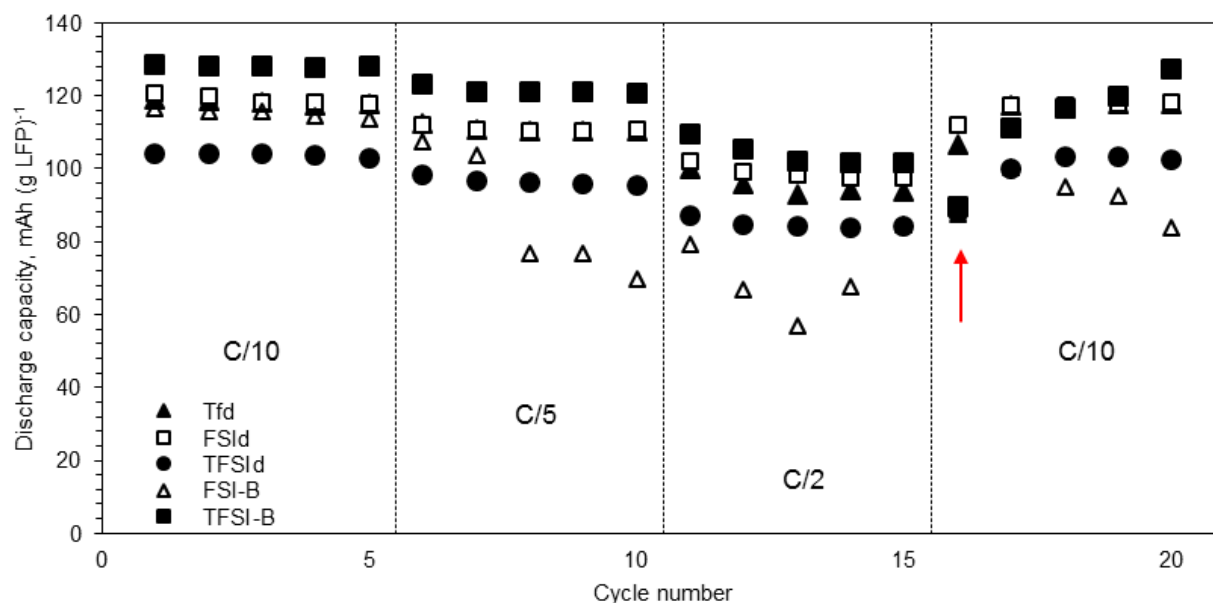


Figure 4.41 Rate study of LFP | P13FSI electrolyte | Li cells with Tfd, FSId, TFSId, FSI-B and TFSI-B separators cycling at C/10, C/5 and C/2 rates between 1.0 and 2.5 V. Red arrow indicates reduced capacity in first cycle at C/10 rate following C/2 charge.

The performance of FSI-B, TFSI-B and the DMAc separators in LFP | P13FSI electrolyte | Li cells at different current densities is shown in Figure 4.41. The TFSI-B cell has the highest discharge capacity during C/10, C/5 and C/2 cycles of 128, 121 and 104 mAh (g LFP)⁻¹, respectively. These are higher than the capacities obtained with FSI-C, the best performing cell in Figure 4.40, which suggests that TFSI-B facilitates better lithium ion mobility in the electrolyte during discharge [350]. Though, the performance of TFSI-B in the final C/10 cycles is not consistent as it shows a low capacity (89 mAh (g LFP)⁻¹) in the first final C/10 cycle, then the capacity steadily increases over the next four cycles to a final C/10 cycle capacity of 127 mAh (g LFP)⁻¹. This suggests that a fault occurred during the first final C/10 cycle that caused reversible capacity loss, which was recovered in subsequent cycles. As discussed above, the FSI-B cell shows erratic behaviour during the C/5, C/2 and final C/10 cycles making comparison of performance impossible.

Of the DMAc separators, FSId and Tfd have the best performance, with very similar performance at all discharge rates except for C/2, where FSId performs slightly better than Tfd (average capacities of 99 and 95 mAh (g LFP)⁻¹, respectively). As above, the drop in discharge capacity at higher rates is not uncommon for IL electrolytes with high viscosities [347]. The lower capacity at C/2 for Tfd, compared to FSId, could be related to the ionic conductivities of the separators with P13FSI electrolyte, 0.36 mS cm⁻¹ for Tfd and 0.53 mS cm⁻¹ for FSId, at higher discharge rates the effect of ionic conductivity on performance is magnified [73]. The lower performance in the cell containing Tfd could be due to separator morphology and the ionic transport, any resistance to

ionic transport in the electrolyte, imposed by the separator, would be exacerbated at higher discharge rates. Lee, et al. [92] suggested that the Gurley number and ionic conductivity of a separator (introduced in Section 2.2.1) can be more strongly correlated to performance, than the more commonly known indicators, thickness and porosity.

The average initial C/10 discharge capacity is approximately 118 mAh (g LFP)⁻¹ (69% theoretical capacity) for both FSI_d and Tfd. This capacity is almost fully recovered following the higher rate discharges with the final C/10 discharge capacity being approximately 117 mAh (g LFP)⁻¹ for both FSI_d and Tfd. TFSI_d consistently has the lowest capacities in Figure 4.41, which is interesting considering the other separator incorporating LiTFSI has the best performance. This suggests that the presence of LiTFSI is not as influential on performance as other separator properties, such as pore morphology, thickness and ionic conductivity with P13FSI electrolyte.

An investigation of IM⁺ and TFSI⁻ based IL electrolytes with different alkyl groups in LFP | GF/A Whatman | Li cells reported a capacity drop of between 7 and 15% when increasing the discharge rate from C/10 to C/2 [349]. Jin, et al. [349] attributed the capacities at different discharge rates to viscosity and ionic conductivity of the electrolytes, as well as characteristics of the electrode-electrolyte interphase formed on the LFP and lithium metal electrodes. Similarly, Xiang, et al. [348] looked at piperidinium⁺ and TFSI⁻ based IL electrolytes in LFP | Li cells, with and without tetramethylene sulfone additive for enhanced electrolyte transport and electrode-electrolyte interphase properties. A capacity drop of approximately 7% was observed when increasing the discharge rate from C/10 to C/2 for the electrolytes incorporating the additive, while the IL electrolyte with no additive (0.3 M LiTFSI n-butyl-methyl-piperidinium bis(trifluoromethanesulfonyl)imide) had a capacity drop of more than 50%. The authors [348] suggested that differences in lithium ion diffusion properties and interphase resistance on the lithium metal electrode may contribute to the capacities observed at different discharge rates.

Kim, et al. [350] reported a similar study of IL electrolytes in LFP | GF | Li cells at different discharge rates. It should be noted that the GF used by Kim, et al. [350] was the same commercial product as used in this work. Specifically, the electrolytes 1 M LiTFSI in P13FSI or EMIFSI ILs were reported, alongside a conventional electrolyte (1 M LiPF₆ EC / EMC 3:7 v/v with 3 wt% vinylene carbonate (VC)) for comparison. It should be noted that LiTFSI was used instead of LiFSI, which the authors [350] justified due to LiTFSI exhibiting lower current collector corrosion, while maintaining similar chemical structure to the IL anion (FSI⁻). Comparing the capacity drop with different electrolytes when increasing the rate from C/10 and C/2, the EMIFSI electrolyte experienced the greatest drop of approximately 11% capacity, while P13FSI and conventional electrolytes lost approximately 7% and 4 %, respectively [350]. The capacity drop was determined by the percentage decrease in average capacity seen at the C/2 discharge rate, compared to the

C/10 discharge rate. A similar comparison can be made in this work, and it was found that a much larger capacity drop was observed with P13FSI electrolyte in this work than reported by Kim, et al. [350]. The lowest capacity drop, 16%, was observed in the FSI-C cell while the largest drop was seen in the GF cell (approximately 21%). The disparity in capacity drops observed in this work compared to Kim, et al. [350] could be due to the different lithium salt in the electrolyte, although the physical properties of the electrode (loading, porosity and thickness) and electrode wetting could have an impact as well. Considering the capacity drop observed at high discharge rates, P13FSI electrolyte, like many other IL electrolytes, may be suitable for low-rate applications [351].

4.4.6 Cycling performance

The cycling performance of GF and separators containing LiFSI salt in LFP | P13FSI electrolyte | LTO cells at 30 °C and C/10 rate is shown in Figure 4.42. The average discharge capacities for GF and the novel separators in the 1st, 10th, 25th and 50th cycles under different testing conditions are shown in Table 4.24. After assembly, the cells underwent formation (three C/20 discharge / charge cycles) then immediately began cycling at C/10 for 50 cycles. The capacity shown for GF and the separators containing LiFSI salt is the average of three cells and the error bars are the corresponding standard deviation. The electrode loadings are such that the coin cells are cathode limited. The theoretical capacity of LFP is 170 mAh (g LFP)⁻¹ [6, 352].

At the start of C/10 cycling with the P13FSI electrolyte, the cells have average capacities of approximately 75-85 mAh (g LFP)⁻¹, well below the theoretical capacity of 170 mAh (g LFP)⁻¹ [6, 352]. The tight grouping from cells with different separators indicates that the low capacities observed are likely not due to the impact of the separators, but rather from interaction between the electrolyte and electrodes, which are constant for the cells shown in Figure 4.42. Compared to the performance of LFP | P13FSI electrolyte | Li cells, which showed initial capacities between 110 and 120 mAh (g LFP)⁻¹ at a C/10 rate (presented in Section 4.4.5), the LFP | P13FSI electrolyte | LTO cells are showing much lower initial capacities at the same cycling rate. One of the main differences is the introduction of an LTO anode instead of lithium metal. The lower capacities with LTO suggests this electrode may not have been fully utilised during cycling. Although no obvious wetting issues were observed between P13FSI electrolyte and the LTO electrode during cell assembly, it should be noted that the ratio of electrolyte volume to the LTO electrode material was not optimised. There may have been incomplete wetting within some electrode pores which would reduce the amount of active material available during cycling. The electrodes used were commercially obtained, which means they have been manufactured for use with conventional electrolytes (i.e. loading, coating thickness, porosity, thermal calendaring); since IL electrolytes generally have higher viscosities than conventional electrolytes, IL electrolytes may not achieve

optimal wetting of the electrode [353].

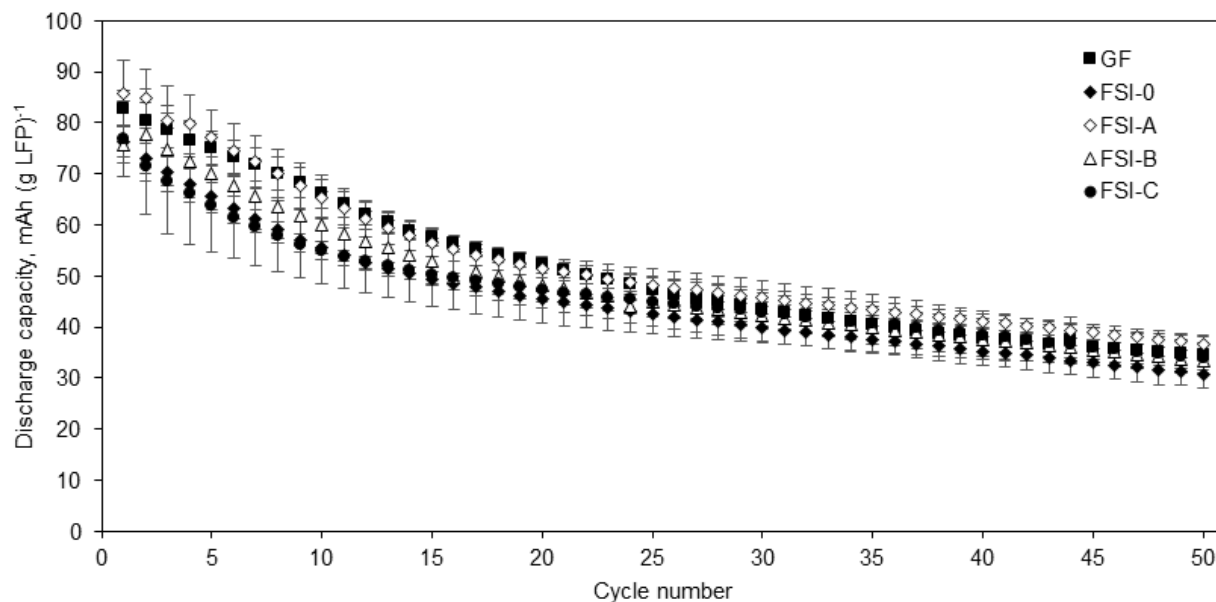


Figure 4.42 Capacity plot of C/10 cycling of LFP | P13FSI electrolyte | LTO cells with GF, FSI-0, FSI-A, FSI-B and FSI-C separators. Average and standard deviation (error bars) presented for three replicate cells for each separator.

Cells containing FSI-A separator exhibited the highest capacity initially and at the end of cycling (Figure 4.42). In the first C/10 cycle the average capacity is 85 mAh (g LFP)⁻¹ and by the 50th cycle the capacity has decreased to approximately 37 mAh (g LFP)⁻¹, capacity loss of approximately 57%. Overall, the average capacity of GF is the second highest in Figure 4.42 during the C/10 cycling, although the profile follows a different trend to that seen in FSI-A. This means that although FSI-A starts and ends with the highest capacity, the capacities of GF and FSI-A are similar during cycles seven through to 24. By the 50th cycle, GF has an average capacity of approximately 34 mAh (g LFP)⁻¹, approximately 58% capacity loss from the initial C/10 cycle capacity (83 mAh (g LFP)⁻¹). FSI-0 shows the highest capacity loss during C/10 cycling, 60%, as well as finishing with the lowest average capacity in the 50th cycle, approximately 31 mAh (g LFP)⁻¹. During the first 15 cycles FSI-B has a higher average capacity than FSI-C, however in the remaining cycles the capacities converge giving very similar final capacities, approximately 34 mAh (g LFP)⁻¹. While FSI-C had one of the lowest capacities at the beginning, the capacity loss during the C/10 cycling (approximately 56%) was the lowest of the separators in Figure 4.42. It should be noted that considering the error bars in Figure 4.42, although there is a small spread of capacities at the beginning of cycling, the error bars actually overlap throughout cycling,

suggesting that there is no substantial difference between the cycling performance of LFP | P13FSI electrolyte | LTO cells with different separators.

Table 4.24 Discharge capacity of LFP | P13FSI electrolyte | LTO cells at current density 0.126 mA cm⁻² with different separators. Average values and standard deviation are taken from three replicate cells with a specific separator.

P13FSI electrolyte at 30 °C	Discharge capacity, mAh (g LFP) ⁻¹			
	Cycle 1	Cycle 10	Cycle 25	Cycle 50
GF (x2)	82.9 ±3.5	66.2 ±2.8	47.4 ±2.2	34.5 ±3.6
FSI-0	76.2 ±2.9	55.5 ±1.2	42.6 ±2.3	30.8 ±2.7
FSI-A	85.9 ±6.4	65.4 ±4.3	48.3 ±1.7	36.7 ±1.7
FSI-B	75.8 ±3.5	59.9 ±6.6	45.0 ±2.9	33.3 ±1.8
FSI-C	76.8 ±7.4	55.0 ±6.6	45.0 ±6.4	34.0 ±3.0
TFSI-B	78.1	57.2	39.5	24.4
FSId	72.8	51.9	37.0	30.9
TFSId	66.7	50.0	37.5	30.4
P13FSI electrolyte at 50 °C	Cycle 1	Cycle 10	Cycle 25	Cycle 50
GF (x2)	40.5	24.8	13.1	6.4
FSI-A	44.6	27.2	19.4	11.0
FSI-B	38.7	27.7	17.1	-
FSI-C	43.1	27.8	19.6	5.5
TFSI-B	48.7	27.3	-	-
P13FSI / PC electrolyte	Cycle 1	Cycle 10	Cycle 25	Cycle 50
FSI-0	76.9	69.6	63.9	55.7
FSI-A	103.9	89.1	76.9	62.4
FSI-B	108.2	93.6	81.4	67.2
FSI-C	83.5	68.9	60.0	51.9
TFSId	105.6	90.1	77.6	63.5
Conventional electrolyte	Cycle 1	Cycle 10	Cycle 25	Cycle 50
GF (x2)	107.7	104.9	102.2	98.2
FSI-A	112.9	111.7	-	-
FSI-B	101.7	98.8	98.1	98.1
FSId	108.1	106.3	105.0	103.0

Balducci, et al. [354] investigated LFP | LTO cells with a GF separator and a N-methyl-N-butyl-pyrrolidinium bis(fluorosulfonyl)imide (P14FSI) electrolyte (P14FSI / LiTFSI 9:1 mole ratio). Cycling was performed at different rates from C/20 up to 2C, 1000 cycles were performed at each rate. The authors [354] observed approximately 85% theoretical capacity at both C/20 and C/10 discharge rates, and the capacities were relatively constant over 1000 cycles. Stability over 1000 cycles is very impressive considering the results observed in this work. Compared to this work, the cells of Balducci, et al. [354] use a similar IL, a longer chain on one of the alkyl side groups, P14FSI, with a different lithium salt, LiTFSI, in the electrolyte, which could contribute to the increased stability observed. Moreno, et al. [355] investigated ternary IL electrolytes, N-methyl-N-propyl-pyrrolidinium bis(trifluoromethanesulfonyl)imide (P13TFSI) / P13FSI and LiTFSI, and saw enhanced

physiochemical properties, which the authors attributed to the combination of advantageous properties from the different materials.

The voltage profile for GF and FSI-B are shown in Figure 4.43 during C/10 cycling for the 1st, 10th, 25th and 50th cycles for comparison (additional plots in Appendix I). The resistance of a cell can be estimated from the voltage difference between plateaus during charging and discharging, when the current is kept constant the difference in voltage can be used as an estimate of cell resistance. Kim, et al. [73] note that the plateau potential gap includes the combined effects of mass transfer, activation energies and charge transfer properties of the electrolyte. In this work the median voltage value during a consecutive charge and discharge were used to determine the cell resistance of a cell during a particular cycle.

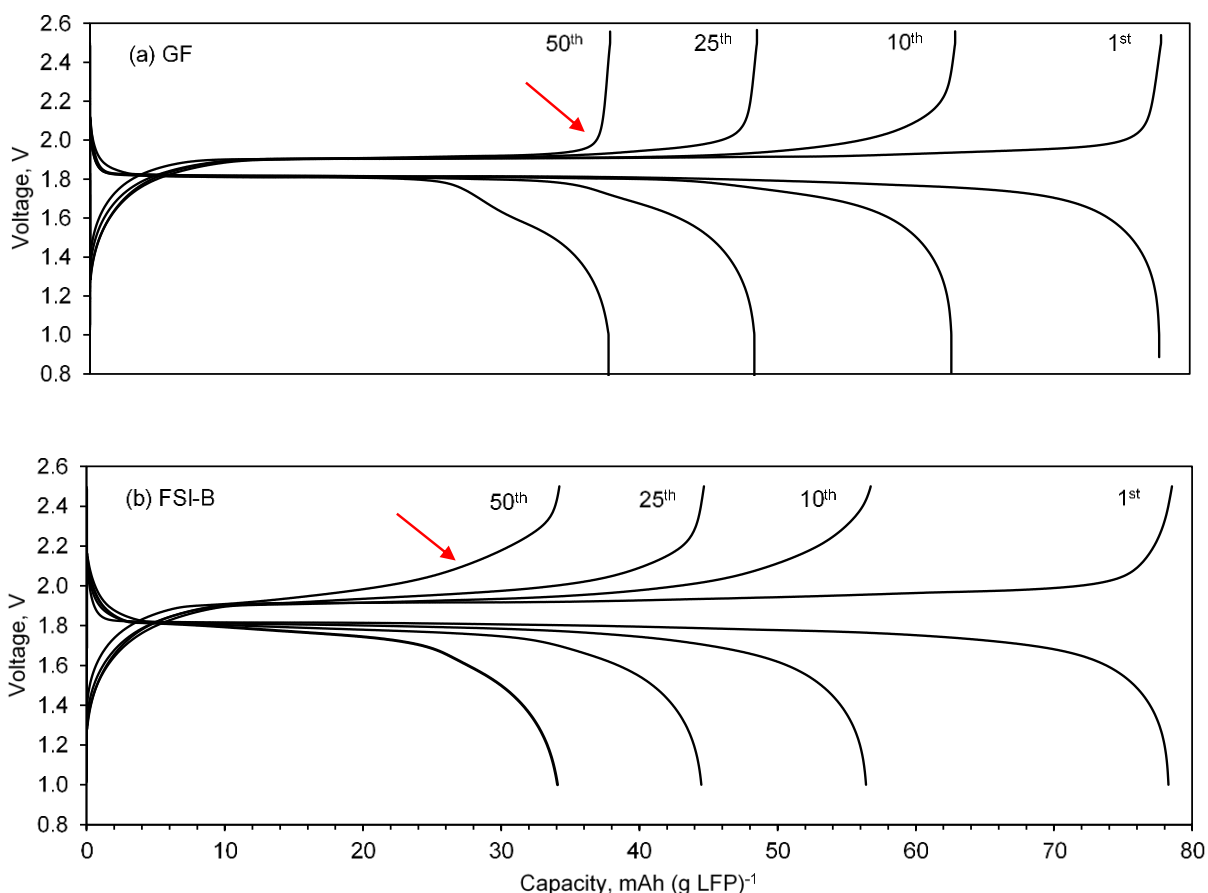


Figure 4.43 Voltage curves for 1st, 10th, 25th and 50th cycles of representative LFP | P13FSI electrolyte | LTO cell with (a) GF and (b) FSI-B separators, cycling at current density 0.126 mA cm⁻². Theoretical capacity 170 mAh (g LFP)⁻¹.

Although the capacity decreases substantially from the 1st to 50th cycle, the voltage remains constant for the majority of the charge and discharge profile, with a sharp voltage change (indicated by a red arrow Figure 4.43a) seen at the end of the charge, even in the 50th cycle. The voltage plateau for FSI-B slowly shortens with increasing cycle number as the voltage change towards the end of charge occurs more gradually (indicated by a red arrow Figure 4.43b). Kim, et al. [66] relate smooth voltage plateaus during charge and discharge to the reversibility of lithium insertion, in both LFP and LTO electrodes, and a small difference between the charge discharge voltage plateaus to a low charge transfer resistance at electrode-electrolyte interphases. The less defined shape of voltage plateaus in FSI-B with ongoing cycling could suggest increased resistance at the electrode-electrolyte interphase, which would contribute to the capacity fade observed.

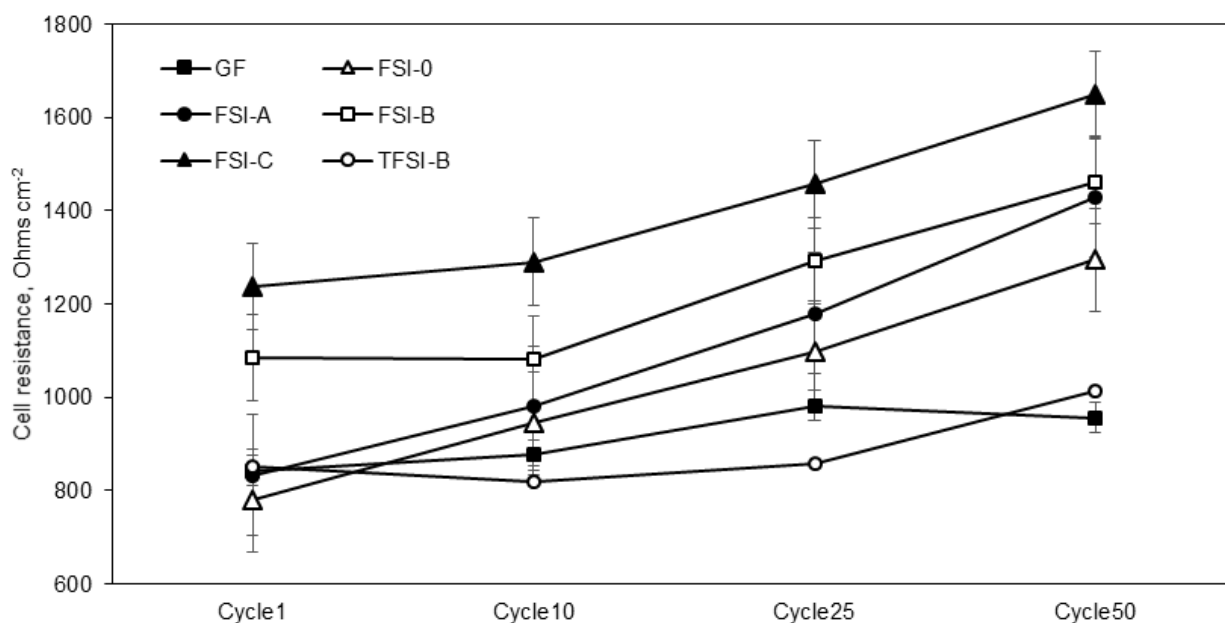


Figure 4.44 Resistances during C/10 cycling of LFP | P13FSI electrolyte | LTO cells with GF, FSI-0, FSI-A, FSI-B, FSI-C and TFSI-B separators. Calculated from difference between voltage plateau median of charge and discharge curves.

The evolution of estimated cell resistance is shown in Figure 4.44 during the 1st, 10th, 25th and 50th cycle at C/10 rate for GF, the separators containing LiFSI salt and TFSI-B. FSI-C has the highest resistance at each cycle and the resistance can be seen to increase with the number of cycles. FSI-B has the second highest cell resistance at each cycle, but the cell resistance appears to be unchanged during the first ten cycles, after which an increase is seen. FSI-A and FSI-0 have the lowest resistances in the first cycle, but show the largest overall increase during cycling. TFSI-B

and GF are among the lowest cell resistance in the first cycle and only a small amount of increase is seen during the cycling resulting in the two lowest resistance values, almost half that of FSI-C, at the end of cycling.

The change in cell resistance during cycling could be related to the electrode-electrolyte interphase formation and stabilisation at the electrode [96]. It can be seen that GF has not only the lowest resistance, but also the least increase during cycling; this suggests that GF has a better interphase composition with the LFP and LTO electrodes, rather than the separators containing LiFSI salt. There is no clear advantage of LiFSI presence or concentration in the separator since the separators with the lowest resistances also show the largest increase in resistance during cycling, indicating a stable electrode-electrolyte interphase was not formed. Of the electrospun separators shown in Figure 4.44, TFSI-B has the lowest cell resistance as well as the smallest increase in resistance during cycling. This suggests that the presence of LiTFSI in the separator may have a positive effect on the cell cycling, possible due to enhanced electrode-electrolyte interphase stability.

The C/10 cycling performance of FSI-B, TFSI-B and two of the DMAc separators is shown in Figure 4.45. The capacities shown for TFSI-B, FSI-B and TFSI-B are from a single coin cell results, therefore no standard deviation is available. FSI-B maintains the highest capacity throughout cycling. Although TFSI-B starts with a similar capacity to FSI-B, by the 50th cycle TFSI-B experiences approximately 69% capacity loss compared to the first C/10 cycle capacity, meaning that it ends with the lowest capacity of all the cells (Figure 4.42 and Figure 4.45) in the 50th cycle. Interestingly, TFSI-B delivered a capacity of only 9 mAh (g LFP)⁻¹ in the 37th cycle, after which the cell capacity was diminished in the remaining cycles. The cause of this low capacity is unknown, however, the fact that the cell could continue cycling indicated that the malfunction was not permanent. TFSI-B and FSI-B have similar capacities, consistently lower than FSI-B. Although the capacity of FSI-B was initially higher than TFSI-B, after the first twenty cycles the capacities converged to a final capacity of approximately 31 mAh (g LFP)⁻¹ in the 50th cycle, only slightly below the average capacity of FSI-B in the 50th cycle (33 mAh (g LFP)⁻¹). It should be noted that although TFSI-B had the second lowest capacity (second only to TFSI-B, after the malfunction), the capacity loss during cycling for this separator was only 54%, comparing the capacities of the first cycle to the 50th C/10 cycle. This lower capacity loss suggests that the electrode-electrolyte interphase formed with TFSI-B separator was more stable than the other separators. This is similar to the results of Section 4.4.5 where the TFSI-B separator was found to have the highest rate performance. Together these results suggest the salt type present in the separator contributes to the electrode-electrolyte interphase during formation and that incorporation of LiTFSI salt into the separator may provide enhanced cycling performance.

To investigate the effects of electrolyte on the capacity loss observed over 50 cycles at C/10, LFP | LTO cells with different separators were assembled with the following electrolytes for comparison to the P13FSI electrolyte cells cycled at 30 °C: (1) P13FSI electrolyte, for cycling at 50 °C, (2) Conventional electrolyte (1.2 M LiPF₆ EC / EMC 2:1 v/v) for cycling at 30 °C, and (3) P13FSI electrolyte with 6.3 wt% PC (P13FSI / PC electrolyte) for cycling at 30 °C. Hybrid electrolytes of P13TFSI ILs with LiTFSI and different solvents (fluoroethylene carbonate, vinylene carbonate and PC) were investigated by Plylahan, et al. [356]. Of the hybrids evaluated, the electrolyte containing PC (6.32 wt%) was found to have the highest discharge capacity in a LFP | Li cell [356]. Therefore, PC was selected to study the effects of a solvent additive on the performance a P13FSI electrolyte cell.

The cycling performance of FSI-B cells with different electrolytes can be seen in Figure 4.46. It is clear that the conventional electrolyte cell has the best capacity retention, with negligible capacity loss observed after 50 cycles. Although it should be noted that the initial capacity of the conventional electrolyte cell was only approximately 100 mAh (g LFP)⁻¹. The P13FSI / PC electrolyte had the highest initial capacity of approximately 108 mAh (g LFP)⁻¹ but gradual capacity loss was seen with cycling, approximately 38% by the 50th cycle. This is a similar trend to the P13FSI electrolyte but a lower percentage of capacity lost.

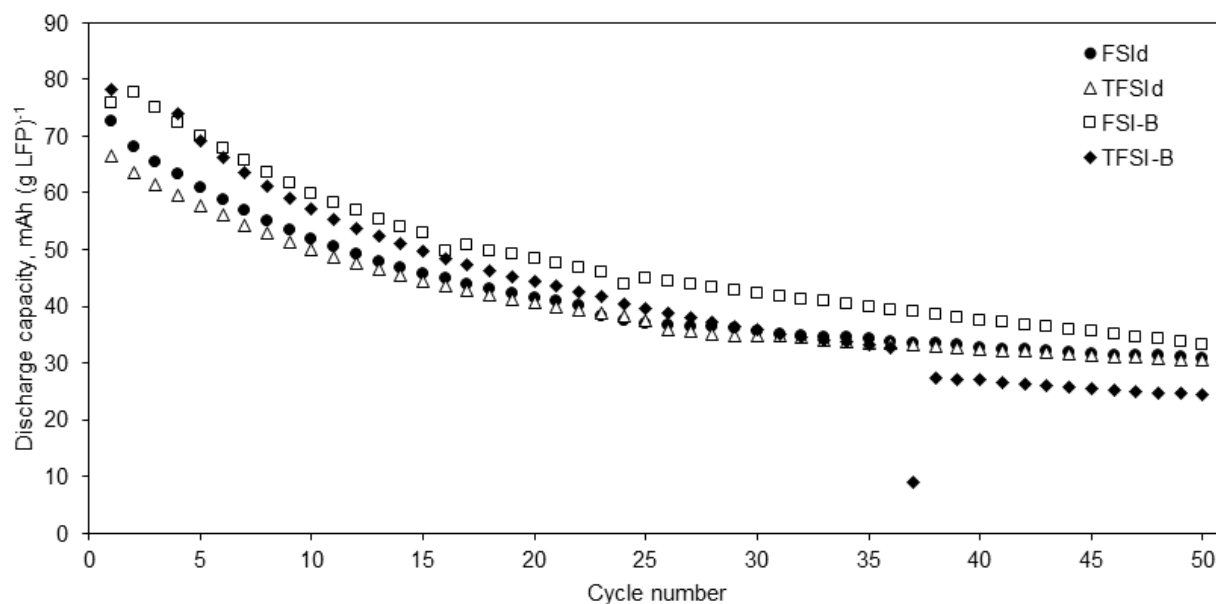


Figure 4.45 Capacity plot of C/10 cycling of LFP | P13FSI electrolyte | LTO cells with FSI, TFSI, FSI1, and TFSI1 separators.

The ionic conductivity of ILs have been reported to increase with added PC, according to the mole fraction, and a corresponding decrease in the solution viscosity is observed [357]. The ionic conductivity was seen to increase with a PC additive in N-butyl-N-methyl-imidazolium tetrafluoroborate (BMIBF₄), N-butyl-N-methyl-imidazolium bis(trifluoromethanesulfonyl)imide (BMITFSI) and N-methyl-N-butyl-pyrrolidinium bis(trifluoromethanesulfonyl)imide (P14TFSI) ILs. Although Lam, et al. [357] only investigated PC additive to ILs, they note that the presence of lithium salts, as is necessary in an IL electrolyte, will cause a decrease in the conductivity. Interestingly the P13FSI electrolyte cell cycled at 50 °C did not have an increased capacity, as was expected with a lower electrolyte viscosity at elevated temperatures [358]. This indicates that although the transport properties of the electrolyte may have been enhanced due to the lower viscosity, the rate of reactions occurring at the electrode-electrolyte interphase appear to have also increased at the higher temperatures, therefore leading to a lowered capacity. Comparing the different electrolytes and cycling temperatures, it can be suggested that the major impediment on cycling performance for P13FSI electrolyte is the low stability of the electrode-electrolyte interphase, which results in gradual capacity loss with continued cycling. The lower conductivity of the electrolyte does not appear to be affecting the P13FSI electrolyte performance at the C/10 rate.

Srouf, et al. [352] report the cycling performance of IM⁺ TFSI⁻ based IL electrolytes in LFP | LTO cells with a glass microfibre separator at 60 °C and C/10 discharge rate. The capacity loss after only 25 cycles, compared to the first C/10 cycle, is less than 7%. This can be compared to the capacity loss by the 25th cycle, in this work, which is between 30 and 40%. This suggests that IM⁺ TFSI⁻ based IL electrolytes investigated by Srouf, et al. [352] form a more stable electrode-electrolyte interphase with LFP and LTO electrodes, than is seen in this work.

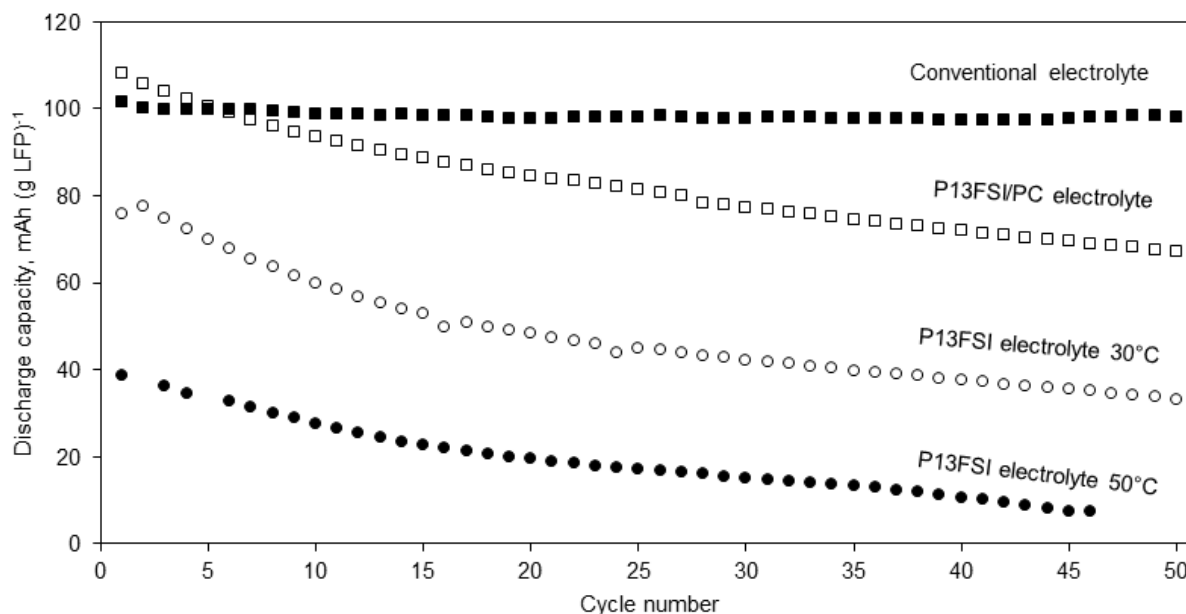


Figure 4.46 Capacity plot of C/10 cycling of LFP | FSI-B | LTO cells with ILE (P13FSI electrolyte), ILE with PC (P13FSI / PC electrolyte) and conventional electrolyte at 30 °C as well as ILE at 50 °C.

The C/10 cycling performance of conventional and P13FSI / PC electrolytes are shown in Figure 4.47 and Figure 4.48 with different separators. A stable cycling capacity is observed for GF, FSI-B and FSI-d separators with conventional electrolyte (Figure 4.47). FSI-d has a consistently higher capacity than FSI-B, 108 and 101 mAh (g LFP)⁻¹ in the first cycle, respectively, which is likely due to the separator morphology (i.e. porosity, pore size, tortuosity etc.) and associated transport properties when wet with conventional electrolyte. While FSI-B and FSI-d have a low capacity loss of approximately 4% over the 50 cycles, GF has a capacity loss of almost 9%. This may be due to the high surface roughness, assumed from large fibre and pore size, of the GF causing disturbance to the electrode-electrolyte interphase formed with conventional electrolyte on the electrodes [96] and the corresponding decrease in capacity with continued cycling from loss of cyclable lithium in interphase reactions.

Gao, et al. [21] investigated P14TFSI IL electrolyte in a LiNi_{0.5}Mn_{1.5}O₄ (LMNO) | Li cell, compared to a EC / diethyl carbonate (DEC) conventional electrolyte. The increased viscosity of the IL electrolyte was seen to result in poor electrode wetting as well as increased resistance of the electrolyte and charge-transfer at the electrode-electrolyte interphase [21]. EIS showed that the P14TFSI electrolyte had a lower SEI resistance than the conventional electrolyte due to the high resistivity of LiF in the SEI, formed from LiPF₆ in the conventional electrolyte. However, the charge transfer resistance was higher for the IL electrolyte, which the authors [21] contributed to the increased viscosity of the IL electrolyte.

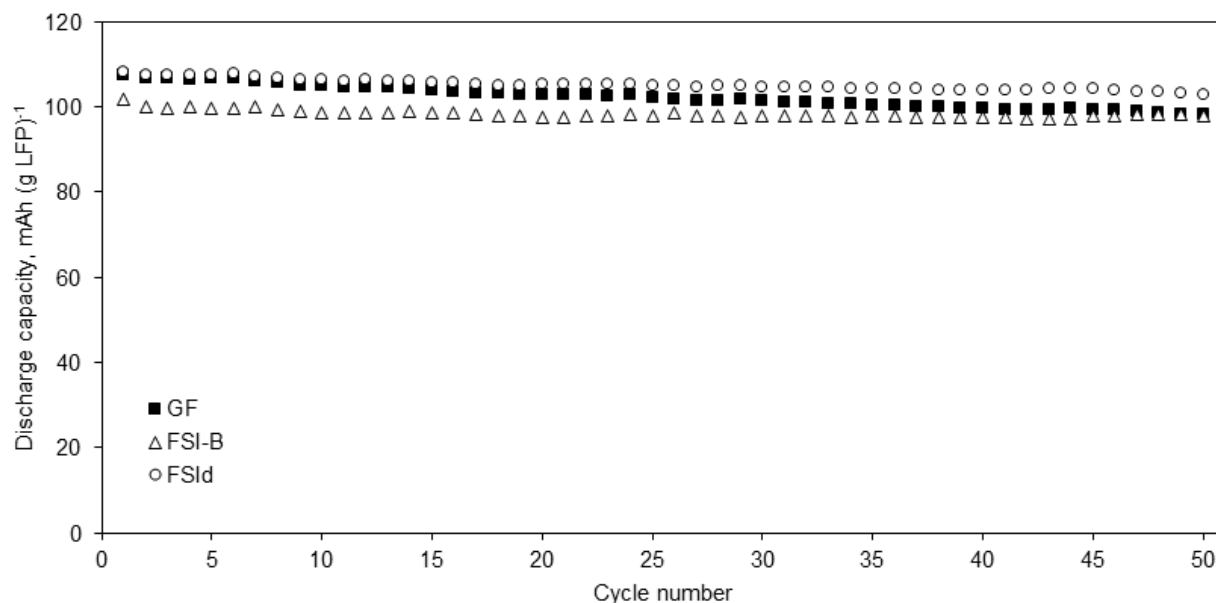


Figure 4.47 Capacity plot of C/10 cycling of LFP | conventional electrolyte | LTO cells with GF, FSI-B and FSI-d separators.

P13FSI / PC electrolyte shows different cycling performance with different separators (Figure 4.48). FSI-A, FSI-B and TFSI-d have initial capacities above 100 mAh (g LFP)⁻¹. While FSI-0 and FSI-C have capacities of approximately 80 mAh (g LFP)⁻¹, not substantially higher than those seen with P13FSI electrolyte. For all separators, a gradual decrease is observed with continued cycling, with a capacity loss of approximately 40% from the first to the 50th cycle, except for FSI-0 which has a lower capacity loss (28%). The lower capacity loss of FSI-0, compared to all other separators in Figure 4.48, suggests enhanced electrode-electrolyte interphase stability. FSI-0 is the only separator without LiFSI or LiTFSI present in the electrospun layer. This may suggest two things. Firstly, the lithium salts present in the separator does have an impact on the performance of the cell, and secondly, that LiFSI and LiTFSI, even in small amounts, may negatively impact the electrode-electrolyte interphase stability.

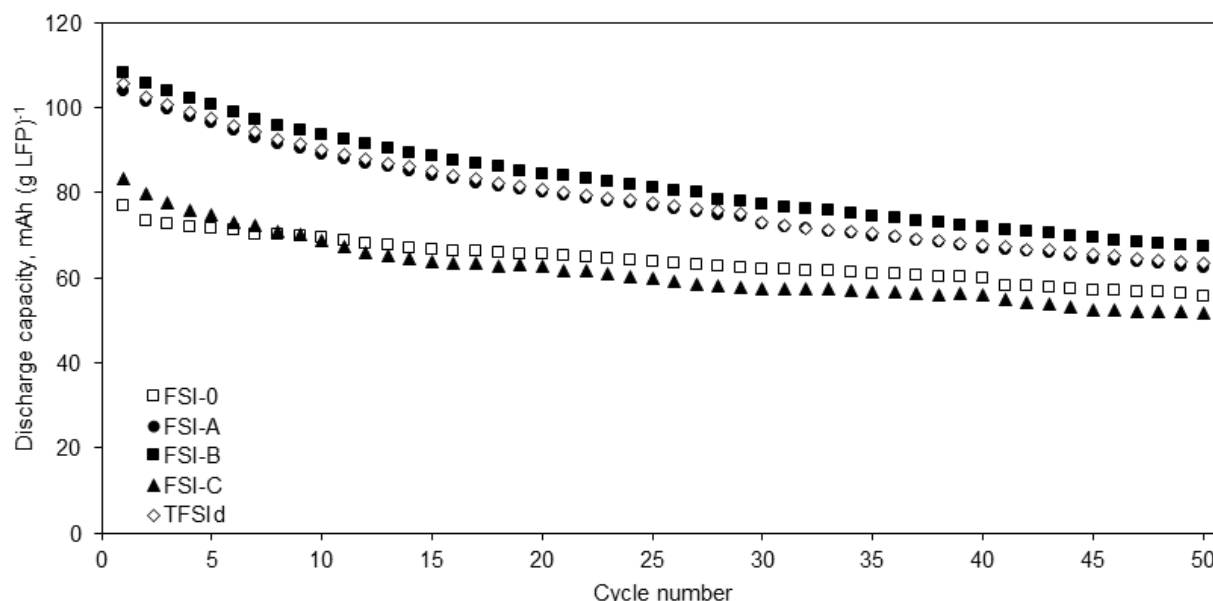


Figure 4.48 Capacity plot of C/10 cycling of LFP | P13FSI / PC electrolyte | LTO cells with FSI-0, FSI-A, FSI-B, FSI-C and TFSId separators.

Lombardo, et al. [323] investigated a Pyr⁺ TFSI IL blends with conventional electrolyte in LFP and LTO half-cells. The authors [323] found that at high concentrations of IL (50:50 weight/weight (w/w)) the solvents present in the conventional electrolyte have a large impact on the electrode-electrolyte interphase stability, specifically the presence of DEC was seen to negatively impact the interphase stability during cycling at C/5. In full cells, LFP | LTO, a blend with 30:70 w/w IL to conventional electrolyte demonstrated minimal capacity loss over ten cycles at C/5 [323]. While, Menne, et al. [321] investigated P14TFSI / PC electrolytes (0.3 M LiTFSI) in LFP | LTO cells and found the blend electrolyte was proven to have enhanced performance over the pure IL electrolyte, with long-term cycling up to 25000 cycles demonstrated at 10C discharge rate. These reports demonstrate that electrolyte additives can have a significant impact on cell performance, and optimisation of P13FSI electrolyte additives may enhance the cycling performance in a LFP | LTO cell.

4.4.7 FTIR changes after cycling

FTIR spectra was collected for the P13FSI electrolyte alone, and each separator FSI-0, FSI-A, FSI-B and FSI-C with P13FSI electrolyte before and after cycling in an LFP | LTO coin cell is shown in Figure 4.49. A small portion of the spectra are shown in Figure 4.49b-c for better peak visualisation. In Figure 4.49c characteristic P13FSI peaks are indicated with red dashed lines. Appendix J contains photos of disassembled cells; separators and electrodes. The FTIR spectrum

for P13FSI electrolyte from this work aligns well with characteristic FTIR peaks previously reported for P13FSI IL by Huang and Hollenkamp [64] and Yoon, et al. [359]. Characteristic peaks indicated in Figure 4.49c can be assigned to the following vibrations: 556 cm^{-1} -SO₂ bending vibration; 641 cm^{-1} -SNS bending vibration; 730 cm^{-1} -SNS symmetrical stretching vibration; $730\text{ to }827\text{ cm}^{-1}$ -SF stretching vibration; 827 cm^{-1} -SNS asymmetrical stretching vibration; 1100 cm^{-1} possible -FSI interactions; $1172\text{ and }1216\text{ cm}^{-1}$ -SO₂ symmetrical stretching vibration; and, $1360\text{ and }1377\text{ cm}^{-1}$ -SO₂ asymmetrical stretching vibration [64].

All the reported characteristic peaks for P13FSI were present in this work plus there were three additional peaks observed in this work for P13FSI electrolyte (indicated with red circles in Figure 4.49a-b). The peaks occurred in the P13FSI electrolyte spectrum as well as all corresponding separator with electrolyte spectrum before and after cycling; the peaks occur consistently at 2980 , 2888 and 1471 cm^{-1} . Since these peaks are absent in the dry separator spectrum it is most likely they are related to the P13FSI electrolyte material. The absence of these peaks from previously published P13FSI spectrum suggests they could be from a small amount of impurity present in the P13FSI electrolyte used in this work.

The grey arrows in Figure 4.49c indicate peak changes in FTIR spectrum of LiFSI containing FSI-A, FSI-B and FSI-C separators after cycling. These changes were not seen after cycling in the PVDF-HFP separator without LiFSI (FSI-0). This suggests that the LiFSI present in the separator fibres does interact with the electrolyte and / or electrode-electrolyte interphase during cell operation.

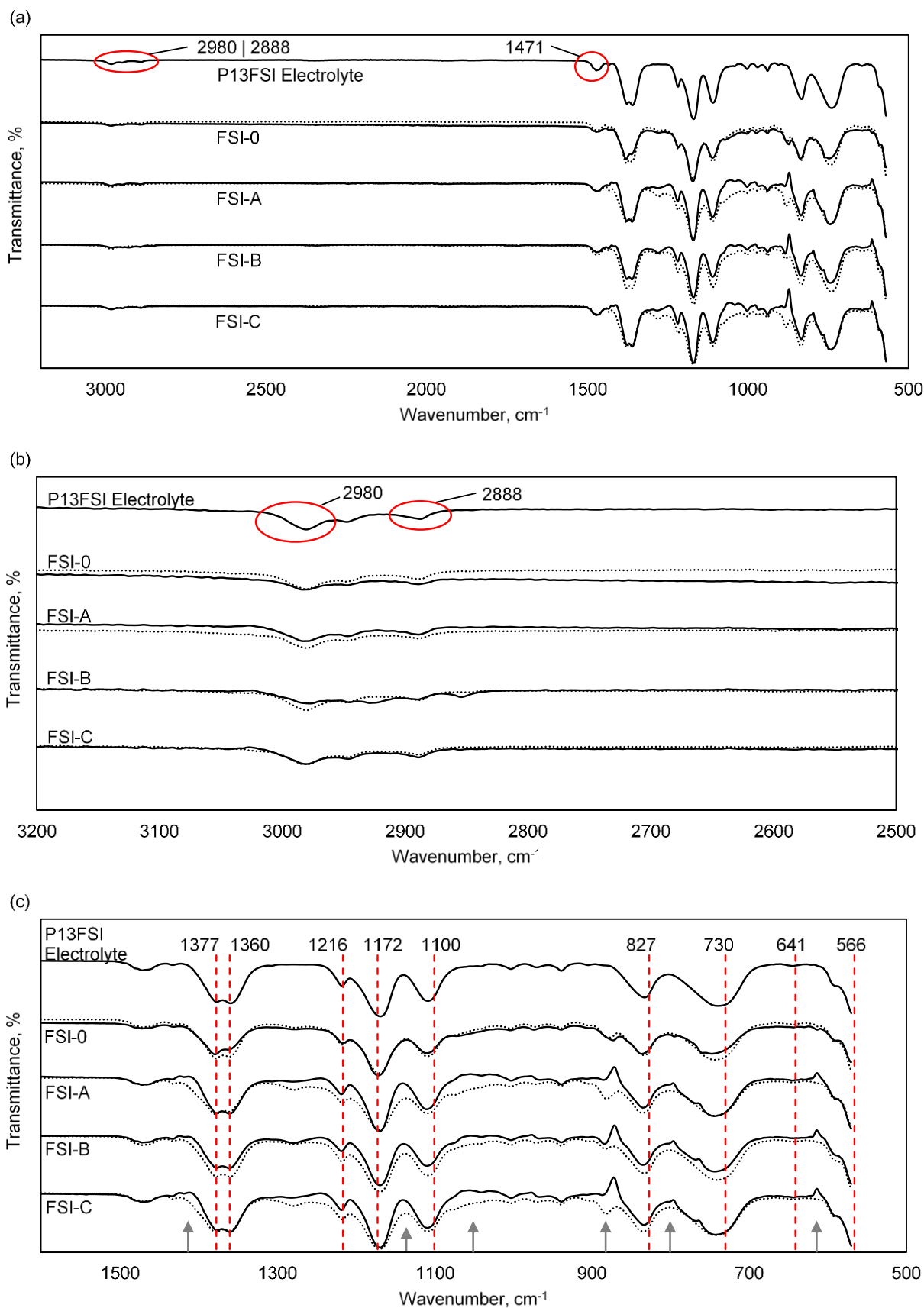


Figure 4.49 (a) FTIR spectra of P13FSI electrolyte alone and each separator with P13FSI electrolyte before (___) and after (.....) cycling in an LFP | LTO coin cell. (b) In range 2500 to 3200 cm^{-1} . (c) In range 500 to 1600 cm^{-1} , characteristic P13FSI electrolyte peaks indicated with red dashed lines. Grey arrows indicate peaks altered after cycling in separator containing LiFSI.

Specifically, at 614 cm^{-1} an upwards peak is observed in all three separators containing LiFSI when wet with P13FSI electrolyte. After cycling this upwards peak is no longer present, the result is consistent across FSI-A, FSI-B and FSI-C separators suggesting there is an interaction occurring during cycling that involves LiFSI in the polymer matrix. The peak at 827 cm^{-1} widens in FSI-A, FSI-B and FSI-C separators following cycling suggesting an interaction occurs between LiFSI in the polymer matrix and P13FSI electrolyte affecting the -SNS asymmetrical stretching vibration of the electrolyte trapped in the separator. Following cycling, a peak appears in FSI-A, FSI-B and FSI-C separators at 882 cm^{-1} ; before cycling there was an upwards peak in FSI-A, FSI-B and FSI-C separators at 871 cm^{-1} . This does not correlate to any vibrational peaks identified for PVDF-HFP, P13FSI or LiFSI in the literature, it is likely from a new component formed at the electrode-electrolyte interphase during cycling that remained on the separator during cell disassembly.

The peak at 1100 cm^{-1} widened in FSI-A, FSI-B and FSI-C separators after cycling and a shoulder peak appeared at 1071 cm^{-1} . This shoulder peak correlates with the characteristic $-\text{CF}_3$ rocking vibration peak seen in the PVDF-HFP spectrum. Widening of the 1172 , 1216 and 1377 cm^{-1} peaks following cycling in FSI-A, FSI-B and FSI-C separators indicates an interaction occurs between LiFSI in the polymer matrix and P13FSI electrolyte affecting the $-\text{SO}_2$ asymmetrical and symmetrical stretching vibration of the electrolyte trapped in the separator. FTIR of separators with P13FSI electrolyte before and after cycling show subtle changes which suggest that the LiFSI present in the separator polymer matrix does interact with P13FSI electrolyte during cell operation.

FTIR of cycled electrodes was performed to detect any changes on the electrode surface from cycling in P13FSI electrolyte. Cycled electrodes harvested from cell containing different separators were compared to determine if the novel separators containing LiFSI salt had an effect on the electrode surface composition after cycling. FTIR of cycled LFP and LTO electrodes from cells with different separators is shown in Figure 4.50 and Figure 4.51. FTIR of each cycled electrode has been plotted alongside dry electrode material and P13FSI electrolyte for peak comparison. The cycled electrode spectra can be seen to have a combined spectrum with peaks that align with peaks in the dry electrode material and in the P13FSI electrolyte.

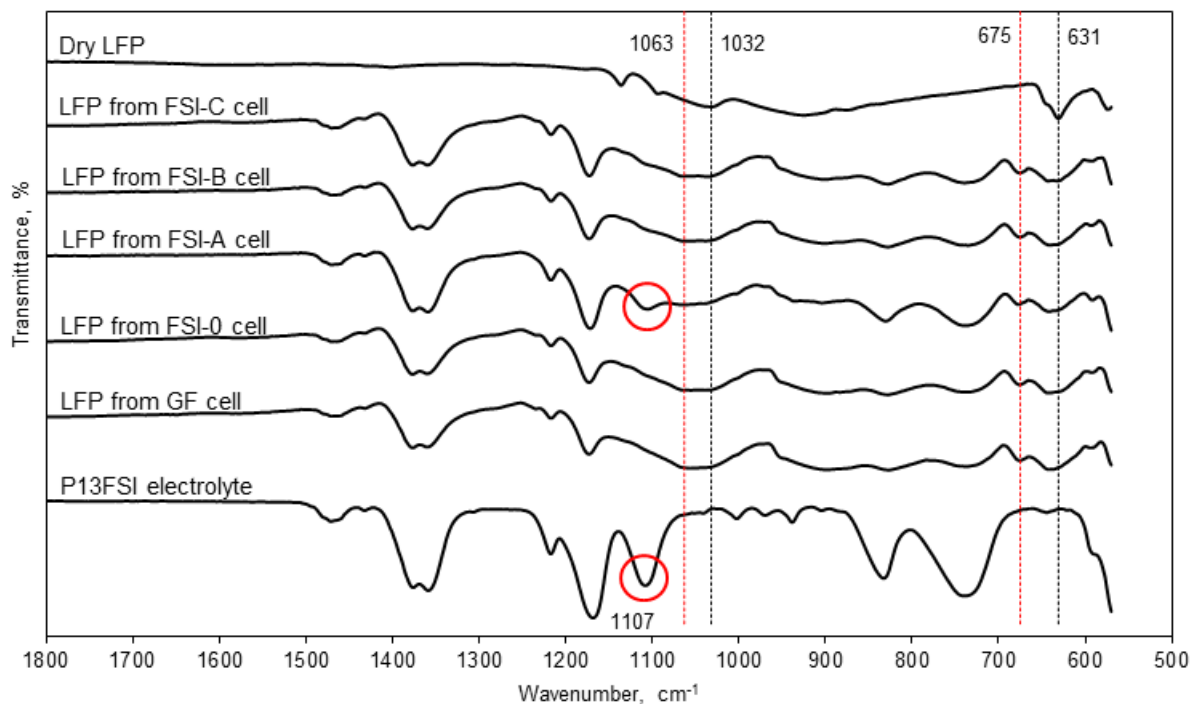


Figure 4.50 FTIR of cycled LFP harvested from P13FSI electrolyte LFP | LTO cells with different separators (GF, FSI-0, FSI-A, FSI-B and FSI-C), alongside dry LFP for comparison. In range 500 to 1800 cm^{-1} . Black dashed lines indicate dry LFP peaks. Red dashed lines indicate peaks that appear on cycling.

In the cycled LFP, there are two peaks (Figure 4.50 red dashed lines) that cannot be attributed to peaks in the electrode or electrolyte materials. The first peak appears at approximately 675 cm^{-1} , on the shoulder of the peak at approximately 630 cm^{-1} which can be seen in the dry LFP material spectrum. The second peak appears at approximately 1062 cm^{-1} as a double trough with another peak that is present on the dry LFP material (approximately 1030 cm^{-1}). The appearance of these peaks after cycling suggests they may be due to a change on the electrode surface from interactions between the electrolyte and LFP during cycling. There is no obvious difference in the LFP electrode surface from cells containing different separators, except for the cycled LFP from the cell containing FSI-A which has a slightly different shape to the other cycled LFP spectra. Most obviously, there is a peak occurring at 1107 cm^{-1} that is not seen in the other cycled LFP spectra (Figure 4.50 circled in red), the peak correlates to a peak in the P13FSI electrolyte and therefore can be contributed to excess electrolyte present on the electrode surface from the electrode harvest.

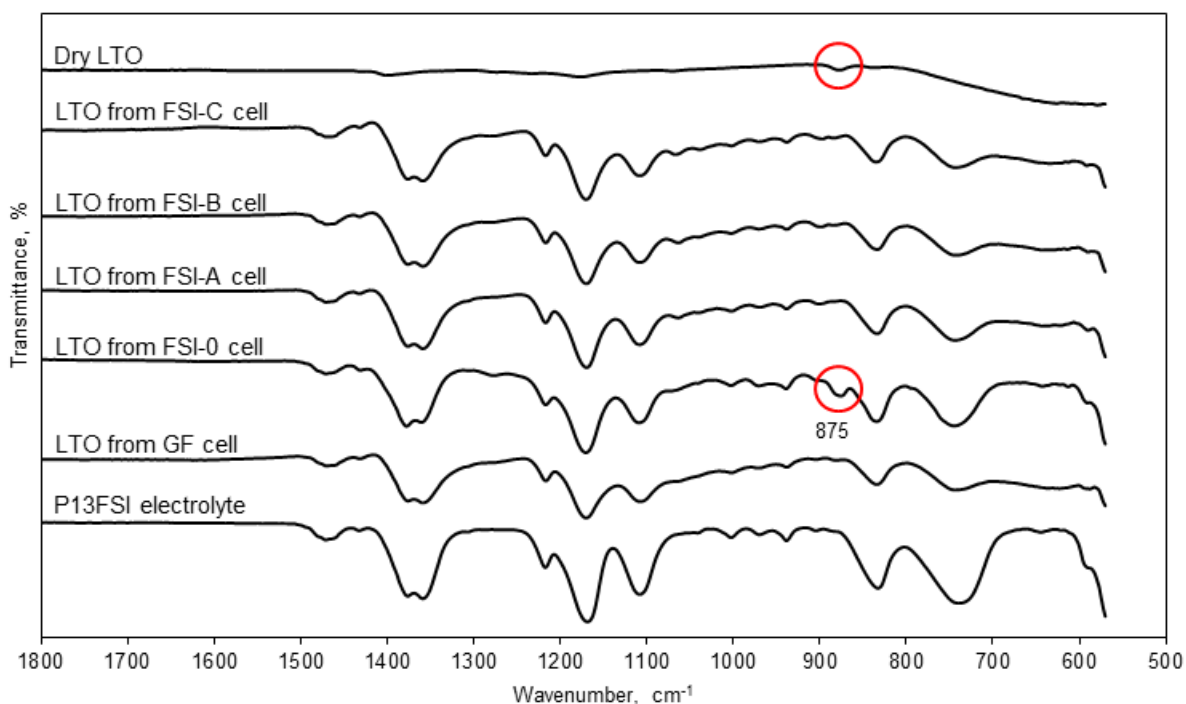


Figure 4.51 FTIR of cycled LTO harvested from P13FSI electrolyte LFP | LTO cells with different separators (GF, FSI-0, FSI-A, FSI-B and FSI-C).

The cycled LTO spectrum from a cell containing FSI-0 has a peak not seen in the other cycled LTO spectra (Figure 4.51 circled in red). The peak occurs at approximately 875 cm^{-1} , however, a corresponding peak can be seen in the dry LTO material spectrum which could correlate to the FSI-0 peak. In the cycled LTO spectra (Figure 4.51) there are no peaks observed on the cycled electrodes that do not correspond to peaks in the P13FSI electrolyte or dry electrode material spectra. This suggests that there are no substantial interactions between the LTO and P13FSI electrolyte that result in changes to the electrode surface during cycling that can be observed by FTIR.

4.5 Conclusion

The electrochemical performance has been investigated for an IL electrolyte cell containing a novel separator incorporating lithium salt in the polymer. The electrochemical and transport properties of P13FSI electrolyte with different novel separators was investigated with CV on a glassy carbon electrode. The stripping peak current densities of both FSI-B and FSI-C were seen to increase with cycling, suggesting that SEI stabilisation improved in each cycle, unlike GF that had a relatively constant stripping current density in each cycle. Overall FSI-B has peak current densities approximately twice that of FSI-C, which indicates enhanced lithium plating and stripping

properties of FSI-B with P13FSI electrolyte. The behaviour of the separator and electrolyte on a lithium metal electrode was investigated with EIS at open circuit voltage and plating and stripping of symmetrical lithium. EIS was used to determine the SEI forming ability of the separator and electrolyte on lithium. Over 15 hours at room temperature and open circuit voltage, FSI-C was found to have the lowest resistance of the separators containing LiFSI salt. This was most likely due to early stabilisation of the SEI; the resistance reached a maximum after 12 hours and then decreased, suggesting formation and stabilisation of the SEI. When comparing the separators with different lithium salts, TFSI-B was found to have the lowest resistance overall, which suggests that LiTFSI could enhance the stability of the SEI formed on lithium metal.

During cycling of symmetrical lithium cells, some fluctuation in overvoltage was observed for all separators containing LiFSI salt. FSI-0 had the lowest overvoltage in the 100th cycle, suggesting the lowest cell resistance, and FSI-B showed voltage spikes characteristics of dendrite formation and detachment. There was no evidence of short circuit on any of the cells indicating the electrospun membranes were able to function as separators with lithium metal electrodes. TFSI-d and FSI-d separators showed very stable overvoltage during cycling which may be due to the morphology of the electrospun layers being more conducive to uniform lithium plating and stripping as well as SEI formation. Again, TFSI-B showed a stable overvoltage profile, which supports the EIS results indicating that a stable SEI was able to be formed.

Discharge capacity of LFP | Li cells at various current densities were investigated with different separators. Of the separators containing LiFSI salt, FSI-C was able to achieve the highest capacity at each discharge rate as well as showing stable cycling performance throughout the test. The other separators containing LiFSI salt showed fluctuating discharge capacities, and in some cases, were not able to complete the testing. This suggests that FSI-C is compatible with lithium metal as well as lithium-ion electrodes. The DMAc separators showed stable discharge capacities over a range of current densities, delivering capacities only slightly lower than FSI-C. Overall, TFSI-B showed the highest discharge capacity at each rate with stable cycling, up to the final C/10 cycles, where the discharge capacity appeared to recover slowly from the high rate discharges.

Cycling of full LFP | LTO cells at C/10 was used to compare separator performance with different cycling conditions and electrolytes. With P13FSI electrolyte cycled at 30 °C, a significant capacity loss was observed for all separators over only 50 cycles, more than 50% capacity was lost. FSI-A had the highest discharge capacity at the end of 50 cycles and the DMAc separators had consistently lower capacities compared to the separators containing LiFSI salt, except for TFSI-B which showed the most capacity loss during cycling. This suggests that separators that perform well with lithium metal electrodes are not necessarily suited to lithium-ion cells. With P13FSI electrolyte cycled at 50 °C the capacity loss was magnified in all cells, indicating that parasitic side

reactions, whose rates are enhanced at higher temperatures, may be contributing to the capacity loss observed at 30 °C with P13FSI electrolyte.

Cells containing conventional electrolyte were cycled for comparison, irrespective of separator the conventional electrolyte cells experienced negligible capacity losses and higher initial capacities. This suggests that conventional electrolyte is able to form a stable electrode-electrolyte interphase with lower loss of cyclable lithium during formation, compared to P13FSI electrolyte. Some of the P13FSI / PC electrolyte cells had higher initial capacities following formation, which suggests that sacrificial reaction of PC may have occurred during electrode-electrolyte interphase formation. Capacity loss was still observed during cycling with P13FSI / PC electrolyte, although the capacity loss was less than for P13FSI electrolyte cells.

FSI-B was the only separator able to complete cycling in all four temperature and electrolyte cells. This is interesting considering the instabilities observed with this separator in lithium symmetrical and LFP | Li half-cells. The ability of FSI-B to perform in LFP | LTO cells could suggest that the separator morphology is not ideal for lithium metal electrodes but may be suitable with lithium-ion electrodes. Although FSI-B was able to be cycled successfully, the low cell resistance of FSI-C, ability to be cycled at various current densities and achieve comparable capacities during cycling lead to FSI-C being selected for pouch cell investigations.

These results confirm that the novel separators are able to function as separator in lithium and lithium-ion based cells with P13FSI electrolyte. In order to investigate the safety performance of P13FSI electrolyte combined with the novel separator, thermal abuse testing of LFP | LTO pouch cells will be presented in Chapter 6. However, before the thermal abuse response of a full cell can be properly analysed, it is important to assess the thermal stability and decomposition profile of individual cell materials, including separators and electrodes cycled with P13FSI electrolyte to analyse the thermal behaviour of any electrode-electrolyte interphase formed on the electrode surface. The thermal stability of separators and a selection of commercial electrodes with P13FSI electrolyte was investigated using DSC, the results are presented in the following chapter.

CHAPTER 5

Thermal Stability of Ionic Liquid Electrolyte Cell Materials

5.1 Introduction

Ionic liquids (ILs) researched for lithium-ion cell electrolytes have been suggested to have superior thermal stabilities over conventional electrolytes. These properties have been investigated with Differential Scanning Calorimetry (DSC) and Thermogravimetric Analysis (TGA) studies of the IL electrolytes alone. However, in a cell environment the complex chemical reactions occurring make it impossible to assess the thermal safety of a cell from individual component properties. The decomposition behaviour of IL electrolytes in a lithium-ion cell has not been widely reported in literature. In this chapter DSC was used to investigate the decomposition behaviour of the IL electrolyte individually and with other cell materials. The measurements were used to suggest possible decomposition reactions occurring within the cell during high temperature events.

A selection of separator and electrode materials identified in Chapter 1, will be investigated with the aim of determining the most thermally stable material for use in a safer lithium-ion cell. The thermal stability of two commercial separators, Celgard 3501 and GF, were compared to a poly(vinylidene fluoride-hexafluoropropylene) (PVDF-HFP) electrospun membrane with 1.17 mol kg^{-1} lithium bis(fluorosulfonyl)imide (LiFSI) in 1-methyl-3-propylpyrrolidinium bis(fluorosulfonyl)imide electrolyte (P13FSI electrolyte). Six commercial electrodes were investigated; $\text{Li}(\text{Ni}_{1/3}\text{Co}_{1/3}\text{Mn}_{1/3})\text{O}_2$ (NMC), LiCoO_2 (LCO), $\text{LiNi}_{0.5}\text{Mn}_{1.5}\text{O}_4$ (LMNO), LiFePO_4 (LFP), graphite and $\text{Li}_4\text{Ti}_5\text{O}_{12}$ (LTO). DSC and TGA were performed on electrode and electrolyte combinations from 25 to 600 °C. A more thermally stable material will be characterised by a lower heat release rate during decomposition as well as a higher decomposition onset temperature. The thermal stability advantage provided by P13FSI electrolyte with each separator and electrode will be considered. Majority of the experimental Section (5.3), along with the results and discussion presented in Sections 5.4.1, 5.4.3 and 5.4.4 in this chapter are part of a published research paper, see Table 1.4 publication #1 for authorship details.

5.2 Literature review

Catastrophic failure of lithium-ion batteries in recent years has led to public safety concerns [19, 25-29]. Cell failure can occur when the cell temperature increases due to high environmental temperatures or ohmic heating inside the cell, i.e. overcharge, lithium plating or short circuit. Increasing temperatures within the cell cause exothermic decomposition reactions of cell materials leading to a state known as thermal runaway [26, 42, 360, 361]. Thermal runaway occurs when heat generation in a cell exceeds the heat dissipation of a cell [42, 362]. The sequence of reactions is typically [30]:

1. Solid Electrolyte Interphase (SEI) decomposition
2. Separator melting and decomposition
3. Negative active material reaction with electrolyte
4. Electrolyte decomposition
5. Positive active material reaction with electrolyte

It is very difficult to stop thermal runaway since the exothermic decomposition reactions contribute to the rising internal temperature causing a runaway reaction chain that continues until all available reaction material has been exhausted. The internal temperature of commercial lithium-ion cells can exceed 850 °C (1562 °F) during thermal runaway, depending on the chemistry [28].

During formation cycling, reactions occur between electrode materials and the electrolyte [7, 20, 340] to form a thin passivation film known as the electrode-electrolyte interphase. Eftekhari, et al. [50] suggests that the electrode-electrolyte interphase forms on both anode and cathode when using IL electrolytes. Unfortunately, limited research has been published on the both the nature and composition of the electrode-electrolyte interphase for these electrolytes to understand the impact on both cell operation and abuse conditions.

On the negative electrode, the passivation film is known as the SEI. Thermal stability of the SEI in conventional electrolyte cells is considered an important factor to increase the thermal runaway onset temperature and overall thermal stability of a cell [363]. The thermal stability of electrode-electrolyte interphase formed on cathodes and anodes with IL electrolytes is similarly important for thermal stability of the cell.

The temperature at which interphase compounds decompose and the heat released upon decomposition could directly impact thermal runaway, especially if interphase decomposition occurs at substantially lower temperatures than cathode, anode or electrolyte decomposition. For example, in a LiCoO₂ (LCO) | graphite cell with a conventional electrolyte consisting of 1 M lithium hexafluorophosphate (LiPF₆) ethylene carbonate (EC) / diethyl carbonate (DEC) (1:1 weight/weight (w/w)), the SEI decomposition is responsible for the first exothermic decomposition reactions observed at temperatures as low as 90 °C [363]. Therefore, an electrode-electrolyte interphase with higher thermal stability, will be critical to improving the thermal stability of a cell.

The onset temperature and amount of heat released during thermal runaway of a lithium-ion cell is dependent on the combination of cell materials and the resulting electrode-electrolyte interphase. It is hypothesised that the composition of the electrode-electrolyte interphase produced by active material reactions with conventional electrolytes will be different to those produced by active material reactions with *solvent-free* electrolytes, such as those made with ILs. If the thermal stability of the electrode-electrolyte interphase can be improved by changing to an IL electrolyte and reducing the organic content of the SEI, this could raise the thermal runaway onset

temperature for the cell. An increased thermal runaway onset temperature would give the battery management and cooling systems a greater opportunity to prevent the cell entering thermal runaway. Replacement of conventional electrolyte with an IL electrolyte could be expected to improve the thermal stability of other cell components by eliminating the electrolyte solvents that react with electrode active materials. To investigate this hypothesis, it is important to characterise the decomposition profile of IL electrolytes at the elevated temperatures that could be experienced by a cell during thermal runaway.

5.2.1 Thermal stability and IL electrolytes

Accelerating Rate Calorimetry (ARC), TGA and DSC thermal studies have been used to investigate thermal runaway events in lithium-ion batteries [33, 364-369]. Thermal gravimetric techniques (i.e. TGA) evaluate the weight loss of a sample at different temperatures, while DSC measures heat flow from exothermic or endothermic events of a sample at different temperatures, the weight loss during TGA can be compared to thermal events during DSC to help determine the reaction type [367, 368]. ARC is excellent for assessing self-heating materials and affords the opportunity to analyse larger samples (i.e. multiple components and whole cells), however, it is not useful for detecting endothermic thermal events [369].

The thermal stability of IL electrolyte-based cells has not been widely investigated at elevated temperatures experienced during thermal runaway events. To determine the benefits of IL electrolytes under thermal runaway conditions, it is crucial to understand how cells containing these electrolytes are going to react at elevated temperatures. For ease of comparison, Table 5.25 summarises literature reports on thermal stability of pyrrolidinium (Pyr⁺) based ILs, IL electrolytes and a conventional EC / dimethyl carbonate (DMC) electrolyte from TGA studies. The thermal stability investigations of Pyr⁺ based and other ILs are discussed in the following paragraphs.

Table 5.25 Summary of thermal stability of carbonate solvent, conventional electrolyte, ILs and IL electrolytes.

Material	Decomposition	Ref.
EC / DMC (1:1 w/w)	Negligible heat flow below 250 °C	[362]
1 M LiPF ₆ EC / DMC (1:1 w/w)	202 °C onset temperature, exothermic peak at 215 °C	[362]
P13FSI	217 °C, decomposition temperature determined by 5% weight loss during TGA	[370]
	210 °C onset for exothermic activity, determined by ARC	[51]
N-n-butyl-N-ethyl-pyrrolidinium TFSI	Decomposition temperature of approximately 368 °C from 10% weight loss by TGA	[371]
N-n-butyl-N-ethyl-pyrrolidinium TFSI 0.4 mol kg ⁻¹ (approximately 0.56 M) LiTFSI	Decomposition temperature of approximately 400 °C from 10% weight loss by TGA	[371]
P13TFSI 1 M LiTFSI	Decomposition temperatures above 400 °C from TGA	[351]

Vijayaraghavan, et al. [51] studied the thermal runaway behaviour of ILs using ARC. ILs with IM⁺ or Pyr⁺ cations were investigated with various anions. Overall the IM⁺ cation was found to have higher thermal stability than the Pyr⁺ cation [51]. This was also found by Ishikawa, et al. [370] who compared the thermal stability of EMIFSI, P13FSI and EMITFSI ILs with TGA. The authors [51] reported EMITFSI had the highest decomposition temperature of 374 °C (determined by 5% weight loss during TGA experiments), while the FSI⁻ based ILs had lower decomposition temperatures of 225 °C for EMIFSI and 217 °C for P13FSI. The consequence of adding lithium salt to the thermal stability of an IL was investigated by Nakagawa [372] using EMIBF₄ IL and lithium tetrafluoroborate (LiBF₄) salt. The authors [372] suggested ionic clusters (Li⁺, EMI⁺ and tetrafluoroborate (BF₄⁻)) formed when LiBF₄ was added to the IL causing a change to the ionic interactions. The neat IL showed a different decomposition profile and a slightly higher decomposition temperature compared to the electrolyte containing LiBF₄ salt.

Huang and Hollenkamp [64] determined the effect of lithium salt on the thermal stability of P13FSI IL electrolytes. The concentration of lithium bis(fluorosulfonyl)imide (LiFSI) and lithium bis(trifluoromethanesulfonyl)imide (LiTFSI) salt was varied and thermal stability was investigated with DSC. No exothermic peaks were observed in the P13FSI sample heated to 200 °C at 10 °C min⁻¹. However, with a LiFSI salt concentration of 0.3 mol kg⁻¹ in P13FSI, a sharp exothermic peak was observed at approximately 120 °C. Comparison between the IL and 0.3 mol kg⁻¹ LiFSI P13FSI electrolyte suggests that the thermal stability of an IL is not a good representation of the thermal stability expected in the corresponding IL electrolyte. Additionally, the effect of impurities on the thermal stability of a lithium salt, particularly LiFSI, was investigated by Kerner, et al. [373]. Three commercial LiFSI salts were compared and differences found in their thermal stability were

directly attributed to the impurities present, which were suggested by the authors to be residual material from the manufacturing method [373]. Therefore, the concentration and purity of lithium salts may have a substantial impact on the overall thermal stability of an IL electrolyte.

N-methyl-N-butyl-pyrrolidinium bis(trifluoromethanesulfonyl)imide (P14TFSI) containing LiFSI salt was investigated by Fericola, et al. [371] as an IL electrolyte. The decomposition temperature of the IL containing 0.4 mol kg^{-1} LiTFSI salt was reported as approximately $400 \text{ }^\circ\text{C}$ (from 10% weight loss by TGA) [371]. Patra, et al. [351] reported N-methyl-N-propyl-pyrrolidinium bis(trifluoromethanesulfonyl)imide (P13TFSI) and P14TFSI IL electrolytes both containing 1M LiTFSI as having decomposition temperatures above $400 \text{ }^\circ\text{C}$ from TGA. However, the authors [351] noted that the thermal ramp method used in TGA could overestimate the decomposition temperature compared to the isothermal method. The decomposition temperature of P13FSI IL electrolyte containing different amount of LiFSI salt was found to be approximately 280 to $295 \text{ }^\circ\text{C}$, using a weight loss of 5% by TGA to determine the decomposition temperature.

The thermal decomposition of an IL can be decreased by the addition of a lithium salt but has been seen to increase with use as a polymer electrolyte. Balducci, et al. [354] reports the thermal stability of P14TFSI LiFSI electrolyte as $150 \text{ }^\circ\text{C}$ while the corresponding polymer electrolyte incorporating Poly(phenylene oxide) (PEO) has a thermal stability $>200 \text{ }^\circ\text{C}$. Polymer electrolytes and the use of ILs in polymer electrolytes for enhanced safety has been recently reviewed by Angell [374] and Shaplov, et al. [375].

The Pyr⁺ based IL electrolytes have a much higher decomposition temperature than the EC / DMC and analogous electrolytes which may lead to increased thermal stability in a cell. Thermal studies of individual materials can help predict possible thermal events. However, due to reactions between cell materials during normal operation – including formation of the electrode-electrolyte interphase – the thermal stability of materials extracted from both cycled and uncycled cells using various anode and cathode materials should also be studied.

Reactions between ILs and charged electrode materials were investigated using ARC by Wang, et al. [376]. $\text{Li}_{0.45}\text{CoO}_2$, $\text{Li}_7\text{Ti}_4\text{O}_{12}$ and Li_1Si electrode materials were cycled in cells containing 1 M LiPF_6 EC / DEC (1:1 volume/volume (v/v)) electrolyte then harvested, rinsed and dried. For the ARC measurement, different IL electrolytes were added to the dried electrode materials for thermal stability testing. The authors [376] compared self-heating rates and the maximum temperature reached by each IL electrolyte with each electrode. They concluded that 1-butyl-2,3-dimethylimidazolium bis(trifluoromethanesulfonyl)imide, n-butyl,methyl-piperidinium bis(trifluoromethanesulfonyl)imide and N-trimethyl-N-butylammonium bis(trifluoromethanesulfonyl)imide were safer than conventional electrolytes; P13FSI and EMITFSI had similar safety to conventional electrolytes; and EMIFSI showed the worst safety

characteristics. Overall, ILs with bis(trifluoromethanesulfonyl)imide (TFSI⁻) were found to be safer than FSI⁻, while EMI-based ILs exhibited the worst thermal stability in the study. However, the electrode-electrolyte interphase formed on the electrodes during cycling in cells containing 1 M LiPF₆ EC / DEC (1:1) electrolyte would not have the same composition or chemical character as a cell which was cycled with IL electrolyte. Since the electrode-electrolyte interphase is an important factor for cell safety, the thermal stability of electrodes cycled in IL electrolytes should be further investigated.

The exothermic onset temperature and total heat generation should both be considered in relation to thermal stability [369, 377, 378]. Heat generation and exothermic onset temperature from DSC analysis have been used to rank thermal stabilities of electrode and electrolyte materials for lithium-ion cell safety [362, 369, 377, 378]. Xiang, et al. [362] stated that thermal runaway onset of most lithium-ion batteries occurs below 200 °C, so their work did not investigate thermal events above 225 °C. This statement may be true for lithium-ion batteries containing conventional electrolytes, however, as has been described, IL electrolytes have increased thermal stability. This means the thermal stability of materials in an IL lithium-ion cell should be investigated up to the point of decomposition to predict critical temperatures for heat release and thermal runaway in a cell.

The thermal stability of the P13FSI electrolyte used in Chapter 3 and Chapter 4, and thermal reactions with lithium-ion separators and electrodes have been investigated using DSC and TGA. DSC is useful for analysing endothermic and exothermic thermal events of electrolytes, separators and electrode materials at high temperatures. TGA is useful for analysing decomposition profiles and suggesting the reaction type for a thermal event observed with DSC; for example, the absence of mass loss in TGA may suggest a thermal event in DSC is due to melting. In the following sections, the onset temperature for the first exothermic event as well as peak temperatures and heat generations for each thermal event were analysed and used to compare thermal stability of separators and electrodes from cells containing P13FSI electrolyte.

5.3 Experimental²

The thermal stability of P13FSI electrolyte, a selection of separators and the electrodes from Chapter 3 and Chapter 4 were investigated individually and in various combinations. In addition to the LFP and LTO electrodes used in Chapter 4, the thermal stability of NMC, LCO, LMNO and

² Section 5.3 has been adapted from a published research paper, see Table 1.4 publication #1 for authorship details.

graphite electrodes were also investigated with P13FSI electrolyte.

5.3.1 Materials

The IL 1-methyl-3-propylpyrrolidinium bis(fluorosulfonyl)imide (P13FSI, >99.5%) and the salt lithium bis(fluorosulfonyl)imide (LiFSI, >99.5%) were purchased from CoorsTek Fluorochemicals (USA). The IL electrolyte used was a commercial product containing 1.57 M (1.17 mol kg⁻¹) LiFSI in P13FSI (P13FSI electrolyte, >99.5%), also purchased from CoorsTek Fluorochemicals (USA).

Commercial microporous polypropylene separator Celgard 3501, 25 µm thickness and 0.064 µm average pore size, was purchased from Celgard, LLC (USA). Glass fibre (GF) membrane (GA558X10IN, Advantech), 210 µm thickness and 0.6 µm nominal pore size, was purchased from Sterlitech Limited (USA). The electrospun PVDF-HFP was produced via electrospinning a 20 wt% polymer solution of PVDF-HFP dissolved in dimethylformamide (DMF) / acetone (7:3 w/w). The electrospinning set up was previously described in Section 3.2.3. The flow rate was 2 mL h⁻¹ and the applied voltage was set to 15 kV. The electrospun PVDF-HFP was collected directly on aluminium foil, no support membrane was used. For DSC testing the PVDF-HFP was peeled off the foil and placed directly into the crucible.

The LFP electrode (10.0 mg cm⁻² coating loading, working voltage range = 3.0 – 3.8 V vs. Li⁺) was purchased from MTI Corporation (USA). A range of commercial electrode materials were supplied through Argonne National Laboratory (USA) Cell Analysis, Modelling, and Prototyping (CAMP) Facility Electrode Library (see Table 5.26 for active material, total loading and working voltage range vs. Li⁺).

Table 5.26 Commercial electrodes supplied by Argonne National Laboratory (USA) Cell Analysis, Modelling, and Prototyping (CAMP) Facility Electrode Library

Electrode	Active material	Total loading, mg cm ⁻²	Voltage range, V vs. Li ⁺
NMC	Li(Ni _{1/3} Co _{1/3} Mn _{1/3})O ₂	6.40	2.7 – 4.7
LCO	LiCoO ₂	14.53	3.0 – 4.3
LMNO	LiMn _{1.5} Ni _{0.5} O ₄	16.07	3.0 – 4.7
LTO	Li ₄ Ti ₅ O ₁₂	13.59	1.0 – 3.0
Graphite	LiC ₆	4.82	0.005 – 3.0

5.3.2 Sample preparation

The separators were cut into 15.9 mm diameter disks and dried overnight in a vacuum oven at 50 °C before transferring into an argon atmosphere glovebox (H₂O <100 ppm, O₂ <50 ppm) at CSIRO (Clayton, VIC). Once inside the glovebox, the separators were assembled into coin cells

(CR2032 sized). Electrodes were cut into 11 mm diameter disks and dried overnight in a vacuum oven at 50 °C before being transferred into an argon atmosphere glovebox. Uncycled electrode sample was scraped off the current collector and placed in a DSC high pressure crucible then a drop of electrolyte was added to the sample. Uncycled separator samples were placed in a DSC high pressure crucible then a drop of electrolyte was added to the sample. The crucible was weighed and sealed inside the glovebox prior to removal to prevent sample contamination. Uncycled samples wet with electrolyte were put on test within 1 hour of preparation. Dry separators and electrode samples were loaded into standard aluminium crucibles with a pierced lid in air atmosphere and weighed prior to testing.

For cycled electrode samples, the electrodes were assembled into half-cells (CR2032 coin cells) inside the glovebox with lithium metal (lithium chips: 12 mm diameter, 0.4 mm thick) as the counter electrode and 150 µL P13FSI IL electrolyte. GF membrane (GA558X10IN, Sterlitech Limited) was used as the separator. For cycled separator samples the separators were assembled into half-cells (CR2032 coin cells) inside the glovebox with lithium metal as the counter electrode and 150 µL P13FSI IL electrolyte. For Celgard 3501 the working electrode was LFP and for GF the working electrode was LTO.

The coin cells were removed from the glovebox and tested at 30 °C on a MACCOR unit (Series 4000) at CSIRO (Clayton, VIC). The cells were initially charged to the upper voltage limit then discharged and recharged at C/20 rate within the specified voltage range. Electrodes for 100% State of Charge (SoC) investigation were harvested after this recharge. Cells used for other SoC investigation underwent an additional discharge to the capacity corresponding to the desired SoC. The following electrodes were assembled into P13FSI electrolyte half-cells: NMC, LCO, LMNO, LFP, graphite and LTO. Representative charge and discharge curves have been shown for each electrode.

The coin cells were transferred back into the glovebox for disassembly. Electrodes and separator were harvested from the coin cells by using a coin cell uncrimping device (MSK 110, MTI Corporation (USA)) at CSIRO (Clayton, VIC) to ensure that the electrodes retained the desired SoC. The electrodes and separators were harvested without washing with solvent to avoid disturbing the electrode-electrolyte interphase film present on the electrode surface. Due to the absence of electrode washing, some excess electrolyte was expected to be present in the DSC sample. It should be noted that the amount was known to vary between samples since the volume of excess electrolyte was not able to be controlled without disturbing or destroying the sample. An electrode sample was scraped off the current collector directly into a DSC high pressure crucible and sealed prior to leaving the glovebox atmosphere. The cycled separators were cut to fit in a DSC high pressure crucible and sealed prior to leaving the glovebox atmosphere.

5.3.3 Thermal characterisation

DSC was performed from 25 to 600 °C using a DSC 3 (Mettler Toledo, Switzerland) at CSIRO (Clayton, VIC). The DSC 3 undergoes calibration every 2-3 months using a two-point calibration with Indium and Zinc calibration standards (>99,999% purity) to validate the sensor performance. The temperature accuracy is ± 0.2 K and the calorimetric data resolution is 0.04 μ W (FRS5+ sensor). Reusable hermetically sealed high pressure stainless steel crucibles (part no. 51140404) with gold plated copper seals (part no. 51140403) were used (Mettler Toledo, Switzerland). These crucibles were chosen specifically for high temperatures and pressures; however, crucible rupture did occur in some cases.

Before sample testing, one high pressure crucible was sealed as received from the manufacturer and used as the reference crucible for future tests. DSC baseline tests were performed with the other two crucibles vs. the reference crucible, in the as-received condition, to determine their similarity. It should be noted that manual subtraction of the baseline crucible test from each sample was not performed because the Mettler Toledo DSC 3 software has a built-in correction for the selected crucible type for each test.

Approximately 5 mg of material was used for each DSC test. The high-pressure crucibles and samples were handled inside an argon atmosphere glovebox (H_2O <100 ppm, O_2 <50 ppm) at CSIRO (Clayton, VIC), excluding the uncycled separator and dry LTO sample. The heat generation (area under curve) for each peak was calculated with thermal analysis STARe Excellent Software using a linear baseline. Changes in the heat flow derivative curve were used to help define the beginning and end of each thermal event.

The high-pressure crucibles were reusable and cleaning was necessary in-between each test. The high-pressure crucibles were unsealed and the gold-plated seal was discarded. Manual mechanical cleaning was employed on the inside surfaces of the crucible lid and base with forceps. The crucible lid and base were placed in an acid bath (10 wt% HCl at 100 °C) for ten minutes with slow mechanical stirring. The lid and base were removed and manual cleaning was employed again. The acid bath was repeated for a further ten minutes along with another manual cleaning step before thorough rinsing in water. After rinsing and drying with KimWipes, the crucible lid and base were placed in an oven at 60 °C for 60 minutes to remove additional moisture. Following oven drying the crucible lid and base were transferred back into the glovebox for reuse with a new gold-plated seal.

TGA was performed under a constant flow of ultra-high purity argon on P13FSI electrolyte, its components and IL electrolyte solutions made with different LiFSI concentrations, from 25 to 600 °C (Pyris1, Perkin Elmer, USA) at CSIRO (Clayton, VIC). The materials were removed from

the glovebox and loaded into the open crucible in an air atmosphere. The sample was weighed and moved to the testing stage as quickly as possible. Sample weights were approximately 5 to 10 mg. The IL electrolyte solutions made with different salt concentrations were mixed inside the glovebox using the LiFSI and P13FSI IL materials as received from manufacturer. The solutions were sealed, removed from the glovebox and then mechanically stirred at 75 °C for five days to ensure the salts dissolved completely.

TGA test methods are outlined in Table 5.27. The first step in the TGA method was to hold the sample under high flow ultra-high purity argon for ten minutes to remove any moisture absorbed during the crucible loading process. At a heating rate of 5 °C min⁻¹ the weight change during P13FSI electrolyte decomposition occurred too rapidly to record realistic weights so the heating rate was slowed to 2 °C min⁻¹ over the decomposition temperature range. The slower TGA test method was used for the P13FSI electrolyte sample as well as the test containing uncycled electrodes with P13FSI electrolyte. A heating rate of 5 °C min⁻¹ was used for all other samples: LiFSI, P13FSI IL and the IL electrolyte solutions made with different salt concentrations.

Table 5.27 TGA test methods for different samples

Method used for samples containing P13FSI electrolyte, including uncycled electrodes with P13FSI electrolyte.		Method used for samples LiFSI, P13FSI IL and electrolytes solutions with different salt concentrations.	
1)	Hold for 10 minutes at 30 °C	1)	Hold for 10 minutes at 30 °C
2)	Heat from 30 °C to 250 °C at 5 °C min ⁻¹	2)	Heat from 30 °C to 600 °C at 5 °C min ⁻¹
3)	Heat from 250 °C to 400 °C at 2 °C min ⁻¹	3)	Cool from 600 °C to 30 °C at 50 °C min ⁻¹
4)	Heat from 400 °C to 600 °C at 5 °C min ⁻¹		
5)	Cool from 600 °C to 30 °C at 25 °C min ⁻¹		

5.4 Results and discussion

DSC was performed using hermetically sealed high pressure stainless steel crucibles to allow for high temperature (up to 600 °C) testing and the associated high pressure that may be experienced during decomposition reactions. The thermograms for dry LTO electrode material are shown in Figure 5.52, in a standard aluminium crucible with pierced lid and a high-pressure crucible. The high-pressure crucibles appear to have a different baseline profile compared to the standard aluminium crucibles, which could be associated with the thermal properties of the stainless steel or aluminium crucible material over the temperature range used. Additionally, the high-pressure crucible appears to be more sensitive than the aluminium crucible, detecting an additional thermal event at approximately 320 °C that was not visible in the standard aluminium crucible thermogram. However, this additional peak could also be due to the sealed high-pressure crucible causing an

altered reaction process during decomposition since vapours / gasses are not vented from crucible.

It should be noted that the high-pressure crucibles were reusable, requiring cleaning in between each use. Therefore, the cleaning stage is crucial to obtaining a true thermogram for each sample. The cleaning process has been described Section 5.3.3. As a crucible aged, the thermogram was seen to become noisier, in some cases, with a more pronounced baseline drift. This could be due to contamination of the crucible from previous samples or mechanical / chemical etching of the crucible from the cleaning process effecting measurement. From Figure 5.52, it is likely that any baseline drift observed for samples tested in high pressure crucibles could be a manifestation of the crucible and not necessarily related to thermal events in the sample. For this reason, changes in the heat flow derivative curve were used to define the beginning and end of each thermal event to help differentiate the thermal effects of the crucible from thermal events of the sample.

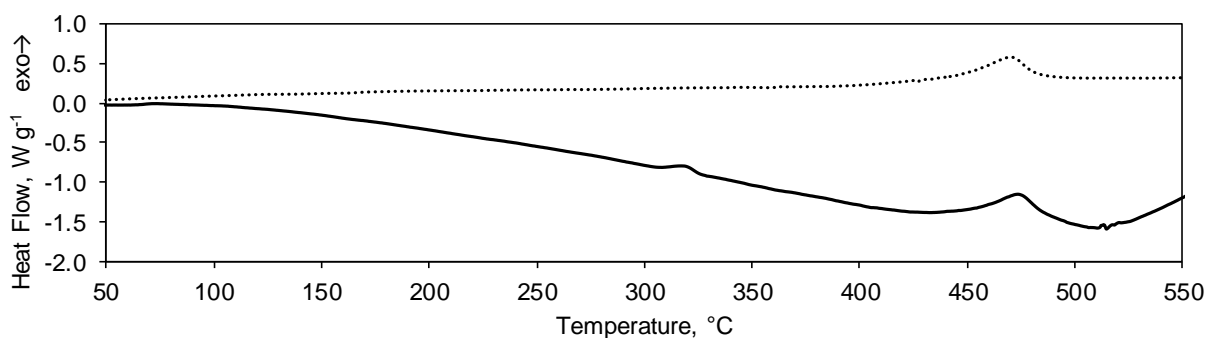


Figure 5.52 DSC thermogram for dry LTO electrode material in different DSC crucibles, hermetically sealed high pressure stainless steel crucible (—) and standard aluminium DSC crucible (.....).

DSC experiments were originally investigated at a heating rate of 10 °C min^{-1} . The DSC thermograms were found to have multiple overlapping peaks (Appendix K), leading to the heating rate being reduced to 5 °C min^{-1} . This allowed for better peak separation as well as decreasing the effects of thermal lag associated with high heating rates [367]. Although peak separation was improved at the lower heating rate, overlapping peaks are still evident at 5 °C min^{-1} . This is specifically noticeable for the LiFSI and LFP and LTO electrodes tested with P13FSI electrolyte (plots in Appendix K). However, the DSC traces obtained are useful for comparison to each other. Since all DSC tests were performed with the same DSC method, the temperatures and magnitude of peaks is quantitatively comparable between traces, while the shape of each peak can be qualitatively compared.

5.4.1 P13FSI electrolyte thermal stability³

The DSC and TGA results for LiFSI salt, IL P13FSI and P13FSI electrolyte from 50 to 550 °C are shown in Figure 5.53. For all figures, positive heat flow is exothermic and negative heat flow endothermic, as indicated on the vertical axis title. The onset temperature, peak temperature and corresponding heat generations are shown in Table 5.28 for P13FSI electrolyte and its components as well as EC / EMC and EC / DMC electrolytes and their components. Corresponding to the above definition of positive heat flow as exothermic, all heat values in tables are positive for exothermic and negative for endothermic.

DSC of LiFSI and P13FSI electrolyte was initially performed at 10 °C min⁻¹, however peak separation for the thermal events was not clear at this rate. A slower heating rate of 5 °C min⁻¹ was used for all subsequent tests. Complex samples, such as the cycled electrodes, still had multiple thermal events overlapping at 5 °C min⁻¹ but the thermograms were clear enough for comparison to each other and strict peak separation was not necessary to make these comparisons.

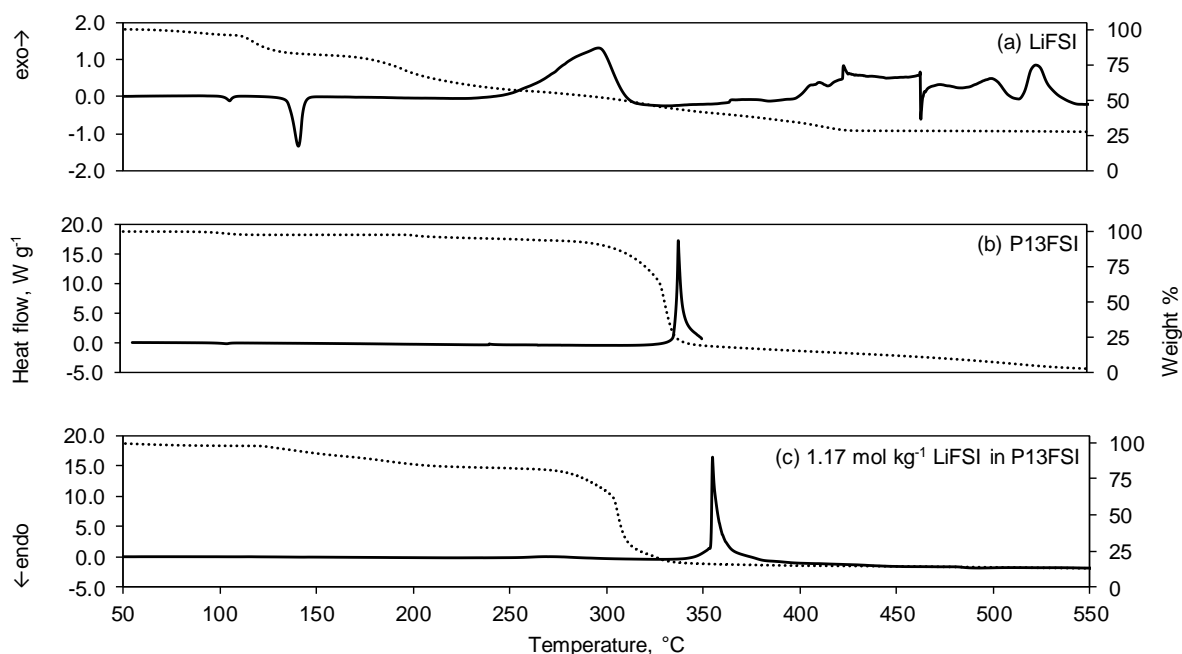


Figure 5.53 DSC thermogram (—) and TGA trace (.....) for (a) LiFSI powder, (b) P13FSI IL and (c) P13FSI electrolyte (1.17 mol kg⁻¹ LiFSI).

³ Section 5.4.1 is from a published research paper, see Table 1.4 publication #1 for authorship details.

5.4.1.1 LiFSI salt

The DSC thermogram and TGA trace for LiFSI is shown in Figure 5.53a. The LiFSI thermogram shows endothermic peaks at 106 and 141 °C and one large exothermic peak at 297 °C with a heat generation of 568 J g⁻¹. Above 350 °C, LiFSI showed multiple overlapping peaks making peak distinction difficult. The high onset temperature for exothermic decomposition of LiFSI confirms the salt is high purity and the crucible is sealed [367]. The sharp endothermic peak at 464 °C could indicate gasses being vented from the crucible. The presence of defined thermal peaks following the abrupt endothermic event suggests that complete crucible rupture did not occur.

Table 5.28 Comparison of DSC thermograms for P13FSI electrolyte components and conventional electrolyte components: LiFSI, LiPF₆, P13FSI IL, EC / EMC (1:1) solvent, P13FSI electrolyte, 1 M LiPF₆ EC / EMC (1:1) electrolyte and 1 M LiPF₆ EC / DMC (1:1 w/w) electrolyte.

	Exothermic onset temperature, °C	*Peak temperature, °C	Heat generation, J g ⁻¹	*Total heat,		Heating rate, °C min ⁻¹	Temperature range, °C	Ref.
				J g ⁻¹	ΔJ cm ⁻³			
LiFSI	230	106 141 297	-6 -87 568	475		5	50-550	This work
LiPF ₆	>350	(180 to 210) [§]		-20 ± 2		10	100-350	[367]
P13FSI	321	339	866*	866	1160	5	50-460	This work
EC / EMC (1:1 v/v)	209	(205 to 250) [§]		11 ± 1		10	100-350	[367]
1.57 M LiFSI P13FSI	248	269 355	54 1029	1083	1635	5	50-550	This work
1 M LiPF ₆ EC / EMC (1:1 v/v)	253	(200 to 250) [§] (250 to >350) [§]		330 ± 30		10	100-350	[367]
1 M LiPF ₆ EC / DMC (1:1 w/w)	202	215		612		0.2	50-300	[362]

* Extreme temperature reached in thermal event (i.e. maximum for exothermic and minimum for endothermic)

± Sum of heat generation

§ Peak temperature not reported, start and end temperatures for each peak shown

Δ Calculated with material densities of P13FSI (1.34 g cm⁻³, from manufacturers datasheet) and P13FSI electrolyte (1.51 g cm⁻³, from manufacturers datasheet).

The DSC curve agrees with results obtained by Eshetu, et al. [31] for LiFSI salt powder at a heating rate of 10 °C min⁻¹, taking into consideration the thermal lag at higher heating rates that results in peaks shifting to higher temperatures with increased heat generation [367]. Eshetu, et al. [31] attribute the endothermic peak at approximately 140 °C to LiFSI melting and the exothermic

peak at approximately 300 °C to thermal degradation.

The LiFSI TGA trace from this work (Figure 5.53a) shows a mass loss corresponding to the 140 °C endothermic peak. This indicates the peak was not solely from salt melting, a small reaction likely also occurred releasing some vapour, causing the decrease in sample weight. The major TGA mass loss correlates to the main DSC exothermic peak, which confirms decomposition of the lithium salt.

Decomposition of LiFSI salt was studied by Li, et al. [379] who performed TGA-DSC-Mass Spectrometry (MS) on LiFSI powder at a heating rate of 10 °C min⁻¹. Detection of SO₂ on the MS during pyrolysis indicated decomposition beginning at approximately 180 °C with the main decomposition event occurring from 320 °C, confirmed by the DSC, TGA and MS results. The decomposition peak observed during DSC of LiFSI in this work occurred at 297 °C, approximately 20 °C lower than that reported by Li, et al. [379]. The lower peak temperature observed in this work can be explained by the lower heating rate used.

The LiFSI DSC thermogram (Figure 5.53a) has a small endothermic event at 106 °C with a heat generation of -6 J g⁻¹. This endothermic peak is also observed in four other samples throughout this work (see Figure 5.56c Figure 5.59a, Figure 5.63c and Figure 5.65b) at 105 ±1 °C with similar heat generations of -3, -5, -7 and -6 J g⁻¹, respectively. As there is no indication this endothermic peak is related to the samples, it could be from evaporation of residue present on the surface of the crucible from sample cleaning and loading processes.

The DSC results obtained for P13FSI electrolyte are shown in Table 5.28 alongside those of conventional electrolytes from other studies. It should be noted that Botte, et al. [367] performed DSC at a heating rate of 10 °C min⁻¹ up to 350 °C and Xiang, et al. [362] performed DSC at a heating rate of 0.2 °C min⁻¹ up to 300 °C, therefore the effects of thermal lag need to be considered. LiFSI melted at approximately 140 °C whereas LiPF₆ did not melt until approximately 190 °C, however this melting peak may have been seen at a lower temperature if it was tested at 5 °C min⁻¹. Yang, et al. [380] found that LiPF₆ underwent an endothermic thermal decomposition between approximately 200 and 250 °C, at a heating rate of 10 °C min⁻¹. Therefore, LiPF₆ decomposes at a temperature of approximately 100 °C lower than LiFSI, which indicates the superior thermal stability of LiFSI [381], although it should be noted that no heat is released by LiPF₆ during decomposition.

The P13FSI IL thermogram (Figure 5.53b) shows one large exothermic peak at 339 °C with a heat generation of 866 J g⁻¹. Crucible rupture occurred at 351 °C towards the end of the peak. Corresponding mass loss observed in the TGA trace confirming the exothermic peak is from a decomposition reaction. The thermal stability of P13FSI IL can be compared to that of the EC /

ethyl methyl carbonate (EMC) (1:1 v/v) solvent mixture used in conventional electrolytes (Table 5.28). EC / EMC (1:1 v/v) solvent mixture undergoes one exothermic event at approximately 210 – 250 °C with a small heat release of 11 J g⁻¹, the peak would occur at a slightly lower temperature if tested at 5 °C min⁻¹. The P13FSI IL has an onset temperature more than 100 °C higher than the solvent mixture indicating a higher thermal stability. However, comparing the total heat released during decomposition, the P13FSI IL releases substantially more. This means comparison of thermal stability based on onset temperature and total heat release will give conflicting results. Since these materials will not exist individually in a cell, it is more important to look at the thermal stability and decomposition profile of the resulting electrolytes.

5.4.1.2 *LiFSI concentration in P13FSI electrolyte*

The TGA traces for LiFSI salt powder, P13FSI IL, P13FSI electrolyte (1.57 M LiFSI) and IL electrolyte solutions made with different salt concentrations: 0.67 M (0.5 mol kg⁻¹), 1.34 M (1.0 mol kg⁻¹), 1.61 M (1.2 mol kg⁻¹) and 2.01 M (1.5 mol kg⁻¹) LiFSI in P13FSI are shown in Figure 5.54. LiFSI shows a definitive mass loss of approximately 13 wt% from 110 to 140 °C. This is followed by a gentle sloping mass loss from bulk decomposition that continues until 430 °C where the residual mass is approximately 28% of the original sample weight. It should be noted that the LiFSI thermal stability trace in Figure 5.54 is most similar to the commercial LiFSI salt identified by Kerner, et al. [373] as the least pure salt in their investigation, as introduced in Section 5.2.1. During TGA the least pure LiFSI salt showed a decomposition event at approximately 160 °C, while the other two commercial salts did not experience any decomposition below 200 °C [373]. The presence of impurities in the LiFSI salt is expected to have an impact on the thermal stability of the salt, as well as possibly impact the thermal stability of materials prepared with the salt, such as the thermal properties of the electrospun FSI-A, FSI-B and FSI-C separators presented in Section 3.3.2.5. The P13FSI ILs do not show any definitive mass loss until 200 °C when approximately 4 wt% is lost between 200 and 280 °C. This is followed by the main decomposition reaction evidenced by a rapid loss of approximately 75% of the sample weight. The IL electrolytes with different salt concentrations show a mass loss starting at approximately 110 °C from the dissolved LiFSI.

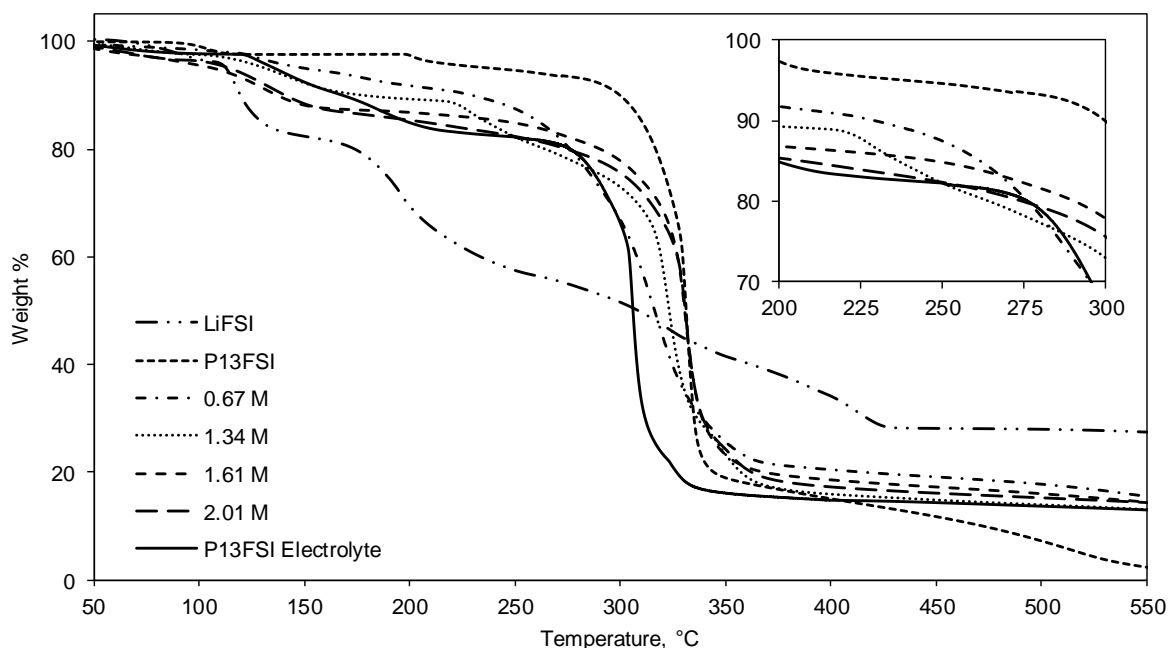


Figure 5.54 TGA trace of LiFSI powder, P13FSI IL, P13FSI electrolyte (1.57 M LiFSI) and P13FSI electrolyte with different salt concentrations: 0.67, 1.34, 1.61 and 2.01 M LiFSI in P13FSI. Inset of 200 to 300 °C temperature range.

The amount of weight loss is lower than the LiFSI sample and approximately corresponds to the salt concentration in the electrolyte. By 150 °C the electrolytes sample weights have reduced to 95.0, 92.3, 88.1 and 88.4% of their initial weight, for the salt concentrations of 0.67, 1.34, 1.61 and 2.01 M electrolytes, respectively. It appears that the addition of LiFSI salt to an IL causes a decrease in the electrolyte thermal stability in proportion to the salt concentration. This is not unexpected since the exothermic onset temperature of LiFSI is 90 °C lower than that of P13FSI IL (Table 5.28). This is likely due to the presence of the lithium cation in the salt since the salt and IL have the same anion. In a DSC study of P13FSI with LiFSI or LiTFSI, Huang and Hollenkamp [64] reported an exothermic peak, at approximately 120 and 140 °C for 0.5 mol kg⁻¹ LiFSI and LiTFSI, respectively. Since the exothermic peak was not present in the P13FSI thermogram, it was suggested to be from the co-presence of Li⁺ and FSI⁻ in the electrolyte [64].

The P13FSI electrolyte specified a salt concentration of 1.57 M. The P13FSI electrolyte TGA trace aligns well with the 1.61 M electrolyte up to approximately 150 °C. After 150 °C the trace falls between the 0.67 and 2.01 M electrolyte traces, displaying a slightly different TGA profile. The major mass loss begins and ends at approximately 270 °C and 350 °C, respectively, approximately 25 °C before the other electrolyte samples. P13FSI electrolyte is a commercial product and there may be a small amount of undisclosed additive or a residual material from the manufacturing process that could be responsible for the different TGA trace observed in this work.

5.4.1.3 P13FSI electrolyte and conventional electrolytes

The P13FSI electrolyte thermogram (Figure 5.53c) shows two exothermic events, a small peak at 269 °C with a heat generation of 54 J g⁻¹ and a major peak at 355 °C with a heat generation of 1029 J g⁻¹. These exothermic peaks observed in the P13FSI electrolyte at 269 and 355 °C most likely correspond to the exothermic decomposition events seen in LiFSI salt and P13FSI IL, at 297 °C and 339 °C, respectively (Figure 5.53). The peak temperatures observed in the electrolyte have shifted slightly from those of the individual materials, this could be due to altered ionic interactions when the salt is dissolved in the IL to form the electrolyte solution. The same two thermal events are visible as definite mass losses in the TGA trace. This indicates that a small amount of decomposition occurs during the first peak but the major decomposition reaction (and mass loss) occurs at approximately 310 °C. This occurs at a lower temperature in the TGA trace than in the DSC due to the slower heating rate used for TGA testing over the P13FSI electrolyte decomposition temperature range.

Compared to 1 M LiPF₆ EC / EMC (1:1) electrolyte (Table 5.28), the P13FSI electrolyte has a slightly lower onset temperature and a much larger total heat value, both indicating inferior thermal stability of the P13FSI electrolyte. When compared to 1 M LiPF₆ EC / DMC (1:1 w/w) electrolyte, P13FSI electrolyte has a higher onset temperature by 40 °C. However, the heating rate should be considered; 1 M LiPF₆ EC / DMC (1:1 w/w) electrolyte would be expected to have a higher exothermic onset temperature if tested at 5 °C min⁻¹. Although the IL electrolyte may have a high onset temperature, the total heat released during decomposition is considerably more than the 1 M LiPF₆ EC / DMC (1:1 w/w) electrolyte. Wang, et al. [382] proposed that the safety of an electrolyte corresponds to its exothermic onset temperature. Applying this suggestion to the electrolytes compared here, thermal stability of the electrolytes can be ranked in the following sequence: 1 M LiPF₆ EC / DMC (1:1 w/w) < P13FSI electrolyte < 1 M LiPF₆ EC / EMC (1:1 v/v). It appears that solvent type in an electrolyte can strongly impact the electrolyte thermal stability. In the next sections, P13FSI electrolyte combined with different separators and electrodes, including potentially formed electrode-electrolyte interphase components, were investigated and discussed to determine thermal stability of the electrolyte in conjunction with other materials present in a lithium-ion cell.

5.4.2 Separators with P13FSI electrolyte

5.4.2.1 Celgard with P13FSI electrolyte

The DSC thermograms for Celgard 3501 alone, with P13FSI electrolyte and harvested from a LFP | P13FSI electrolyte | lithium metal (Li) cell are shown in Figure 5.55. The corresponding onset temperature, peak temperatures, heat generations and total heat values for each thermogram in

Figure 5.55 can be found in Table 5.29. Celgard 3501 (Figure 5.55a) has two overlapping endothermic peaks between 128 and 173 °C, with a peak temperature of 164 °C and a total heat of -90 J g^{-1} . The peak at 164 °C appears to be from melting of the polypropylene (PP) polymer. The melting peak for Celgard 2400, also a monolayer PP separator, has been previously observed at 162 °C during DSC [222]. The split peak that appears in this work may be due to the surfactant coating on Celgard 3501, however, it does not appear to impact the polymer melting temperature.

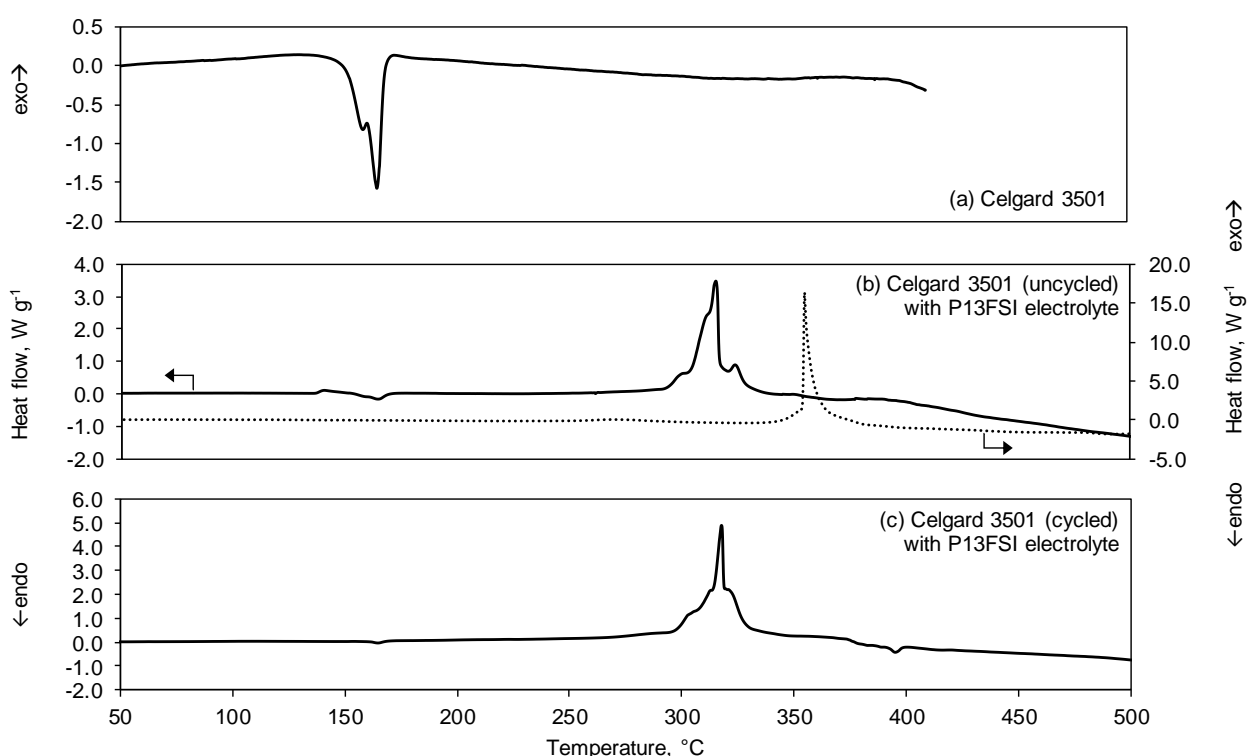


Figure 5.55 DSC thermogram (—) for (a) Celgard 3501, (b) Celgard 3501 (uncycled) with P13FSI electrolyte (including P13FSI electrolyte (.....)), and (c) Celgard 3501 (cycled) in P13FSI electrolyte LFP | Li cell.

Celgard 3501 with P13FSI electrolyte (Figure 5.55b) has two exothermic events and one endothermic event, with a total heat of 533 J g^{-1} . It should be noted that the DSC sample was approximately 25 wt% Celgard 3501 and the balance made up by P13FSI electrolyte. When Celgard 3501 is combined with P13FSI electrolyte, the melting peak magnitude diminished according to the separator wt% in the sample however the melting peak temperature remained constant at 164 °C. A small exothermic event appeared at 140 °C, immediately before the separator melting peak. The main exothermic event occurred at 316 °C and consisted of multiple overlapping exothermic events between 241 and 348 °C. The main exothermic event is likely due

to decomposition of P13FSI electrolyte, however the peak occurs at approximately 40 °C lower than the decomposition peak for P13FSI electrolyte (dotted line in Figure 5.55b, peak values in Table 5.28). This suggests that Celgard 3501 may interact with P13FSI electrolyte, resulting in a lower thermal stability than the P13FSI electrolyte alone.

Table 5.29 Comparison of DSC results for Celgard 3501, GF and electrospun PVDF-HFP: alone, with P13FSI electrolyte (uncycled) and harvested from a P13FSI electrolyte cell.

	Onset temperature [§] , °C		*Peak temperature, °C	Heat generation, J g ⁻¹	*Total heat, J g ⁻¹	Heating rate, °C min ⁻¹	Temperature range, °C	Ref.
	Endo	Exo						
Celgard 3501	128		164	-90	-90	5	50-550	This work
Celgard 3501 (uncycled) with P13FSI electrolyte	151	135	140 164 316	8 -21 546	533	5	50-550	This work
Celgard 3501 (cycled) in P13FSI electrolyte	154	294	165 319 395	-6 567 -42	519	5	50-550	This work
GF		217	229	5	5	5	50-550	This work
GF (uncycled) with P13FSI electrolyte	311	188	254 302 311 391	238 678 -79 -91	746	5	50-550	This work
GF (cycled) in P13FSI electrolyte	96	151	105 160 231 313	-3 3 159 651	810	5	50-550	This work
PVDF-HFP	108	333	157 377 461	-44 75 123	154	5	50-550	This work
PVDF-HFP (uncycled) with P13FSI electrolyte		137	221 322 394	563 332	895	5	50-550	This work

[§] Endo = endothermic, Exo = exothermic

* Extreme temperature reached in thermal event (maximum for exothermic and minimum for endothermic)

‡ Sum of heat generation

Celgard 3501 harvested from a LFP | P13FSI electrolyte | Li cell (Figure 5.55c) has a similar thermogram to the uncycled Celgard 3501 with P13FSI electrolyte (Figure 5.55b), two endothermic events and one exothermic event with a total heat of 519 J g⁻¹. A melting peak for Celgard is seen at 165 °C, which correlates to the other Celgard thermograms in Figure 5.55. The main exothermic event occurs at approximately the same temperature (319 °C) as the uncycled Celgard with P13FSI electrolyte (316 °C), and has a similar total heat value. However, the small exothermic event at 140 °C does not appear and multiple overlapping endothermic appear to occur between

374 and 401 °C that were not visible in the uncycled Celgard 3501 with P13FSI electrolyte. The endothermic region is likely due to interactions between Celgard 3501 and P13FSI electrolyte during cycling, or perhaps electrode-electrolyte interphase compounds formed on the lithium metal and / or LFP electrode/s during cycling being left on the separator during cell disassembly. It can be seen from Figure 5.55b-c that interactions between Celgard 3501 and P13FSI electrolyte during cell cycling are negligible, although the consistent reduced temperature of P13FSI electrolyte decomposition in the presence of Celgard 3501 should be noted.

5.4.2.2 GF with P13FSI electrolyte

The DSC thermograms for GF alone, with P13FSI electrolyte and harvested from a LFP | P13FSI electrolyte | Li cell are shown in Figure 5.56. The corresponding onset temperature, peak temperatures, heat generations and total heat values for each thermogram in Figure 5.56 can be found in Table 5.29. The GF thermogram (Figure 5.56a) has one small exothermic event at 217 °C with a heat generation of 5 J g⁻¹. There are two small instabilities in the DSC thermogram at approximately 150 and 280 °C, however, no defined peaks are visible. DSC of a glass microfibre membrane made via the paper making process, reported in literature, showed no thermal events between 60 and 280 °C [222]. The exothermic peak observed at 217 °C is of unknown origin since the GF used in this work was binder free.

When GF is combined with P13FSI electrolyte (Figure 5.56b), two exothermic events and two endothermic regions are observed, with a total heat of 746 J g⁻¹. The exothermic events at 254 and 302 °C could be related to the decomposition peaks in the P13FSI electrolyte at 269 and 355 °C, respectively (dotted line in Figure 5.56b, peak values in Table 5.28). However, the peaks occur approximately 20 and 50 °C earlier for GF with P13FSI electrolyte, compared to P13FSI electrolyte alone. This suggests that the thermal stability of P13FSI electrolyte may be decreased in the presence of GF. There are two regions with overlapping endothermic events between 311 to 331 °C and 384 to 438 °C that do not correlate to any peaks in either of the separate GF or P13FSI electrolyte thermograms, which suggests that some interaction may have occurred between GF and the P13FSI electrolyte.

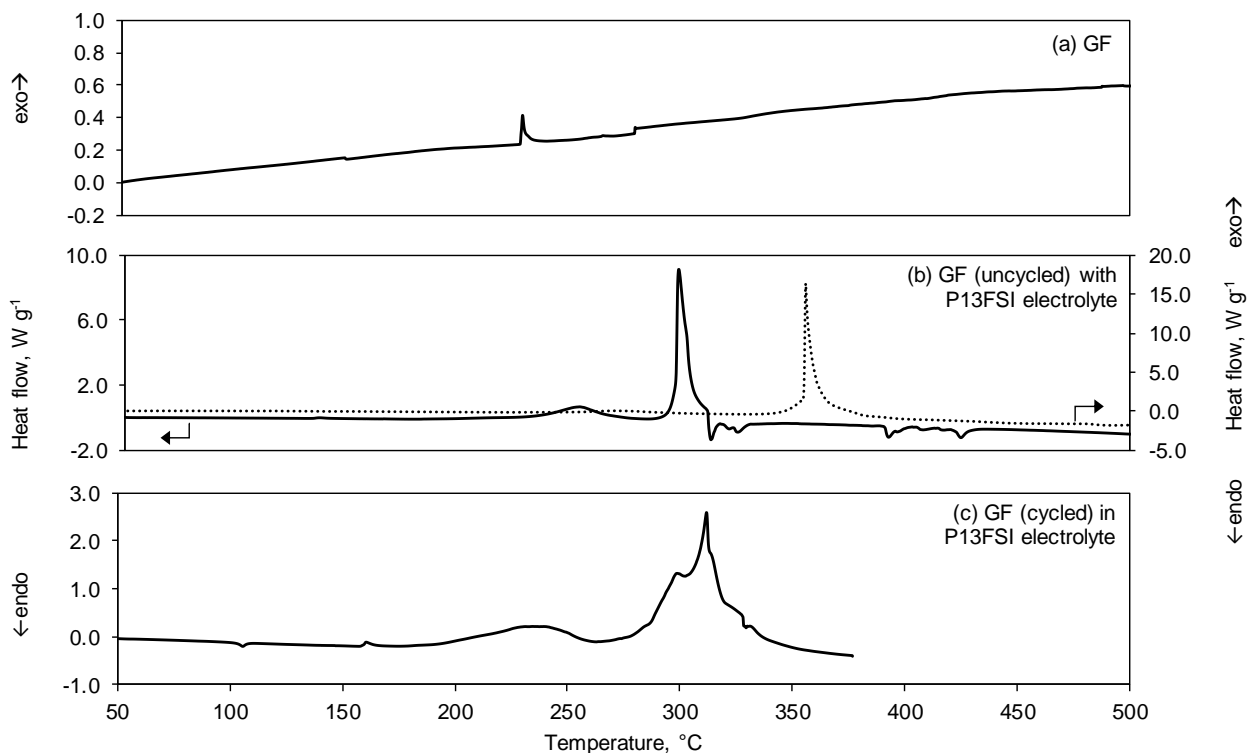


Figure 5.56 DSC thermogram (—) for (a) GF, (b) GF (uncycled) with P13FSI electrolyte (including P13FSI electrolyte (.....)) and (c) GF (cycled) in P13FSI electrolyte LTO | Li cell.

The thermogram of GF harvested from a LTO | P13FSI electrolyte | Li cell (Figure 5.56c) has one small endothermic event and three exothermic events, with a total heat generation of 810 J g^{-1} . The endothermic event at $105 \text{ }^\circ\text{C}$ is likely due to evaporation of residue present on the crucible surface, as discussed previously. There is a small exothermic event at $160 \text{ }^\circ\text{C}$ that was not present in the uncycled GF with P13FSI electrolyte thermogram. The next exothermic peak at $213 \text{ }^\circ\text{C}$ could correlate to the $254 \text{ }^\circ\text{C}$ peak in the uncycled GF with P13FSI electrolyte, however it occurs over a wider temperature range, with the peak occurring approximately $40 \text{ }^\circ\text{C}$ lower and less heat is generated. The main exothermic peak is at $313 \text{ }^\circ\text{C}$, slightly higher than that seen in the uncycled GF with P13FSI electrolyte, the exothermic event appears to be a combination of multiple overlapping peaks occurring over a wider temperature range. The three exothermic peaks observed in the cycled GF thermogram, compared to the uncycled GF with P13FSI electrolyte. This suggests that GF is interacting with the P13FSI electrolyte during cycling or perhaps electrode-electrolyte interphase compounds formed on the electrode/s (lithium metal and / or LTO) during cycling were present on the separator following cell disassembly.

For both Celgard 3501 and GF with P13FSI electrolyte (uncycled and cycled), the main exothermic peak occurs between 300 to $320 \text{ }^\circ\text{C}$. However, overall, the Celgard 3501 could be considered

more thermally stable due to the additional exothermic peak occurring with GF at approximately 230 to 255 °C, lowering the main exothermic onset temperature for GF, compared to Celgard 3501. The total heat generation of GF with P13FSI electrolyte (cycled and uncycled) is higher than that of Celgard 3501 with P13FSI electrolyte. This may be due to the higher porosity and wettability of GF, compared to Celgard 3501, resulting in a higher weight ratio of electrolyte to separator material in the GF samples and could account for more heat being generated.

5.4.2.3 *Electrospun PVDF-HFP with P13FSI electrolyte*

The DSC thermograms for electrospun PVDF-HFP (no salt) alone and with P13FSI electrolyte are shown in Figure 5.57. The corresponding onset temperature, peak temperatures, heat generations and total heat values for each thermogram in Figure 5.57 can be found in Table 5.29. Electrospun PVDF-HFP (Figure 5.57a) has one endothermic event and two exothermic events, with a total heat generation of 154 J g⁻¹. The endothermic peak occurs at 157 °C, which is most likely due to PVDF-HFP melting, similar to published DSC results showing a melting point of 159 °C for PVDF-HFP [280]. There is a mild extended exotherm between 333 and 432 °C and an exothermic peak at 461 °C. As PVDF-HFP is the only material present in this sample, the exothermic events seen above 300 °C are likely due to decomposition reactions of PVDF-HFP. This agrees with the DSC and TGA results presented in Section 3.3.2.5.

When electrospun PVDF-HFP is combined with P13FSI electrolyte (Figure 5.57b), there are multiple exothermic events that can be divided into two groups, exothermic peaks below 312 °C and exothermic peaks above 312 °C. Below 312 °C, there is one main exothermic peak at 221 °C as well as an extended mild exothermic event occurring from approximately 137 to 312 °C, with a heat generation of 563 J g⁻¹. Above 312 °C there are two main exothermic peaks, joined by smaller overlapping exothermic events, occurring at 322 and 394 °C. The peak at 322 °C has a similar shape to that of the main decomposition peak for P13FSI electrolyte (dotted line in Figure 5.57b, peak values in Table 5.28) which suggests it may be from decomposition of P13FSI electrolyte, however the peak occurs approximately 30 °C lower for PVDF-HFP with P13FSI electrolyte compared to P13FSI electrolyte alone. The peak at 394 °C could be associated with PVDF-HFP decomposition, although it occurs approximately 60 °C lower than for PVDF-HFP alone (Figure 5.57a), suggesting that P13FSI electrolyte interacts PVDF-HFP resulting in a lower thermal stability. It is likely that polymer swelling occurs when P13FSI electrolyte is added which may change the intermolecular interactions and reduce the thermal stability of the polymer phase. The degree of polymer swelling, and therefore effect on thermal stability, may also be affected by the wetting time before thermal analysis. The peak at 221 °C does not correlate to peaks in either individual PVDF-HFP or P13FSI electrolyte thermograms. There is a small exothermic peak at 269 °C in P13FSI electrolyte (Figure 5.53 and Table 5.28) which is suggested to be from decomposition of LiFSI present in the P13FSI electrolyte. This is the closest event that could

correlate to the 221 °C exothermic peak for PVDF-HFP with P13FSI electrolyte. This could indicate that the 221 °C peak may be due to decomposition of LiFSI in the P13FSI electrolyte and possibly the subsequent interaction between the LiFSI decomposition products and the PVDF-HFP polymer.

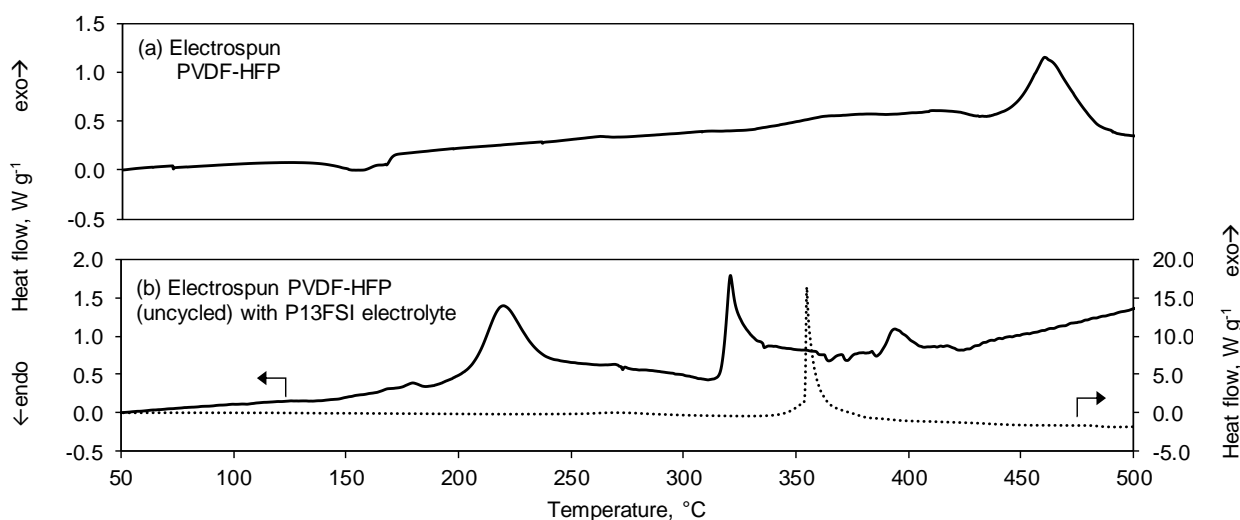


Figure 5.57 DSC thermogram (—) for (a) Electrospun PVDF-HFP, (b) Electrospun PVDF-HFP (uncycled) with P13FSI electrolyte (including P13FSI electrolyte (.....)) and (c) Electrospun PVDF-HFP (uncycled) with conventional electrolyte.

Based on exothermic onset temperatures, Celgard 3501 and PVDF-HFP have similar thermal stability with P13FSI electrolyte, whereas GF is more stable as it has an exothermic onset temperature approximately 50 °C higher with P13FSI electrolyte present than the other two separators. When comparing thermal stabilities based on total heat generation, Celgard 3501 has the lowest heat generation in the presence of P13FSI electrolyte, followed by GF, and PVDF-HFP, indicating that the electrospun PVDF-HFP is less thermally stable than the other two separator materials. Overall, the DSC results for each separator with P13FSI electrolyte suggests that the thermal stability of a separator may change when electrolyte is added due to polymer swelling after wetting. Therefore, it is recommended that the thermal stability of separators is evaluated for separators wet with electrolyte to obtain results more relevant to a separator in an assembled cell. Additionally, irrespective of the separator material, the thermal stability of P13FSI electrolyte appears to be decreased when absorbed in a separator matrix. This should be taken into consideration when comparing the thermal stability of electrolyte for use in lithium-ion cells.

5.4.3 Commercial electrodes with P13FSI electrolyte⁴

5.4.3.1 NMC with P13FSI electrolyte

The charge and discharge curves of a NMC vs. lithium metal coin cell with P13FSI electrolyte is shown in Figure 5.58. Approximately 75% of the theoretical capacity was extracted from the electrode (NMC electrode porosity was 36.1%). This result correlates to other reported data for this material with Pyr⁺ and TFSI⁻ based IL electrolytes [74, 351]. At a discharge rate of 35 mA (g NMC)⁻¹, Patra, et al. [351] observed cell capacities of approximately 110 to 160 mAh (g NMC)⁻¹ for Pyr⁺ TFSI⁻ based IL electrolytes with different cation chain lengths, similar to the capacity obtained in this work (158 mAh (g NMC)⁻¹). The difference in capacities observed by Patra, et al. [351] with different IL electrolytes was attributed to the higher conductivity and lower viscosity of one electrolyte over the other. This suggests that the lower conductivity and higher viscosity of IL electrolytes, compared to conventional electrolytes, is likely to result in decreased capacities, even at lower discharge rates. It should be noted that the high viscosity P13FSI electrolyte may not have completely wetted the commercial electrodes which had been calendared for use with conventional electrolytes, which would mean it would not be possible to extract all the theoretical capacity. The upper voltage cut-off was set to 4.7 V, however this was not reached and charge was terminated after double the expected charge time had passed.

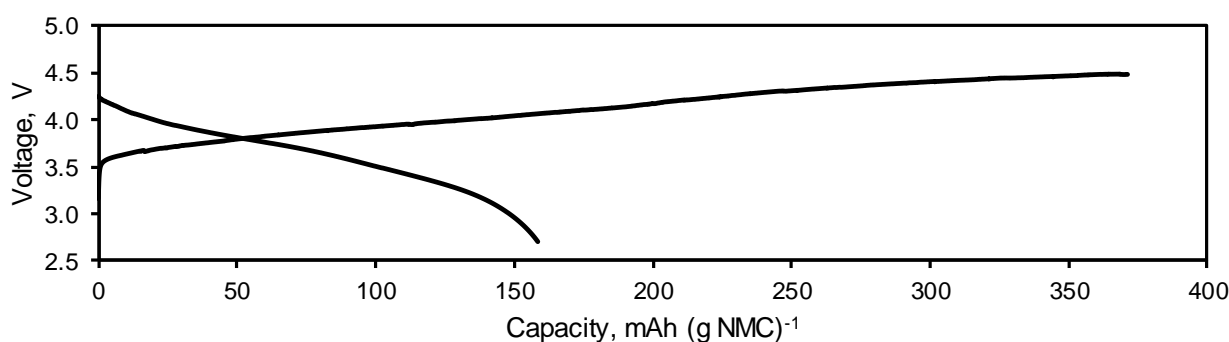


Figure 5.58 Discharge and recharge curve of NMC vs lithium metal with P13FSI electrolyte. Reversible capacity 210 mAh (g NMC)⁻¹. Current density 0.242 mA cm⁻².

The DSC thermogram for (a) NMC (uncycled) with 1.2 M LiPF₆ EC / EMC (2:1 v/v) electrolyte, (b) NMC (uncycled) with P13FSI electrolyte, (c) delithiated NMC from a half-cell with P13FSI electrolyte and (d) lithiated NMC from a half-cell with P13FSI electrolyte are shown in Figure 5.59. Delithiated electrodes refer to cathode materials charged to the upper voltage limit prior to

⁴ Section 5.4.3 is from a published research paper, see Table 1.4 publication #1 for authorship details.

disassembly. Lithiated electrodes refer to cathode material discharged to the lower voltage limit prior to disassembly. The corresponding onset temperature, peak temperatures, heat generations and total heat values are shown in Table 5.30 for the thermograms in Figure 5.59, alongside results of conventional electrolyte studies from other works.

Uncycled NMC with 1.2 M LiPF₆ EC / EMC (2:1 v/v) electrolyte (Figure 5.59a) has an onset temperature of 115 °C for a small exothermic event at 131 °C with a heat generation of 21 J g⁻¹. The main exothermic peak occurs at 286 °C with a heat generation of 644 J g⁻¹, including an overlapping smaller exothermic event at approximately 268 °C. There is also a small endothermic event at 104 °C with a heat generation of -5 J g⁻¹, as discussed previously.

Uncycled NMC with P13FSI electrolyte (Figure 5.59b) has an onset temperature of 163 °C for the main exothermic event at 297 °C with a heat generation of 766 J g⁻¹. The TGA trace confirms decomposition occurs with the sample undergoing a major mass loss at the same temperature as the exothermic peak. Uncycled NMC with P13FSI electrolyte has an onset temperature 48 °C higher than with 1.2 M LiPF₆ EC / EMC (2:1 v/v) electrolyte. This indicates a higher thermal stability of uncycled NMC with P13FSI electrolyte. However, using overall heat generation, uncycled NMC with 1.2 M LiPF₆ EC / EMC (2:1 v/v) electrolyte is more thermally stable than with P13FSI electrolyte. Considering these conflicting results for thermal stability, the investigation of cycled electrode materials becomes more important to determine the effects of the electrode-electrolyte interphase formed with different electrolytes on thermal stability.

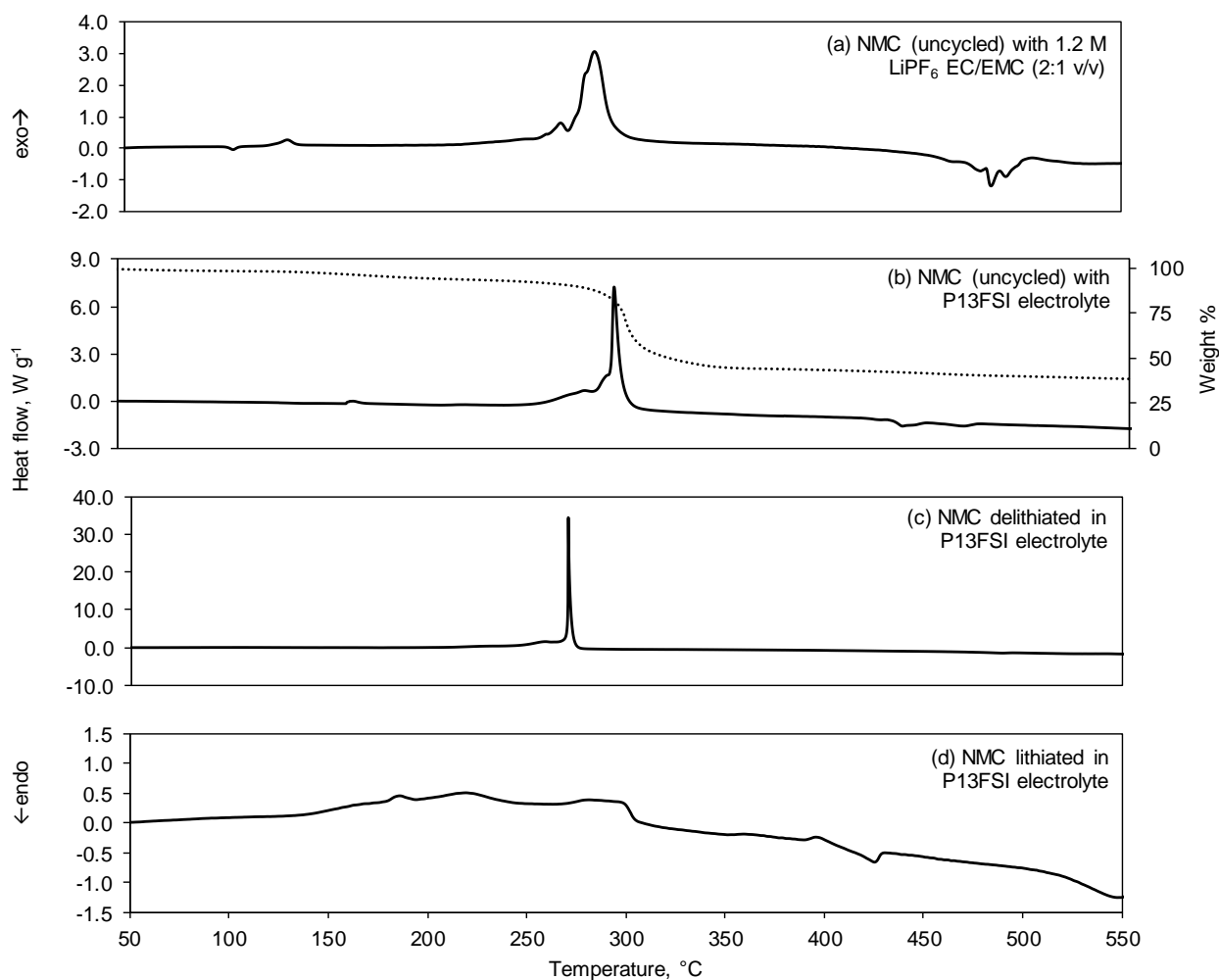


Figure 5.59 DSC thermograms (—) and TGA trace (.....) for (a) uncycled NMC with 1.2 M LiPF₆ EC / EMC (2:1 v/v) electrolyte, (b) uncycled NMC with P13FSI electrolyte, (c) delithiated NMC from half-cell with P13FSI electrolyte and (d) lithiated NMC from half-cell with P13FSI electrolyte.

The delithiated NMC from a half-cell with P13FSI electrolyte (Figure 5.59c) has one sharp exothermic peak at 271 °C with a heat release of 1289 J g⁻¹. This peak overlaps a smaller exothermic event with an onset temperature of 180 °C. The lithiated NMC from a P13FSI electrolyte cell (Figure 5.59d) has a small but prolonged exothermic event starting at approximately 123 °C and continuing until approximately 300 °C with a total heat generation of 610 J g⁻¹. The lithiated NMC (discharged state) releases approximately half the total heat of the delithiated NMC (charged state). This suggests P13FSI electrolyte is more reactive with NMC in the charged state. The sharp peak in the delithiated NMC (Figure 5.59c) is similar to that in the thermogram for P13FSI electrolyte alone (Figure 5.53c), however, it occurs approximately 84 °C lower in the delithiated NMC thermogram. This could indicate reactivity of P13FSI electrolyte with the delithiated NMC resulting in electrolyte decomposition at a lower temperature. The delithiated NMC

has a higher onset temperature than both uncycled samples possibly indicating high thermal stability of the electrode-electrolyte interphase components formed on the electrode. However, when exothermic decomposition occurs the total heat generated by delithiated NMC is approximately twice that of the other samples (Figure 5.59a, b and d). The exothermic onset temperatures as well as the magnitude of total heat released by NMC with P13FSI electrolyte should be considered when determining the thermal stability.

Table 5.30 Comparison of DSC results for uncycled NMC with 1.2 M LiPF₆ EC / EMC (2:1 v/v) electrolyte, uncycled NMC with P13FSI electrolyte, delithiated NMC from half-cell with P13FSI electrolyte, lithiated NMC from half-cell with P13FSI electrolyte and Li_xNMC cycled with 1 M LiPF₆ EC / DMC (1:1 w/w) electrolyte.

	Exothermic onset temperature, °C	*Peak temperature, °C	Heat generation, J g ⁻¹	*Total heat,		Heating rate, °C min ⁻¹	Temperature range, °C	Ref.
				J g ⁻¹	ΔJ cm ⁻³			
Uncycled NMC with 1.2 M EC / EMC (2:1 v/v)	115	104 131 286 485 570	-5 21 644 -219 30	471		5	50-550	This work
Uncycled NMC with P13FSI electrolyte	163	166 297 437	12 766 -91	687	1253	5	50-550	This work
Delithiated NMC from half-cell with P13FSI electrolyte	180	271	1289	1289	2351	5	50-550	This work
Lithiated NMC from half-cell with P13FSI electrolyte	123	220	610	610	1113	5	50-550	This work
Li _x NMC cycled with 1 M LiPF ₆ EC / DMC (1:1 w/w)	146	191 215 252		600		0.2	50-300	[362]

* Extreme temperature reached in thermal event (maximum for exothermic and minimum for endothermic)

± Sum of heat generation

Δ Calculated with material densities of P13FSI electrolyte (1.51 g cm⁻³, from manufacturers datasheet) and NMC electrode (2.38 g cm⁻³, from [30]). Electrode porosity used to estimate volume ratio of electrode : electrolyte present in DSC sample.

The thermogram for charged (delithiated) NMC from a half-cell with P13FSI electrolyte (Figure 5.59c) can be compared to $\text{Li}_x\text{Ni}_{0.33}\text{Co}_{0.33}\text{Mn}_{0.33}\text{O}_2$ (Li_xNMC) cycled with 1 M LiPF_6 EC / DMC (1:1 w/w) electrolyte investigated by Xiang, et al. [362] (Table 5.30). It should be noted that Xiang, et al. [362] measured thermal stability with a C80 calorimeter at a heating rate of $0.2\text{ }^\circ\text{C min}^{-1}$. The exothermic onset temperature for NMC with P13FSI electrolyte in this work is $34\text{ }^\circ\text{C}$ higher than for NMC with 1 M LiPF_6 EC / DMC (1:1 w/w) electrolyte reported by Xiang, et al. [362]. However, at a heating rate of $5\text{ }^\circ\text{C min}^{-1}$ the peak observed in the Li_xNMC cycled with 1 M LiPF_6 EC / DMC (1:1 w/w) electrolyte would shift to a higher temperature meaning the exothermic onset temperatures could be comparable. The heat release is more than doubled for the NMC cycled with P13FSI electrolyte suggesting charged NMC is more reactive with P13FSI electrolyte than with 1 M LiPF_6 EC / DMC (1:1 w/w) electrolyte. This means that based on total heat generated, charged NMC with 1 M LiPF_6 EC / DMC (1:1 w/w) electrolyte is more thermally stable than with P13FSI electrolyte. This suggests perhaps there is no clear advantage of using P13FSI electrolyte compared to a conventional electrolyte with NMC electrode materials.

5.4.3.2 LCO with P13FSI electrolyte

The discharge and recharge curves of a LCO vs. lithium metal coin cell with P13FSI electrolyte is shown in Figure 5.60. The voltage range was set to 3.0 - 4.3 V, however, the upper voltage limit was not reached and charge was terminated after double the expected charge time had passed. Approximately 86% of the theoretical capacity was extracted from the electrode; this could be related to low porosity (35%) of the electrode making wetting more difficult with higher viscosity electrolytes, like P13FSI electrolyte. Increased electrolyte viscosity can result in slow or inhibited electrode wetting [73, 356] and electrolyte wettability can affect the reversible capacity of a cell [353]. The wettability of IL electrolytes with different electrodes and separators was studied by Huie, et al. [18] and they found that wettability (as measured by contact angle) could have a greater impact on cell performance than the electrolyte conductivity. In a study of LCO with different IL electrolytes, Matsumoto, et al. [291] observed a low capacity in the first cycle with piperidinium-FSI based electrolyte, which they attributed to wettability of the electrode, and the capacity increase observed in successive cycles was attributed to improved wettability of the electrode. It should be noted that the viscosity of the piperidinium-FSI based electrolyte was more than twice that of the Pyr^+ FSI^- based electrolyte [291], therefore viscosity related wetting issues experienced with piperidinium-FSI based electrolyte are expected to be more severe than wetting issues expected with Pyr^+ FSI^- based electrolyte. However, this does not mean that issues would not be expected with a Pyr^+ FSI^- based electrolyte when wetting commercial electrodes that have been manufactured for use with conventional electrolytes, since Pyr^+ FSI^- based electrolytes are more viscous than conventional electrolytes.

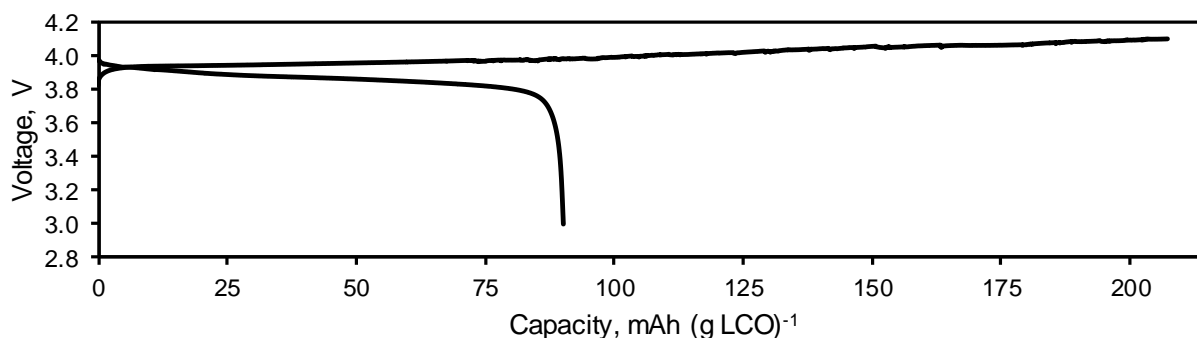


Figure 5.60 Discharge and recharge curve of LCO vs lithium metal with P13FSI electrolyte. Reversible capacity 105 mAh (g LCO)⁻¹. Current density 0.316 mA cm⁻².

The DSC thermograms for (a) LCO (uncycled) with P13FSI electrolyte and (b) delithiated LCO from a half-cell with P13FSI electrolyte are shown in Figure 5.61. The corresponding onset temperature, peak temperatures, heat generations and total heat values are shown in Table 5.31 for each thermogram in Figure 5.61, alongside results of conventional electrolyte studies from other works.

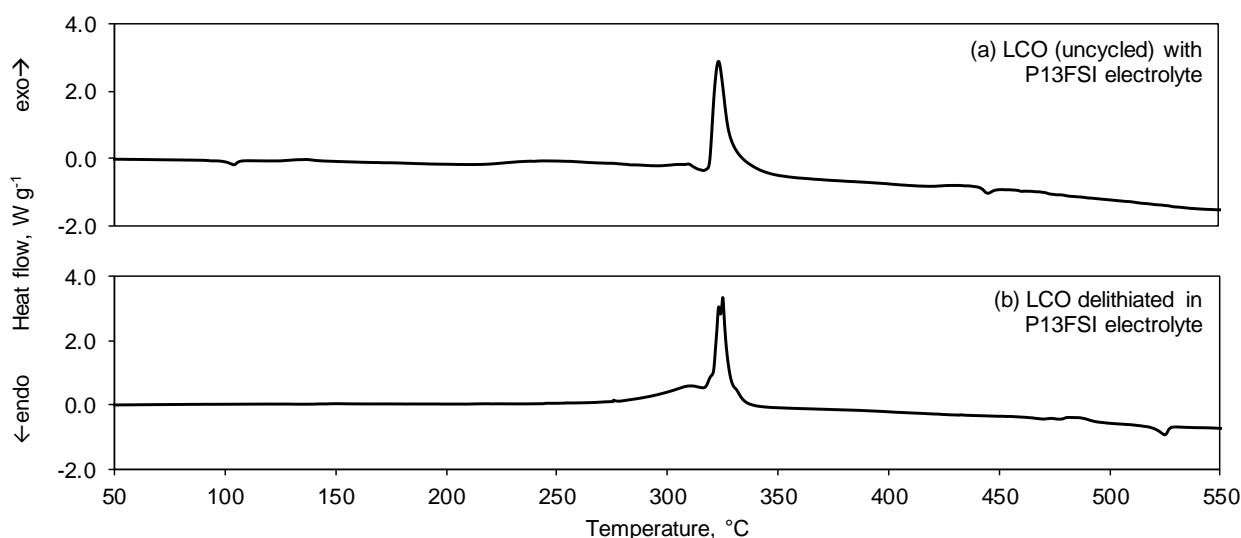


Figure 5.61 DSC thermogram for (a) uncycled LCO with P13FSI electrolyte and (b) delithiated LCO from half-cell with P13FSI electrolyte.

Uncycled LCO with P13FSI electrolyte (Figure 5.61a) has an onset temperature of 211 °C for the first exothermic peak at 245 °C with a heat generation of 66 J g⁻¹. The main exothermic peak

occurs at 324 °C and has a heat generation of 241 J g⁻¹. Including the three endothermic events at 104, 316 and 445 °C, the total heat for uncycled LCO with P13FSI electrolyte is 276 J g⁻¹. The delithiated LCO thermogram (Figure 5.61b) shows one exothermic peak at 326 °C, overlapping a smaller peak at approximately 310 °C. The onset temperature is 237 °C and the heat generation is 452 J g⁻¹.

Table 5.31 Comparison of DSC results for uncycled LCO with P13FSI electrolyte, delithiated LCO from half-cell with P13FSI electrolyte and Li_xCoO₂ cycled with 1 M LiPF₆ EC / DMC (1:1 w/w) electrolyte.

	Exothermic onset temperature, °C	*Peak temperature, °C	Heat generation, J g ⁻¹	*Total heat,		Heating rate, °C min ⁻¹	Temperature range, °C	Ref.
				J g ⁻¹	ΔJ cm ⁻³			
Uncycled LCO with P13FSI electrolyte	211	104 245 316 324 445	-8 66 -14 241 -9	276	512	5	50-550	This work
Delithiated LCO from half-cell with P13FSI electrolyte	237	326	452	452	839	5	50-550	This work
Li _x CoO ₂ with 1 M LiPF ₆ EC / DMC (1:1 w/w)	168	193 212 240		692		0.2	50-300	[362]
Li _x CoO ₂ with 1 M LiPF ₆ EC / DMC (1:1 v/v)	<249 [§]	249 276		759		5	50-350	[383]

* Extreme temperature reached in thermal event (maximum for exothermic and minimum for endothermic)

± Sum of heat generation

§ Assume exothermic onset occurs before first exothermic peak

Δ Calculated with material densities of P13FSI electrolyte (1.51 g cm⁻³, from manufacturers datasheet) and LCO electrode (2.50 g cm⁻³, from [30]). Electrode porosity used to estimate volume ratio of electrode : electrolyte present in DSC sample.

The delithiated LCO thermogram (Figure 5.61b) can be compared to cycled Li_xCoO₂ with 1 M LiPF₆ EC / DMC (1:1) electrolyte [362, 383] (Table 5.31) to discuss potential differences in LCO thermal stability in the presence of P13FSI electrolyte and conventional electrolytes. The onset temperature is 70 °C higher for LCO with P13FSI electrolyte and the heat release is less, however, due to the effects of thermal lag, the lower heating rate should be considered when comparing onset temperatures. Yi, et al. [383] used the same heating rate as for this work and saw

the first exothermic peak at 249 °C, 77 °C lower than the LCO from the P13FSI electrolyte cell. Yi, et al. [383] suggested the peaks at 249 and 276 °C were due to electrolyte oxidation and solvent decomposition on the reactive electrode surface along with oxygen released from the electrode.

DSC investigations of Li_xCoO_2 in LiPF_6 electrolytes (various solvents) showed a mild exothermic process occurring approximately 70 to 80 °C which the authors [362, 383] considered to be decompositions of the electrode-electrolyte interphase. No exothermic peaks were visible below 230 °C in the delithiated LCO from the P13FSI electrolyte cell, therefore, suggesting the electrode-electrolyte interphase potentially present on the electrode may be more thermally stable than on the electrode surface with conventional electrolytes. LCO delithiated with P13FSI electrolyte has a higher thermal stability than LCO delithiated with 1 M LiPF_6 EC / DMC (1:1 w/w) electrolyte.

Katayama, et al. [384] investigated $\text{Li}_{0.49}\text{CoO}_2$ with electrolytes containing $(-\text{SO}_2\text{C}_n\text{F}_{2n+1})$ lithium salts in EC / propylene carbonate (PC) (1:1 v/v) and observed a peak at approximately 200 °C that they attributed to evolved oxygen from the electrode reacting with solvents. This peak is not seen in LCO with P13FSI electrolyte, which could be due to the lack of reactive solvents in the IL electrolyte.

5.4.3.3 LMNO with P13FSI electrolyte

The charge and discharge curves of a LMNO vs. lithium metal coin cell with P13FSI electrolyte is shown in Figure 5.62. The voltage range was set to 3.0 - 4.7 V however the upper voltage limit was not reached and charge was terminated after double the expected charge time had passed. Approximately 28% of the theoretical capacity was extracted from the electrode. This result correlates poorly to other reported results of LMNO with $\text{Pyr}^+ \text{TFSI}^-$ based IL electrolyte at elevated temperatures (40 and 60 °C) [62], the lower temperature (30 °C) used in this work could account for some of the capacity lost through the higher electrolyte viscosities at lower temperatures. The extraction of 28% of the theoretical capacity is suspected to be from the combined effects of the higher electrolyte viscosity and the low LMNO electrode porosity (33.1%) resulting in poor electrode wetting.

The DSC thermogram for (a) LMNO (uncycled) with P13FSI electrolyte, (b) delithiated LMNO from P13FSI electrolyte cell and (c) lithiated LMNO from P13FSI electrolyte cell are shown in Figure 5.63. The corresponding onset temperature, peak temperatures, heat generations and total heat values are shown in Table 5.32 for each thermogram in Figure 5.63, alongside results of conventional electrolyte studies from other works.

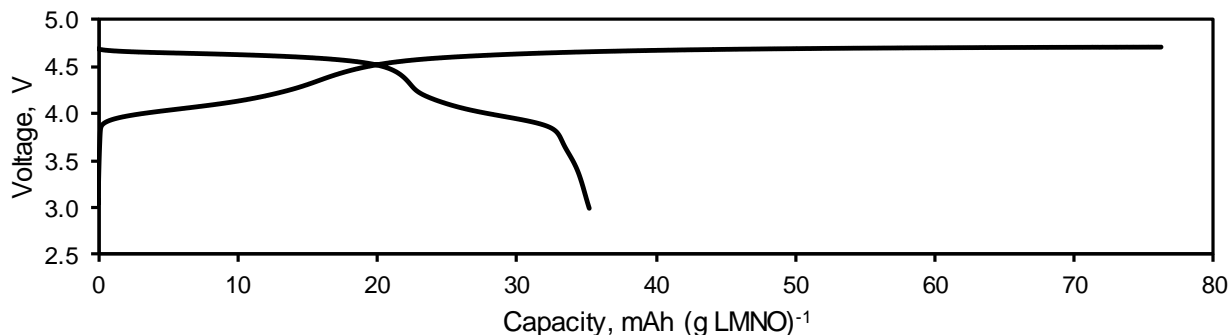


Figure 5.62 Discharge and recharge curve of LMNO vs lithium metal with P13FSI electrolyte. Reversible capacity 125 mAh (g LMNO)⁻¹. Current density 0.100 mA cm⁻².

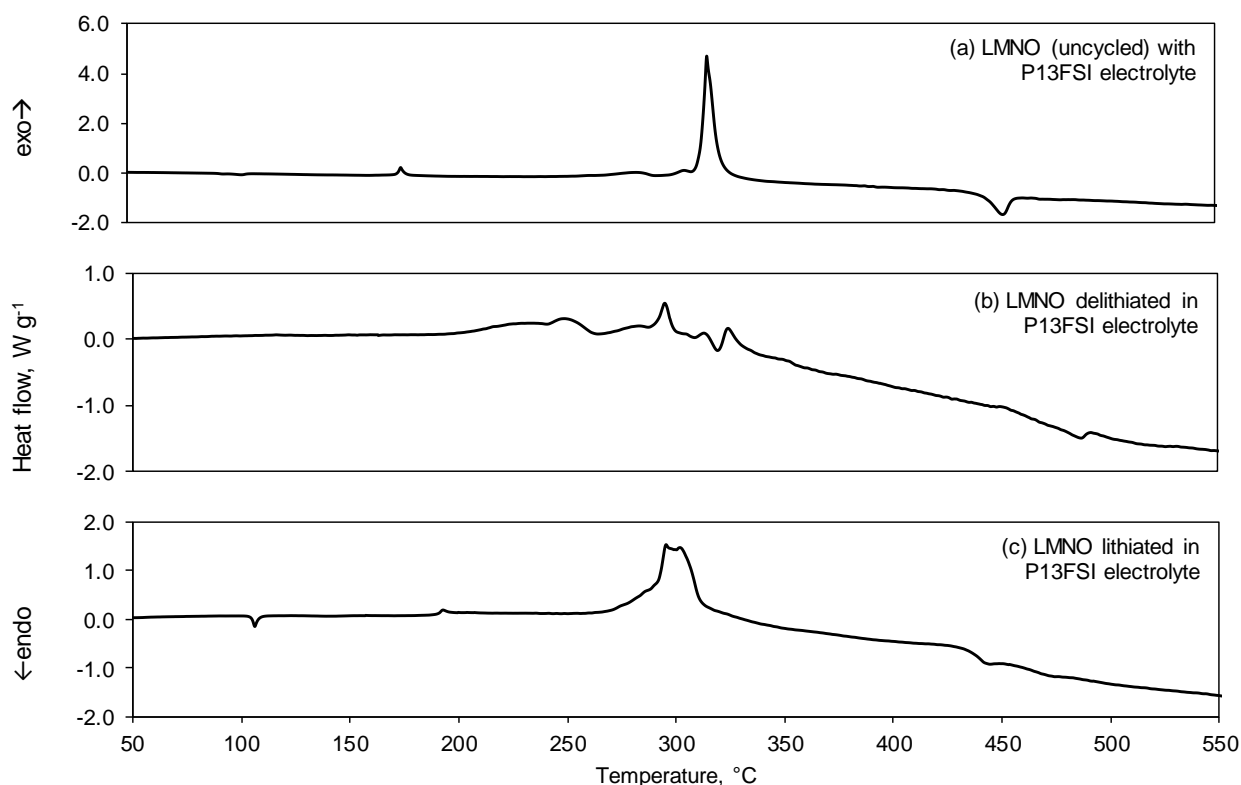


Figure 5.63 DSC thermogram for (a) uncycled LMNO with P13FSI electrolyte, (b) delithiated LMNO from half-cell with P13FSI electrolyte and (c) lithiated LMNO from half-cell with P13FSI electrolyte.

Uncycled LMNO with P13FSI electrolyte (Figure 5.63a) has an onset temperature of 167 °C for the first exothermic event at 176 °C with a small heat generation of 12 J g⁻¹. The main exothermic peak occurs at 318 °C with a heat generation of 346 J g⁻¹. Including the two endothermic events at 102 and 452 °C, the total heat for uncycled LMNO with P13FSI electrolyte is 299 J g⁻¹.

The thermogram for delithiated LMNO from a half-cell with P13FSI electrolyte (Figure 5.63b) shows several overlapping exothermic and endothermic peaks in the temperature range 200 to 350 °C. Two defined exothermic peaks occur at 249 and 295 °C with heat generations of 97 and 54 J g⁻¹, respectively. One endothermic event is observed at approximately 320 °C with a heat generation of -18 J g⁻¹. The total heat for delithiated LMNO from a P13FSI electrolyte cell is 133 J g⁻¹. The lithiated LMNO from a P13FSI electrolyte cell (Figure 5.63c) has one main exothermic peak at 296 °C with a heat generation of 323 J g⁻¹. The exothermic onset temperature is 181 °C for a small exothermic peak at 193 °C. Including the small endothermic event at 106 °C (discussed previously), the total heat is 326 J g⁻¹.

Table 5.32 Details of DSC results for uncycled LMNO with P13FSI electrolyte, delithiated LMNO from half-cell with P13FSI electrolyte, lithiated LMNO from half-cell with P13FSI electrolyte and Li_xMn_{1.5}Ni_{0.5}O₄ cycled with 1 M LiPF₆ EC / DMC (1:1 w/w) electrolyte.

	Exothermic onset temperature, °C	*Peak temperature, °C	Heat generation, J g ⁻¹	±Total heat,		Heating rate, °C min ⁻¹	Temperature range, °C	Ref.
				J g ⁻¹	ΔJ cm ⁻³			
Uncycled LMNO with P13FSI electrolyte	167	102 176 283 318 452	-5 12 28 346 -82	299	486	5	50-550	This work
Delithiated LMNO from half-cell with P13FSI electrolyte	194	249 295 320	97 54 -18	133	216	5	50-550	This work
Lithiated LMNO from half-cell with P13FSI electrolyte	181	106 193 296	-7 10 323	326	530	5	50-550	This work
Li _x Mn _{1.5} Ni _{0.5} O ₄ with 1 M LiPF ₆ EC / DMC (1:1 w/w)	78	106 150 240		630		0.2	50-300	[362]

* Extreme temperature reached in thermal event (maximum for exothermic and minimum for endothermic)

± Sum of heat generation

Δ Calculated with material densities of P13FSI electrolyte (1.51 g cm⁻³, from manufacturers datasheet) and LMNO electrode (1.857 g cm⁻³, from [83]). Electrode porosity used to estimate volume ratio of electrode : electrolyte present in DSC sample.

Comparing uncycled LMNO (Figure 5.63a) to delithiated LMNO from a P13FSI electrolyte cell (Figure 5.63b) there is an additional mild exothermic reaction beginning at approximately 190 °C that is not present in the uncycled LMNO thermogram. This suggests the peak may be due to

decomposition of electrode-electrolyte interphase components formed on the electrode during cycling. The total heat for lithiated LMNO is higher than delithiated LMNO suggesting delithiated LMNO is more thermally stable than lithiated LMNO from a P13FSI electrolyte cell. The higher heat generation of lithiated LMNO compared to delithiated LMNO was unexpected.

The delithiated LMNO from a P13FSI cell can be compared to $\text{Li}_x\text{Mn}_{1.5}\text{Ni}_{0.5}\text{O}_4$ with 1 M LiPF_6 EC / DMC (1:1 w/w) electrolyte [362] (Table 5.32). The onset temperature is 116 °C higher for LMNO with P13FSI electrolyte, however, if $\text{Li}_x\text{Mn}_{1.5}\text{Ni}_{0.5}\text{O}_4$ with 1 M LiPF_6 EC / DMC (1:1 w/w) electrolyte was tested at a higher heating rate it is likely that the onset temperature would increase too, although probably not above that of the cycled LMNO with P13FSI electrolyte. The low onset temperature for LMNO with 1 M LiPF_6 EC / DMC (1:1 w/w) electrolyte was suggested to be due to higher solubility of the Mn ion in the electrolyte [362]. The absence of exothermic peaks below 200 °C for LMNO with P13FSI electrolyte suggests that Mn ion solubility may not be an issue with P13FSI electrolyte. The heat release of LMNO with P13FSI electrolyte is approximately one quarter of that with 1 M LiPF_6 EC / DMC (1:1 w/w) electrolyte. Considering both onset temperature and total heat, thermal stability of cycled LMNO with P13FSI electrolyte is greater than with 1 M LiPF_6 EC / DMC (1:1 w/w) electrolyte.

5.4.3.4 LFP with P13FSI electrolyte

The charge and discharge curves of a LFP vs. lithium metal coin cell with P13FSI electrolyte is shown in Figure 5.64. The voltage range was set to 3.0 – 3.8 V. Approximately 89% of the theoretical capacity was extracted from the electrode (LFP electrode porosity was approximately 48%).

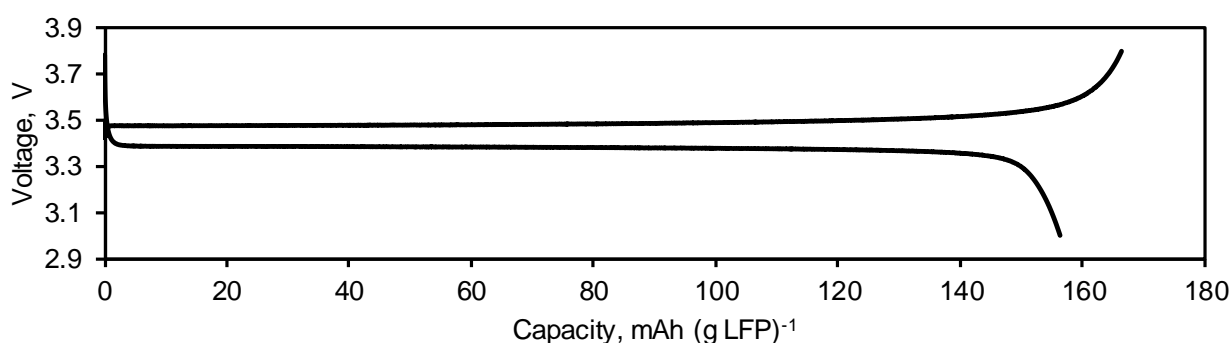


Figure 5.64 Discharge and recharge curve of LFP vs lithium metal with P13FSI electrolyte. Theoretical capacity 170 mAh (g LFP)⁻¹ [6, 352]. Current density 0.063 mA cm⁻².

The DSC thermogram for (a) LFP (uncycled) with P13FSI electrolyte, Li_xFePO_4 from half-cells with P13FSI electrolyte charged to (b) 100% SoC (c) 75% SoC, (d) 50% SoC, (e) 25% SoC and (f) 0% SoC are shown in Figure 5.65. DSC was performed up to 600 °C, however the thermograms did not indicate any further reaction above 450 °C so the higher temperatures are not shown here. The corresponding onset temperature, peak temperatures, heat generations and total heat values are shown in Table 5.33 for each thermogram shown in Figure 5.65, alongside results of conventional electrolyte studies from other works.

Uncycled LFP with P13FSI electrolyte (Figure 5.65a) has an onset temperature of 130 °C for a small exothermic event at 136 °C. Three larger exothermic events occur at 235, 291 and 312 °C with heat generations of 150, 49 and 372 J g⁻¹, respectively. TGA shows two different mass loss slopes that correlate approximately to the exothermic peaks observed in the DSC. This suggests that the exothermic peak at 291 °C is responsible for some decompositions but the main reactions occur during the 312 °C peak. Unfortunately, the crucible ruptured following the 312 °C peak meaning the high temperature (>350 °C) data could not be analysed for uncycled LFP with P13FSI electrolyte. Repeatable crucible rupture was observed for this sample when scanned at a heating rate of 10 °C min⁻¹ (see Appendix K). Similar thermal events and profiles can be seen at both heating rates, however, the rupture occurred approximately 30 °C higher at the faster heating rate (10 °C min⁻¹) due to thermal lag effects.

LFP electrode was charged in a LFP half-cell containing P13FSI electrolyte to different SoC to investigate the effect of different lithiation states on the electrode thermal stability. LFP at 100% SoC (Figure 5.65b) shows two endothermic peaks and three exothermic peaks. The endothermic peak at 106 °C could be due to evaporation of residue from the crucible surface, as discussed previously. Exothermic peaks occur at 204, 307 and 352 °C with heat generations of 33, 7 and 76 J g⁻¹, respectively. The second endothermic peak occurs at 345 °C, directly before the main exothermic peak. The total heat for 100% SoC LFP from a P13FSI electrolyte cell is 106 J g⁻¹.

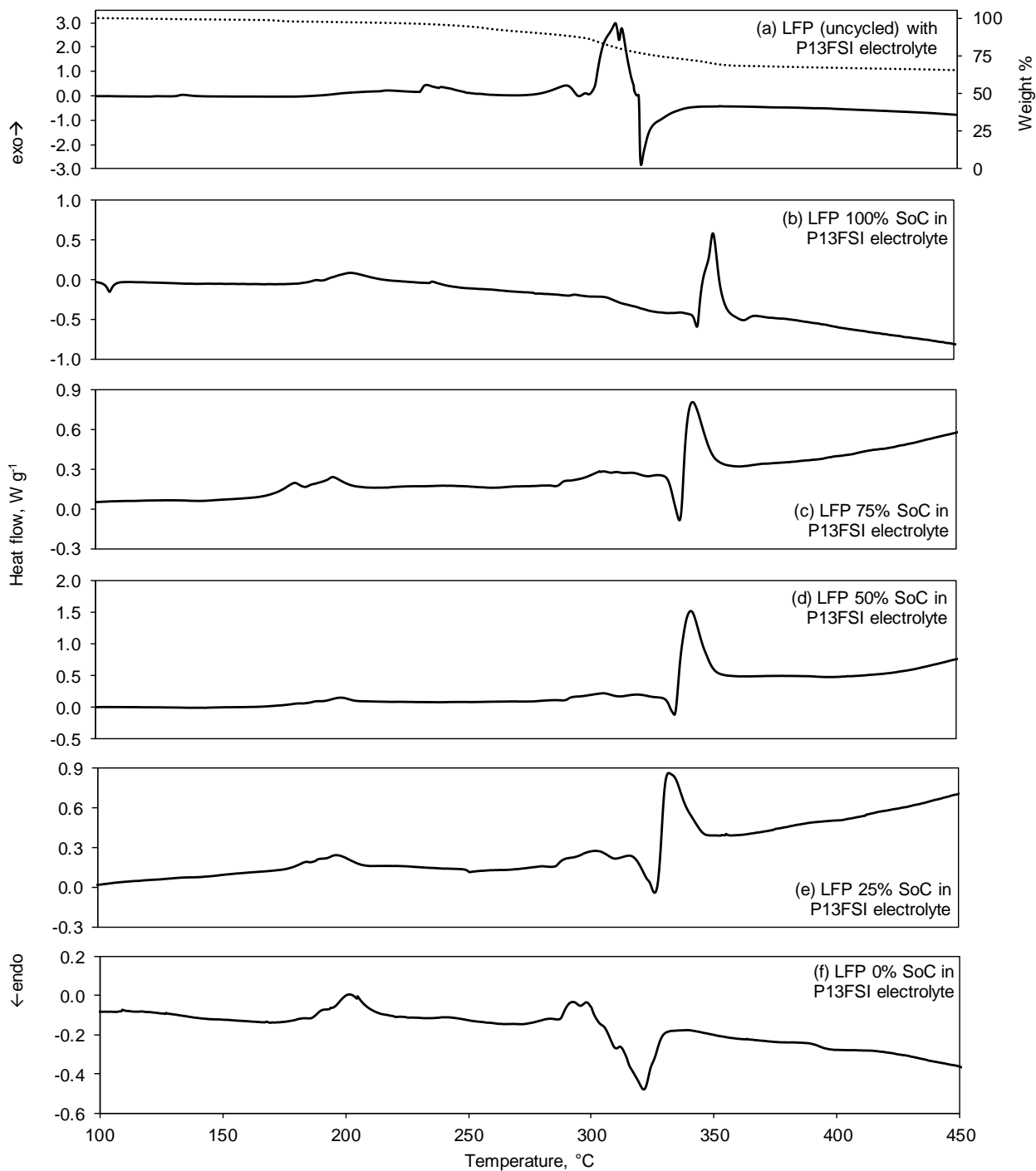


Figure 5.65 DSC thermogram (—) and TGA trace (.....) for (a) uncycled LFP with P13FSI electrolyte, LFP from half-cell with P13FSI electrolyte charged to (b) 100% SoC (c) 75% SoC, (d) 50% SoC, (e) 25% SoC and (f) 0% SoC.

Table 5.33 Details of DSC results for uncycled LFP with P13FSI electrolyte, LFP from half-cell with P13FSI electrolyte charged to 100% SoC, 75% SoC, 50% SoC, 25% SoC and 0% SoC, and Li_xFePO_4 cycles with 1 M LiPF_6 EC / DMC (1:1 w/w) electrolyte.

	Exothermic onset temperature, °C	*Peak temperature, °C	Heat generation, J g^{-1}	*Total heat,		Heating rate, °C min^{-1}	Temperature range, °C	Ref.
				J g^{-1}	AJ cm^{-3}			
Uncycled LFP with P13FSI electrolyte	130	136 235 291 312	4 150 49 372	575*	1445	5	50-450	This work
LFP from half-cell with P13FSI electrolyte charged to 100% SoC	179	106 204 307 345 352	-6 33 7 -4 76	106	266	5	50-450	This work
LFP from half-cell with P13FSI electrolyte charged to 75% SoC	142	196 305 337 343	25 23 -15 58	91	229	5	50-450	This work
LFP from half-cell with P13FSI electrolyte charged to 50% SoC	164	199 306 335 342	19 27 -12 128	162	407	5	50-450	This work
LFP from half-cell with P13FSI electrolyte charged to 25% SoC	137	197 302 327 332	26 23 -16 69	102	256	5	50-450	This work
LFP from half-cell with P13FSI electrolyte charged to 0% SoC	172	202 293 321	46 23 -44	25	63	5	50-450	This work
Li_xFePO_4 with 1 M LiPF_6 EC / DMC (1:1 w/w)	218	246 268 285		260		0.2	50-300	[362]

	Exothermic onset temperature, °C	*Peak temperature, °C	Heat generation, J g ⁻¹	*Total heat,		Heating rate, °C min ⁻¹	Temperature range, °C	Ref.
				J g ⁻¹	ΔJ cm ⁻³			
Li _x FePO ₄ with 1 M LiPF ₆ EC / DMC (1:1 v/v)	<257 [§]	257	537			5	50-350	[383]

* Extreme temperature reached in thermal event (maximum for exothermic and minimum for endothermic)

± Sum of heat generation

§ Assume exothermic onset occurs before first exothermic peak

Δ Calculated with material densities of P13FSI electrolyte (1.51 g cm⁻³, from manufacturers datasheet) and LFP electrode (3.60 g cm⁻³, from [30]). Electrode porosity used to estimate volume ratio of electrode : electrolyte present in DSC sample.

The LFP electrodes at other states of charge (Figure 5.65c-f) show similar thermogram profiles with a mild sustained exothermic event occurring at approximately 200 °C and again at approximately 300 °C, followed by the endothermic event directly before the major exothermic peak. The exothermic reaction at approximately 200 °C is observed in all cycled electrodes (Figure 5.65b-f) but is absent in the uncycled electrode (Figure 5.65a). This suggests the thermal event at approximately 200 °C may be from decomposition of electrode-electrolyte interphase components formed on the LFP during cycling with P13FSI electrolyte. Reaction of IL electrolytes and conventional - IL hybrid electrolytes with LFP electrode at the electrode-electrolyte interphase has been suggested for a variety of ILs [322, 323, 342, 348, 349]. The low onset temperature of the uncycled electrode with P13FSI electrolyte could be due to reactions between the electrode and electrolyte that were not observed for cycled LFP where a passivation film was believed to be present to protect the electrode from reaction with the electrolyte.

The set of thermal events above 250 °C is reproduced in all charged LFP thermograms occurring at successively lower temperatures as the SoC decreases (Figure 5.65b-e). The main exothermic peaks occur at 352, 343, 342 and 332 °C for LFP at 100%, 75%, 50% and 25% SoC, respectively. The repeated profile with decreasing SoC indicates reproducibility in the decomposition thermals of charged LFP electrodes from a P13FSI electrolyte cell. This also suggests that the SoC of an LFP electrode can be related to the major exothermic event peak temperature. Contrary to what is expected, a lower SoC results in the major exothermic peak occurring at a lower temperature. The LFP at 0% SoC (Figure 5.65f) has the exothermic reaction at approximately 300 °C followed by an endothermic event, similar to the other LFP thermograms, however, the major exothermic reaction immediately following is absent. This could indicate reactivity of LFP in the fully discharged state is lower than LFP with any amount of charge present.

The thermal stability of LFP at different states of charge can be ranked. Comparing thermal stabilities based on exothermic onset temperature at different SoCs:

$$\text{SoC of } 25\% < 75\% < 50\% < 0\% < 100\%$$

Ranking the thermal stability based on total heat released gives a different result:

$$\text{SoC of } 50\% < 100\% < 25\% < 75\% < 0\%$$

The second ranking of thermal stability gives a more expected result of the fully charged electrode being less stable than the discharged electrode. The LFP at 50% SoC was not expected to be the least stable, however the trend of thermogram profiles changing with SoC suggests the data is reproducible and that the thermal peak position can be related to the electrode SoC. The heat release does not appear to be related to SoC. This could be due to variation in the amount of electrolyte present on harvested electrodes since the electrodes were used directly from the cell without washing with solvent. A larger amount of electrolyte present in the DSC sample would most likely increase the total heat released and could account for higher heat generation in a particular sample. Since the main exothermic peak for LFP at higher SoCs occurred at approximately the same temperature as the main decomposition for P13FSI electrolyte (355 °C peak), it is possible that the main peaks observed in the 100% and 75% SoC LFP thermograms could include heat contributions from excess electrolyte. However, the unexpected higher heat release observed for 0% and 25% SoC LFP are likely not related to excess P13FSI electrolyte since there is no corresponding decomposition peak visible at approximately 355 °C. It is clear from onset temperature and total heat that the thermal stability of uncycled LFP with P13FSI electrolyte is lower than the cycled LFP from P13FSI electrolyte cells. This suggests that electrode-electrolyte interphase formed on the LFP electrode in P13FSI electrolyte has a high thermal stability, increasing the electrode thermal stability.

The LFP at 100% SoC thermogram (Figure 5.65b) can be compared to Li_xFePO_4 delithiated in 1 M LiPF_6 EC / DMC (1:1) (Table 5.33). The onset temperature for LFP with 1 M LiPF_6 EC / DMC (1:1 w/w) electrolyte was 218 °C compared to the lower onset temperature of 179 °C for LFP from a P13FSI electrolyte cell. Considering the heating rate, the onset temperature for LFP with 1 M LiPF_6 EC / DMC (1:1 w/w) electrolyte would be expected to occur at a higher temperature if a comparable heating rate was used. Therefore, comparing thermal stability based on onset temperatures, LFP with 1 M LiPF_6 EC / DMC (1:1 w/w) is more thermally stable than LFP with P13FSI electrolyte.

There is a difference in the total heats reported in literature for delithiated LFP with 1 M LiPF_6 EC / DMC (1:1) electrolyte (Table 5.33). The total heat reported by Yi, et al. [383] is approximately twice

that reported by Xiang, et al. [362], but this can be explained by the difference in heating rates used. In both cases, the total heat for charged LFP with 1 M LiPF₆ EC / DMC electrolyte is larger than with P13FSI electrolyte. Based on total heat release, delithiated LFP is more thermally stable with P13FSI electrolyte than with 1 M LiPF₆ EC / DMC (1:1 w/w) electrolyte. This contradicts the thermal stability as indicated by exothermic onset temperatures, which suggests there may not be a clear thermal advantage to using P13FSI electrolyte with LFP electrodes. Both indicators of thermal stability are important for cell safety and should be considered before selecting an electrolyte.

5.4.3.5 Graphite with P13FSI electrolyte

The charge and discharge curves of a graphite vs. lithium metal coin cell with P13FSI electrolyte is shown in Figure 5.66. The lower voltage cut-off was set to 0.005 V. Approximately 58% of the theoretical capacity was extracted from the electrode. The extraction of only half the theoretical capacity is suspected to be from the combined effects of high viscosity of the P13FSI electrolyte and the low porosity (58.2 %) of the graphite electrode resulting in poor wetting and subsequent low utilisation of the active material.

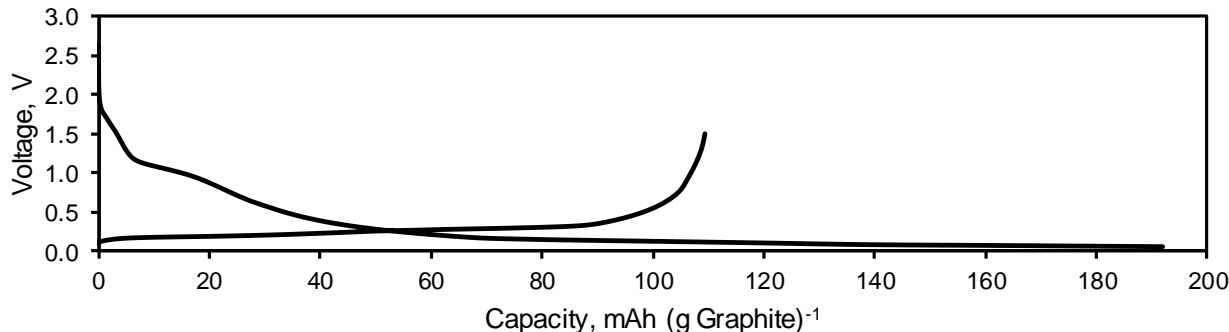


Figure 5.66 Discharge and recharge curve of LiC₆ vs lithium metal with P13FSI electrolyte. Reversible capacity 330 mAh (g Graphite)⁻¹. Current density 0.400 mA cm⁻².

The DSC thermogram for (a) graphite (uncycled) with P13FSI electrolyte, (b) lithiated graphite from a half-cell with P13FSI electrolyte and (c) delithiated graphite from a half-cell with P13FSI electrolyte are shown in Figure 5.67. The corresponding onset temperature, peak temperatures, heat generations and total heat values are shown in Table 5.34 for each thermogram in Figure 5.67, alongside results of conventional electrolyte studies from other works.

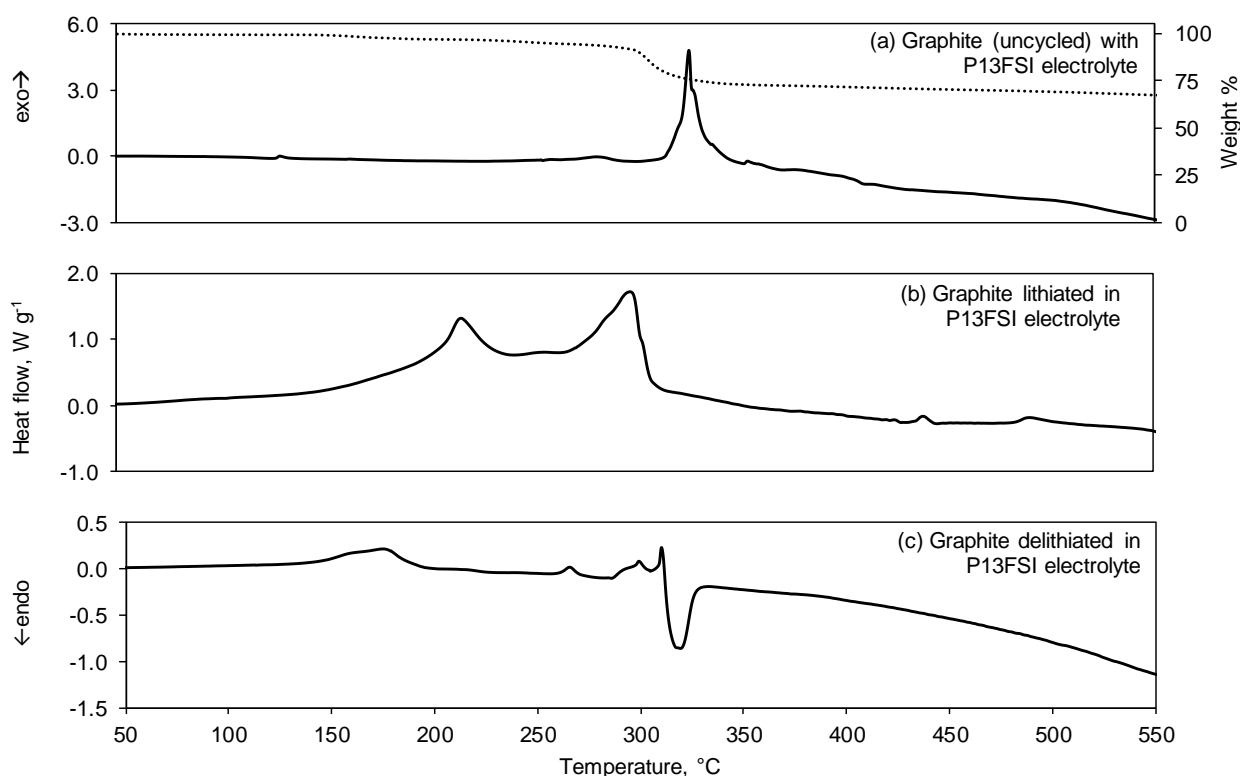


Figure 5.67 DSC thermogram (—) and TGA trace (.....) for (a) uncycled graphite with P13FSI electrolyte, (b) lithiated graphite from half-cell with P13FSI electrolyte and (c) delithiated graphite from half-cell with P13FSI electrolyte.

Uncycled LiC_6 with P13FSI electrolyte (Figure 5.67a) has an onset temperature of 124 °C for a small exothermic event at 129 °C, this could be from electrolyte reactions at the electrode surface in the absence of a passivating SEI film. Two more exotherms occur at 281 and 327 °C with heat generations of 55 and 564 J g^{-1} , respectively. The TGA results correspond to the thermogram, with the major mass loss occurring at approximately the same temperature as the main exothermic peak. There is, however, a noticeable prolonged weight loss occurring before the main exothermic reaction which suggests some decomposition reactions may take place from temperatures as low as 150 °C. The main exothermic reaction for uncycled LiC_6 with P13FSI electrolyte occurs 33 °C lower than that of the P13FSI electrolyte suggesting the electrolyte reactivity increases in the presence of uncycled LiC_6 , or its reaction products at the SEI.

Table 5.34 Comparison of DSC results for uncycled LiC_6 with P13FSI electrolyte, lithiated graphite from half-cell with P13FSI electrolyte, delithiated graphite from half-cell with P13FSI electrolyte, lithiated graphite with 1 M LiPF_6 EC / DEC (1:1) and charged graphite with 1 M LiPF_6 EC / DMC (1:1 w/w) electrolyte.

	Exothermic onset temperature, °C	*Peak temperature, °C	Heat generation, J g^{-1}	*Total heat,		Heating rate, °C min^{-1}	Temperature range, °C	Ref.
				J g^{-1}	$\Delta\text{J cm}^{-3}$			
Uncycled LiC_6 with P13FSI electrolyte	124	129 281 327	5 55 564	624	1360	5	50-500	This work
Lithiated graphite from half-cell with P13FSI electrolyte	146	216 298 439 490	179 7 14	200	436	5	50-500	This work
Delithiated graphite from half-cell with P13FSI electrolyte	119	175 266 310 319	81 7 47 -81	54	118	5	50-500	This work
Lithiated graphite with 1 M LiPF_6 EC / DEC (1:1 w/w)	57	99 214 228 243		393		0.2	50-300	[377]
Charged graphite with 1 M LiPF_6 EC / DMC (1:1 v/v)	<287 [§]	287		355 [∅]		5	50-400	[385]

* Extreme temperature reached in thermal event (maximum for exothermic and minimum for endothermic)

± Sum of heat generation

§ Assume exothermic onset occurs before appearance of first exothermic peak

∅ Approximated from total sample weight of 2mg for electrolyte and electrode

Δ Calculated with material densities of P13FSI electrolyte (1.51 g cm^{-3} , from manufacturers datasheet) and graphite electrode (2.66 g cm^{-3} , from [30]). Electrode porosity used to estimate volume ratio of electrode : electrolyte present in DSC sample.

The lithiated graphite from a half-cell with P13FSI electrolyte (Figure 5.67b) shows two overlapping exothermic events with peaks at 216 and 298 °C, and a combined heat generation of 179 J g^{-1} . Above 400 °C, two small exothermic peaks are seen at 439 and 490 °C with heat generations of 7 and 14 J g^{-1} , respectively. The total heat for lithiated graphite from a P13FSI electrolyte cell is 200 J g^{-1} . The delithiated graphite from a half-cell with P13FSI electrolyte (Figure 5.67c) has an onset temperature of 119 °C for an exothermic peak at 175 °C with a heat generation of 81 J g^{-1} . Between 250 and 325 °C there are a few overlapping exothermic peaks immediately before the

main endothermic event starting at 310 °C, with a heat generation of -81 J g^{-1} . The total heat for delithiated graphite with P13FSI electrolyte is 54 J g^{-1} .

The endothermic event at 310 °C in delithiated graphite aligns with an endothermic event seen in 0% SoC LFP. The endothermic peak occurs at 319 and 321 °C for delithiated graphite and 0% SoC LFP electrodes, respectively, from P13FSI electrolyte half-cells. There is also evidence of aligned thermal events occurring at 300 and 310 °C in both electrodes. Both electrodes are in what would be a state of discharge if they were assembled into a full cell, this means delithiated for the graphite anode and lithiated for the LFP cathode. This indicates that the endothermic reaction is not likely to be from the reaction of lithium with P13FSI electrolyte or the electrode compound, it is more likely to be related to reaction of P13FSI electrolyte, which is present in both samples.

Comparing total heat generation with P13FSI electrolyte, lithiated graphite is less stable than delithiated graphite. This is expected due to exothermic reactions between P13FSI electrolyte and the intercalated lithium present in the lithiated graphite electrode. Comparing thermal stability based on exothermic onset temperatures, lithiated graphite is more thermally stable than delithiated graphite from a P13FSI electrolyte cell. However, both thermograms for lithiated and delithiated graphite from a P13FSI electrolyte cell appear to have an exothermic slope from a very early temperature. Therefore, determining thermal stability based on exothermic onset temperature may not be reliable for graphite electrodes with P13FSI electrolyte.

In a study of graphite with 1 M LiFSI EC / DMC: EMC electrolyte, a sharp exothermic peak was seen at approximately 200 °C that was suggested to be from electrochemical reduction of the LiFSI salt [32]. This could account for the first exothermic peak seen in the lithiated graphite occurring at 216 °C (Figure 5.67b). The peak at 175 °C in the delithiated graphite could also be due to LiFSI reduction, although it is occurring at a lower temperature than observed by Forestier, et al. [32]. The absence of a sharp exothermic peak from P13FSI electrolyte decomposition in the lithiated graphite thermogram suggests that the P13FSI electrolyte reacted with lithium present in the graphite structure before the P13FSI electrolyte decomposition temperature was reached. The two overlapping peaks in lithiated graphite are not present in the delithiated graphite thermogram which supports the suggestion that they are likely due to reaction between the P13FSI electrolyte and intercalated lithium.

In other studies, lithiated graphite with 1 M LiPF₆ EC / DEC (1:1) electrolyte showed an exothermic peak from approximately 100 to 150 °C with additional exotherms above 200 °C [377, 386-388]. The first peak has been suggested by the authors [377, 386-388] to be from SEI breakdown and subsequent electrolyte reactions with the electrode surface. In this study, cycled graphite with P13FSI electrolyte (Figure 5.67b-c) showed noticeable exothermic events from approximately 150 up to 300 °C, which were not present in the uncycled graphite (Figure 5.67a). These exothermic

events could similarly be attributed to decomposition reactions of the SEI and subsequent reactions between the electrolyte and electrode as the SEI decomposes and reforms on the electrode surface.

Lithiated graphite with P13FSI electrolyte from this work is compared in Table 5.34 to graphite with 1 M LiPF₆ EC / DEC (1:1) electrolyte from other studies. It should be noted that the heating rate used by Wang, et al. [377] was 0.2 °C min⁻¹ so the thermograms are not directly comparable, although Doi, et al. [385] used the same heating rate as this work. Charged graphite with 1 M LiPF₆ EC / DMC (1:1 w/w) showed only one major peak at 287 °C. Doi, et al. [385] attributed this peak to SEI reductive decomposition with the charged electrode. Additional peaks were observed at lower temperatures with the 1 M LiPF₆ EC / DEC (1:1) electrolyte, which Wang, et al. [377] suggested this was also due to SEI decomposition. This suggests that different SEI components form on the electrode surface depending on the electrolyte solvents, and that this can directly influence the thermal stability of a charged graphite electrode.

The total heat of lithiated graphite with P13FSI electrolyte is lower than lithiated graphite with both conventional electrolytes, suggesting the thermal stability of lithiated graphite with P13FSI electrolyte is greater than with conventional electrolytes. The onset temperature is approximately 100 °C lower with 1 M LiPF₆ EC / DEC (1:1 w/w) electrolyte compared to the P13FSI electrolyte indicating a higher thermal stability of P13FSI electrolyte. However, the lower heating rate for graphite with 1 M LiPF₆ EC / DEC (1:1 w/w) electrolyte should be considered, the exothermic onset temperature is expected to occur at a higher temperature if the same heating rate were used. The high onset temperature with P13FSI electrolyte compared to other studies with conventional electrolyte indicates the increased thermal stability of SEI components formed on the electrode surface with P13FSI electrolyte.

5.4.3.6 LTO with P13FSI electrolyte

The charge and discharge curves of a LTO vs. lithium metal coin cell with P13FSI electrolyte is shown in Figure 5.68. The lower voltage range was set to 1.0 – 3.0 V. Approximately 95% of the theoretical capacity was extracted from the electrode (LTO electrode porosity was 31.7%). Figure 5.69 shows the TGA trace for LTO (uncycled) with P13FSI electrolyte (a), DSC thermograms for (a) LTO (uncycled) with P13FSI electrolyte, Li_xTi₅O₁₂ harvested from a half-cell with P13FSI electrolyte charged to (b) 100% SoC (c) 75% SoC, (d) 50% SoC, (e) 25% SoC and (f) 0% SoC. The corresponding onset temperature, peak temperatures, heat generations and total heat values are shown in Table 5.35 for each thermogram in Figure 5.69, alongside results of conventional electrolyte studies from other works.

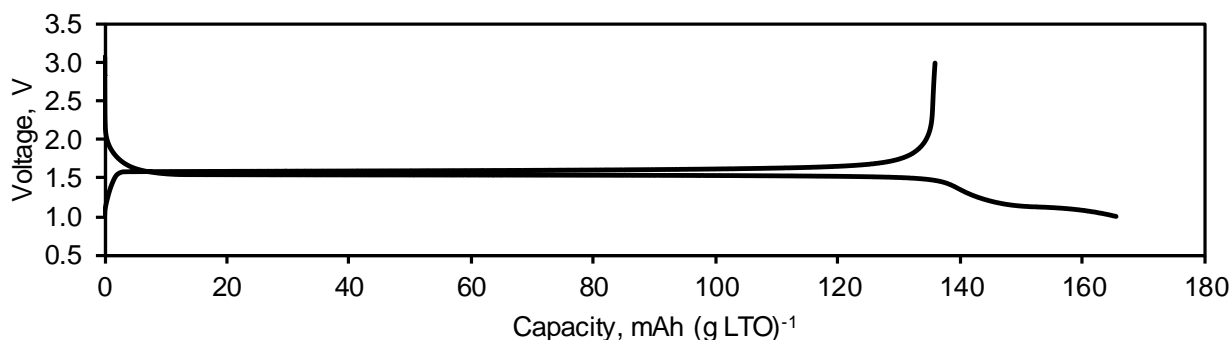


Figure 5.68 Discharge and recharge curve of LTO vs lithium metal with P13FSI electrolyte. Theoretical capacity 175 mAh (g LTO)⁻¹ [6, 389]. Current density 0.071 mA cm⁻².

The uncycled LTO with P13FSI electrolyte (Figure 5.69a) has an onset temperature of 131 °C for a small exothermic event at 140 °C. Two main exothermic peaks overlap at 213 and 282 °C with a combined heat generation of 576 J g⁻¹. Endothermic events occur at approximately 437 and 527 °C with heat generations of -36 and -5 J g⁻¹, respectively. The endothermic event at 437 °C appears to be the overall result of multiple overlapping peaks. The TGA curve shows a considerable decrease in sample weight supporting a decomposition reaction corresponding to the exothermic peak observed at 282 °C in the DSC thermogram. The peak at 213 °C does not correspond to a mass loss; this suggests the heat release may not be associated with a decomposition reaction.

LTO electrode was charged in a LTO half-cell containing P13FSI electrolyte to different SoC to investigate the effect of different lithiation states on thermal stability of the electrode. LTO at 100% SoC (Figure 5.69b) shows one large exothermic peak at 294 °C overlapping another exothermic peak immediately following. The onset temperature is 263 °C and the exothermic heat generation is 267 J g⁻¹. There is a small exothermic event at 318 °C with a heat generation of 7 J g⁻¹ and one endothermic event at 520 °C with a heat generation of -10 J g⁻¹. There is an exothermic peak at approximately 200 °C in the uncycled LTO with P13FSI electrolyte (Figure 5.69a) that is not present in the 100% SoC LTO (Figure 5.69b). The peak at 200 °C could be from reactions between the P13FSI electrolyte and the electrode active material due to the absence of a passivating SEI film on the electrode surface.

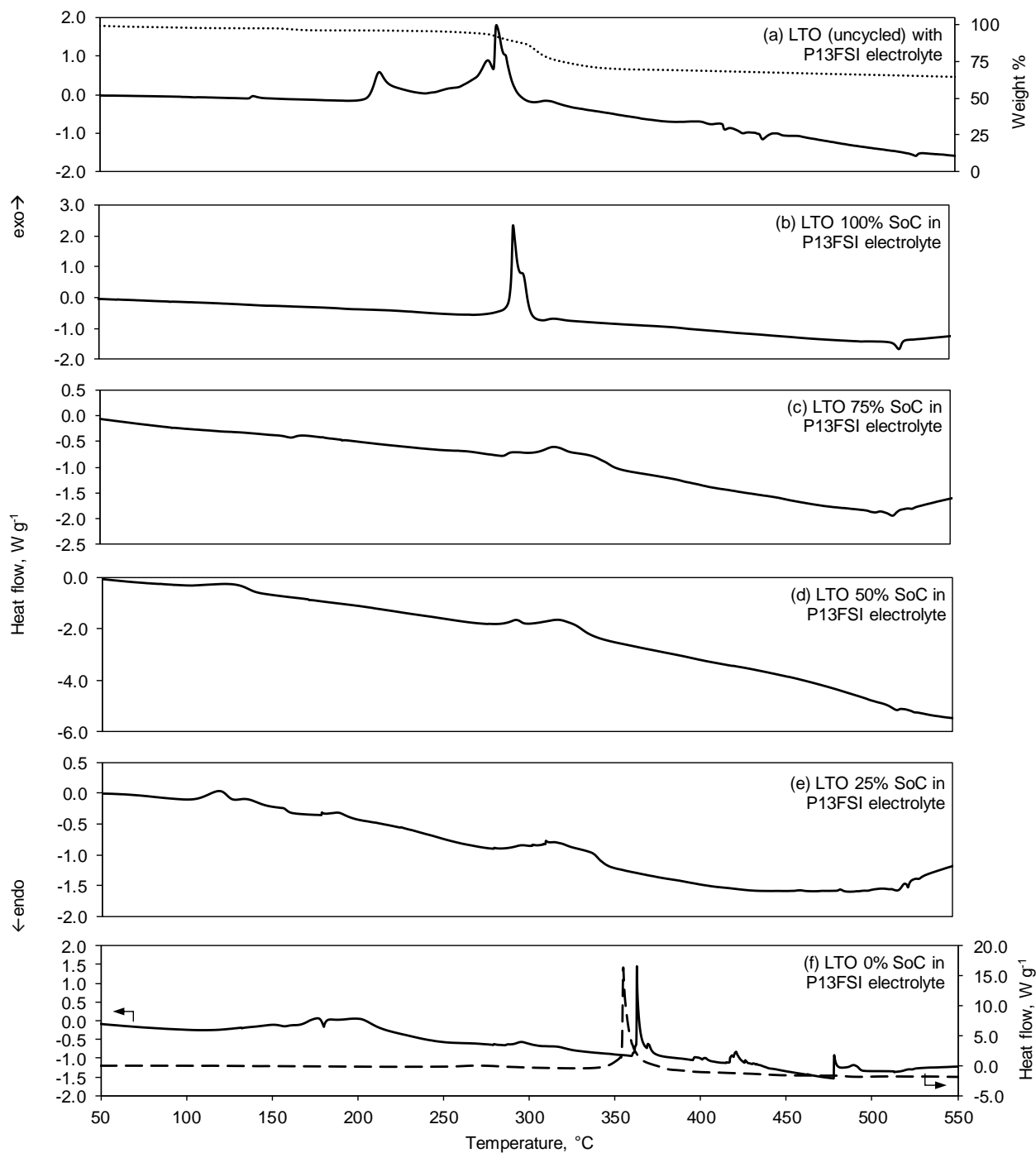


Figure 5.69 DSC thermogram (—) and TGA trace (.....) for (a) uncycled LTO with P13FSI electrolyte, LTO from half-cell with P13FSI electrolyte charged to (b) 100% SoC (c) 75% SoC, (d) 50% SoC, (e) 25% SoC and (f) 0% SoC and P13FSI electrolyte (- - -).

Table 5.35 Comparison of DSC results for uncycled LTO with P13FSI electrolyte, LTO from half-cell with P13FSI electrolyte charged to 100% SoC, 75% SoC, 50% SoC, 25% SoC, 0% SoC and $\text{Li}_x\text{Ti}_5\text{O}_{12}$ with 1 M LiPF_6 EC / DMC (1:1 w/w) electrolyte.

	Exothermic onset temperature, °C	*Peak temperature, °C	Heat generation, J g^{-1}	*Total heat,		Heating rate, °C min ⁻¹	Temperature range, °C	Ref.
				J g^{-1}	$\Delta\text{J cm}^{-3}$			
Uncycled $\text{Li}_4\text{Ti}_5\text{O}_{12}$ with P13FSI electrolyte	131	140 213 282 437 527	3 576 -36 -5	538	1153	5	50-550	This work
LTO from half-cell with P13FSI electrolyte charged to 100% SoC	263	294 318 520	267 7 -20	254	545	5	50-550	This work
LTO from half-cell with P13FSI electrolyte charged to 75% SoC	285	162 317 516	-8 135 -10	117	251	5	50-550	This work
LTO from half-cell with P13FSI electrolyte charged to 50% SoC	103	122 319	59 211	270	579	5	50-550	This work
LTO from half-cell with P13FSI electrolyte charged to 25% SoC	99	120 189 311	71 9 130	210	450	5	50-550	This work
LTO from half-cell with P13FSI electrolyte charged to 0% SoC	111	200 296 363 403 420 478	379 28 72 8 32 72	591	1267	5	50-550	This work
$\text{Li}_x\text{Ti}_5\text{O}_{12}$ with 1 M LiPF_6 EC / DMC (1:1 v/v)	<109 [§]	109 199 265 306		454		5	50-350	[383]

* Extreme temperature reached in thermal event (maximum for exothermic and minimum for endothermic)

± Sum of heat generation

§ Assume exothermic onset occurs before appearance of first exothermic peak

Δ Calculated with material densities of P13FSI electrolyte (1.51 g cm^{-3} , from manufacturers datasheet) and LTO electrode (3.51 g cm^{-3} , from [390]). Electrode porosity used to estimate volume ratio of electrode : electrolyte present in DSC sample.

LTO from a half-cell containing P13FSI electrolyte charged to 75, 50 and 25% SoC (Figure 5.69c-e) all have a mild exothermic event at approximately 310 to 320 °C with heat generations of 135,

211 and 130 J g⁻¹, respectively. In the 0% SoC LTO (Figure 5.69f) there is a similar exothermic peak occurring at a slightly lower temperature (296 °C) with a smaller heat generation of 28 J g⁻¹. There is a sharp peak in the 100% SoC LTO at 294 °C which is not present at lower SoC. This suggests LTO is more reactive at the fully charged state than at lower states of charge, however there is no discernible relationship between the electrode SoC and the amount of heat generated. An endothermic event occurs in the 75% SoC LTO thermogram that does not show up in the other thermograms, a small peak at 162 °C with a heat generation of -8 J g⁻¹. The thermograms of LTO at 50, 25 and 0% SoC have mild exothermic events in the 100 to 200 °C temperature region not seen in the 75% and 100% SoC LTO.

The LTO at 0% SoC (Figure 5.69f) has a sharp exothermic peak at 363 °C with a heat generation of 72 J g⁻¹. This peak is likely due to decomposition of excess P13FSI electrolyte present on the electrode as it corresponds to the main peak observed in the P13FSI electrolyte thermogram (Figure 5.53c). There are multiple overlapping thermal events in the temperature region 400 to 500 °C that are not seen in any other cycled LTO electrodes but could correspond to multiple overlapping peaks observed in the same temperature region in the uncycled LTO with P13FSI electrolyte (Figure 5.69a).

The thermal stability of LTO at different states of charge can be ranked. Comparing thermal stabilities based on onset temperature for the first exothermic event:

$$\text{SoC of } 25\% < 50\% < 0\% < \text{uncycled} < 100\% < 75\%$$

Similar to LFP electrodes, ranking the thermal stability of LTO based on total heat released gives a different result:

$$\text{SoC of } 0\% < \text{uncycled} < 50\% < 100\% < 25\% < 75\%$$

Neither of these ranking methods follow any discernible pattern relating to the SoC of an LTO electrode and the thermal stability. As stated previously, the amount of electrolyte present on harvested electrodes may be variable since the electrodes were used directly from the cell without washing with solvent and this would directly influence the total heat released.

The LTO at 100% SoC can be compared to Li_xTi₅O₁₂ delithiated in 1 M LiPF₆ EC / DMC (1:1 w/w) electrolyte (Table 5.35). Yi, et al. [383] saw peaks at approximately 190 and 300 °C which they attributed to intercalated lithium reaction with solvents and electrolyte decomposition of lithiated LTO, respectively. The latter may account for the exothermic event at 294 °C seen in the charged LTO from a P13FSI electrolyte cell (Figure 5.69b), since the peak occurs at approximately the same temperature. The onset temperature is 70 °C higher for LTO with the P13FSI electrolyte and the heat release is slightly less, meaning the charged LTO with P13FSI electrolyte is more

thermally stable than with 1 M LiPF₆ EC / DMC (1:1 w/w) electrolyte.

5.4.4 Comparison of electrode thermal stability

Thermal stability rankings of fully charged electrodes from P13FSI electrolyte cells can be presented based on exothermic onset temperatures or total heat values. Andersson, et al. [378] argued that thermal stability could be indicated by the onset temperature of the first exothermic reaction since this temperature would be used to set the operating temperature range of a cell. The total heat and exothermic onset temperature is shown in Figure 5.70 for the cycled electrodes from P13FSI electrolyte half-cells in this work.

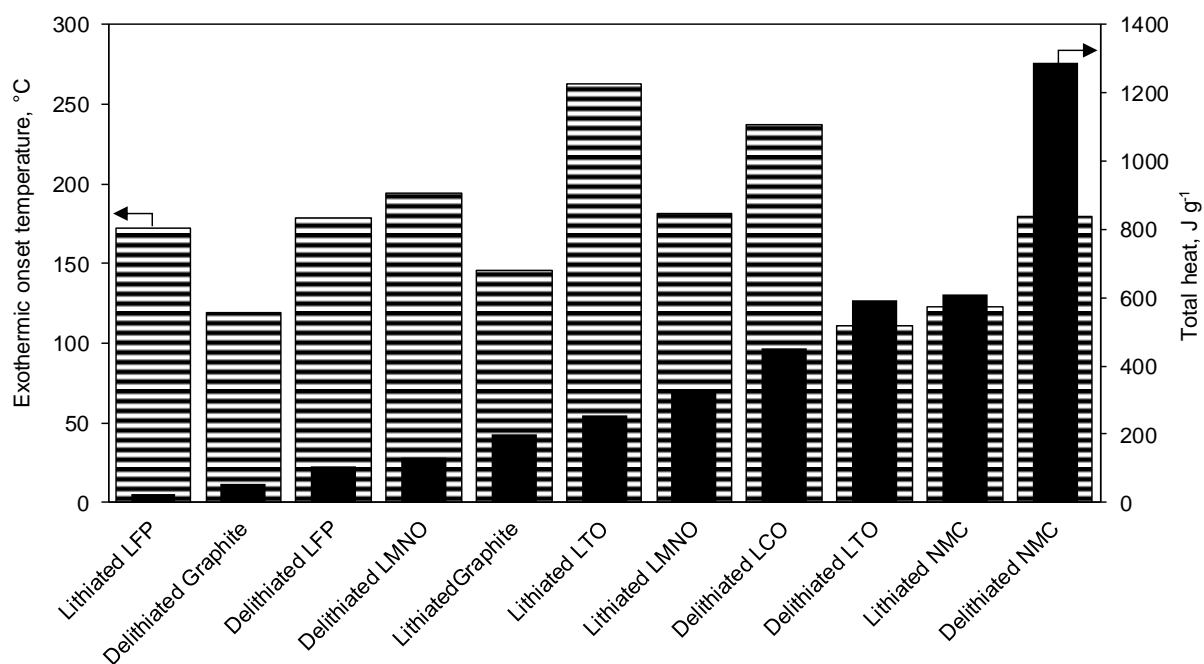


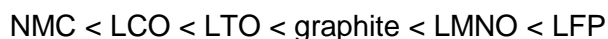
Figure 5.70 Total heat and exothermic onset temperature for cycled electrodes from P13FSI electrolyte cells. The instrument measurement error for temperature and heat values displayed is 0.2 K and 0.04 μ W, respectively.

Based on onset temperature, the ranked thermal stability of fully charged electrodes (delithiated cathodes, lithiated anodes) from P13FSI electrolyte cells are as follows:

$$\text{Graphite} < \text{LFP} < \text{NMC} < \text{LMNO} < \text{LCO} < \text{LTO}$$

It seems that LFP and LCO have swapped positions from what would be commonly expected for these electrodes with a conventional electrolyte that contains solvent. In a study of LCO with

conventional electrolytes, Wang, et al. [369] reasoned that a higher energy release indicated lower thermal stability since the first reaction provides energy for the following reactions. The ranked thermal stabilities for charged electrodes based on total heat generated are as follows:



This order of electrode thermal stability for the P13FSI electrolyte is less surprising with NMC as the most reactive electrode and LFP as the least. Based on these results it may be more useful to compare total heat generation rather than just the exothermic onset temperature when considering P13FSI electrolyte and thermal stabilities. The thermal stability of each electrode with conventional electrolyte from literature was compared to P13FSI electrolyte in this work. For all six electrodes, both onset temperature and total heat rankings indicated that P13FSI electrolyte is more thermally stable, with two exceptions. First, NMC, both charged (delithiated) and discharged (lithiated), is more thermally stable with conventional electrolyte when ranked based on total heat generated. The heat released by NMC with P13FSI electrolyte was more than double that with conventional electrolyte. This would suggest there is no definite thermal advantage to using P13FSI electrolyte with an NMC electrode.

Second, LFP, both charged (delithiated) and discharged (lithiated), is found to be less thermally stable with P13FSI electrolyte than with conventional electrolyte when comparing exothermic onset temperatures. LFP with P13FSI electrolyte releases less than half the total heat of LFP with conventional electrolyte. However, the exothermic onset temperature of LFP is 179 °C with P13FSI electrolyte, at least 44 °C lower than with conventional electrolyte, considering the different heating rates used. It should also be noted that the thermal stability of graphite with P13FSI electrolyte is superior to conventional electrolytes when total heat values are compared. However, the onset temperature of graphite with conventional electrolytes appears to change with different solvent types. Therefore, the thermal stability of graphite with P13FSI electrolyte compared to conventional electrolyte depends on the conventional electrolyte solvents.

The importance of the exothermic onset temperature for reactions in the cathode should be considered alongside the onset temperatures of other heat sources in the cell, i.e. exothermic reactions in the anode and separator melting (short circuit) temperature which would cause ohmic heating. For example, if P13FSI electrolyte was used in a LFP | LTO cell with a polyethylene (PE) commercial separator the thermal stability of materials would be ranked:



In this case, the critical thermal event would be the separator melting because a higher onset temperature for the cathode decomposition will not further increase the cell thermal stability. But a

lower heat release by the cathode during decomposition could be advantageous during thermal runaway. The thermal stability of all materials in a cell should be considered including the total heat generation as well as the onset temperature for exothermic reactions (or ohmic heating). For many types of electrodes, P13FSI electrolyte provides a thermal advantage over conventional electrolytes in high temperature situations. However, the higher cost of ILs and potential selected electrode incompatibilities should be noted when considering the thermal advantages of IL electrolytes. Investigating the thermal stability of whole cells is the next step to determining thermal stability of IL electrolyte lithium-ion cells.

5.5 Conclusion

P13FSI IL is thermally stable up to 321 °C, however P13FSI electrolyte, containing 1.17 mol kg⁻¹ (1.57 M) LiFSI, is only stable up to 248 °C, and the electrolyte has a higher heat release during decomposition compared to the P13FSI IL alone. When compared to a 1 M LiPF₆ EC / DMC (1:1 w/w) conventional electrolyte, the P13FSI electrolyte has a higher exothermic onset temperature but generates more heat during decomposition. The thermal stability of P13FSI electrolyte, when combined with a separator, was found to be reduced. Based on exothermic onset temperature, GF with P13FSI electrolyte was found to be the most thermally stable separator, however when comparing the total heat Celgard 3501 with P13FSI electrolyte was found to be more thermally stable than GF. In both instances, PVDF-HFP with P13FSI electrolyte was found to be the least thermally stable, compared to Celgard 3501 and GF. This suggests that the thermal stability of a separator and electrolyte may be altered when tested in combination.

When investigating P13FSI electrolyte with commercial electrodes it was observed that P13FSI electrolyte does not provide a thermal stability advantage over EC / DMC (1:1 w/w) conventional electrolyte when used with an NMC electrode. Graphite and LFP electrodes with P13FSI electrolyte release less heat during decomposition than with EC / DMC (1:1 w/w) conventional electrolyte, however the exothermic reactions begin at lower temperatures which could impact the operating temperatures for a cell. LMNO and LTO electrodes had a higher thermal stability with P13FSI electrolyte than a EC / DMC (1:1 w/w) conventional electrolyte seen by a higher onset temperature and lower heat release with the P13FSI electrolyte. An investigation of LFP and LTO with P13FSI electrolyte at different SoC showed that SoC does impact the electrode thermal stability, however, the thermal stability is not necessarily proportional to the electrode SoC.

Electrodes in a charged and discharged state from a P13FSI electrolyte lithium metal half-cell were grouped by thermal stability based on the onset temperature of the first exothermic event. Discharged LTO, discharged NMC and graphite (charged and discharged) all had an onset

temperature below 150 °C which means that with these electrodes the exothermic decomposition of electrodes and electrolyte would likely initiate thermal runaway process as it would occur before short circuit heating from the separator melting. LFP (charged and discharged), charged NCM and LMNO (charged and discharged) had intermediate onset temperatures between 150 and 200 °C, while charged LCO and charged LTO had onset temperatures above 200 °C for their first exothermic event which means the thermal runaway process would likely be initiated by another event, such as separator melting causing short circuit heating.

Although the onset temperature for exothermic decomposition is an important factor for thermal runaway, the amount of heat released during decomposition should also be considered when comparing thermal stability of electrodes. The electrodes can be ranked according to total heat generation:

NMC (charged and discharged) > discharged LTO > charged LCO > discharged LMNO > charged LTO > graphite (charged and discharged) > charged LMNO > LFP (charged and discharged)

LFP in both charged and discharged state released the least heat during decomposition of all the electrodes investigated with P13FSI electrolyte. Although LFP charged and discharged had an exothermic onset temperature at approximately 170 °C, the first exothermic peak is mild with a small heat generation, the cell may be able to dissipate this heat effectively without entering thermal runaway. The thermal stability results vary greatly when comparing onset temperature vs. total heat generation, while both indicators are important, it is also necessary to consider the DSC thermogram profile to inform a material decision for lithium-ion batteries. Following on from DSC, ARC studies would allow thermal analysis to be conducted on an assembled cell in different states of charge to test material compatibility and investigate the expected thermal stability of a full cell.

LFP and LTO were both found to have high thermal stabilities with P13FSI electrolyte. The thermal stability of IL electrolytes has been seen to increase the onset temperature for exothermic decomposition of electrodes, however in many cases more heat is generated when decomposition does occur. The impact on thermal stability of substituting safer materials into a lithium-ion cell can only be investigated by assembly of a full cell and subsequent testing. The thermal stability of a LFP | LTO pouch cell containing P13FSI electrolyte and FSI-C separator will be investigated through thermal abuse testing and the development of a thermal abuse model in the next chapter.

CHAPTER 6

Thermal Runaway of Ionic Liquid Electrolyte Pouch Cells

6.1 Introduction

The use of an ionic liquid (IL) electrolyte in a lithium-ion cell is hypothesised to increase the onset temperature for decomposition of the electrolyte and associated materials within the cell, as discussed in Chapter 5. IL electrolytes with increased thermal stability and heat capacity may delay the onset temperature of thermal runaway, therefore allowing cell cooling to dissipate the heat being generated before the cell enters thermal runaway. For these properties to improve the safety of a cell it must be coupled with a separator that also has an increased thermal stability to delay internal short circuit ohmic heating as a result of separator melting.

There is a critical temperature that a cell reaches at which point the cell will self-fuel its own decomposition called the thermal runaway onset temperature. Once reached, the cell will continue to heat up due to exothermic decomposition of all cell components, discussed in Section 6.2.1 below. As introduced in Section 5.2, the sequence of reactions in a cell containing conventional electrolyte is typically Solid Electrolyte Interphase (SEI) decomposition; separator melting; anode decomposition; gasification of electrolyte; and lastly cathode decomposition. Once separator melting occurs, the cell will likely go into thermal runaway from the combined effects of ohmic heating and exothermic reactions causing heat accumulation within the cell. In Chapter 5, the thermal stabilities of various cell material combinations were characterised. This information provides an insight into individual material failure, although it cannot predict how multiple combinations within an assembled cell will fail, hence whole cells need to be tested. However, these experiments are time consuming and expensive to conduct. Modelling, in particular thermal abuse modelling, may be able to help predict these failures.

Computational models have been developed to describe thermal abuse of a lithium-ion cell and used to predict the most likely response of a lithium-ion cell under thermal runaway conditions, discussed in Section 6.2.3 below. In this chapter, a review is presented on thermal test methods and thermal abuse models for lithium-ion cells in the literature. A thermal model for a cell consisting of one cathode and one anode separated by a separator will be applied to an IL electrolyte pouch cell, based on a conventional electrolyte lithium-ion cell model from literature [85]. The heat generation terms are described by Arrhenius equations for decomposition reactions of each material. The decomposition reaction kinetics for each material were obtained from analysis of the Differential Scanning Calorimetry (DSC) thermograms presented in Chapter 5. Modelling of IL electrolyte lithium-ion cells is not well reported in literature. As such, the model was used to investigate the expected response of an IL electrolyte cell under thermal abuse conditions.

The thermal stability of IL electrolytes with various electrode materials at high temperatures was discussed in Chapter 5. Of these electrodes, LiFePO_4 (LFP) | $\text{Li}_4\text{Ti}_5\text{O}_{12}$ (LTO) cells were selected

for further investigation in a pouch cell with 1.17 mol kg^{-1} lithium bis(fluorosulfonyl)imide (LiFSI) in 1-methyl-3-propylpyrrolidinium bis(fluorosulfonyl)imide electrolyte (P13FSI electrolyte) and the novel separator, FSI-C. In Chapter 5, LFP and LTO were both found to have high thermal stabilities with P13FSI electrolyte. LFP | LTO pouch cells were assembled with different separators and either P13FSI electrolyte or conventional electrolyte. The pouch cells were subjected to oven testing to assess the impact of the separator and the electrolyte on the cell response to a thermal abuse condition. A thermal abuse model was applied to a LFP | P13FSI electrolyte | LTO cell. Kinetic analysis was performed on the DSC exothermic peaks for P13FSI electrolyte as well as 100% State of Charge (SoC) LFP and LTO to obtain reaction model parameters to describe decomposition reactions in the thermal abuse model. The model was used to simulate and analyse the thermal runaway of P13FSI electrolyte and conventional electrolyte pouch cells.

6.2 Literature review

Common causes of cell failure are associated with improper management of the cell during operation [391]. Abuse conditions include internal and external short circuit [392-395]; overcharge and over discharge [396-400]; and operating in a high temperature environment [35, 43, 401-404]. The ultimate result of these abuse conditions is thermal runaway of the cell [405], sometimes leading to catastrophic failure including the cell fires or explosion due to a build up of gasses from internal reactions. Therefore, in addition to the performance testing presented in Chapter 4, it is important to test the cell response to abuse conditions. The occurrence of thermal runaway in lithium-ion cells was discussed in Section 5.2. The response of a cell to abuse conditions must be known in order to design effective safety precautions around the cell. In this literature review, the concept of thermal runaway will be summarised, the characterisation techniques important to thermal runaway will be assessed, and available models that predict thermal abuse conditions will be evaluated for their efficacy.

6.2.1 Thermal runaway

Thermal runaway occurs when heat accumulates in the cell. Heat sources include electrical (ohmic) heat, entropic (reaction) heat and / or external heat from the surroundings. The reactions that occur during thermal runaway of a conventional electrolyte lithium-ion cell have been introduced in Section 5.2. These events occur at different temperatures depending on the material composition of the cell components, i.e. electrode materials, separator type and electrolyte solvents. The thermal runaway process of a $\text{Li}(\text{Ni}_{1/3}\text{Co}_{1/3}\text{Mn}_{1/3})\text{O}_2$ (NMC) | graphite lithium-ion cell with conventional electrolyte is shown in Figure 6.71. Most of these reactions are exothermic and

therefore contribute to heat accumulation in the cell.

Figure has been removed due to Copyright restrictions.

Figure 6.71 Temperature ranges for different stages of thermal runaway in a NMC | graphite lithium-ion cell with conventional electrolyte from Accelerating Rate Calorimetry (ARC) testing. Taken from Feng, et al. [365].

Increasing the safety of individual cell components can therefore improve the overall safety of a lithium-ion cell. Thermal stability can be increased by either decreasing the energy released during exothermic decomposition or increasing the onset temperature of decomposition reactions. Anode and cathode materials can be selected to increase the thermal stability of a cell at high temperatures [15]. As discussed in Section 1.1.2, the electrolyte is a major contributor to cell safety [31-34].

The self-heating properties and thermal runaway profile of a 25 Ah conventional electrolyte NMC | graphite prismatic cell has been investigated with Accelerating Rate Calorimetry (ARC) by Feng, et al. [365]. The thermal runaway process was divided into six stages, as shown in Figure 6.71, with the following reactions: stage 1 SEI decomposition begins; stage 2 anode-electrolyte reactions; stage 3 separator shutdown occurs (if relevant); stage 4 micro short circuits from separator melting; stage 5 more short circuits, cathode and electrolyte decomposition reactions; and stage 6 all reaction material used up and maximum temperature reached. The temperature for each stage changed with the heating rate used during the ARC experiment. The temperature was recorded on the surface of the cell as well as with one thermocouple placed inside for comparison, the internal temperature was found to reach a maximum of 870 °C during thermal runaway.

The thermal runaway of a conventional electrolyte LiCoO₂ (LCO) | graphite cell was studied with a micro-calorimeter by Ping, et al. [363]. Calorimetry was performed on individual materials: electrolyte, cathode with electrolyte, anode with electrolyte and the separator and a deconvolution method was developed using a Gaussian function to separate overlapping peaks seen in the calorimetry. Full cells were then investigated and the individual material peaks were used to identify the reactions occurring during calorimetry of the full cells. From these reactions, Ping, et al. [363] identified three critical factors that impact the thermal stability of a cell; thermal stability of the SEI, heat generation during cathode reactions and the melting temperature of the separator.

Abuse testing of IL electrolyte-based lithium-ion cells has not been widely reported in the literature. One example is the work of Kalhoff, et al. [39] who undertook abuse testing on 0.8 Ah LFP | LTO

pouch cells containing N-methyl-N-butyl-pyrrolidinium bis(fluorosulfonyl)imide (P14FSI) lithium bis(trifluoromethanesulfonyl)imide (LiTFSI) IL electrolyte by. The IL cells underwent extended cycling (300 cycles) including ageing (3 years open circuit voltage storage at room temperature) before being subjected to nail penetration and overcharge testing. The nail penetration test was performed on fully charged cells and revealed that the surface temperature did not exceed 30 °C during the test and the authors [39] also noted the lack of fire and gas production. This demonstrated a safety level not possible with commercial lithium-ion cells containing conventional electrolytes. Similarly, during the overcharge test a temperature increase of only 7 °C was observed in the cell. Kalhoff, et al. [39] attributed the high safety observed to the combination of LTO and LFP, electrodes known to have enhanced safety [406-411], along with the non-volatile / non-flammable IL electrolyte.

6.2.2 Thermal characterisation

To understand what is occurring within a cell during thermal abuse testing, thermal characterisation of a lithium-ion cell is required under different conditions. Thermal characterisation information is useful for input parameters required for modelling, which will be covered in Section 6.2.3. When analysing the thermal characteristics of a cell the material thermal properties are important, including heat capacity and thermal conductivity. In lithium-ion cell modelling, average thermal properties of the cell core have been commonly used to predict the overall thermal response of a lithium-ion cell under abuse conditions. In order to characterise the properties, experimental methods for measurement of average cell core thermal parameters have been developed for this purpose. Bazinski and Wang [412] modified an isothermal calorimeter to measure the specific heat capacity and perpendicular thermal conductivity of a pouch cell core at various temperature and SoC conditions for a commercial LFP pouch cell. The authors [412] found that specific heat capacity does not significantly change with SoC but does depend strongly on temperature, whereas the perpendicular thermal conductivity was found to be independent of temperature but can be related to the SoC. The perpendicular thermal conductivity of the core is the overall thermal conductivity of the cell in the direction perpendicular to the layers, which takes into account thermal contact resistance that exists between the layers when assembled into a cell stack [41, 413]. The thermal conductivity of a lithium-ion cell is important as it dictates the potential dissipation of heat within the cell to reduce the severity of localised high temperature regions, such as in the occurrence of an internal short circuit.

Alternate methods of temperature sensing have been applied to lithium-ion cells to enhance the spatial resolution of temperature monitoring. Thermal imaging has been applied to lithium-ion cells to investigate temperature distribution. Heubner, et al. [414] applied microscopic thermal imaging

to the cross section of a single cell stack to investigate the thermal characteristics. The authors [414] investigated heat evolution and diffusion of each cell component layer during charge and discharge separately. The microscopic imaging technique showed that inhomogeneity of the electrodes can have a significant impact on heat transport within the cell stack. Veth, et al. [415] also applied thermal imaging to lithium-ion cell temperature measurement to monitoring the external cell temperature. Heat generation and temperature distribution within a cell was studied at various charge and discharge rates, SoC, environmental temperatures and cell ages. The thermal imaging technique was used in conjunction with PT-100 electrical sensors and an optical fibre (5 mm resolution) applied to the surface of the pouch to evaluate the temperature measurement accuracy. Agreement between the measurement methods was found to be ± 0.2 K. Veth, et al. [415] suggest that optical fibres may present a three dimensional (3D) temperature monitoring solution inside a battery module. Although Heubner, et al. [414] and Veth, et al. [415] only measured cell temperatures under normal charge and discharge conditions, their methods could be extended to monitor formation of local hot spots that may precede thermal runaway processes in a cell.

6.2.3 Modelling

Lithium-ion battery models including IL electrolytes have not been widely reported in the literature. Yoo, et al. [416] proposed a transport equation for IL electrolytes based on Maxwell-Stefan diffusivities from molecular dynamic simulations, however no thermal properties were included in this model. Since no thermal abuse models for IL electrolyte cells could be located in the literature, thermal abuse models for conventional electrolyte lithium-ion cells will be reviewed for application to IL electrolyte cells.

Thermal characterisation of a lithium-ion cell is very important for design considerations. Estimating the thermal runaway onset temperature and expected heat generation in a cell is key to estimating the cell response under thermal abuse conditions. One way to predict the behaviour of a cell undergoing thermal runaway is to create a thermal model that includes decomposition reactions for each component present in the cell. Modelling can be used to simulate dangerous or long-term tests with a considerable decrease in time, resources and risk. Therefore, modelling is a useful tool to optimise the design process. However, with all modelling, the accuracy of the output is dependent on the equations and parameters input, including the accuracy and standard deviation of experimentally determined parameters. Thermal modelling of batteries under abuse conditions is achieved through a thermal energy balance that includes heat from chemical reactions that take place when the cell is operated outside of standard conditions. Decomposition profiles, thermal material properties and the thermal design of a cell become the most important to simulate cell

safety. The standard outputs for a thermal abuse model are onset temperature for thermal runaway, heat generation rates and temperature profile for the cell. The heat generation term consists of heat sources from exothermic reactions. Thermal abuse models available in the literature are discussed below to determine the most appropriate model for application to IL electrolyte cells.

Abada, et al. [1] surveyed the literature for models focussing on lithium-ion safety under abuse conditions and found that models for normal operation and ageing effects have been more widely reported than for abuse conditions. The abuse models that have been reported are generally poorly validated, which limits confidence in the accuracy of this type of model. Effat, et al. [78] also reviewed models for lithium-ion batteries including abuse condition thermal models and the authors focussed on module level models that consider heat propagation between cells within a pack.

An electrochemical-thermal coupled model for lithium-ion cells during self-heating and thermal runaway conditions was developed by Wang, et al. [38]. The heat generation included terms for reversible, irreversible and ohmic heat experienced during charge and discharge operations, as well as the heat contributions from material decomposition reactions at elevated temperatures. The decomposition reactions were anode, cathode, electrolyte and SEI decomposition reactions as well as electrolyte solvent gasification and subsequent decomposition reactions. The reactions were described by Arrhenius equations. The Arrhenius equation is widely used to model the temperature dependence of a reaction rate constant (k) [417-422] is described by Eq. (8):

$$k = A \exp \left[-\frac{E}{RT} \right] \quad \text{Eq. (8)}$$

where A is the frequency factor (or pre-exponential factor), E is the activation energy, R is the universal gas constant and T is the temperature in K.

Wang, et al. [38] obtained the reaction parameters for each component from kinetic analysis of DSC experiments; carbon based anode, LFP based cathode and 1 M lithium hexafluorophosphate (LiPF₆) in ethylene carbonate (EC) / diethyl carbonate (DEC) / dimethyl carbonate (DMC) (1:1:1, volume/volume (v/v)) electrolyte, DSC of the separator was not performed. Wang, et al. [38] focussed on determining the effects of the separator melt-down temperature on the self-heating and thermal runaway process within a cell at elevated temperatures. The simulations commenced from 125 °C and ran until thermal runaway was reached, visible by a simultaneous vertical increase in temperature and heating rate. Wang, et al. [38] found that in an adiabatic environment at 125 °C (beginning of simulation) an increase in cell temperature was observed from heat generated by SEI decomposition reactions. Once the SEI has been depleted endothermic solvent gasification occurs simultaneously with exothermic electrolyte decomposition causing the

temperature to continue increasing. Then the separator melts and the electrodes begin reacting. Wang, et al. [38] found the model predicted that the cell entered thermal runaway regardless of the separator meltdown temperature. When a separator with a low meltdown temperature was used, the separator melting and resulting internal short circuit initiated thermal runaway, whereas when a separator with high meltdown temperature was used the electrode decomposition reactions initiated thermal runaway. A higher separator meltdown temperature delayed the thermal runaway event but did not prevent it.

Hatchard, et al. [84] developed a one dimensional (1D) thermal model for oven test simulations of lithium-ion cells. LCO | graphite cells were considered with cylindrical and prismatic geometries. Heat generation reactions were modelled as Arrhenius equations. Anode heat generation was split into two reactions: lithium-containing species in the SEI and intercalated lithium in the electrode. The cathode heat generation was described by one equation for the cathode-electrolyte reaction. The jelly roll was assumed to be one homogeneous core with volume averaged thermal parameters, i.e. density and heat capacity. The model was validated by oven test experiments on cylindrical and prismatic cells. The authors [84] saw good agreement between the model and the oven test experiments. They did note a difference in the time of thermal runaway and maximum cell temperature predicted by the model and seen in the tests. The variation in time of thermal runaway prediction was attributed to cell venting events that were not accounted for in the model. The underestimation of maximum cell temperature by the model was attributed to the absence of a heat generation term for electrolyte decomposition reactions. The Arrhenius equation parameters for each material were fitted only to the first exothermic event meaning additional exothermic reactions that occurred during thermal runaway were not included in the heat generation terms.

Kim, et al. [423] used the 1D model proposed by Hatchard, et al. [84] to develop a 3D model for a cylindrical cell. A 3D model allows for consideration of individual component geometries and a 3D profile for temperature within the cell. The heat generation terms were included as described by Hatchard, et al. [84] with the addition of a heat term for electrolyte decomposition. To decrease computational effort the thermal parameters of materials were included as a single volumetric heat capacity value for the jelly roll. Anisotropic thermal conductivity was included with description in the layer-normal and layer-parallel directions using thickness-averaged properties. Reactions were validated by comparing simulations to the 1D model by Hatchard, et al. [84]. Kim, et al. [423] used the 3D model to investigate internal short circuit hot spots and temperature non-uniformity in a cell during thermal runaway. They found that thermal behaviours in a cell are multidimensional and that the 3D cell geometry, including cell volume to surface area ratio, is important during thermal abuse conditions to predict cell response.

Lopez, et al. [80] developed a thermal model based on the work of Hatchard, et al. [84] and Kim, et

al. [423]. Lopez, et al. [80] applied the model to spiral wound cylindrical and prismatic cell geometries. Thermal properties were calculated as weight averaged from individual materials in each layer. Radiative and convective heat flux were applied as boundary conditions for the cell. Heat generation terms for SEI, anode, cathode and electrolyte decomposition were included as Arrhenius equations. The influence of oven temperature, convective heat coefficient and abuse reactions were investigated. The authors [80] applied the model to a constant heater power abuse test. The abuse process began with SEI decomposition during the initial heating stage from convection effects in the oven. The exothermic SEI reaction increases the cell temperature and the anode-electrolyte reactions begin, which further increases the temperature, and cathode-electrolyte reaction also occurs increasing the cell temperature. Once the active materials are consumed the temperature begins to decrease as the heat generation slows down. Cell cooling to the oven temperature occurs from the convective heat effects.

Yang, et al. [83] developed an exothermic reaction model for a $\text{LiNi}_{0.5}\text{Mn}_{1.5}\text{O}_4$ | C cell. The reaction parameters were obtained from individual DSC of the electrolyte, cycled anode and cycled cathode. The heat flow results were fitted to Arrhenius equations and used to model heat generated by each material in the cell. The thermal runaway model was validated with ARC of the whole cell. The authors [83] concluded that for a $\text{LiNi}_{0.5}\text{Mn}_{1.5}\text{O}_4$ (LMNO) | C cell, once the temperature reached $162.9\text{ }^\circ\text{C}$ and the heating rate reached $0.04\text{ }^\circ\text{C s}^{-1}$ the cell was in a critical state of thermal runaway. The first anode reaction was responsible for the initial heating rate increase but the cathode reaction was the main reason for thermal runaway.

The abuse testing and modelling in this chapter is focussed on LFP | P13FSI electrolyte | LTO cells. Unfortunately, models which include abuse reactions of LTO are not widely available in the literature. One of the few examples, by Ping, et al. [424], models the cycling behaviour and thermal runaway response of a conventional electrolyte NMC | LTO cell. The thermal abuse model included heat sources from SEI decomposition, anode-electrolyte reaction, short-circuit after separator melting, cathode decomposition and cathode-electrolyte reaction. The reactions were described by n^{th} order autocatalytic-controlled and diffusion-controlled reaction models with the Arrhenius equation [424], Arrhenius equation described in Section 6.3.4. Kinetic analysis of ARC data was used obtain the reaction parameters. The thermal runaway simulation was validated against ARC test data. Ping, et al. [424] found that thermal runaway occurred at an ambient temperature as low as $152\text{ }^\circ\text{C}$.

In the literature, the exothermic decomposition of a conventional electrolyte cell is typically described by an Arrhenius reaction model [30, 80, 83-85, 424]. However, the reaction mechanism in a cell containing in IL electrolyte, more specifically P13FSI electrolyte, is expected to be different from that of a conventional electrolyte cell. This is due to the increased thermal stability of P13FSI

electrolyte, discussed in Chapter 5, as well as the reactions relating to the electrode-electrolyte interphase decomposition.

The decomposition reactions for an IL electrolyte lithium-ion cell are not well understood. In the next section, a thermal abuse model is applied to a P13FSI electrolyte cell, including five decomposition reactions that contributed to cell heating. The DSC results obtained for thermal stability of each cell component in Chapter 5 were used to obtain the kinetic parameter for the decomposition reactions in the simulation.

6.3 Physical and mathematical model

The zero dimensional (0D) lumped thermal abuse model presented by Coman, et al. [85] was established to be appropriate for a pouch cell containing a LFP cathode, P13FSI IL electrolyte and LTO anode. In their model, Coman, et al. [85] used the reaction equations set out by Hatchard, et al. [84], discussed in Section 6.2.3, to develop a lumped thermal abuse model including heat from an internal short circuit. This model will be applied to an IL electrolyte cell to predict the reaction temperatures and heat released during thermal abuse, based on and Arrhenius equations and the kinetic data from Chapter 5. The overall thermal equations are described in Section 6.4. The IL electrolyte cell reaction equations are described in Section 6.4.1, followed by the kinetic parameter estimation method in Section 6.4.2. The conventional electrolyte cell reaction equations used for comparison are described in Section 6.4.3. Finally, the modelling procedure is presented in Section 6.4.4.

6.4 Thermal energy model

The single cell thermal model can be simulated as a lumped model due to the small Biot number [85]. The Biot number is the ratio of the external and internal heat transfer in a defined system [425]. For the P13FSI electrolyte pouch cell dimensions investigated, the Biot number was calculated to be $7.4E-5$ or $1.8E-3$ depending on the thermal conductivity used to describe the cell stack, in-plane or through plane, respectively (calculations in Appendix M). For thermal conductivity in both directions the Biot number is $\ll 0.1$, therefore the internal heat transfer is negligible and the external heat transfer effects dominate and a lumped cell model is appropriate [425]. The lumped thermal model has been adapted from Coman, et al. [85] to be applicable to an IL electrolyte pouch cell. A list of symbols used in the thermal model is shown in Table 6.36.

Table 6.36 Symbols used in thermal model, including units and description.

Symbol	Units	Description
A	s^{-1}	Frequency factor
A_{surf}	m^2	Surface area of cell stack
C_p	$J\ kg^{-1}\ K^{-1}$	Specific heat capacity
E	$J\ mol^{-1}$	Reaction activation energy
h	$W\ m^{-2}\ K^{-1}$	Equivalent heat transfer coefficient
H	$J\ kg^{-1}$	Reaction heat
M	kg	Material weight in cell
n	dimensionless	Reaction order
q	J	Heat release for a reaction
Q	W	Heat generation for a reaction
Q_{gen}	W	Total heat generation
Q_{ht}	W	Heat transfer at the boundary
R_{gas}	$J\ mol^{-1}\ K^{-1}$	Universal gas constant
T	K	Temperature
t	s	Time
T_{amb}	K	ambient temperature
V_{cell}	m^3	Volume of cell stack
x	dimensionless	Material available for reaction
ρ	$kg\ m^{-3}$	Density

The thermal energy balance for a lumped thermal model is described by Eq. (9):

$$V_{cell}\rho C_p \frac{dT}{dt} = Q_{ht} + Q_{gen} \quad \text{Eq. (9)}$$

where V_{cell} is the volume of the cell stack (calculation given in Appendix M). The density, ρ ($kg\ m^{-3}$), and heat capacity, C_p ($J\ kg^{-1}\ K^{-1}$), are weight-averaged properties over the whole cell stack. T is the average cell temperature (K). Q_{ht} is the heat transfer between the cell and the surroundings (W).

Q_{gen} is the internal heat generation of the cell (W).

Density and heat capacity have been included as weight-averaged properties for cathode, anode and electrolyte material based on their weight fraction in the cell. For example, the weight-averaged heat capacity was calculated by Eq. (10):

$$C_p = \sum_j \frac{M_j}{M_{total}} C_{p,j} \quad \text{Eq. (10)}$$

where C_p is the heat capacity ($\text{J kg}^{-1} \text{K}^{-1}$), j indicates a specific material and M_{total} is the sum of all M_j values for the cell.

The heat transfer between the cell and the surroundings (Q_{ht}) includes conductive, convective and radiative heat effects on the cell boundary. For a lumped model, the boundary is described by the total surface area of the cell. The heat transfer in the thermal model is described by Eq. (11):

$$Q_{ht} = -A_{surf} [h(T - T_{amb})] \quad \text{Eq. (11)}$$

where A_{surf} is the total surface area of the cell (m^2). h is the equivalent heat transfer coefficient ($\text{W m}^{-2} \text{K}^{-1}$). T_{amb} is the ambient oven temperature.

6.4.1 Reaction models for P13FSI electrolyte cell

The reaction models for the P13FSI electrolyte cell are based on the DSC results obtained in Chapter 5. The LFP reaction model is based on the thermogram of LFP from half-cell with P13FSI electrolyte charged to 100% SoC (Figure 5.10b) which shows two main exothermic peaks. Therefore, the decomposition of charged LFP in the presence of P13FSI electrolyte is described by two reactions in Section 6.4.1.1 below. The LTO reaction model is based on the thermogram of LTO from half-cell with P13FSI electrolyte charged to 100% SoC (Figure 5.12b) which shows one main exothermic peak. Therefore, the decomposition of charged LTO in the presence of P13FSI electrolyte is described by one reaction in Section 6.4.1.2 below. The P13FSI electrolyte reaction model is based on the thermogram of P13FSI electrolyte (Figure 5.2c) which shows two exothermic peaks. Therefore, the decomposition of P13FSI electrolyte is described by two reactions in Section 6.4.1.3 below.

The heat generation (Q_{gen}) includes heat sources from internal cell reactions. For the P13FSI electrolyte cell, heat generation is described by Eq. (12):

$$Q_{gen} = Q_i + Q_{e1} + Q_a + Q_c + Q_{e2} \quad \text{Eq. (12)}$$

where Q_i is the heat generated by decomposition of electrode-electrolyte interphase. Q_c is the heat generated by reactions between the cathode and electrolyte. Q_a is the heat generated by reactions between the anode and electrolyte. Q_{e1} and Q_{e2} are the heat generated by electrolyte reactions and decomposition. Exothermic reactions of cell materials are typically modelled by Arrhenius equations [30, 80, 83-85, 424]. Due to the small capacity of the pouch cell in this thesis, separator melting and the subsequent internal short circuit ohmic heating was assumed negligible and therefore not included in the heat generation equation (Eq. (12)). The inclusion of internal short circuit ohmic heating is investigated in Section 6.6.2.5

6.4.1.1 Cathode reactions

Two exothermic reactions were observed during DSC of charged LFP with P13FSI electrolyte (Section 5.4.3.4). The first exothermic event observed in charged LFP was assumed to be from reaction of electrode-electrolyte interphase compounds formed on the cathode during cycling with P13FSI electrolyte. Consequently, the interphase material available for the reaction is assumed to be a weight fraction (x_i) of the total cathode material available (M_c). The weight fraction of interphase material available for reaction at the start of the simulation, time = 0 seconds ($x_{i,0}$), was estimated to be 0.1 from the amount of capacity drop seen during formation cycling, the capacity drop was assumed to be from electrode-electrolyte interphase formation reactions. Since the charged LTO DSC did not appear to have any reactions attributed to decomposition of electrode-electrolyte interphase compounds, the interphase was assumed to be entirely on the cathode for the purposes of this model. The remaining cathode material (x_c) is assumed to be consumed during the second exothermic event observed for charged LFP.

The electrode-electrolyte interphase decomposition reaction and heat generation are described by Eq. (13) and Eq. (14):

$$\frac{dx_i}{dt} = -x_i A_i \exp\left[-\frac{E_i}{R_{gas} T}\right] \quad \text{Eq. (13)}$$

$$Q_i = -H_i M_c \frac{dx_i}{dt} \quad \text{Eq. (14)}$$

where x_i is the weight fraction of cathode material available for reaction of the electrode-electrolyte interphase. A_i is the electrode-electrolyte interphase reaction frequency factor (s^{-1}). E_i is the electrode-electrolyte interphase reaction activation energy ($J mol^{-1}$). R_{gas} is the universal gas

constant ($8.314 \text{ J mol}^{-1} \text{ K}^{-1}$). T is the average cell temperature, described by Eq. (9). H_i is the reaction heat for decomposition of the electrode-electrolyte interphase (J kg^{-1}). M_c is the total cathode material in the cell (kg).

The second exothermic reaction for charged LFP was assumed to be from reaction between the cathode and electrolyte. The cathode-electrolyte reaction and heat generation are described by Eq. (15) and Eq. (16):

$$\frac{dx_c}{dt} = -x_c A_c \exp\left[-\frac{E_c}{R_{gas}T}\right] \quad \text{Eq. (15)}$$

$$Q_c = -H_c M_c \frac{dx_c}{dt} \quad \text{Eq. (16)}$$

where x_c is the weight fraction of cathode material available for reaction with electrolyte. A_c is the cathode decomposition reaction frequency factor (s^{-1}). E_c is the cathode decomposition reaction activation energy (J mol^{-1}). H_c is the reaction heat for the cathode-electrolyte reaction (J kg^{-1}).

6.4.1.2 Anode reactions

The amount of anode material available for reaction has been initially set to $x_{a,0} = 0.75$, as is standard for electrode materials in published models [30, 80, 84, 85, 423]. The anode decomposition reaction and heat generation are described by Eq. (17) and Eq. (18):

$$\frac{dx_a}{dt} = -x_a A_a \exp\left[-\frac{E_a}{R_{gas}T}\right] \quad \text{Eq. (17)}$$

$$Q_a = -H_a M_a \frac{dx_a}{dt} \quad \text{Eq. (18)}$$

where x_a is the weight fraction of anode material available for reaction with electrolyte. A_a is the anode decomposition reaction frequency factor (s^{-1}). E_a is the anode decomposition reaction activation energy (J mol^{-1}). H_a is the reaction heat for the anode-electrolyte reaction (J kg^{-1}). M_a is the total anode material in the cell (kg).

6.4.1.3 Electrolyte reactions

Two exothermic reactions were observed during DSC of P13FSI electrolyte (Section 5.4.1). The first exothermic reaction was suggested to be from decomposition of lithium bis(fluorosulfonyl)imide (LiFSI) in the electrolyte. Therefore, the weight fraction of electrolyte material available for this reaction (x_{el}) has been set to the weight fraction of LiFSI in the electrolyte, $x_{el,0} = 0.18$. The total amount of electrolyte material was set to the weight of electrolyte material (M_e) in the pouch cell.

The first electrolyte reaction and heat generation are described by Eq. (19) and Eq. (20):

$$\frac{dx_{e1}}{dt} = -x_{e1}A_{e1}\exp\left[-\frac{E_{e1}}{R_{gas}T}\right] \quad \text{Eq. (19)}$$

$$Q_{e1} = -H_{e1}M_e\frac{dx_{e1}}{dt} \quad \text{Eq. (20)}$$

A_{e1} is the first electrolyte reaction frequency factor (s^{-1}). E_{e1} is the first electrolyte reaction activation energy ($J\ mol^{-1}$). H_{e1} is the reaction heat for the first electrolyte reaction ($J\ kg^{-1}$).

The second exothermic event during DSC of P13FSI electrolyte was assumed to be from decomposition of P13FSI IL in the electrolyte. The second electrolyte decomposition reaction and heat generation are described by Eq. (21) and Eq. (22):

$$\frac{dx_{e2}}{dt} = -x_{e2}A_{e2}\exp\left[-\frac{E_{e2}}{R_{gas}T}\right] \quad \text{Eq. (21)}$$

$$Q_{e2} = -H_{e2}M_e\frac{dx_{e2}}{dt} \quad \text{Eq. (22)}$$

where x_{e2} is the weight fraction of P13FSI IL available for decomposition in the electrolyte material. A_{e2} is the electrolyte decomposition reaction frequency factor (s^{-1}). E_{e2} is the electrolyte decomposition reaction activation energy ($J\ mol^{-1}$). H_{e2} is the reaction heat for decomposition of the electrolyte ($J\ kg^{-1}$).

6.4.2 Estimation of kinetic parameters

Kinetic analysis of DSC data (from Sections 5.4.1.3, 5.4.3.4 and 5.4.3.6) was undertaken to obtain reaction model parameters for the P13FSI electrolyte cell materials: specific heat release H_i , H_c , H_a , H_{e1} and H_{e2} ; activation energies E_i , E_c , E_a , E_{e1} and E_{e2} ; and frequency factors A_i , A_c , A_a , A_{e1} and A_{e2} . For P13FSI electrolyte, analysis was performed on the main exothermic peaks at 269 and 355 °C in the thermogram (Figure 5.2c), labelled with the subscripts $e1$ and $e2$ in the thermal abuse model, respectively. The charged LFP from a P13FSI electrolyte cell also had two main exothermic peaks, at 204 and 352 °C, which have been included in the thermal abuse model; labelled with the subscripts i and c , respectively. There was only one main exothermic peak in the charged LTO from a P13FSI electrolyte cell at 294 °C; labelled with the subscript a in the thermal abuse model.

Kinetic reaction parameters for each DSC peak were extracted using the Arrhenius equation. The Arrhenius equation is described by Eq. (23) [420, 426]:

$$k = A \exp\left(-\frac{E}{R_{gas}T}\right) \quad \text{Eq. (23)}$$

where k is the rate constant. E is the activation energy. A is the frequency factor. T is the temperature. R_{gas} is the universal gas constant.

From DSC data, the rate constant was determined by Eq. (24) [426]:

$$k = \frac{\left(\frac{\alpha_{tot}}{C_0}\right)^{n-1} \beta}{(\alpha_{tot} - \alpha)^n} \quad \text{Eq. (24)}$$

where α_{tot} is the total area under the DSC peak for a particular reaction, α is the area up to a temperature, C_0 is a normalisation factor, β is the heating rate (K s^{-1}) and n is the reaction order. C_0 was set to one in this case as the DSC data used was normalised using the sample weight prior to kinetic analysis (heat flow in W g^{-1}).

The rate constant, k , was calculated at intervals of 3°C over the temperature range of the DSC peak. A 0th order reaction was used, as has been previously found suitable for decomposition of ILs [420]. The natural logarithm of k , $\ln(k)$, was plotted against $1/T$. Using Eq. (23), E and A can be extracted from a linear fit of $\ln(k)$ vs $1/T$; E is determined from the slope and A is determined from the intercept.

6.4.3 Reaction models for conventional electrolyte cell

The reaction models for the conventional electrolyte cell are based on the LTO decomposition mechanism reported by Ping, et al. [424] along with the LFP decomposition and electrolyte decomposition mechanisms reported by Peng and Jiang [30]. Ping, et al. [424] found good agreement between their reaction model and ARC testing by including two reactions associated with thermal decomposition of LTO with conventional electrolyte: (1) SEI decomposition, from the surface of LTO and (2) reaction between the LTO electrode and the electrolyte. The SEI and anode reactions are described below in Sections 6.4.3.1 and 6.4.3.2, respectively. Peng and Jiang [30] includes a single reaction for the cathode between the LFP electrode and the electrolyte. There was no reaction model reported to describe cathode-electrolyte interphase decomposition, therefore, heat generation from decomposition of cathode-electrolyte interphase compounds formed in conventional electrolyte cells has been assumed to be negligible for the purposes of this model. The cathode reaction is described below in Section 6.4.3.3. Peng and Jiang [30] also

include a single reaction for decomposition of the electrolyte, described below in Section 6.4.3.4.

The heat generation (Q_{gen}) for the conventional electrolyte pouch cell includes the heat from reactions occurring inside the cell. The generated heat is described by Eq. (25):

$$Q_{gen} = Q_{sei} + Q_a + Q_c + Q_e \quad \text{Eq. (25)}$$

where Q_{sei} is the heat generated by SEI decomposition. Q_c is the heat generated by reaction between the cathode and electrolyte. Q_a is the heat generated by reaction between the anode and electrolyte. Q_e is the heat generated by electrolyte decomposition. Heat generated by decomposition and exothermic reactions of cell materials have been estimated with Arrhenius equations in published models [30, 80, 82, 85, 424].

6.4.3.1 SEI reaction

The amount of material available for decomposition as the SEI has been initially set to $x_{sei,0} = 0.15$, as is standard for graphite anode materials in published literature [30, 80, 85]. Unfortunately, this parameter was not provided by Ping, et al. [424] for the LTO anode model. The SEI decomposition reaction and heat generation are described by Eq. (26) and Eq. (27) [424]:

$$\frac{dx_{sei}}{dt} = -x_{sei}A_{sei} \exp\left[-\frac{E_{sei}}{R_{gas}T}\right] \quad \text{Eq. (26)}$$

$$Q_{sei} = -H_{sei}M_a \frac{dx_{sei}}{dt} \quad \text{Eq. (27)}$$

where x_{sei} is the weight fraction of anode material available for reaction in the SEI. A_{sei} is the SEI reaction frequency factor (s^{-1}). E_{sei} is the SEI reaction activation energy ($J \text{ mol}^{-1}$). H_{sei} is the reaction heat for reaction of the SEI ($J \text{ kg}^{-1}$). M_a is the total anode material in the cell (kg).

6.4.3.2 Anode reactions

The amount of anode material available for reaction has been initially set to $x_{a,0} = 0.75$, as is standard for electrode materials in published literature [30, 80, 85]. The anode-electrolyte reaction and heat generation are described by Eq. (28) and Eq. (29) [424]:

$$\frac{dx_a}{dt} = -x_a^{n_{a1}}(1-x_a)^{n_{a2}}[-\ln(1-x_a)]^{n_{a3}}A_a \exp\left[-\frac{E_a}{R_{gas}T}\right] \quad \text{Eq. (28)}$$

$$Q_a = -H_aM_a \frac{dx_a}{dt} \quad \text{Eq. (29)}$$

where x_a is the weight fraction of anode material available for reaction with electrolyte. n_{a1} , n_{a2} and n_{a3} are the kinetic exponents for the reaction equation [424]. A_a is the anode-electrolyte reaction

frequency factor (s^{-1}). E_a is the anode-electrolyte reaction activation energy ($J mol^{-1}$). H_a is the reaction heat for the anode-electrolyte reaction ($J kg^{-1}$).

6.4.3.3 Cathode reactions

The amount of cathode material available for conversion has been initially set to $x_{c,0} = 0.04$, as is standard for cathode materials in published literature [30, 80, 84, 85]. The reaction between LFP and conventional electrolyte and the heat generation are described by Eq. (30) and Eq. (31) [30]:

$$\frac{dx_c}{dt} = x_c^{n_c}(1 - x_c)^{n_c}A_c \exp\left[-\frac{E_c}{R_{gas}T}\right] \quad \text{Eq. (30)}$$

$$Q_c = H_c M_c \frac{dx_c}{dt} \quad \text{Eq. (31)}$$

where x_c is weight fraction of cathode material available for reaction with electrolyte. n_c is the reaction order. A_c is the cathode-electrolyte reaction frequency factor (s^{-1}). E_c is the cathode-electrolyte reaction activation energy ($J mol^{-1}$). H_c is the reaction heat for the cathode-electrolyte reaction ($J kg^{-1}$). M_c is the total cathode material in the cell (kg).

6.4.3.4 Electrolyte reactions

The electrolyte decomposition reaction and heat generation are described by Eq. (32) and Eq. (33) [30]:

$$\frac{dx_e}{dt} = -x_e A_e \exp\left[-\frac{E_e}{R_{gas}T}\right] \quad \text{Eq. (32)}$$

$$Q_e = -H_e M_e \frac{dx_e}{dt} \quad \text{Eq. (33)}$$

where x_e is the weight fraction of electrolyte material available. A_e is the electrolyte decomposition reaction frequency factor (s^{-1}). E_e is the electrolyte decomposition reaction activation energy ($J mol^{-1}$). H_e is the reaction heat for the electrolyte decomposition ($J kg^{-1}$). M_e is the total electrolyte material in the cell (kg).

6.4.4 Modelling procedure

The model was implemented in COMSOL Multiphysics software package. COMSOL Multiphysics is applicable to battery modelling due to the ease of implementation and flexibility with model description [427]. The lumped thermal model energy balance Eq. (9); heat transfer Eq. (11); heat generation Eq. (12) or Eq. (25); and reaction equations Eq. (13) to Eq. (22) or Eq. (26) to Eq. (33)

were implemented as user defined Ordinary Differential Equations (ODEs) in a 0D COMSOL model. The parameters used for the P13FSI electrolyte and conventional electrolyte cell thermal models are shown in Table 6.37 and Table 6.38, respectively.

Table 6.37 IL electrolyte model parameters

Symbol	Units	Value*
H_i	J kg^{-1}	3.279E4
H_c		7.622E4
H_a		2.669E5
H_{e1}		5.346E4
H_{e2}		1.029E6
M_c	kg	7.005E-4
M_a		7.891E-4
M_e		9.06E-3
A_i	s^{-1}	1.21E13
A_c		3.5E67
A_a		5.06E30
A_{e1}		8.85E23
A_{e2}		1.58E44
E_i	J mol^{-1}	1.45E5
E_c		8.44E5
E_a		3.71E5
E_{e1}		2.81E5
E_{e2}		5.86E5
$X_{i,0}$	dimensionless	0.1
$X_{c,0}$		0.75
$X_{a,0}$		0.75
$X_{e1,0}$		0.18
$X_{e2,0}$		0.82
ρ_c	kg m^{-3}	3600 [30]
ρ_a		3510 [390]
ρ_e		1510 (from manufacturers datasheet)
ρ_{cell}		1798
$C_{p,c}$	$\text{J kg}^{-1} \text{K}^{-1}$	1369 [30]
$C_{p,a}$		1437 [390]
$C_{p,e}$		1325 (calculated with [48])
$C_{p,cell}$		1336
V_{cell}	m^3	6.4194E-6
A_{surf}	m^2	1.57E-2
T_0	K	293

* the kinetic parameters were extracted from DSC results with a sample size of 1, therefore experimental errors are not available for these values.

Table 6.38 Conventional electrolyte model parameters

Symbol	Units	Value*	Ref.
H_{sei}	J kg ⁻¹	1.772E5	[424]
H_c		1.947E5	[30]
H_a		3.83E5	[424]
H_e		1.55E5	[30]
M_c	kg	7.005E-4	
M_a		7.891E-4	
M_e		5.12E-3	
A_{sei}	s ⁻¹	1.2	[424]
A_c		2E8	[30]
A_a		1.1E24	[424]
A_e		5.14E25	[30]
E_{sei}	J mol ⁻¹	4.46E4	[424]
E_c		1.03E5	[30]
E_a		2.2E5	[424]
E_e		2.74E5	[30]
n_{a1}	dimensionless	1	[424]
n_{a2}		0.3	[424]
n_{a3}		0.2	[424]
n_c		1	[30]
$x_{sei,0}$	dimensionless	0.15	[30]
$x_{c,0}$		0.04	[30]
$x_{a,0}$		0.75	[30]
$x_{e,0}$		1	[30]
ρ_c	kg m ⁻³	3600	[30]
ρ_a		3510	[390]
ρ_e		1280	[428]
ρ_{cell}		1792	
$C_{p,c}$	J kg ⁻¹ K ⁻¹	1369	[30]
$C_{p,a}$		1437	[390]
$C_{p,e}$		229	[428]
$C_{p,cell}$		493	
V_{cell}	m ³	4.4194E-6	
A_{surf}	m ²	1.561E-2	
T_0	K	293	

* kinetic parameters were obtained from published literature in which no errors were provided.

The system of ODEs was solved using a backward differentiation formula (BDF) solver, with a step size of one second. A smaller step size (1E-6) was found to give the same results, even over regions of thermal runaway where the simulation solution became unstable. Smaller step sizes came with a cost of high simulation time, therefore a step size of one second was used to reduce the computational time and effort.

6.5 Experimental

LFP | LTO pouch cells were assembled with different separators and either P13FSI electrolyte or a conventional electrolyte, for comparison. The pouch cells underwent formation cycling before being subjected to thermal abuse oven testing followed by disassembly for inspection.

6.5.1 Materials

The IL electrolyte was a commercial product containing 1-methyl-3-propylpyrrolidinium bis(fluorosulfonyl)imide (P13FSI) with 1.17 mol kg^{-1} LiFSI (P13FSI electrolyte, >99.5%) purchased from CoorsTek Fluorochemicals (USA). The conventional electrolyte was 1.2 M lithium hexafluorophosphate (LiPF_6) in EC / ethyl methyl carbonate (EMC) 2:1 v/v, purchased from soubrain MI (USA). FSI-C separator was prepared as described in Section 3.2. Glass fibre (GF) membrane (GA558X10IN, Advantech), $210 \mu\text{m}$ thickness and $0.6 \mu\text{m}$ nominal pore size, was purchased from Sterlitech Limited (USA). Commercial microporous polypropylene separator (Celgard 3501), $25 \mu\text{m}$ thickness and $0.064 \mu\text{m}$ average pore size, was purchased from Celgard, LLC (USA). LiFePO_4 (LFP, 10.0 mg cm^{-2} coating loading, approximately 48% porosity) was purchased from MTI Corporation (USA). $\text{Li}_4\text{Ti}_5\text{O}_{12}$ (LTO, 11.78 mg cm^{-2} coating loading, 50.2% porosity) was supplied through Argonne National Laboratory (USA) Cell Analysis, Modelling, and Prototyping (CAMP) Facility Electrode Library. Both electrodes used aluminium current collectors.

6.5.2 Pouch cell preparation and formation

For thermal abuse testing, pouch cells were used, instead of coin cells, to allow for temperature distribution measurement over the surface of the cell during thermal runaway.

LFP and LTO electrodes were cut into seven by 11 cm sheets with a connected strip of uncoated current collector for the tab. A tab extension was applied to LFP electrodes using a spot welder and $20 \mu\text{m}$ aluminium foil. No tab extension was necessary on the LTO electrode. The separators were cut into eight by 12 cm sheets. A cell stack was assembled with one cathode, one separator and one anode (sequentially), the assembly was taped together to prevent electrode misalignment in future handling. A pouch was cut from aluminium laminated film, with at least 1 cm pouch clearance on all four sides of the electrode stack. The cell stack was placed in the pouch and heat sealed on three sides. The open pouch was dried overnight in a vacuum oven at $50 \text{ }^\circ\text{C}$ before being transferred into an argon atmosphere glovebox ($\text{H}_2\text{O} < 100 \text{ ppm}$, $\text{O}_2 < 50 \text{ ppm}$) at CSIRO (Clayton, VIC).

Once inside the glovebox, electrolyte was added to the pouch, taking specific care to distribute the

electrolyte. Where possible, the electrolyte was added directly onto the separator to facilitate electrolyte distribution in the cell. Two different electrolytes were used for comparison. P13FSI electrolyte cells used 6 mL of P13FSI electrolyte (8 mL in GF cell due to increased separator thickness requiring more electrolyte volume for sufficient wetting). Conventional cells used 4 mL of 1.2 M $\text{LiPF}_6/\text{EC} / \text{EMC}$ (2:1 v/v) (6 mL in GF cell). The electrolyte filled pouch was left standing in the glovebox overnight to aid electrolyte absorption and distribution before vacuum sealing. After pouch standing, vacuum was applied twice to the pouch to remove trapped gasses then a vacuum seal was applied to seal the last side of the pouch (MTI Corporation (USA), MSK-115-III) at CSIRO (Clayton, VIC).

The 0.1 Ah pouch cells were removed from the glovebox and tested on a MACCOR unit (Series 4000, MACCOR, Inc., USA) at CSIRO (Clayton, VIC). Cells underwent formation cycling at room temperature in the voltage range 1.2 to 2.4 V at a C/20 rate (current density of 0.071 mA cm^{-2}). The cells underwent an initial charge to the upper voltage limit, then three cycles were performed for cell formation. One cycle is defined as a discharge followed by a recharge at the same rate with three minutes rest at the end of each discharge and charge. After completing formation, the pouch cells were subjected to thermal abuse testing, described below.

6.5.3 Thermal abuse testing

A pouch cell was placed lying down on a wire rack in a fan forced oven (ODWF24, LABEC, Laboratory Equipment Pty Ltd (Australia)) at PMB (Osborne, SA). Five K-type thermocouples (labelled A-E) were attached to the pouch cell surface with Kapton tape, as shown in Figure 6.72. Temperature was logged at one second intervals with a dataTaker (DT85, Thermo Fisher Scientific Inc. (Australia)). After attaching the thermocouples, the logger was set to record. The cell was left to equilibrate at room temperature in the oven for 15 minutes. The oven was then turned on and set to 150 °C. Once the oven temperature was stable at 150 °C, the cell was left for 60 minutes. Then the oven temperature was increased (to 180 or 200 °C) and left for a further 60 minutes. At the end of the test the oven was switched off and left to cool. In case of thermal runaway and / or cell venting, the oven exhaust was connected to an air scrubber (DefendAir HEPA 500 (F284), Dri-Eaz Products (USA)) drawing air at approximately $7 \text{ m}^3 \text{ min}^{-1}$. The exhaust was turned on at the end of the test, for 30 minutes before opening the oven door, to clear any gases or vapours present.

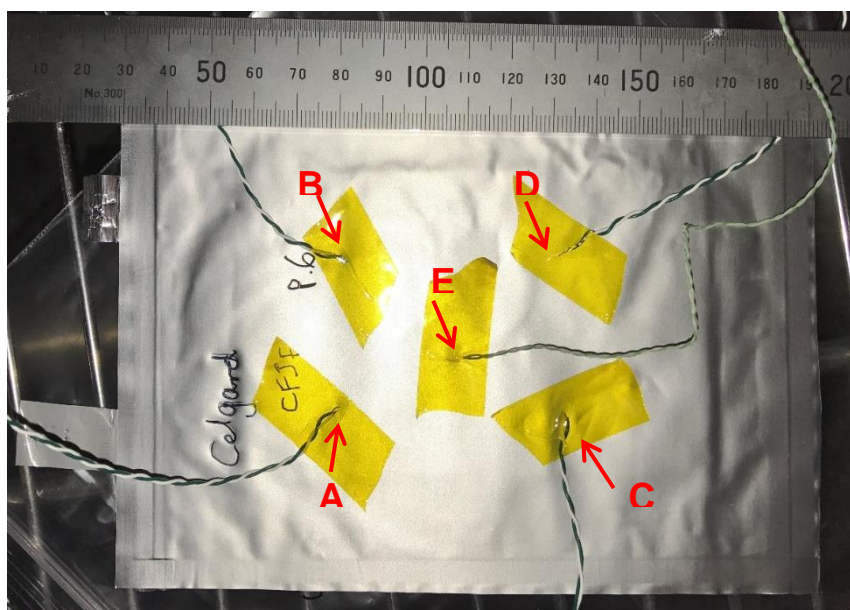


Figure 6.72 Thermocouple placement for oven test.

6.5.4 Pouch cell disassembly

After thermal abuse testing was complete, pouch cells were disassembled to inspect the electrodes and separator. A pouch cell was placed in a fume hood. The pouch was cut open along three sides, leaving the tab-sealed edge intact. A plastic spatula was used to separate and lift each cell layer. The cathode, separator and anode were inspected individually and photographed.

6.6 Results and discussion

6.6.1 Thermal abuse tests

LFP and LTO electrodes were selected, to combine with the P13FSI electrolyte, for thermal abuse tests of pouch cells with enhanced safety. These electrodes were found to have good thermal stability with P13FSI electrolyte in Section 5.4.3 and have also been reported in literature to have superior safety with conventional electrolytes [39, 353].

6.6.1.1 Formation

Each pouch cell underwent formation cycling at C/20 rate (current density 0.071 mA cm^{-2}) to facilitate electrode-electrolyte interphase formation, along with verifying that the pouch cells assembled were functioning cells prior to thermal abuse testing. Pouch cells were assembled with the novel separator (FSI-C), a commercial separator (Celgard 3501) and GF separator for comparison. as in Chapter 4, the GF cells contained two GF membranes to prevent short circuiting due to the large pore size. LFP | LTO cells containing P13FSI electrolyte were compared to

identical cells containing conventional electrolyte. The number of cells assembled and the cycling capacities for each material combination can be found in Table 6.39. Voltage plots of cycling for each cell type can be seen in Figure 6.73.

Table 6.39 Formation cycling capacities of LFP | LTO cells at current density $0.0315 \text{ mA cm}^{-2}$ with different separators and P13FSI electrolyte or conventional electrolyte (1.2 M LiPF_6 EC / EMC (2:1 v/v)). Values shown with standard deviation are average capacity calculated from replicate cells with a specific separator.

		No. of cells	Initial Charge	Cycle 1, mAh (g LFP)^{-1}		Cycle 2, mAh (g LFP)^{-1}		Cycle 3, mAh (g LFP)^{-1}	
				Dis.	Ch.	Dis.	Ch.	Dis.	Ch.
P13FSI electrolyte	GF	1	95.3	86.3	85.8	83.4	83.8	79.8	80.2
	Celgard 3501	1	7.5	6.0	60.2	56.0	101.4	86.1	84.6
	FSI-C	3	109.0 ± 6.8	97.1 ± 5.6	96.2 ± 5.8	93.4 ± 4.2	93.3 ± 3.9	89.3 ± 3.4	89.7 ± 3.2
Conventional electrolyte	GF	1	N/A*						
	Celgard 3501	1	121.8	107.9	106.6	104.5	102.7	101.2	99.7
	FSI-C	2	119.1 ± 0.3	111.8 ± 0.7	111.2 ± 0.9	109.3 ± 0.8	108.8 ± 0.8	107.3 ± 1.0	107.0 ± 1.1

* conventional electrolyte / GF cell not able to undergo cycling

The capacities (in mAh (g LFP)^{-1}) obtained during the 3rd formation cycle of the P13FSI electrolyte pouch cells are comparable to the capacities obtained in equivalent coin cells in Section 4.4.5. However, the capacities are substantially lower than the LFP theoretical capacity of $170 \text{ mAh (g LFP)}^{-1}$ [6, 352], LFP is the limiting electrode in the pouch cells. Among the P13FSI electrolyte cells, FSI-C cells appear to have better performance than the other separator cells. The higher voltage plateau difference of the GF cell (129 mV) compared to the FSI-C cell (89 mV) suggests the GF cell has a higher internal resistance. This is likely related to the increased thickness of the GF separator, compared to the thickness of FSI-C. It should be noted that the Celgard 3501 cell experiences extremely poor cycle capacity during the first charge and subsequent discharge, as seen in the voltage profile Figure 6.73b. In the following cycles, the cell capacity improves, which could indicate gradual wetting of the electrodes and separator. The absence of this trend in the other P13FSI electrolyte cells, with identical electrode materials, suggests that the gradual wetting is likely due to the separator material. Contrary to expectation, the Celgard 3501 cell outperformed the GF cell in the third formation cycle.

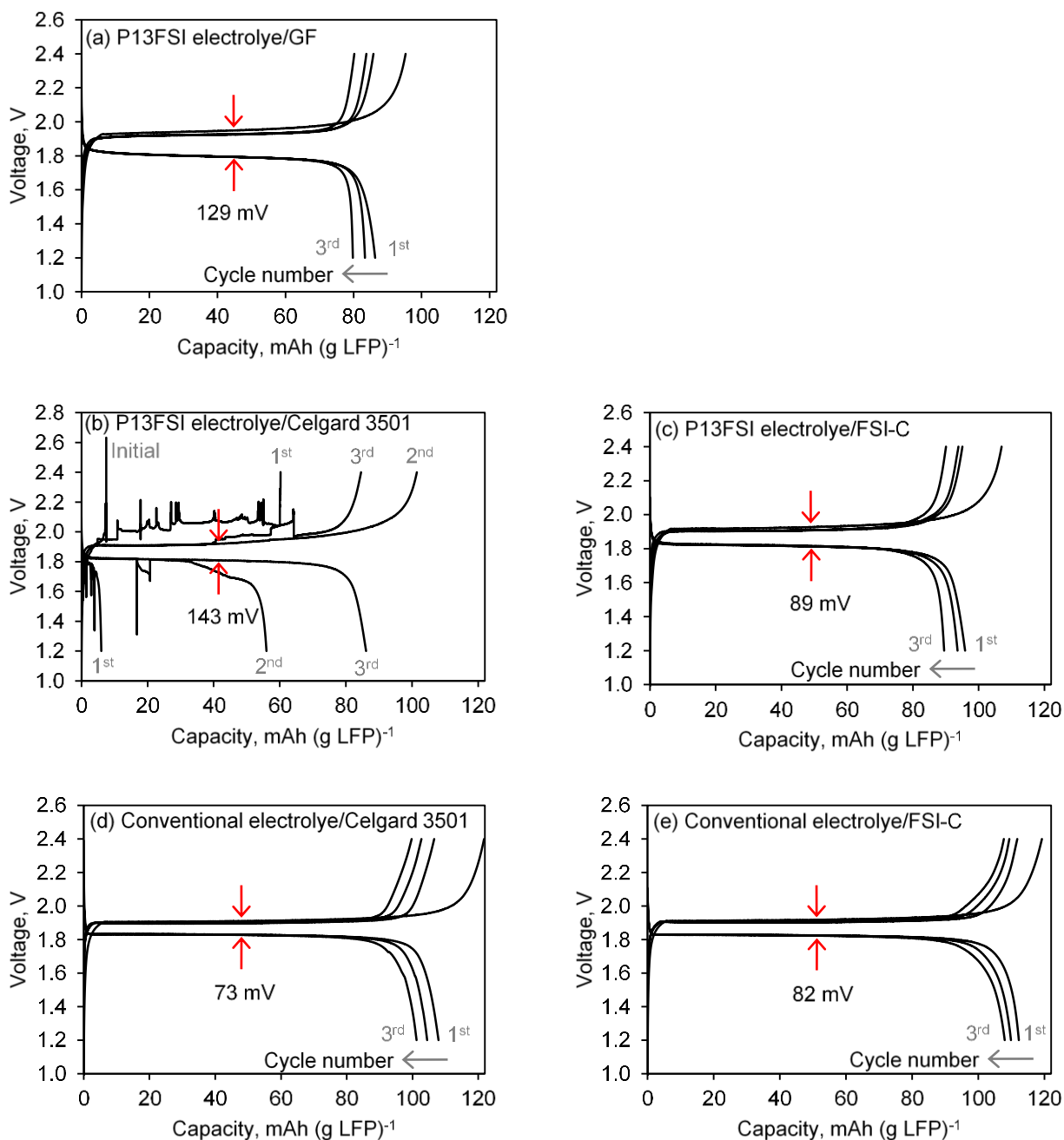


Figure 6.73 Voltage plots of formation cycles at current density 0.0315 mA cm⁻² with different separators and P13FSI electrolyte or conventional electrolyte (1.2 M LiPF₆ EC / EMC (2:1 v/v)). Cycle number indicated in grey. Plateau voltage difference (for 3rd cycle) indicated by red arrows.

Overall the conventional electrolyte pouch cells consistently outperformed the P13FSI electrolyte cells. The capacity in the 3rd formation cycle of the conventional electrolyte FSI-C cell is comparable to the results obtained in Section 4.4.5 for a conventional electrolyte FSI-B coin cell. The conventional electrolyte cells containing the FSI-C separator appear to have higher capacities than the conventional electrolyte cell with Celgard 3501. This suggests the FSI-C separator has better wetting with conventional electrolyte compared to the commercial Celgard 3501 separator.

6.6.1.2 Oven tests

LFP | LTO pouch cells with different separators and electrolytes were thermally abused in an oven test with exposure to 150 and 180 °C for approximately 60 minutes each. A two-step temperature profile was chosen based on the expected reaction temperatures for LFP | LTO pouch cell materials with P13FSI electrolyte or conventional electrolyte. At 150 °C the conventional electrolyte cells were expected to experience decomposition of the SEI as well as anode-electrolyte reaction, onset temperatures of 80 and 117 °C, respectively, determined by Ping, et al. [424] for LTO with a conventional electrolyte; while the P13FSI electrolyte cells were expected to have negligible heat release at 150 °C, based on the DSC results in Section 5.4.1 and 5.4.3. Increasing the temperature to 180 °C was hypothesised to initiate the decomposition reaction, presumed to be electrode-electrolyte interphase on the LFP electrode, with an onset temperature of 179 °C observed for charged LFP with P13FSI electrolyte in Section 5.4.3.4. All pouch cells were subjected to the two-step temperature profile, irrespective of electrolyte type, to allow a direct comparison to be made between the two electrolyte types during oven testing.

The surface temperature of the pouch was monitored with five thermocouples distributed over the surface (Figure 6.72). The oven test results of a LFP | P13FSI electrolyte-Celgard 3501 | LTO pouch cell are shown in Figure 6.74. The ambient oven temperature thermocouple (black line Figure 6.74) appears to be noisy, likely due to the fan forced effects causing constant circulation of the oven environment. The cell thermocouples also show some noise, but noticeably less than the ambient thermocouple. There is no sign of thermal runaway during the oven test, as is expected since the first exothermic event for P13FSI electrolyte cell materials should not occur until approximately 180 °C. Charged LFP with P13FSI electrolyte was observed to have an exothermic peak at approximately 200 °C with an onset temperature of approximately 180 °C (Section 5.4.3.4). It appears that the LFP | P13FSI electrolyte-Celgard 3501 | LTO pouch cell did not reach the onset temperature for this exothermic reaction, or if the reaction did occur it may not have been detected due to the amount of heat generated being negligible relative to the size of the pouch cell.

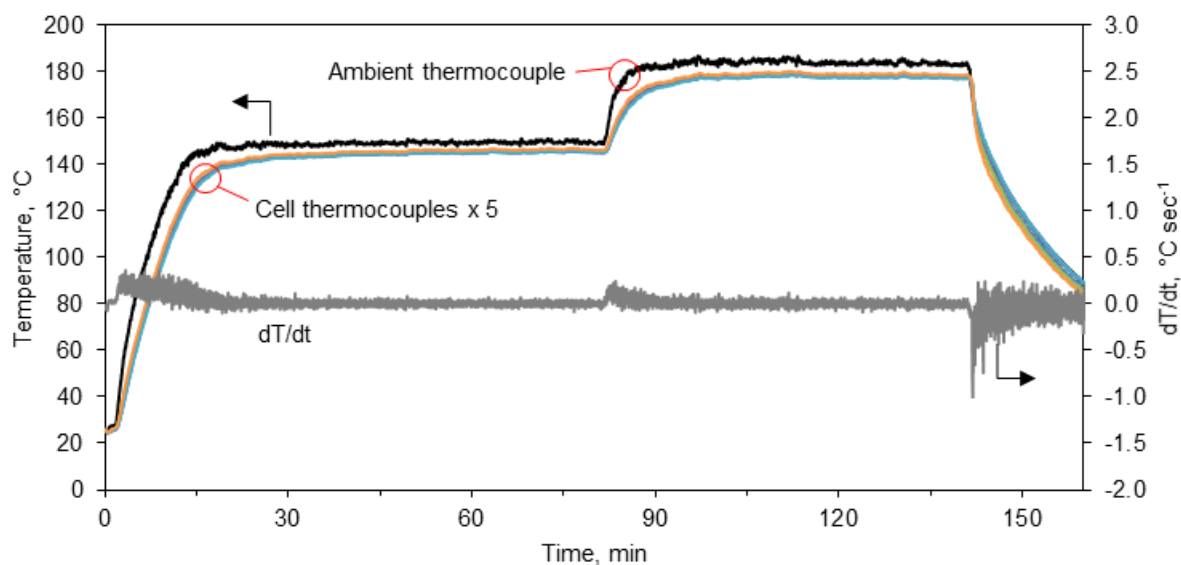


Figure 6.74 Temperature vs time plot for oven test of LFP | P13FSI electrolyte-Celgard 3501 | LTO pouch cell. Oven temperature at 150 °C for approximately 60 minutes, then raised to 180 °C for approximately 45 minutes. Including ambient thermocouple, five thermocouples recorded temperature over the surface of the pouch and provided average dT/dt from cell thermocouples.

The oven test before and after photos for a LFP | P13FSI electrolyte-Celgard 3501 | LTO pouch cell are shown in Figure 6.75. After exposure to 180 °C there is some discolouration visible on the top right corner of the pouch cell (circled in red Figure 6.75). This discolouration is most likely from some pouch leakage resulting in P13FSI electrolyte being present on the pouch surface prior to the oven test. As can be seen in Figure 6.75a, there is a slight discolouration in the before photo with the same pattern. There is evidence of some pouch swelling after exposure to 180 °C. In Section 5.4.3.4, a small exothermic event was detected at approximately 180 °C in charged LFP harvested from a P13FSI electrolyte cell; if the same reaction(s) occurred while the pouch cell was held at 180 °C with gas production, this may account for the pouch swelling observed during the oven testing.



Figure 6.75 Oven test (a) before and (b) after photos of LFP | P13FSI electrolyte-Celgard 3501 | LTO pouch cell. Discolouration on pouch surface before and after oven testing circled in red.

The oven test results of a LFP | conventional electrolyte-Celgard 3501 | LTO pouch cell is shown in Figure 6.76. Similar to the P13FSI electrolyte cell, there is no evidence of temperature rise associated with thermal runaway. The oven test before and after photos for a LFP | conventional electrolyte-Celgard 3501 | LTO pouch cell are shown in Figure 6.77. There is evidence of pouch swelling. The thermal stability of individual materials was discussed in Section 5.4.3. Charged LFP with 1 M LiPF₆ EC / DMC (1:1) electrolyte did not show any exothermic peaks below 200 °C [362, 383]. 1 M LiPF₆ EC / EMC (1:1 v/v) electrolyte alone, similar to 1.2 M LiPF₆ EC / EMC (2:1 v/v) used in this work, did not show exothermic behaviour until approximately 250 °C. Both material thermal stabilities agree with the absence of thermal runaway observed for the LFP | conventional electrolyte-Celgard 3501 | LTO pouch cell.

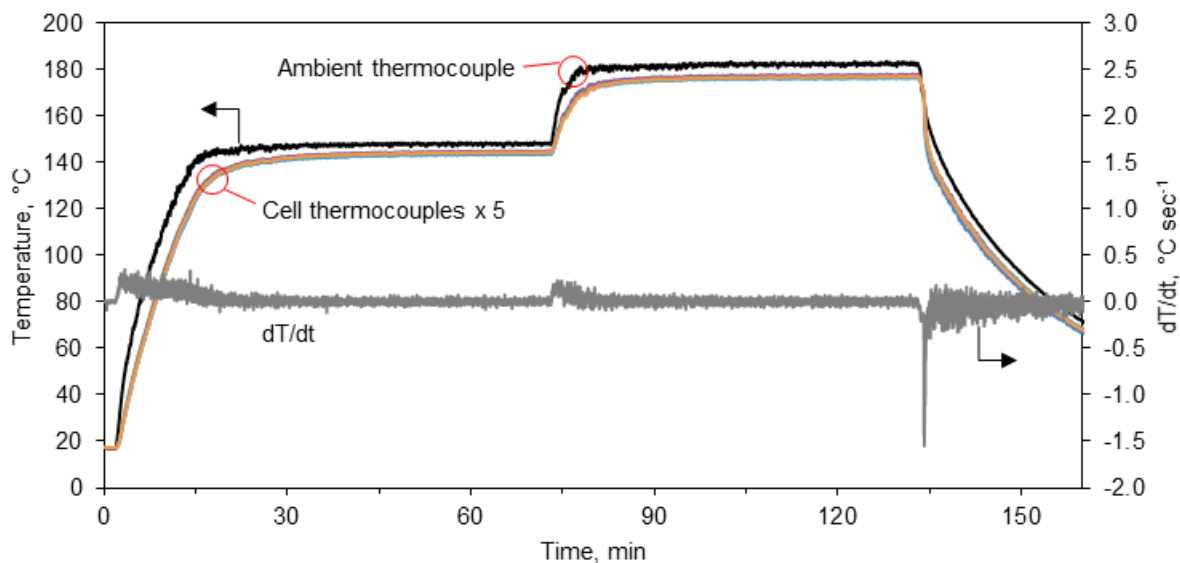


Figure 6.76 Temperature vs time plot for oven test of LFP | conventional electrolyte-Celgard 3501 | LTO pouch cell. Oven temperature at 150 °C for approximately 60 minutes, then raised to 180 °C for approximately 45 minutes. Including ambient thermocouple, five thermocouples over surface of the pouch and average dT/dt from cell thermocouples.

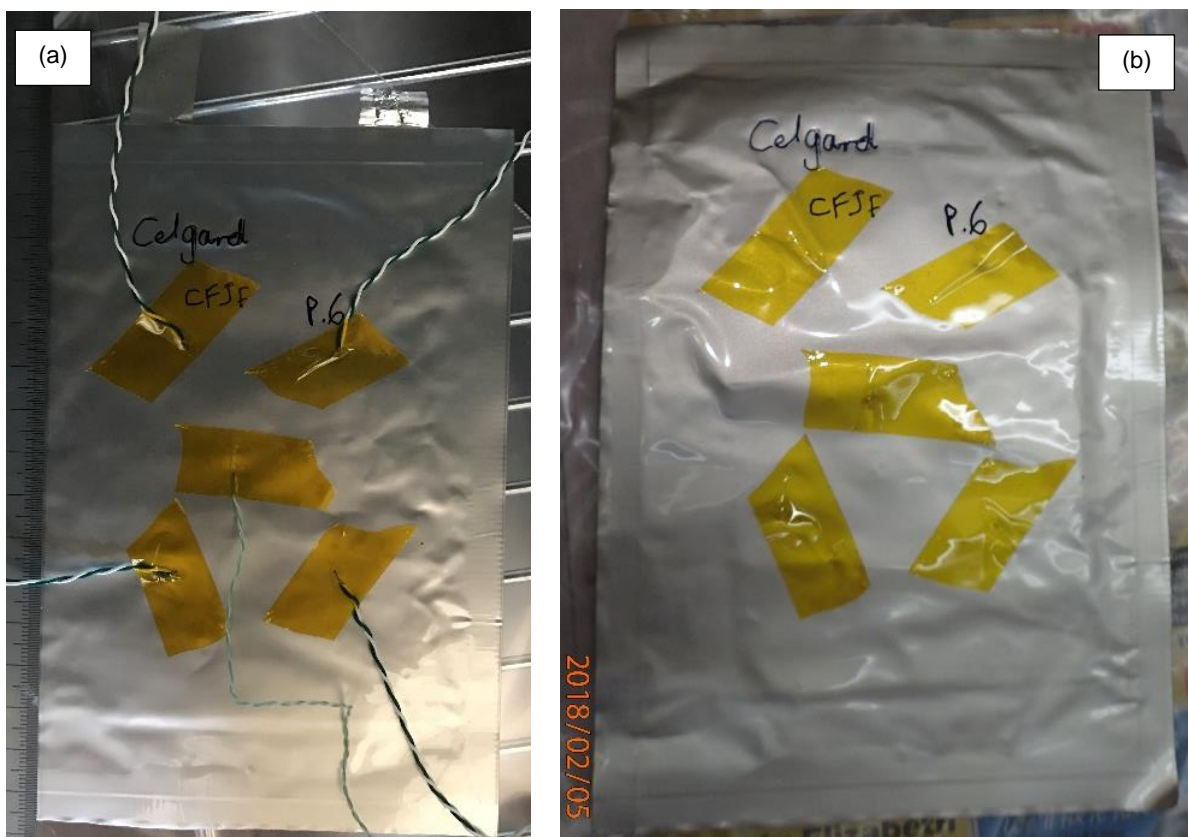


Figure 6.77 Oven test (a) before and (b) after photos of LFP | conventional electrolyte-Celgard 3501 | LTO pouch cell.

Charged LTO with 1 M LiPF₆ EC / DMC (1:1 v/v) has been reported to have a small exothermic peak at approximately 110 °C, due to SEI reaction and re-formation, but the LTO-electrolyte reaction peak does not occur until approximately 300 °C [383]. It is possible that the exothermic reaction at 110 °C may have been dwarfed by the temperature rise of the cell, approximately 20 to 145 °C, as the oven heated up. Additionally, the thermocouple distribution and pouch size relative to the heat generated by the small exothermic reaction at approximately 110 °C may have contributed to no obvious temperature increase being observed. The small amount of pouch swelling visible in Figure 6.77 may be from by-products of LTO SEI decomposition and subsequent formation reactions at approximately 110 °C described by Yi, et al. [383].

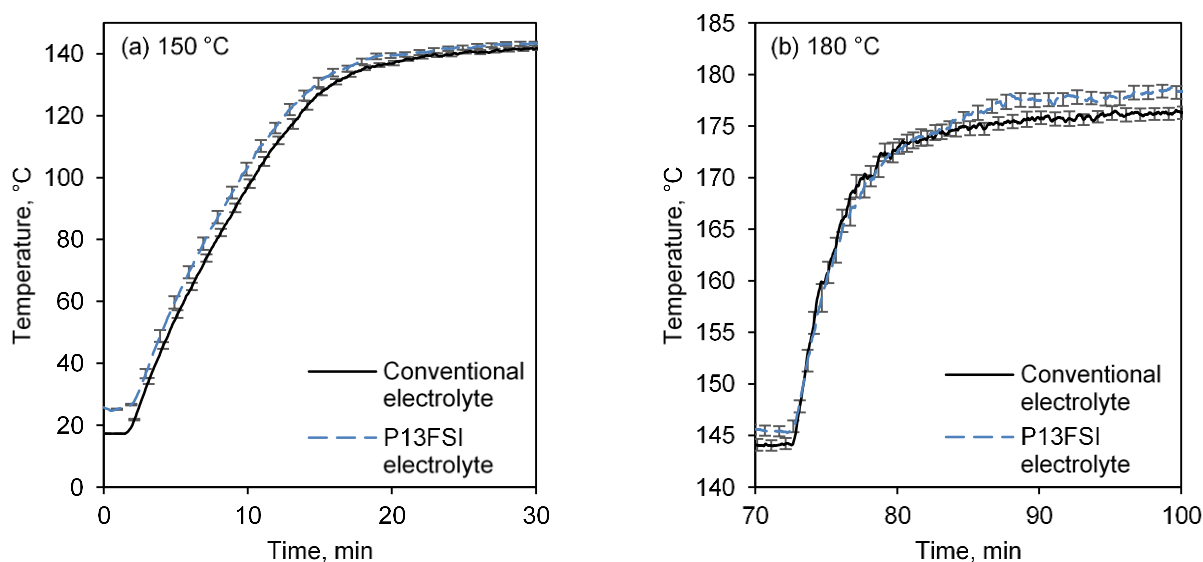


Figure 6.78 Temperature vs time plot for LFP | Celgard 3501 | LTO pouch cells during the temperature increased region of the oven tests. Overlay of the average cell temperature of pouch cells with P13FSI electrolyte (dashed blue line) and conventional electrolyte (solid black line). Standard deviation for five thermocouple measurements over the surface of the cell is shown every minute during the test.

The temperature profiles of LFP | Celgard 3501 | LTO pouch cells with P13FSI electrolyte and conventional electrolyte are shown in Figure 6.78, overlaid for comparison of the temperature response during heating stages of the oven test. When the oven was set to 150 °C (Figure 6.78a) the two cells increased in temperature following the same trend, which is likely due to the convection effects of the oven being similar in both tests. When the temperature was increased to 180 °C, the cells again follow the same temperature profile during the main increased, however, at approximately 175 °C the temperatures diverge slightly. The conventional electrolyte cell remains at approximately 175 ±2 °C for the rest of the test, while the P13FSI electrolyte cell increases further to approximately 178 °C. Unfortunately the LFP | Celgard 3501 | LTO cell oven tests were

not replicated therefore repeatability could not be confirmed for the temperature rise observed in the conventional electrolyte cell, compared to the P13FSI electrolyte cell.

Oven testing of LFP | FSI-C | LTO pouch cells with P13FSI electrolyte and conventional electrolyte was also performed (see Appendix N), since no evidence of thermal runaway had been observed at 180 °C for the IL electrolyte cells, the second hold temperature was increased to 200 °C.

Unfortunately, this resulted in a sawtooth pattern during the 200 °C hold which can be related to the oven automatically toggling on and off, due to a maximum operating temperature of 200 °C.

The temperature profiles, where similar to the Celgard 3501 cells, showing no evidence of thermal runaway.

The temperature profile of a LFP | conventional electrolyte-GF | LTO pouch cell during an oven test is shown in Figure 6.79. This cell differs from the cell in Figure 6.76 because it has a different separator material, as well as not having undergone formation cycling due to a faulty tab making connection not possible. The lack of formation cycling means that the SEI stability in this cell will be different than other cells. Since the thermal stability of the SEI has been previously related to the thermal stability of a cell overall [363], the behaviour of this cell is expected to be different. There is a small event towards the end of the 150 °C temperature increase (indicated by red arrow in Figure 6.79) that could suggest the presence of an exothermic reaction. The event occurred in all the thermocouples on the cell and does not coincide with a temperature increase in the ambient thermocouple, this indicates the event observed is a result of an internal cell reaction.

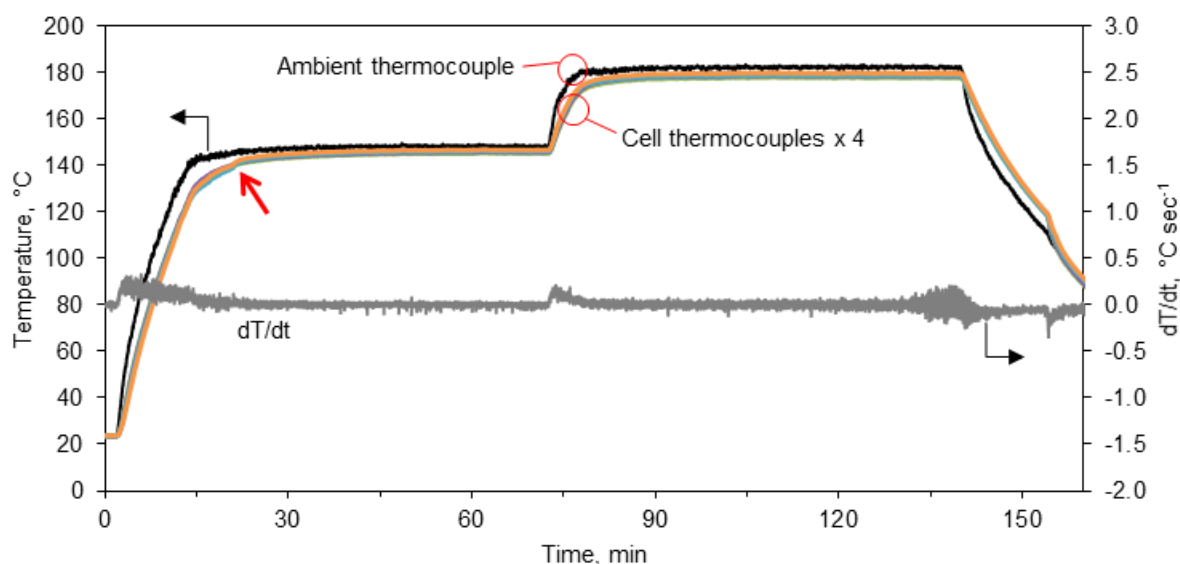


Figure 6.79 Temperature vs time plot for oven test of LFP | conventional electrolyte-GF | LTO pouch cell. Oven temperature at 150 °C for approximately 60 minutes, then raised to 180 °C for approximately 45 minutes. Including ambient thermocouple, five thermocouples over surface of the pouch and average dT/dt from cell thermocouples.

Inspection of the LFP | conventional electrolyte-GF | LTO pouch cell following oven testing revealed extreme swelling of the pouch most likely from electrolyte gassing (see Figure 6.80), however, it does not appear that pouch rupture occurred during the test. Compared to the conventional electrolyte-Celgard 3501 pouch cell (Figure 6.77b), there was substantially more swelling visible in the GF cell, which may be related to the larger electrolyte volume used in the GF cells. It is not possible to determine the direct cause of the swelling; although the pouch cells had different separators, there was also a difference in the formation performed on the cells. The GF separator was expected to be thermally stable and have little impact on the cell thermal stability, as discussed in Section 5.4.2. The most likely reason for the swelling is the difference in SEI stability in the conventional electrolyte-GF cell. The reaction observed by Yi, et al. [383] at 110 °C on LTO with a conventional electrolyte was due to decomposition of the SEI on the LTO surface. As there was no formation cycling on the conventional electrolyte-GF cell, there was likely a less stable SEI present to protect the electrolyte from reaction with the anode material when the cell reached 110 °C. This may have resulted in more heat being generated and more gas produced.



Figure 6.80 Oven test after photos of LFP | conventional electrolyte-GF | LTO pouch cell, showing severe swelling (a) pouch surface and (b) pouch side.

6.6.1.3 Cell disassembly

Following oven testing, each pouch cell was opened for inspection of the materials: anode, cathode, separator and electrolyte. The inside of a LFP | P13FSI electrolyte-Celgard 3501 | LTO pouch cell following oven testing is shown in Figure 6.81. Figure 6.81a confirms the presence of P13FSI electrolyte, although discolouration is evident. Melted polymer from the separator can be seen at the bottom of the pouch cell in Figure 6.81b. It appears that the separator has discoloured after melting at elevated temperatures in the presence of P13FSI electrolyte. Some delamination of the cathode coating occurred when separating the cell layers (Figure 6.81c) but the anode coating appears to be intact following the oven test. In all Figure 6.81 photos, free liquid electrolyte is visible, and appears to be well distributed over the electrodes.

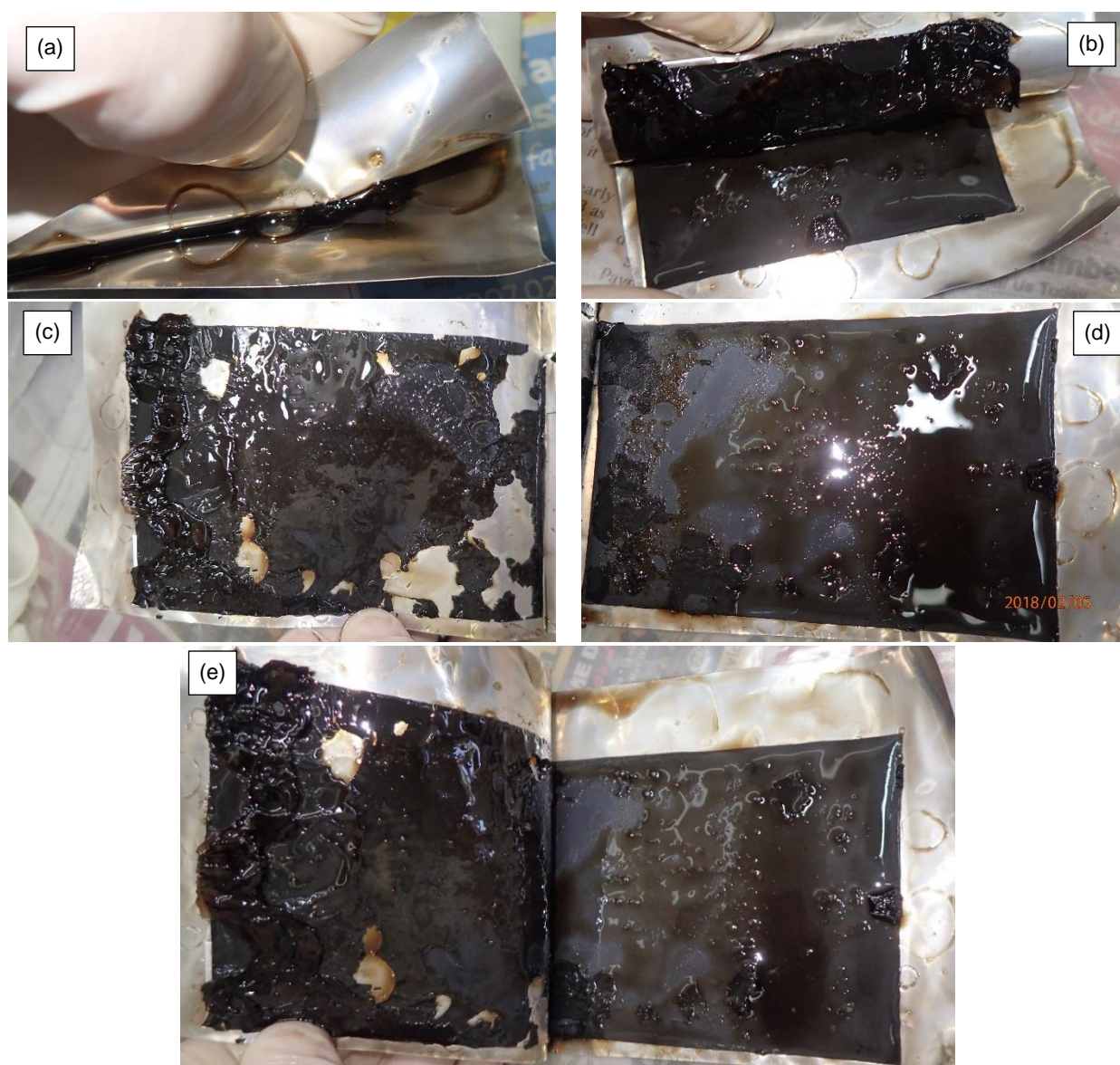


Figure 6.81 Disassembly photos of a LFP | P13FSI electrolyte-Celgard 3501 | LTO pouch cell following oven testing.

The inside of a LFP | conventional electrolyte-Celgard 3501 | LTO pouch cell following oven testing is shown in Figure 6.82. Some liquid electrolyte is present, but the presence of electrode bubbling (Figure 6.82a) and dry spots (Figure 6.82d) suggest that some electrolyte gasification has occurred during the oven test, which agrees with the pouch swelling observed (Figure 6.77). The separator (Figure 6.82b,c) shows thermal shrinkage during melting, similar to Figure 6.81, however, separator discoloration was not observed in the conventional electrolyte cell. Again, the cathode was substantially delaminated. Other than the presence of some bubbles, the anode is relatively intact which suggests that the LTO electrode had better adherence between the coating and the current collector foil, than the LFP electrode. Note, the green tape visible was used to secure the cell stack together during assembly and does not appear to have undergone any reaction in the cell environment.



Figure 6.82 Disassembly photos of a LFP | conventional electrolyte-Celgard 3501 | LTO pouch cell following oven testing.

The inside of a LFP | P13FSI electrolyte-FSI-C | LTO pouch cell following oven testing is shown in Figure 6.83. There is some liquid electrolyte visible in Figure 6.83a, but the electrodes appear to be covered in a gelatinous layer, which is most likely the FSI-C separator wet with P13FSI electrolyte. There appears to be no distinct separator layer to maintain electrode separation therefore an internal short circuit most likely occurred. The cell voltage prior to disassembly was approximately 0.4 V which also suggests a partial internal short circuit occurred during the oven test. This could be due to thermal shrinkage of the separator at increased temperatures, as expected based on the thermal dimensional stability discussed in Section 3.3.2.5. The melting temperature of poly(vinylidene fluoride-hexafluoropropylene) (PVDF-HFP) is approximately 160 °C (Section 5.4.2) and shrinkage of the PVDF-HFP layers in the FSI-C separator may have occurred during the 180 °C hold in the oven test. The cathode appears to have preferentially adhered to the gelatinous separator over the current collector in some areas, as shown in Figure 6.83a. During cell disassembly, the gelatinous separator mostly remained on the anode surface (Figure 6.83e), however, there are some areas in the anode that appear to have no separator and very little electrolyte (Figure 6.83b).

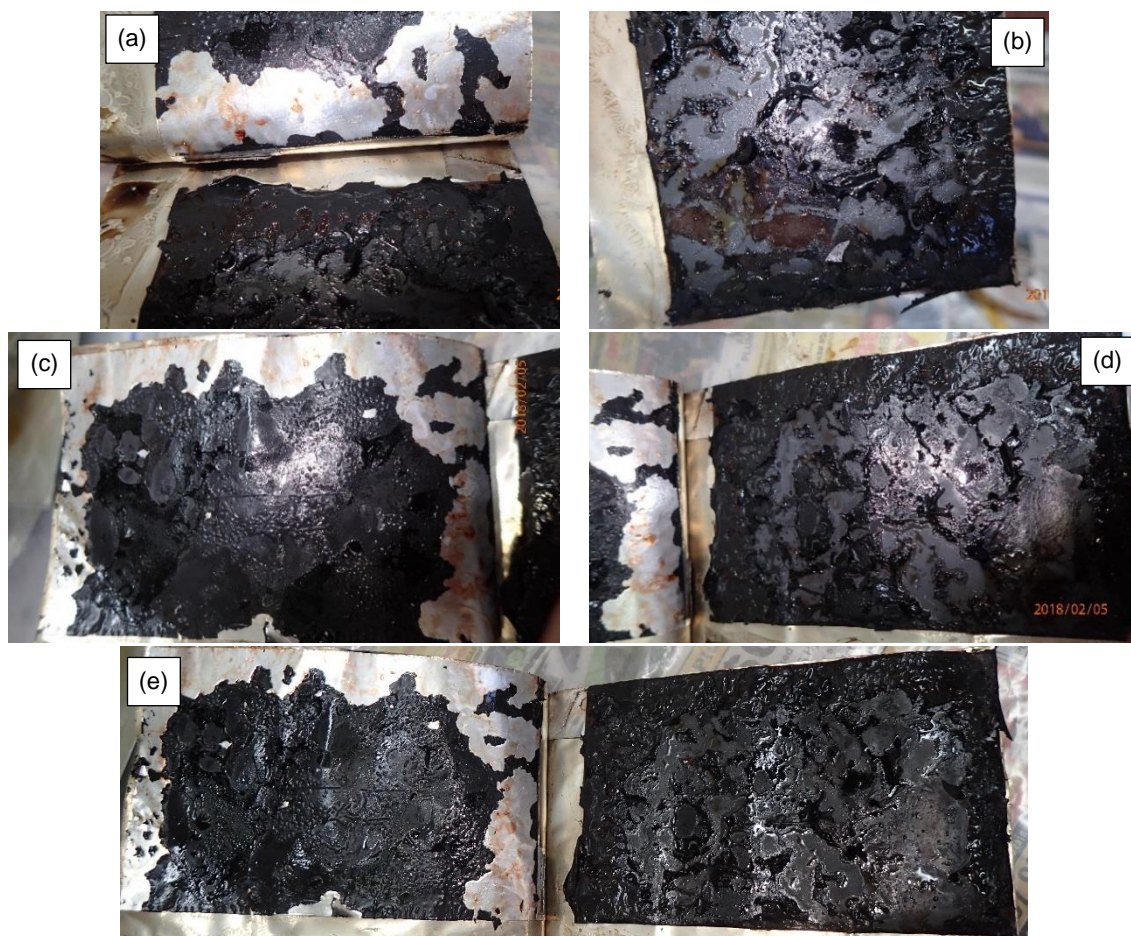


Figure 6.83 Disassembly photos of a LFP | P13FSI electrolyte-FSI-C | LTO pouch cell following oven testing.

The inside of a LFP | conventional electrolyte-FSI-C | LTO pouch cell following oven testing is shown in Figure 6.84. There is very little electrolyte visible which suggests some electrolyte gasification occurred, similar to the conventional electrolyte-Celgard 3501 pouch cell (Figure 6.82). Figure 6.84, however, has a yellow substance visible on both electrode surfaces and on the interior of the pouch (Figure 6.84a). Since there is no clear separator layer remaining on the electrode surface this substance could be the result of interaction between the conventional electrolyte solvents and the FSI-C separator polymers. The electrolyte solvents appear to have undergone gasification during the oven test, leaving behind the yellowish substance. It is clear in Figure 6.84d that some of the cathode has adhered to the anode during cell disassembly and there appears to be melted polymer around the edges, which may have encouraged the adherence.

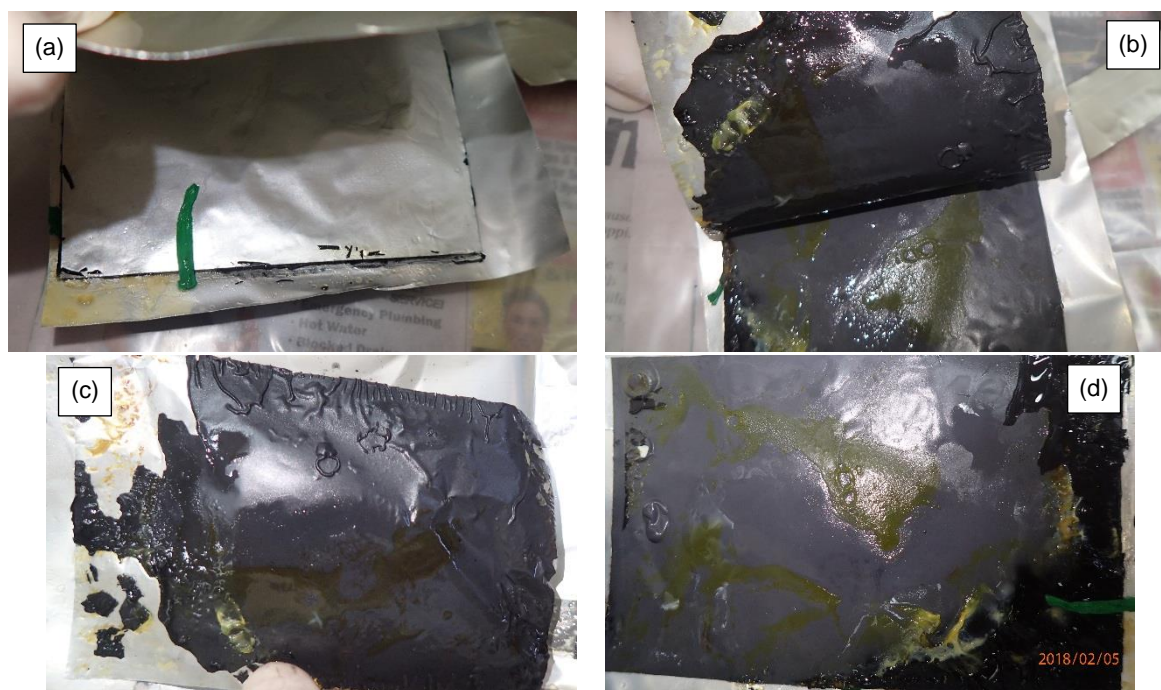


Figure 6.84 Disassembly photos of a LFP | conventional electrolyte-FSI-C | LTO pouch cell following oven testing.

The inside of a LFP | conventional electrolyte-GF | LTO pouch cell following oven testing is shown in Figure 6.85. Severe pouch swelling was visible (Figure 6.85a) and when the pouch was opened it appeared that the electrodes had moved apart in the pouch due to this (Figure 6.85b), despite the use of tape during assembly to secure the cell stack (melted green tape visible in Figure 6.85e). The GF separator layers (note two GF membranes were used) appear to be intact and each GF membrane adhered to an electrode during pouch swelling. Some anode delamination occurred when lifting the GF off the LTO electrode (Figure 6.85e). The GF separator and

electrodes also appeared dry (Figure 6.85c-e) which indicates gasification of the electrolyte during oven testing.



Figure 6.85 Disassembly photos of a LFP | conventional electrolyte-GF | LTO pouch cell following oven testing.

In both Celgard 3501 cells, separator melting was obvious and liquid electrolyte was present in both pouch cells, suggesting very little interaction between either electrolyte and Celgard 3501 (except for discolouration in P13FSI electrolyte). In the conventional electrolyte-GF cell the GF membrane was intact and electrolyte vaporisation was evident, also indicating little or no interaction between the separator and the electrolyte. However, in the FSI-C cells, the separator was not immediately visible. In the P13FSI electrolyte cell the FSI-C separator appeared to have

formed a gel with the electrolyte and was unevenly distributed over the electrode surface after oven testing. Meanwhile in the conventional electrolyte cell the FSI-C separator appears to have partially dissolved and / or melted during oven testing. In both cases, the FSI-C separator interacts with the electrolyte and the interactions may compromise the separator functionality and integrity in the cell at elevated temperatures.

6.6.2 Thermal abuse model

6.6.2.1 Kinetic parameter estimation

The temperature range and heat release of the five DSC peaks selected to describe the thermal abuse of a LFP | P13FSI electrolyte | LTO pouch cell is given in Figure 6.86. These peaks were selected from DSC thermograms of P13FSI electrolyte and charged LFP and LTO from P13FSI electrolyte cells, peak descriptions provided in Table 6.40. The onset and endset temperature for each peak as well as the specific heat release (J g^{-1}) was obtained from analysis of the DSC peaks (previously discussed in Section 5.4). Kinetic analysis of these peaks was undertaken as described in Section 6.3.4 to obtain the model parameters for the thermal abuse of a LFP | P13FSI electrolyte | LTO cell.

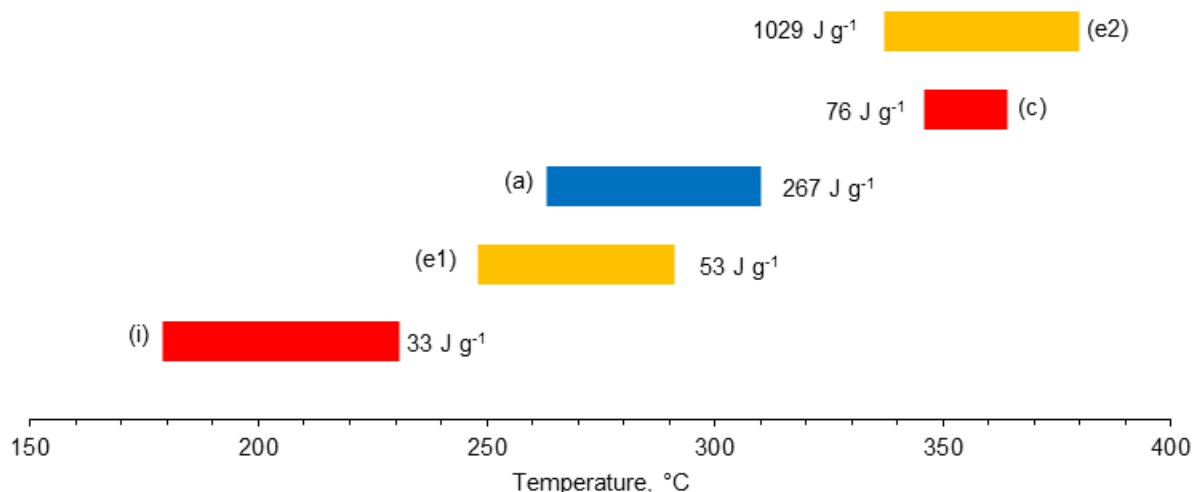


Figure 6.86 Temperature range and heat release for sequence of reactions selected to simulate thermal abuse of LFP | P13FSI electrolyte | LTO cell: (i) electrode-electrolyte interphase decomposition on cathode, (e1) first reaction of P13FSI electrolyte, (a) anode-electrolyte reaction, (c) cathode-electrolyte reaction and (e2) decomposition of P13FSI electrolyte. Cathode reactions shown in red. Anode reaction shown in blue. Electrolyte reactions shown in yellow.

For each reaction peak included in the P13FSI electrolyte reaction model (described in Section 6.4.1), the DSC data (heat flow versus temperature) was used to extract kinetic parameters using the Arrhenius equation, as described in Section 6.4.2. As an example, Figure 6.87 shows the $\ln(k)$ vs $1/T$ plot for the 355 °C peak in the P13FSI electrolyte thermogram (Figure 5.2c). The linear fit equation and R^2 value are shown. The fit equation slope was used to determine the reaction activation energy, $E: -E/R_{gas} = -70470.91$, and the fit equation intercept was used to determine the reaction frequency factor, $A: \ln(A) = 101.77$.

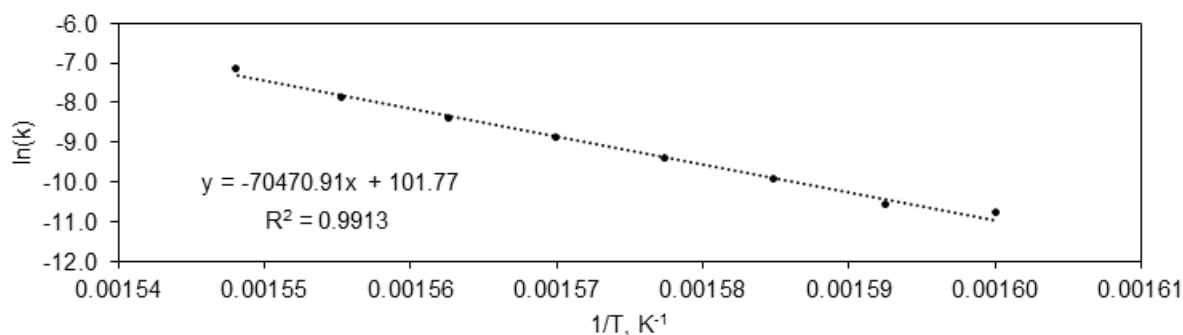


Figure 6.87 $\ln(k)$ vs $1/T$ plot for e2, the 355 °C peak in P13FSI electrolyte thermogram, used to calculate E and A reaction parameters for $n = 1$. Markers are data points and the dotted line is the linear fit. Fit equation and R^2 value shown in plot.

The linear fit equation and R^2 values for each DSC peak used to determine the kinetic parameters for the LFP | P13FSI electrolyte | LTO cell model are shown in Table 6.40. $\ln(k)$ vs $1/T$ plots for the other four reaction peaks are in Appendix O. It can be seen from Table 6.40 that the R^2 of linear fit for the other four reactions are not as close to one as e2 ($R^2 = 0.9913$). The lower R^2 values are likely to be from the fitted peaks containing multiple overlapping thermal events, therefore the overall linear fit pertains to the shape of the combined peak, which was not always a smooth peak.

Table 6.40 $\ln(k)$ vs $1/T$ linear fit equations for P13FSI electrolyte cell reactions: i, c, a, e1 and e2. Resulting kinetic parameters are shown in Table 6.37.

Model label	Reaction peak Description	In(k) vs 1/T linear fit equation				
		*Onset, °C	*Endset, °C	Slope	Intercept	R ²
<i>i</i>	204 °C peak of charged LFP with P13FSI electrolyte	179	231	-17474.61	30.13	0.9106
<i>c</i>	352 °C peak of charged LFP with P13FSI electrolyte	346	364	- 101583.28	155.53	0.8963
<i>a</i>	294 °C peak of charged LTO with P13FSI electrolyte	263	310	-44606.22	70.70	0.8749
<i>e1</i>	269 °C peak of P13FSI electrolyte	248	291	-33769.81	55.14	0.9021
<i>e2</i>	355 °C peak of P13FSI electrolyte	337	380	-70470.91	101.77	0.9913

* peak temperatures have an error of ± 0.2 K, from temperature accuracy of DSC instrument.

6.6.2.2 Model validation

The thermal abuse model was compared to the oven test results by including temperature steps in the model ambient temperature to reflect the oven test procedure (Figure 6.88 and Figure 6.89). The stepped model ambient temperature (T_{amb}) (green dashed line Figure 6.88 and Figure 6.89) was described by a piecewise function set to 150 °C for 50 minutes (stage 1), 180 °C for 70 minutes (stage 2) then 60 °C for 20 minutes (stage 3) without transitions regions. The experimental and simulation oven test results for a LFP | P13FSI electrolyte | LTO pouch cell are shown in Figure 6.88, using an equivalent heat transfer coefficient of $h = 4.5 \text{ W m}^{-2} \text{ K}^{-1}$ in the simulation. An equivalent heat transfer coefficient has been used to incorporate the combined effects of radiative, convective and conductive heat transfer in a simulation [30, 82, 84]. The effects of variation in heat transfer coefficient is discussed in the next section. The equivalent heat transfer coefficient used in the model was selected to have the same temperature profile shape during the heating steps at the start of stage 1 and 2. Appendix P shows the oven profile simulation with different h values. The equivalent heat transfer coefficient of $4.5 \text{ W m}^{-2} \text{ K}^{-1}$ was selected because although the experimental temperature is approximately five minutes behind the simulation, the simulation temperature shape during the temperature increase is closest to that of the experimental temperature.

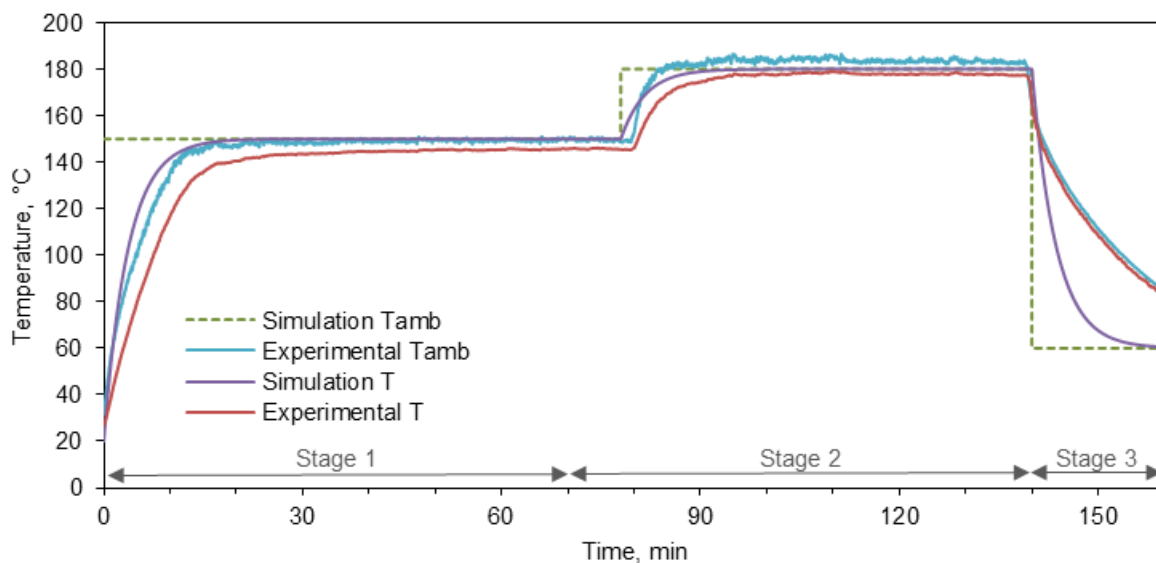


Figure 6.88 Simulation and experimental temperature evolution of LFP | P13FSI electrolyte | LTO pouch cell oven test, oven temperature of 150 °C for 70 minutes and 180 °C for 50 minutes. $h = 4.5 \text{ W m}^{-2} \text{ K}^{-1}$.

During the temperature increase in stage 1, the cell temperature appears to reach an equilibrium a little faster in the simulation (approximately 23 minutes) than in the experiment (approximately 26 minutes). However, the experimental cell reaches a temperature equilibrium of approximately 144 °C and does not reach 150 °C. This is likely an artefact of the oven used in the oven tests. During stage 1 the experimental temperature does not go above 145 °C, which indicates that the average ambient temperature in the oven was approximately 145 °C during the test, not 150 °C as set. The temperature increase is slightly less steep in the experimental results compared to the simulations results, which suggests there may be complex heat transfer properties during the temperature increase that are not reflected in the constant equivalent heat transfer coefficient used in the simulation.

The timing for the beginning of the oven test stage 2 does not match up in the experimental and simulation results. This is due to the experimental nature of the procedure followed during the oven test experiments; the oven temperature was set to 150 °C, and the 60 minutes was not started until the oven thermostat stabilised at 150 °C., therefore the time profile for the experimental cell does not exactly align with T_{amb} profile used in the simulation. Although the experimental stage 2 begins a few minutes behind the simulation, the shape of the temperature profiles during the increase is similar. It should be noted that during stage 2 the experimental cell has a holding temperature of approximately 178 °C, which aligns more closely with the simulation results than in stage 1.

Stage 3 was intended to simulate cell cooling at the end of the oven test. The simulation temperature decreased more rapidly than the experimental temperature because in reality the cooling process was slower as it also includes cooling of the oven itself. Considering the P13FSI electrolyte cell does not undergo any thermal events below 180 °C (Figure 6.86), the thermal model is an acceptable simulation of the pouch cell temperature during the oven test.

The conventional electrolyte cell was observed to experience some thermal events during the oven test, evidenced by pouch swelling (Figure 6.80), so a more eventful temperature profile was expected from oven test simulations for a LFP | conventional electrolyte | LTO pouch cell (Figure 6.89). A large variation is seen for the simulation and experimental temperature profiles during stage 1. While the experimental cell appears to increase in temperature affected only by the oven temperature, the simulation results reveal a temperature spike. During the simulated oven test, the temperature spikes to approximately 152 °C, approximately eight minutes into the simulation suggesting a heating source other than heat transfer from ambient oven temperature, i.e. an internal reaction causing the temperature to increase above 150 °C. This could have been from a small exothermic reaction of SEI decomposition on the LTO surface at approximately 110 °C reported in literature for charged LTO with 1 M LiPF₆ EC / DMC (1:1 v/v) [383].

Based on the pouch swelling observed following oven testing of conventional electrolyte cells it was clear that internal reactions had occurred. The absence of the temperature rise in the profile during the experimental oven test may be related to the pouch swelling. When pouch swelling occurs the pouch surface, with the attached thermocouples, is forced away from the cell stack by gas production and the resulting pouch distortions observed. When this occurs, the thermocouples are no longer in close proximity to the active materials undergoing reaction, effectively insulating the thermocouples from heat being generated by the reactions. Considering the small amount of active material available in the 0.1 Ah pouch cells and the related heat generation, it is possible that the thermocouple displacement was enough during swelling to result in a negligible temperature change at each thermocouple position. Additionally, the thermal abuse model does not include the pouch and tab materials [429], which are present in the oven test experiments. The pouch and tab materials provide additional thermal mass and surface area to the system, which could also contribute to the lower cell temperatures observed during the experimental oven test, compared to the simulation results. Therefore, inclusion of cell tabs and pouch material in the thermal abuse model may have improved the agreement between the simulation and experiment.

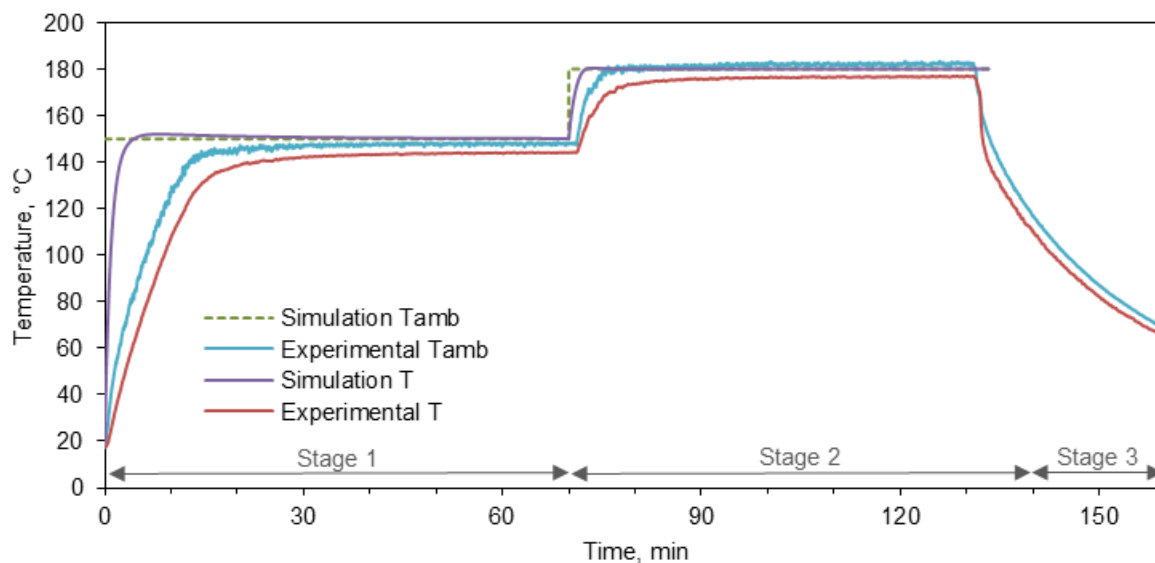


Figure 6.89 Simulation and experimental temperature evolution of LFP | conventional electrolyte | LTO pouch cell oven test, oven temperature of 150 °C for 70 minutes and 180 °C for 50 minutes. $h = 4.5 \text{ W m}^{-2} \text{ K}^{-1}$.

6.6.2.3 Heat transfer coefficient

The heat dissipation rate for the cell, Q_{heat} , is described by Eq. (11), which includes the surface area (A_{surf}), an equivalent heat transfer coefficient (h) and the difference in temperature between the cell (T) and the surroundings (T_{amb}). The cell surface area is constant for all P13FSI electrolyte simulations and the difference in temperature is dictated by the test procedure, i.e. ambient oven test temperature. The equivalent heat transfer coefficient, however, varies depending on the experimental set up and conditions used. The heat transfer coefficient used in this work is an equivalent coefficient that includes the combined effects of three types of heat transfer [82]: radiation, convection and conduction. The selection of coefficient is based on the work of Peng, et al. [82] who developed a LCO | graphite conventional electrolyte cell thermal abuse model and varied the equivalent heat transfer coefficient, h , from 0.1 up to $45 \text{ W m}^{-2} \text{ K}^{-1}$. Peng, et al. [82] suggested that the smaller h value corresponds to heat conduction effects only, as would be experienced by a cell in the centre of a battery pack, while the larger h value includes radiation, convection and conduction effects as could be experienced by a cell on the edge of a battery pack [82].

The results of varying the equivalent heat transfer coefficient in an oven test simulation for a LFP | P13FSI electrolyte | LTO pouch cell with an ambient oven temperature of 250 °C are shown in Figure 6.90. Since no evidence of thermal runaway was observed at 200 °C for the IL electrolyte cells during oven testing, the oven test simulation was conducted at a higher temperature. At an oven temperature of 250 °C none of the simulations result in thermal runaway, no matter what h

value was used. The time taken for the cell to reach the ambient oven temperature is directly related to the h value; as h increases, the time taken for the cell to reach 250 °C decreases (indicated by arrow in Figure 6.90).

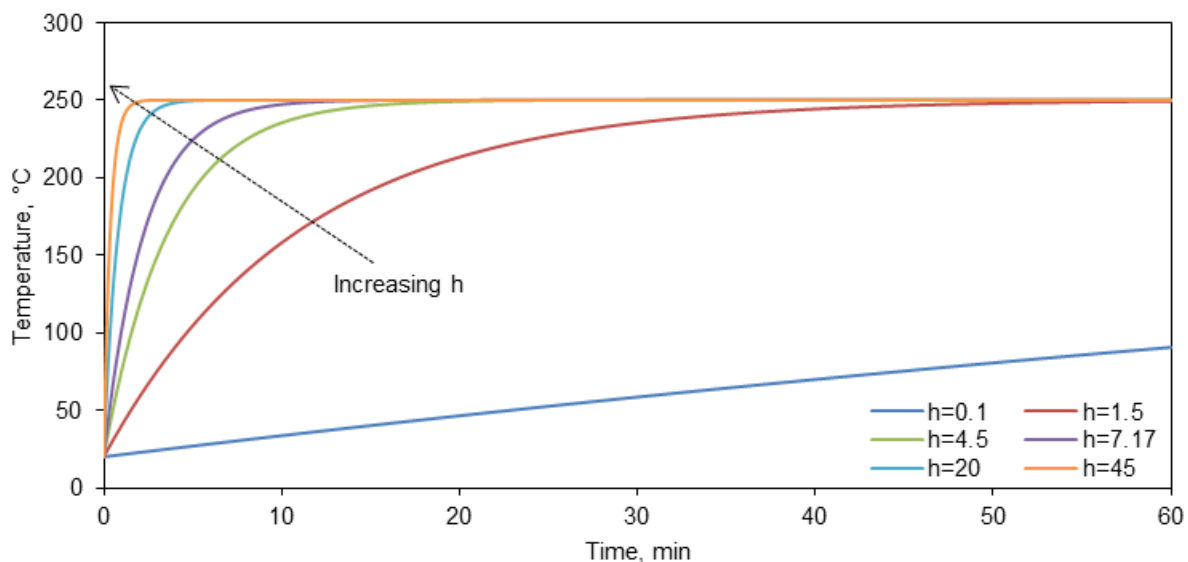


Figure 6.90 Temperature profile of LFP | P13FSI electrolyte | LTO pouch cell during 250 °C oven test simulations, $h = 0.1, 1.5, 4.5, 7.17, 20$ and $45 \text{ W m}^{-2} \text{ K}^{-1}$.

The heat generation rate for different reactions in a LFP | P13FSI electrolyte | LTO pouch cell are shown in Figure 6.91 during a 250 °C oven test simulation with $h = 4.5$ and $20 \text{ W m}^{-2} \text{ K}^{-1}$. In both cases the electrode-electrolyte interphase decomposition reaction, Q_i , occurs first and continues until the reaction material is used up. Before the Q_i reaction is completed, the first electrolyte reaction, Q_{e1} , begins and continues until the simulation ends after 60 minutes. The other reactions produce negligible heat at 250 °C and do not contribute to the overall heat generation. The overall heat generation, Q_{gen} , is shown in Figure 6.92 for all the h values used. The same overall heat generation profile is seen for all h values, except as the h value increases the peaks sharpen and occur earlier in the simulation.

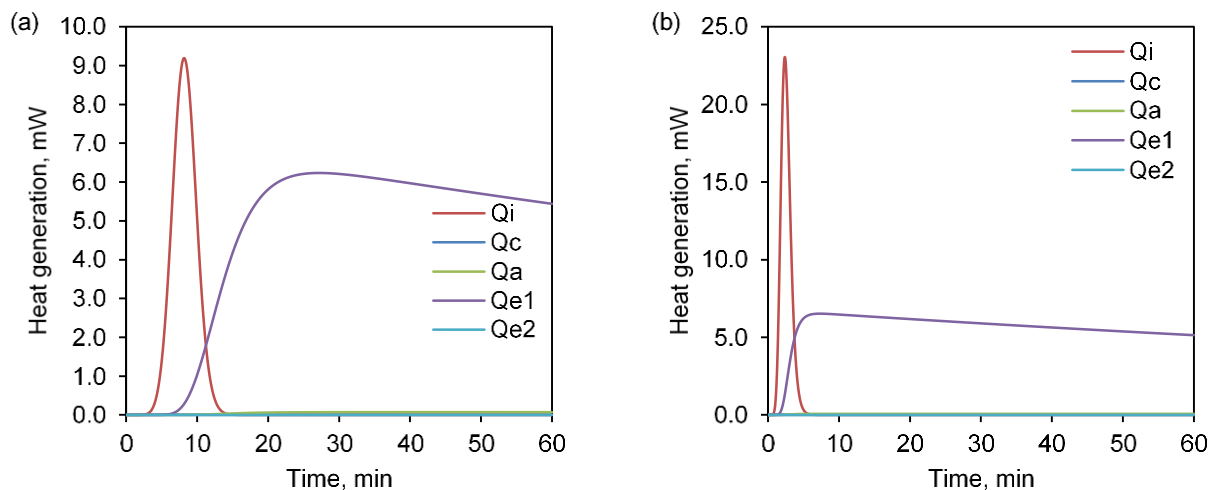


Figure 6.91 Heat generation contributions of different reactions for LFP | P13FSI electrolyte | LTO pouch cell during 250 °C oven test simulation (a) $h = 4.5 \text{ W m}^{-2} \text{ K}^{-1}$ and (b) $h = 20 \text{ W m}^{-2} \text{ K}^{-1}$; electrode-electrolyte interphase heat generation Q_i , cathode heat generation Q_c , anode heat generation Q_a , and electrolyte heat generation Q_{e1} and Q_{e2} .

The total heat generation was used to calculate the total heat release, q_{exo} (J), during the simulation (area under Q_{gen} curve) for comparison of the different equivalent heat transfer coefficients (Figure 6.93). The total heat was found to increase with increasing h value, towards a limit of approximately 23.3 J, determined by material and reaction parameters for the pouch cell in the simulation. The increase in total heat can be attributed to the amount of electrolyte reaction (x_{e1}) that occurs during the simulation, since the heat released by the electrode-electrolyte interphase reaction, q_i from Q_i curve, is limited by the amount of active material available to react, however the Q_{e1} reaction does not go to completion during the simulation (only run for 60 minutes), therefore the onset and duration of the first electrolyte reaction influences the amount of heat it generates (q_{e1}). From Figure 6.91 it can be seen that with a h value of $4.5 \text{ W m}^{-2} \text{ K}^{-1}$, the Q_{e1} reaction rate does not substantially increase until approximately 12 minutes however with a h value of $20 \text{ W m}^{-2} \text{ K}^{-1}$ the Q_{e1} reaction takes off within three minutes of the simulation beginning, therefore generating more heat during the simulation than the initial simulation. In all cases the total heat generation was not sufficient to cause a thermal runaway process in the cell, therefore exposing the 0.1 Ah LFP | P13FSI electrolyte | LTO pouch cells in this work to an ambient temperature of 250 °C for 60 minutes will not result in thermal runaway.

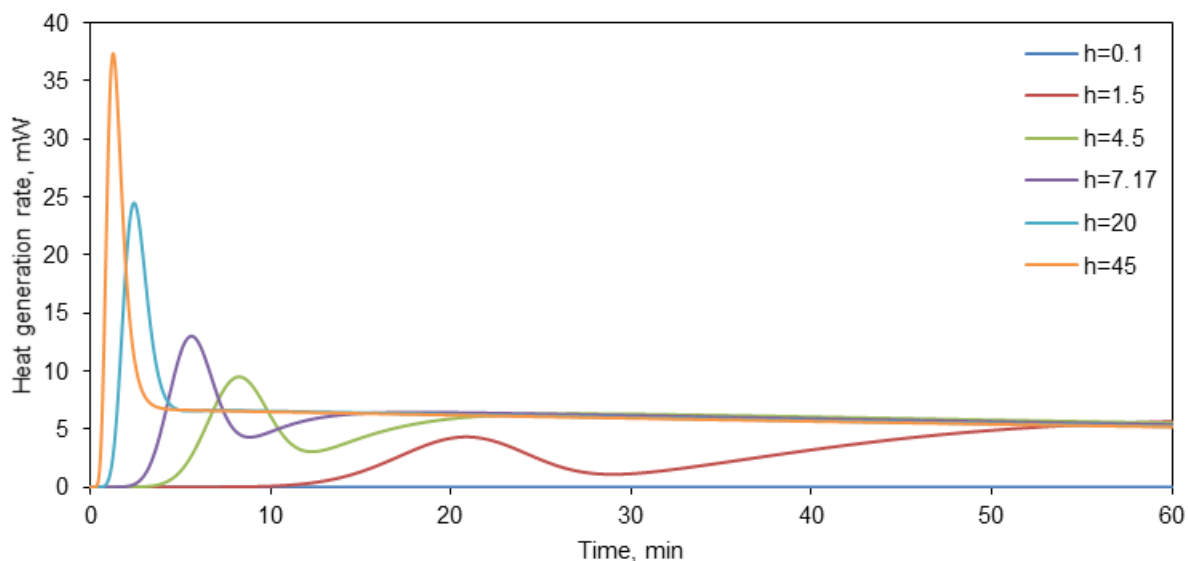


Figure 6.92 Heat generation profile of LFP | P13FSI electrolyte | LTO pouch cell during 250 °C oven test simulations, total heat generation (Q_{gen}). $h = 0.1, 1.5, 4.5, 7.17, 20$ and $45 \text{ W m}^{-2} \text{ K}^{-1}$.

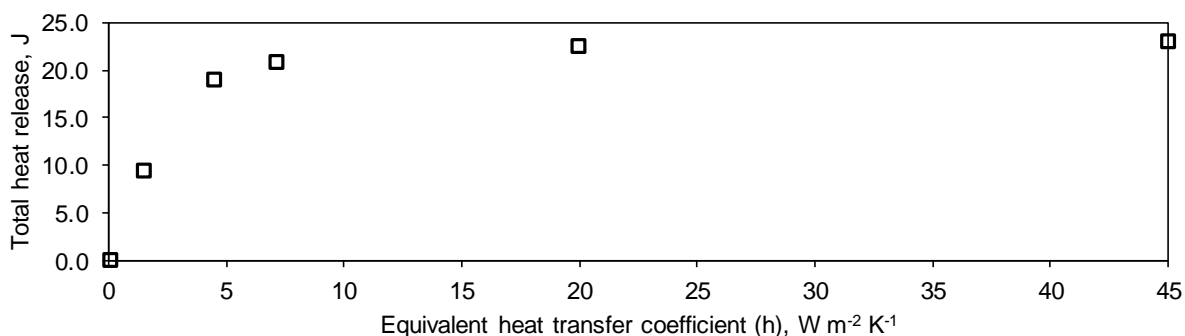


Figure 6.93 Equivalent heat transfer coefficient (h) vs total heat release for LFP | P13FSI electrolyte | LTO pouch cell during 250 °C oven test simulations.

6.6.2.4 Oven test temperature simulations

Oven test simulations of LFP | P13FSI electrolyte | LTO pouch cells at different ambient temperatures are shown in Figure 6.94. The oven tests at 150, 200, 300 and 350 °C did not result in thermal runaway, but the oven test at 370 °C did. In the event of a thermal runaway the simulation solution became unstable and was terminated, as can be observed at 640 °C in the 370 °C oven test (orange line, Figure 6.94). The degree of conversion for each material in the cell during the 200, 300 and 370 °C oven test simulations is shown in Figure 6.95; x_i - electrode-electrolyte interphase decomposition; x_a - anode electrolyte reactions; x_c - cathode electrolyte reactions; x_{e1} - first electrolyte decomposition; x_{e2} - second electrolyte decomposition. As the first

exothermic reaction does not occur until approximately 180 °C (see Figure 6.86), the 150 °C oven test simulation responded as expected with no temperature events and no further analysis was performed.

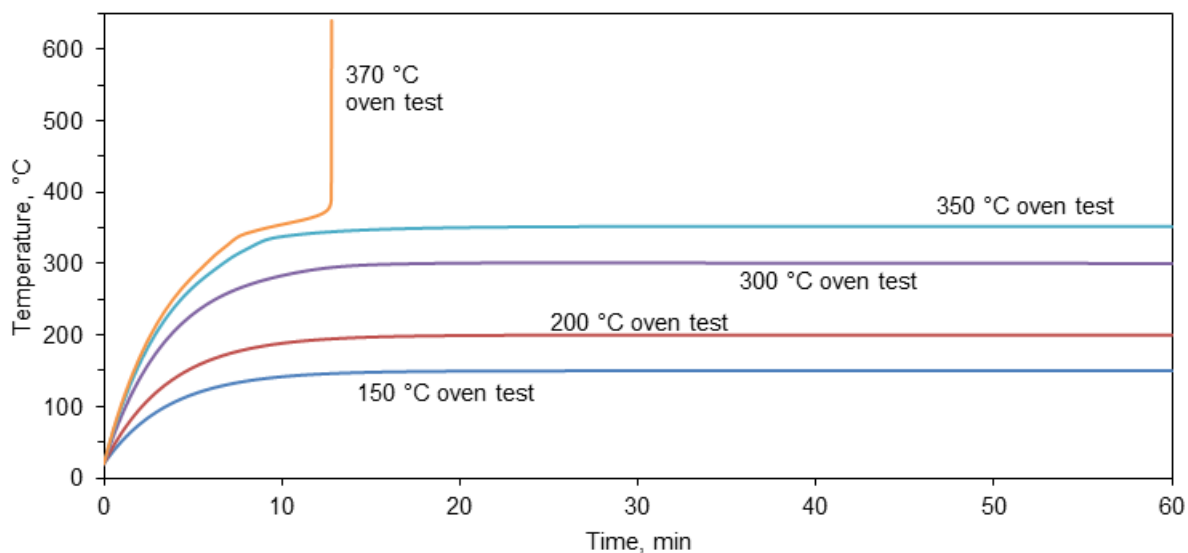


Figure 6.94 LFP | P13FSI electrolyte | LTO pouch cell temperature evolution during 150, 200, 300, 350 and 370 °C oven test simulations. $h = 4.5 \text{ W m}^{-2} \text{ K}^{-1}$.

In the 200 °C oven test simulation the only reaction that occurred was decomposition of the electrode-electrolyte interphase, x_i , which began slowly at 2.6 minutes and the reaction rate increased as the simulation continued (Figure 6.95a). The heat generation from this reaction is not enough to cause thermal runaway in the cell. Since the reaction temperature for the next exothermic reaction in the cell is at approximately 250 °C (Figure 6.86), no further reaction occurs during the 200 °C oven test simulation. It is expected that in a real cell that some of the electrode-electrolyte interphase would reform as it decomposed and therefore the reactions could continue for longer than the simulation indicated, since the simulation x_i reaction is limited by the $x_{i,0}$ value specified. However, it is still expected that the heat released from this reaction would not be enough to push the cell into thermal runaway.

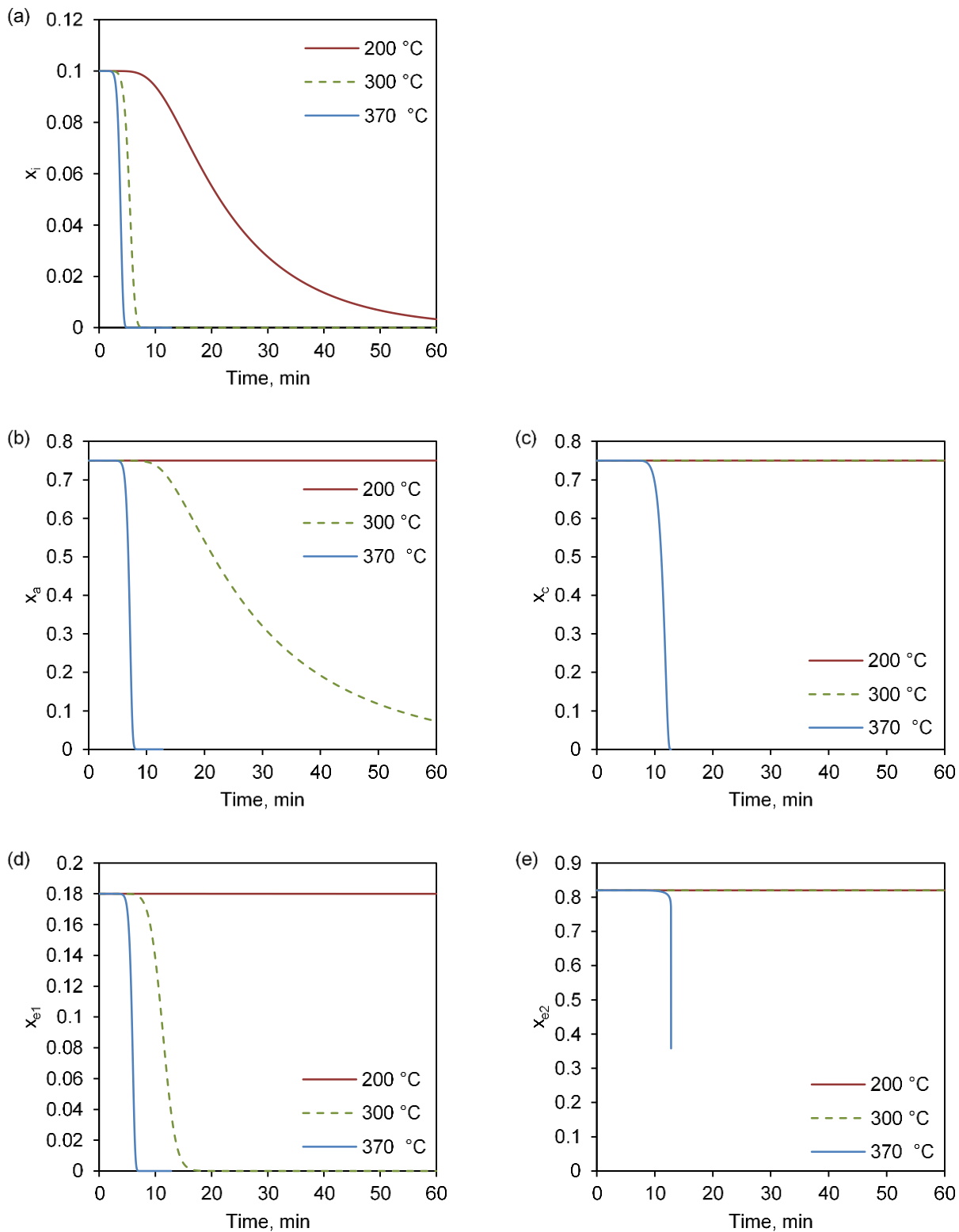


Figure 6.95 LFP | P13FSI electrolyte | LTO pouch cell 200, 300 and 370 °C oven test simulations conversion degree in for (a) electrode-electrolyte interphase decomposition x_i , (b) anode electrolyte reactions x_a , (c) cathode electrolyte reactions x_c , (d) first electrolyte decomposition x_{e1} and (e) second electrolyte decomposition x_{e2} . $h = 4.5 \text{ W m}^{-2} \text{ K}^{-1}$.

When the simulated ambient oven temperature is increased to 300 °C, more reactions begin to occur. The first reaction is the electrode-electrolyte interphase decomposition x_i (Figure 6.95a), this occurs in the first ten minutes of the simulation. As the interphase reaction concludes from exhausting the available material in the simulation, the first electrolyte decomposition reaction commences, x_{e1} , approximately eight minutes into the simulation (Figure 6.95d). Similarly, this reaction also continues to completion by approximately 18 minutes when the reaction material has been used up. Simultaneously, the anode-electrolyte reaction starts, x_a , and a steady decrease in available material is observed for the remainder of the simulation (Figure 6.95b). Since the cell temperature does not exceed the anode-electrolyte reaction peak temperature (294 °C) by more than a few degrees, the reaction continues slowly and by the end of the simulation x_a has dropped to approximately 5%.

The heat generation from each reaction during the 300 °C oven test simulation is shown in Figure 6.96. Heat generation contributions (Figure 6.96b) agree with the reaction conversion plots (Figure 6.95), both show that the cathode-electrolyte (x_c) and electrolyte decomposition (x_{e2}) reactions do not occur during the 300 °C oven test simulation. The results show that even at 300 °C for 60 minutes, the LFP | P13FSI electrolyte | LTO pouch cell does not enter thermal runaway and the heat generated by Q_i , Q_{e1} and Q_a reactions does not push the cell into thermal runaway. A similar result was seen for the 350 °C oven test simulation, with no thermal runaway occurring during the 60 minutes simulation.

The 370 °C oven test simulation goes into thermal runaway after approximately 13 minutes (Figure 6.94). The reaction conversion degree and the heat generation rates are shown in Figure 6.95 and Figure 6.97, respectively, for the 370 °C oven test simulation. The electrode-electrolyte interphase decomposition, first electrolyte reaction and anode-electrolyte reaction (x_i , x_{e1} and x_a) all go to completion within the first ten minutes of the simulation. This is not unexpected considering these reactions all have peak reaction temperatures below 300 °C. At approximately ten minutes the cathode-electrolyte reaction (x_c) begins as the cell temperature approaches 350 °C. This reaction began slowly then the heat released caused a temperature rise, increasing the reaction rate. As the temperature increased from the cathode reactions, the cell approached the second electrolyte decomposition temperature (355 °C). The vertical temperature increase in Figure 6.94, indicating thermal runaway, corresponds with a sharp decrease in the x_{e2} reaction conversion (Figure 6.95e) and a rapid increase in the total heat generation (Figure 6.95a). This indicates that once the second electrolyte decomposition reaction occurs, the cell will enter thermal runaway. The heat released by each reaction during thermal runaway agrees with the corresponding DSC results to within $\pm 1 \text{ J g}^{-1}$ except for the second electrolyte reaction. The second electrolyte reaction has a heat release of 1029 and $2.14 \times 10^{13} \text{ J g}^{-1}$ for the DSC and simulations results, respectively, which highlights the instability experienced by the simulation during the decomposition reaction of the

electrolyte (x_{e2}).

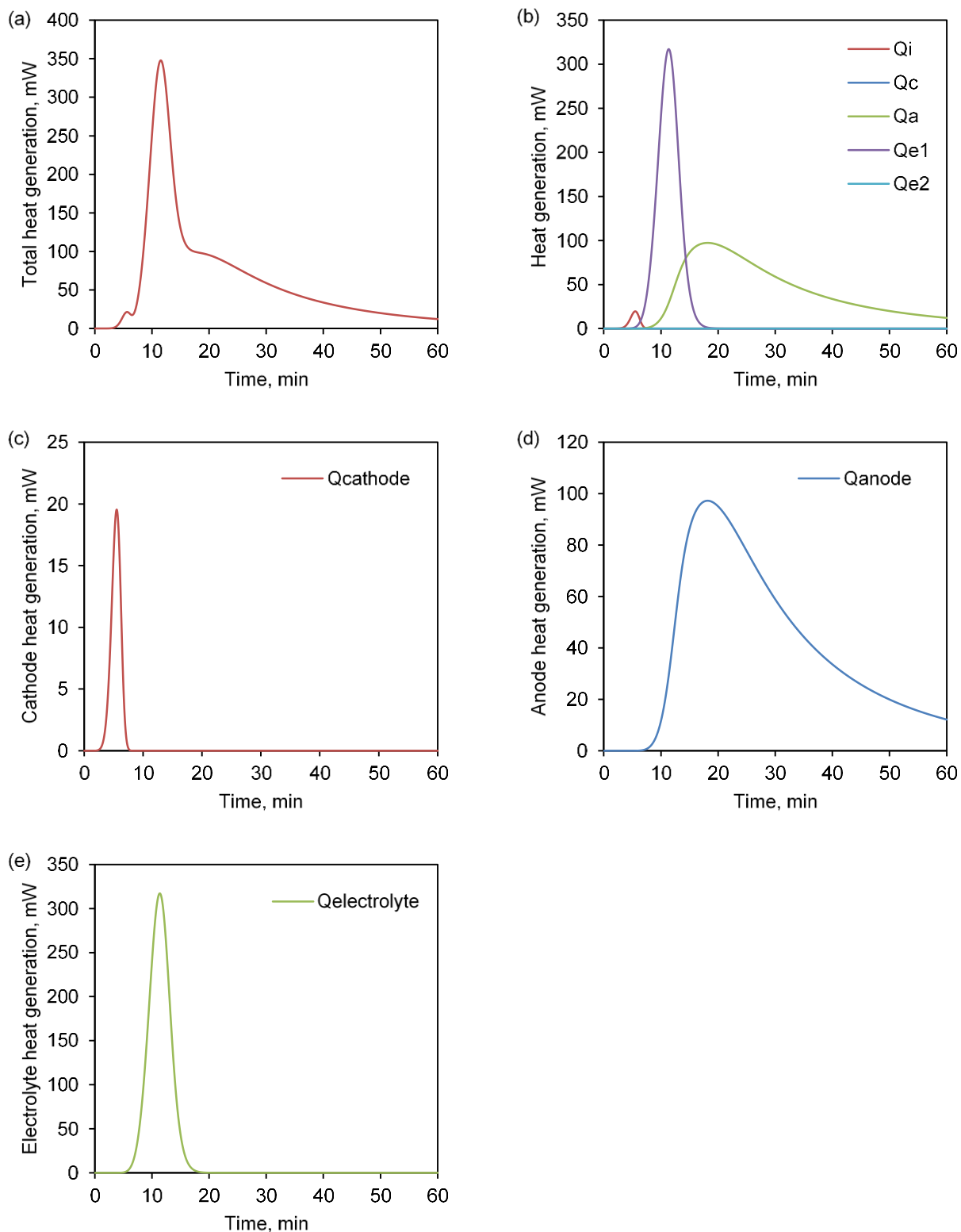


Figure 6.96 Heat generation profile during LFP | P13FSI electrolyte | LTO pouch cell 300 °C oven test simulation, (a) total heat generation Q_{gen} , (b) exothermic heat generation for different reactions, (c) cathode heat generation $Q_i + Q_c$, (d) anode heat generation Q_a , and (e) electrolyte heat generation $Q_{e1}+Q_{e2}$. $h = 4.5 \text{ W m}^{-2} \text{ K}^{-1}$.

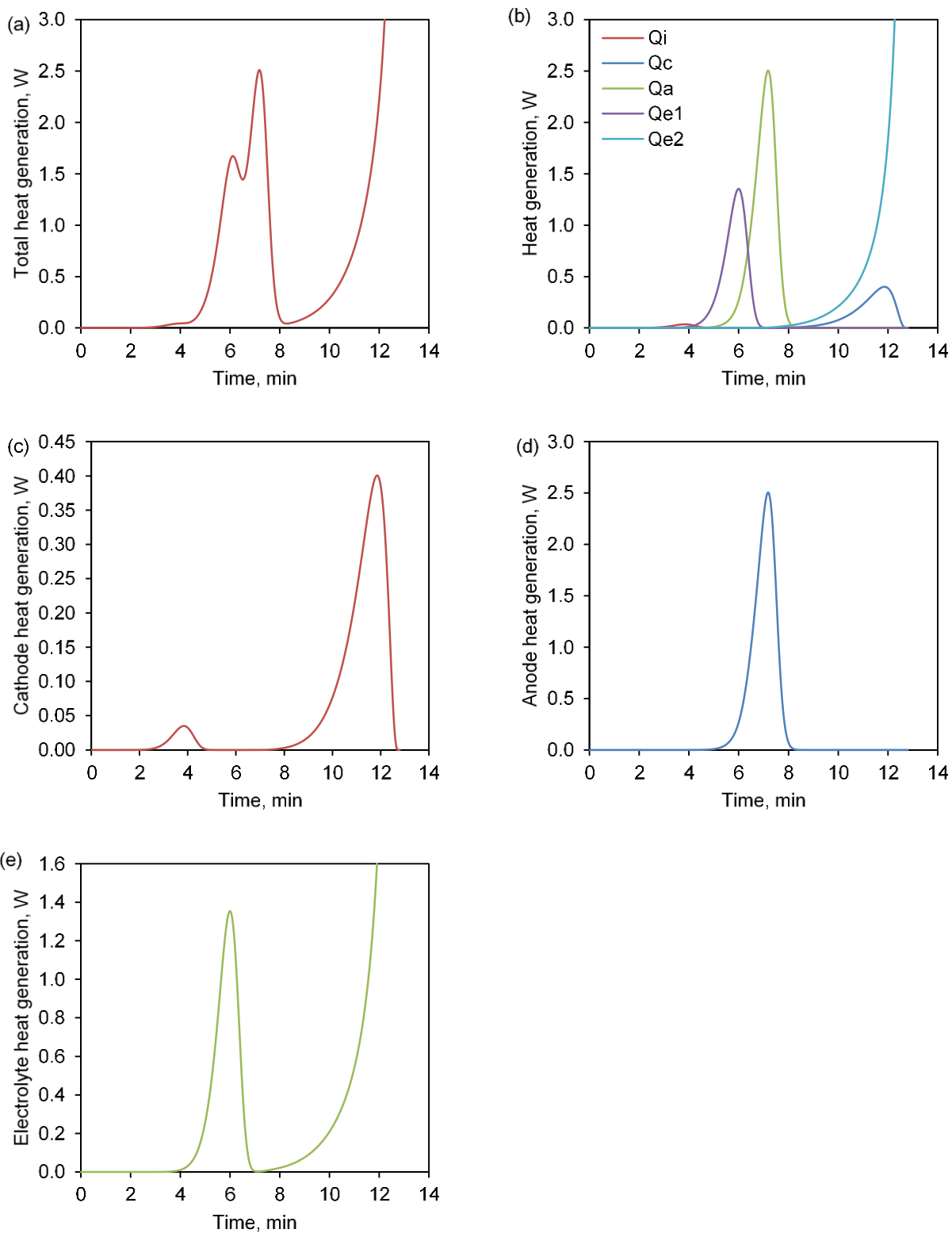


Figure 6.97 Heat generation profile during LFP | P13FSI electrolyte | LTO pouch cell 350 °C oven test simulation, (a) total heat generation Q_{gen} , (b) exothermic heat generation for different reactions, (c) cathode heat generation $Q_i + Q_c$, (d) anode heat generation Q_a , and (e) electrolyte heat generation $Q_{e1} + Q_{e2}$. $h = 4.5 \text{ W m}^{-2} \text{ K}^{-1}$.

Oven test simulations of a LFP | conventional electrolyte | LTO pouch cell at 150 and 200 °C are shown in Figure 6.98. As discussed previously during model validation, simulation with a 150 °C ambient oven temperature experiences a temperature of approximately 152 °C, approximately eight minutes into the simulation. The degree of conversion and the heat generation rate for each reaction can be seen in Figure 6.99 and Figure 6.100, respectively. During the 150 °C oven test simulation the only reaction that underwent substantial conversion was the anode-electrolyte reaction x_a (Figure 6.99b). The anode reaction began a few minutes into the simulation and continued until the end of the simulation when x_a was approximately 0.1. It appears that a small amount of reaction also occurred for x_f and x_c (Figure 6.99a,c), however these reactions continued at a negligible rate for the rest of the simulation. It appears that in a LFP | conventional electrolyte | LTO pouch cell at an ambient temperature of 150 °C, anode-electrolyte reactions will occur, resulting in a slight temperature increase, however, this does not cause thermal runaway in the cell.

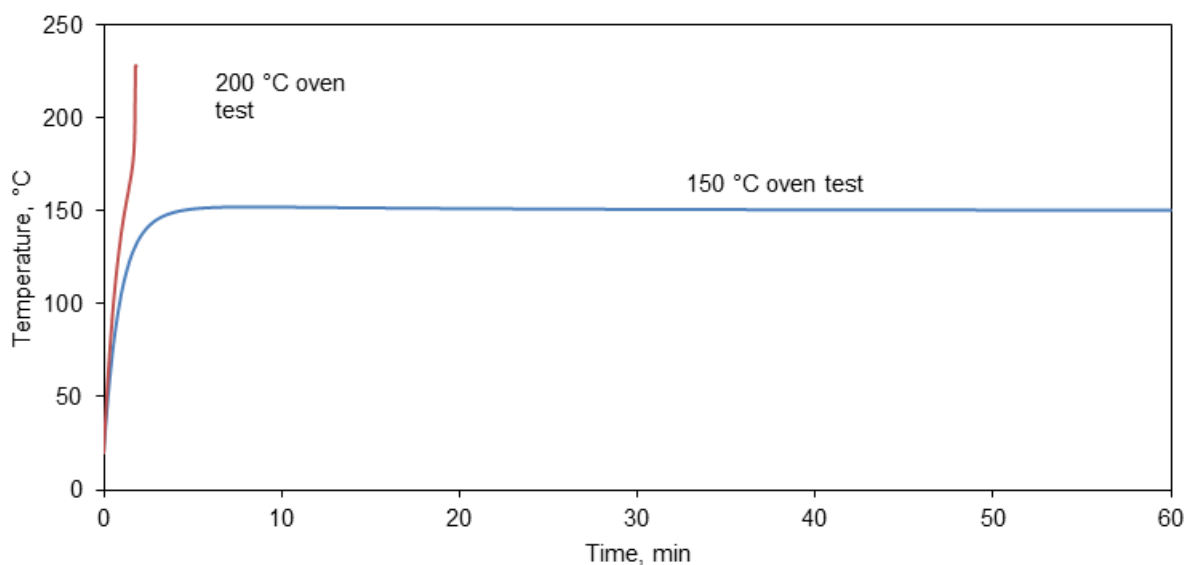


Figure 6.98 LFP | conventional electrolyte | LTO pouch cell temperature evolution during 150 and 200 °C oven test simulations. $h = 4.5 \text{ W m}^{-2} \text{ K}^{-1}$.

In an electro-thermal model for a NMC | LTO cell with conventional electrolyte, Ping, et al. [424] found that thermal runaway occurred at ambient temperatures as low as 152 °C. The authors [424] report SEI decomposition and anode-electrolyte reactions initiate at 80 and 117 °C, respectively however the cell does not enter thermal runaway until 152 °C. This indicates that the heat generated by SEI decomposition and anode-electrolyte reactions in the cell investigated by Ping, et al. [424] did not result in cell thermal runaway.

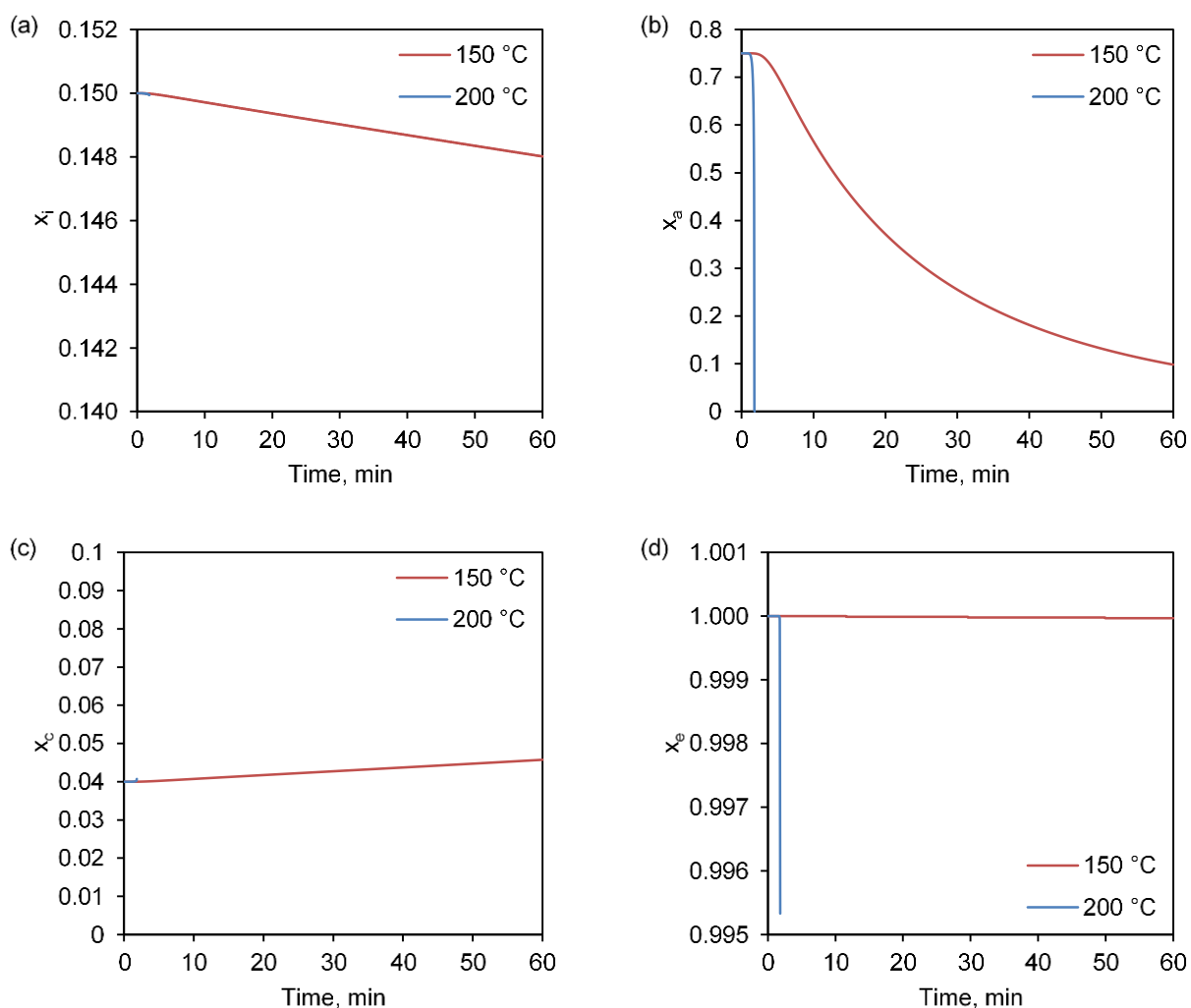


Figure 6.99 LFP | conventional electrolyte | LTO pouch cell 150 and 200 °C oven test simulations conversion degree in for (a) electrode-electrolyte interphase decomposition x_i , (b) anode electrolyte reactions x_a , (c) cathode electrolyte reactions x_c and (d) electrolyte decomposition x_e . $h = 4.5 \text{ W m}^{-2} \text{ K}^{-1}$.

At an ambient oven temperature of 200 °C, a LFP | conventional electrolyte | LTO pouch cell enters thermal runaway approximately two minutes into the simulation (Figure 6.98). As in the 150 °C oven test simulation, the anode-electrolyte (x_a) reaction proceeds first (Figure 6.99b). The Q_a reaction reaches a maximum heat generation of approximately 100 W at the peak, which causes the cell temperature to increase rapidly and the electrolyte decomposition reaction (x_e) begins (Figure 6.99d). It appears that once the electrolyte reaction begins the system becomes unstable, probably from the sharp x_e reaction and the corresponding large heat generation, Q_e (Figure 6.101). A few seconds after x_e starts reacting the simulation solution becomes unstable. It is suspected that once the electrolyte reaction begins the cell will enter thermal runaway, as suggested by the rapid temperature increase immediately before the simulation stops.

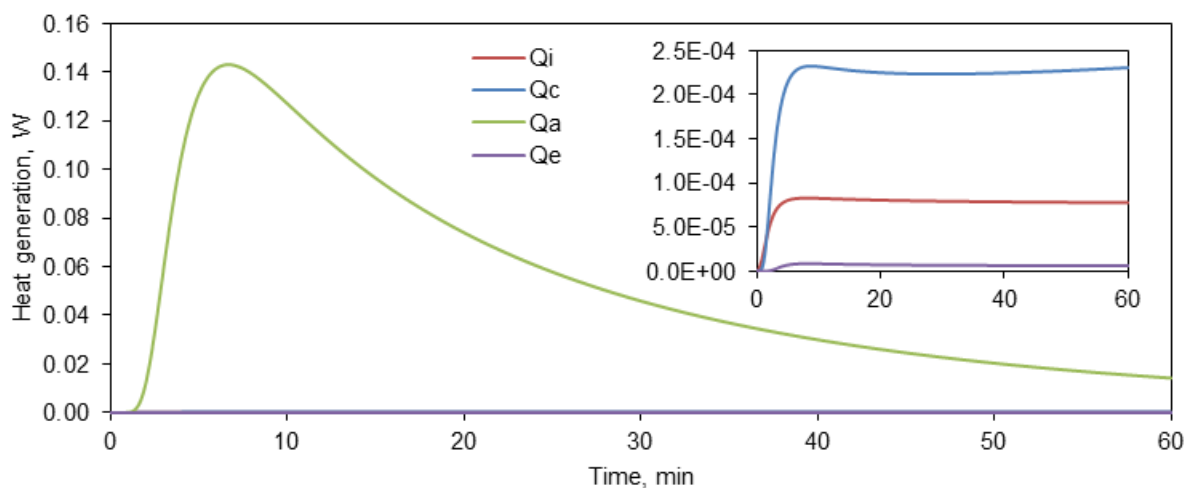


Figure 6.100 Heat generation contribution of different reactions for LFP | conventional electrolyte | LTO pouch cell during 150 °C oven test simulation; electrode-electrolyte interphase heat generation Q_i , cathode heat generation Q_c , anode heat generation Q_a , and electrolyte heat generation Q_e . Inset shows Q_i , Q_c and Q_e . $h = 4.5 \text{ W m}^{-2} \text{ K}^{-1}$.

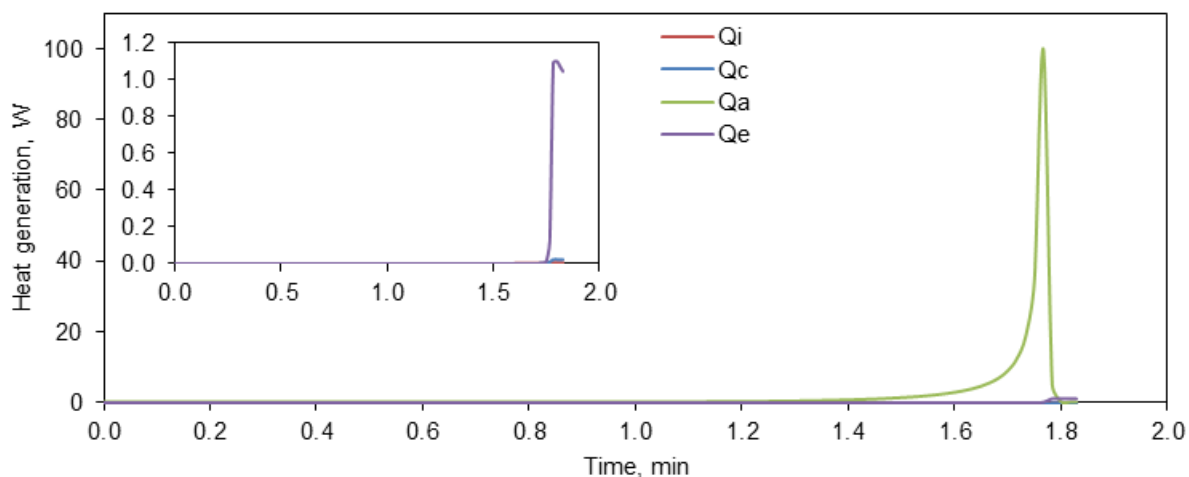


Figure 6.101 Heat generation contribution of different reactions for LFP | conventional electrolyte | LTO pouch cell during 200 °C oven test simulation; electrode-electrolyte interphase heat generation Q_i , cathode heat generation Q_c , anode heat generation Q_a , and electrolyte heat generation Q_e . Inset shows Q_i , Q_c and Q_e . $h = 4.5 \text{ W m}^{-2} \text{ K}^{-1}$.

Comparing the oven test simulations of a LFP | LTO pouch cell with P13FSI electrolyte and the conventional electrolyte (Figure 6.94 and Figure 6.98), it appears that the P13FSI electrolyte cell is thermally stable to at least 350 °C, while the conventional electrolyte cell undergoes an exothermic event at 150 °C and proceeds into thermal runaway before the cell reaches 200 °C. This indicates that the thermal runaway onset temperature for the P13FSI electrolyte cell is approximately 150 °C higher than for the conventional electrolyte cell. However, as discussed in Chapter 5, the onset temperature is not the only indicator for thermal stability, the amount of heat released should also be considered. The theoretical total heat released by each cell is calculated for the case of thermal runaway, when all available reaction material is consumed (the initial x_0 for each reaction). This can be calculated based on the simulation parameters used for each model. Theoretical heat release for the P13FSI electrolyte cell is described by Eq. (34):

$$\text{Theoretical heat} = x_{i,0}M_cH_i + x_{c,0}M_cH_c + x_{a,0}M_aH_a + x_{e1,0}M_eH_{e1} + x_{e2,0}M_eH_{e2} \quad \text{Eq. (34)}$$

Theoretical heat release for the conventional electrolyte cell is described by Eq. (35):

$$\text{Theoretical heat} = x_{i,0}M_aH_i + x_{a,0}M_aH_a + (1 - x_{c,0})M_cH_c + x_{e,0}M_eH_e \quad \text{Eq. (35)}$$

The theoretical heat for each reaction as well as the cell total for LFP | LTO pouch cells with either P13FSI electrolyte or conventional electrolyte is given in Table 6.41. In both cells, the main heat source is electrolyte decomposition. The theoretical heat from decomposition of the P13FSI electrolyte cell is approximately eight times larger than the conventional electrolyte cell. Based on

total heat release, the conventional electrolyte pouch cell is much more stable than the P13FSI electrolyte cell. This conflicts with the thermal stability based on onset temperature where P13FSI electrolyte cell has superior thermal stability with a thermal runaway onset temperature approximately 150 °C higher than the conventional electrolyte cell. This could be related to the difference in heat capacities of the electrolytes; the conventional electrolyte has a heat capacity of approximately 229 J kg⁻¹ K⁻¹ [428] while the P13FSI electrolyte has a heat capacity of approximately 1325 J kg⁻¹ K⁻¹ [48]. Both thermal stability ranks should be considered, along with the intended application, when looking at P13FSI electrolyte as a safer alternative to conventional electrolytes.

Table 6.41 Theoretical heat values for the LFP | LTO pouch cells with P13FSI electrolyte or conventional electrolyte.

P13FSI electrolyte cell		Conventional electrolyte cell	
Reaction	Theoretical heat, J	Reaction	Theoretical heat, J
Electrode-electrolyte interphase, i	2.3	Electrode-electrolyte interphase, i	21.0
Cathode-electrolyte, c	40.0	Cathode-electrolyte, c	130.9
Anode-electrolyte, a	158.0	Anode-electrolyte, a	226.7
Electrolyte 1	87.2	Electrolyte	793.6
Electrolyte 2	7644.6		
Total for cell	7932.1	Total for cell	1172.2

6.6.2.5 Ohmic heating from internal short circuit

Cells with a larger capacity may not maintain the level of thermal stability observed in the 0.1 Ah pouch cells in this thesis. A cell with increased capacity is expected to experience substantial ohmic heating due to internal short circuiting upon separator melting, depending on the cell capacity and SoC [430]. Therefore, there would be an additional heat term contributing to total heat generation along with the material decomposition reactions included in this thesis. In that case, the melt down temperature of the separator would be a critical parameter to include in the model as it would determine the initiation temperature for the ohmic heating generation, as discussed by Wang, et al. [38] for their conventional electrolyte LFP | graphite cell simulation investigations. In addition to heat contributions from ohmic heating, the material volume-to-surface area ratio of a larger capacity cell would be higher and therefore the cell may experience diminished heat transfer between the cell and the environment which may affect heat accumulation within the cell and consequently the thermal runaway process.

In order to validate the assumption of negligible heat contribution from an internal short circuit, the heat from an internal short circuit was investigated for IL electrolyte pouch cells with varying

capacity. The short circuit parameters and reactions reported by Coman, et al. [85] were used to estimate the ohmic heating (electrochemical reaction) contribution. The SoC, short circuit heat term and ohmic heat generation are described by Eq. (36), Eq. (37) and Eq. (38) [85]:

$$\frac{dSoC}{dt} = -ISC_{cond} SoC A_{ec} \exp \left[-\frac{E_{ec}}{R_{gas}T} \right] \quad \text{Eq. (36)}$$

$$H_{ec} = V C 3600 \eta \quad \text{Eq. (37)}$$

$$Q_{ec} = -H_{ec} \frac{dSoC}{dt} \quad \text{Eq. (38)}$$

where SoC is the cell state of charge, initially one (fully charged) and decreases when the short circuit occurs. ISC_{cond} is the internal short circuit condition of the cell, equal to either one or zero. ISC_{cond} was initially set to 0 (no short circuit) and switches to one (short circuit) at a set temperature (T_{ISC}). A_{ec} is the short circuit electrochemical reaction frequency factor (s^{-1}). E_c is the short circuit electrochemical reaction activation energy ($J mol^{-1}$). H_c is the reaction heat for the electrochemical ($J kg^{-1}$). V is the cell open circuit voltage (V). C is the cell capacity (Ah). η is the efficiency factor which describes the amount of electrochemical energy that is converted into ohmic heat during the short circuit. The internal short circuit reaction parameters are shown in Table 6.42.

Table 6.42 Internal short circuit reaction parameters

Symbol	Units	Value*	Ref.
T_{ISC}	°C	57	[85]
A_{ec}	s^{-1}	3.37E12	[85]
E_{ec}	$J mol^{-1}$	9.51E4	[85]
V	V	1.8	This Work
C	Ah	0.1	This work
η	-	0.28	[85]

Temperature profiles of LFP | P13FSI electrolyte | LTO pouch cells with 0.1, 1, 2 and 5 Ah capacities are shown in Figure 6.102 during an oven test simulation at 200 °C, including a heat generation term for internal short circuit ohmic heating. The 0.1 Ah pouch cell shows a slight peak at approximately 100 °C, but the overall trend follows the same temperature profile as observed in the 200 °C oven test without the heat generation term for internal short circuit ohmic heating (Figure 6.94). Increasing the cell capacity to 1 Ah results in a different temperature profile with a rapid temperature increase from approximately 60 °C up to 185 °C, due to internal short circuit ohmic heating, after which the cell temperature continues to slowly increase until it reaches an equilibrium with the 200 °C oven temperature.

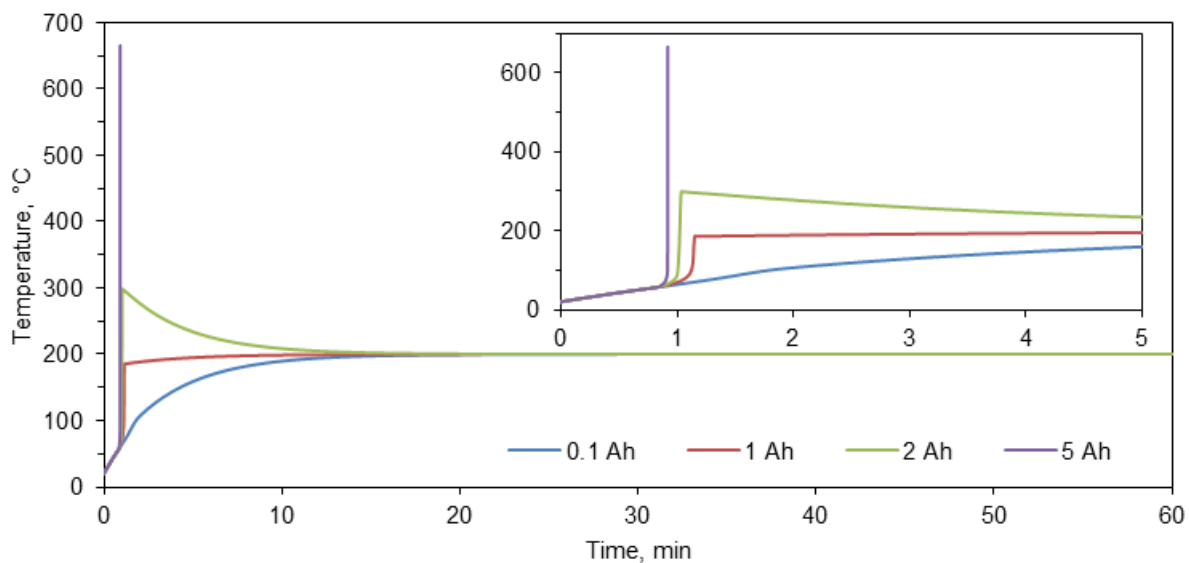


Figure 6.102 Temperature profile of LFP | P13FSI electrolyte | LTO pouch cells of varying capacity, during 200 °C oven test simulations including internal short circuit ohmic heating, $h = 4.5 \text{ W m}^{-2} \text{ K}^{-1}$.

The pouch cell with 2 Ah capacity (Figure 6.102) shows a similar profile except the rapid temperature increase reaches a maximum of approximately 298 °C before slowly decreasing to 200 °C. In the above three cases the cell did not enter into thermal runaway, which indicates that the amount of heat generated during internal short circuit ohmic heating was able to be dissipated by the cell. Since the cell temperature did not reach a high enough temperature to initiate the cathode-electrolyte reaction or the second electrolyte decomposition, thermal runaway did not occur, as found in the IL electrolyte pouch cell simulations in Section 6.6.2.4. When the capacity is increased to 5 Ah the cell goes into thermal runaway within one minute of the oven test simulation commencing. This suggests that the heat from the internal short circuit ohmic heating of the 5 Ah cell caused the temperature to increase until the exothermic cathode-electrolyte and second electrolyte decomposition reactions began.

Temperature profiles of oven test simulations, including a heat generation term for internal short circuit ohmic heating, at 350 °C for LFP | P13FSI electrolyte | LTO pouch cells with 0.1, 1, 2 and 5 Ah capacities are shown in Figure 6.103. The results of the 350 °C oven test with an internal short circuit are similar to the 200 °C oven test; the 0.1, 1 and 2 Ah cells did not go into thermal runaway but the 5 Ah cell did. Even though the internal short circuit reactions use a trigger temperature of only 57 °C [85], the study validates the assumption that the internal short circuit ohmic heat released is negligible in the 0.1 Ah pouch cell modelled in this work, therefore the internal short circuit reactions can be left out of the oven test simulations without substantially changing the results.

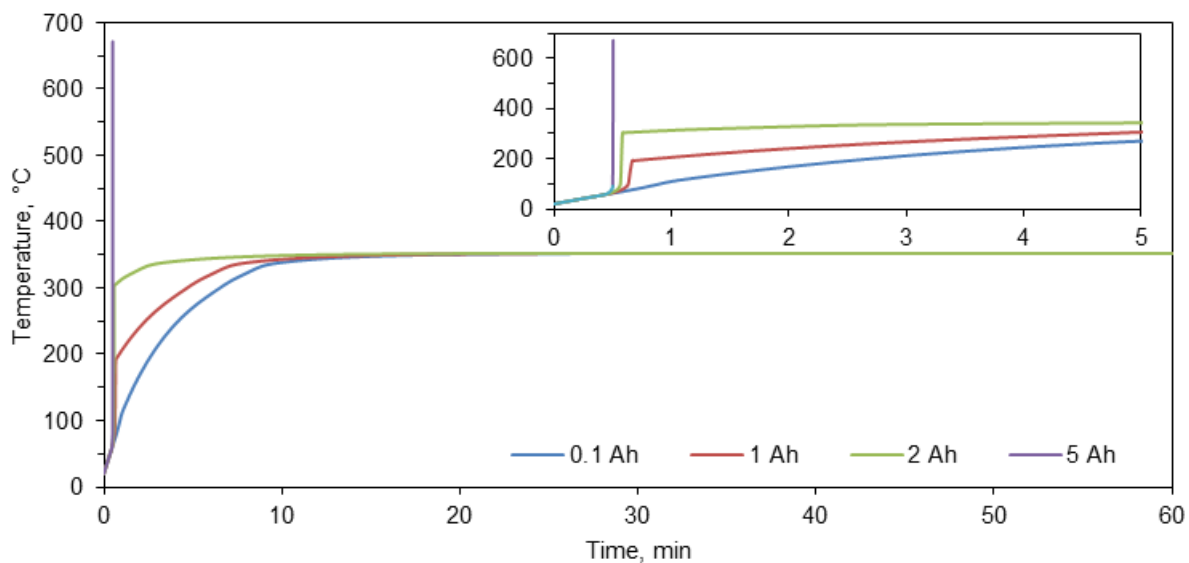


Figure 6.103 Temperature profile of LFP | P13FSI electrolyte | LTO pouch cells of varying capacity, during 350 °C oven test simulations including internal short circuit ohmic heating, $h = 4.5 \text{ W m}^{-2} \text{ K}^{-1}$.

6.7 Conclusion

Thermal abuse of single-plate pair pouch cells assembled with LFP and LTO electrodes, different separators and either P13FSI electrolyte or conventional electrolyte was completed. Cells successfully underwent formation cycling, overall the conventional electrolyte cells exhibited higher capacities and for both types of electrolyte the FSI-C separator showed the highest capacity. Oven testing of the pouch cells at 150 and 180 °C did not show evidence of thermal runaway, except for pouch swelling in conventional electrolyte cells. However, conventional electrolyte pouch swelling was not accompanied by any temperature increase on the pouch surface. The P13FSI electrolyte cells were not expected to undergo thermal runaway at a temperature of 180 °C so the oven test results were as expected. Disassembly of the pouch cells after oven testing showed that interactions between the separator and electrolyte can impact cell safety. The Celgard 3501 separator was found to have melted and appeared to have negligible interaction with either electrolyte. On the other hand, the FSI-C separator showed interactions with both electrolytes, forming a gelatinous layer with P13FSI electrolyte and dissolving / melting in the conventional electrolyte cell. The P13FSI electrolyte was present in liquid form following oven testing and the conventional electrolyte appeared to have partially or fully vaporised during oven testing.

A thermal abuse model was successfully applied to simulate a LFP | P13FSI electrolyte | LTO cell, and compared to a conventional electrolyte cell. Anode, cathode and P13FSI electrolyte decomposition kinetic parameters were obtained from the DSC results in Chapter 5 and used to implement a thermal abuse model for a 0.1 Ah LFP | P13FSI electrolyte | LTO pouch cell. The

abuse model reactions included: electrode-electrolyte interphase decomposition, the first electrolyte decomposition, anode-electrolyte reaction, cathode-electrolyte reaction and second electrolyte decomposition. Literature parameters were used to model a LFP | conventional electrolyte | LTO pouch cell, for comparison. Oven testing was used to determine an equivalent heat transfer coefficient ($4.5 \text{ W m}^{-2} \text{ K}^{-1}$) for the pouch cell thermal abuse simulations. Simulations showed that P13FSI electrolyte pouch cells were thermally stable at an ambient temperature of $350 \text{ }^\circ\text{C}$ for 60 minutes, while at $370 \text{ }^\circ\text{C}$ thermal runaway occurred after approximately 13 minutes. For comparison, the conventional electrolyte cells went into thermal runaway after approximately two minutes at an ambient temperature of $200 \text{ }^\circ\text{C}$ when the electrolyte decomposition reaction began.

In P13FSI electrolyte cells, the electrode-electrolyte interphase decomposition, the first electrolyte reaction and the anode-electrolyte reactions occurred below $300 \text{ }^\circ\text{C}$, however, the heat generated by these reactions did not cause thermal runaway. In P13FSI electrolyte cells, the cathode-electrolyte reaction and second electrolyte decomposition reactions occur almost simultaneously, since they have similar peak temperatures. However, thermal runaway only occurs when the electrolyte decomposition reaction begins, possibly due to the extremely large heat generation of P13FSI electrolyte decomposition resulting in high cell temperatures. Although the P13FSI electrolyte cell is stable up to $350 \text{ }^\circ\text{C}$, $150 \text{ }^\circ\text{C}$ higher than the conventional electrolyte cell, it should be noted that the heat released during thermal runaway of the P13FSI electrolyte cell is approximately ten times larger than the heat released by the conventional electrolyte cell.

Since ohmic heating was not included in the lumped thermal model, the separator material was not accounted for in the simulations results. When simulating thermal abuse of larger cells with substantial capacity, the separator melting temperature should be included as it would determine the initiation temperature for the ohmic heating generation. Depending on the cell capacity and SoC, the separator melting may be a critical event in the thermal runaway process for larger capacity cells.

CHAPTER 7

Summary and Conclusions

7.1 Summary

The overall aim of this thesis was to address ionic liquid (IL) electrolyte wetting issues with commercial separators through the development of a novel separator and investigate the resulting thermal characteristics of IL electrolyte-based lithium-ion cells. This concluding chapter summarises the findings of the previous six chapters and provides suggested directions for future work.

Lithium-ion batteries, their application and the safety issues surrounding their use were introduced in Chapter 1. Background information was provided on the components that make up a lithium-ion cell, including, electrode, separator and electrolyte materials. The impact of electrolytes and separators on the safety of a cell was discussed, along with the need for alternative electrolyte materials to increase the overall safety of lithium-ion cells. IL electrolytes were presented as a highly researched alternative electrolyte material, with potentially superior thermal stability over conventional electrolytes. However, compared to conventional electrolytes, IL electrolytes have poor wetting properties with other cell components, which can negatively affect the performance of a cell. The need for a separator with enhanced wetting for IL electrolyte was introduced to improve the performance of lithium-ion cells containing IL electrolytes. Additionally, the thermal advantages of a cell containing IL electrolyte under thermal runaway conditions was postulated.

The characteristics and functionality of separator materials were presented in Chapter 2. Commercial separators and advancements in the literature for conventional electrolyte separator materials were summarised. A literature review was presented on separators for IL electrolytes, including commercial separator compatibility studies as well as novel separators designed for enhanced wetting with IL electrolytes. Typically, nonwoven separators were found to have higher ionic conductivities than microporous separators due to the high porosity and open pore structure of nonwoven membranes providing minimal resistance to lithium ion transport the IL electrolyte. Correlations were suggested between different separator properties and performance of the separator with IL electrolytes. Overall, the porosity of a separator was found to strongly correlate to the ionic conductivity of the separator when wet with IL electrolyte. This highlights the impact separators can have on cell performance even through the separator is not an active material in cell reactions.

A novel separator was developed for use with 1.17 mol kg^{-1} lithium bis(fluorosulfonyl)imide (LiFSI) in 1-methyl-3-propylpyrrolidinium bis(fluorosulfonyl)imide electrolyte (P13FSI electrolyte) and tested in Chapter 3. The separator was manufactured via electrospinning poly(vinylidene fluoride-hexafluoropropylene) (PVDF-HFP) containing a lithium salt onto a polyacrylonitrile (PAN) support membrane, the support membrane was to provide mechanical and thermal stability to the

separator. The lithium salt type, salt concentration and solvent type in the PVDF-HFP electrospinning solution were varied and physical properties of the resulting separators were analysed. Electrospun PVDF-HFP containing 0.5 wt% LiFSI showed the most uniform membrane morphology, however, overall the separators electrospun with N,N-Dimethylacetamide (DMAc) solvent showed improved fibre formation during electrospinning. The tensile strength of the novel separator coated with PVDF-HFP containing 2 wt% LiFSI was found to be higher than GF, but not as high as the commercial Celgard 3501 separator. Of the novel separators, the separator coated with PVDF-HFP containing 0.5 wt% LiFSI showed the best thermal stability and thermal dimensional stability. The wetting characteristics of the novel separator with P13FSI electrolyte were shown to increase with the presence of LiFSI in the polymer matrix. The novel separator coated with PVDF-HFP containing 1 wt% LiFSI showed the highest electrolyte uptake and ionic conductivity with P13FSI electrolyte. The physical and wetting characteristics of the novel separators indicated they may be suitable for use in lithium-ion batteries with IL electrolyte, which was investigated in the next chapter.

The electrochemical performance and cycling ability of the novel separator developed in Chapter 3 with P13FSI electrolyte in both lithium symmetrical and lithium-ion cells was investigated in Chapter 4. In a P13FSI electrolyte lithium symmetrical cell at open circuit voltage for 15 hours, the separator coated with PVDF-HFP containing 2 wt% LiFSI was found to have a lower interfacial resistance than the separators containing lower concentrations of LiFSI. However, overall the separator coated with PVDF-HFP containing 1 wt% lithium bis(trifluoromethanesulfonyl)imide (LiTFSI) had the lowest resistance, which suggests that LiTFSI could enhance the stability of SEI formed on lithium metal. During cycling of lithium symmetrical cells, novel separators containing LiFSI or LiTFSI salt showed very stable overpotentials, which may be due to the electrospun layer morphology being more conducive to SEI formation and uniform lithium plating / stripping. In LiFePO₄ (LFP) half-cells, the separator coated with PVDF-HFP containing 1 wt% LiTFSI had the highest capacity at all discharge rates, followed closely by the separator coated with PVDF-HFP containing 2 wt% LiFSI. When cycled in a lithium-ion cell, LFP | P13FSI electrolyte | Li₄Ti₅O₁₂ (LTO), the novel separators all showed a considerable capacity loss, more than 50% over 50 cycles at C/10. It should be noted that the commercial electrode materials used were not optimised for IL electrolytes therefore the full capacity may not have been delivered due to electrode wetting issues. Cycling of the novel separators in LFP | LTO cells containing a conventional electrolyte had improved cycling capacities. These results demonstrate that the novel separators are able to function as a separator in lithium metal and lithium-ion cells with P13FSI electrolyte.

The thermal stability of separators and a selection of commercial electrodes with P13FSI electrolyte using Differential Scanning Calorimetry (DSC) was investigated in Chapter 5. Electrospun PVDF-HFP with P13FSI electrolyte was found to have a lower thermal stability than

Celgard 3501 and GF with P13FSI electrolyte. This suggests that the thermal stability of a separator and electrolyte may be altered when tested in combination. The decomposition profile of P13FSI electrolyte with different electrodes was compared, including electrodes cycled with P13FSI electrolyte to analyse the thermal behaviour of electrode-electrolyte interphase films that may have formed on the electrode surface. Discharged LTO, discharged $\text{Li}(\text{Ni}_{1/3}\text{Co}_{1/3}\text{Mn}_{1/3})\text{O}_2$ (NMC) and charged and discharged graphite all had an onset temperature below 150 °C. Exothermic onset temperatures below 150 °C suggests that with exothermic decomposition these electrodes P13FSI electrolyte would likely initiate thermal runaway, as it would occur before short circuit heating from the separator melting. Charged and discharged LFP, charged NCM, and charged and discharged $\text{LiNi}_{0.5}\text{Mn}_{1.5}\text{O}_4$ (LMNO) had intermediate onset temperatures between 150 and 200 °C, while charged LiCoO_2 (LCO) and charged LTO had onset temperatures above 200 °C for their first exothermic event. Exothermic onset temperatures above 150 °C suggests the thermal runaway process would likely be initiated by another event, such as separator melting causing a short circuit and ohmic heating. The thermal stability of P13FSI electrolyte has been seen to increase the onset temperature for exothermic decomposition of most electrodes, however in many cases more heat is released during electrode decomposition in the presence of the P13FSI electrolyte.

The analysis of materials thermal stability in the previous chapter does not provide enough detail to assess how a cell containing these materials will behave in thermal abuse testing. Further work was completed in Chapter 6, where the thermal abuse response of single plate pair LFP | LTO pouch cells, containing P13FSI electrolyte was analysed and compared the response of cells containing a conventional electrolyte. Oven testing of the pouch cells at 150 and 180 °C did not show evidence of thermal runaway, except for pouch swelling in the conventional electrolyte cells. A thermal abuse model was developed for IL electrolyte pouch cells using kinetic parameters obtained from the results in Chapter 5. The following reactions were included in the abuse model: electrode-electrolyte interphase decomposition, the first electrolyte reaction, anode-electrolyte reaction, cathode-electrolyte reaction and electrolyte decomposition. Simulated oven tests showed that the P13FSI electrolyte pouch cell was stable at 350 °C for 60 minutes and only went into thermal runaway after approximately 13 minutes at 370 °C. For comparison, the simulated conventional electrolyte cells went into thermal runaway as electrolyte decomposition reactions began after being exposed to 200 °C for approximately two minutes. In the simulations of LFP | LTO pouch cells containing P13FSI electrolyte, electrode-electrolyte interphase decomposition, the first electrolyte reaction and anode-electrolyte reactions all occurred below 300 °C, however, the heat generated by these reactions did not cause thermal runaway. Thermal runaway only occurred when the electrolyte decomposition reaction began at approximately 355 °C. It appears that the P13FSI electrolyte pouch cell is stable at higher temperatures than the conventional electrolyte cell, although, the theoretical heat released by the P13FSI electrolyte cell during thermal runaway

is approximately ten times more than the conventional electrolyte cell.

7.2 Implications for IL electrolyte lithium-ion batteries

Use of a multi-layer separator can take advantage of the properties of multiple materials in a single separator, such as a mechanically and thermally stable support membrane coated with a material to enhance compatibility with P13FSI electrolyte, both electrolyte uptake and retention. Using a separator with enhanced compatibility with IL electrolyte can improve electrolyte wetting and distribution in the cell, however, electrode wetting and stability with the IL electrolyte still needs to be improved in order to improve the capacity obtained from IL electrolyte lithium-ion batteries.

In Chapter 1 some issues associated with IL electrolytes were introduced, including high viscosity and poor wetting. The high viscosity of ILs affects the wetting properties of the separator and electrode by decreasing electrolyte pore infiltration. ILs also typically have a low ionic conductivity and low lithium-ion diffusivity, compared to conventional electrolytes, as demonstrated by cell performance results in Section 4.4.6. The P13FSI electrolyte is recommended for applications in which high rate performance is not required, therefore the lower ionic conductivity would not be an issue. As for the wetting, the IL electrolyte wetting has been seen to improve with an enhanced separator material, but the wettability of electrode with P13FSI electrolyte still requires attention to ensure all the active material in the cell is accessible.

The thermal stability advantages of IL electrolyte have been shown to result in a delayed exothermic onset temperature for decomposition and therefore delayed thermal runaway, as expected; however, the substantial increase in heat released during thermal decomposition of IL electrolyte compared to conventional electrolyte should be considered when recommending IL electrolytes as safer alternatives to conventional electrolytes.

7.3 Conclusions

Separator wetting with P13FSI electrolyte was improved with a novel separator; a PAN support coated with electrospun PVDF-HFP containing lithium salt. In conjunction with P13FSI electrolyte, the novel separator was found to be applicable to lithium metal and lithium-ion cells, although investigation into the wetting and stability of lithium-ion electrodes with P13FSI electrolyte is recommended. Overall, P13FSI electrolyte was found to delay the onset temperature for thermal decomposition reactions in a cell, compared to conventional electrolyte, however, the heat released during decomposition of cells containing P13FSI electrolyte was typically higher than cells

containing conventional electrolyte. IL electrolytes, specifically P13FSI electrolyte, could be suitable for improved safety lithium-ion batteries for low rate applications through the use of a novel separator with enhanced wetting along with electrodes optimised for IL electrolytes.

7.4 Limitations of work

There are some limitations of the research conducted in this thesis, summarised here.

- The electrospinning process was not optimised therefore the ionic transport properties of the separator wet with electrolyte may have been hindered by the presence of beading and melted polymer regions in the PVDF-HFP layers, discussed in Section 3.3.2.1.
- The electrodes used to assemble cells were not optimised for wetting with high viscosity IL electrolytes therefore the cell capacities may have been lower than the theoretical capacity of the electrode, discussed in Sections 4.4.5 and 4.4.6.
- The high-pressure crucibles used for DSC were reusable and required cleaning which may have introduced baseline shift and uncertainty into the origin of unexpected thermal events observed, discussed in Section 5.4.
- The electrode and separator samples harvested from cycled cells were not washed with solvents prior to DSC testing therefore excess electrolyte may have been present and could have affected the comparison of total heat release of samples during decomposition, discussed in Section 5.3.2.
- The P13FSI electrolyte pouch cells did not enter thermal runaway during oven testing therefore model validation was not possible for the thermal runaway stage of the model, discussed in Section 6.5.2.2.
- The ohmic heat due to separator melting was assumed to be negligible during thermal abuse simulations therefore the heat generation during thermal runaway may have been underestimated in the model, discussed in Section 6.5.2.4.
- A zero dimensional (0D) lumped thermal model was developed meaning the impact of cell geometry and thermal conductivity effects were assumed to be negligible therefore the model results may be limited to small single cell simulations, discussed in Section 6.5.2.4.

These limitations could be addressed in future works to investigate their impact on the results.

7.5 Directions for future work

The inclusion of a lithium salt was shown to improve the wetting properties of electrospun PVDF-HFP with the P13FSI electrolyte, however, the electrospun membrane was not optimised. The electrospun membrane experienced beading and issues with poorly evaporated solvent during electrospinning, both of which contributed to the highly non-homogeneous morphology of the electrospun membrane. These issues could be improved with optimisation of the electrospinning solution, i.e. solvent type and polymer concentration; and the electrospinning variables, i.e. applied voltage, collector distance, environmental temperature and humidity. Measurement of the electrospinning solution conductivity and viscosity could also be used to help future optimisation.

Inclusion of LiFSI and LiTFSI salt in the separator showed promise for improved separator performance with P13FSI electrolyte. Although inclusion of LiFSI was the focus of this work, the inclusion of LiTFSI salt was also promising and the interphase behaviour of LiTFSI based separators should be investigated further. The electrode-electrolyte interphase layers formed with different salts incorporated in the separator could be investigated with XPS and Raman surface techniques.

The thickness of PVDF-HFP electrospun layer required to enhance the separator wetting should be investigated. Maintaining a minimum thickness of the separator is important (discussed in Section 2.2.1) and a thicker support membrane would be expected to increase the mechanical and thermal stability of the separator. Therefore, minimising the electrospun PVDF-HFP layer thickness would allow for a thicker support membrane to be employed without increasing the overall thickness of the separator.

The support membrane, PAN, was selected to improve the thermal and mechanical properties of the separator. However, the novel separator was found to be less mechanically robust than the commercial Celgard 3501 separator and in thermal dimensional stability investigations the lower melting temperature of PVDF-HFP was found to affect the overall membrane thermal stability. Treatments, such as thermal- or ultra-violet (UV)- crosslinking, were introduced in Section 2.2.1 to improve separator thermal and mechanical stability. Post-process treatments could also be investigated to improve the separator thermal and mechanical integrity as well as adherence of the PVDF-HFP layers.

Selection of another support membrane could also provide increased thermal stability to the separator. Alternate polymer materials investigated as separators, along with mechanical and thermal properties, were presented in Table 2.3. Specifically, polyimide or aramid polymer based support materials could provide higher thermal stability than the PAN support, if they are compatible with the PVDF-HFP electrospun layer and the IL electrolyte.

Since PVDF-HFP separator materials have been widely investigated with a range of IL electrolytes (Table 2.5), it is expected that the novel separator may be suitable for a range of IL electrolytes. Investigation of the novel separator with other IL electrolytes is suggested to confirm its compatibility before recommending the novel separator for broader use.

The compatibility of P13FSI electrolyte with electrodes is suggested to be investigated further. Specifically, the electrode wettability could be studied by optimising to the electrode loading, porosity and / or calendaring to enhance electrode wetting with P13FSI electrolyte. Additionally, characterisation of the electrode-electrolyte interphase possibly present on different electrodes after cycling with P13FSI electrolyte should be undertaken, i.e. Scanning Electron Microscopy (SEM), Energy Dispersive X-Ray (EDX) and Raman spectroscopy, to further understand the chemical and thermal stability of the interphase components, as well as potentially point to ways of increasing the electrode-electrolyte interphase stability.

Thermal analysis of assembled P13FSI electrolyte cells with ARC is recommended to investigate the expected thermal stability of a full cell. Full cell ARC is expected to provide insight into possible interactions between the reactions identified during DSC analysis. ARC results could also be used to validate and potentially improve the thermal abuse model.

Abuse testing of larger pouch cells (approximately 10 Ah) is suggested to investigate the contribution of internal short circuit ohmic heating to overall cell heating and thermal runaway initiation. Larger pouch cells would also provide a more realistic material volume-to-surface area ratio for heat generation and thermal dissipation investigation in pouch cells including tabs and the pouch material. Additionally, surface characterisation of cell materials after thermal abuse, such as FTIR, SEM and EDX, could be undertaken to further understand the reactions occurring during decomposition.

The thermal decomposition products of the P13FSI should be analysed to determine the flammability, reactivity and toxicity of the gases released. Specifically, gas chromatography and mass spectroscopy characterisation of the gases produced during thermal decomposition and the remaining residue following decomposition could be conducted to inform cell design and safety controls surrounding the application of IL electrolyte in lithium-ion cells.

Lastly, the thermal abuse model dimensionality should be increased in order to simulate thermal abuse of larger cells, including the effects of thermal conductivity within the pouch. A heat generation term for ohmic heating could be included to account for an internal short circuit associated with separator melting at elevated temperatures.

References

- [1] S. Abada, G. Marlair, A. Lecocq, M. Petit, V. Sauvant-Moynot, F. Huet, *Journal of Power Sources*, 306 (2016) 178-192.
- [2] F. Cheng, J. Liang, Z. Tao, J. Chen, *Advanced Materials*, 23 (2011) 1695-1715.
- [3] V. Etacheri, R. Marom, R. Elazari, G. Salitra, D. Aurbach, *Energy and Environmental Science*, 4 (2011) 3243-3262.
- [4] H. Li, Z. Wang, L. Chen, X. Huang, *Advanced Materials*, 21 (2009) 4593-4607.
- [5] M.-H. Ryou, D.J. Lee, J.-N. Lee, Y.M. Lee, J.-K. Park, J.W. Choi, *Advanced Energy Materials*, 2 (2012) 645-650.
- [6] N. Nitta, F. Wu, J.T. Lee, G. Yushin, *Materials Today*, 18 (2015) 252-264.
- [7] P. Roy, S.K. Srivastava, *Journal of Materials Chemistry A*, 3 (2015) 2454-2484.
- [8] M. Armand, J.-M. Tarascon, *Nature*, 451 (2008) 652-657.
- [9] J.B. Goodenough, K.S. Park, *Journal of the American Chemical Society*, 135 (2013) 1167-1176.
- [10] L. Croguennec, M.R. Palacin, *Journal of the American Chemical Society*, 137 (2015) 3140-3156.
- [11] C.M. Hayner, X. Zhao, H.H. Kung, *Annual review of chemical and biomolecular engineering*, 3 (2012) 445-471.
- [12] W. Xu, J. Wang, F. Ding, X. Chen, E. Nasybulin, Y. Zhang, J.-G. Zhang, *Energy and Environmental Science*, 7 (2014) 513-537.
- [13] J. Hassoun, B. Scrosati, *Journal of The Electrochemical Society*, 162 (2015) A2582-A2588.
- [14] R. Zhao, S. Zhang, J. Liu, J. Gu, *Journal of Power Sources*, 299 (2015) 557-577.
- [15] P.G. Balakrishnan, R. Ramesh, T. Prem Kumar, *Journal of Power Sources*, 155 (2006) 401-414.
- [16] Q. Li, J. Chen, L. Fan, X. Kong, Y. Lu, *Green Energy & Environment*, 1 (2016) 18-42.
- [17] C.S. Stefan, D. Lemordant, B. Claude-Montigny, D. Violleau, *Journal of Power Sources*, 189 (2009) 1174-1178.
- [18] M.M. Huie, R.A. DiLeo, A.C. Marschilok, K.J. Takeuchi, E.S. Takeuchi, *ACS Applied Materials and Interfaces*, 7 (2015) 11724-11731.
- [19] C. Hendricks, N. Williard, S. Mathew, M. Pecht, *Journal of Power Sources*, 297 (2015) 113-120.
- [20] J. Kalhoff, G.G. Eshetu, D. Bresser, S. Passerini, *ChemSusChem*, 8 (2015) 2154-2175.
- [21] X.-W. Gao, C.-Q. Feng, S.-L. Chou, J.-Z. Wang, J.-Z. Sun, M. Forsyth, D.R. MacFarlane, H.-K. Liu, *Electrochimica Acta*, 101 (2013) 151-157.
- [22] J.P. Schmidt, D. Manka, D. Klotz, E. Ivers-Tiffée, *Journal of Power Sources*, 196 (2011) 8140-8146.
- [23] B. John, G. Cheruvally, *Polymers for Advanced Technologies*, 28 (2017) 1528-1538.
- [24] Y. Xiang, J. Li, J. Lei, D. Liu, Z. Xie, D. Qu, K. Li, T. Deng, H. Tang, *ChemSusChem*, 9 (2016) 3023-3039.
- [25] D. Lisbona, T. Snee, *Process Safety and Environmental Protection*, 89 (2011) 434-442.
- [26] Q. Wang, P. Ping, X. Zhao, G. Chu, J. Sun, C. Chen, *Journal of Power Sources*, 208 (2012) 210-224.
- [27] N. Williard, W. He, C. Hendricks, M. Pecht, *Energies*, 6 (2013) 4682-4695.
- [28] A.W. Golubkov, D. Fuchs, J. Wagner, H. Wiltsche, C. Stangl, G. Fauler, G. Voitc, A. Thaler, V. Hacker, *RSC Advances*, 4 (2014) 3633-3642.
- [29] H.U. Escobar-Hernandez, R.M. Gustafson, M.I. Papadaki, S. Sachdeva, M.S. Mannan, *Journal of The Electrochemical Society*, 163 (2016) A2691-A2701.
- [30] P. Peng, F. Jiang, *International Journal of Heat and Mass Transfer*, 103 (2016) 1008-1016.
- [31] G.G. Eshetu, S. Grugeon, G. Gachot, D. Mathiron, M. Armand, S. Laruelle, *Electrochimica Acta*, 102 (2013) 133-141.
- [32] C. Forestier, S. Grugeon, C. Davoisne, A. Lecocq, G. Marlair, M. Armand, L. Sannier, S. Laruelle, *Journal of Power Sources*, 330 (2016) 186-194.
- [33] G. Gachot, S. Grugeon, G.G. Eshetu, D. Mathiron, P. Ribiere, M. Armand, S. Laruelle,

- Electrochimica Acta, 83 (2012) 402-409.
- [34] J. Lamb, C.J. Orendorff, E.P. Roth, J. Langendorf, Journal of The Electrochemical Society, 162 (2015) A2131-A2135.
- [35] B. Gaulupeau, B. Delobel, S. Cahen, S. Fontana, C. Hérold, Journal of Power Sources, 342 (2017) 808-815.
- [36] S. Hess, M. Wohlfahrt-Mehrens, M. Wachtler, Journal of The Electrochemical Society, 162 (2015) A3084-A3097.
- [37] A. Guéguen, D. Streich, M. He, M. Mendez, F.F. Chesneau, P. Novák, E.J. Berg, Journal of The Electrochemical Society, 163 (2016) A1095-A1100.
- [38] S. Wang, L. Lu, X. Liu, Journal of Power Sources, 244 (2013) 101-108.
- [39] J. Kalhoff, G.-T. Kim, S. Passerini, G. Appetecchi, Journal of Power and Energy Engineering, 4 (2016) 9-18.
- [40] F. Richter, S. Kjelstrup, P.J.S. Vie, O.S. Burheim, Journal of Power Sources, 359 (2017) 592-600.
- [41] V. Vishwakarma, C. Waghela, Z. Wei, R. Prasher, S.C. Nagpure, J. Li, F. Liu, C. Daniel, A. Jain, Journal of Power Sources, 300 (2015) 123-131.
- [42] S.-i. Tobishima, J.-i. Yamaki, Journal of Power Sources, 81-82 (1999) 882-886.
- [43] S. Yayathi, W. Walker, D. Doughty, H. Ardebili, Journal of Power Sources, 329 (2016) 197-206.
- [44] A. Lewandowski, A. Świdarska-Mocek, Journal of Power Sources, 194 (2009) 601-609.
- [45] Q. Zhou, W.A. Henderson, G.B. Appetecchi, M. Montanino, S. Passerini, Journal of Physical Chemistry B, 112 (2008) 13577-13580.
- [46] N. De Vos, C. Maton, C.V. Stevens, ChemElectroChem, 1 (2014) 1258-1270.
- [47] M. Armand, F. Endres, D.R. MacFarlane, H. Ohno, B. Scrosati, Nature Materials, 8 (2009) 621-629.
- [48] D.R. MacFarlane, N. Tachikawa, M. Forsyth, J.M. Pringle, P.C. Howlett, G.D. Elliott, J.H. Davis, M. Watanabe, P. Simon, C.A. Angell, Energy and Environmental Science, 7 (2014) 232-250.
- [49] M.A. Navarra, MRS Bulletin, 38 (2013) 548-553.
- [50] A. Eftekhari, Y. Liu, P. Chen, Journal of Power Sources, 334 (2016) 221-239.
- [51] R. Vijayaraghavan, M. Surianarayanan, V. Armel, D. MacFarlane, V. Sridhar, Chemical Communications, 41 (2009) 6297-6299.
- [52] N. Meine, F. Benedito, R. Rinaldi, Green Chemistry, 12 (2010) 1711-1714.
- [53] C.A. Nieto de Castro, M.J.V. Lourenço, A.P.C. Ribeiro, E. Langa, S.I.C. Vieira, P. Goodrich, C. Hardacre, Journal of Chemical & Engineering Data, 55 (2010) 653-661.
- [54] A. Seeberger, A.-K. Andresen, A. Jess, Physical Chemistry Chemical Physics, 11 (2009) 9375-9381.
- [55] J.A. Lazzús, G. Pulgar-Villaruel, Journal of Molecular Liquids, 211 (2015) 981-985.
- [56] M. Watanabe, M.L. Thomas, S. Zhang, K. Ueno, T. Yasuda, K. Dokko, Chemical Reviews, 117 (2017) 7190-7239.
- [57] G. Gebresilassie Eshetu, M. Armand, B. Scrosati, S. Passerini, Angewandte Chemie, International Edition, 53 (2014) 13342-13359.
- [58] X. Cao, S. Röser, B. Rezaeirad, X. He, B. Streipert, M. Winter, I. Cekic-Laskovic, Zeitschrift fuer Anorganische und Allgemeine Chemie, 641 (2015) 2536-2542.
- [59] C.A. Berger, M.U. Ceblin, T. Jacob, ChemElectroChem, 4 (2017) 261-265.
- [60] B. Garcia, S. Lavallée, G. Perron, C. Michot, M. Armand, Electrochimica Acta, 49 (2004) 4583-4588.
- [61] T. Sugimoto, Y. Atsumi, M. Kikuta, E. Ishiko, M. Kono, M. Ishikawa, Journal of Power Sources, 189 (2009) 802-805.
- [62] X. Cao, X. He, J. Wang, H. Liu, S. Röser, B.R. Rad, M. Evertz, B. Streipert, J. Li, R. Wagner, M. Winter, I. Cekic-Laskovic, ACS Applied Materials and Interfaces, 8 (2016) 25971-25978.
- [63] J.S. Moreno, Y. Deguchi, S. Panero, B. Scrosati, H. Ohno, E. Simonetti, G.B. Appetecchi, Electrochimica Acta, 191 (2016) 624-630.
- [64] J. Huang, A.F. Hollenkamp, Journal of Physical Chemistry C, 114 (2010) 21840-21847.
- [65] A.S. Best, A.I. Bhatt, A.F. Hollenkamp, Journal of The Electrochemical Society, 157 (2010)

A903-A911.

- [66] G.T. Kim, S.S. Jeong, M.Z. Xue, A. Balducci, M. Winter, S. Passerini, F. Alessandrini, G.B. Appetecchi, *Journal of Power Sources*, 199 (2012) 239-246.
- [67] E. Cho, J. Mun, O.B. Chae, O.M. Kwon, H.-T. Kim, J.H. Ryu, Y.G. Kim, S.M. Oh, *Electrochemistry Communications*, 22 (2012) 1-3.
- [68] A. Basile, A.F. Hollenkamp, A.I. Bhatt, A.P. O'Mullane, *Electrochemistry Communications*, 27 (2013) 69-72.
- [69] A. Basile, A.I. Bhatt, A.P. O'Mullane, *Electrochimica Acta*, 215 (2016) 19-28.
- [70] S. Wilken, S. Xiong, J. Scheers, P. Jacobsson, P. Johansson, *Journal of Power Sources*, 275 (2015) 935-942.
- [71] J.A. Choi, E.G. Shim, B. Scrosati, D.W. Kim, *Bulletin of the Korean Chemical Society*, 31 (2010) 3190-3194.
- [72] S.Y. Bae, E.G. Shim, D.W. Kim, *Journal of Power Sources*, 244 (2013) 266-271.
- [73] K. Kim, Y.H. Cho, H.C. Shin, *Journal of Power Sources*, 225 (2013) 113-118.
- [74] Y.S. Fung, Y. Yang, J. Zheng, D. Zhu, *ECS Transactions*, 50 (2012) 57-68.
- [75] Y. Wang, W.-H. Zhong, *ChemElectroChem*, 2 (2015) 22-36.
- [76] H.-S. Jeong, S.-Y. Lee, *Journal of Power Sources*, 196 (2011) 6716-6722.
- [77] D. Wang, Z. Zhao, L. Yu, K. Zhang, H. Na, S. Ying, D. Xu, G. Zhang, *Journal of Applied Polymer Science*, 131 (2014) 40543.
- [78] M.B. Effat, C. Wu, F. Ciucci, *Asia-Pacific Journal of Chemical Engineering*, 11 (2016) 399-406.
- [79] R. Spotnitz, J. Franklin, *Journal of Power Sources*, 113 (2003) 81-100.
- [80] C.F. Lopez, J.A. Jeevarajan, P.P. Mukherjee, *Journal of The Electrochemical Society*, 162 (2015) A2163-A2173.
- [81] P.T. Coman, S. Rayman, R.E. White, *Journal of Power Sources*, 307 (2016) 56-62.
- [82] P. Peng, Y. Sun, F. Jiang, *Heat and Mass Transfer*, 50 (2014) 1405-1416.
- [83] K. Yang, X. Liu, L. Lu, S. Wang, P. Liu, *Journal of Power Sources*, 302 (2016) 1-6.
- [84] T.D. Hatchard, D.D. MacNeil, A. Basu, J.R. Dahn, *Journal of The Electrochemical Society*, 148 (2001) A755-A761.
- [85] P.T. Coman, E.C. Darcy, C.T. Veje, R.E. White, *Journal of The Electrochemical Society*, 164 (2017) A587-A593.
- [86] M. Xiong, H. Tang, Y. Wang, M. Pan, *Carbohydrate Polymers*, 101 (2014) 1140-1146.
- [87] C.M. Costa, M.M. Silva, S. Lancers-Mendez, *RSC Advances*, 3 (2013) 11404-11417.
- [88] V. Deimede, C. Elmasides, *Energy Technology*, 3 (2015) 453-468.
- [89] S.S. Zhang, *Journal of Power Sources*, 164 (2007) 351-364.
- [90] H.Y. Guan, F. Lian, Y. Ren, Y. Wen, X.R. Pan, J.L. Sun, *International Journal of Minerals Metallurgy and Materials*, 20 (2013) 598-603.
- [91] H. Lee, M. Yanilmaz, O. Toprakci, K. Fu, X. Zhang, *Energy and Environmental Science*, 7 (2014) 3857-3886.
- [92] Y. Lee, J. Park, H. Jeon, D. Yeon, B.-H. Kim, K.Y. Cho, M.-H. Ryou, Y.M. Lee, *Journal of Power Sources*, 325 (2016) 732-738.
- [93] X.S. Huang, *J Solid State Electrochem*, 15 (2011) 649-662.
- [94] C.J. Weber, S. Geiger, S. Falusi, M. Roth, *AIP Conference Proceedings*, 1597 (2014) 66-81.
- [95] Y.B. Truong, P. Kao, I.L. Kyratzis, C. Huynh, F.H.M. Graichen, A.I. Bhatt, A.S. Best, *Australian Journal of Chemistry*, 66 (2013) 252-261.
- [96] M. Kirchhöfer, J. von Zamory, E. Paillard, S. Passerini, *International Journal of Molecular Sciences*, 15 (2014) 14868-14890.
- [97] A. Sheidaei, X. Xiao, X. Huang, J. Hitt, *Journal of Power Sources*, 196 (2011) 8728-8734.
- [98] G. Venugopal, J. Moore, J. Howard, S. Pandalwar, *Journal of Power Sources*, 77 (1999) 34-41.
- [99] Y. Liao, C. Sun, S. Hu, W. Li, *Electrochimica Acta*, 89 (2013) 461-468.
- [100] IEEE Std 1725-2011(Revision to IEEE Std 1725-2006), (2011) 1-91.
- [101] IEEE Std 1625-2008 (Revision of IEEE Std 1625-2004), (2008) 1-79.
- [102] P. Arora, Z. Zhang, *Chemical Reviews*, 104 (2004) 4419-4462.
- [103] J. Chen, Y. Yan, T. Sun, Y. Qi, X. Li, *RSC Advances*, 4 (2014) 14904-14914.
- [104] J. Nunes-Pereira, M. Kundu, A. Gören, M.M. Silva, C.M. Costa, L. Liu, S. Lancers-Méndez,

Composites Part B: Engineering, 96 (2016) 94-102.

- [105] T. Evans, J.-H. Lee, V. Bhat, S.-H. Lee, *Journal of Power Sources*, 292 (2015) 1-6.
- [106] W. Yi, Z. Huaiyu, H. Jian, L. Yun, Z. Shushu, *Journal of Power Sources*, 189 (2009) 616-619.
- [107] M. Alcoutlabi, H. Lee, J.V. Watson, X. Zhang, *Journal of Materials Science*, 48 (2013) 2690-2700.
- [108] J. Nunes-Pereira, C.M. Costa, S. Lanceros-Méndez, *Journal of Power Sources*, 281 (2015) 378-398.
- [109] T. Nestler, R. Schmid, W. Munchgesang, V. Bazhenov, J. Schilm, T. Leisegang, D.C. Meyer, *AIP Conference Proceedings*, 1597 (2014) 155-184.
- [110] I.C. Halalay, M.J. Lukitsch, M.P. Balogh, C.A. Wong, *Journal of Power Sources*, 238 (2013) 469-477.
- [111] C. Huang, C.-C. Lin, C.-Y. Tsai, R.-S. Juang, *Plasma Processes and Polymers*, 10 (2013) 407-415.
- [112] R.-S. Juang, C.-H. Liang, W.-C. Ma, C.-Y. Tsai, C. Huang, *Journal of the Taiwan Institute of Chemical Engineers*, 45 (2014) 3046-3051.
- [113] J. Son, M.S. Kim, H.W. Lee, J.S. Yu, K.H. Kwon, *Journal of Nanoscience and Nanotechnology*, 14 (2014) 9368-9372.
- [114] M. Baginska, B.J. Blaiszik, T. Rajh, N.R. Sottos, S.R. White, *Journal of Power Sources*, 269 (2014) 735-739.
- [115] C. Cao, L. Tan, W. Liu, J. Ma, L. Li, *Journal of Power Sources*, 248 (2014) 224-229.
- [116] L.F. Fang, J.L. Shi, J.H. Jiang, H. Li, B.K. Zhu, L.P. Zhu, *RSC Advances*, 4 (2014) 22501-22508.
- [117] X. Gao, W. Sheng, Y. Wang, Y. Lin, Y. Luo, B.-G. Li, *Journal of Applied Polymer Science*, 132 (2015) 42169.
- [118] W. Ji, B. Jiang, F. Ai, H. Yang, X. Ai, *RSC Advances*, 5 (2015) 172-176.
- [119] C. Man, P. Jiang, K.-w. Wong, Y. Zhao, C. Tang, M. Fan, W.-m. Lau, J. Mei, S. Li, H. Liu, D. Hui, *Journal of Materials Chemistry A*, 2 (2014) 11980-11986.
- [120] J.Y. Sohn, J.S. Im, J. Shin, Y.C. Nho, *J Solid State Electrochem*, 16 (2012) 551-556.
- [121] J.L. Shi, L.F. Fang, H. Li, H. Zhang, B.K. Zhu, L.P. Zhu, *Journal of Membrane Science*, 437 (2013) 160-168.
- [122] R.-S. Juang, C.-T. Hsieh, P.-A. Chen, Y.-F. Chen, *Journal of Power Sources*, 286 (2015) 526-533.
- [123] T. Lee, W.K. Kim, Y. Lee, M.H. Ryou, Y.M. Lee, *Macromolecular Research*, 22 (2014) 1190-1195.
- [124] X.Y. Lv, H. Li, Z.Q. Zhang, H.N. Chang, L. Jiang, H.Z. Liu, *Physics Procedia*, 25 (2012) 227-232.
- [125] Z. Wang, F. Guo, C. Chen, L. Shi, S. Yuan, L. Sun, J. Zhu, *ACS Applied Materials and Interfaces*, 7 (2015) 3314-3322.
- [126] W. Zhengduo, S. Lijun, L. Zhongwei, C. Qiang, in: 2012 Abstracts IEEE International Conference on Plasma Science (ICOPS), IEEE, 2012, pp. 3P-105.
- [127] K.J. Kim, H.K. Kwon, M.-S. Park, T. Yim, J.-S. Yu, Y.-J. Kim, *Physical Chemistry Chemical Physics*, 16 (2014) 9337-9343.
- [128] H.Y. Liu, Z.H. Dai, J. Xu, B.H. Guo, X.M. He, *Journal of Energy Chemistry*, 23 (2014) 582-586.
- [129] J.-H. Park, J.-H. Cho, W. Park, D. Ryoo, S.-J. Yoon, J.H. Kim, Y.U. Jeong, S.-Y. Lee, *Journal of Power Sources*, 195 (2010) 8306-8310.
- [130] K. Prasanna, T. Subburaj, W.J. Lee, C.W. Lee, *Electrochimica Acta*, 137 (2014) 273-279.
- [131] W.-K. Shin, D.-W. Kim, *Journal of Power Sources*, 226 (2013) 54-60.
- [132] P. Zhang, L. Chen, C. Shi, P. Yang, J. Zhao, *Journal of Power Sources*, 284 (2015) 10-15.
- [133] X. Li, J. He, D. Wu, M. Zhang, J. Meng, P. Ni, *Electrochimica Acta*, 167 (2015) 396-403.
- [134] J. Fang, A. Kellarakis, Y.-W. Lin, C.-Y. Kang, M.-H. Yang, C.-L. Cheng, Y. Wang, E.P. Giannelis, L.-D. Tsai, *Physical Chemistry Chemical Physics*, 13 (2011) 14457-14461.
- [135] M. Kim, J.H. Park, *Journal of Power Sources*, 212 (2012) 22-27.
- [136] W. Chen, L. Shi, Z. Wang, J. Zhu, H. Yang, X. Mao, M. Chi, L. Sun, S. Yuan, *Carbohydrate Polymers*, 147 (2016) 517-524.

- [137] J.M. Ko, B.G. Min, D.W. Kim, K.S. Ryu, K.M. Kim, Y.G. Lee, S.H. Chang, *Electrochimica Acta*, 50 (2004) 367-370.
- [138] X. Zhu, X. Jiang, X. Ai, H. Yang, Y. Cao, *Journal of Membrane Science*, 504 (2016) 97-103.
- [139] K.J. Kim, Y.H. Kim, J.H. Song, Y.N. Jo, J.S. Kim, Y.J. Kim, *Journal of Power Sources*, 195 (2010) 6075-6080.
- [140] K.J. Kim, J.H. Kim, M.S. Park, H.K. Kwon, H. Kim, Y.J. Kim, *Journal of Power Sources*, 198 (2012) 298-302.
- [141] S.J. Gwon, J.H. Choi, J.Y. Sohn, Y.E. Ihm, Y.C. Nho, *Nuclear Instruments & Methods in Physics Research Section B-Beam Interactions with Materials and Atoms*, 267 (2009) 3309-3313.
- [142] M.N. Tamaño-Machiavello, B. Bracke, C.M. Costa, S. Lanceros-Mendez, R. Sabater i Serra, J.L. Gómez Ribelles, *Journal of Polymer Science Part B: Polymer Physics*, 54 (2016) 672-679.
- [143] D.W. Kim, J.M. Ko, J.H. Chun, S.H. Kim, J.K. Park, *Electrochemistry Communications*, 3 (2001) 535-538.
- [144] Y.-B. Jeong, D.-W. Kim, *Journal of Power Sources*, 128 (2004) 256-262.
- [145] T. Chen, Y. Liao, X. Wang, X. Luo, X. Li, W. Li, *Electrochimica Acta*, 191 (2016) 923-932.
- [146] L.F. Fang, J.L. Shi, H. Li, B.K. Zhu, L.P. Zhu, *Journal of Applied Polymer Science*, 131 (2014) 41036.
- [147] R. Xu, X. Huang, X. Lin, J. Cao, J. Yang, C. Lei, *Journal of Electroanalytical Chemistry*, 786 (2017) 77-85.
- [148] H.-S. Jeong, S.C. Hong, S.-Y. Lee, *Journal of Membrane Science*, 364 (2010) 177-182.
- [149] H.-S. Jeong, D.-W. Kim, Y.U. Jeong, S.-Y. Lee, *Journal of Power Sources*, 195 (2010) 6116-6121.
- [150] Y.-S. Lee, Y.B. Jeong, D.-W. Kim, *Journal of Power Sources*, 195 (2010) 6197-6201.
- [151] W.K. Shin, Y.S. Lee, D.W. Kim, *Journal of Nanoscience and Nanotechnology*, 13 (2013) 3705-3710.
- [152] M.Y. An, H.T. Kim, D.R. Chang, *J Solid State Electrochem*, 18 (2014) 1807-1814.
- [153] H.-S. Jeong, J.H. Noh, C.-G. Hwang, S.H. Kim, S.-Y. Lee, *Macromolecular Chemistry and Physics*, 211 (2010) 420-425.
- [154] K.M. Kim, L.R. Hepowit, J.-C. Kim, Y.-G. Lee, J.M. Ko, *Korean Journal of Chemical Engineering*, 32 (2015) 717-722.
- [155] J.-A. Choi, S.H. Kim, D.-W. Kim, *Journal of Power Sources*, 195 (2010) 6192-6196.
- [156] Y. Ko, H. Yoo, J. Kim, *RSC Advances*, 4 (2014) 19229-19233.
- [157] C. Shi, P. Zhang, L.X. Chen, P.T. Yang, J.B. Zhao, *Journal of Power Sources*, 270 (2014) 547-553.
- [158] S.M. Kang, M.H. Ryou, J.W. Choi, H. Lee, *Chemistry of Materials*, 24 (2012) 3481-3485.
- [159] M. Kim, Y.S. Kim, Y.G. Lee, J.H. Park, *RSC Advances*, 3 (2013) 16708-16713.
- [160] D. Yeon, Y. Lee, M.H. Ryou, Y.M. Lee, *Electrochimica Acta*, 157 (2015) 282-289.
- [161] Y. Liu, H. Ma, B.S. Hsiao, B. Chu, A.H. Tsou, *Polymer*, 107 (2016) 163-169.
- [162] H. Lee, M. Alcoutlabi, J.V. Watson, X.W. Zhang, *Journal of Applied Polymer Science*, 129 (2013) 1939-1951.
- [163] M. Yanilmaz, C. Chen, X.W. Zhang, *Journal of Polymer Science Part B: Polymer Physics*, 51 (2013) 1719-1726.
- [164] H. Wang, H. Gao, *Electrochimica Acta*, 215 (2016) 525-534.
- [165] H.Y. Liu, J. Xu, B.H. Guo, X.M. He, *Ceramics International*, 40 (2014) 14105-14110.
- [166] D. Fu, B. Luan, S. Argue, M.N. Bureau, I.J. Davidson, *Journal of Power Sources*, 206 (2012) 325-333.
- [167] X. Li, M. Zhang, J. He, D. Wu, J. Meng, P. Ni, *Journal of Membrane Science*, 455 (2014) 368-374.
- [168] H. Lee, M. Alcoutlabi, O. Toprakci, G.J. Xu, J.V. Watson, X.W. Zhang, *J Solid State Electrochem*, 18 (2014) 2451-2458.
- [169] D. Ihm, J. Noh, J. Kim, *Journal of Power Sources*, 109 (2002) 388-393.
- [170] J.-L. Shi, L.-F. Fang, H. Li, Z.-Y. Liang, B.-K. Zhu, L.-P. Zhu, *Journal of Membrane Science*, 429 (2013) 355-363.
- [171] D. Djian, F. Alloin, S. Martinet, H. Lignier, *Journal of Power Sources*, 187 (2009) 575-580.
- [172] J.Y. Han, H.H. Oh, K.J. Choi, B.R. Min, *Journal of Applied Polymer Science*, 122 (2011)

2653-2665.

- [173] H.Y. Hwang, D.J. Kim, H.J. Kim, Y.T. Hong, S.Y. Nam, *Transactions of Nonferrous Metals Society of China*, 21 (2011) S141-S147.
- [174] X.S. Huang, *J Solid State Electrochem*, 17 (2013) 591-597.
- [175] M. Bolloli, C. Antonelli, Y. Molm  ret, F. Alloin, C. Iojoiu, J.-Y. Sanchez, *Electrochimica Acta*, 214 (2016) 38-48.
- [176] Y.S. Zhu, F.X. Wang, L.L. Liu, S.Y. Xiao, Y.Q. Yang, Y.P. Wu, *Scientific Reports*, 3 (2013) 3187.
- [177] Y. Liang, S. Cheng, J. Zhao, C. Zhang, S. Sun, N. Zhou, Y. Qiu, X. Zhang, *Journal of Power Sources*, 240 (2013) 204-211.
- [178] M. Kim, G.Y. Han, K.J. Yoon, J.H. Park, *Journal of Power Sources*, 195 (2010) 8302-8305.
- [179] Z. Liu, W. Jiang, Q. Kong, C. Zhang, P. Han, X. Wang, J. Yao, G. Cui, *Macromolecular Materials and Engineering*, 298 (2013) 806-813.
- [180] X. Zhou, L. Yue, J. Zhang, Q. Kong, Z. Liu, J. Yao, G. Cui, *Journal of The Electrochemical Society*, 160 (2013) A1341-A1347.
- [181] W. Pu, X. He, L. Wang, C. Jiang, C. Wan, *Journal of Membrane Science*, 272 (2006) 11-14.
- [182] R. Sousa, J. Nunes-Pereira, C.M. Costa, M.M. Silva, S. Lanceros-Mendez, J. Hassoun, B. Scrosati, G.B. Appetecchi, *Journal of Power Sources*, 263 (2014) 29-36.
- [183] Z.Y. Cui, Y.Y. Xu, L.P. Zhu, J.Y. Wang, B.K. Zhu, *Ionics*, 15 (2009) 469-476.
- [184] L. Ye, X. Shi, Z. Zhang, J. Liu, X. Jian, M. Waqas, W. He, *Advanced Materials Interfaces*, 4 (2017) 1601236.
- [185] A. Subramania, N.T.K. Sundaram, A.R.S. Priya, G.V. Kumar, *Journal of Membrane Science*, 294 (2007) 8-15.
- [186] Y. Ansari, B. Guo, J.H. Cho, K. Park, J. Song, C.J. Ellison, J.B. Goodenough, *Journal of the Electrochemical Society*, 161 (2014) A1655-A1661.
- [187] M. Raja, T.P. Kumar, G. Sanjeev, L. Zolin, C. Gerbaldi, A.M. Stephan, *Ionics*, 20 (2014) 943-948.
- [188] D. Song, C. Xu, Y. Chen, J. He, Y. Zhao, P. Li, W. Lin, F. Fu, *Solid State Ionics*, 282 (2015) 31-36.
- [189] Y. Ding, P. Zhang, Z. Long, Y. Jiang, F. Xu, W. Di, *Journal of Membrane Science*, 329 (2009) 56-59.
- [190] F. Huang, Y. Xu, B. Peng, Y. Su, F. Jiang, Y.-L. Hsieh, Q. Wei, *ACS Sustainable Chemistry and Engineering*, 3 (2015) 932-940.
- [191] M. Xiong, H. Tang, Y. Wang, Y. Lin, M. Sun, Z. Yin, M. Pan, *Journal of Power Sources*, 241 (2013) 203-211.
- [192] N. Angulakshmi, A.M. Stephan, *Electrochimica Acta*, 127 (2014) 167-172.
- [193] A.K. Solarajan, V. Murugadoss, S. Angaiah, *Journal of Applied Polymer Science*, 134 (2017) 45177.
- [194] K.-W. Kim, H.W. Kim, Y. Kim, J.-K. Kim, *Electrochimica Acta*, 236 (2017) 394-398.
- [195] C.M. Costa, L.C. Rodrigues, V. Sencadas, M.M. Silva, J.G. Rocha, S. Lanceros-Mendez, *Journal of Membrane Science*, 407 (2012) 193-201.
- [196] C.M. Costa, V. Sencadas, J.G. Rocha, M.M. Silva, S. Lanceros-Mendez, *J Solid State Electrochem*, 17 (2013) 861-870.
- [197] J. Zhang, Z. Liu, Q. Kong, C. Zhang, S. Pang, L. Yue, X. Wang, J. Yao, G. Cui, *ACS Applied Materials and Interfaces*, 5 (2013) 128-134.
- [198] S.-J. Chun, E.-S. Choi, E.-H. Lee, J.H. Kim, S.-Y. Lee, S.-Y. Lee, *Journal of Materials Chemistry*, 22 (2012) 16618-16626.
- [199] R. Pan, O. Cheung, Z. Wang, P. Tammela, J. Huo, J. Lindh, K. Edstr  m, M. Str  mme, L. Nyholm, *Journal of Power Sources*, 321 (2016) 185-192.
- [200] Q. Xu, Q. Kong, Z. Liu, X. Wang, R. Liu, J. Zhang, L. Yue, Y. Duan, G. Cui, *ACS Sustainable Chemistry and Engineering*, 2 (2014) 194-199.
- [201] Q. Xu, Q. Kong, Z. Liu, J. Zhang, X. Wang, R. Liu, L. Yue, G. Cui, *RSC Advances*, 4 (2014) 7845-7850.
- [202] B.S. Lalia, Y.A. Samad, R. Hashaikeh, *Journal of Applied Polymer Science*, 126 (2012) E441-E447.

- [203] J. Zhang, L. Yue, Q. Kong, Z. Liu, X. Zhou, C. Zhang, Q. Xu, B. Zhang, G. Ding, B. Qin, Y. Duan, Q. Wang, J. Yao, G. Cui, L. Chen, *Scientific Reports*, 4 (2014) 3935.
- [204] H. Zhang, X. Wang, Y. Liang, *Heliyon*, 1 (2015) e00032.
- [205] W. Yi, D. Xiaoli, Y. Yunzhen, L. Yun, H. Jian, Z. Huaiyu, *Textile Research Journal*, 82 (2012) 1659-1665.
- [206] X. Huang, J. Hitt, *Journal of Membrane Science*, 425–426 (2013) 163-168.
- [207] B. Zhang, Q. Wang, J. Zhang, G. Ding, G. Xu, Z. Liu, G. Cui, *Nano Energy*, 10 (2014) 277-287.
- [208] T.H. Cho, T. Sakai, S. Tanase, K. Kimura, Y. Kondo, T. Tarao, M. Tanaka, *Electrochemical and Solid-State Letters*, 10 (2007) A159-A162.
- [209] T.-H. Cho, M. Tanaka, H. Onishi, Y. Kondo, T. Nakamura, H. Yamazaki, S. Tanase, T. Sakai, *Journal of Power Sources*, 181 (2008) 155-160.
- [210] P. Carol, P. Ramakrishnan, B. John, G. Cheruvally, *Journal of Power Sources*, 196 (2011) 10156-10162.
- [211] Y.-J. Kim, H.-S. Kim, C.-H. Doh, S.H. Kim, S.-M. Lee, *Journal of Power Sources*, 244 (2013) 196-206.
- [212] X. Ma, P. Kolla, R. Yang, Z. Wang, Y. Zhao, A.L. Smirnova, H. Fong, *Electrochimica Acta*, 236 (2017) 417-423.
- [213] G. Zainab, X. Wang, J. Yu, Y. Zhai, A. Ahmed Babar, K. Xiao, B. Ding, *Materials Chemistry and Physics*, 182 (2016) 308-314.
- [214] A.I. Gopalan, P. Santhosh, K.M. Manesh, J.H. Nho, S.H. Kim, C.G. Hwang, K.P. Lee, *Journal of Membrane Science*, 325 (2008) 683-690.
- [215] X.S. Huang, D. Bahroloomi, X.R. Xiao, *J Solid State Electrochem*, 18 (2014) 133-139.
- [216] M. Yanilmaz, Y. Lu, M. Dirican, K. Fu, X.W. Zhang, *Journal of Membrane Science*, 456 (2014) 57-65.
- [217] M. Yanilmaz, Y. Lu, Y. Li, X. Zhang, *Journal of Power Sources*, 273 (2015) 1114-1119.
- [218] M. Yanilmaz, Y. Lu, J. Zhu, X. Zhang, *Journal of Power Sources*, 313 (2016) 205-212.
- [219] D. Li, D. Shi, K. Feng, X. Li, H. Zhang, *Journal of Membrane Science*, 530 (2017) 125-131.
- [220] Z. Li, T. Cao, Y. Zhang, Y. Han, S. Xu, Z. Xu, *Journal of Membrane Science*, 540 (2017) 422-429.
- [221] Q. Wang, Y. Yu, J. Ma, N. Zhang, J. Zhang, Z. Liu, G. Cui, *Journal of Power Sources*, 327 (2016) 196-203.
- [222] Q. Wang, *Electrochimica Acta*, 182 (2015) 334-341.
- [223] K. Peng, B. Wang, C. Ji, *Journal of Applied Polymer Science*, 134 (2017) 44907.
- [224] H. Zhang, Y. Zhang, T. Xu, A.E. John, Y. Li, W. Li, B. Zhu, *Journal of Power Sources*, 329 (2016) 8-16.
- [225] Y. Zhai, N. Wang, X. Mao, Y. Si, J. Yu, S.S. Al-Deyab, M. El-Newehy, B. Ding, *Journal of Materials Chemistry A*, 2 (2014) 14511-14518.
- [226] W. Kang, N. Deng, X. Ma, J. Ju, L. Li, X. Liu, B. Cheng, *Electrochimica Acta*, 216 (2016) 276-286.
- [227] Q.-Y. Wu, H.-Q. Liang, L. Gu, Y. Yu, Y.-Q. Huang, Z.-K. Xu, *Polymer*, 107 (2016) 54-60.
- [228] S.-R. Park, Y.-C. Jung, W.-K. Shin, K.H. Ahn, C.H. Lee, D.-W. Kim, *Journal of Membrane Science*, 527 (2017) 129-136.
- [229] J.H. Lee, J. Manuel, H. Choi, W.H. Park, J.-H. Ahn, *Polymer*, 68 (2015) 335-343.
- [230] R. Lv, Y. Zhu, H. Liu, B. Na, Y. Huang, X. Xie, *Journal of Applied Polymer Science*, 134 (2017) 44515.
- [231] R. l'Abée, F. DaRosa, M.J. Armstrong, M.M. Hantel, D. Mourzagh, *Journal of Power Sources*, 345 (2017) 202-211.
- [232] X. Huang, *Journal of Power Sources*, 216 (2012) 216-221.
- [233] L. Kong, B. Liu, J. Ding, X. Yan, G. Tian, S. Qi, D. Wu, *Journal of Membrane Science*, 549 (2018) 244-250.
- [234] Y. Zhai, K. Xiao, J. Yu, B. Ding, *Electrochimica Acta*, 154 (2015) 219-226.
- [235] H. Wang, T. Wang, S. Yang, L. Fan, *Polymer*, 54 (2013) 6339-6348.
- [236] H. Zhang, C.-E. Lin, M.-Y. Zhou, A.E. John, B.-K. Zhu, *Electrochimica Acta*, 187 (2016) 125-133.

- [237] Q.J. Wang, W.L. Song, L.N. Wang, Y. Song, Q. Shi, L.Z. Fan, *Electrochimica Acta*, 132 (2014) 538-544.
- [238] W. Ye, J. Zhu, X. Liao, S. Jiang, Y. Li, H. Fang, H. Hou, *Journal of Power Sources*, 299 (2015) 417-424.
- [239] L. Cao, P. An, Z. Xu, J. Huang, *Journal of Electroanalytical Chemistry*, 767 (2016) 34-39.
- [240] J.-E. Lim, M.-S. Oh, J.-H. Ahn, J.-K. Kim, *Electrochimica Acta*, 238 (2017) 107-111.
- [241] W. Jiang, Z. Liu, Q. Kong, J. Yao, C. Zhang, P. Han, G. Cui, *Solid State Ionics*, 232 (2013) 44-48.
- [242] L. Kong, L. Yuan, B. Liu, G. Tian, S. Qi, D. Wu, *Journal of The Electrochemical Society*, 164 (2017) A1328-A1332.
- [243] Y. Wang, S. Wang, J. Fang, L.-X. Ding, H. Wang, *Journal of Membrane Science*, 537 (2017) 248-254.
- [244] J. Shayapat, O.H. Chung, J.S. Park, *Electrochimica Acta*, 170 (2015) 110-121.
- [245] W.Y. Chen, Y.B. Liu, Y. Ma, W.X. Yang, *Journal of Power Sources*, 273 (2015) 1127-1135.
- [246] D. Wu, C. Shi, S. Huang, X. Qiu, H. Wang, Z. Zhan, P. Zhang, J. Zhao, D. Sun, L. Lin, *Electrochimica Acta*, 176 (2015) 727-734.
- [247] W. Chen, Y. Liu, Y. Ma, J. Liu, X. Liu, *Materials Letters*, 133 (2014) 67-70.
- [248] J. Lee, C.L. Lee, K. Park, I.D. Kim, *Journal of Power Sources*, 248 (2014) 1211-1217.
- [249] J. Hao, G. Lei, Z. Li, L. Wu, Q. Xiao, L. Wang, *Journal of Membrane Science*, 428 (2013) 11-16.
- [250] H. He, X. Wang, W. Liu, *Solid State Ionics*, 294 (2016) 31-36.
- [251] J.H. Kim, J.H. Kim, K.H. Choi, H.K. Yu, J.H. Kim, J.S. Lee, S.Y. Lee, *Nano Letters*, 14 (2014) 4438-4448.
- [252] W. Xiao, Z. Gao, S. Wang, J. Liu, C. Yan, *Materials Letters*, 145 (2015) 177-179.
- [253] M. Xie, M. Yin, G. Nie, J. Wang, C. Wang, D. Chao, X. Liu, *Journal of Polymer Science Part A: Polymer Chemistry*, 54 (2016) 2714-2721.
- [254] Q. Xiao, Z. Li, D. Gao, H. Zhang, *Journal of Membrane Science*, 326 (2009) 260-264.
- [255] J. Zhang, Q. Kong, Z. Liu, S. Pang, L. Yue, J. Yao, X. Wang, G. Cui, *Solid State Ionics*, 245-246 (2013) 49-55.
- [256] J. Li, W. Tian, H. Yan, L. He, X. Tuo, *Journal of Applied Polymer Science*, 133 (2016) 43623.
- [257] S.-O. Tung, S. Ho, M. Yang, R. Zhang, N.A. Kotov, *Nature Communications*, 6 (2015) 6152.
- [258] S.S. Zhang, M.H. Ervin, K. Xu, T.R. Jow, *Electrochimica Acta*, 49 (2004) 3339-3345.
- [259] S.S. Zhang, M.H. Ervin, K. Xu, T.R. Jow, *Solid State Ionics*, 176 (2005) 41-46.
- [260] W. Pu, X. He, L. Wang, Z. Tian, C. Jiang, C. Wan, *Journal of Membrane Science*, 280 (2006) 6-9.
- [261] P. Zhang, H.P. Zhang, G.C. Li, Z.H. Li, Y.P. Wu, *Electrochemistry Communications*, 10 (2008) 1052-1055.
- [262] J. Shi, Y. Xia, Z. Yuan, H. Hu, X. Li, H. Zhang, Z. Liu, *Scientific Reports*, 5 (2015) 8255.
- [263] J. Ding, Y. Kong, P. Li, J. Yang, *Journal of The Electrochemical Society*, 159 (2012) A1474-A1480.
- [264] M. Xia, Q. Liu, Z. Zhou, Y. Tao, M. Li, K. Liu, Z. Wu, D. Wang, *Journal of Power Sources*, 266 (2014) 29-35.
- [265] J. Ding, Y. Kong, J.R. Yang, *Journal of the Electrochemical Society*, 159 (2012) A1198-A1202.
- [266] E.-S. Choi, S.-Y. Lee, *Journal of Materials Chemistry*, 21 (2011) 14747-14754.
- [267] H.-S. Jeong, E.-S. Choi, S.-Y. Lee, J.H. Kim, *Journal of Membrane Science*, 415-416 (2012) 513-519.
- [268] J.H. Kim, J.H. Kim, E.S. Choi, J.H. Kim, S.Y. Lee, *RSC Advances*, 4 (2014) 54312-54321.
- [269] Y.-E. Miao, G.-N. Zhu, H. Hou, Y.-Y. Xia, T. Liu, *Journal of Power Sources*, 226 (2013) 82-86.
- [270] X. Yan, Y. Wang, T. Yu, H. Chen, Z. Zhao, S. Guan, *Electrochimica Acta*, 216 (2016) 1-7.
- [271] J. Shi, T. Shen, H. Hu, Y. Xia, Z. Liu, *Journal of Power Sources*, 271 (2014) 134-142.
- [272] M. Jassal, S. Ghosh, *Indian Journal of Fibre and Textile Research*, 27 (2002) 290-306.
- [273] A. Balducci, *Topics in Current Chemistry*, 375 (2017) 20 (21-27).
- [274] W. Zhai, H.J. Zhu, L. Wang, X.M. Liu, H. Yang, *Electrochimica Acta*, 133 (2014) 623-630.

- [275] C.M. Costa, J.L. Gomez Ribelles, S. Lanceros-Méndez, G.B. Appetecchi, B. Scrosati, *Journal of Power Sources*, 245 (2014) 779-786.
- [276] M. Li, L. Yang, S. Fang, S. Dong, Y. Jin, S.-i. Hirano, K. Tachibana, *Journal of Power Sources*, 196 (2011) 6502-6506.
- [277] C.M. Costa, H.M. Rodrigues, A. Gören, A.V. Machado, M.M. Silva, S. Lanceros-Méndez, *ChemistrySelect*, 2 (2017) 5394-5402.
- [278] M. Rao, X. Geng, Y. Liao, S. Hu, W. Li, *Journal of Membrane Science*, 399-400 (2012) 37-42.
- [279] G. Cheruvally, J.-K. Kim, J.-W. Choi, J.-H. Ahn, Y.-J. Shin, J. Manuel, P. Raghavan, K.-W. Kim, H.-J. Ahn, D.S. Choi, C.E. Song, *Journal of Power Sources*, 172 (2007) 863-869.
- [280] P. Raghavan, X. Zhao, J. Manuel, G.S. Chauhan, J.-H. Ahn, H.-S. Ryu, H.-J. Ahn, K.-W. Kim, C. Nah, *Electrochimica Acta*, 55 (2010) 1347-1354.
- [281] J.-K. Kim, G. Cheruvally, X. Li, J.-H. Ahn, K.-W. Kim, H.-J. Ahn, *Journal of Power Sources*, 178 (2008) 815-820.
- [282] C.L. Yang, H.Y. Liu, Q.L. Xia, Z.H. Li, Q.Z. Xiao, G.T. Lei, *Arabian Journal for Science and Engineering*, 39 (2014) 6711-6720.
- [283] B.S. Lalia, Y. Abdul Samad, R. Hashaikeh, *J Solid State Electrochem*, 17 (2013) 575-581.
- [284] J. Saunier, F. Alloin, J.Y. Sanchez, G. Caillon, *Journal of Power Sources*, 119-121 (2003) 454-459.
- [285] C.T. Love, *Journal of Power Sources*, 196 (2011) 2905-2912.
- [286] S. Yan, X. Xiao, X. Huang, X. Li, Y. Qi, *Polymer*, 55 (2014) 6282-6292.
- [287] F. Mueller, N. Loeffler, G.-T. Kim, T. Diemant, R.J. Behm, S. Passerini, *ChemSusChem*, 9 (2016) 1290-1298.
- [288] H. Sakaebe, H. Matsumoto, K. Tatsumi, *Electrochimica Acta*, 53 (2007) 1048-1054.
- [289] C. Arbizzani, G. Gabrielli, M. Mastragostino, *Journal of Power Sources*, 196 (2011) 4801-4805.
- [290] M. Galiński, A. Lewandowski, I. Stępnia, *Electrochimica Acta*, 51 (2006) 5567-5580.
- [291] H. Matsumoto, H. Sakaebe, K. Tatsumi, M. Kikuta, E. Ishiko, M. Kono, *Journal of Power Sources*, 160 (2006) 1308-1313.
- [292] M.J. Lee, J.H. Kim, H.-S. Lim, S.Y. Lee, H.K. Yu, J.H. Kim, J.S. Lee, Y.-K. Sun, M.D. Guiver, K.D. Suh, Y.M. Lee, *Chemical communications*, 51 (2015) 2068-2071.
- [293] J. Nunes-Pereira, A.C. Lopes, C.M. Costa, L.C. Rodrigues, M.M. Silva, S. Lanceros-Mendez, *Journal of Electroanalytical Chemistry*, 689 (2013) 223-232.
- [294] H.Y. Liu, J. Xu, B.H. Guo, X.M. He, *Journal of Applied Polymer Science*, 131 (2014) 41156.
- [295] W. Xiao, L. Zhao, Y. Gong, J. Liu, C. Yan, *Journal of Membrane Science*, 487 (2015) 221-228.
- [296] J. Liu, X. Wu, J. He, J. Li, Y. Lai, *Electrochimica Acta*, 235 (2017) 500-507.
- [297] J. Wan, J. Zhang, J. Yu, J. Zhang, *ACS Applied Materials & Interfaces*, 9 (2017) 24591-24599.
- [298] J. Cui, J. Liu, C. He, J. Li, X. Wu, *Journal of Membrane Science*, 541 (2017) 661-667.
- [299] F.G.B. Ooms, E.M. Kelder, J. Schoonman, N. Gerrits, J. Smedinga, G. Calis, *Journal of Power Sources*, 97-98 (2001) 598-601.
- [300] D. Djian, F. Alloin, S. Martinet, H. Lignier, J.Y. Sanchez, *Journal of Power Sources*, 172 (2007) 416-421.
- [301] C. Martinez-Cisneros, C. Antonelli, B. Levenfeld, A. Varez, J.Y. Sanchez, *Electrochimica Acta*, 216 (2016) 68-78.
- [302] C.J. Orendorff, *Electrochemical Society Interface*, Summer (2012) 61-65.
- [303] M. Kim, J.-Y. Shon, Y.C. Nho, T.-W. Lee, J.H. Park, *Journal of The Electrochemical Society*, 157 (2010) A31-A34.
- [304] U. Schadeck, K. Kyrgyzbaev, T. Gerdes, M. Willert-Porada, R. Moos, *Journal of Membrane Science*, 550 (2018) 518-525.
- [305] S. Kalnaus, Y. Wang, J.A. Turner, *Journal of Power Sources*, 348 (2017) 255-263.
- [306] B. Morin, C. Hu, P. Khokhlov, J. Kaschmitter, S.-J. Cho, *ECS Transactions*, 72 (2016) 1-12.
- [307] S. Jenkins, *Chemical Engineering*, 120 (2013) 17-23.
- [308] M. Xu, M. Wang, H. Xu, H. Xue, H. Pang, *Chemistry – An Asian Journal*, 11 (2016) 2967-

2995.

- [309] D.H. Reneker, A.L. Yarin, *Polymer*, 49 (2008) 2387-2425.
- [310] Z.-M. Huang, Y.Z. Zhang, M. Kotaki, S. Ramakrishna, *Composites Science and Technology*, 63 (2003) 2223-2253.
- [311] H. Fong, I. Chun, D.H. Reneker, *Polymer*, 40 (1999) 4585-4592.
- [312] G.A. Elia, U. Ulissi, F. Mueller, J. Reiter, N. Tsiouvaras, Y.-K. Sun, B. Scrosati, S. Passerini, J. Hassoun, *Chemistry—A European Journal*, 22 (2016) 6808-6814.
- [313] J. Cao, Y.M. Shang, L. Wang, X.M. He, L.F. Deng, H. Chen, *RSC Advances*, 5 (2015) 8258-8262.
- [314] S.A. Smith, B.P. Williams, Y.L. Joo, *Journal of Membrane Science*, 526 (2017) 315-322.
- [315] P. Raghavan, X. Zhao, H. Choi, D.-H. Lim, J.-K. Kim, A. Matic, P. Jacobsson, C. Nah, J.-H. Ahn, *Solid State Ionics*, 262 (2014) 77-82.
- [316] R.E. Sousa, M. Kundu, A. Goren, M.M. Silva, L. Liu, C.M. Costa, S. Lanceros-Mendez, *RSC Advances*, 5 (2015) 90428-90436.
- [317] M.P.S. Mousavi, A.J. Dittmer, B.E. Wilson, J. Hu, A. Stein, P. Bühlmann, *Journal of The Electrochemical Society*, 162 (2015) A2250-A2258.
- [318] G.A. Giffin, A. Moretti, S. Jeong, S. Passerini, *Journal of Power Sources*, 342 (2017) 335-341.
- [319] S. Horiuchi, M. Yoshizawa-Fujita, Y. Takeoka, M. Rikukawa, *Journal of Power Sources*, 325 (2016) 637-640.
- [320] H. Li, J. Pang, Y. Yin, W. Zhuang, H. Wang, C. Zhai, S. Lu, *RSC Advances*, 3 (2013) 13907-13914.
- [321] S. Menne, R.S. Kühnel, A. Balducci, *Electrochimica Acta*, 90 (2013) 641-648.
- [322] N. Salem, S. Zavorine, D. Nucciarone, K. Whitbread, M. Moser, Y. Abu-Lebdeh, *Journal of The Electrochemical Society*, 164 (2017) H5202-H5209.
- [323] L. Lombardo, S. Brutti, M.A. Navarra, S. Panero, P. Reale, *Journal of Power Sources*, 227 (2013) 8-14.
- [324] C. Liu, X. Ma, F. Xu, L. Zheng, H. Zhang, W. Feng, X. Huang, M. Armand, J. Nie, H. Chen, Z. Zhou, *Electrochimica Acta*, 149 (2014) 370-385.
- [325] B. Gélinas, M. Natali, T. Bibienne, Q.P. Li, M. Dollé, D. Rochefort, *The Journal of Physical Chemistry C*, 120 (2016) 5315-5325.
- [326] A.I. Bhatt, A.S. Best, J. Huang, A.F. Hollenkamp, *Journal of The Electrochemical Society*, 157 (2010) A66-A74.
- [327] T. Evans, J. Olson, V. Bhat, S.-H. Lee, *Journal of Power Sources*, 265 (2014) 132-139.
- [328] T. Osaka, D. Mukoyama, H. Nara, *Journal of The Electrochemical Society*, 162 (2015) A2529-A2537.
- [329] M. Itagaki, K. Honda, Y. Hoshi, I. Shitanda, *Journal of Electroanalytical Chemistry*, 737 (2015) 78-84.
- [330] C. Fernández-Sánchez, C.J. McNeil, K. Rawson, *TrAC Trends in Analytical Chemistry*, 24 (2005) 37-48.
- [331] D. Aurbach, I. Weissman, A. Zaban, O. Chusid, *Electrochimica Acta*, 39 (1994) 51-71.
- [332] H. Lin, C. Liang, C. Liu, C. Dai, Y. Xiong, *ChemistrySelect*, 2 (2017) 6090-6096.
- [333] J.E.B. Randles, *Discussions of the Faraday Society*, 1 (1947) 11-19.
- [334] D. Aurbach, A. Zaban, Y. Gofer, Y.E. Ely, I. Weissman, O. Chusid, O. Abramson, *Journal of Power Sources*, 54 (1995) 76-84.
- [335] A. Zaban, D. Aurbach, *Journal of Power Sources*, 54 (1995) 289-295.
- [336] P.C. Howlett, N. Brack, A.F. Hollenkamp, M. Forsyth, D.R. MacFarlane, *Journal of The Electrochemical Society*, 153 (2006) A595-A606.
- [337] R. de Levie, *Electrochimica Acta*, 9 (1964) 1231-1245.
- [338] S. Seki, Y. Ohno, Y. Kobayashi, H. Miyashiro, A. Usami, Y. Mita, H. Tokuda, M. Watanabe, K. Hayamizu, S. Tsuzuki, M. Hattori, N. Terada, *Journal of The Electrochemical Society*, 154 (2007) A173-A177.
- [339] A. Budi, A. Basile, G. Opletal, A.F. Hollenkamp, A.S. Best, R.J. Rees, A.I. Bhatt, A.P. O'Mullane, S.P. Russo, *The Journal of Physical Chemistry C*, 116 (2012) 19789-19797.
- [340] H. Guk, D. Kim, S.-H. Choi, D.H. Chung, S.S. Han, *Journal of The Electrochemical Society*,

- 163 (2016) A917-A922.
- [341] F. Leng, C.M. Tan, M. Pecht, *Scientific Reports*, 5 (2015) 12967.
- [342] S. Theivaprakasam, D.R. MacFarlane, S. Mitra, *Electrochimica Acta*, 180 (2015) 737-745.
- [343] G.A. Snook, A.S. Best, A.G. Pandolfo, A.F. Hollenkamp, *Electrochemistry Communications*, 8 (2006) 1405-1411.
- [344] X.-G. Sun, S. Dai, *Electrochimica Acta*, 55 (2010) 4618-4626.
- [345] A.I. Bhatt, P. Kao, A.S. Best, A.F. Hollenkamp, *Journal of The Electrochemical Society*, 160 (2013) A1171-A1180.
- [346] N.-W. Li, Y.-X. Yin, J.-Y. Li, C.-H. Zhang, Y.-G. Guo, *Advanced Science*, 4 (2017) 1600400.
- [347] J.-K. Kim, L. Niedzicki, J. Scheers, C.-R. Shin, D.-H. Lim, W. Wiczczonek, P. Johansson, J.-H. Ahn, A. Matic, P. Jacobsson, *Journal of Power Sources*, 224 (2013) 93-98.
- [348] J. Xiang, F. Wu, R. Chen, L. Li, H. Yu, *Journal of Power Sources*, 233 (2013) 115-120.
- [349] Y. Jin, S. Fang, M. Chai, L. Yang, K. Tachibana, S.I. Hirano, *Journal of Power Sources*, 226 (2013) 210-218.
- [350] H.-T. Kim, O.M. Kwon, J. Mun, S.M. Oh, T. Yim, Y.G. Kim, *Electrochimica Acta*, 240 (2017) 267-276.
- [351] J. Patra, P.P. Dahiya, C.-J. Tseng, J. Fang, Y.-W. Lin, S. Basu, S.B. Majumder, J.-K. Chang, *Journal of Power Sources*, 294 (2015) 22-30.
- [352] H. Srour, L. Chancelier, E. Bolimowska, T. Gutel, S. Mailley, H. Rouault, C.C. Santini, *Journal of Applied Electrochemistry*, 46 (2016) 149-155.
- [353] A. Guerfi, M. Dontigny, P. Charest, M. Petitclerc, M. Lagacé, A. Vijh, K. Zaghib, *Journal of Power Sources*, 195 (2010) 845-852.
- [354] A. Balducci, S.S. Jeong, G.T. Kim, S. Passerini, M. Winter, M. Schmuck, G.B. Appetecchi, R. Marcilla, D. Mecerreyes, V. Barsukov, V. Khomenko, I. Cantero, I. De Meatza, M. Holzappel, N. Tran, *Journal of Power Sources*, 196 (2011) 9719-9730.
- [355] M. Moreno, E. Simonetti, G.B. Appetecchi, M. Carewska, M. Montanino, G.-T. Kim, N. Loeffler, S. Passerini, *Journal of The Electrochemical Society*, 164 (2017) A6026-A6031.
- [356] N. Plylahan, M. Kerner, D.-H. Lim, A. Matic, P. Johansson, *Electrochimica Acta*, 216 (2016) 24-34.
- [357] P.H. Lam, A.T. Tran, D.J. Walczyk, A.M. Miller, L. Yu, *Journal of Molecular Liquids*, 246 (2017) 215-220.
- [358] B. Yang, C. Li, J. Zhou, J. Liu, Q. Zhang, *Electrochimica Acta*, 148 (2014) 39-45.
- [359] H. Yoon, A.S. Best, M. Forsyth, D.R. MacFarlane, P.C. Howlett, *Physical Chemistry Chemical Physics*, 17 (2015) 4656-4663.
- [360] P. Röder, N. Baba, H.D. Wiemhöfer, *Journal of Power Sources*, 248 (2014) 978-987.
- [361] T.D. Hatchard, D.D. MacNeil, D.A. Stevens, L. Christensen, J.R. Dahn, *Electrochemical and Solid-State Letters*, 3 (2000) 305-308.
- [362] H.F. Xiang, H. Wang, C.H. Chen, X.W. Ge, S. Guo, J.H. Sun, W.Q. Hu, *Journal of Power Sources*, 191 (2009) 575-581.
- [363] P. Ping, Q. Wang, P. Huang, J. Sun, C. Chen, *Applied Energy*, 129 (2014) 261-273.
- [364] D.P. Abraham, E.P. Roth, R. Kostecky, K. McCarthy, S. MacLaren, D.H. Doughty, *Journal of Power Sources*, 161 (2006) 648-657.
- [365] X. Feng, M. Fang, X. He, M. Ouyang, L. Lu, H. Wang, M. Zhang, *Journal of Power Sources*, 255 (2014) 294-301.
- [366] Y. Fu, S. Lu, K. Li, C. Liu, X. Cheng, H. Zhang, *Journal of Power Sources*, 273 (2015) 216-222.
- [367] G.G. Botte, R.E. White, Z. Zhang, *Journal of Power Sources*, 97 (2001) 570-575.
- [368] Y. Baba, S. Okada, J.-i. Yamaki, *Solid State Ionics*, 148 (2002) 311-316.
- [369] Q. Wang, J. Sun, X. Chen, G. Chu, C. Chen, *Materials Research Bulletin*, 44 (2009) 543-548.
- [370] M. Ishikawa, T. Sugimoto, M. Kikuta, E. Ishiko, M. Kono, *Journal of Power Sources*, 162 (2006) 658-662.
- [371] A. Fernicola, F. Croce, B. Scrosati, T. Watanabe, H. Ohno, *Journal of Power Sources*, 174 (2007) 342-348.
- [372] H. Nakagawa, *Electrochemistry*, 83 (2015) 707-710.
- [373] M. Kerner, N. Plylahan, J. Scheers, P. Johansson, *RSC Advances*, 6 (2016) 23327-23334.

- [374] C.A. Angell, *Electrochimica Acta*, 250 (2017) 368-375.
- [375] A.S. Shaplov, R. Marcilla, D. Mecerreyes, *Electrochimica Acta*, 175 (2015) 18-34.
- [376] Y. Wang, K. Zaghbi, A. Guerfi, F.F.C. Bazito, R.M. Torresi, J.R. Dahn, *Electrochimica Acta*, 52 (2007) 6346-6352.
- [377] Q. Wang, J. Sun, X. Yao, C. Chen, *Thermochimica Acta*, 437 (2005) 12-16.
- [378] A.M. Andersson, M. Herstedt, A.G. Bishop, K. Edström, *Electrochimica Acta*, 47 (2002) 1885-1898.
- [379] L. Li, S. Zhou, H. Han, H. Li, J. Nie, M. Armand, Z. Zhou, X. Huang, *Journal of The Electrochemical Society*, 158 (2011) A74-A82.
- [380] H. Yang, G.V. Zhuang, P.N. Ross, *Journal of Power Sources*, 161 (2006) 573-579.
- [381] H.-B. Han, S.-S. Zhou, D.-J. Zhang, S.-W. Feng, L.-F. Li, K. Liu, W.-F. Feng, J. Nie, H. Li, X.-J. Huang, M. Armand, Z.-B. Zhou, *Journal of Power Sources*, 196 (2011) 3623-3632.
- [382] Q. Wang, J. Sun, X. Yao, C. Chen, *Journal of Loss Prevention in the Process Industries*, 19 (2006) 561-569.
- [383] J. Yi, C. Wang, Y. Xia, *Electrochemistry Communications*, 33 (2013) 115-118.
- [384] N. Katayama, T. Kawamura, Y. Baba, J.-i. Yamaki, *Journal of Power Sources*, 109 (2002) 321-326.
- [385] T. Doi, L. Zhao, M. Zhou, S. Okada, J.-i. Yamaki, *Journal of Power Sources*, 185 (2008) 1380-1385.
- [386] Q. Wang, J. Sun, C. Chen, *Journal of Hazardous Materials*, 167 (2009) 1209-1214.
- [387] Y.-S. Park, S.-M. Lee, *Electrochimica Acta*, 54 (2009) 3339-3343.
- [388] Y.-S. Park, H.J. Bang, S.-M. Oh, Y.-K. Sun, S.-M. Lee, *Journal of Power Sources*, 190 (2009) 553-557.
- [389] H. Nakagawa, S. Izuchi, K. Kuwana, T. Nukuda, Y. Aihara, *Journal of The Electrochemical Society*, 150 (2003) A695-A700.
- [390] J. Jaguemont, N. Omar, F. Martel, P. Van den Bossche, J. Van Mierlo, *Journal of Power Sources*, 367 (2017) 24-33.
- [391] P. Andersson, P. Blomqvist, A. Lorén, F. Larsson, *Fire and Materials*, 40 (2016) 999-1015.
- [392] Y. Xia, T. Li, F. Ren, Y. Gao, H. Wang, *Journal of Power Sources*, 265 (2014) 356-362.
- [393] X. Feng, J. Sun, M. Ouyang, F. Wang, X. He, L. Lu, H. Peng, *Journal of Power Sources*, 275 (2015) 261-273.
- [394] T.H. Dubaniewicz, J.P. DuCarme, *Journal of Loss Prevention in the Process Industries*, 43 (2016) 575-584.
- [395] D.P. Finegan, B. Tjaden, T. M. M. Heenan, R. Jarvis, M.D. Michiel, A. Rack, G. Hinds, D.J.L. Brett, P.R. Shearing, *Journal of The Electrochemical Society*, 164 (2017) A3285-A3291.
- [396] A. Devie, M. Dubarry, B.Y. Liaw, *Journal of The Electrochemical Society*, 162 (2015) A1033-A1040.
- [397] H. Wang, A. Tang, K. Huang, *Chinese Journal of Chemistry*, 29 (2011) 27-32.
- [398] Y. Liu, J. Xie, *Journal of The Electrochemical Society*, 162 (2015) A2208-A2217.
- [399] Q.F. Yuan, F. Zhao, W. Wang, Y. Zhao, Z. Liang, D. Yan, *Electrochimica Acta*, 178 (2015) 682-688.
- [400] J. Ye, H. Chen, Q. Wang, P. Huang, J. Sun, S. Lo, *Applied Energy*, 182 (2016) 464-474.
- [401] Z. Chen, Y. Ren, E. Lee, C. Johnson, Y. Qin, K. Amine, *Advanced Energy Materials*, 3 (2013) 729-736.
- [402] X. Liu, S.I. Stolarov, M. Denlinger, A. Masias, K. Snyder, *Journal of Power Sources*, 280 (2015) 516-525.
- [403] T. Wu, H. Chen, Q. Wang, J. Sun, *Journal of Hazardous Materials*, 344 (2018) 733-741.
- [404] F. Larsson, S. Bertilsson, M. Furlani, I. Albinsson, B.-E. Mellander, *Journal of Power Sources*, 373 (2018) 220-231.
- [405] A. Lecocq, G.G. Eshetu, S. Grugeon, N. Martin, S. Laruelle, G. Marlair, *Journal of Power Sources*, 316 (2016) 197-206.
- [406] F. Xu, H. He, C. Dun, Y. Liu, M.-x. Wang, Q. Liu, Y. Ren, J. Xie, *ECS Transactions*, 41 (2012) 1-12.
- [407] D. Li, D. Danilov, Z. Zhang, H. Chen, Y. Yang, P.H.L. Notten, *Journal of The Electrochemical Society*, 162 (2015) A858-A869.

- [408] M. Mastali, M. Farkhondeh, S. Farhad, R.A. Fraser, M. Fowler, *Journal of The Electrochemical Society*, 163 (2016) A2803-A2816.
- [409] I. Belharouak, Y.-K. Sun, W. Lu, K. Amine, *Journal of The Electrochemical Society*, 154 (2007) A1083-A1087.
- [410] R. Bernhard, S. Meini, H.A. Gasteiger, *Journal of The Electrochemical Society*, 161 (2014) A497-A505.
- [411] P. Huang, P. Ping, K. Li, H. Chen, Q. Wang, J. Wen, J. Sun, *Applied Energy*, 183 (2016) 659-673.
- [412] S.J. Bazinski, X. Wang, *Journal of Power Sources*, 293 (2015) 283-291.
- [413] R. Ponnappan, T.S. Ravigururajan, *Journal of Power Sources*, 129 (2004) 7-13.
- [414] C. Heubner, C. Lämmel, N. Junker, M. Schneider, A. Michaelis, *Electrochemistry Communications*, 48 (2014) 130-133.
- [415] C. Veth, D. Dragicevic, C. Merten, *Journal of Power Sources*, 267 (2014) 760-769.
- [416] K. Yoo, A. Deshpande, S. Banerjee, P. Dutta, *Electrochimica Acta*, 176 (2015) 301-310.
- [417] S. Vyazovkin, C. Wight, *Annual review of physical chemistry*, 48 (1997) 125-149.
- [418] A.K. Burnham, R.L. Braun, *Energy & Fuels*, 13 (1999) 1-22.
- [419] P. Navarro, M. Larriba, J. García, F. Rodríguez, *Thermochimica Acta*, 588 (2014) 22-27.
- [420] M.T. Clough, K. Geyer, P.A. Hunt, J. Mertes, T. Welton, *Physical Chemistry Chemical Physics*, 15 (2013) 20480-20495.
- [421] Y. Cao, T. Mu, *Industrial & Engineering Chemistry Research*, 53 (2014) 8651-8664.
- [422] A. Chowdhury, S.T. Thynell, *Propellants, Explosives, Pyrotechnics*, 35 (2010) 572-581.
- [423] G.-H. Kim, A. Pesaran, R. Spotnitz, *Journal of Power Sources*, 170 (2007) 476-489.
- [424] P. Ping, Q. Wang, Y. Chung, J. Wen, *Applied Energy*, 205 (2017) 1327-1344.
- [425] B.R. Becker, B.A. Fricke, *International Journal of Refrigeration*, 27 (2004) 540-551.
- [426] S.J. Swarin, A.M. Wims, A Method for Determining Reaction Kinetics by Differential Scanning Calorimetry, in: R.S. Porter, J.F. Johnson (Eds.) *Analytical Calorimetry: Volume 4*, Springer US, Boston, MA, 1977, pp. 155-171.
- [427] E.J.F. Dickinson, H. Ekström, E. Fontes, *Electrochemistry Communications*, 40 (2014) 71-74.
- [428] P. Bohn, G. Liebig, L. Komsijska, G. Wittstock, *Journal of Power Sources*, 313 (2016) 30-36.
- [429] U.S. Kim, J. Yi, C.B. Shin, T. Han, S. Park, *Journal of Power Sources*, 196 (2011) 5115-5121.
- [430] R. Zhao, J. Liu, J. Gu, *Applied Energy*, 173 (2016) 29-39.
- [431] M. Dahbi, D. Violleau, F. Ghamouss, J. Jacquemin, F. Tran-Van, D. Lemordant, M. Anouti, *Industrial and Engineering Chemistry Research*, 51 (2012) 5240-5245.
- [432] Y.-B. He, Z.-Y. Tang, Q.-S. Song, H. Xie, Q. Xu, Y.-G. Liu, G.-W. Ling, *Thermochimica Acta*, 480 (2008) 15-21.
- [433] S.C. Chen, C.C. Wan, Y.Y. Wang, *Journal of Power Sources*, 140 (2005) 111-124.

Appendices

Appendix A Ideal separator properties

Table A.43 Ideal separator properties including typical measurement standards and methods.

Property	Impact		Ideal	Measurement method	Ref.
	Performance	Safety			
Stability (electrochemical)	✓	✓	No evidence of reaction after ten days immersion and cycling to extreme voltage limits	Immersion Linear sweep voltammetry	[89, 91]
Thickness	✓	✓	≤25 µm	Micrometre ASTM D5947-96 ASTM D2103	[87, 89, 91, 93]
Porosity	✓	✓	≥40%	ASTM D2873	[87, 89, 91]
Pore dimension / structure	✓	✓	<1 µm Uniform	Scanning Electron Microscopy (SEM) Capillary Flow Porometer ASTM E128-99 ASTM 1294	[87, 89, 91, 93]
Permeability	✓	✓	25 seconds / 10 cm ³	Gurley number ASTM D726	[89, 93]
Wettability	✓		Low angle (<90° indicates favourable interaction with electrolyte) Fast wetting time Fast wicking rate	Contact angle Time to wet Wicking behaviour	[89, 91, 93-95, 431]
Dimensional stability		✓	No skew <5% (machine direction and transverse direction)	Curling/flat Dimensions when wet	[87, 89, 91]
Electrical resistance (MacMullin number)	✓	✓	1 (reality <8)	<i>In situ</i> impedance	[87, 89, 91, 93]
Ionic conductivity	✓		10 ⁻³ -10 ⁻¹ S cm ⁻¹	Electrochemical Impedance Spectroscopy (EIS)	[91]
Tensile strength		✓	≥98.06 MPa	Dynamic Mechanical Analyser (DMA) ASTM D882 ASTM D638	[89, 91, 93]
Puncture strength		✓	≥300 g for 25 µm thickness	ASTM F1306-90 ASTM D3763	[91, 93]
Melt integrity temperature		✓	≥200°C	Differential Scanning Calorimetry (DSC) Thermal Mechanical Analysis (TMA)	[87, 93]
Thermal dimensional stability		✓	<5% after 60 minutes at 90°C	Hot oven test Hot iron tip test Accelerating Rate Calorimetry (ARC) ASTM D1204	[89, 93]
Shutdown temperature		✓		Overheating test with impedance measurement	[89, 93, 98]

Appendix B Commercial separator data sheets

Celgard® 2400

Figure has been removed due to Copyright restrictions.

Celgard® 3501

Figure has been removed due to Copyright restrictions.

Solupor® 7P03A

Figure has been removed due to Copyright restrictions.

Separion® S240 P30

Figure has been removed due to Copyright restrictions.

Dreamweaver Gold™

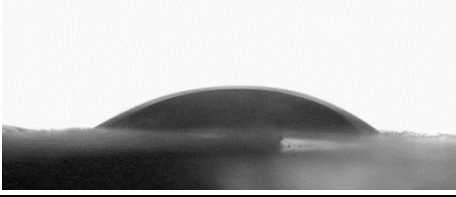
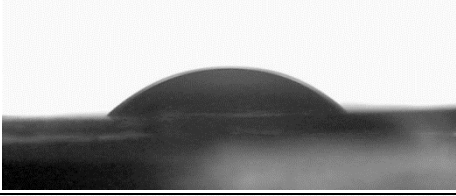
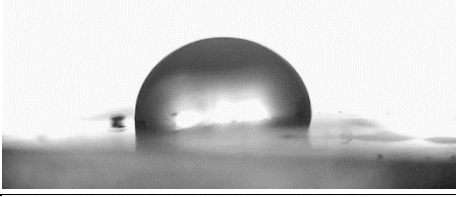
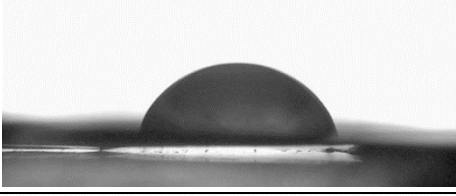
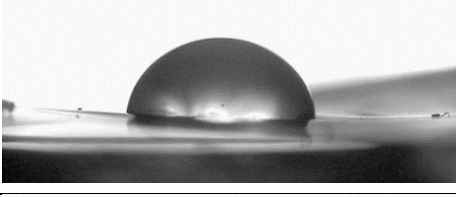
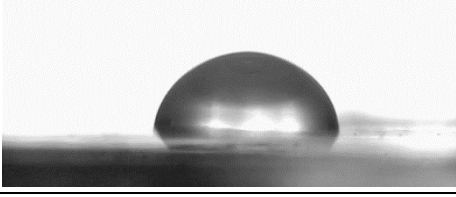
Figure has been removed due to Copyright restrictions.

Dreamweaver Silver™

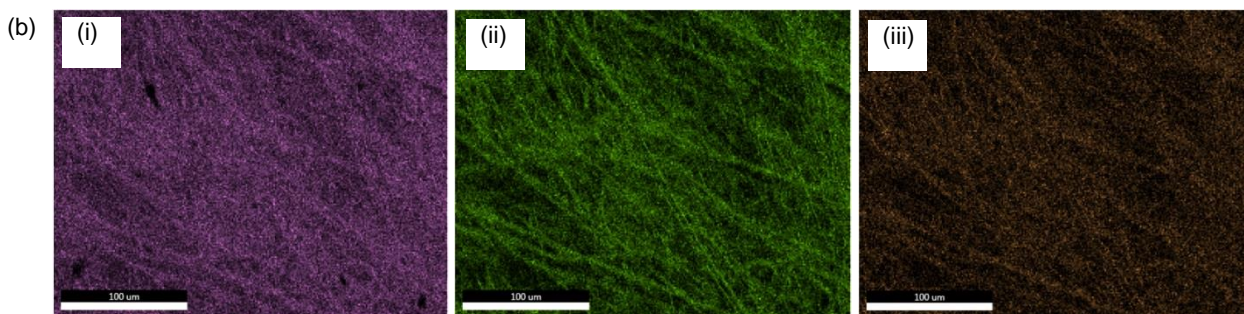
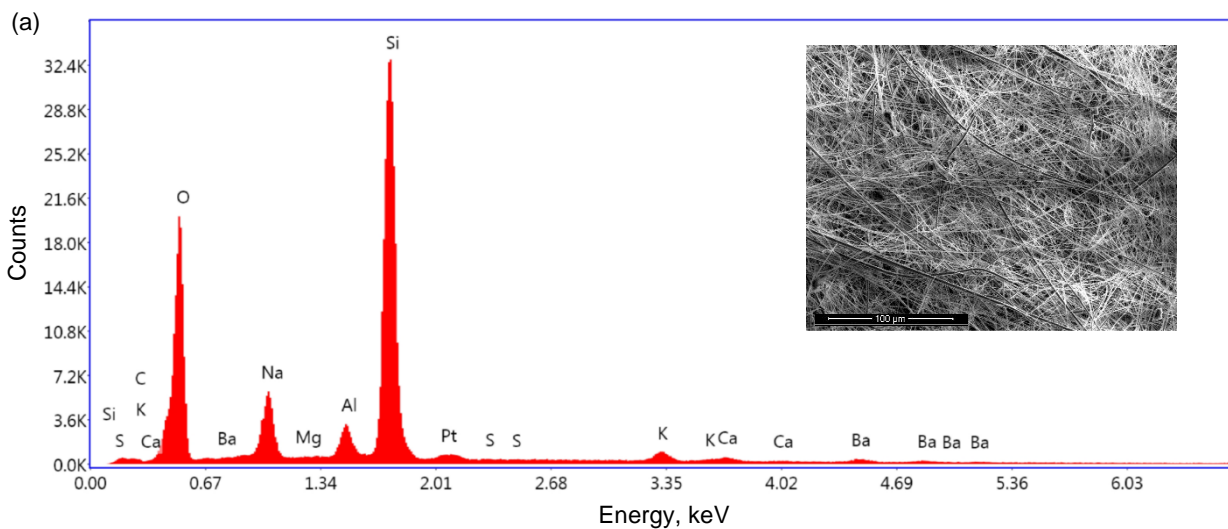
Figure has been removed due to Copyright restrictions.

Appendix C Commercial separator wetting

Table A.44 Representative contact angle image for eight commercial separators with P13FSI electrolyte at time = 0.2 seconds.

DW Silver 40	
DW Gold 40	
Separion S240 P30	
Celgard 5550	
Celgard 3501	
Celgard 2500	
Solupor 7P03A	
Celgard 2400	

Appendix D Energy Dispersive X-Ray of glass fibre membrane



(c)

	OK	NaK	AlK	SiK	KK
At%	39.47	7.70	3.28	43.87	2.53

Figure A.104 EDX spectrum of GF: (a) elemental count with SEM image (insert); (b) distribution mapping (i) silicon, (ii) oxygen and (iii) sodium; and (c) atomic percentage on surface.

Appendix E Energy Dispersive X-Ray of separators containing LiFSI

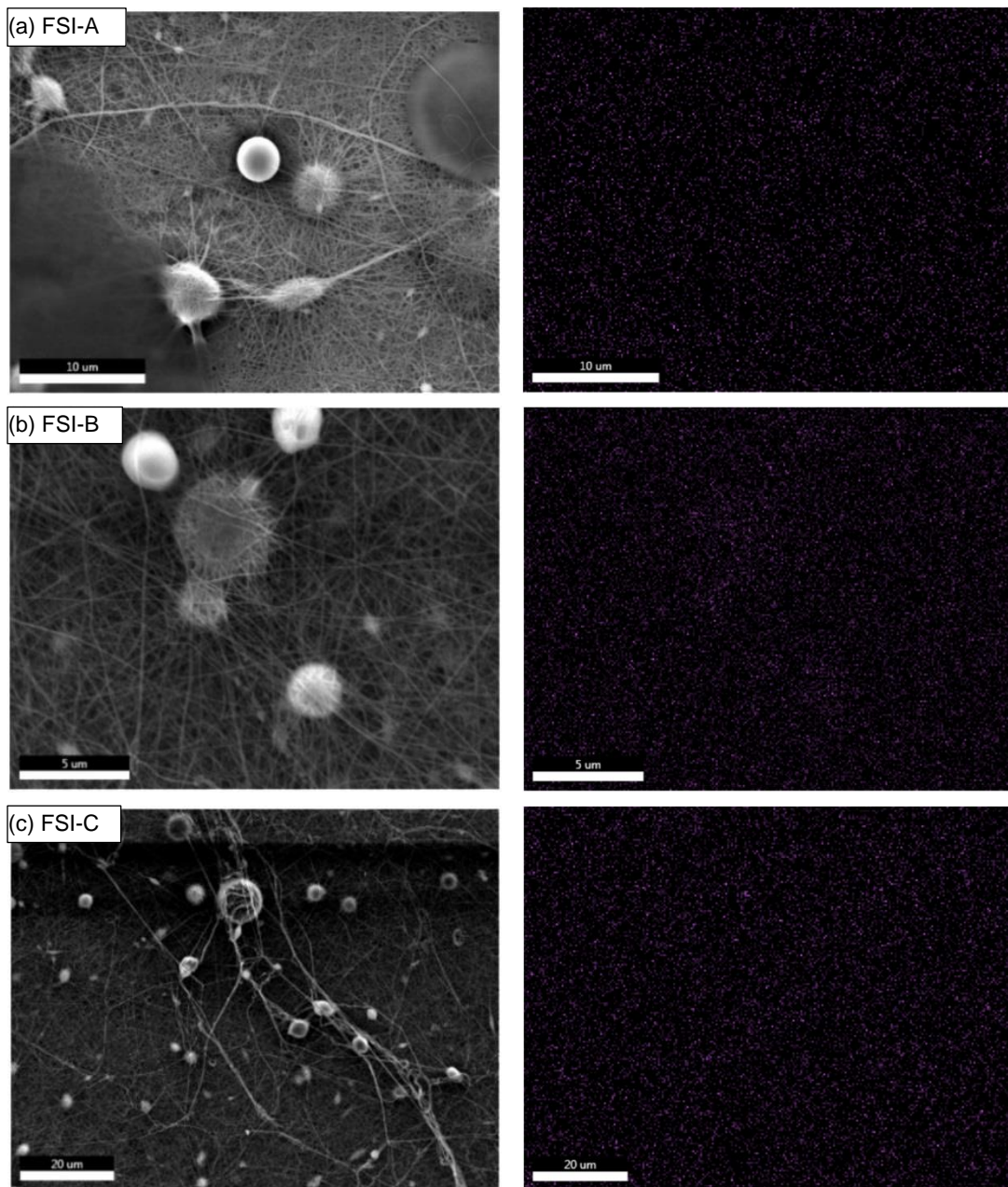


Figure A.105 EDX spectrum of (a) FSI-A, (b) FSI-B and (c) FSI-C. Left: SEM image of EDX region. Right: sulphur distribution map.

Appendix F Scanning Electron Microscopy images

FSI-0

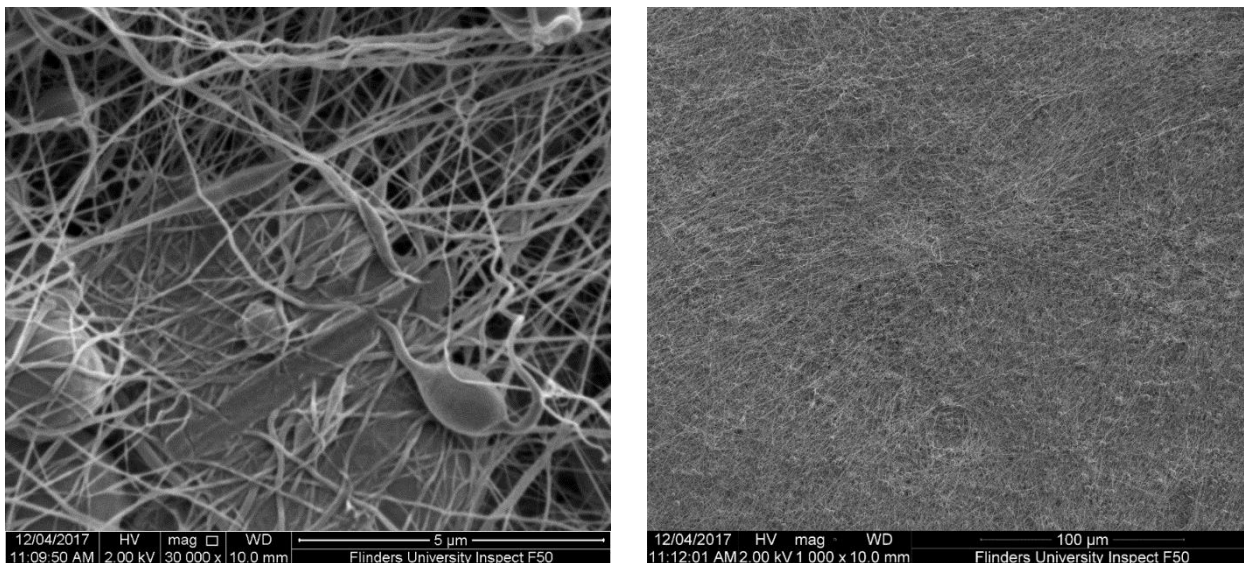


Figure A.106 SEM image of FSI-0, magnification 30000x and 1000x.

FSI-A

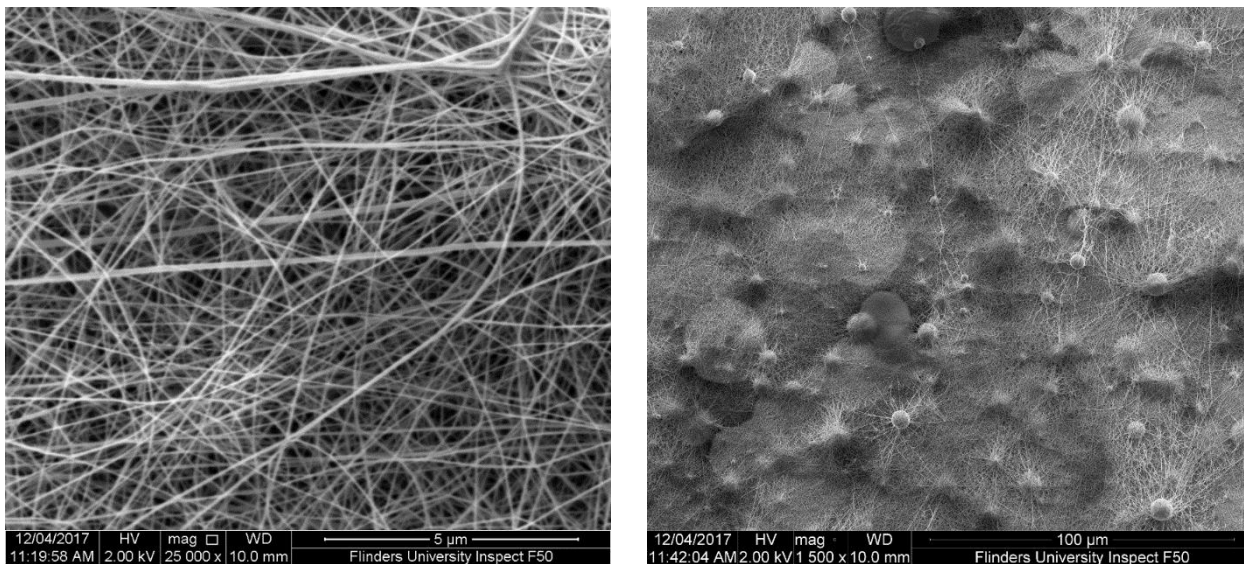


Figure A.107 SEM image of FSI-A, magnification 25000x and 1500x.

FSI-B

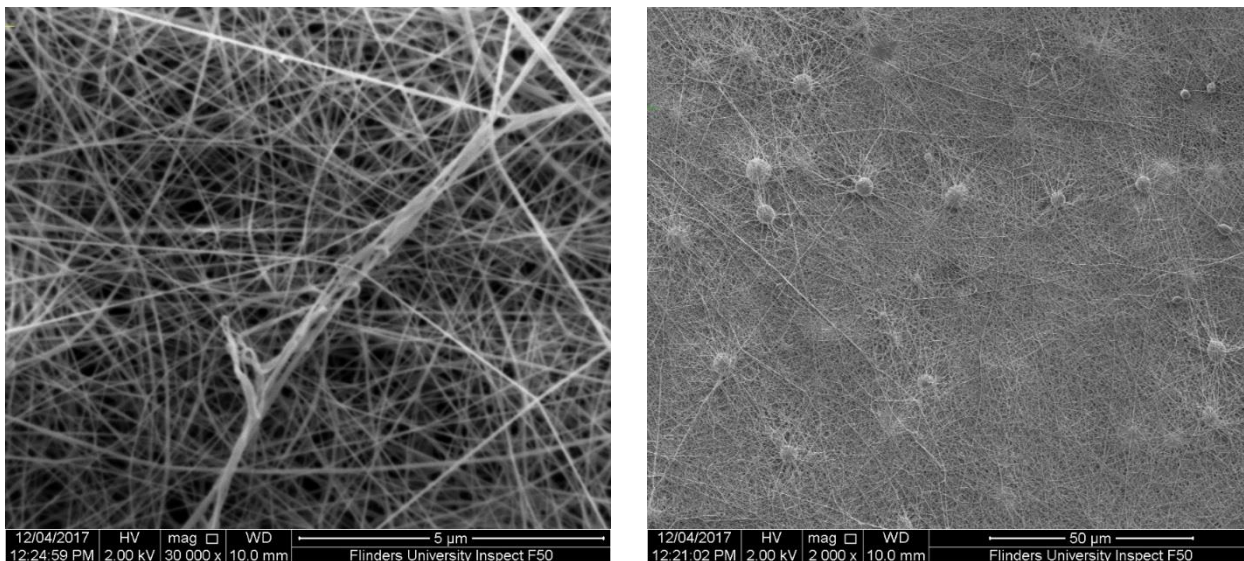


Figure A.108 SEM image of FSI-B, magnification 30000x and 2000x.

FSI-C

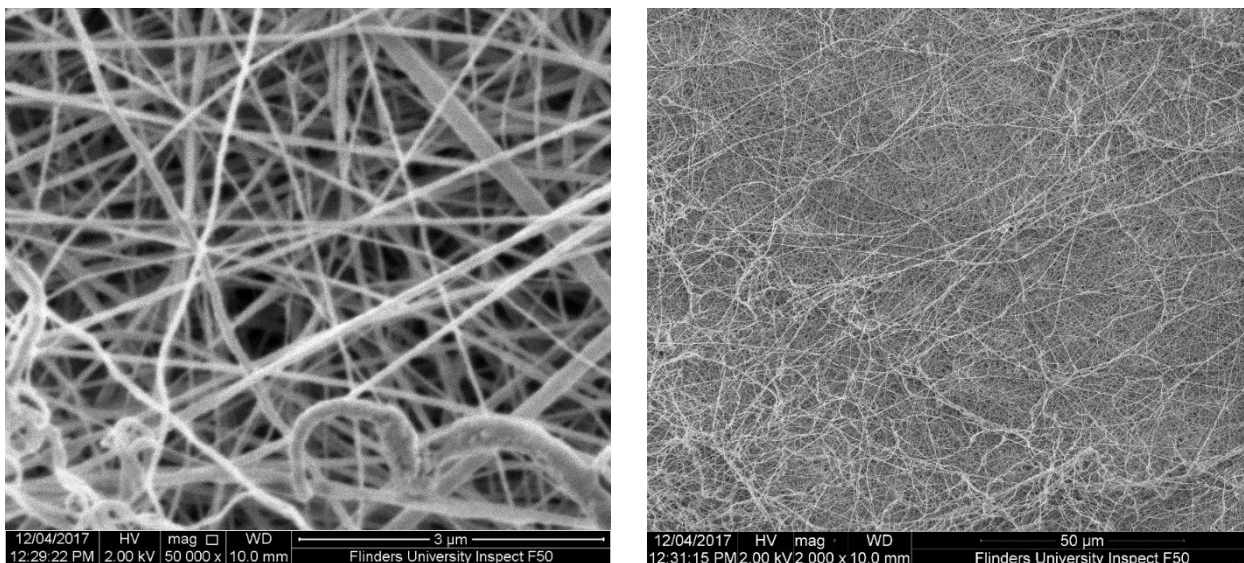


Figure A.109 SEM image of FSI-C, magnification 50000x and 2000x.

TFSI-B

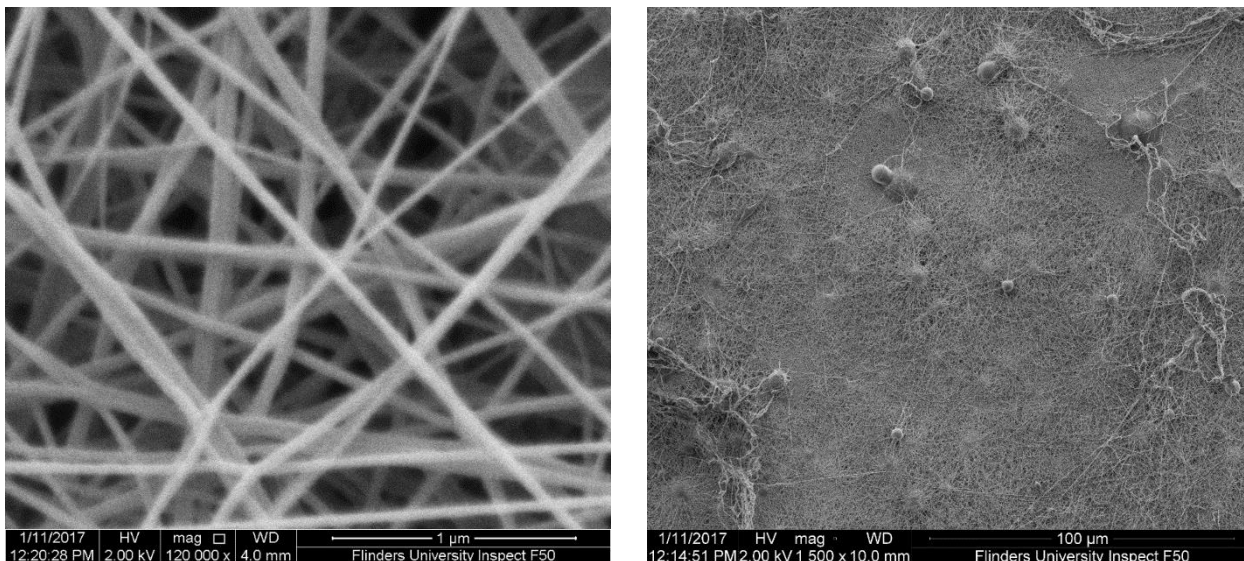


Figure A.110 SEM image of TFSI-B, magnification 120000x and 1500x.

Tfd

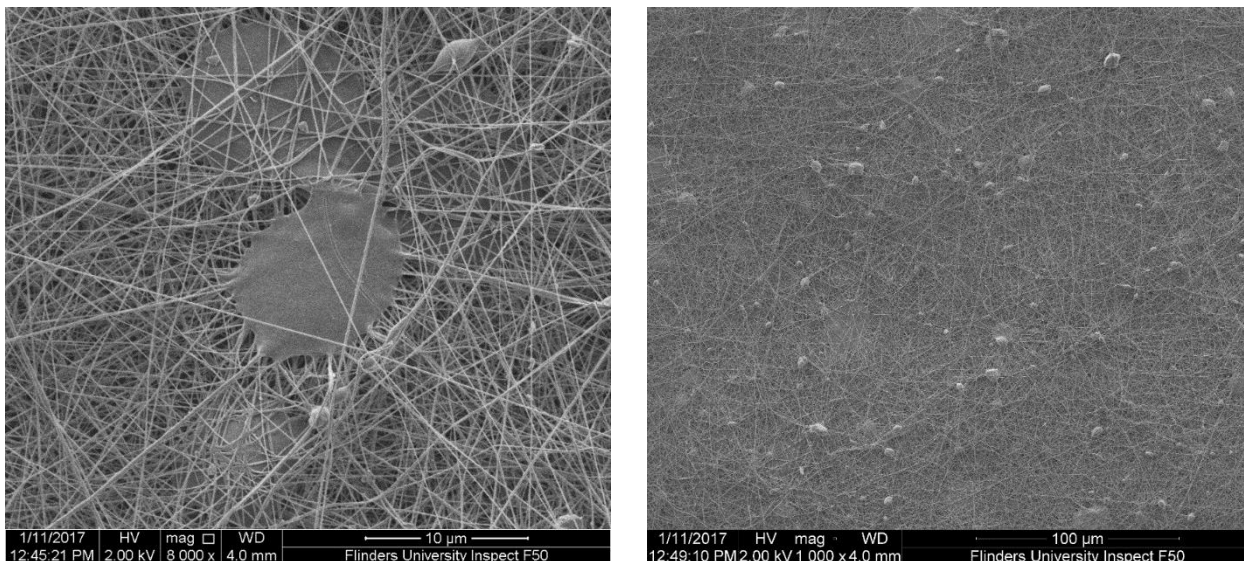


Figure A.111 SEM image of Tfd, magnification 8000x and 1000x.

FSId

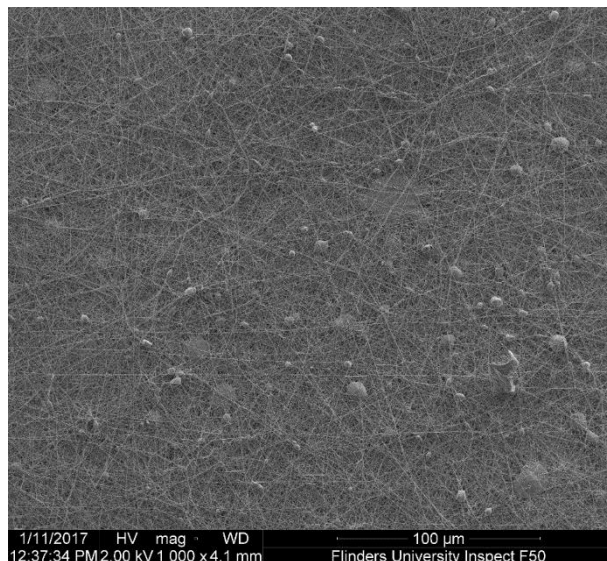
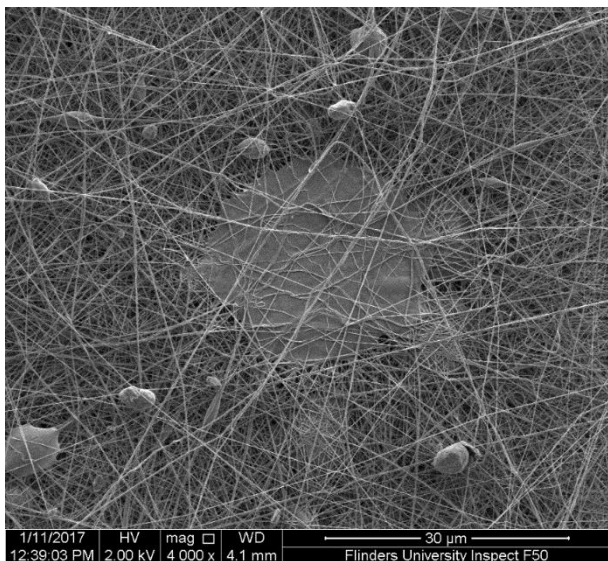


Figure A.112 SEM image of FSId, magnification 4000x and 1000x.

TFSId

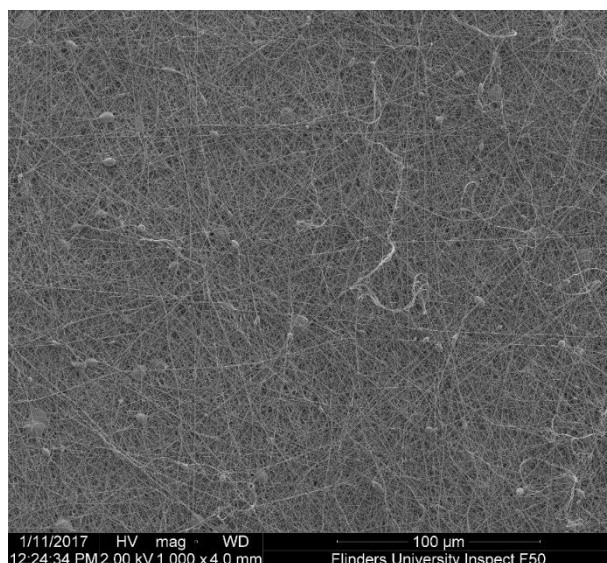
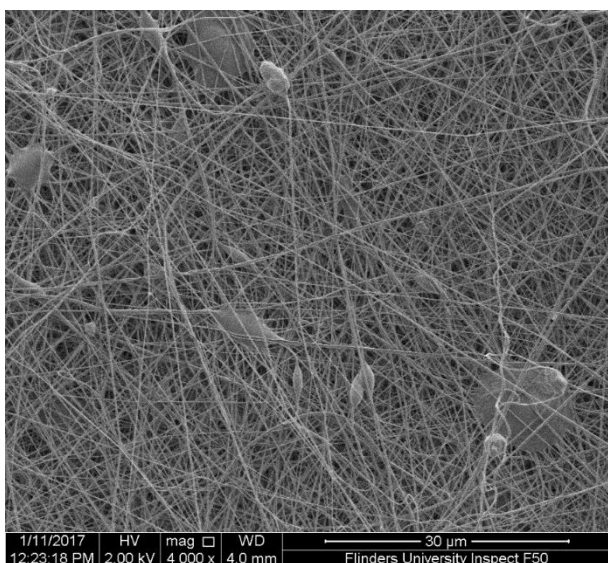
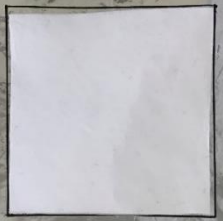


Figure A.113 SEM image of TFSId, magnification 4000x and 1000x.

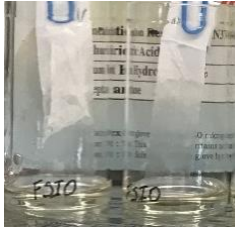
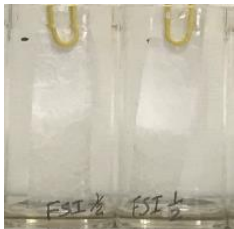
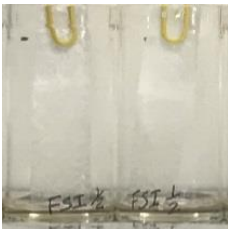
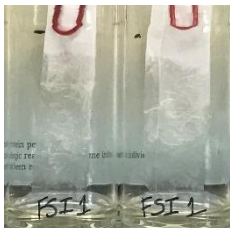
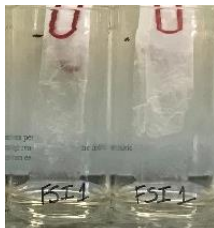
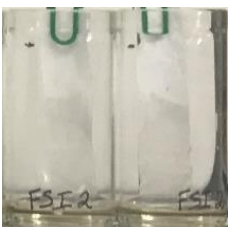
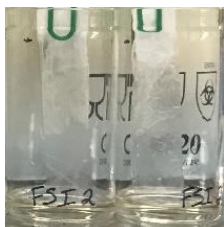
Appendix G Thermal dimensional stability

Table A.45 Images of shrinkage of Celgard, PAN and the four separators manufactured in this work after exposure to 150 °C for 60 minutes.

	Before 150 °C	After 150 °C
Celgard		
PAN		
FSI-0		
FSI-A		
FSI-B		
FSI-C		

Appendix H Wicking rate images

Table A.46 Images of wicking rate of separators containing LiFSI salt with P13FSI.

Separator	Time							
FSI0	10 minutes		35 minutes		42 minutes		92 minutes	
FSI½	8 minutes		18 minutes		34 minutes		52 minutes	
FSI1	6 minutes		15 minutes		32 minutes		48 minutes	
FSI2	5 minutes		15 minutes		30 minutes		56 minutes	

Appendix I Cycling voltage-capacity

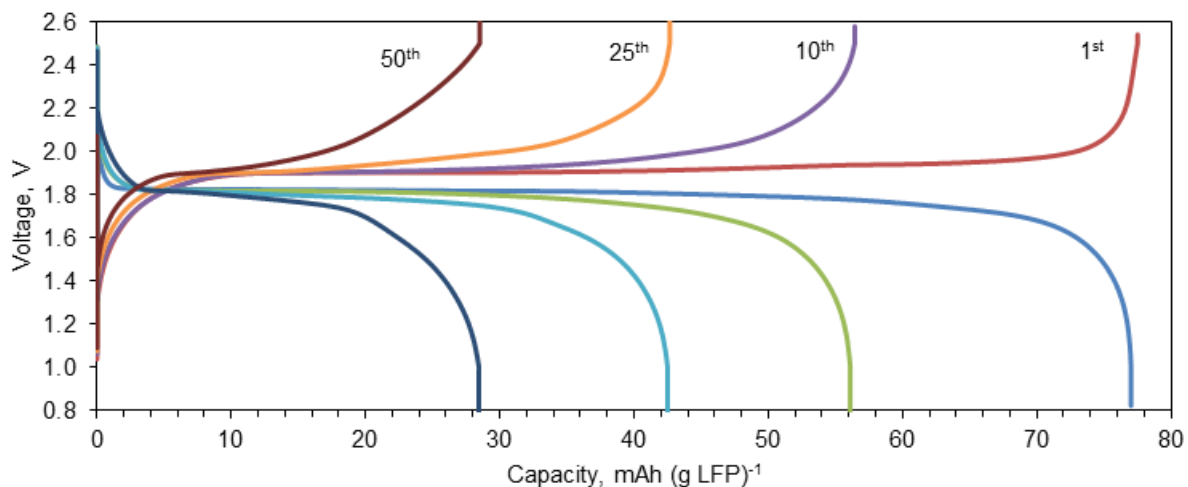
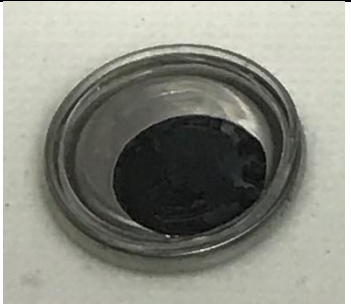
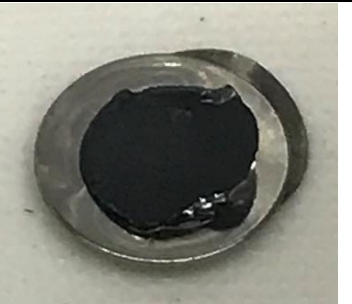
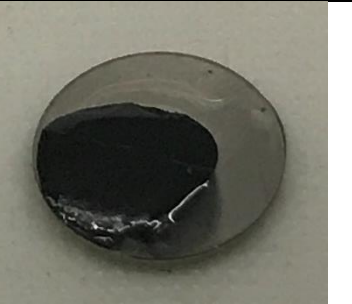


Figure A.114 Voltage curves for 1st, 10th, 25th and 50th cycles of representative LFP | P13FSI electrolyte | LTO cell with FSI-0 separator, cycling at current density 0.126 mA cm⁻². Theoretical capacity 127 mAh (g LFP)⁻¹.

Appendix J Disassembly images

Table A.47 Images of LFP | P13FSI electrolyte | LTO cells with GF, FSI-0, FSI-A, FSI-B and FSI-C separators, following 50 cycles at C/10 discharge rate.

	LFP	Separator	LTO
GF			
FSI-0			
FSI-A			
FSI-B			
FSI-C			

Appendix K DSC at different heating rates

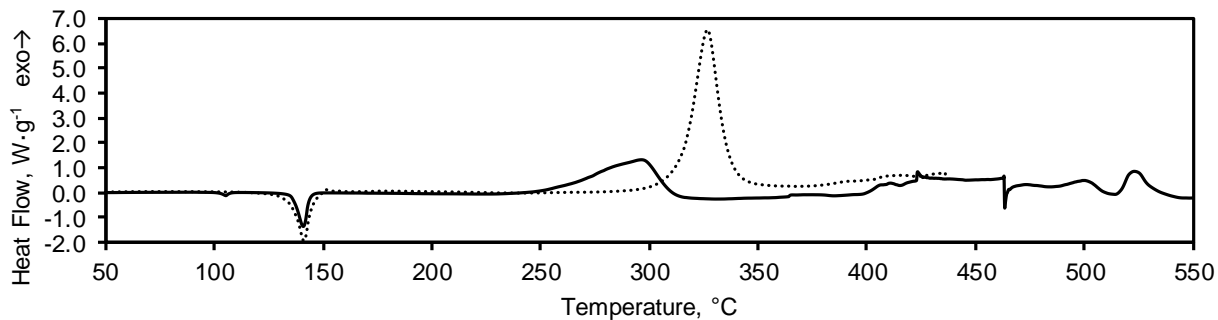


Figure A.115 DSC thermogram of LiFSI powder at 5 °C min⁻¹ (—) and 10 °C min⁻¹ (.....) heating rates.

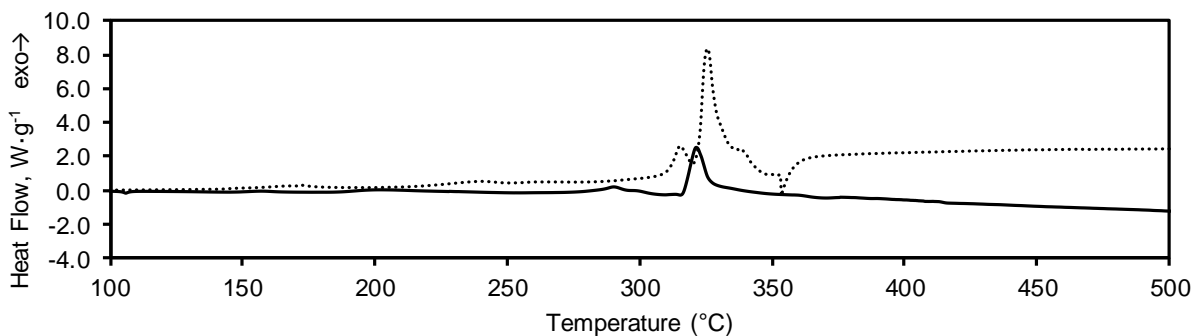


Figure A.116 DSC thermogram of uncycled LFP with P13FSI electrolyte at 5 °C min⁻¹ (—) and 10 °C min⁻¹ (.....) heating rates.

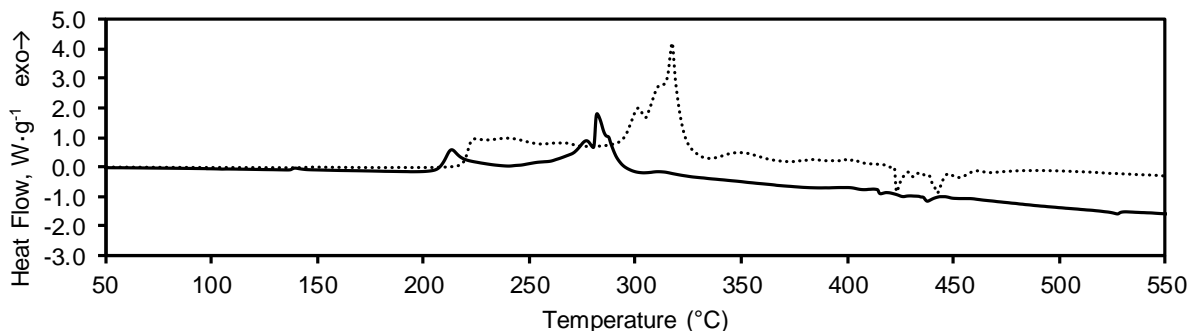


Figure A.117 DSC thermogram of uncycled LTO with P13FSI electrolyte at 5 °C min⁻¹ (—) and 10 °C min⁻¹ (.....) heating rates.

Appendix L DSC graphite and LFP overlay

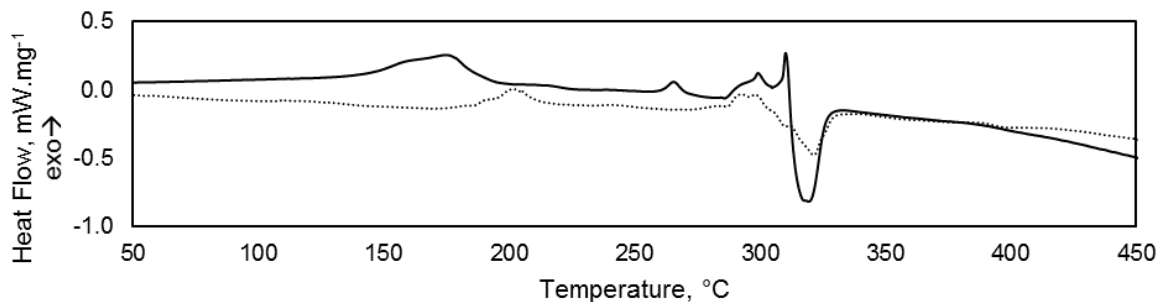


Figure A.118 DSC thermogram overlay of discharged (delithiated) graphite (—) and discharged (0% SoC) LFP (.....) from half-cells with P13FSI electrolyte.

Appendix M Biot number and V_{cell} calculations

Biot number equation

The Biot number for heat transport applications can be calculated with the following equation [432]:

$$Bi = \frac{hL_C}{k}$$

where Bi is the Biot number (dimensionless), h is the heat transfer coefficient ($\text{W m}^{-2} \text{K}^{-1}$), L_C is the characteristic length (m) and k is the thermal conductivity ($\text{W m}^{-1} \text{K}^{-1}$).

The same heat transfer coefficient used in the simulations was used to calculate the Biot number, $h = 4.5 \text{ W m}^{-2} \text{K}^{-1}$.

The characteristic length (L_C) for a rectangle can be described by the following equation:

$$L_C = \frac{V}{SA}$$

where V is the volume (V_{cell} in this case) and SA is the surface area (A_{surf} in this case).

V_{cell} and A_{surf}

For the P13FSI electrolyte cell, since excess electrolyte was used to ensure good electrode wetting the cell volume is larger than that of the dry cell stack, which would be equal to the stack thickness multiplied by the electrode surface area (77 cm^2). Where the stack thickness ($589 \text{ }\mu\text{m}$) is equal to the cathode thickness ($83 \text{ }\mu\text{m}$) plus the anode thickness ($96 \text{ }\mu\text{m}$) plus the separator thickness (maximum $2 \times 210 \text{ }\mu\text{m}$ for GF separator). This gives a dry volume of $4.5\text{E-}6 \text{ m}^3$. However, considering the excess electrolyte, the wet cell would occupy a larger volume (V_{cell}). V_{cell} was determined by calculating the volume of anode, cathode and electrolyte material actually in the cell ($6.4194\text{E-}6 \text{ m}^3$).

The surface area (A_{surf}) was then determined by assuming that the electrode thickness and area were fixed, therefore the variable property was the separator thickness, which could be increased to include the excess electrolyte material and obtain the real V_{cell} . For the P13FSI electrolyte cell, an effective separator and electrolyte thickness of $655 \text{ }\mu\text{m}$ was used in the simulation so that the V_{cell} and A_{surf} parameters matched up with the actual amount of material present. The A_{surf} could then be calculated with the new separator and electrolyte thickness to be 0.0157 m^2 . The same process was followed for the conventional electrolyte cell: $V_{\text{cell}} = 4.4194\text{E-}6 \text{ m}^3$ and $A_{\text{surf}} = 0.01561 \text{ m}^2$.

Therefore, the characteristic length for the P13FSI electrolyte cell can be calculated from V_{cell} and A_{surf} . $L_C = 4.1\text{E-}4$ m.

Thermal conductivity property

The thermal conductivity of a lithium-ion cell is very different depending on the direction, the in-plane thermal conductivity ($24.840 \text{ W m}^{-1} \text{ K}^{-1}$) is much greater than the through plane thermal conductivity ($1.035 \text{ W m}^{-1} \text{ K}^{-1}$) [433].

Biot number calculation

Since there is a large difference in the directionality of thermal conductivity, the Biot number will be calculated for thermal conductivity in both directions.

Biot number (in-plane) = $7.4\text{E-}5$.

Biot number (through plane) = $1.8\text{E-}3$.

Appendix N Additional oven tests

Note: the sawtooth pattern during the oven test 200 °C hold in Figure A.119 and Figure A.121 can be related to the oven, which had a maximum operating temperature of 200 °C. This meant that when the oven reached 200 °C, heating would stop for approximately 2 minutes before resuming. This occurred multiple times during the 200 °C hold.

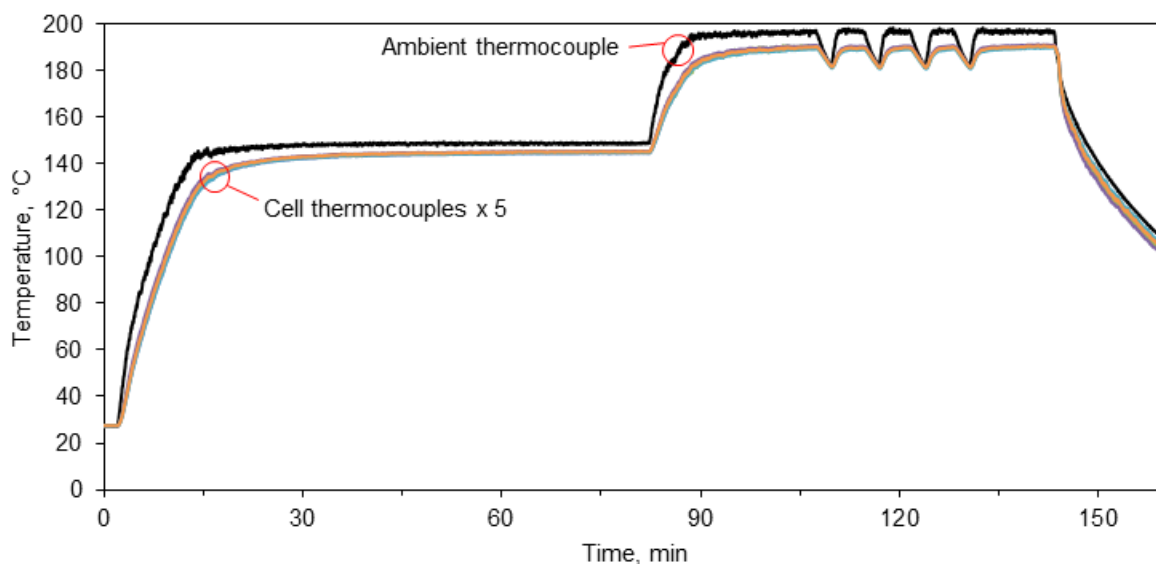


Figure A.119 Temperature vs time plot for oven test of LFP | P13FSI electrolyte-FSI-C | LTO pouch cell. Oven temperature at 150 °C for approximately 60 minutes, then raised to 200 °C for approximately 60 minutes. Including ambient thermocouple and five thermocouples over surface of the pouch.

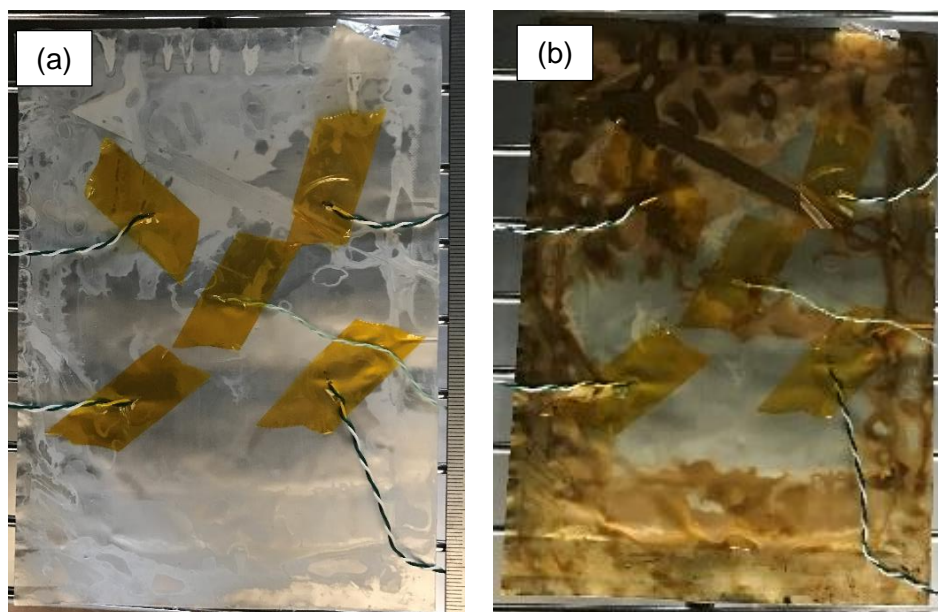


Figure A.120 Oven test (a) before and (b) after photos of LFP | P13FSI electrolyte-FSI-C | LTO pouch cell. Discolouration from electrolyte leakage from pouch cell prior to oven test.

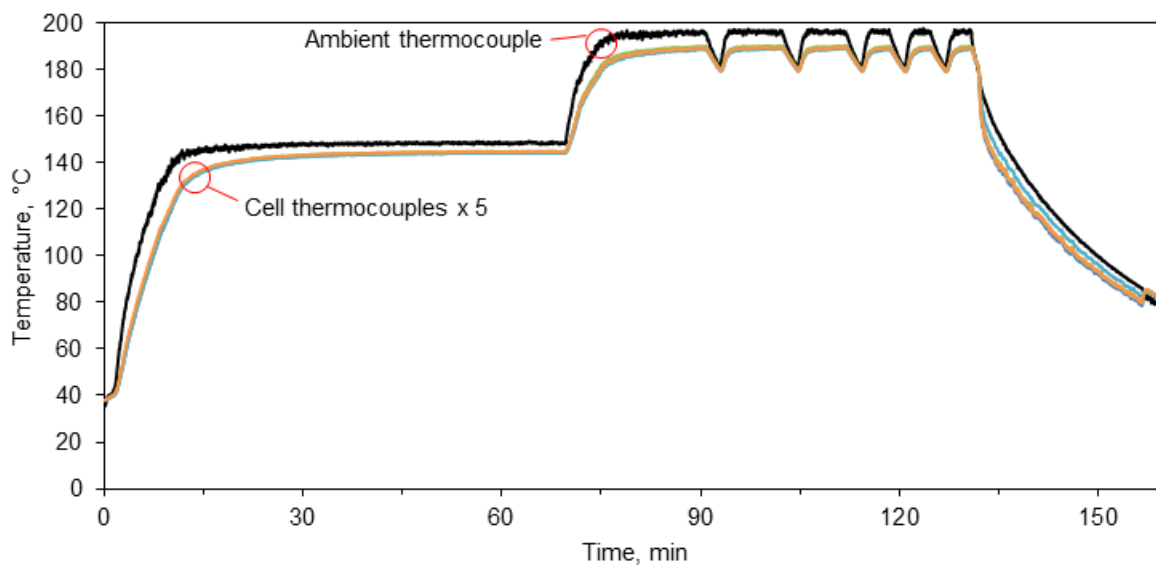


Figure A.121 Temperature vs time plot for oven test of LFP | conventional electrolyte-FSI-C | LTO pouch cell. Oven temperature at 150 °C for approximately 60 minutes, then raised to 200 °C for approximately 60 minutes. Including ambient thermocouple and five thermocouples over surface of the pouch.

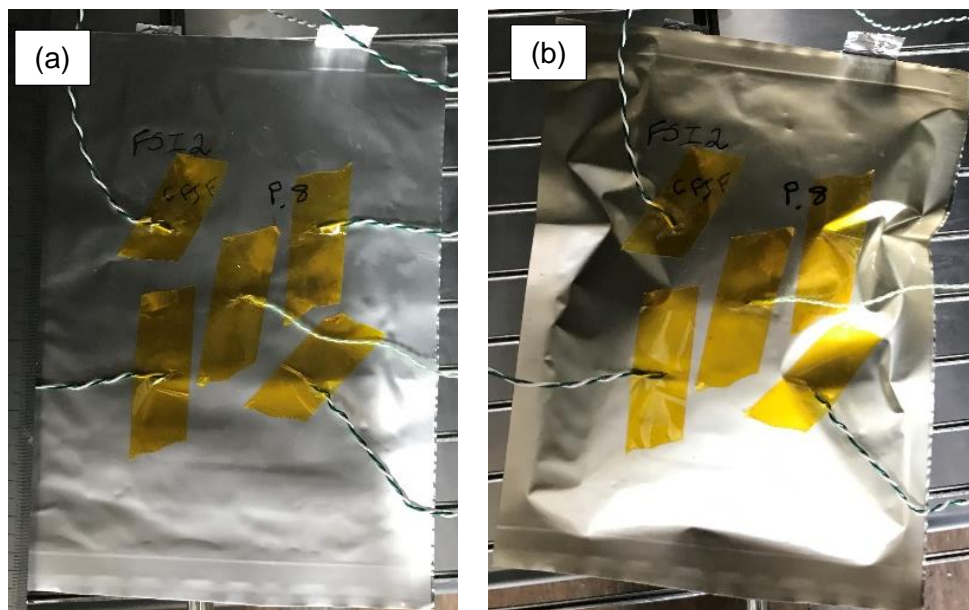


Figure A.122 Oven test (a) before and (b) after photos of LFP | conventional electrolyte-FSI-C | LTO pouch cell. Swelling obvious after oven test.

Appendix O Kinetic parameter estimation

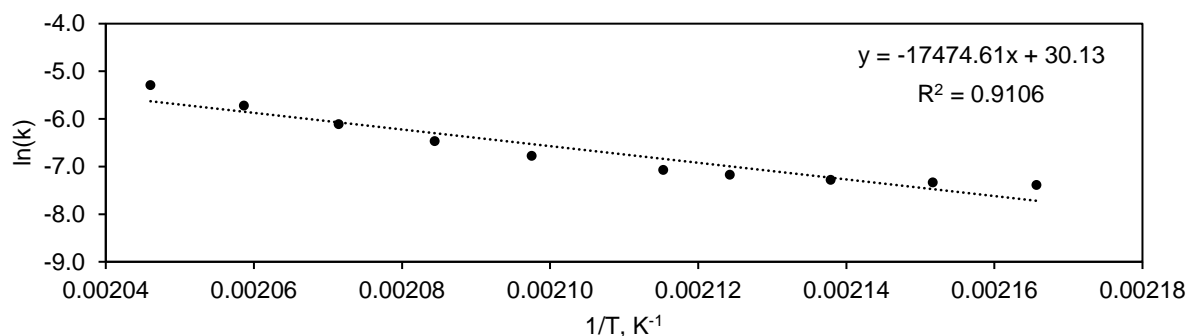


Figure A.123 log(k) vs 1/T plot for i, the 204 °C peak in charged LFP P13FSI electrolyte thermogram, used to calculate E and A reaction parameters for n=1. Markers are data points and the dotted line is the linear fit. Fit equation and R² value shown in plot.

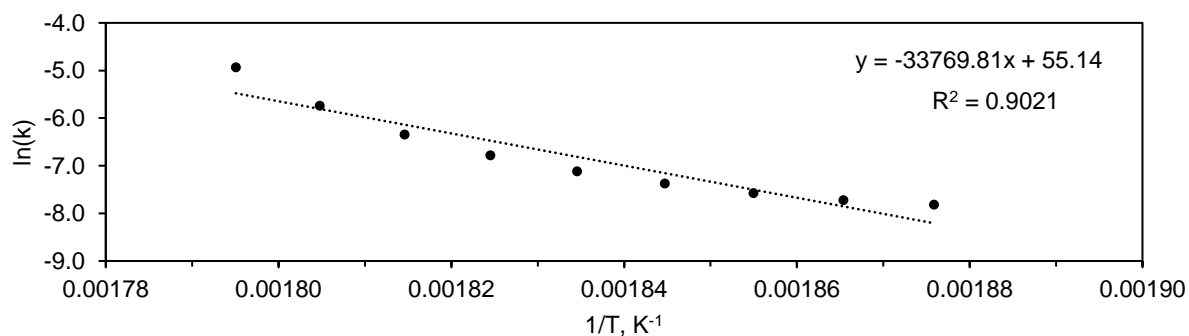


Figure A.124 log(k) vs 1/T plot for e1, the 269 °C peak in P13FSI electrolyte thermogram, used to calculate E and A reaction parameters for n=1. Markers are data points and the dotted line is the linear fit. Fit equation and R² value shown in plot.

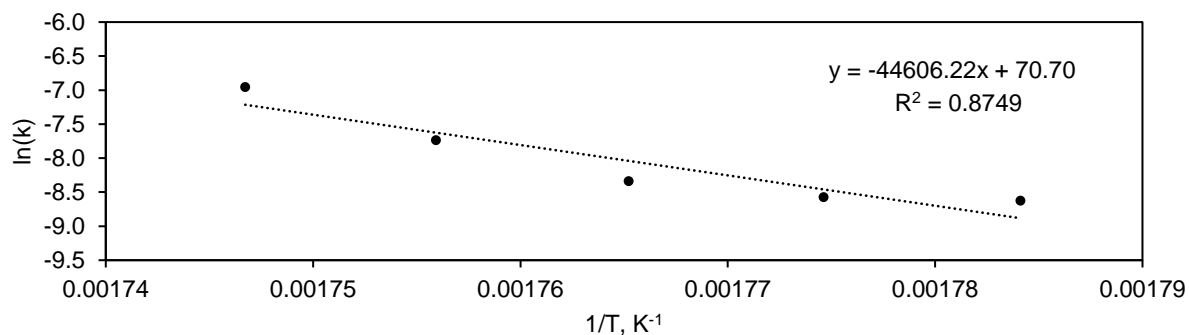


Figure A.125 log(k) vs 1/T plot for a, the 294 °C peak in charged LTO P13FSI electrolyte thermogram, used to calculate E and A reaction parameters for n=1. Markers are data points and the dotted line is the linear fit. Fit equation and R² value shown in plot.

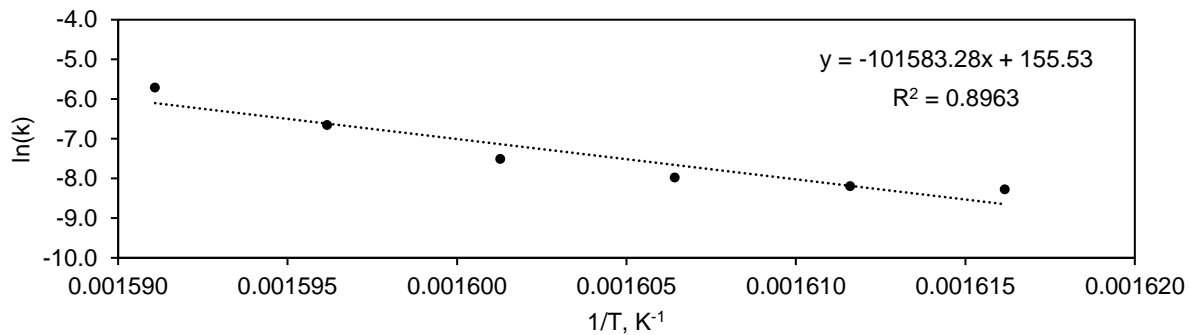


Figure A.126 log(k) vs 1/T plot for c, the 352 °C peak in charged LFP P13FSI electrolyte thermogram, used to calculate E and A reaction parameters for n=1. Markers are data points and the dotted line is the linear fit. Fit equation and R² value shown in plot.

Appendix P Different h values for oven test simulations

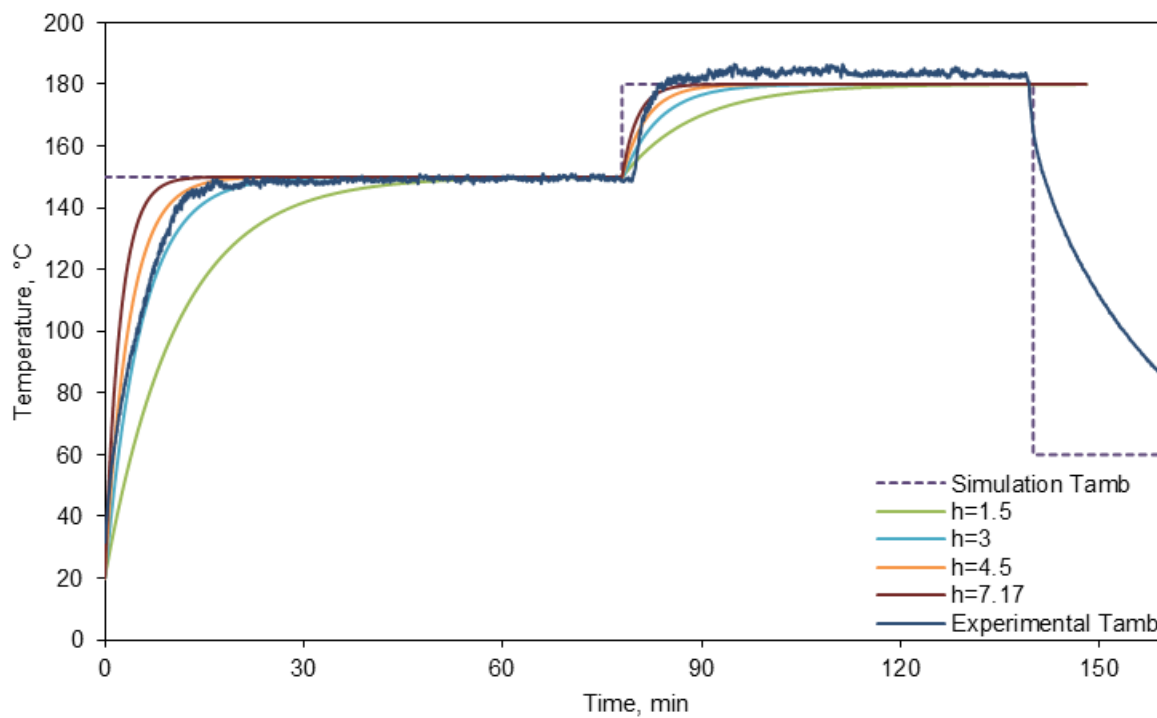


Figure A.127 Temperature profile of LFP | P13FSI electrolyte | LTO pouch cell during oven profile experimental temperature and simulated temperature with $h = 1.5, 3, 4.5$ and $7.17 \text{ W m}^{-2} \text{ K}^{-1}$.